



DIN
GMA

Quaderni di ricerca

Settima giornata di studio Ettore Funaioli

19 luglio 2013

A cura di
Umberto Meneghetti, Alberto Maggiore e Vincenzo Parenti Castelli



SOCIETÀ EDITRICE
ESCULAPIO

Alm@DL



Quaderni del **DIN** – **GMA**

Atti di giornate di studio – 7

A cura di:

U. Meneghetti , A. Maggiore , V. Parenti Castelli

Coordinatore di redazione:

Alessandro Zanarini

DIN

Dipartimento di Ingegneria Industriale

<http://www.ingegneriaindustriale.unibo.it>

GMA

Gruppo di Meccanica Applicata

http://wpage.unina.it/dellaval/GMA/GMA_home.htm

Accademia delle Scienze dell'Istituto di Bologna

<http://www.accademiascienzebologna.it/AccademiaScienze/default.htm>

Settima giornata di studio

Ettore Funaioli

19 luglio 2013

A cura di:
Umberto Meneghetti, Alberto Maggiore e Vincenzo Parenti Castelli

Proprietà letteraria riservata
© Copyright 2014 degli autori
Tutti i diritti riservati

Settima giornata di studio Ettore Funaioli – 19 luglio 2013 / A cura di
Umberto Meneghetti, Alberto Maggiore, Vincenzo Parenti Castelli
Bologna: 2014 – p. 336; 17 cm

ISBN 978-88-7488-795-8

Versione elettronica disponibile alla pagina
<http://amsacta.unibo.it/4064/>

Stampa a richiesta eseguita da:



40131 Bologna – Via U. Terracini 30 – Tel. 051- 6340113 – Fax 051- 6341136

www.editrice-esculapio.com

INDICE

Prefazione

<i>E. Liverani, A. Fortunato, A. Ascari, L. Tomesani, M. Carricato</i> Laser-assisted cold bending: an innovative forming process for high strength steels	1
<i>E. Salsi, R. Squatrito, I. Todaro, L. Tomesani</i> Prediction of ductile iron microstructures in sand cast processes	15
<i>A. Carminelli, G. Catania</i> Application of an automatic refinement technique for B2-spline finite element modeling of thin-walled mechanical components	29
<i>A. O. Andrisano, L. I. Manevitch, F. Pellicano, M. Strozzi</i> Nonlinear vibrations and energy distribution of carbon nanotubes	47
<i>F. Meoni, A. Fortunato, M. Carricato</i> Servo pressa biassiale con architettura isostatica	57
<i>F. Oscari, G. Rosati, A. Rossi, C. Pacchierotti, D. Prattichizzo</i> First results on the role of cutaneous feedback during the learning of a force field in reaching tasks	69
<i>N. Sancisi, M. Conconi, M. Forlani, V. Parenti Castelli</i> Improved rig for the analysis of knee behaviour under dynamic motion tasks	83
<i>A. O. Andrisano, F. Leali, F. Pini, M. Ansaloni</i> Lavorazioni meccaniche robotizzate di precision nell'industria automotive: una prospettiva europea	95
<i>A. Rossi, G. Rosati, S. Minto</i> Celle robotizzate flessibili a configurazione variabile	107
<i>A. Freddi</i> Parametric modeling of experimental data	115
<i>E. Dragoni</i> Optimal design of paired tapered roller bearings under central radial and axial static loads	137
<i>A. Strozzi, A. Baldini, M. Giacomini, A. Lazzarini, A. Valgimigli</i> Optimization methodology for an automotive composite hood	157

<i>E. Carraro, E. Mucchi, G. Dalpiaz</i>	171
Tuned mass damper design for vibration suppression of stacker cranes	
<i>F. Nardini, N. Sancisi, V. Parenti Castelli</i>	183
Stiffness analysis of spatial strip-driven devices	
<i>A. Strozzi, A. Baldini, M. Giacomini, G. A. Mulas, S. Mantovani</i>	191
Forzamento albero-mozzo in presenza di momento flettente: valore del momento flettente che provoca il distacco tra albero e mozzo	
<i>E. Prati, A. Tasora</i>	201
Studio teorico della lubrificazione idrodinamica con caratterizzazione viscoelastica di anelli di tenuta in elastomero	
<i>A. Strozzi, M. Giacomini, A. Baldini, S. Sissa</i>	213
On the complementarity formulaton of lubricated cavitated contacts	
<i>N. Golinelli, A. Spaggiari, E. Dragoni</i>	229
Viscoelastic and magnetorheological properties of the magnetic silly putty	
<i>D. Castagnetti</i>	245
A low frequency energy converter for electromagnetic or piezoelectric energy harvesting	
<i>R. Vertechy, M. Fontana, M. Bergamasco</i>	255
Dielectric elastomer machines for the conversion of ocean wave energy	
<i>G. Scirè Mammano, D. Castagnetti, E. Dragoni</i>	265
Closed-form modal analysis of flexural beam resonators ballasted by a rigid mass	
<i>E. Mucchi, G. Dalpiaz</i>	293
On the use of piezoelectric strain sensors for experimental modal analysis	
<i>G. Curcurù, M. Cocconcelli, R. Rubini</i>	303
Multivariate analysis for bearing classification	
<i>A. Zanarini</i>	313
Full field optical measurements for operational modal analysis and model updating	
Indice degli autori	335

Prefazione

Questo volume raccoglie 24 delle 27 memorie presentate alla settimana "Giornata di studio Ettore Funaioli", svoltasi il 19 luglio 2013. A tutti i partecipanti, e in particolare agli autori delle memorie qui raccolte, va il nostro più vivo ringraziamento: a loro si deve il permanente successo della manifestazione, chiaramente legato anche al ricordo del Prof. Ettore Funaioli, che ricordiamo sempre con grande stima e gratitudine per l'appassionato insegnamento scientifico e la profonda umanità.

La folta adesione a queste Giornate di Studio conferma anche l'apprezzamento dei partecipanti per l'occasione che esse offrono di ritrovarsi amichevolmente fra colleghi, per scambiarsi idee e opinioni sulle ricerche in corso e sui problemi generali della nostra comunità scientifica.

È motivo di grande soddisfazione per tutti, e sicuramente ragione di orgoglio per i nostri Maestri, constatare l'elevata qualità scientifica dei lavori presentati e il costante impegno dei Ricercatori di Meccanica che hanno partecipato alla manifestazione.

Questa Giornata di studio si è svolta con il patrocinio dell'Accademia delle Scienze dell'Istituto di Bologna e del GMA – Gruppo di Meccanica Applicata. Di ciò ingratiamo vivamente il Presidente dell'Accademia delle Scienze, Prof. Emilio Pasquini e il Presidente del GMA, Prof. Aldo Rossi.

La Giornata ha potuto svolgersi anche grazie alla collaborazione della Scuola di Ingegneria e Architettura e del DIN – Dipartimento di Ingegneria Industriale dell'Alma Mater Studiorum – Università di Bologna. Ringraziamo il Presidente della Scuola di Ingegneria e Architettura, Prof. Pier Paolo Diotallevi, e il Direttore del DIN, Prof. Gianni Caligiana, che hanno consentito queste collaborazioni e hanno voluto aprire la Giornata porgendo il loro saluto ai partecipanti.

Bologna, 25 giugno 2014

Umberto Meneghetti – Alberto Maggiore – Vincenzo Parenti Castelli

LASER-ASSISTED COLD BENDING: AN INNOVATIVE FORMING PROCESS FOR HIGH STRENGTH STEELS

Erica Liverani
*Department of Industrial Engineering,
University of Bologna, Italy
E-mail: erica.liverani2@unibo.it*

Alessandro Fortunato
*Department of Industrial Engineering,
University of Bologna, Italy
E-mail: alessandro.fortunato@unibo.it*

Alessandro Ascari
*Department of Industrial Engineering,
University of Bologna, Italy
E-mail: a.ascari@unibo.it*

Luca Tomesani
*Department of Industrial Engineering,
University of Bologna, Italy
E-mail: luca.tomesani@unibo.it*

Marco Carricato
*Department of Industrial Engineering,
University of Bologna, Italy
E-mail: marco.carricato@unibo.it*

Abstract. *This paper presents the feasibility of an innovative application of laser-assisted bending process. The high strength steel sheets bending, carried out after a laser heat treatment is reviewed. Several strategies aimed to obtain a ductile structure along the bending line, suitable for cold forming, were investigated. The influence of laser processing parameters on the microstructure, hardness and strength of the sheets are discussed and analyzed. In order to predict the temperature and ensure the repetability and the reliability of the process, a model for heat treatment simulation was developed. The study of the experimental data and the simulation led to the definition of parameters resulting in reduced steel strength, positive to bend the sheet avoiding breakage.*

Keywords: *Laser assisted-bending, high strength steel, laser simulation, AISI 1070 sheet, AISI 1090 sheet*

1. INTRODUZIONE

Negli ultimi anni, l'esigenza di progettare tenendo conto della sostenibilità ambientale e della necessaria riduzione dei consumi, ha spinto diversi settori di la ricerca verso lo studio di nuovi acciai ad alta resistenza che permettano la costruzione di componenti ad elevate proprietà meccaniche, ma leggeri. Deformare in modo permanente un componente, necessita di forze sufficientemente elevate da superare il limite di snervamento del materiale e per acciai alto-resistenziali questa soglia raggiunge valori dell'ordine dei 1000 N/mm^2 . Come conseguenza la maggior parte dei processi convenzionali di formatura non sono adatti per questa classe di acciai. Il processo che verrà di seguito descritto nasce come proposta per risolvere il problema di formabilità di acciai alto-resistenziali e prevede l'utilizzo di una sorgente laser che, riscaldando selettivamente il componente, porta alla riduzione delle forze necessarie alla formatura. Il laser è stato utilizzato moltissimo nel campo della piegatura di lamiera, come descritto in [1–3], per evitare l'uso di punzoni, ma questo processo si adatta solo al caso in cui l'ampiezza dell'angolo di piegatura sia molto limitata. Angoli maggiori possono essere ottenuti riscaldando il percorso di piegatura con passaggi successivi della sorgente laser, ma ad aumenti considerevoli del tempo di processo corrispondono comunque ampiezze ristrette. L'utilizzo di una sorgente laser per la formatura di lamiera diventa, quindi, vantaggiosa e competitiva solo se utilizzata in diverse fasi del processo produttivo oppure se combinata ad altre operazioni di formatura allo scopo di ridurre le forze in gioco [4]. In letteratura è possibile trovare diversi lavori che riguardano l'integrazione di una sorgente laser alla pressa piegatrice [5–7]. In questi articoli viene proposto di effettuare la piegatura della lamiera subito dopo la fase di riscaldamento, ma questo tipo di soluzione presenta alcuni inconvenienti rilevanti:

1. L'irraggiamento di percorsi lunghi all'interno della pressa può essere complesso e richiedere l'utilizzo di azionamenti lineari da integrare in macchina.
2. Temperature di riscaldamento omogenee lungo tutto il percorso possono essere ottenute solo utilizzando ottiche speciali [8] oppure disponendo di laser a velocità e potenza molto elevate. Quest'ultima alternativa richiede l'utilizzo di specchi galvanometrici che, però, risentono delle variazioni causate dai movimenti della pressa e quindi richiedono un corretto isolamento [9].
3. Gli utensili di piegatura sono sottoposti ad alte temperature e questo causa l'usura prematura degli stessi.

Per i motivi elencati, l'approccio affrontato in questo articolo, prevede un pre-riscaldamento della lamiera tramite una sorgente laser e la successiva piegatura a freddo. Il lavoro è stato svolto attraverso prove sperimentali su acciai ad alto contenuto di carbonio (AISI1070 e AISI1090) e con l'ausilio della simulazione numerica, per predire i cicli termici al variare dei parametri di processo.

2. SETUP SPERIMENTALE

La piegatura assistita al laser prevede il riscaldamento della superficie del componente, utilizzando una fascio laser ad alta potenza che viene guidato lungo il percorso di piegatura. Le variabili più importanti che influenzano il processo sono: velocità di avanzamento, dimensione dello spot e potenza del laser. Questi parametri devono essere ottimizzati per ottenere

il gradiente termico voluto in tutto il percorso di piegatura e in profondità . Per quanto riguarda la velocità di avanzamento, deve essere scelta in modo che la temperatura rimanga elevata, senza che si verifichino fenomeni di fusione superficiale della lamiera. Le dimensioni delle lamiere di AISI1070 e AISI1090, utilizzate per le prove sperimentali erano: 76 mm di lunghezza, 19 mm di larghezza e 1.3 mm di spessore. I campioni sono stati forniti rinvenuti e con una durezza pari a 515 HV (AISI1070) e 785 HV (AISI1090). Il laser utilizzato è una sorgente allo stato solido Nd:YAG con potenza massima pari ad 1 kW (TRUMPF HL 1003) e il diametro dello spot è stato impostato pari a 4 mm. Tutti i parametri di processo utilizzati sono riportati in Tab. 1, 2 e 3 e ciascuna prova è stata ripetuta due volte. Sono stati valutati gli effetti del riscaldamento laser utilizzando tre diverse strategie, due delle quali sono state testate solo sulle lamiere in AISI1070. La prima strategia prevedeva un singolo passaggio del laser lungo il percorso stabilito: l'idea era valutare se attraverso il riscaldamento della linea di piegatura tramite un fascio con dimensione dello spot maggiore rispetto all'area di contatto lamiera-punzone, consentisse il rinvenimento di tutto lo spessore della lamiera. La seconda strategia analizzata consisteva nel passaggio del laser sulla lamiera lungo due percorsi paralleli, distanziati l'uno dall'altro (variabile di processo), in modo tale che il secondo passaggio portasse ad un rinvenimento dell'area tra i due percorsi, precedentemente riscaldata. Infine, sulla base dei risultati ottenuti dalle prime due strategie di processo, si è proceduto con una scansione multi-passata della linea di piegatura a bassa potenza. Le microstrutture ottenute con le diverse strategie di riscaldamento, sono state analizzate tramite un microscopio ottico e successivamente sono state valutate le durezze, sia lungo lo spessore che sotto-pelle, con un micro-durometro Vickers (Ernst Leitz Wetzlar 2175); la distanza tra ciascuna indentazione è stata impostata pari a 200 μm . Tutti i campioni trattati termicamente sono stati successivamente sottoposti alla prova di piegatura, utilizzando una pressa INSTRON 8033, sulla quale è stata montata una coppia stampo-punzone apposita, con un angolo di piegatura di 90° e raggio del punzone pari a 0.5 mm. Le prove sono state svolte variando la velocità di avanzamento del punzone per determinare l'influenza della velocità di deformazione sul processo.

Tabella 1. Parametri del primo set di prove.

Strategia	Potenza	Velocità di avanzamento
	[W]	[mm/min]
Mono-passata	1000	1500
	1000	1700
	1000	1900
	1000	2100
	1000	2300
	1000	2500
	1000	2700
	1000	2900
	1000	3100
	1000	3300
	1000	3500

Tabella 2. Parametri del secondo set di prove.

Strategia	Potenza [W]	Velocità s1 [mm/min]	Velocità s2 [mm/min]	Distanza tra i percorsi [mm]
Doppia passata	1000	2500	2500	2
	1000	2500	2800	
	1000	2500	3100	
	1000	2500	3400	
	1000	2500	2500	3
	1000	2500	2800	
	1000	2500	3100	
	1000	2500	3400	
	1000	2500	3400	3.5
	1000	2500	3400	4
	750	1875	2250	3
	750	1875	2250	3.5
	750	1875	2250	4
	500	1250	1700	3
	500	1250	1700	3.5
	500	1250	1700	4

Tabella 3. Parametri del terzo set di prove.

Strategia	Potenza [W]	Velocità [mm/min]	Tempo di scansione [s]	Acciaio
Multi-pass	200	4000	300	AISI1070
	300	4000	75	AISI1070
	400	4000	45	AISI1070
	200	4000	300	AISI1090
	200	4000	150	AISI1090
	300	4000	20	AISI1090
	300	4000	30	AISI1090
	300	4000	50	AISI1090
	300	4000	60	AISI1090
	300	4000	75	AISI1090
	400	4000	25	AISI1090
	400	4000	45	AISI1090

3. SIMULAZIONE DEL PROCESSO

Per definire i parametri di processo e ottenere elevate velocità di riscaldamento lungo l'intero percorso di piegatura, senza la fusione della superficie della lamiera, è stato sviluppato un modello agli elementi finiti per la previsione del campo termico. Il modello comprende la

lamiera di acciaio e l'attrezzatura in alluminio per l'afferraggio della stessa, discretizzati con una mesh ad elementi tetraedrici. Il modulo termico utilizzato tiene conto dei fenomeni di conduzione del calore, tramite la risoluzione dell'equazione di Fourier, di convezione e irraggiamento. Il laser è stato modellato come sorgente superficiale: questa semplificazione è stata fatta sulla base dell'equazione di Beer-Lambert, per cui la densità di potenza generata da una sorgente laser diminuisce con legge esponenziale negativa molto ripida lungo lo spessore del componente in esame. Per componenti metallici già a $0,05 \mu\text{m}$ di profondità si ha una riduzione del 86.5% della densità di potenza [10]. L'Eqn.1 esprime la densità di potenza di un fascio laser.

$$Q(x, y) = Q_0(1 - R_c) \frac{2}{\pi w(z)^2} e^{-\left[\frac{2(x-x_0)^2}{w(z)^2} + \frac{2(y-y_0)^2}{w(z)^2} \right]} \quad (1)$$

Q_0 è la potenza in ingresso, R_c è il coefficiente di riflessione, $w(z)$ è il raggio dello spot ad una distanza z rispetto alla posizione focale e $x_0, y_0 =$ sono le coordinate del centro della sorgente, rispettivamente lungo x e lungo y , all'inizio della simulazione. La qualità del fascio laser di una sorgente Nd:YAG pompata a lampade è molto inferiore a quella descritta del tipico fascio gaussiano, quindi, vista l'influenza non trascurabile di questo valore sulla caustica del fascio (come è evidente dall'Eqn. 2), è stata fatta una stima del valore di M^2 in modo da rendere i risultati della simulazione più accurati:

$$w^2(z) = w_0^2 \left[1 + \left(\frac{\lambda z M^2}{\pi w_0^2} \right)^2 \right] \quad (2)$$

$w_0 =$ è il raggio del fascio focalizzato, $\lambda =$ è la lunghezza d'onda della radiazione e M^2 esprime la qualità del fascio. I parametri che compaiono nelle equazioni mostrate precedentemente, ed in particolare il coefficiente di riflessione, sono stati calibrati tramite un processo di validazione della simulazione. Per questa validazione sono state utilizzate lamiere di spessore pari a 3 mm, sulle quale sono state collocate 5 termocoppie per monitorare l'andamento della temperatura durante il processo. Per acquisire gli andamenti reali della temperatura sono state fatte diverse prove e i risultati sono stati confrontati con quelli ottenuti tramite la simulazione del processo.

4. RISULTATI

4.1 AISI 1070

In ciascuna prova svolta con la strategia della mono-passata è stata individuata la presenza di martensite, con un conseguente aumento della durezza e quindi della fragilità della lamiera (Fig. 1). Questo ha causato la rottura di ciascun campione durante la fase di piegatura. Risultati negativi sono stati ottenuti anche con la seconda strategia: in questo caso è stata rilevata una diminuzione di durezza tra i due percorsi, dovuta al rinvenimento dell'acciaio (Fig.2), tuttavia questa diminuzione non ha portato ad un miglioramento di duttilità sufficiente ad evitare la rottura delle lamiere in fase di piegatura. Per quanto riguarda il terzo set di prove, sono stati utilizzati i parametri ottenuti tramite la simulazione del processo. Da questi risultati, come mostrato nelle Fig. 3, 4 e 5, la temperatura superficiale raggiunta è minore della temperatura di austenitizzazione per le prove a bassa potenza, mentre utilizzando potenze pari a 300 W e 400 W la temperatura supera A_{c3} . L'andamento teorico delle temperature mostra chiaramente il ciclo termico al quale viene sottoposto il campione durante il processo

stabilito dalla strategia multi-passata: la temperatura massima viene raggiunta velocemente lungo tutto il percorso e rimane costante per 240 s nella prima prova, 20 s nella seconda e per pochi secondi nella terza, poi si ha un rapido raffreddamento in aria.

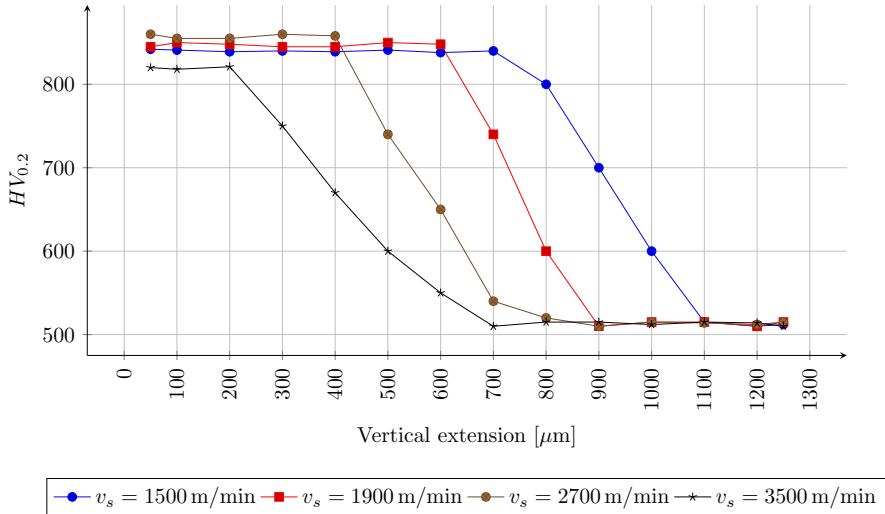


Figura 1. Andamento delle micro-durezze dei campioni trattati secondo la prima strategia.

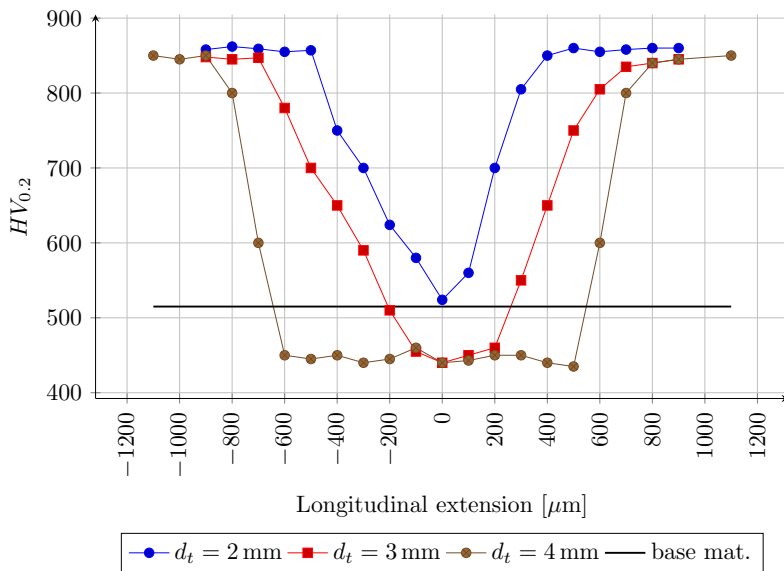


Figura 2. Andamento delle micro-durezze dei campioni trattati secondo la seconda strategia.

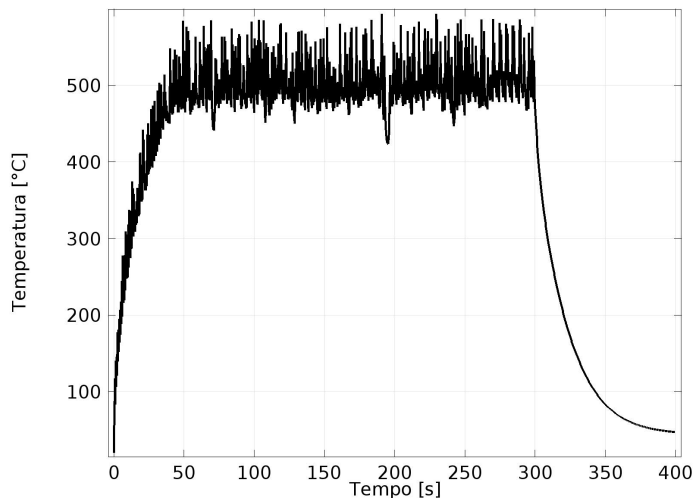


Figura 3. Distribuzione delle temperature sulla superficie dei campioni trattati a 200 W.

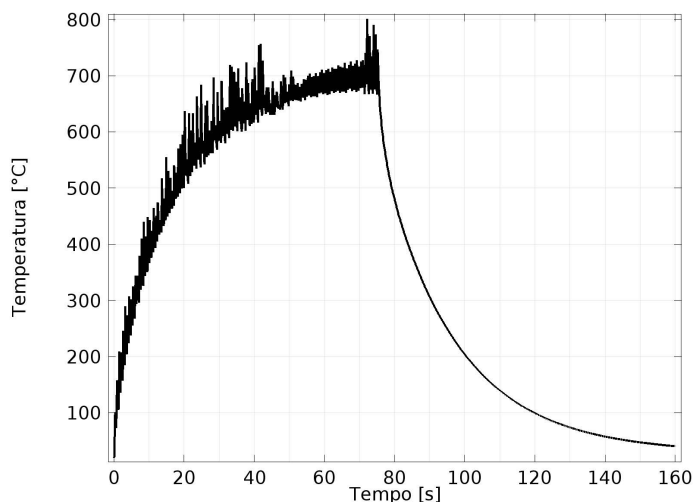


Figura 4. Distribuzione delle temperature sulla superficie dei campioni trattati a 300 W.

Per individuare le microstrutture ottenute i campioni sono stati studiati tramite microscopio ottico e poi sottoposti alle prove di micro-durezza. Il grafico che riporta i valori di durezza sottopelle mostra una diminuzione notevole della durezza della lamiera lungo il percorso di piegatura, come si vede in Fig.6, con una riduzione fino al 60% rispetto all'acciaio allo stato di fornitura. L'andamento, per le prove ad alta potenza, mostra un minimo relativo al centro del percorso; la differenza tra questi valori di durezza e i valori ottenuti nelle due zone adiacenti che mostrano durezza inferiori, è pari a circa 150 HV per $P = 400$ W. Questo comportamento può essere spiegato ricordando le temperature ottenute dalla simulazione: nelle

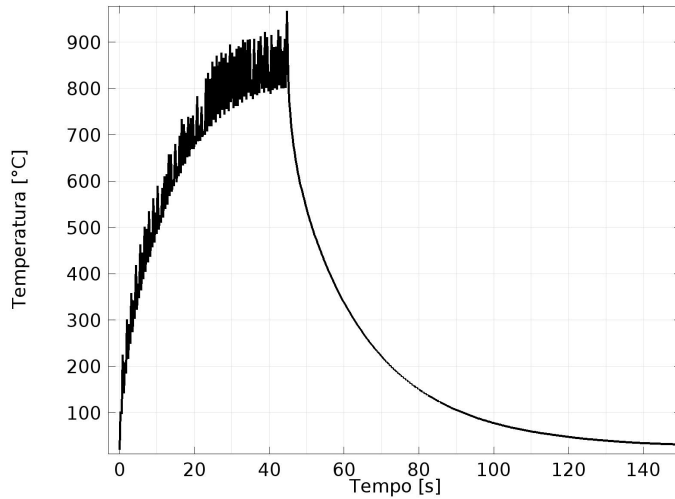


Figura 5. Distribuzione delle temperature sulla superficie dei campioni trattati a 400 W.

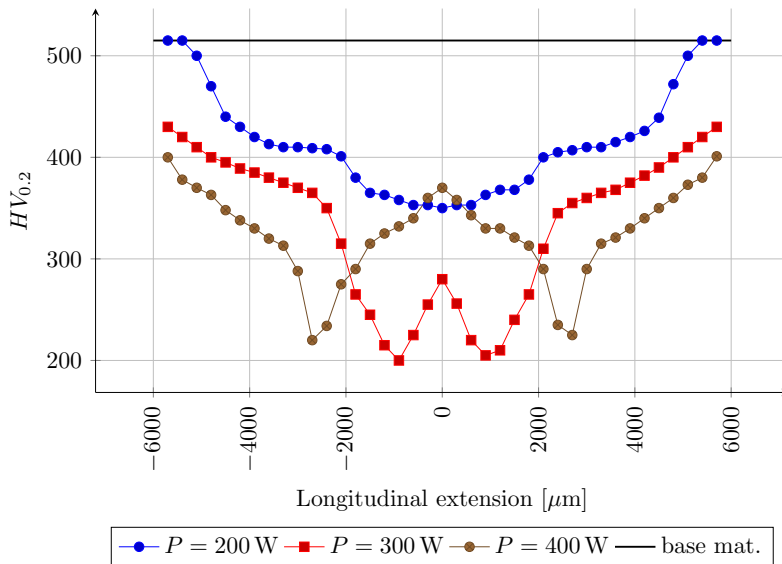


Figura 6. Micro-durezze sotto-pelle dei campioni trattati con la terza strategia.

prove svolte a 400 W, viene raggiunta la temperatura di austenitizzazione e quindi parte dell'austenite si trasforma in martensite a seguito del raffreddamento. Lo stesso risultato è stato ottenuto nel caso di 300 W, ma per queste prove il valore massimo della temperatura risulta inferiore al caso precedente e quindi una percentuale inferiore di austenite riesce a trasformarsi in martensite; questo spiega gli aumenti meno ripidi di durezza. Allo scopo di valutare il gradiente termico lungo lo spessore, sono state eseguite anche le prove di micro-durezza in

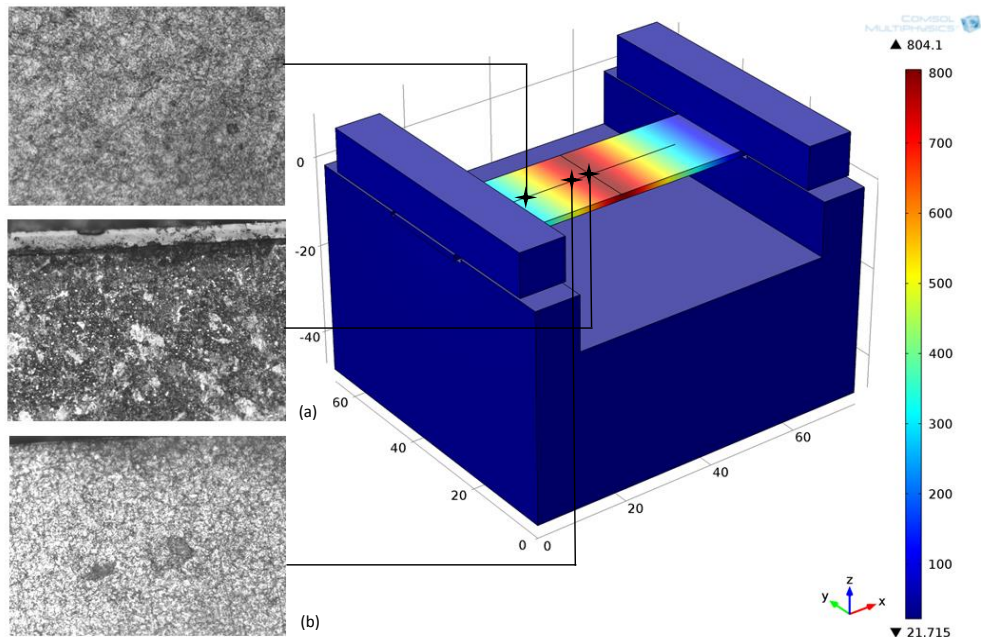


Figura 7. Microstruttura dei campioni trattati a 400 W.

questa direzione, sia nella zona centrale (a), sia nelle due aree adiacenti (b) a minore durezza; i risultati sono mostrati in Fig. 7. Dai grafici si vede che il riscaldamento non è perfettamente omogeneo: nel primo caso si hanno durezza elevate in superficie, mentre nel secondo i risultati sono opposti (Fig. 8). Il motivo di questo comportamento è legato al rinvenimento dei campioni: se si rimane sotto la temperatura di austenitizzazione, si ottengono strutture più duttili e durezza minori (prove eseguite a 200 W), mentre se si entra in campo austenitico la martensite che si forma porta a durezza maggiori. Allo scopo di verificare se le modificazione strutturale fossero sufficienti ad evitare la rottura delle lamiere durante la piegatura, sono state fatte prove alla pressa. Inizialmente è stata impostata una velocità di avanzamento del punzone pari a 1 mm/s, una corsa di 19 mm e un carico di 25 kN. Con questi parametri nessun campione si è rotto (Fig.9). La velocità di piegatura è stata successivamente incrementata e sono state svolte prove con i parametri riportati in Tab. 4, ottenendo i risultati di Fig. 10.

Tabella 4. Velocità di piegatura.

Test	Velocità di avanzamento [mm/s]
1	1
2	5
3	10
4	15

Infine, per controllare l'integrità superficiale delle lamiere piegate, tutti i campioni sono stati

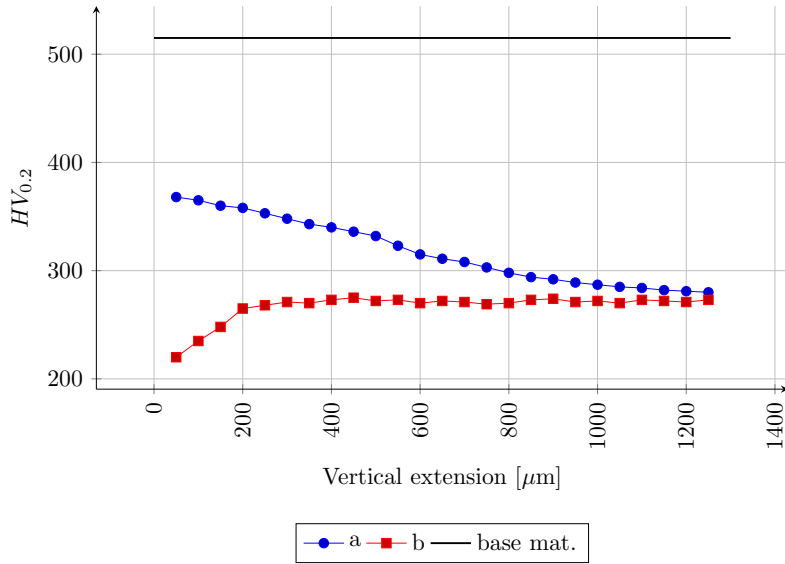


Figura 8. Micro-durezza lungo lo spessore nella zona centrale (a) e nell'area adiacente (b).

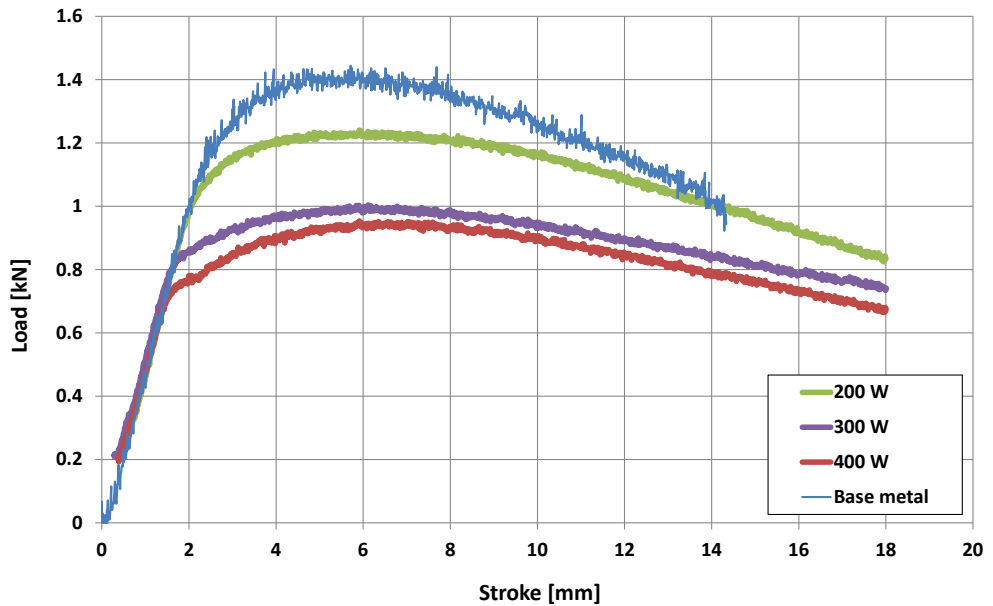


Figura 9. Diagramma forza-corsa della prova di piegatura.

osservati al SEM (Scanning Electron Microscope). Nelle prove condotte a 200 W e 300 W non sono state rilevate microfratture. Piccole cricche sono state invece osservate nel caso dei campioni riscaldati a 400 W, come mostrato in Fig. 11. Tutti i risultati ottenuti con le lamiere in AISI1070 sono stati confermati ripetendo le stesse prove nel caso di lamiere di AISI1090.

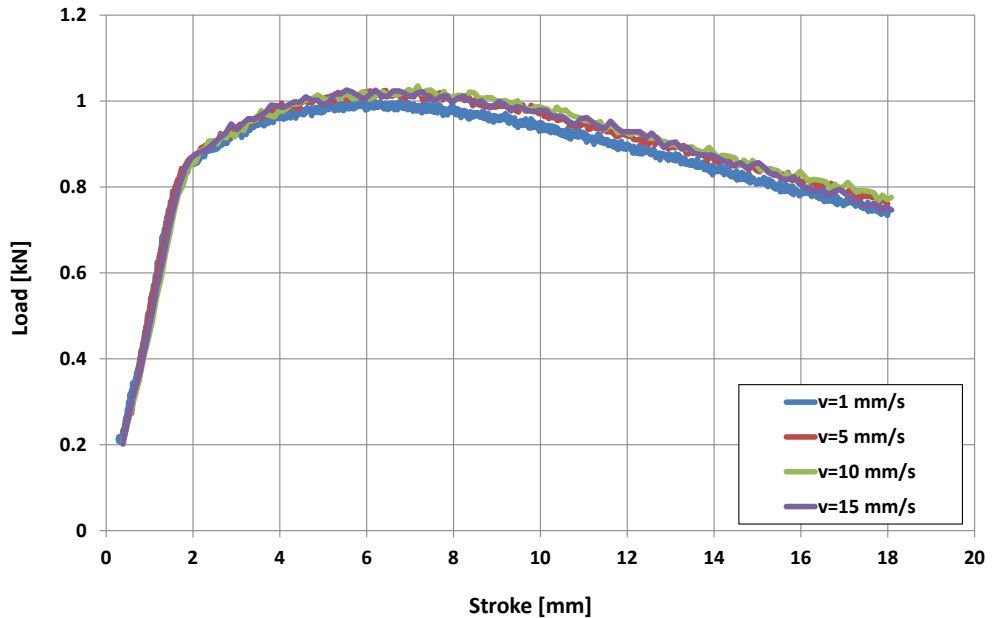


Figura 10. Diagramma forza-corsa al variare della velocità di piegatura.

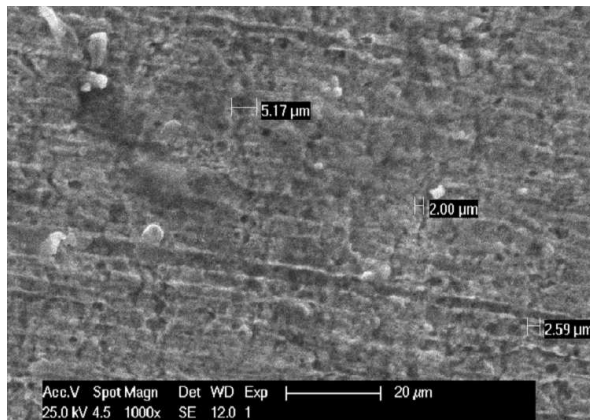


Figura 11. Campioni trattati a 400 W, visti al SEM.

4.2 AISI1090

Le prove svolte sulle lamiere in AISI1090 sono state pianificate tenendo conto dei risultati ottenuti per le lamiere in AISI1070. Per questo motivo le strategie di singola e doppia passata sono state escluse. I parametri utilizzati sono riportati nella Tab. 3 e i risultati più significativi sono mostrati in Fig. 12 - 14. Anche in questo caso è stata raggiunta una riduzione di durezza pari al 60%, a conferma di quanto precedentemente descritto. Le prove di piegatura hanno dato i risultati di Fig. 15: il diagramma forza-corsa mostra chiaramente come durezza e dutti-

lità sono legate tra loro e quindi l'influenza del pre-trattamento laser influenza notevolmente la formabilità. Mentre le lamiere non trattate si rompono dopo una corsa di 6 mm, la lamiera riscaldata con un ciclo termico corretto non si fratturano fino a corse pari a 17 mm.

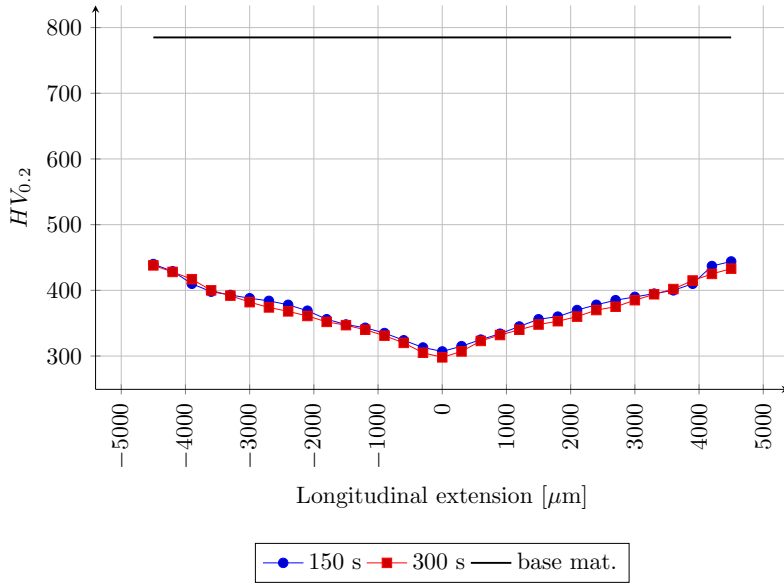


Figura 12. Andamento delle micro-durezze delle lamiere in AISI1090 trattate a 200 W.

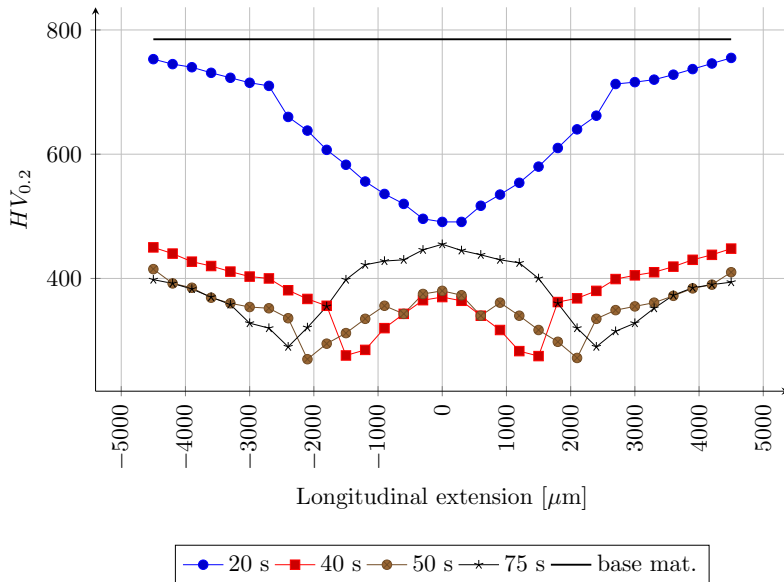


Figura 13. Andamento delle micro-durezze delle lamiere in AISI1090 trattate a 300 W.

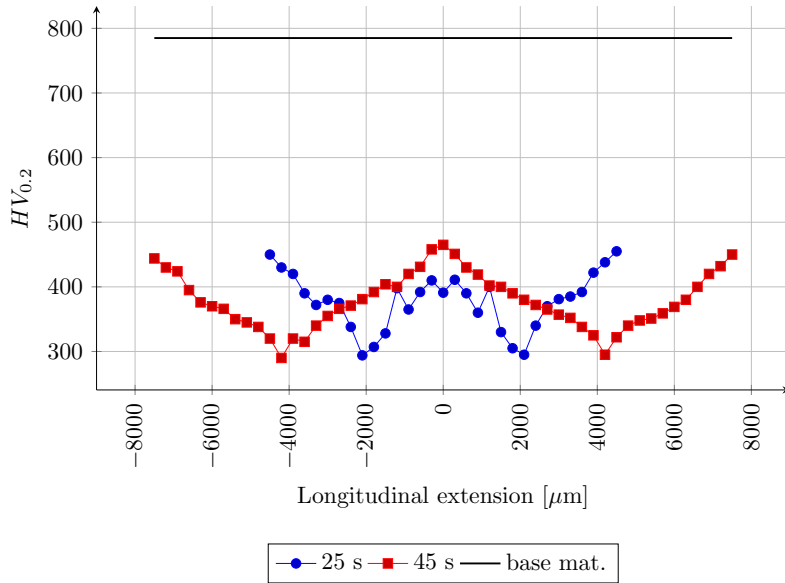


Figura 14. Andamento delle micro-durezze delle lamiere in AISI1090 trattate a 400 W.

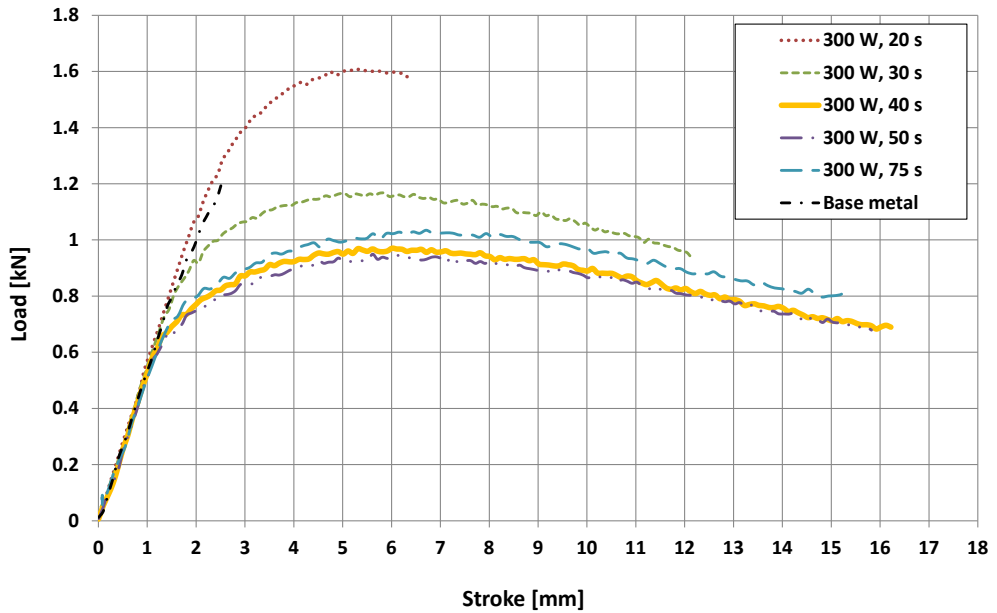


Figura 15. Diagramma forza-corsa per la piegatura dei campioni in AISI1090.

5. CONCLUSIONI

In questo articolo è stato presentato un processo ottimizzato per la piegatura assistita al laser, la cui fattibilità è stata dimostrata attraverso prove sperimentali e numeriche. Sono stati valutati gli effetti di diverse strategie di processo e tra queste è stata individuata la multi-passata per ottenere i risultati il trattamento adatto ad addolcire la lamiera. È stata condotta una campagna sperimentale su lamiere in acciaio AISI1070 e AISI1090 per valutare le variazioni microstrutturali al variare dei parametri di processo, potenza e tempo di esposizione al fascio laser. Per ciascuna coppia di parametri sono state fatte due prove per verificare la validità del risultato. Attraverso lo studio della microstruttura, per mezzo di microscopio ottico e SEM, e tramite prove di piegatura, è stato dimostrato come sia possibile ottenere un aumento di duttilità in un'area sufficiente a garantire la piegatura senza rottura delle lamiere. Il miglioramento della formabilità delle lamiere permette anche di diminuire i carichi necessari alla piegatura. Entrambi gli aspetti descritti, sono fondamentali in diverse applicazioni e la relativa semplicità di integrazione del laser all'interno di una macchina, può essere uno stimolo allo sviluppo del processo a livello industriale.

REFERENCES

- [1] Dearden, G., and Edwardson, S., 2003. "Laser assisted forming for ship building". *SAIL, Williamsburg, VA*.
- [2] Hennige, T., Holzer, S., Vollertsen, F., and Geiger, M., 1997. "On the working accuracy of laser bending". *Journal of Materials Processing Technology*, **71**, pp. 422–432.
- [3] Geiger, M., Merklein, M., and Pitz, M., 2004. "Laser and forming technology an idea and the way of implementation". *Journal of Materials Processing Technology*, **151**(1-3), Sept., pp. 3–11.
- [4] Amir Roohi, H., Hoseinpour Gollo, M., and Moslemi Naeini, H., 2012. "External force-assisted laser forming process for gaining high bending angles". *Journal of Manufacturing Processes*, pp. 269–276.
- [5] Lield, G., Kratky, A., and Schuocker, D., 2002. "Laser assisted shaping of metallic sheets and wires - a promising new application of high power lasers". In *High-Power Laser Ablation IV*, C. R. Phipps, ed., Vol. 4760, pp. 633–644.
- [6] Bammer, F., Schumi, T., Otto, A., and Schuöcker, D., 2011. "Laser assisted bending for efficient light-weight-production". *Technical Gazette*, pp. 571–576.
- [7] Brecher, C., Emonts, M., and Eckert, M., 2011. "Laser-Assisted Sheet Metal Working of High Strength Steels in Serial Production". *Physics Procedia*, **12**, Jan., pp. 617–626.
- [8] Bammer, F., Schuöcker, D., Schumi, T., Holzinger, B., and Humenberger, G., 2011. "A Diode-Laser-System for Laser-Assisted Bending of Brittle Materials". *Advances in Optical Technologies*, **2011**, pp. 1–4.
- [9] Brecher, C., Emonts, M., and Eckert, M., 2012. "Laser-Assisted Sheet Metal Working by the Integration of Scanner System Technology into a Progressive Die". *Physics Procedia*, **39**, Jan., pp. 249–256.
- [10] Steen, W. M., and Mazumder, J., 2010. *Laser Material Processing*. Springer London, London.

PREDICTION OF DUCTILE IRON MICROSTRUCTURES IN SAND CAST PROCESSES

Emilio Salsi

*Department of Industrial Engineering DIN,
University of Bologna, Italy
E-mail: emilio.salsi2@unibo.it*

Rosario Squatrito

*Interdepartmental Center for Industrial Research CIRI-MAM,
University of Bologna, Italy
E-mail: rosario.squatrito2@unibo.it*

Ivan Todaro

*Interdepartmental Center for Industrial Research CIRI-MAM,
University of Bologna, Italy
E-mail: ivan.todaro2@unibo.it*

Luca Tomesani

*Department of Industrial Engineering DIN,
University of Bologna, Italy
E-mail: luca.tomesani@unibo.it*

Abstract. *This paper focuses on process modeling and microstructure prevision validation of sand ductile iron castings. Cast iron microstructure is deeply influenced by process parameters such as alloy chemical composition, melt treatment and cooling rates which can be very different in each part of castings. Therefore, a casting equipment made of cubic structures with different thermal modules has been designed to evaluate the influence of process parameters on microstructure in a wide range of cooling conditions. Temperatures of alloy were recorded directly in the centre of each cube with thermocouples coated with ceramic material. Metallographic samples were extracted from each cube to evaluate microstructural features gradient throughout the whole thickness. All of the experimental castings have been studied by means of numerical process simulation. Thermal simulations were performed using commercial models for microstructure prevision coupled with dynamic databases for the calculations of local alloy thermo-physical characteristics in function of the local solidification conditions. By comparing with recorded temperature data, the prediction of cooling curves in each point of casting was enhanced allowing to obtain a good prevision of microstructures. Indeed predicted and measured microstructures show an overall good accordance.*

Keywords: *ductile iron, sand cast, heavy sections, solidification models, process modelling, thermal analysis, numerical simulation, microstructure prediction.*

1. INTRODUCTION

The mechanical properties of cast irons depend on their microstructural features (e.g. graphite shape and distribution, as well as metal matrix microstructure), which are strongly influenced by chemical composition, technological treatment of the melt and cooling conditions [1-5]. In the case of Ductile Cast Iron (SG), the microstructure depends both on solidification (mainly for the size, shape and distribution of graphite nodules) and on the eutectoid transformation (mainly for the metal matrix) [5-11].

Different parts of complex castings, because of different thicknesses and heat dissipations, may cool at a wide range of cooling rates. This leads to a variety of microstructures in different parts of the casting and consequently to different local mechanical properties. An accurate evaluation of the cooling conditions of the casting and their effect on the final microstructures is therefore essential for the study and improvement of the casting process.

Some new empiric-numerical models have been added to mathematical models for the prediction of microstructures in castings. Today the main commercial codes of simulation processes use these new models that may be coupled with the fluid-dynamic and thermal models (calculation of dynamics of mould filling, local cooling rates and solidification trends) in order to also evaluate the chemical and kinetic aspects of the process that lead to the final microstructures. Diffusivity of carbon and other chemical elements are some examples of the evaluated phenomena. These models have not yet been investigated in all the ranges of process conditions, although experimental campaigns on a laboratory scale have been carried out to define the empirical constraints in the mathematical equations and to validate these models [6,8,9,12-18]. The variability of the process conditions, in fact, is strongly influenced by many different factors: size and variability of casting thickness, instability of process conditions and problems in the measurement of process parameters, in particular for heavy sections [15,19,20].

In this investigation, the numerical-experimental characterisation of a sand casting process of ductile iron was aimed to validate numerical models of the casting simulation software on a wide range of process conditions, with particular attention to the prediction of microstructure.

The activities were carried out by means of specific casting equipment designed to study a wide range of process conditions and to allow their direct measurement also in massive areas of casting.

In particular, an “in mould” thermal analysis system has been developed for monitoring the eutectic and eutectoid transformations during cooling, in areas with different thermal modules. Thermal analysis, in fact, is the main instrument for the monitoring of casting processes and it is widely used both in industrial and scientific fields [8, 20-22]. This system can ride the problems of standard thermal analyses out. In fact measurements with small standard cups is not representative of a wide ranges of cooling rate. Moreover, in the industrial practice, the temperature monitoring experiences were normally carried out in boundary areas of the moulds, which are systematically influenced and perturbed by phenomena due to the solidification of the centre of the casting, such as the thermal flux of the released latent heat during the eutectic transformation. These problems were resolved using ceramic coatings in order to record the temperatures in the central volume of heavy section castings for long times without any damage for the thermocouples.

The monitoring of temperature allowed to validate the thermal simulation of the casting process in all casting parts. This allowed estimation of the microstructure in the castings with good accuracy through a commercial casting simulation code. Consequently, the

implementation of empirical relationships between the main microstructural features and mechanical properties in the casting simulation software allows the evaluation of the local mechanical properties of the castings with good confidence.

2. DESIGN OF EXPERIMENTS

Casting equipment, measurement system and numerical simulation

The casting equipment was designed to obtain different solidification conditions and, consequently, different microstructures and mechanical properties of the cast iron. The layout is shown in Fig. 1. The equipment includes a conical basin and properly dimensioned runners and gates, which fill a cluster of seven cubes of different sides (60, 75, 100, 120, 150, 180, 210 mm, named respectively with progressive numbers from 1 to 7) which allow investigation of a large range of solidification and cooling rates. The equipment has runners, gates and casting in drag; this may cause a turbulent fall of metal inside the mould cavity but allows a simple and cheap construction; anyway two filters allow a more homogenous filling in the mould.

During the experimental activities, three ductile iron castings were poured with the described equipment. The pouring of the ladle, inoculation, magnesium treatment, and filling were monitored continuously. The chemical composition of the alloy was evaluated by means of a spectrometer, before and after the magnesium treatment. The chemical compositions of the melt are reported in Tab. 1 in different phases of the activities (before the magnesium treatment, after the magnesium treatment and before the pouring of the last casting). The magnesium content does not show significant differences between the first and the third pouring.

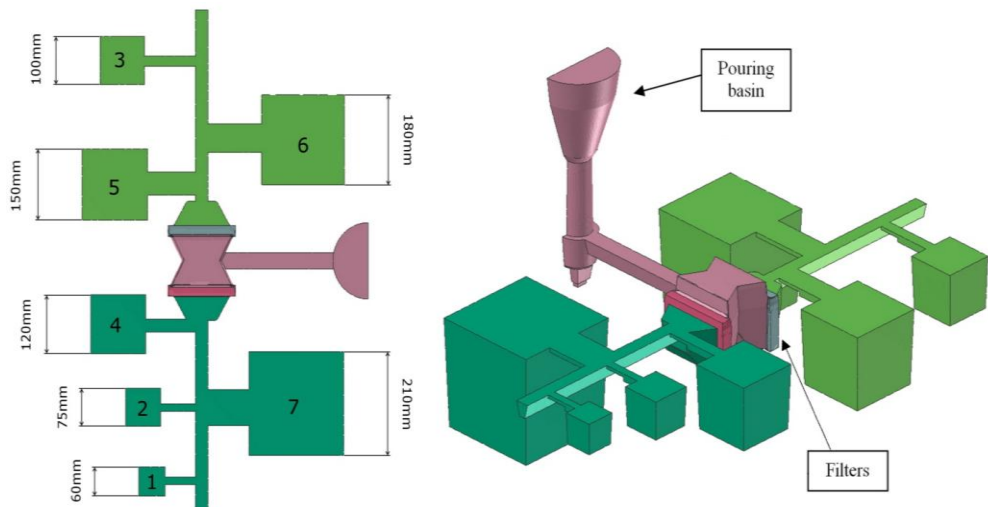


Figure 1. Schemes of the experimental casting equipment

Table 1. Schemes of the experimental casting equipment

	C	Si	Mn	P	S	Ni	Cr	Cu	Mo	Mg	Sn	Ti	Pb	Al
Before Mg Treatment	3.82	1.88	0.191	0.021	0.002	0.032	0.057	0.065	0.001	0.001	0.023	0.035	0.007	0.016
First Pouring	3.72	2.19	0.197	0.020	0.001	0.031	0.058	0.066	0.002	0.048	0.021	0.035	0.007	0.017
Last Pouring	3.78	2.21	0.196	0.025	0.000	0.031	0.059	0.064	0.001	0.046	0.022	0.036	0.006	0.019

Thermal analysis of the castings was carried out both on a standard sample cup, (by means of ITACA v.7 system) poured from the ladle before filling, and also directly inside the mould, by means of type K thermocouples (Chromel/Alumel) covered with alumina. This material was selected for his high strength at high temperature, elevated thermal conductivity and chemical stability. Coatings of different diameters were used for different cube sizes. The coated thermocouples were vertically inserted using sand cores to position them in order to measure temperatures at the centre of the cubes (Fig. 2). The thermocouples were connected to an AGILENT 34970A Data Acquisition/Data Logger Switch Unit and the acquisition of the cooling curves was carried out until shake out (around 35 hours). The direct measurement of the temperature in the castings allows for:

- Identification of the temperature and duration of the eutectic and eutectoid transformations.
- Definition of the correct boundary conditions and the process parameters for the numerical simulations.
- Arrangement of the information of the solidification conditions.

During the experimental activities, two ductile iron castings were monitored as previously described, while the third casting was not monitored in order to allow the extraction of samples for mechanical and microstructural characterisation.

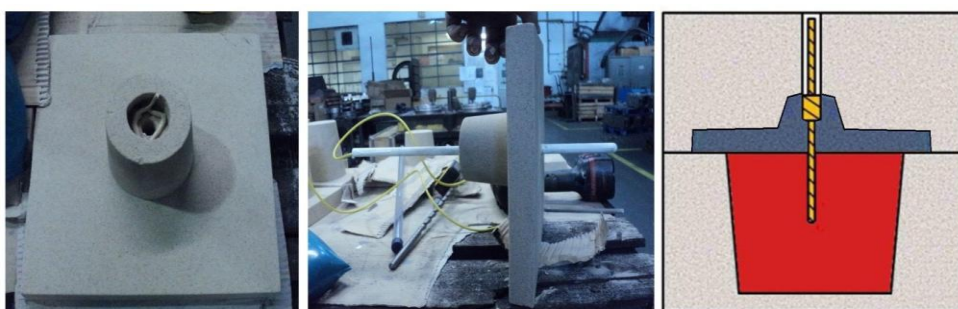


Figure 1. Thermal acquisition system “in mold” with thermocouples covered with alumina.

Numerical simulation

Numerical simulation was carried out by means of the FEM numerical code PROCAST v.2011 that solve the heat transfer equations in presence of liquid-solid phase change. A specific implemented model coupled with COMPUTHERM [23] database for the calculation of thermo-physical properties in function of the local chemical composition, was also adopted to predict the microstructural characteristics.

In ductile iron, due to a carbon equivalent value close to eutectic, the amount of primary dendritic austenite grains is often very low and the main phenomena which take place during the alloy solidification is the formation of eutectic structures composed by graphite nodules surrounded by a austenite shells [6]. The calculation of nucleation of eutectic grains was carried out using the following equation based upon the model proposed by Oldfield [12] in 1966:

$$N_{\text{eut}} = A_e(\Delta T)^n \quad (1)$$

Where:

- N_{eut} is the number of eutectic graphite nuclei in the volume unit.
- ΔT is the undercooling with respect to the stable eutectic temperature (the eutectic temperature used to define the local undercooling is given by Computherm that calculate the phase diagram of alloy for each time step in function of local chemical composition).
- A_e , n are empirical nucleation constants that depend on chemical composition and melt treatments (the values suggested for Ductile Iron [24] : $A_e=1000[\text{K}^{-n}/\text{cm}^3]$, $n=2$).

Several models [15,16], which consider also parameters such as graphite nodule and diffusion of carbon through austenite shell, have been proposed in literature to describe the kinetic growth of the eutectic grains. In this study, the following empirical equation, which relates the eutectic growing with a quadratic power of the undercooling, was adopted:

$$\frac{dR_{\text{eut}}}{dt} = \mu_e(\Delta T)^2 \quad (2)$$

Where:

- dR_{eut}/dt is the growth rate of eutectic grain
- μ_e is an empirical eutectic growth coefficient (for Ductile Iron the suggested value [24] is: $A_e = 3.87 \cdot 10^{-6} [\text{cm}/\text{sK}^2]$).

If the complete solidification of liquid is not achieved when the metastable eutectic temperature is reached, cementite forms. During the end of solidification, the grains impinge on each other. This is taken into consideration by using the Avrami-Johnson-Mehl approximation [6,24].

After the solidification, during the cooling of casting, take place the eutectoid reaction that leads to the decomposition of austenite into ferrite and graphite for the case of the stable eutectoid and to pearlite for the metastable eutectoid transformation. Usually, slower cooling rates lead to stable eutectoid structure (Ferrite). In ductile iron, the eutectoid transformation is strongly influenced by the diffusion distance for carbon through the ferrite shell and then also by the parameters of microstructures formed during eutectic solidification such as nodule count and graphite radius which is correlated to R_{eut} . If the complete transformation of austenite is not achieved when the metastable eutectoid temperature is reached, pearlite forms and grows in competition with ferrite. In literature [9-11], models of pearlite nucleation and growth are described as power laws of the undercooling with respect to the metastable eutectoid temperature (ΔT_{eutd}) that depends on

local chemical composition. In this study, the following empirical equation for nucleation and growth of pearlite grains was adopted :

$$\frac{dN_{\text{pearl}}}{dt} = 5.07 \cdot 10^6 \exp \left(-\frac{370}{\Delta T_{\text{eud}}} \right) \quad (3)$$

$$\frac{dR_{\text{pearl}}}{dt} = 0.0168 \exp \left(-\frac{94.8}{\Delta T_{\text{eud}}} \right) \quad (4)$$

Microstructural analyses

Metallographic specimens were extracted according to the scheme shown in Figure 3. The aim is to obtain experimental data for the validation of casting simulation in a wide range of cooling conditions. Between central and boundary parts of each cube, there are very different cooling rates which involve microstructures shapes, especially the nucleation and growth of spheroids. Therefore, metallographic analyses were carried out along the profile starting from the centre of each cube and ending on its lower edge (dotted line in Fig. 3). According to ISO 945 and ISO 16112, microstructural analyses were carried out to evaluate:

- the percentage of graphite (G [%])
- graphite nodule density (ND [1/mm²])
- mean graphite nodule area (NA [μm²])
- nodularity (N [%])

The specimens were prepared by standard metallographic techniques, including mechanical grinding, polishing and etching. According to ASTM E883, the Nital2 etchant was used to evaluate:

- the percentage fraction of ferrite (F [%])
- the percentage fraction of pearlite (P [%]).

Metallographic analyses were carried out by means of digital image analysis software and the numerical results, together with tensile tests data, were statistically elaborated by using the XLstat® software.

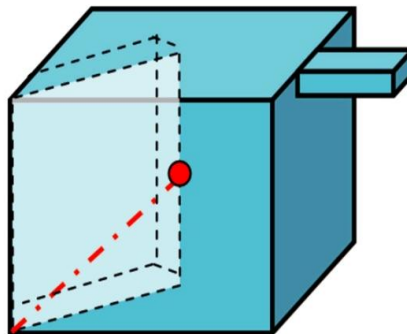


Figure 2. Schemes of the extraction areas of metallographic specimens (red dotted line represent the profile analyzed from centre to lower edge of each cube).

3. RESULTS

Microstructural analyses

Representative optical micrographs of the ductile iron studied in this paper are reported in Fig. 4, showing rounded graphite nodules within a ferritic-perlitic matrix. Different ferrite to perlite ratios and graphite nodule density and size were observed, depending on the wide range of thermal modules of the cubes and on the distance from the external surface of the casting consequently on their different solidification and cooling conditions.

The cooling rates during the solidification (near the eutectic temperature) mainly influences density and size of graphite nodules. Indeed, central parts of cubes (Fig. 4a) show a low density of big graphite nodules in comparison with more external parts (Fig.4b) which show an high density of small graphite nodule due to high cooling rates during the eutectic. In central areas of cubes, a decrease of the thermal modulus of the castings leads to: an increase of the graphite nodule density (from 41 mm^{-2} to 122 mm^{-2}), a decrease of the graphite nodule area (from $2576 \mu\text{m}^2$ to $1455 \mu\text{m}^2$), mainly due to an increase of cooling rates during solidification and an increase of the perlite fraction in the matrix (from 40% to 70%), mainly due to an increase of cooling rates during the eutectoid transformation.

The average values of the main microstructural parameters measured in each casting are reported in Tab. 2.

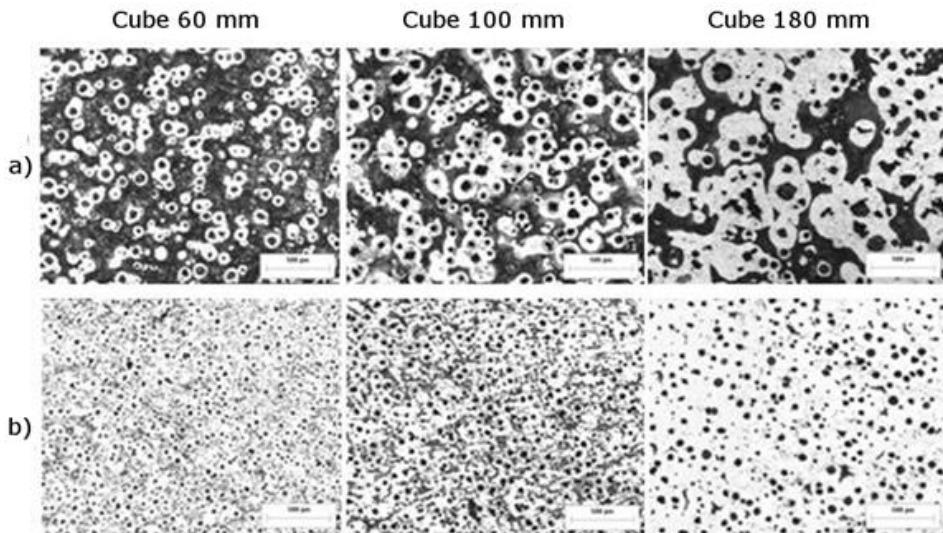


Figure 3. Representative optical microstructures of 60, 100, 210 mm edge ductile iron cube: (a) Central parts of cubes with low density of big spheroids within a ferritic-perlitic matrix; (b) Boundary parts under the skin of cubes with high density of little spheroids within a ferritic-perlitic matrix.

Table 1. Results (average values) of the microstructural analyses carried out on specimens extracted from central areas of cubes (G = % fraction of graphite, F = % fraction of ferrite, P = % fraction of perlite, NA = average area of the graphite nodules μm^2 , NC = graphite nodule density [mm^{-2}], N = % graphite nodularity).

Casting Thickness	Microstructural Parameters					
	G	F	P	NA	NC	N
	%	%	%	μm^2	mm^{-2}	%
210 mm	10.4	46.3	43.2	2576	41	64
180 mm	8.1	50.9	41.1	1725	47	71
150 mm	9.1	45	45.9	1931	47	71
120 mm	10.9	33.4	55.8	2139	51	83
75 mm	7.6	24	68.4	1455	52	82

Thermal Analyses

The cooling curves acquired in five points of measurement in the center of cubes are shown in Fig. 5. By observing the first six hours of acquisition, it is possible to analyse the cooling process, in particular the eutectic and eutectoid transformations. The temperatures of eutectic and eutectoid transformations are consistent with the theoretical temperatures of the Fe-C phase diagram for the present cast iron (1152 °C for the stable eutectic, 738 °C for the eutectoid transformation).

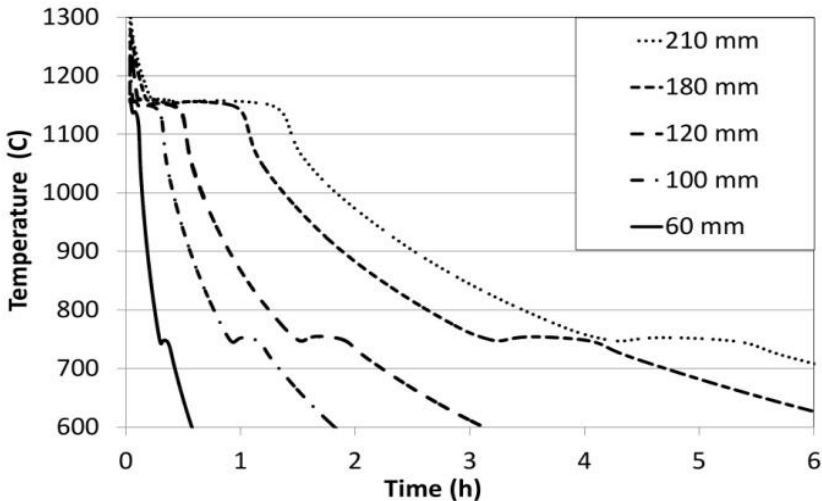


Figure 4. Temperature – Time profiles measured in the centre of 60, 100, 120, 180 and 210 mm edge cubes.

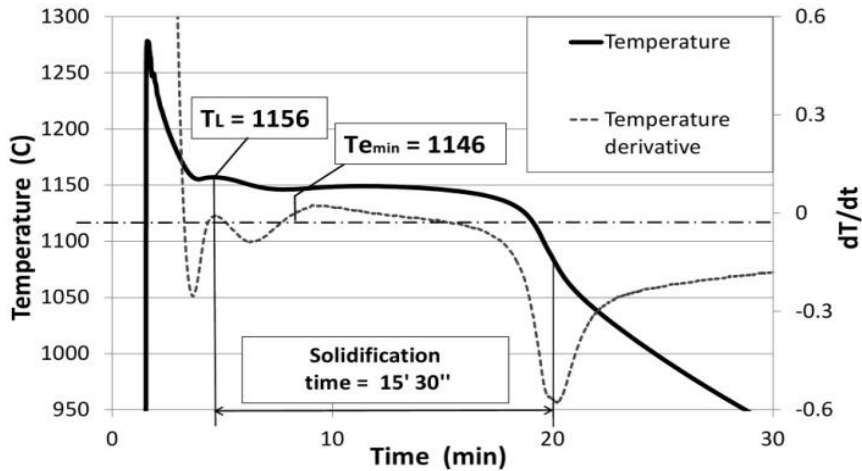


Figure 5. Example of derivative analysis of the acquired cooling curves in the 100 mm edge cube.

In order to obtain an accurate determination of start and end points of the eutectic transformations in the different thermal modules, the analysis of the derivative of measured cooling curves (Fig. 6) was carried out, detecting:

- The temperature of primary phase nucleation, $T_{\text{liquidus}} (T_l)$, at the first relative maximum of the derivative.
- The minimum temperature reached during eutectic transformation (T_{emin}), at the subsequent point where derivative goes to 0.

The analysis of the first derivative gave different temperatures of phase transformation, depending on different thermal modules and then different cooling rates; for lower cooling rates, lower undercooling and higher temperatures of eutectic transformation (typical of stable eutectic) were found.

4. COMPARISONS BETWEEN NUMERICAL AND EXPERIMENTAL RESULTS

Cooling Curves

A comparison between the cooling curves acquired in the center of the cubes (with sides of 60, 100, 180 mm, respectively) and the predicted cooling curves, are reported in Fig. 7. A good correspondence between numeric and measured values can be seen during the initial phases of cooling, due to a correct set-up of the process parameters and boundary conditions. In the initial phases (high thermal gradients), the system is strongly influenced by the value of Heat Thermal Conductivity (HTC) assigned to the metal/sand interface and by the thermo-physical characterisation of the materials (cast iron, sand). An accurate analysis of the eutectic transformation (Fig. 7) show a good correspondence between measured and predicted solidification times, also for different cooling rates. A good accordance between measured and simulated cooling curves was obtained after an iterative optimization of simulation parameters that describes boundary conditions and thermo-

physical proprieties of the materials involved in the process. The monitoring of temperature allowed to validate the thermal simulation of the casting process in all casting parts.

Table 3 shows the minimum eutectic temperatures measured and predicted in cubes of 60, 100 and 180 mm. Only the measured T_{liquidus} are shown because the predicted ones were not evaluable, due to the near-eutectic chemical composition; in this case, the prediction model underestimates the formation of the primary phase and the analysis detects only the eutectic solidification. For comparison, also the results obtained by the thermal analysis of the alloy with standard cup, by means ITACA v.7, are reported in Table 3.

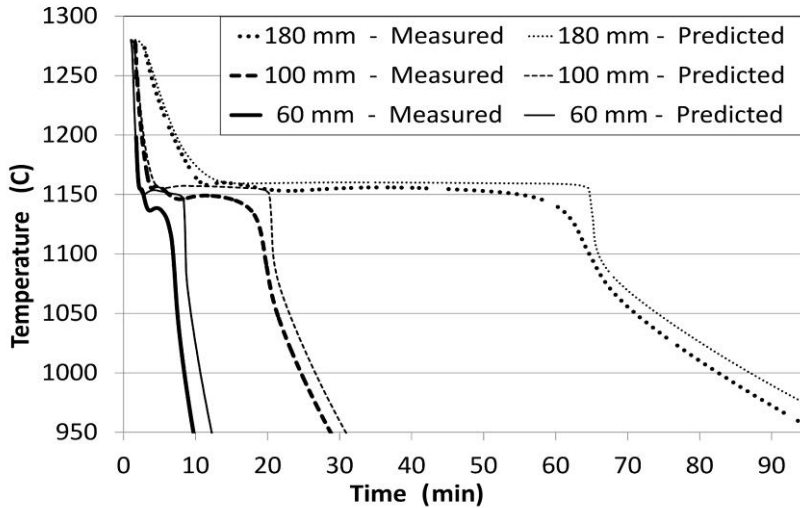


Figure 6. Comparison of the measured (thick) and simulated (thin) cooling curves logged in the centre of 60, 100 and 180 mm edge cubes.

Table 2. Comparison of measured (meas.) and simulated (pred.) T_{liquidus} and T_{eutectic} for the casting.

		T liquidus (C)	T eutectic (C)
TA Standard Cup	Measured	1148	1137
	Predicted		
Cube 60 mm	Measured	1154	1141
	Predicted		1151
Cube 100 mm	Measured	1156	1145
	Predicted		1156
Cube 180 mm	Measured	1160	1153
	Predicted		1159

The importance of a correct numerical prevision of eutectic temperatures is correlated with the influence of the solidification phase on the microstructure formation. Indeed, the matrix morphology is highly influenced by the cooling conditions during both eutectic and eutectoid transformations. It is well known that low cooling rates during the solid state transformation promote ferrite formation. On the other hand, low solidification cooling rates lead to large austenitic grains, promoting perlite formation. Carbon atoms, in fact, are hindered to move through large diffusion paths and remain entrapped in the austenite matrix favouring perlite formation when the metastable eutectoid temperature is reached ¹⁴. For this reason, correct evaluation of the phenomena that take place during solidification is necessary also for the correct prevision of metal matrix.

Prediction of microstructures

Commercial software as Procast allows to predict the microstructure in all parts of casting by means of implemented numerical models [6,8,12-18,24]. These models take into account phenomena such as nucleation and growth of primary and eutectic phases, eutectoid transformation in the solid state which are dependent on local chemical composition and local cooling conditions of alloy.

The reliability of numerical models for the prevision of microstructures was evaluated by comparing predicted and measured microstructural parameters, in terms of: fraction of graphite, ferrite and perlite, nodule count, average nodule radius and nodularity (Fig. 8).

Since the simulation code estimates a volumetric value of the nodule count, the Wienceck relation (Eqn.(5)) was used to convert this value into a bidimensional value, in order to compare the data obtained with the process simulation with those of the microstructural analysis [25].

$$N = \sqrt{\frac{N_p^3}{f_{gr}}} \quad (5)$$

Where:

- N : Nodule count for volume unit.
- N_p : Nodule count for surface unit.
- f_{gr} : Fraction of graphite.

By way of example, a comparison between measured and predicted values of main microstructural parameters within the 180 mm edge cube is reported in fig. 8.

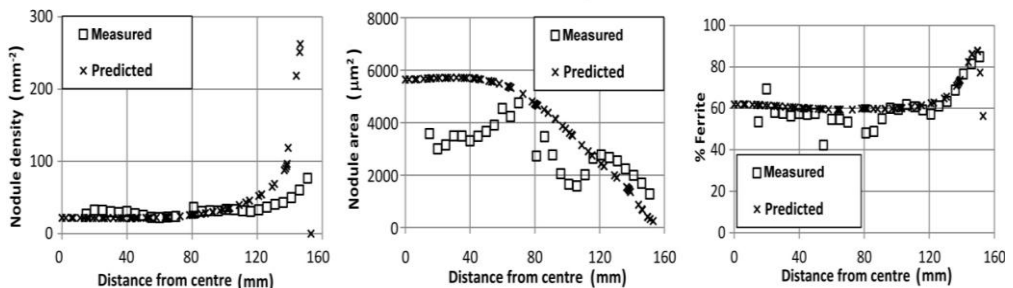


Figure 7. Comparison between measured and predicted values of main microstructural parameters within the 180 mm edge cube (along the profile represented in fig. 3)

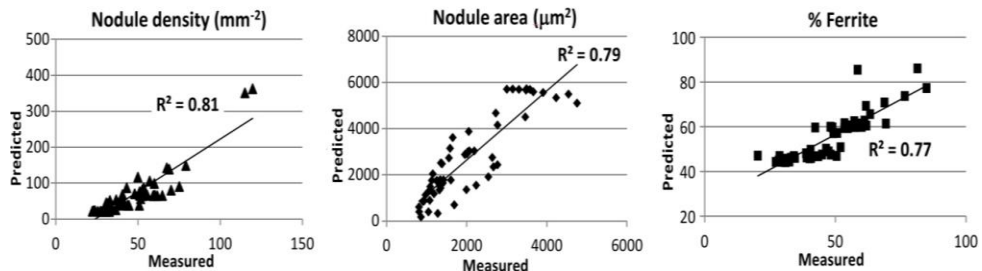


Figure 9. Overall comparison between main predicted and measured microstructural parameters for each area of castings: Nodule density, Nodule area, % Ferrite

Figure 9 report the overall comparison between predicted and measured microstructural data that show good correlation with R^2 indices between 0.81 and 0.77. The differences of measured and predicted values for some microstructural data do not depend only on accuracy of thermal simulations and microstructural models but also on measurement uncertainty of the optical analysis and on other phenomena such as segregation and porosity in the analyzed areas.

The evaluation of local microstructures allowed the prediction of the local mechanical properties of castings (by means of the implementation in the casting simulation of empirical relationships between the main microstructural parameters and the tensile properties) giving useful data for structural analysis.

5. CONCLUSIONS

The results of the present investigation lead to the design of a thermal analysis system able to work directly “in-mould”, to mirror the real process conditions for both small and large castings.

The monitoring of temperature allowed to validate the thermal simulation of the casting process in all casting parts. This lead to the estimation of the local microstructure in the castings with good accuracy through a commercial casting simulation code also in heavy section of ductile iron castings.

Acknowledgments

The research was carried out in collaboration with the laboratory CRIF – Research Centre for the Foundry Industry SCM Group SpA (RN), with the ex- Department of Metallurgy of University of Bologna (ex-SMETEC).

REFERENCES

- [1] M. Koenig, M. Wessén, 2010 “Influence of alloying elements on microstructure and mechanical properties of CGI”, *Int. J. of Cast Met. Research*, **23**(3), pp. 97–110.
- [2] T. Sjoegren, I. L. Svensson, 2004. “Modelling the effect of graphite morphology on the modulus of elasticity in cast irons”, *Int. J. of Cast Met. Research*, **17**(5), pp. 271–279.
- [3] C. F. Yeung, H. Zhao, W. B. Lee, 1998. “The Morphology of Solidification of Thin-Section Ductile Iron Castings”, *Mater. Characterization*, **40**, pp. 201–208.

- [4] L. Alvarez et al. 2004, "Analysis of the influence of chemical composition on the mechanical and metallurgical properties of engine cylinder blocks in grey cast iron", *J. of Mater. Process. Technol.*, **153–154**, pp. 1039–1044.
- [5] R.A. Gonzaga, J.F. Carrasquilla. 2005, "Influence of an appropriate balance of the alloying elements on microstructure and on mechanical properties of nodular cast iron", *J. of Mater. Process. Technol.*, **162–163**, pp. 293–297.
- [6] M. Stefanescu. 2005, "Solidification and modelling of cast iron-A short history of the defining moments", *Mater. Sci. and Eng.*, **413–414A**, pp. 322–333.
- [7] M. Hafiz, 2001 "Mechanical properties of SG-iron with different matrix structure", *J. of Mater. Sci.*, **36**, pp. 1293–1300.
- [8] J. Sertucha, R. Suarez, J. Legazpi, 2006, "Prediction of solid state structure based on eutectic and eutectoid transformation parameters in spheroidal graphite irons", *Int. J. of Cast Met. Research*, **19(6)**, pp. 315–322.
- [9] J. Lacaze, V.Gerval, 1998, "Modelling of the eutectoid reaction in Spheroidal Graphite Fe-C-Si Alloys", *ISIJ International*, **38(7)**, pp. 714–722.
- [10] J. Lacaze, C. Wilson, C. Bak, 1994, "Experimental Study of the eutectoid transformation in Spheroidal Graphite Cast Iron", *Scandinavian J. of Metall.*, **23**, pp. 151–163.
- [11] J. Lacaze et al 1997, "The role of manganese and copper in the eutectoid transformation of spheroidal graphite cast iron", *Metall. and Mater. Trans.*, **28A**, pp. 2015–2025.
- [12] W. Oldfield, 1996, *ASM Trans.*, **59**, pp. 945.
- [13] M. Koenig, 2010, "Literature review of microstructure formation in compacted graphite Iron", *Int. J. of Cast Met. Research*, **23(3)**, pp. 185–192.
- [14] In Proceedings, J. Guo, M. T. Samonds, 2007, "Modelling and experimental validation of microstructure and mechanical properties of ductile during solidification", 5rd Decennial Int. Conf. on 'Solidification Processing', Sheffield, 447-451.
- [15] P. Donelan, 2000, "Modelling microstructural and mechanical properties of ferritic ductile cast iron", *Mater. Sci. and Tech.*, **16**, pp. 261–269.
- [16] G. Lesoult, M. Castro, 1998, "Solidification of spheroidal graphite cast irons – I. Physical Modelling", *Acta Mater*, **46(3)**, pp. 983–995.
- [17] J. Lacaze, M. Castro, 1998, "Solidification of spheroidal graphite cast irons – II. Numerical Simulation", *Acta Mater*, 1998, **46(3)**, pp. 997–1010.
- [18] G. Lacaze, 1998, "Solidification of spheroidal graphite cast irons – III. Microsegregation Related Effects", *Acta Mater*, 1999, Vol. **47(14)**, pp. 3779–3792.
- [19] P. Ferro et al, 2013, "Effect of inoculant containing rare earth metals and bismuth on microstructure and mechanical properties of heavy-section near-eutectic ductile iron castings", *J. of Mater. Process. Technol.*, **213**, pp. 1601–1608.
- [20] J. Sertucha et al., 2009, "Thermal Analysis of the formation of chunky graphite during solidification of heavy-section Spheroidal Graphite Iron Parts", *ISIJ Int.*, **49(2)**.
- [21] D. Emadi et al. 2005, "Applications of thermal analysis in quality control of solidification processes", *J. of Therm. Analysis and Calorimetry*, **81**, pp. 235–242.
- [22] M.J. Oliveira et al., 1999, "Evaluation of the heat of solidification of cast irons from continuous cooling curves", *J. of Mater. Process. Technol.*, **92–93**, pp. 25–30.

- [23] Misc, CompuTherm, “Information on the Thermodynamic Database for Iron-Based Alloy: Pan Iron 5”, Madison, USA, see also www.computherm.com.
- [24] Misc, Esi Group, 1996, “Procast Casting User Manual”, Version3.1.0, see also www.esi-group.com.
- [25] E. Fras, M. Gorny, 2008, “Eutectic cell and nodule count as the quality factors of cast iron”, *AFE Archives of Foundry Eng*, **8**(3), pp. 53–58.

APPLICATION OF AN AUTOMATIC REFINEMENT TECHNIQUE FOR B2-SPLINE FINITE ELEMENT MODELING OF THIN-WALLED MECHANICAL COMPONENTS

Antonio Carminelli
DIN, CIRI-MAM
University of Bologna, Italy
e-mail: antonio.carminelli@unibo.it

Giuseppe Catania
DIN, CIRI-MAM
University of Bologna, Italy
e-mail: giuseppe.catania@unibo.it

Abstract. This paper presents a technique for the automatic refinement of a B-spline degenerate shell finite element model for the vibration analysis of curved thin and moderately thick walled structures. A B2-spline finite element shell is defined as a generalization of the B-spline shell element. The proposed element makes it possible the finite element solution on a subdomain inside a selected element to be locally refined without affecting the discretization of the connected elements. A degrees of freedom constraint condition is imposed so that the C^0 continuity of the displacement field is restored on the boundaries of the refined subdomains. The choice of the elements to be refined, the position and the extension of the refining subdomains are carried out automatically by means of an iterative procedure. The adaptive technique adopts a point-wise error functional based on the system total potential energy density and a two-step process. The subdomains to be refined are identified by means of the functional value. The number of shape functions on a subdomain is iteratively increased until the difference of the total potential energy, calculated between two consecutive iterations, is below a user defined tolerance. A numerical example is presented in order to test the proposed approach. Strengths and limits of the approach are critically discussed.

1. INTRODUCTION

Several papers on Finite Element (FE) models based on B-spline shape functions were published in recent years [1-3]. B-spline FE models convergence properties were studied and good characteristics were shown for several applications such as vibration analysis [4-5]. Despite the benefits of using a B-spline FE model, the major drawbacks preventing its adoption, for the study of structures of practical interest, is the tensorial definition of a B-spline patch: a single

B-spline patch cannot be mapped to the complicated shapes often adopted for thin walled structures or components in industry.

In order to solve this problem, the most popular approach in literature is to define and adopt generalizations of the B-spline FE model in which the tensorial definition is not used, so that complicated shapes of thin-walled structures can be represented and local features can be effectively modeled. Dorfel et al. [6] and Bazilevs et.al [7] proposed using T-spline functions as FE shape functions. Efficient local refinement methods were proposed by making use of the T-spline knot-insertion algorithm proposed by Sederberg [8-9] for geometric applications. However, these refinement methods can insert some additional and unnecessary degrees of freedom (dofs) [6] in order to satisfy some constraints resulting from the Sederberg's T-spline definition. Moreover, the T-spline knot-insertion algorithm can lead to rational functions even if the input functions were polynomials, mainly because of the normalization technique adopted in the definition of the T-spline model. Very recently polynomial splines over Locally Refined (LR) box-partitions were presented in the literature [10]. The refinement is obtained by means of a combination of subdivision and scaling operators applied on the B-spline functions. The adoption of the LR-spline functions preserves some important properties of the B-spline functions and also fixes some drawbacks of T-spline model: the functions remain polynomial even after using the LR-spline knot-insertion algorithm and a smaller number of superfluous dofs are generated.

A common drawback of both T-spline and LR-spline n -variate ($n > 1$) models is that the shape functions are not defined as the tensorial product of univariate functions, as is the case with B spline models. For a bivariate, tensor product, p, q degree B-spline model, a point evaluation requires $p+q$ function evaluations, while for T-spline and LR-spline it requires, in general, $p \times q$ function evaluations, so that the computational cost of these latter models is generally heavier with respect to the former model, being for this reason generally preferred for finite element industrial applications.

A different approach in literature adopts a multi patch B-spline FE shell so as to model thin-walled structures with complex shapes. Using this approach, several B-spline FE shell with identical parameterization are connected as usual in FE technique. However, the refinement of a single patch remains a problem. In fact, the knot-insertion [11] procedure can be adopted for refining the solution in a patch, but augmented knot vectors associated to this patch generally result. As a matter of fact, the same procedure should be applied to every boundary patches so that continuity is preserved. In this way, a high increase of dofs generally results and a global refinement procedure is generally applied instead. With reference to a multi patch FE shell model, Kagan et al.[1-2] and Hughes et al.[3-5] proposed various techniques for local refinement of the finite element solution making use of the knot-insertion algorithm [11]. They proposed to eliminate the superfluous dofs, i.e. those being far from the subdomain to be refined, by employing some constraint equations [2,5]. However the procedure can be inefficient when a lot of dofs have to be eliminated.

The purpose of the present paper is the development of a procedure for the automatic refinement of a FE model based on a generalization of B-spline shape functions. The FE model adopts a multi patch approach, and the generalized B-spline shape functions are introduced in order to allow a single patch to be refined without affecting the other patches. The technique makes it possible the local refinement of the FE solution while maintaining the low

computational cost of the tensorial product of functions. An automatic refinement procedure based on the gradient of the energy density function is then proposed. The solution can be improved by locally refining the discretization on a limited sub-domain of a single patch without influencing adjacent patches. Numerical examples are used to test the proposed approach by comparing the obtained solutions with those obtained by means of standard FE models with fine mesh size and proved convergence.

2. THE LOCAL REFINABLE B2-SPLINE SHELL MODEL

A shell midsurface geometry can be efficiently described by means of B-spline functions mapping the parametric domain (ξ, η) (with $0 \leq \xi, \eta \leq 1$) into the surface $\Omega(\xi, \eta)$ in the tridimensional Euclidean space (x, y, z) [12]. A linear variation of both geometry and displacement is considered along the thickness by means of the ζ parametric coordinate. A generalized B-spline FE model with local refinement properties is introduced starting from the standard global B-spline model described in [13]. This model, indicated as B2-spline shell model from this point, can be defined by adding on $\Omega^* = [\xi_a, \xi_b] \times [\eta_a, \eta_b] \subset \Omega$, a tensorial set of polynomial B-spline functions, defined on local clamped knot vectors on the subdomain Ω^* , and normalizing all the functions with respect to their sum, so that, on the whole domain Ω , the displacement field is defined as in Eq.1:

$$\begin{aligned}
 \mathbf{d}(\xi, \eta, \zeta) = & \\
 = & \frac{\sum_{i=1}^m \sum_{j=1}^n N_i^p(\xi) N_j^q(\eta)}{\sum_{i=1}^m \sum_{j=1}^n N_i^p(\xi) N_j^q(\eta) + \sum_{r=1}^{m'} \sum_{s=1}^{n'} N_r^{*p}(\xi) N_s^{*q}(\eta)} \left(\begin{Bmatrix} u_{ij} \\ v_{ij} \\ w_{ij} \end{Bmatrix} + t_{ij} \left(\zeta - \frac{1}{2} \right) [-\mathbf{v}_{ij}^2 \quad \mathbf{v}_{ij}^1] \begin{Bmatrix} \alpha_{ij} \\ \beta_{ij} \end{Bmatrix} \right) + \\
 + & \frac{\sum_{r=1}^{m'} \sum_{s=1}^{n'} N_r^{*p}(\xi) N_s^{*q}(\eta)}{\sum_{i=1}^m \sum_{j=1}^n N_i^p(\xi) N_j^q(\eta) + \sum_{r=1}^{m'} \sum_{s=1}^{n'} N_r^{*p}(\xi) N_s^{*q}(\eta)} \left(\begin{Bmatrix} u_{rs} \\ v_{rs} \\ w_{rs} \end{Bmatrix} + t_{rs} \left(\zeta - \frac{1}{2} \right) [-\mathbf{v}_{rs}^2 \quad \mathbf{v}_{rs}^1] \begin{Bmatrix} \alpha_{rs} \\ \beta_{rs} \end{Bmatrix} \right) \quad (1)
 \end{aligned}$$

where:

- $N_i^p(\xi)$ and $N_r^{*p}(\xi)$ are the univariate normalized B-spline functions of degree p , defined with respect to the curvilinear coordinates ξ by means of the knot vectors, respectively:

$$\mathbf{U} = \{\xi_1, \dots, \xi_r\} = \left\{ \underbrace{0, \dots, 0}_{p+1}, \xi_{p+1}, \dots, \xi_{r-p-1}, \underbrace{1, \dots, 1}_{p+1} \right\}$$

and

$$\begin{aligned} \mathbf{U}^* &= \{\xi^*_1, \dots, \xi^*_{m'+p+1}\} = \\ &= \left\{ \underbrace{\xi_a, \dots, \xi_a}_{p+1}, \xi^*_{p+1}, \dots, \xi^*_{m'}, \underbrace{\xi_b, \dots, \xi_b}_{p+1} \right\} \end{aligned}$$

- $N_j^q(\eta)$ and $N_s^{*q}(\eta)$ are the univariate normalized B-spline functions of degree q , defined with respect to the curvilinear coordinates η by means of the knot vectors, respectively:

$$\mathbf{V} = \{\eta_1, \dots, \eta_r\} = \left\{ \underbrace{0, \dots, 0}_{q+1}, \eta_{q+1}, \dots, \eta_{s-q-1}, \underbrace{1, \dots, 1}_{q+1} \right\}$$

and

$$\begin{aligned} \mathbf{V}^* &= \{\eta^*_1, \dots, \eta^*_{n'+q+1}\} = \\ &= \left\{ \underbrace{\eta_a, \dots, \eta_a}_{q+1}, \eta^*_{q+1}, \dots, \eta^*_{n'}, \underbrace{\eta_b, \dots, \eta_b}_{q+1} \right\}. \end{aligned}$$

$(\mathbf{v}_{ij}^1, \mathbf{v}_{ij}^2, \mathbf{v}_{ij}^3)$ is an orthonormal set defined on the midsurface contro points (CPs) starting from the vector \mathbf{v}_{ij}^3 [13], u_{ij}, v_{ij}, w_{ij} are the three translational dofs, α_{ij} and β_{ij} are two rotational dofs for each CP.

As a consequence, because of the partition of unity property of B-spline functions [12], the following equation results:

$$\sum_{i=1}^m \sum_{j=1}^n N_i^p(\xi) N_j^q(\eta) = \sum_{r=1}^{m'} \sum_{s=1}^{n'} N_r^{*p}(\xi) N_s^{*q}(\eta) = 1 \quad (2)$$

so that the shape functions in Eq.1 are not modified, with respect to the unrefined model, outside Ω^* and are polynomial inside Ω^* . However, the displacement field in Eq.1 presents a discontinuity on the boundary of Ω^* . In order to impose the C^0 continuity of the displacement

field a procedure, based on the knot-insertion algorithm, is proposed. This procedure makes it possible to evaluate the displacement on the boundary of Ω^* as a linear combination of the unrefined shell model dofs. The proposed technique can be applied on a subdomain of either a B-spline shell model or a B2-spline shell model. Actually, both the position and the displacement models need to be B2-refined because the shell model is based on an isoparametric formulation. The B2-refining strategy is mainly the same for both the position and the displacement models, but a different transformation matrix is applied at the end of the algorithm.

For ease of presentation, the proposed technique will be applied to a generic parametric function $Q(\xi, \eta)$, Q being a scalar quantity representing one of the components of either the geometry position vector or the displacement vector of the unrefined B-spline shell patch:

$$Q(\xi, \eta) = \sum_{i=1}^m \sum_{j=1}^n N_i^p(\xi) N_j^q(\eta) P_{ij} = \mathbf{S} \cdot \mathbf{P} \quad (3)$$

The procedure allows the B2-refinement of Q within the parametric domain $\Omega(\xi, \eta) = [0, 1] \times [0, 1]$. Hence, the linear dependence on ζ can be omitted, for ease of explanation, without loss of generality. As a consequence of Eqs.1-2, the function Q can be expressed as:

$$Q(\xi, \eta) = \begin{cases} \mathbf{S} \cdot \mathbf{P} & \text{on } \Omega^L \\ \frac{\mathbf{S} \cdot \mathbf{P} + \mathbf{S}^* \cdot \mathbf{P}^*}{2} & \text{on } \Omega^* \end{cases} \quad (4)$$

where \mathbf{S}^* and \mathbf{P}^* are vector arrangement of, respectively, the B-spline functions and the control coefficients just introduced on Ω^* (Eq.1), and $\Omega^L = \{(x, y, z) \in \Omega : (x, y, z) \notin \Omega^*\}$.

The resulting function Q is generally discontinuous on the boundary of Ω^* . Nevertheless, if Q represents a component of the finite element model displacement vector, it needs to be at least C^0 . Some of the elements of \mathbf{P}^* , influencing the displacement vector value on the boundary of Ω^* , can then be evaluated as a linear combination of \mathbf{P} . In order to accomplish this task, the control coefficients \mathbf{P}^* are divided into:

- control coefficients P_b^* influencing the value of Q on the boundary of Ω^*
- control coefficients P_i^* influencing the value of Q on the interior of Ω^* only.

By means of the Oslo knot-insertion algorithm [11], it is possible to properly choose the values of either the P_b^* or all of the control coefficients \mathbf{P}^* , by means of a transformation matrix T . By applying the Oslo algorithm $p+1$ times both in ξ_a and in ξ_b , and $q+1$ times in η_a and η_b at least (more times if \mathbf{U}^* and \mathbf{V}^* have interior knots), a matrix T is obtained so that:

$$\mathbf{P}^* = \begin{Bmatrix} \mathbf{P}_b^* \\ \mathbf{P}_i^* \end{Bmatrix} = \mathbf{T} \cdot \mathbf{P} = \begin{Bmatrix} \mathbf{T}_b \\ \mathbf{T}_i \end{Bmatrix} \cdot \mathbf{P} \quad (5)$$

The continuity on the boundary of Ω^* is assured by adopting the following:

$$Q(\xi, \eta) = \begin{cases} \mathbf{S} \cdot \mathbf{P} & \text{on } \Omega^L \\ \frac{(\mathbf{S} + \mathbf{S}_b^* \cdot \mathbf{T}_b) \cdot \mathbf{P} + \mathbf{S}_i^* \cdot \mathbf{P}_i^*}{2} & \text{on } \Omega^* \end{cases} \quad (6)$$

where

$$\mathbf{S}^* = \{\mathbf{S}_b^* \quad \mathbf{S}_i^*\} \quad (7)$$

The displacement component can thus be expressed as:

$$Q(\xi, \eta) = \begin{cases} \mathbf{S} \cdot \mathbf{P} & \text{on } \Omega^L \\ \mathbf{SS} \cdot \begin{Bmatrix} \mathbf{P} \\ \mathbf{P}_i^* \end{Bmatrix} & \text{on } \Omega^* \end{cases} \quad (8)$$

where the dofs \mathbf{P}_i^* added on Ω^* are clearly outlined. As a consequence the displacement field on Ω^* , for a single B2-spline patch, can be finally defined as:

$$\begin{aligned} \begin{Bmatrix} d_x \\ d_y \\ d_z \end{Bmatrix} &= \hat{\mathbf{N}} \cdot \begin{Bmatrix} \boldsymbol{\delta} \\ \boldsymbol{\delta}_b^* \end{Bmatrix} = \hat{\mathbf{N}} \cdot \boldsymbol{\delta}_G \\ &= \sum_{k=1}^h SS_k(\xi, \eta) \left(\begin{Bmatrix} u_k \\ v_k \\ w_k \end{Bmatrix} + t_k \left(\zeta - \frac{1}{2} \right) [-\mathbf{v}_k^2 \quad \mathbf{v}_k^1] \begin{Bmatrix} \alpha_k \\ \beta_k \end{Bmatrix} \right) \end{aligned} \quad (9)$$

where $h = m \cdot n + (m' - 2) \cdot (n' - 2)$ and $SS_k(\xi, \eta)$ is the k-th functions in the vector \mathbf{SS} .

Equation 9 is the displacement field discretization adopted to obtain the equilibrium equations of the system by means of the principle of minimum total potential energy.

3. AUTOMATIC REFINEMENT PROCEDURE

The automatic refinement strategy is based on the gradient of the density of total potential energy. The potential energy, of internal and inertia forces, of a system modeled by means of the FE method is:

$$\begin{aligned}\Pi &= \delta_{\mathbf{G}}^T \cdot \mathbf{M} \cdot \ddot{\delta}_{\mathbf{G}} + \frac{1}{2} \delta_{\mathbf{G}}^T \cdot \mathbf{K} \cdot \delta_{\mathbf{G}} = \\ &= \delta_{\mathbf{G}}^T \cdot \int_{\Omega^p} \rho \hat{\mathbf{N}}^T \hat{\mathbf{N}} d\Omega \cdot \ddot{\delta}_{\mathbf{G}} + \frac{1}{2} \delta_{\mathbf{G}}^T \cdot \int_{\Omega^p} \mathbf{B}^T \mathbf{E} \mathbf{B} d\Omega \cdot \delta_{\mathbf{G}}\end{aligned}\quad (10)$$

where \mathbf{B} is the matrix defining the strain vector, \mathbf{E} is the constitutive matrix linking stress and strain vectors, Ω^p being the solid structure domain under analysis. By integrating only along the thickness, with a two points Gauss rule:

$$\Pi = \delta_{\mathbf{G}}^T \cdot \int_0^1 \int_0^1 (\tilde{\mathbf{m}}(\xi, \eta) \cdot \ddot{\delta}_{\mathbf{G}} + \frac{1}{2} \cdot \tilde{\mathbf{k}}(\xi, \eta) \cdot \delta_{\mathbf{G}}) \cdot d\xi \cdot d\eta \quad (11)$$

where

$$\tilde{\mathbf{k}}(\xi, \eta) = \sum_{i=1}^2 w_i \mathbf{B}^T(\xi, \eta, \zeta_i) \mathbf{E} \mathbf{B}(\xi, \eta, \zeta_i) \det J(\xi, \eta, \zeta_i) \quad (12)$$

and

$$\tilde{\mathbf{m}}(\xi, \eta) = \sum_{i=1}^2 w_i \rho \hat{\mathbf{N}}(\xi, \eta, \zeta_i)^T \hat{\mathbf{N}}(\xi, \eta, \zeta_i) \det J(\xi, \eta, \zeta_i) \quad (13)$$

Introducing the solution:

$$\begin{aligned}\delta_{\mathbf{G}} &= \Phi \cdot \mathbf{q}(t) = \sum_{r=1}^n \Phi_r \cdot Q_r \cdot e^{j\omega t} = \sum_{r=1}^n \Phi_r \cdot q_r \\ \ddot{\delta}_{\mathbf{G}} &= -\omega^2 \cdot \delta_{\mathbf{G}}\end{aligned}\quad (14)$$

in Eq.(12), the following equation holds:

$$\begin{aligned}\Pi &= \int_{\Omega} d\Pi = \int_0^1 \int_0^1 g(\xi, \eta) d\xi d\eta = \\ &= \int_0^1 \int_0^1 \left[\sum_{r=1}^n q_r^2 \Phi_r^T \left(\frac{1}{2} \tilde{\mathbf{k}}(\xi, \eta) - \omega^2 \tilde{\mathbf{m}}(\xi, \eta) \right) \Phi_r \right] d\xi d\eta\end{aligned}\quad (15)$$

As a consequence, the surface density of the total potential energy is:

$$g(\xi, \eta) = \sum_{r=1}^n \gamma_r \cdot \psi_r(\xi, \eta) \quad (16)$$

with $\gamma_r = q_r^2$ and:

$$\psi_r(\xi, \eta) = \boldsymbol{\Phi}_r^T \left(\frac{1}{2} \tilde{\mathbf{k}}(\xi, \eta) - \omega^2 \tilde{\mathbf{m}}(\xi, \eta) \right) \boldsymbol{\Phi}_r \quad (17)$$

The local indicator $LI(\xi, \eta)$ is defined:

$$\begin{aligned} LI(\xi, \eta) &= \left(\frac{\partial g}{\partial \xi} \right)^2 + \left(\frac{\partial g}{\partial \eta} \right)^2 = \\ &= \left(\sum_r \gamma_r \frac{\partial \psi_r}{\partial \xi} \right)^2 + \left(\sum_r \gamma_r \frac{\partial \psi_r}{\partial \eta} \right)^2 \end{aligned} \quad (18)$$

where only a few modes, $r \in [r_{\min}, r_{\max}]$, are generally taken into account.

A grid of LI values can be evaluated with a predefined uniform resolution on the patch to be refined: $n^\xi \cdot n^\eta$ evaluation points on the (ξ, η) parametric space result. Each calculated LI value is compared with the following value:

$$GI = \frac{\alpha}{n^\xi n^\eta} \sum_{i=1}^{n^\xi} \sum_{j=1}^{n^\eta} LI(\xi_i, \eta_j) \quad (19)$$

Each value $LI > GI$ identifies a point where a refinement could be needed. Rectangular sub-domains of the grid where condition $LI > GI$ applies are identified as well. Singular sub-domains including only one point are not considered by the refinement procedure. .

The B2-spline refinement algorithm is then applied on the identified subdomains. The number of added dofs are iteratively increased until, for more than one point on the refining subdomain at the k -th step, the following condition holds:

$$\frac{|GI^{k-1} - GI^k|}{GI^{k-1}} < \beta \quad (20)$$

where GI^k is the GI value calculated at the k -th step of the iterative procedure, and β is a user defined value used to stop the iteration if the percent change of the GI indicator, between two successive steps, is below the β value.

4. NUMERICAL TESTS AND RESULTS

4.1. L-shape plate clamped on four points

The free vibration behavior of a L-shaped plate is studied. The B-spline shell model is made by means of three B-spline patches, with $p=q=6$, connected as shown in Fig.1. Each patch is defined by means of 10×10 CPs and sixth degree B-spline functions defined on the knot vectors

$$\mathbf{U} = \mathbf{V} = \left\{ \underbrace{0, \dots, 0}_{7 \text{ times}}, 0.25, 0.5, 0.75, 1, \dots, 1 \right\}. \text{ The geometry position and the displacement field are}$$

C^0 on the boundaries connecting the patches. Moreover, the following parameters are used:

- Young's modulus $E = 2.1 \cdot 10^{11} \text{ N/m}^2$;
- Poisson's ratio $\nu = 0.3$;
- Density $\rho = 7850 \text{ kg/m}^3$;
- Longer edges $L = 2 \text{ m}$;
- Shorter edges $l = 1 \text{ m}$;
- Thickness $t = 0.05 \text{ m}$.

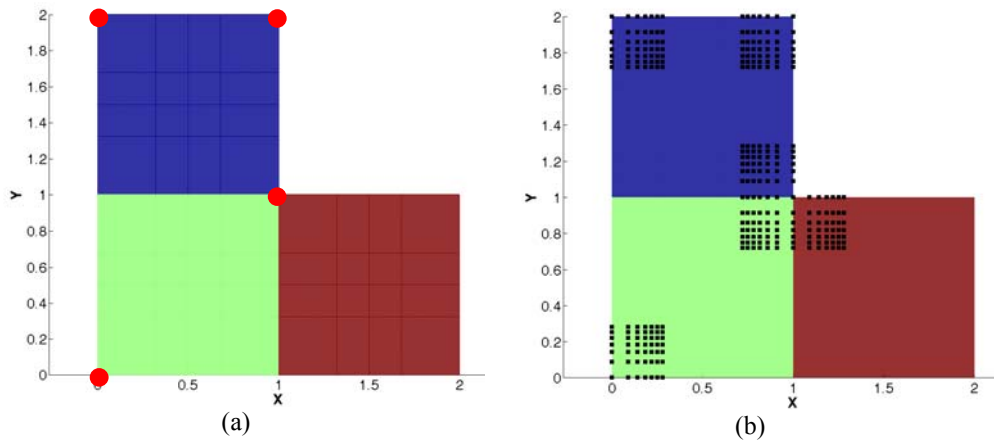


Figure 1. (a) L-plate geometry: the plate is fully constrained on the red dots. (b) The refined subdomains: black dots are the added CPs

Table 1. L-shape plate: numerical frequencies results (Hz).

Mode index	B-spline model unrefined (1400 dofs)	B2-spline model refined (2150 dofs)	Standard FEM coarse mesh (4905 dofs)	Standard FEM refined mesh (73605 dofs)
1	18.72	18.22	19.45	18.197
2	49.02	48.29	50.30	48.1
3	60.28	58.74	62.14	58.641
4	98.84	96.95	101.00	98.285
5	129.33	128.32	133.87	128.05
6	166.83	166.56	170.50	165.62
7	203.18	202.28	206.18	200.61
8	228.33	227.81	237.59	225.78

With respect to the coordinate system in Fig.1, the L-shaped plate are fully constrained on points (red dots in Fig.1 (a)):

$$V_1 = (1,1,0)$$

$$V_2 = (1,2,0)$$

$$V_3 = (0,2,0)$$

$$V_4 = (0,0,0)$$

A singularity is moreover expected in the corner V_1 [24], with respect to some free vibration mode shapes. Hence, a refinement is applied on each patch near the V_i ($i=1,\dots,4$) points by adopting $m'=n'=7$: this is the minimum allowable number of CPs that can be used since $p=q=6$. The refined subdomain are:

1. patch 1 (upper left in Fig.1):
REF1= $[0.8,1] \times [0,0.2]$

- REF2=[0, 0.2]×[0.8,1]
 REF3=[0.8,1]×[0.8,1]
 2. Patch 2 (bottom left in Fig.1):
 REF4=[0.8,1]×[0.8,1]
 REF5=[0, 0.2]×[0, 0.2]
 3. Patch 3 (bottom right in Fig.1):
 REF6=[0, 0.2]×[0.8,1]

A plot of the refined structure is shown in Fig.1 (b), where the added CPs (black dots) of the refined subdomains are visible.

The first eight natural frequencies of the refined B-spline L-shaped structure are reported in Table 1 where the natural frequencies of the unrefined B-spline L-shaped plate and of a standard polynomial 8-node shell finite element with both a coarse and converged solution, used as a reference, are also reported. The plot of the fifth mode shape is reported in Fig.2. Fig.3 shows a zoom of the refined zone where the continuity of the displacement field is clearly visible.

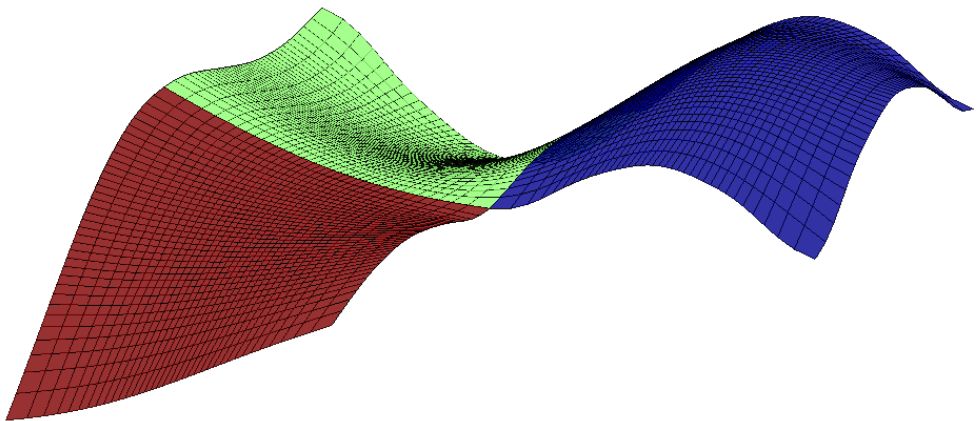


Figure 2: L-plate: fifth modeshape.

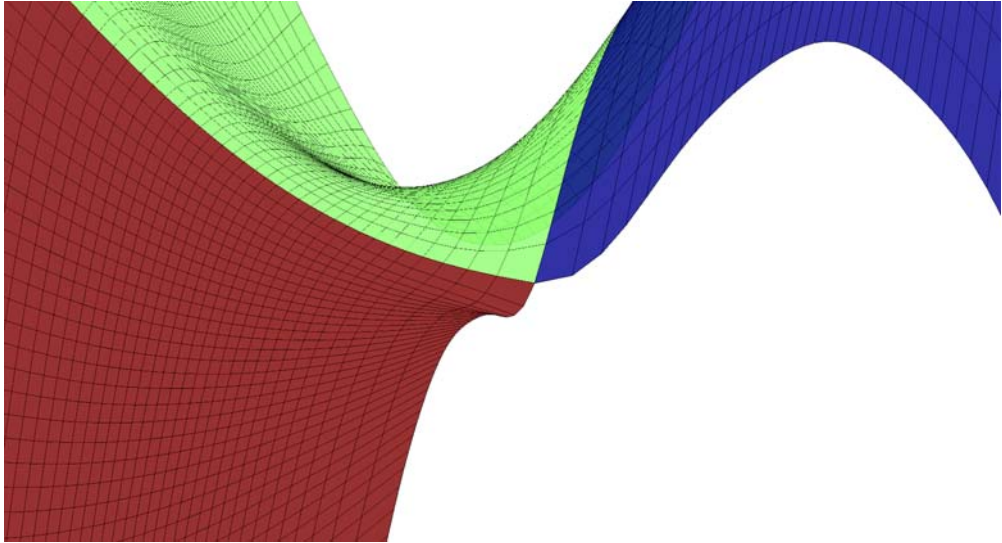


Figure 3: L-plate: close view of the fifth modeshape near the refined corner.

4.2. Automatic refinement of a curved shell roof

An example case is considered for testing the automatic refinement procedure. The example concerns a curved roof with a circular section and a small cutout (Fig.4). The roof is fully constrained on one edge ($y=1$) and loaded with a constant pressure on the subdomain Ω^F delimited by the black lines in Fig.4. A stress singularity is expected near the corner C (red circle in Fig.4).

The B-spline shell model is made by means of four B-spline patches, connected as shown in Fig.4. Each patch is defined by means of 7×7 CPs and sixth degree B-spline functions defined on the knot vectors $\mathbf{U} = \mathbf{V} = \left\{ \underbrace{0, \dots, 0}_7, \underbrace{1, \dots, 1}_7 \right\}$. A discretization made of 6×6 and fifth degree B-spline functions revealed the ineffectiveness of the LI indicator to locate high gradient of the energy if a little number of dofs is adopted to model the problem.

The geometry position vector and the displacement field are C^0 on the boundary connecting the patches. Moreover, the following parameters are used:

- Young's modulus $E = 2.3 \cdot 10^9 \text{ N/m}^2$;
- Poisson's ratio $\nu=0.35$;

- Density $\rho= 1000 \text{ kg/m}^3$;
- Thickness $t= 0.005\text{m}$.

The automatic refinement strategy is adopted in a forced vibration problem. A uniform pressure $p=1000 \text{ N/m}^2$, directed along the negative z axis, is applied inside the domain Ω^F , corresponding to half the domain of the upper-left patch. The forcing function Φ is:

$$\Phi = \begin{Bmatrix} 0 \\ 0 \\ -p \end{Bmatrix} e^{j\omega t}$$

with $\omega=16\text{Hz}$. With this forcing frequency, given the starting eigensolutions in Tab.2, an approximated solution can be obtained by considering only the fourth mode in Eqs.18-20, so that $\gamma_4=6.8121\text{e-}4$ results. The model damping is not considered in the example but real modal damping can be easily included.

The adaptive refinement procedure is started using $\alpha=20$, $n^x=n^y=40$ and $\beta=0.05$ (Eqs.19-20). With these values the subdomains to be refined near the point C are identified (Fig.5) so that the iterative part of the procedure, in which the dofs are added at each step, can be started.

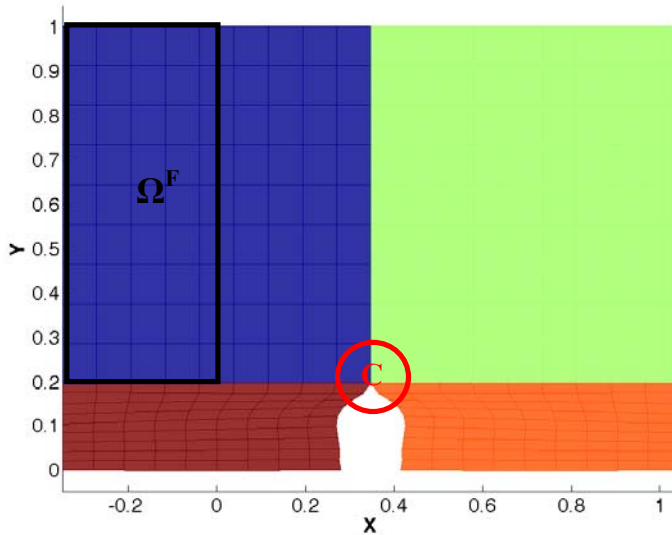


Figure 4. Top view of the shell roof: the forcing pressure is applied on Ω^F (bounded by black lines) and a singularity is expected near the point C (red circle).

The procedure added the dofs on four subdomains near the point C (Fig.6) whose parametric coordinates $[\xi_0, \xi_1] \times [\eta_0, \eta_1]$ are:

- Patch 1 $[0.8, 1] \times [0.8, 1]$
- Patch 2 $[0, 0.3] \times [0.575, 1]$
- Patch 3 $[0.8, 1] \times [0, 0.2]$
- Patch 4 $[0, 0.3] \times [0, 0.425]$

The eigensolutions after the refinement are reported in Tab.2: the fourth mode shows a good improvement.

Tab2. Numerical frequencies results (Hz) for the shell roof model.

Mode index	B-spline unrefined (875 dofs)	B2-spline refined (3315 dofs)
1	6.7310	6.4986
2	6.7581	6.7339
3	9.8154	9.8531
4	15.603	14.451
5	20.140	19.691
6	20.193	20.130
7	33.487	30.418
8	35.185	32.593
9	35.777	35.603
10	39.979	39.904

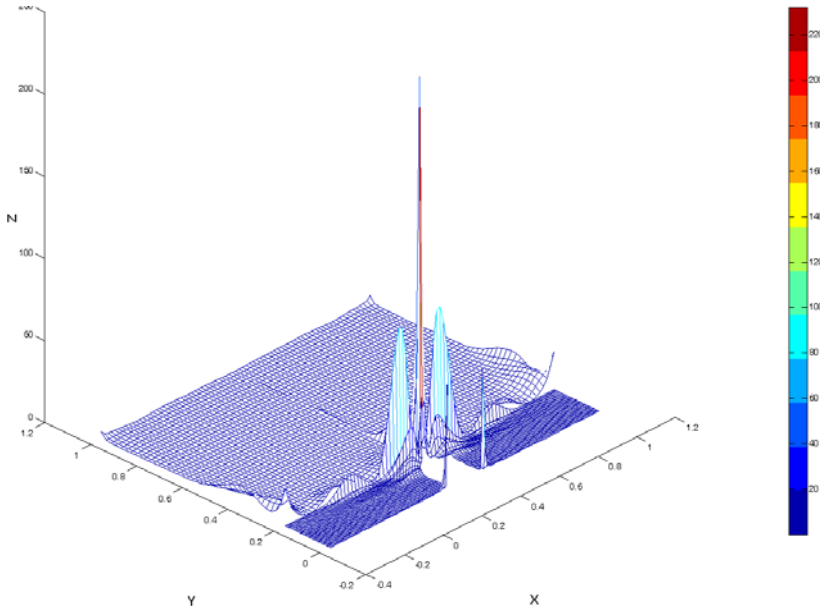


Figure 5. Plot of the local indicator LI .

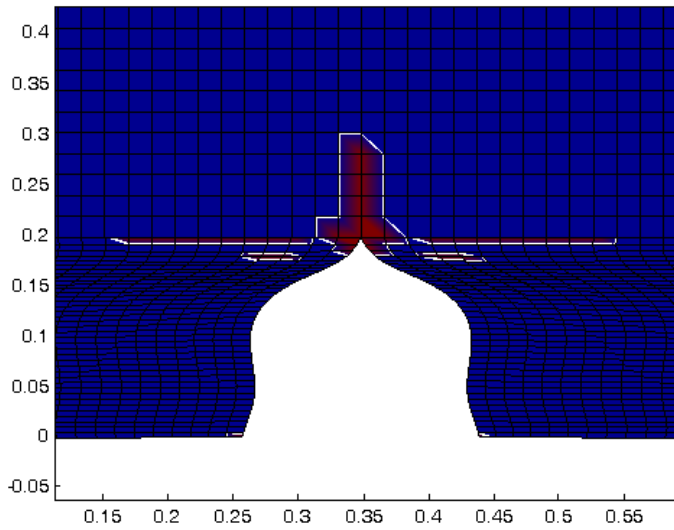


Figure 6. In red the subdomain to be refined.

5. CONCLUSIONS

An FE technique for modeling shell structures, based on a generalization of B-spline functions, was developed and an algorithm for the automatic refinement of this proposed FE model was presented. As a main benefit, the presented FE technique makes it possible a structure to be modeled by means of several connected patches, as in standard FE shell technique. The refinement of a single patch is also possible without affecting the discretization of connected patches. Moreover, the technique makes it possible a very small subdomain inside a single patch to be refined without inserting unwanted additional dofs, as it may happen with the application of the T-spline refinement algorithm. The automatic refinement procedure adopts a local indicator LI , based on the gradient of the total energy density function, in order to locate the subdomains to be refined and a global indicator GI in order to stop the iterative procedure. The proposed numerical examples showed the validity of the refinement technique and of the automatic procedure as well. However, the second example showed that the LI functional may not perform correctly if a small number of dofs are used in the unrefined model. This can happen whenever the starting solution is not able to model high gradients of the total energy density function. The impact of the starting solution choice will be investigated in future studies as well as the optimal choice of the α and β values.

ACKNOWLEDGEMENTS

The present study was supported by the Regione Emilia-Romagna, Progetto Tecnopolo POR FESR 2007-2013, Asse 1 Attività I.1.1.

REFERENCES

- [1] Kagan, P., Fischer, A., 2000, "Integrated mechanically based CAE system using B-Spline finite elements", *Computer-Aided Design*, **32**, pp. 539-552.
- [2] Kagan, P., Fischer, A., Bar-Yoseph, P.Z., 2003, "Mechanically based models: Adaptive refinement for B-spline finite element", *International Journal for Numerical Methods in Engineering*, **57**, pp. 1145-1175.
- [3] Hughes, T.J.R., Cottrell, J.A., Bazilevs, Y., 2005, "Isogeometric analysis: CAD, finite elements, NURBS, exact geometry and mesh refinement", *Computer methods in Applied Mechanical Engineering*, **194**, pp. 4135-4195.
- [4] Cottrell, J.A., Reali, A., Bazilevs, Y., Hughes, T.J.R., 2006, "Isogeometric analysis of structural vibrations", *Computer methods in Applied Mechanical Engineering*, **195**, pp. 5257-5296.
- [5] Cottrell, J.A., Hughes, T.J.R., Reali, A., 2007, "Studies of refinement and continuity in isogeometric analysis", *Computer Methods in Applied Mechanics and engineering*, **196**:4160–4183.
- [6] Dörfel, M.R., Jüttler, B., Simeon, B., 2010, "Adaptive Isogeometric Analysis by Local h-Refinement with T-Splines", *Computer Methods in Applied Mechanics and Engineering*, **199**(5-8), pp.264-275.

- [7] Bazilevs, Y., Calo, V.M., Cottrell, J.A., Evans, J.A., Hughes, T.J.R., Lipton, S., Scott, M.A., Sederberg, T.W., 2010, "Isogeometric analysis using T-splines", *Computer Methods in Applied Mechanics and Engineering*, **199**(5-8), pp. 229-263.
- [8] Sederberg, T.W., Zheng, J., Bakenov, A., Nasri, A., 2003, "T-splines and TNURCCs", *ACM Transactions on Graphics* **22** (3), pp. 161–172.
- [9] Sederberg, T.W., Cardon, D.L., Finnigan, G.T., North, N.S., Zheng, J., Lyche, T., 2004, "T-spline simplification and local refinement", *ACM Transactions on Graphics* **23** (3), pp. 276–283.
- [10] Dokken, T., Lyche, T., 2013, "Polynomial splines over locally refined box-partitions", *Computer Aided Geometric Design*, 30(3), pp. 331-356.
- [11] Goldman, R.N., Lyche, T., 1993, *Knot Insertion and Deletion Algorithms for B-Spline Curves and Surfaces*, 1993, SIAM, Philadelphia.
- [12] Piegl, L., Tiller, W., 1997, *The NURBS book*. 2nd ed. Springer.
- [13] Carminelli A., Catania G., "B-spline laminate shell finite element updating by means of FRF measurements". *Modal Analysis Topics*, Volume 3, Conference Proceedings of the Society for Experimental Mechanics Series 2011, pp- 127-139.

NONLINEAR VIBRATIONS AND ENERGY DISTRIBUTION OF CARBON NANOTUBES

Angelo Oreste Andrisano
*Department of Engineering “Enzo Ferrari”,
University of Modena and Reggio Emilia, Italy
E-mail: angelooreste.andrisano@unimore.it*

Leonid I. Manevitch
*N.N. Semenov Institute of Chemical Physics,
Russian Academy of Sciences, Moscow, Russia
E-mail: lmanev@chph.ras.ru*

Francesco Pellicano
*Department of Engineering “Enzo Ferrari”,
University of Modena and Reggio Emilia, Italy
E-mail: francesco.pellicano@unimore.it*

Matteo Strozzi
*Department of Engineering “Enzo Ferrari”,
University of Modena and Reggio Emilia, Italy
E-mail: matteo.strozzi@unimore.it*

Abstract. *The nonlinear vibrations of Single-Walled Carbon Nanotubes are analysed. The Sanders-Koiter thin shell theory is applied in order to obtain the elastic strain and kinetic energy. The carbon nanotube deformation is described in terms of axial, circumferential and radial displacement fields. The theory considers geometric nonlinearities due to large amplitude of vibration. The displacement fields are expanded by means of a double series based on harmonic functions for the circumferential variable and Chebyshev polynomials for the longitudinal variable. The Rayleigh-Ritz method is applied to obtain approximate natural frequencies and mode shapes. Free boundary conditions are considered. In the nonlinear analysis, the three displacement fields are re-expanded by using approximate eigenfunctions. An energy approach based on the Lagrange equations is then considered to obtain a set of nonlinear ordinary differential equations. The total energy distribution of the shell is studied by considering combinations of different vibration modes. The effect of the conjugate modes is analysed.*

Keywords: *nonlinear vibrations, energy distribution, carbon nanotubes*

1. INTRODUCTION

Carbon Nanotubes were discovered in 1991 by Iijima [1], who first analysed the synthesis of molecular carbon structures in the form of fullerenes and reported the preparation of the carbon nanotubes, as helical microtubules of graphitic carbon.

Rao et al. [2] studied the vibrations of SWNTs by Raman scattering experimental techniques with laser excitation wavelengths in the range of the nanometres. They observed Raman peaks, which correspond to vibrational modes of the nanotubes.

Gupta et al. [3] simulated the mechanical behaviour of SWNTs with free edges by using the MD potential. They considered the effect of the chirality and geometry on the natural frequencies of longitudinal, torsional and inextensional modes.

Arghavan and Singh [4] carried out a numerical study on the free and forced vibrations of SWNTs considering the FE method. They studied different boundary conditions, obtaining natural frequencies, mode shapes, time histories and spectra.

Wang et al. [5] examined applicability and limitations of different simplified models of elastic cylindrical shells for general cases of static buckling and free vibrations. They considered Flugge, Donnell thin shell and Donnell shallow shell models.

Strozzi et al. [6] considered the linear vibrations of SWNTs for different boundary conditions in the framework of the Sanders-Koiter thin shell theory. They studied several types of nanotubes by varying aspect ratio and chirality in a wide range of the natural frequency spectrum.

In the present paper, the nonlinear vibrations of SWNTs are analysed. The Sanders-Koiter thin shell theory is applied. The displacement fields are expanded by means of a double series based on harmonic functions for the circumferential variable and Chebyshev polynomials for the longitudinal variable.

The Rayleigh-Ritz method is applied to obtain approximate natural frequencies and mode shapes. Free boundary conditions are considered.

In the nonlinear analysis, the three displacement fields are re-expanded by using approximate eigenfunctions.

The Lagrange equations are considered in order to obtain a set of nonlinear ordinary differential equations.

The total energy distribution is studied by considering different combined modes. The effect of the conjugate modes participation on the energy distribution is analysed.

2. SANDERS-KOITER THEORY

In Figure 1, a circular cylindrical shell having radius R , length L and thickness h is shown; a cylindrical coordinate system ($O; x, \theta, z$) is considered to take advantage from the axial symmetry of the structure, the origin O of the reference system is located at the centre of one end of the cylindrical shell.

Three displacement fields are represented: longitudinal $u(x, \theta, t)$, circumferential $v(x, \theta, t)$ and radial $w(x, \theta, t)$, where the radial displacement field w is considered positive outward, (x, θ) are the longitudinal and angular coordinates of an arbitrary point on the middle surface, z is the radial coordinate along the thickness h and t denotes the time variable.

Parameter ($\eta = x/L$) is the nondimensional longitudinal coordinate of the shell, ($\beta = h/L$) denotes a nondimensional parameter and τ is the nondimensional time variable, which is obtained by introducing a reference natural frequency ω_0 .

3. ELASTIC STRAIN ENERGY

The nondimensional elastic strain energy of a cylindrical shell, by neglecting the transverse normal stress σ_z (plane stress) and shear strains ($\gamma_{xz}, \gamma_{\theta z}$) (Kirchhoff's hypothesis), is written in the form

$$\begin{aligned} \tilde{U} = & \frac{1}{2} \int_0^1 \int_0^{2\pi} \left(\tilde{\varepsilon}_{x,0}^2 + \tilde{\varepsilon}_{\theta,0}^2 + 2\nu\tilde{\varepsilon}_{x,0}\tilde{\varepsilon}_{\theta,0} + \frac{(1-\nu)}{2}\tilde{\gamma}_{x\theta,0}^2 \right) d\eta d\theta \\ & + \frac{1}{2} \frac{\beta^2}{12} \int_0^1 \int_0^{2\pi} \left(\tilde{k}_x^2 + \tilde{k}_\theta^2 + 2\nu\tilde{k}_x\tilde{k}_\theta + \frac{(1-\nu)}{2}\tilde{k}_{x\theta}^2 \right) d\eta d\theta \end{aligned} \quad (1)$$

where $(\tilde{\varepsilon}_{x,0}, \tilde{\varepsilon}_{\theta,0}, \tilde{\gamma}_{x\theta,0})$ denote the nondimensional middle surface strains and $(\tilde{k}_x, \tilde{k}_\theta, \tilde{k}_{x\theta})$ denote the nondimensional middle surface changes in curvature and torsion.

4. KINETIC ENERGY

The nondimensional kinetic energy of a cylindrical shell is given by

$$\tilde{T} = \frac{1}{2} \int_0^1 \int_0^{2\pi} (\tilde{u}^2 + \tilde{v}^2 + \tilde{w}^2) d\theta d\eta = \frac{1}{2} \int_0^1 \int_0^{2\pi} \left[\left(\frac{d\tilde{u}}{d\tau} \right)^2 + \left(\frac{d\tilde{v}}{d\tau} \right)^2 + \left(\frac{d\tilde{w}}{d\tau} \right)^2 \right] d\theta d\eta \quad (2)$$

where $(\tilde{u}, \tilde{v}, \tilde{w})$ denote the nondimensional displacement fields and $(\tilde{u}', \tilde{v}', \tilde{w}')$ denote the nondimensional velocity fields.

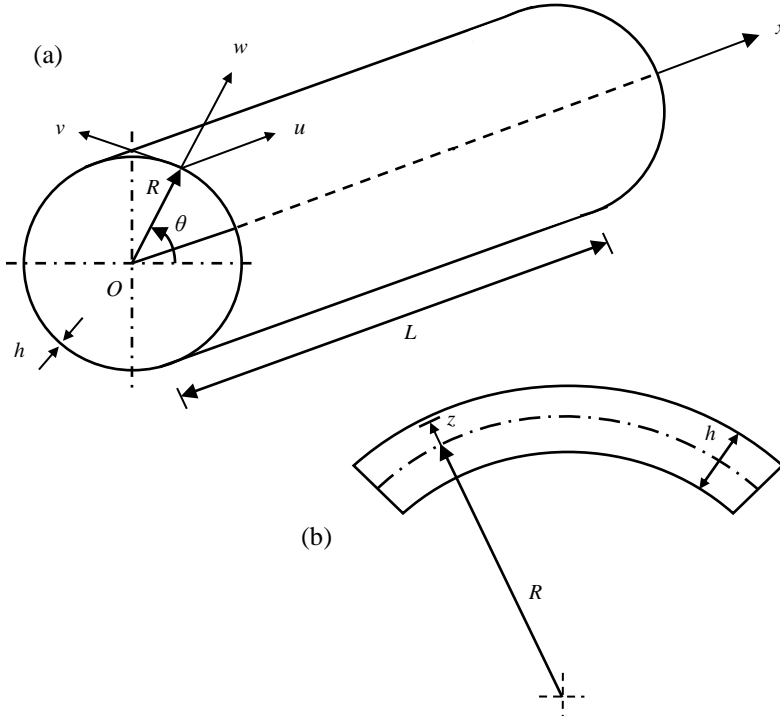


Figure 1. Geometry of the shell. (a) Complete shell; (b) cross-section of the shell surface.

5. LINEAR VIBRATION ANALYSIS

A modal vibration can be written in the form

$$\tilde{u}(\eta, \theta, \tau) = \tilde{U}(\eta, \theta)\varphi(\tau) \quad \tilde{v}(\eta, \theta, \tau) = \tilde{V}(\eta, \theta)\varphi(\tau) \quad \tilde{w}(\eta, \theta, \tau) = \tilde{W}(\eta, \theta)\varphi(\tau) \quad (3)$$

where $\tilde{U}(\eta, \theta)$, $\tilde{V}(\eta, \theta)$, $\tilde{W}(\eta, \theta)$ is the linear mode shape previously obtained and $\varphi(\tau)$ is the nondimensional time law.

The mode shape is expanded by means of a double mixed series in terms of Chebyshev polynomials $T_m^*(\eta)$ in the axial direction and harmonic functions ($\cos n\theta$, $\sin n\theta$) in the circumferential direction

$$\tilde{U}(\eta, \theta) = \sum_{m=0}^{M_u} \sum_{n=0}^N \tilde{U}_{m,n} T_m^*(\eta) \cos n\theta \quad (4)$$

$$\tilde{V}(\eta, \theta) = \sum_{m=0}^{M_v} \sum_{n=0}^N \tilde{V}_{m,n} T_m^*(\eta) \sin n\theta \quad (5)$$

$$\tilde{W}(\eta, \theta) = \sum_{m=0}^{M_w} \sum_{n=0}^N \tilde{W}_{m,n} T_m^*(\eta) \cos n\theta \quad (6)$$

where $T_m^* = T_m(2\eta - 1)$, m denotes the Chebyshev polynomials order and n is the number of nodal diameters.

6. BOUNDARY CONDITIONS

Free-free boundary conditions are given by

$$\tilde{N}_x = 0 \quad \tilde{N}_{x\theta} + \tilde{M}_{x\theta} = 0 \quad \tilde{Q}_x + \frac{\partial \tilde{M}_{x\theta}}{\partial \theta} = 0 \quad \tilde{M}_x = 0 \quad \eta = 0, 1 \quad (7)$$

where the nondimensional force ($\tilde{N}_x, \tilde{N}_{x\theta}, \tilde{Q}_x$) and moment ($\tilde{M}_x, \tilde{M}_{x\theta}$) resultants are

$$\begin{aligned} \tilde{N}_x &= \tilde{\varepsilon}_{x,0} + \nu \tilde{\varepsilon}_{\theta,0} & \tilde{N}_{x\theta} &= \frac{(1-\nu)}{2} \tilde{\gamma}_{x\theta,0} & \tilde{M}_x &= \frac{\beta^2}{12} (\tilde{k}_x + \nu \tilde{k}_\theta) \\ \tilde{M}_{x\theta} &= \frac{\beta^2}{12} \frac{(1-\nu)}{2} \tilde{k}_{x\theta} & \tilde{Q}_x &= \frac{\beta^2}{12} \left[\tilde{k}_{x,x} + \nu \tilde{k}_{\theta,x} + \frac{(1-\nu)}{2} \tilde{k}_{x\theta,\theta} \right] \end{aligned} \quad (8)$$

7. RAYLEIGH RITZ METHOD

The maximum number of variables needed for describing a general vibration mode with n nodal diameters is obtained by the relation ($N_p = M_u + M_v + M_w + 3 - p$), where ($M_u = M_v = M_w$) denote the order of the Chebyshev orthogonal polynomials and p describes the number of equations for the boundary conditions to be respected.

For a multi-mode analysis with different values of nodal diameters n , the number of degrees of freedom of the system is computed by the relation ($N_{max} = N_p \times (N + 1)$), where N represents the maximum value of the nodal diameters n considered.

Equations (3) are inserted into the expressions of the potential energy \tilde{U} (1) and kinetic energy \tilde{T} (2) to compute the Rayleigh quotient $R(\tilde{q}) = \tilde{U}_{\max} / \tilde{T}^*$, where $\tilde{U}_{\max} = \max(\tilde{U})$ is the maximum of the potential energy in a modal vibration, $\tilde{T}^* = \tilde{T}_{\max} / \omega^2$, $\tilde{T}_{\max} = \max(\tilde{T})$ is the maximum of the kinetic energy during a modal vibration, ω is the circular frequency of the motion $\varphi(\tau) = \cos \omega \tau$ and $\tilde{q} = [\dots, \tilde{U}_{m,n}, \tilde{V}_{m,n}, \tilde{W}_{m,n}, \dots]^T$ is the vector of the unknowns.

After imposing the stationarity to the Rayleigh quotient, the following eigenvalue problem is obtained

$$(-\omega^2 \tilde{M} + \tilde{K})\tilde{q} = \mathbf{0} \quad (9)$$

which furnishes approximate natural frequencies and mode shapes.

The approximate mode shape of the j -th mode is given by equations (4-6), where the coefficients $(\tilde{U}_{m,n}, \tilde{V}_{m,n}, \tilde{W}_{m,n})$ are substituted with $(\tilde{U}_{m,n}^{(j)}, \tilde{V}_{m,n}^{(j)}, \tilde{W}_{m,n}^{(j)})$, as the components of the j -th eigenvector \tilde{q}_j of the equation (9).

The vector function

$$\tilde{Q}^{(j)}(\eta, \theta) = [\tilde{U}^{(j)}(\eta, \theta), \tilde{V}^{(j)}(\eta, \theta), \tilde{W}^{(j)}(\eta, \theta)]^T \quad (10)$$

is the approximation of the j -th eigenfunction vector of the original problem.

8. NONLINEAR VIBRATION ANALYSIS

The three displacement fields $\tilde{u}(\eta, \theta, \tau)$, $\tilde{v}(\eta, \theta, \tau)$, $\tilde{w}(\eta, \theta, \tau)$ are expanded by using both the linear mode shapes $\tilde{U}(\eta, \theta)$, $\tilde{V}(\eta, \theta)$, $\tilde{W}(\eta, \theta)$ previously obtained and the conjugate mode shapes $\tilde{U}_c(\eta, \theta)$, $\tilde{V}_c(\eta, \theta)$, $\tilde{W}_c(\eta, \theta)$ in the form

$$\begin{aligned} \tilde{u}(\eta, \theta, \tau) &= \sum_{j=1}^{N_u} \sum_{n=1}^N [\tilde{U}^{(j,n)}(\eta, \theta) \varphi_{u,j,n}(\tau) + \tilde{U}_c^{(j,n)}(\eta, \theta) \varphi_{u,j,n,c}(\tau)] \\ \tilde{v}(\eta, \theta, \tau) &= \sum_{j=1}^{N_v} \sum_{n=1}^N [\tilde{V}^{(j,n)}(\eta, \theta) \varphi_{v,j,n}(\tau) + \tilde{V}_c^{(j,n)}(\eta, \theta) \varphi_{v,j,n,c}(\tau)] \\ \tilde{w}(\eta, \theta, \tau) &= \sum_{j=1}^{N_w} \sum_{n=1}^N [\tilde{W}^{(j,n)}(\eta, \theta) \varphi_{w,j,n}(\tau) + \tilde{W}_c^{(j,n)}(\eta, \theta) \varphi_{w,j,n,c}(\tau)] \end{aligned} \quad (11)$$

The Lagrange equations of motion for free vibrations are expressed in the form

$$\frac{d}{d\tau} \left(\frac{\partial \tilde{L}}{\partial \dot{\tilde{q}}_i} \right) - \frac{\partial \tilde{L}}{\partial \tilde{q}_i} = 0 \quad i \in [1, N_{\max}] \quad (\tilde{L} = \tilde{T} - \tilde{U}) \quad (12)$$

Using the Lagrange equations (12), a set of nonlinear ordinary differential equations is then obtained; such system is then solved by using numerical methods.

Table 1. Effective and equivalent parameters of the Single-Walled Carbon Nanotube [5].

Effective thickness h_0 (nm)	0.10 ÷ 0.15
Equivalent thickness h (nm)	0.066
Effective Young's modulus E_0 (TPa)	1.0 ÷ 2.0
Equivalent Young's modulus E (TPa)	5.5
Effective Poisson's ratio ν_0	0.12 ÷ 0.28
Equivalent Poisson's ratio ν	0.19
Surface density of graphite σ (kg/m ²)	7.718×10^{-7}
Equivalent mass density ρ (kg/m ³)	11700

9. NUMERICAL RESULTS

In order to study the discrete carbon nanotube as a continuum elastic thin shell, equivalent parameters must be considered [5]. These parameters are reported in Table 1.

The present model is then validated with the molecular dynamics data available in the literature [3]; the results reported in Table 2 show that the present model is accurate.

In Figures 2 (a-f), three mode shapes of a free-free carbon nanotube are presented, such modes are considered for the development of the semi-analytic nonlinear model of the carbon nanotube in the re-expansion of Equation (11).

In Figures 3-5, energy distributions in linear and nonlinear field are shown. Different modes are studied. The carbon nanotube is unwrapped on a plane to allow the energy representation. The damping is not considered and the total energy is constant (integral of density over the surface).

The sequence of Figures 3 (a-d) shows the distribution of the energy density [Jm⁻²] in linear field for the modes (0,2), (2,2) in a time range.

The analysis of the total energy distribution over the nanotube surface shows a periodicity along the circumferential direction. Moreover, the energy is distributed symmetrically with respect to the longitudinal direction because two symmetric modes (0,2) and (2,2) are combined.

Figures 4 (a-d) show the distribution of the energy density in nonlinear field for the combined modes (0,2) and (2,2) in a time range. By comparing the linear and nonlinear analyses (with the same modal initial conditions), the nonlinear distribution evolves in a more complex pattern, where the total energy periodicity and symmetry are preserved along the circumferential and longitudinal direction, respectively.

Table 2. Natural frequencies of the radial breathing mode ($j = 0, n = 0$): comparisons between Sanders-Koiter theory (SKT) and Molecular Dynamics Simulations (MDS).

Natural frequency (THz)			Difference %
(r, s)	SKT - Present model	MDS - Ref. [3]	
(10, 0)	8.966	8.718	2.84
(6, 6)	8.636	8.348	3.45
(12, 0)	7.478	7.272	2.83
(7, 7)	7.399	7.166	3.25
(8, 8)	6.473	6.275	3.15
(14, 0)	6.414	6.235	2.87
(16, 0)	5.606	5.455	2.77
(10, 10)	5.184	5.026	3.14

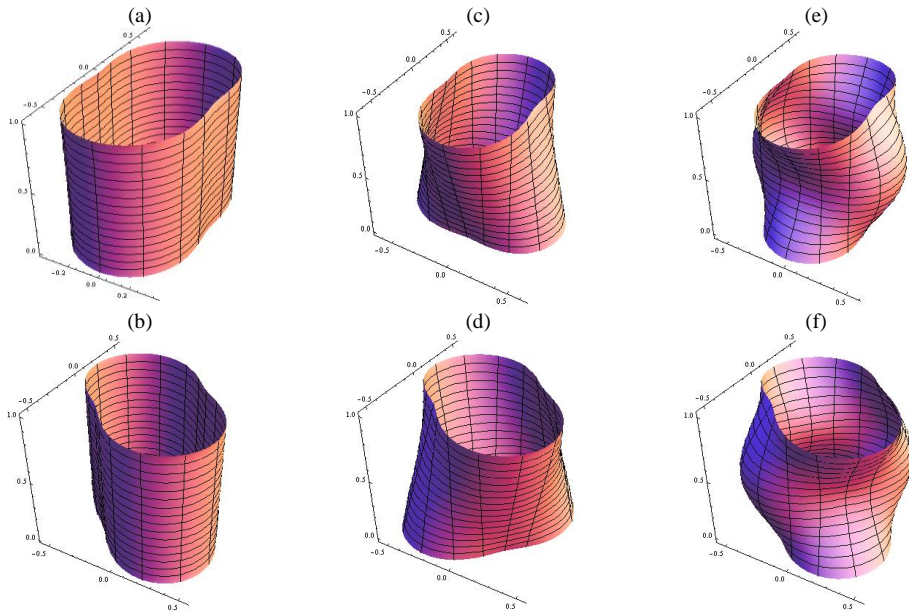


Figure 2. Mode shapes of the SWNT ($r = 10$, $s = 0$, $L = 10$ nm). Equivalent parameters. Free edges. Conjugate modes. (a),(b) Modes (0,2). (c),(d) Modes (1,2). (e),(f) Modes (2,2).

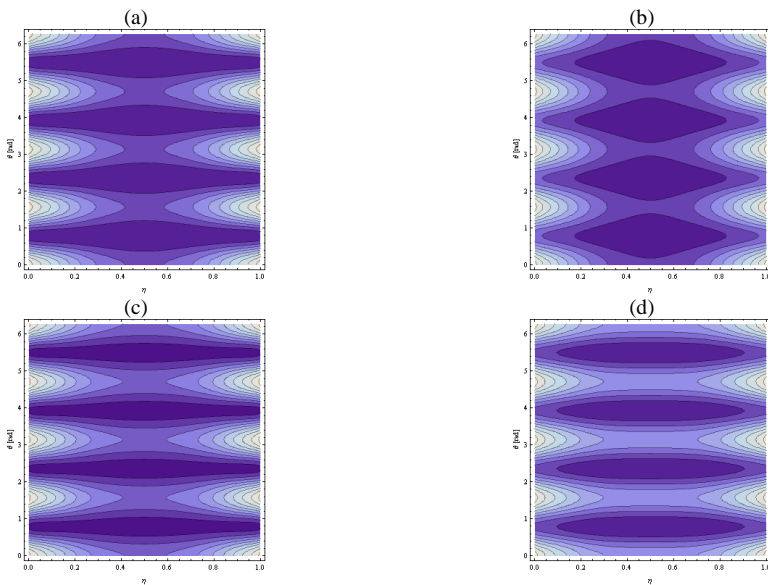


Figure 3. Total energy distribution $\tilde{E}(\eta, \theta, \tau)$. Combined modes (0,2), (2,2). Linear analysis. (a) $\tau = 0.00$. (b) $\tau = 1.26$. (c) $\tau = 2.51$. (d) $\tau = 3.77$.

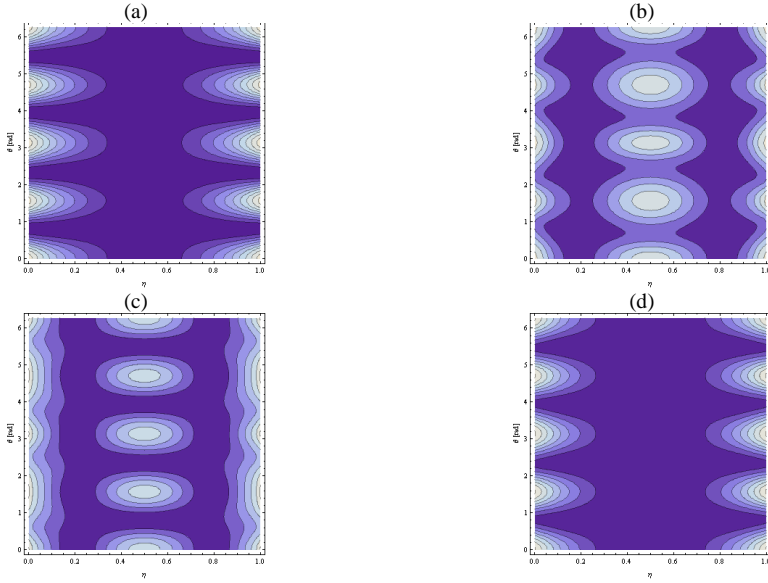


Figure 4. Total energy distribution $\tilde{E}(\eta, \theta, \tau)$. Combined modes (0,2), (2,2). Nonlinear analysis. (a) $\tau = 0.00$. (b) $\tau = 1.26$. (c) $\tau = 2.51$. (d) $\tau = 3.77$.

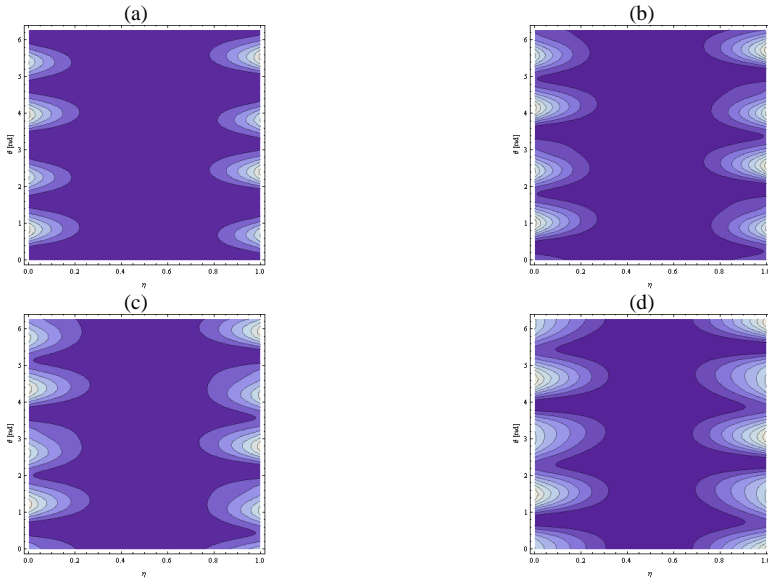


Figure 5. Total energy distribution $\tilde{E}(\eta, \theta, \tau)$. Conjugate modes (1,2). Nonlinear analysis. (a) $\tau = 8.00$. (b) $\tau = 8.02$. (c) $\tau = 8.04$. (d) $\tau = 8.06$.

The sequence of Figures 5 (a-d) shows the energy density distribution in nonlinear field for the two conjugate modes (1,2) in a time range. The periodicity along the circumferential direction is preserved.

The activation of the second mode implies an energy transfer between the conjugate modes. The participation of both the two conjugate modes gives rise to a travelling wave which moves circumferentially around the shell.

10. CONCLUSIONS

In this paper, the nonlinear vibrations of SWNTs are studied within the framework of the Sanders-Koiter elastic shell theory. The Rayleigh-Ritz method is applied in order to obtain approximate natural frequencies and mode shapes. The present model is validated in linear field with data available in the literature. An energy approach based on the Lagrange equations is considered to obtain a set of nonlinear ordinary differential equations. The total energy distribution is analysed in linear and nonlinear fields by assuming suitable initial conditions. The nonlinear energy distribution evolves in a complex pattern with periodicity along the circumferential direction. The participation of two conjugate modes gives rise to an energy transfer between the modes. The periodicity along the circumferential direction is preserved. A travelling wave moving circumferentially around the shell takes place.

REFERENCES

- [1] Iijima S, 1991. "Helical microtubules of graphitic carbon", *Nature*, **354**, pp. 56-58.
- [2] Rao AM, Richter E, Bandow S, Chase B, Eklund PC, Williams KA., Fang S, Subbaswamy K, Menon M, Thess A, Smalley RE, Dresselhaus G, and Dresselhaus MS, 1997. "Diameter-Selective Raman Scattering from Vibrational Modes in Carbon Nanotubes", *Science*, **275**, pp. 187-191.
- [3] Gupta SS, Bosco FG, and Batra RC, 2011. "Wall thickness and elastic moduli of single-walled carbon nanotubes from frequencies of axial, torsional and inextensional modes of vibration", *Computational Materials Science*, **47**, pp. 1049-1059.
- [4] Arghavan S, Singh AV, 2011. "On the Vibrations of Single-Walled Carbon Nanotubes", *Journal of Sound and Vibration*, **330**, pp. 3102-3122.
- [5] Wang CY, Ru CQ, and Mioduchowski A, 2004. "Applicability and Limitations of Simplified Elastic Shell Equations for Carbon Nanotubes", *Journal of Applied Mechanics*, **71**, pp. 622-631.
- [6] Strozzi M, Manevitch LI, Pellicano F, Smirnov VV, and Shepelev DS, 2014. "Low-frequency linear vibrations of Single-Walled Carbon Nanotubes: analytical and numerical models", *Journal of Sound and Vibration*, **333**, pp. 2936-2957.

SERVO PRESSA BIASSIALE CON ARCHITETTURA ISOSTATICA

Francesco Meoni
*Department of Industrial Engineering,
University of Bologna, Italy
E-mail: francesco.meoni2@unibo.it*

Marco Carricato
*Department of Industrial Engineering,
University of Bologna, Italy
E-mail: marco.carricato@unibo.it*

Alessandro Fortunato
*Department of Industrial Engineering,
University of Bologna, Italy
E-mail: alessandro.fortunato@unibo.it*

Abstract. *Le servo presse attuate con assi elettrici sono in grado esercitare la forza massima di pressata indipendentemente dalla posizione della slitta, analogamente a quanto avviene nelle presse idrauliche. Esse offrono dei vantaggi in termini di precisione nonché di semplicità costruttiva, vista l'assenza del circuito idraulico. Esistono sul mercato diversi modelli di servo presse per deformazione di lamiera attuate con assi elettrici, ma generalmente si trascurano le problematiche di iperstaticità legate alle architetture multiassiali. Questo lavoro presenta un'architettura a due assi isostatica, ottenuta tramite l'utilizzo di un meccanismo parallelo. É inoltre effettuato lo studio dettagliato di un prototipo, attualmente in fase di costruzione.*

Keywords: *servo pressa, architettura isostatica, multi asse*

1. INTRODUZIONE

Gli assi elettrici azionati da servomotori sono solitamente usati nelle macchine utensili o nelle macchine automatiche per compiti di posizionamento. Recentemente hanno visto il loro impiego diffondersi anche nell'attuazione di presse elettriche, principalmente nell'industria della plastica e occasionalmente nel campo della deformazione di lamiera. Questa tipologia di pressa, chiamata *servo pressa* in breve, mantiene la flessibilità di una pressa idraulica, poiché la massima forza di pressata è disponibile in ogni posizione della slitta, con corse di lavoro elevate. Allo stesso tempo presenta, però, i vantaggi propri di una pressa meccanica, come ad esempio l'alta ripetibilità del processo ed una elevata precisione di lavorazione; l'assenza di olio tecnologico permette inoltre di eliminare il circuito idraulico, con conseguenti vantaggi

logistici e miglioramenti in termini di eco-sostenibilità.

Le prime applicazioni di servomotori controllati su presse per deformazione lamiera vedono l'impiego delle architetture classiche utilizzate nelle presse meccaniche: la presenza di un dispositivo a ginocchiera permette di ottenere il picco di forza per eseguire l'operazione. Vista la stretta dipendenza della forza esercitabile dalla posizione della slitta, queste macchine sono intrinsecamente poco flessibili. Sebbene le possibilità di controllo offerte dai servozionamenti offrano un ulteriore grado di libertà (si veda per approfondimenti [1–4]), queste macchine rimangono confinate nel campo degli alti volumi di produzione per semplici operazioni, dove la forza massima è richiesta per una breve corsa (es. tranciatura, coniatura).

Per avere completa flessibilità di processo, la forza deve poter essere disponibile in ogni posizione della slitta, come avviene nelle macchine idrauliche. Per far fronte a questa necessità, sono state sviluppate presse attuate da appositi *servo assi*, a sostituzione del classico cilindro idraulico. Solitamente, i servo assi sono composti da un motore rotativo e da una trasmissione meccanica in grado di trasformare il moto rotativo proprio del motore in moto traslatorio (e.g. vite a ricircolo). Poiché non ci sono dispositivi di moltiplicazione della forza, il servo asse deve essere in grado di esercitare con continuità la forza nominale; poiché la forza massima esercitabile dal singolo asse è limitata, per raggiungere carichi più elevati si utilizzano più assi in parallelo accoppiati ad un'unica slitta portastampo (architetture *multiassiali*, ormai molto diffuse). Lo stato dell'arte delle servo presse è presentato in [5]. Esempi di servo presse multiassiali si possono trovare ad esempio tra i cataloghi commerciali di Hoden Seimitsu Kako (HSK) [6], Heitkamp and Tumann [7] e Synchronpress [8].

Nella creazione di una servo pressa elettrica ad architettura multiassiale, ci si limita spesso a implementare l'architettura standard delle presse idrauliche, trascurando che attuare la slitta con un numero di motori maggiore dei gradi di libertà necessari può generare problematiche rilevanti. L'implementazione di un'architettura iperstatica infatti porta conseguenze non trascurabili. Questo lavoro si propone di risolvere tali problematiche, proponendo un'architettura multiassiale isostatica, introducendo un cinematismo parallelo che raccolga il moto degli attuatori per trasmetterlo al membro terminale. Particolare attenzione è rivolta alla *modularità* dell'architettura della pressa, in modo da poter estendere agevolmente il numero degli assi impiegati, per raggiungere "tonnellaggi" che sono in genere appannaggio delle sole presse idrauliche.

È infine presentato nel dettaglio un *case study* specifico di un prototipo industriale: una servo pressa elettrica a due assi, attualmente in costruzione, realizzabile con componenti commerciali. Il prototipo in questione è stato progettato per effettuare operazioni di stampaggio caratterizzate da carichi variabili nel tempo e per effettuare grandi corse, compiendo cicli di lavoro a ritmi industriali. Il progetto del servoasse e la selezione dei componenti meccanici sono stati effettuati con il supporto di un modello dinamico creato *ad hoc*, in grado di simulare il comportamento della catena cinematica costituita da motore elettrico, riduttore e vite a ricircolo di sfere.

2. ARCHITETTURE ISOSTATICHE

Un servo asse può esercitare una forza costante lungo una corsa elevata: sotto questo punto di vista, esso può sostituire completamente un pistone idraulico. Le forze massime esercitabili, tuttavia, non sono comparabili. L'impiego di trasmissioni a corpi volventi è da un lato indispensabile per ottenere la trasformazione del moto rotatorio in moto traslatorio con alta efficienza; dall'altro lato, la fragilità di queste trasmissioni, quando sottoposte a cicli di

carico molto intensivi (come quelli di una macchina per stampaggio) pone un limite tecnico alla forza massima esercitabile. Una soluzione a questa problematica consiste nell'impiego di una architettura multiassiale modulare, dove il numero di servo assi installato dipende dal tonnellaggio globale della pressa.

Nel momento in cui si connettono piú attuatori alla singola slitta, questa è libera di muoversi se e solo se gli assi condividono la stessa direzione, e se si muovono in maniera perfettamente sincronizzata. Questi requisiti sono necessari dal momento che un'architettura di questo tipo è iperstatica, poiché il numero di attuatori è maggiore del numero di gdl dell'output, che risulta essere uno.

Il moto in queste condizioni è possibile solo sotto stringenti condizioni di vincolo, che all'atto pratico non sempre sono rispettabili. Ad esempio, giochi, tolleranze di lavorazione ed imprecisioni di montaggio possono impedire che gli assi siano perfettamente paralleli. Inoltre, anche con il piú raffinato controllo elettronico, non potranno essere evitati piccoli errori di inseguimento e di sincronizzazione tra i motori. Queste situazioni possono far sì che i servomotori lavorino in conflitto l'uno con l'altro, portando alla nascita di sovratensioni interne che influenzano a loro volta le prestazioni dei motori e della trasmissione a vite.

Per ovviare alle problematiche sovraccitate, in questo lavoro si propone l'impiego di un cinematismo parallelo che colleghi gli attuatori rendendo l'architettura isostatica. Per fare questo, il cinematismo in questione deve possedere un numero di gdl pari al numero di attuatori. Viene presentato in questa sede un meccanismo a due gdl, adatto quindi ad un'architettura biassiale, ma il ragionamento può essere esteso anche ad architetture con un numero di assi maggiore.

Meccanismo a due gradi di libertà

In questo paragrafo è presentato (vedi Fig. 1) un meccanismo piano a due gradi di libertà, idoneo per una architettura isostatica a due assi verticali paralleli. Due coppie prismatiche agiscono lungo gli assi di attuazione a_1 e a_2 , con relativi cursori, le cui posizioni sono indicate da A_1 e A_2 . Le coppie rotoidali in A_1 e A_2 sono collegate tramite due aste ad una doppia coppia rotoidale centrale in B , dalla quale una terza asta trasmette il moto alla slitta, libera di traslare lungo c . Nel piano, il meccanismo è staticamente determinato, come può essere verificato attraverso la formula di Grubler:

$$m = 3(n_c - 1) - 2(f_1) = 3(7 - 1) - 2(8) = 2 \quad (1)$$

dove n_c è il numero di componenti, incluso il telaio, e f_1 è il numero di coppie cinematiche ad 1 gdl che esercitano due vincoli. L'Eq. (1) fornisce la corretta mobilità, m , del meccanismo. In caso di disallineamento, h , tra i punti A_1 e A_2 , l'asta centrale ruota di α e il punto B ruota attorno al punto C . Questa rotazione "assorbe" il disallineamento h , evitando che si creino momenti flettenti nella struttura.

La componente verticale della forza trasmessa in C (cioè la forza utile di pressata) è in ogni caso pari alla somma dei moduli delle forze esercitate dagli attuatori, in questo caso $Q_n = 2Q_i$. Questo valore è quindi indipendente dall'angolo di rotazione α (che assume valore nullo in assenza di disallineamenti), mentre non lo è il valore della componente orizzontale, controbilanciata dal sistema di guida. Impiegando un controllo elettronico appropriato, si può assumere che h , e quindi α , siano prossimi allo zero. La rotazione del meccanismo è quindi trascurabile, mentre il sistema beneficia comunque dell'assenza di vincoli supplementari. L'angolo β , definito come l'angolo tra la verticale e una delle due aste, può essere conside-

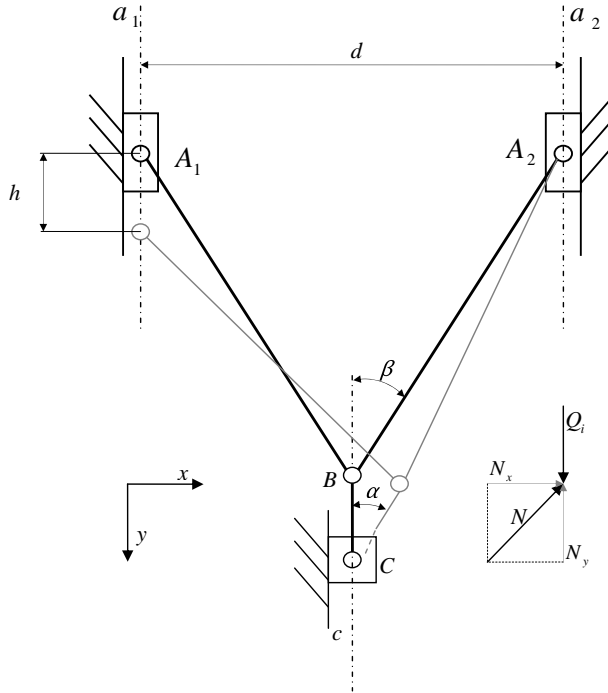


Figura 1. Meccanismo a due gradi di libertà.

rato costante durante la lavorazione, per i motivi sopracitati. Quest'angolo, che influenza la distribuzione dei carichi orizzontali sulle guide, può essere considerato un parametro di progetto e venire quindi ottimizzato. Applicare una forza pari a Q_i lungo le coppie prismatiche, rispettivamente a_1 and a_2 , porta alla nascita di una reazione N che agisce lungo la direzione delle aste di collegamento A_1B e A_2B .

$$N = \frac{Q_i}{\cos \beta} \quad (2)$$

N è la forza di compressione che l'asta deve sopportare (ne determina quindi le dimensioni), ed aumenta all'aumentare di β . Un valore più basso di β porta quindi a valori più piccoli di N , a vantaggio di pesi e ingombri. La forza N può essere scomposta in due componenti, N_y e N_x , rispettivamente verticale e orizzontale.

$$N = \sqrt{N_y^2 + N_x^2} = \sqrt{Q_i^2 + (Q_i \tan \beta)^2} \quad (3)$$

Il carico $N_x = Q_i \tan \beta$, funzione di β , è trasmesso lateralmente alla struttura della pressa attraverso le guide prismatiche, e potrebbe compromettere la funzionalità della trasmissione a vite, se troppo elevato; è opportuno quindi che non assuma valori troppo alti. D'altra parte, un valore troppo basso di β , fissata la distanza assiale d , porta ad un ingombro verticale della

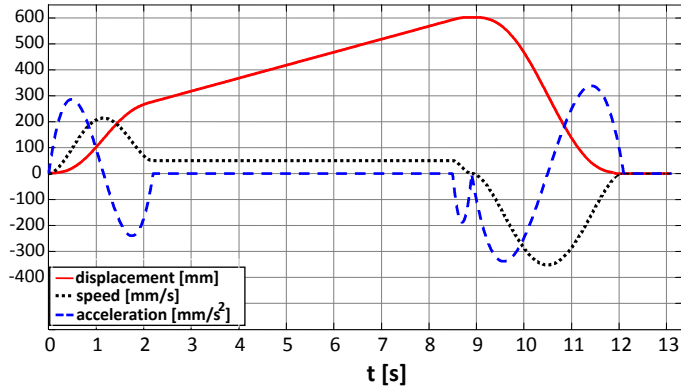


Figura 2. Ciclo di riferimento.

pressa molto elevato. Viste tali esigenze, β deve essere ottimizzato tenendo conto sia della distribuzione delle forze sia dei vincoli spaziali. Per il prototipo sviluppato si è visto che il valore di $\beta = 30^\circ$ porta ad un valore accettabile N_x e al contempo rispetta i vincoli di ingombro.

3. PROTOTIPO DI PRESSA BIASIALE

È attualmente in costruzione un prototipo industriale di una servo pressa a due assi. L'obiettivo del prototipo è la dimostrazione della validità del concetto di architettura multiassiale isostatica. È stato quindi implementato il meccanismo a due gradi di libertà presentato nel paragrafo precedente, in grado di combinare l'azione dei servo assi. Si è proceduto al dimensionamento dei componenti principali per dimostrare che il prototipo è effettivamente realizzabile con relativa semplicità costruttiva utilizzando componenti commerciali.

Specifiche del prototipo

Il prototipo sarà in grado di esercitare una forza massima di pressata di 1200 kN , sommando il contributo di due assi da 600 kN ciascuno. Il ciclo di lavorazione di riferimento è stato determinato tenendo conto dei vincoli cinematici e tecnologici indicati dal partner industriale Gigant. La corsa di lavorazione è di 300 mm , mentre la corsa totale, incluso il posizionamento, è 600 mm . La massima velocità di lavorazione è di 50 mm/s . La potenza nominale di processo, P , ammonta quindi a $P_p = 1200 \text{ kN} \cdot 50 \text{ mm/s} = 60 \text{ kW}$. Il prototipo deve poter operare secondo cicli di lavoro a ritmi industriali, con una produttività di 5 cicli al minuto. Rispettando queste specifiche, è stato definito il ciclo di lavoro per la slitta. Per evitare discontinuità nell'accelerazione, i tratti sono stati raccordati con polinomi di quinto grado.

Il moto della slitta è mostrato in Fig. 2. Nella prima parte la slitta viene posizionata ad alta velocità; la velocità viene poi ridotta a 50 mm/s durante il processo di deformazione lamiera, e rimane costante da $t = 2.5 \text{ s}$ a $t = 9 \text{ s}$; a fine operazione, la slitta torna nella posizione iniziale.

Il prototipo presenta nella parte inferiore un cuscinio premilamiera, anch'esso attuato elettricamente, in grado di fornire una controforza durante lo stampaggio fino a 600 kN ,

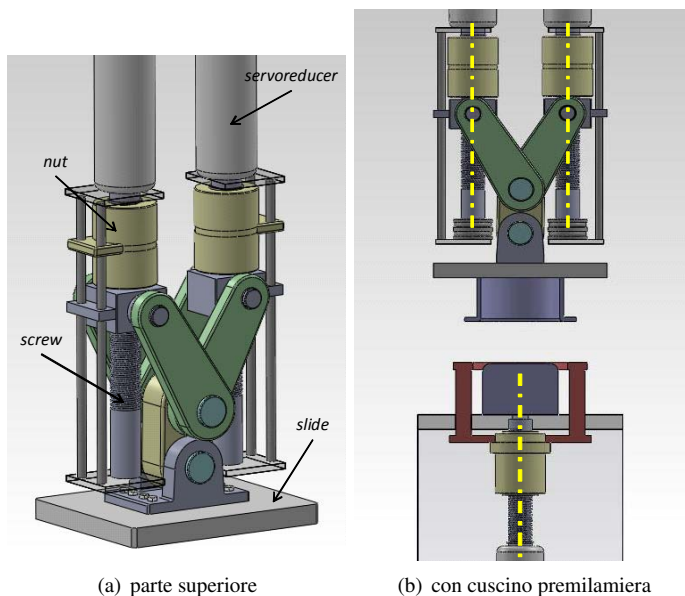


Figura 3. Layout funzionale.

cioè metà della forza totale. La corsa del premilamiera è pari alla corsa di lavorazione, ossia 300 mm . Lo stesso layout del servo asse può quindi essere utilizzato sia nella parte inferiore sia in quella superiore della pressa. Un layout funzionale di tutta la pressa è mostrato in Fig. 3.

Modello Dinamico

Per descrivere il comportamento dinamico del sistema e per permettere il dimensionamento dei componenti meccanici, è stato sviluppato un modello a parametri concentrati del singolo servo asse, formato da servomotore, riduttore e vite a ricircolo di sfere. La legge di moto di ogni asse (i.e. lo spostamento, q , la velocità, \dot{q} , e l'accelerazione, \ddot{q}) è nota, poiché si assume che sia uguale a quella della slitta che porta lo stampo¹. Nel modellare il sistema, sono stati utilizzati due tipi di elementi:

- 1) *elementi inerziali*, che modellano le inerzie ma non le perdite di energia.
- 2) *elementi di trasmissione*, che tengono conto delle variazioni di velocità e coppia (o forza, se il moto è traslatorio) dovute alla trasmissione meccanica, nonché dell'efficienza energetica dei componenti.

¹Nei precedenti paragrafi è stato osservato come, a causa della sincronizzazione fornita dal controllo elettronico, i disallineamenti h e α in Fig. 1 assumono valori molto bassi. Gli effetti dovuti alle variazioni di questi due parametri possono quindi essere trascurati.

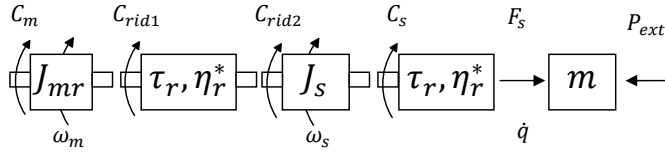


Figura 4. Modello a parametri concentrati di un servoaasse.

In generale, ogni componente meccanico può essere modellato con due elementi: uno che rappresenti la sua inerzia e l'altro che tenga conto del rendimento e del rapporto di trasmissione. In Fig. 4 è mostrato il modello dell'intera catena cinematica.

La velocità di rotazione della vite, ω_s , la sua accelerazione, $\dot{\omega}_s$, la velocità del motore, ω_m , e la sua accelerazione, $\dot{\omega}_m$, possono essere espresse in funzione della legge di moto fornita, introducendo il rapporto di trasmissione del riduttore, τ_r , e il rapporto di trasmissione della vite, τ_s :

$$\omega_s = \frac{\dot{q}}{\tau_s}, \quad \dot{\omega}_s = \frac{\ddot{q}}{\tau_s} \quad (4)$$

$$\omega_m = \frac{\omega_s}{\tau_r} = \frac{\dot{q}}{\tau_s \tau_r}, \quad \dot{\omega}_m = \frac{\dot{\omega}_s}{\tau_r} = \frac{\ddot{q}}{\tau_s \tau_r} \quad (5)$$

Per ogni elemento si può scrivere la relazione tra coppia in ingresso e coppia in uscita. Ad esempio, considerando l'elemento che rappresenta motore e riduttore, la relazione è:

$$C_m - C_{rid1} = J_{mr} \dot{\omega}_m \quad (6)$$

dove C_m è la coppia motore, C_{rid1} è la coppia in ingresso al riduttore e J_{mr} è l'inerzia combinata di motore e riduttore. Per gli elementi di trasmissione, si può imporre la conservazione dell'energia. Ad esempio, per il riduttore vale:

$$C_{rid2} = \frac{\eta_r^*}{\tau_r} C_{rid1} \quad (7)$$

dove C_{rid2} è la coppia in uscita dal riduttore e η_r^* è una funzione a gradino che varia a seconda della direzione del flusso di potenza:

$$\eta_r^* = \begin{cases} \eta_r & C_{rid1} \geq 0 \\ \frac{1}{\eta_r} & C_{rid1} < 0 \end{cases} \quad (8)$$

η_r è il rendimento meccanico del riduttore quando il flusso di potenza va dal motore al carico e $\bar{\eta}_r$ è il rendimento meccanico quando il flusso va dal carico al motore (in generale diverso da η_r). Ripetendo questo processo per tutta la catena cinematica, si può modellare il comportamento dell'intera trasmissione. L'equazione del moto che ne risulta è:

$$C_m - C_r^* = J^* \dot{\omega}_m \quad (9)$$

J^* è l'inerzia equivalente di tutti i componenti ridotta all'albero motore, che in dettaglio vale:

Tabella 1. Lista dei componenti.

Componente	Modello	Marca
Motore	IPH8226 – 1DB45	Siemens
Riduttore	CI160 – 3.15	Rossi
Vite a ricircolo di sfere	VRS160	UmbrAGroup

$$J^* = J_{mr} + J_s \cdot \frac{\tau_r^2}{\eta_r^*} + m \cdot \frac{\tau_r^2 \cdot \tau_s^2}{\eta_r^* \cdot \eta_s^*} \quad (10)$$

dove J_s and η_s^* sono inerzia equivalente e rendimento meccanico della vite, ottenuti come nell' Eq. (8). C_r^* è la coppia ridotta data dalla risultante delle forze esterne agenti sulla slitta, P_{ext} :

$$C_r^* = \frac{\tau_r \cdot \tau_s}{\eta_r^* \cdot \eta_s^*} \cdot P \quad (11)$$

Scelta dei componenti

La progettazione del singolo servo asse è indipendente dalla taglia della pressa. I componenti commerciali sono stati selezionati in modo da fornire una forza assiale $Q_i = 600kN$. Il modello è stato usato per simulare il comportamento dinamico dell'asse e per determinare forze e coppie agenti in ogni componente. Nei paragrafi successivi verranno presentati brevemente i criteri di selezione per ogni componente principale. In Tab. 1 è presentata una lista di componenti adatti all'applicazione .

Vite a ricircolo di sfere. Le viti a ricircolo di sfere sono tipicamente usate quando vi è la necessità di avere alta precisione e alta efficienza. Per le applicazioni di deformazione lamiera, a queste caratteristiche va aggiunta la durabilità nel tempo per cicli di servizio molto probanti. Sono pochi i fornitori che producono viti a corpi volventi in grado di sopportare alti carichi. Infatti, le viti a ricircolo di sfere presentano molte problematiche legate a sollecitazioni cicliche: le superfici di contatto, a causa delle alte pressioni, sono soggette a rotture a fatica e ad altri problemi tribologici. Le viti a rulli satelliti, offrendo superfici di contatto più estese, presentano carichi massimi esercitabili in genere più alti, ma risultano meno efficienti e più costose rispetto alla soluzione a sfere. UmbrAGroup, produttore di viti a sfere leader nel settore aeronautico, fornisce, a parità di dimensioni, prodotti con carichi accettabili paragonabili a quelli di una vite a rulli. Per questo motivo, la vite a sfere è stata preferita per ragioni di costo e di efficienza meccanica.

Per questa applicazione, il parametro fondamentale da valutare è la capacità di sopportare il carico dinamico, dato che la vita utile di una pressa è una grandezza fondamentale nella progettazione di un prototipo industriale. Ogni modello di vite a sfere è caratterizzato da uno specifico *coefficiente di carico dinamico*, C_a , diverso a seconda della taglia della vite, usato per calcolare la vita a fatica. Esso viene definito come il carico assiale, applicato costante e perfettamente centrato, che permette di raggiungere la durata di un milione di cicli. Per

valutare la vita utile, deve essere calcolato il carico dinamico affaticante equivalente, F_{sm} , definito come il carico ipotetico costantemente che, se applicato, avrebbe gli stessi effetti di quello reale:

$$F_{sm} = \sqrt[3]{\frac{\int_L |F_s|^3 dl}{L}} \quad (12)$$

F_s è il carico istantaneo agente nell'elemento di corsa dl ; la corsa totale è pari a L . Per valutare il carico agente sulla chiocciola in funzione del tempo $F_s(t)$, e di conseguenza F_{sm} , è necessario conoscere i parametri della vite (i.e. passo, inerzia etc.) e del servomotore, per tenere conto degli effetti inerziali. Poiché questi dati non sono noti prima della scelta del componente, viene effettuata una scelta di tentativo senza tenere conto dei transitori inerziali. Ad esempio, una scelta di primo tentativo della vite può essere effettuata basandosi sulla fase di lavoro, dove la forza è massima e la velocità costante. Successivamente è effettuata l'analisi dinamica per aggiornare il valore del carico ed effettuare una nuova selezione. Il processo può essere iterato se necessario. La vita utile della vite, L_{10} , espressa in milioni di cicli, è valutata come:

$$L_{10} = \left(\frac{C_a}{F_{sm}} \right)^3 \quad (13)$$

L'equazione (13) permette di determinare il coefficiente di carico dinamico necessario al raggiungimento del valore obiettivo di 5 milioni di cicli pressa, corrispondenti a $L_{10} = 150$. Ad esempio, una possibile scelta è il modello *VRS160* [9], con diametro $d = 160 \text{ mm}$, passo $p_h = 40 \text{ mm}$ e coefficiente di carico dinamico $C_a = 1866 \text{ kN}$. Il coefficiente richiesto è $C_a = 1973 \text{ kN}$.

Servomotore e riduttore. Per attuare il servo asse è stato scelto un motore asincrono controllato con inverter. Una possibile alternativa potrebbe essere un motore brushless a magneti permanenti; le potenze nominali disponibili per i motori brushless, tuttavia, sono piuttosto basse se comparate con i valori richiesti dalle operazioni di deformazione di lamiera (i motori brushless sono principalmente usati per applicazioni di precisione con carichi puramente inerziali, come macchine automatiche, posizionamento assi, ecc.) Un motore asincrono controllato con inverter fornisce alte potenze ad un costo relativamente basso, pur essendo in grado di assicurare prestazioni dinamiche adatte all'applicazione. Nella scelta e nel dimensionamento del motore, non si può prescindere dall'influenza che il rapporto di riduzione $\tau_r = 1/i$ ha sulle prestazioni del motore stesso. Il processo di selezione del motore può essere affrontato analogamente a quanto fatto con la vite. In una scelta di primo tentativo, si determina il parametro fondamentale, in questo caso la potenza necessaria per compiere la lavorazione, P_p . Il processo può essere iterato implementando i transitori ed aggiornando di volta in volta la lista dei componenti. Per quanto riguarda l'influenza del rapporto di riduzione, in Fig. 5 è mostrata la potenza meccanica da fornire all'asse, P , al variare di τ_r . Valori negativi indicano che il sistema sta restituendo energia. I dati mostrati si riferiscono a simulazioni effettuate con i componenti indicati in Tab. 1.

Si possono distinguere tre fasi differenti: nella prima fase, la slitta viene prima accelerata e poi frenata, per fare in modo che si trovi in posizione di lavorazione ad una velocità adeguata; nella fase centrale, sia la velocità sia la forza applicata sono costanti, così come il consumo di energia; nella terza fase, la slitta viene riportata in posizione iniziale. È importante notare

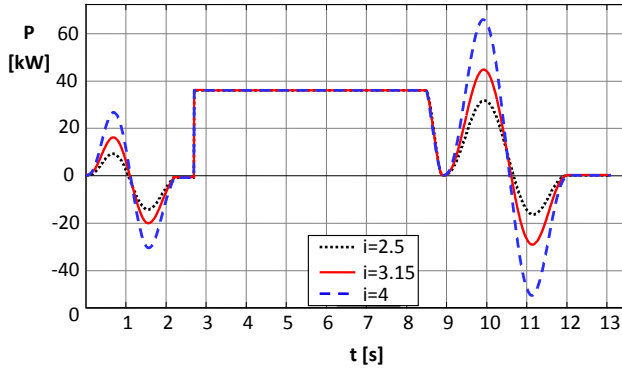


Figura 5. Potenza meccanica da fornire all'asse.

l'effetto del rapporto di riduzione sul consumo di energia durante le fasi di posizionamento. Ad un valore piú alto di τ_r (i.e. un valore piú basso di i) corrisponde un picco di potenza piú basso nelle fasi di movimentazione. Dall'altra parte, un valore piú basso di τ_r porta ad una coppia motrice piú bassa, dovuta ad una ω_s piú alta, come si evinve nell'Eq. (5). Quest'ultima situazione favorisce l'impiego di motori asincroni, dato che sono caratterizzati da velocità nominali relativamente alte. Una buona scelta per τ_r è un valore abbastanza basso da minimizzare la coppia motrice richiesta, ma comunque abbastanza alto da mantenere il picco di potenza assorbita sotto il valore nominale di potenza di processo. Ad esempio, impiegando un riduttore con $\tau_r = 3.15$ a singolo stadio, disponibile da catalogo Rossi [10], una scelta ragionevole per il motore è il modello Siemens *IPH8226-IDB45* [11]. La Fig. 6 mostra la caratteristica meccanica del servomotore in questione durante il ciclo pressa. Il punto di lavorazione è rappresentato da un cerchio.

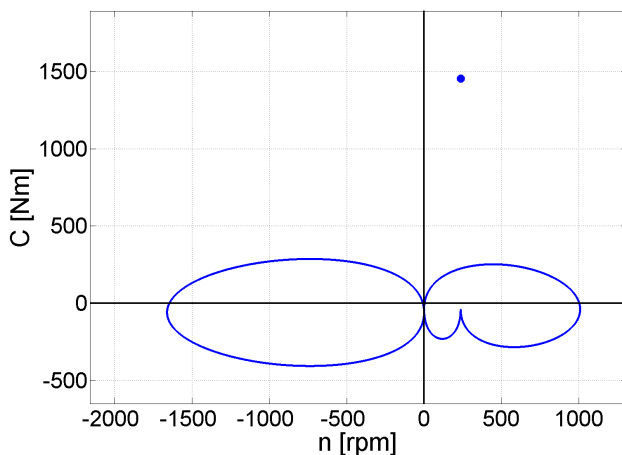


Figura 6. Caratteristica meccanica.

4. CONCLUSIONI

In questo lavoro è stata presentata un'architettura biassiale isostatica per servo presse ad azionamento elettrico destinate alla deformazione di lamiera. È stato creato un modello dinamico del singolo asse servoattuatori per simularne il suo comportamento dinamico e determinare i carichi agenti sui componenti. Il servo asse può essere progettato indipendentemente dalla taglia globale della pressa, poiché l'architettura multiassiale è modulare. È stato infine dimostrato che un prototipo può essere realizzato con relativa semplicità impiegando componenti commerciali.

REFERENCES

- [1] Kirecci, A. et Canan Dulger, L., 1999. "A study on a hybrid actuator". *Mechanism and Machine Theory*, **35**, pp. 1141–1149.
- [2] Hui Li, et Lihui Fu, e. Y. Z., 2010. "Optimum design of a hybrid-driven mechanical press based on inverse kinematics". *Journal of Mechanical Engineering*, **56**, pp. 301–306.
- [3] Hui Li, e. Y. Z., 2010. "Seven-bar mechanical press with hybrid-driven mechanism for deep drawing; part 1: kinematics analysis and optimum design". *Journal of Mechanical Science and Technology*, **24**, pp. 2153–2160.
- [4] Soong, R.-C., 2010. "A new design method for single dof mechanical presses with variable speeds and length-adjustable driving links". *Mechanism and Machine Theory*, **45**, pp. 496–510.
- [5] Osakada, K., Mori, K., Altan, T., and Groche, P., 2011. "Mechanical servo press technology for metal forming". *CIRP Annals - Manufacturing Technology*, **60**(60), pp. 651–672.
- [6] Yoneda, T., 2008. "Features of direct driving ZEN former". *Press Working*, **46**(10), pp. 18–21.
- [7] Huelshorst, J., 2008. "Merging manufacturing processes (MMP)". *Proceedings of the 19th Forming Technology Conference*, Hannover, pp. 161–169.
- [8] Stahlmann, J., Damavandi, K., and Groche, P., 2009. "First experiences by the application of a servo-motor press in cold forging". *Jahrestreffen der Kalt-Massivumformer*.
- [9] UMBRA CUSCINETTI, 2011. *Ballscrew for Industrial Applications, Dimensional Tables*. <http://www.umbragroup.it/en/home>, June.
- [10] ROSSI GROUP, 2011. *G05-Parallel (standard and long) and right angle shaft gear reducers and gearmotors*. <http://www.rossi-group.com/index>, June.
- [11] SIEMENS, 2012. *Main Motors for SINAMICS S120*. <http://www.industry.siemens.com/drives/global/en/motor/>, May.

FIRST RESULTS ON THE ROLE OF CUTANEOUS FEEDBACK DURING THE LEARNING OF A FORCE FIELD IN REACHING TASKS

Fabio Oscari

*Department of Management and Engineering,
University of Padua, Italy
E-mail: fabio.oscari@unipd.it*

Giulio Rosati

*Department of Management and Engineering,
University of Padua, Italy
E-mail: giulio.rosati@unipd.it*

Aldo Rossi

*Department of Management and Engineering,
University of Padua, Italy
E-mail: aldo.rossi@unipd.it*

Claudio Pacchierotti

*Department of Advanced Robotics,
Istituto Italiano di Tecnologia, Italy
E-mail: pacchierotti@dii.unisi.it*

Domenico Prattichizzo

*Department of Information Engineering and Mathematics,
University of Siena, Italy
E-mail: prattichizzo@ing.unisi.it*

Abstract. According to International Labour Organization (ILO), more than two million people die or lose the working capability every year because of accidents or work-related diseases. The insufficient degree of interaction between human and machine (HMI) is one of the major causes. Developments in HMI have been achieved in several fields of robotics research. However, the translational relevance of such innovations is often underestimated. To date, several findings have generated some preliminary indications about the way to facilitate learning of motor tasks with the assistance of robotic devices. This general goal, initially raised by the community of rehabilitation robotics researchers, is also extendable to different application fields since faster learning of a task by the user means more productivity and safety. Haptic stimulation can help humans learn perceptual motor skills, but the precise way in which it influences the learning process has not yet been clarified. This study investigates the role of the kinesthetic and cutaneous components of haptic feedback during the learning of a viscous curl field, taking also into account the influence of visual feedback. Results indicate that kinesthetic stimuli played a primary role during motor adaptation to the viscous field, which is a fundamental premise to motor learning and rehabilitation. On the other hand, cutaneous stimulation alone appeared not to bring significant direct or adaptation effects, although it needs further investigations. The experimental conditions with visual cancellation of position error seems to show slower adaptation rates, indicating that visual feedback actively helps to the formation of internal models. However, modest learning effects were shown when the visual information was used to substitute the viscous field.

Keywords: cutaneous stimulation, haptic force feedback, motor learning, adaptation, perturbation

1. INTRODUCTION

The International Labour Organization (ILO) indicates that the working sectors with the highest number of injuries correspond to those requiring a human-machine interaction (HMI). HMI is one of the major problems since the operator's safety cannot rely on his/her ability and experience solely, and new technological solutions should help in reducing risks and improving performance, providing the operator with reliable and intuitive information on the task at hand. Research on haptics and interactive robotics has reached important results in the last decades in this field, however no general guidelines have been released on how different forms of feedback can be provided by a human-machine interface to maximize operator's safety and task performance/learning at the same time.

For instance, current commercial robotic systems, especially for medical applications (e.g., surgery [1]), still underexploit haptic feedback at master side, due to the difficulty of avoiding unwanted and unsafe movements of the operator's hands that in turn means undesired and dangerous movements of the slave robot's end-effector. Interpretation of force by using visual feedback has been the only solution used so far [1]. However, the absence of such feedback makes HMI more difficult or even non-realistic, thus reducing both task execution performance and safety.

To date, several evidences [2–5] have generated some preliminary indications about the way to facilitate learning of motor tasks with the assistance of robotic devices [3, 5]. This general goal, initially raised by the community of rehabilitation robotics researchers, is also extendable to different application fields since faster learning of a task by the user means more productivity and safety.

Many researchers have studied motor adaptation to altered dynamic environments. A typical setting in this field consists of applying a viscous curl field during the execution of point-to-point reaching movements in the horizontal plane [6, 7]. Following the initial deviation from a straight trajectory (direct effect), subjects tended to adapt to the altered dynamic environment restoring the initial motion path (adaptation). The presence of aftereffects, as a result of perturbation removal, proved that the nervous system creates an internal model of the environment, able to predict the expected perturbing forces [2]. Feygin et al. investigated the use of haptics for skill training [8]. Results indicated that haptic guidance is effective in training: while visual training was better for teaching the trajectory shape, temporal aspects of the task were more effectively learned from haptic guidance. Regarding the interaction between visual and haptic feedback during the adaptation of human reaching movements, Scheidt et al. showed when visual feedback of movement was eliminated entirely, proprioception was enough to guide adaptive recovery of straight and smooth hand trajectories directed towards the final target [9]. Finally, Morris et al. showed that, during the use of haptic feedback to teach an abstract motor skill which requires recalling a sequence of forces, recall following visuohaptic training was significantly more accurate than recall following visual or haptic training alone, although haptic training was inferior to visual training [10].

Although many works analyze the role of haptics in the learning of a perceptual motor skill, it is still not clear how the central nervous system combines concurrent stimulation, such as proprioceptive, visual or haptic feedback.

Focusing on haptic feedback, most of the grounded haptic and rehabilitation devices provide a combination of kinesthetic *and* cutaneous stimuli to the user, if we assume that the interaction is mediated by a stylus, a ball, or any other tool mounted on the device [11, 12]. Cutaneous stimuli are sensed by pressure receptors in the skin, and they are useful for recognizing the local properties of objects, such as shape, edges, embossings and recessed features [13, 14]. On the other hand, through muscle spindles and the Golgi tendon organ, kinesthesia allows the user to sense the movement of neighbouring parts of the body and the forces being exerted [15–17].

The cutaneous and kinesthetic stimuli applied by a grounded haptic device, however, cannot be decoupled: the force provided is felt by the user both at the fingertips (cutaneous component), and at the muscle and joint level (kinesthetic component) [11, 12]. An interesting approach consists of using cutaneous devices to activate only the cutaneous component of the haptic interaction, which has been found to be a simple but effective solution for reducing the mechanical complexity of haptic devices, while guaranteeing adequate performance [11, 18–21]. On the other hand, using a cutaneous device together with a grounded haptic interface allows one to independently control how much kinesthetic and cutaneous stimulation is provided to the user [12]. The authors of [22], for example, exploited this idea to design a stability controller which enhanced transparency of passive teleoperation systems with force reflection. A similar approach was used in [23] to enhance the transparency of a 7-DoF robotic teleoperation system.

The aim of this paper is to show first preliminary results on the role of the two components of haptic interaction during the learning of a viscous curl field, taking into account at the same time the influence of visual feedback in such a process.

In the following, Section 2. describes the design of the experiment and hardware setup, Sec. 3. presents the results of statistical analysis, and Sec. 4. addresses the discussion and outlines prospective work.

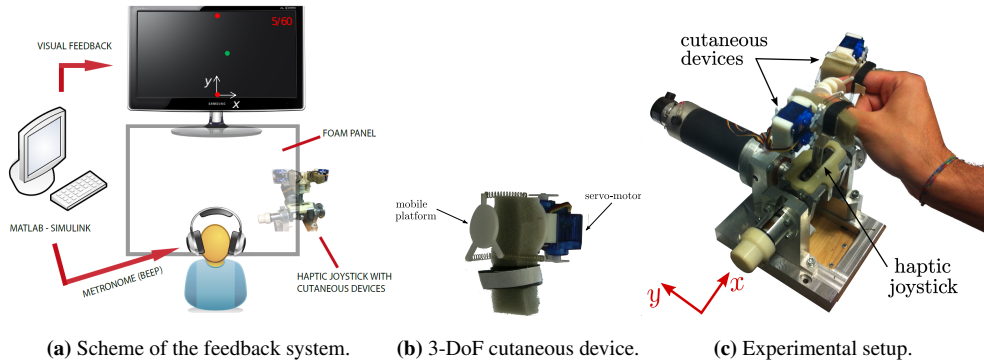


Figure 1. Feedback system and experimental setup. A 2-DoF haptic joystick, equipped with two cutaneous devices, was placed on a table in front of a LCD screen, while a white panel prevented the subject from seeing the hand and the joystick. Users had to grasp the joystick while wearing two cutaneous devices, one on the thumb and one on the index finger.

2. METHODS

2.1 Subjects

A total of 17 healthy subjects participated in the experiment. They were aged between 20 and 29 years (mean age 23.6 ± 3.0 years, 13 males, 4 females), 16 right-handed and one left-handed. All participants reported normal vision with no color blindness, and no hearing or cutaneous-sensibility problems. Written informed consent for participation in the experiments and for the publication of this report was obtained from all the subjects. The experiment received the ethical approval of the Scientific Commission of the University of Padua.

2.2 Setup

The experimental setup is shown in Fig. 1a. The subject sat on a chair, in front of an LCD screen and a 2-DoF haptic joystick [24]. A white panel prevented the subject from seeing the hand and the joystick. A custom plastic support was mounted at the top of the handle, housing two cutaneous devices, one for the thumb and one for the index finger (Fig. 1c). The other fingers were closed into a fist. In this way, the subject grasped the handle only with the fingers wearing the cutaneous devices. The direction of grasping (x) was always transversal with respect to the direction of motion (y), which was parallel to the sagittal plane of the subject. To prevent changes in the perceived direction of force and allow for a comfortable grasp, the subjects were instructed to keep the wrist slightly extended (Fig. 1c).

Each cutaneous device consisted of a static part, connected to the joystick, and a mobile platform (Fig. 1b). Three springs kept the platform in a reference configuration when the device was not actuated. Three servo-motors controlled the length of three wires connecting the static part to the mobile platform, allowing the latter to apply the requested force at the user's fingertip [23]. An estimation of the exerted force was derived through a simple elastic model of the fingertip, with a linear relationship between platform displacement and resultant wrench. In our experiments the cutaneous interfaces were used as 1-DoF devices (all motors pulled the cables together), so that only the forces in the sagittal plane of the finger were generated, roughly normal to the longitudinal axis of the distal phalanx.

2.3 Experimental protocol

Subjects were asked to perform forward (+ y direction) and backward ($-y$ direction) 13 cm-long reaching movements (*reaches*) between two fixed targets, as straight as possible. The exercise was divided into groups of 60 reaches (*task*), corresponding to 30 forward and 30 backward movements. The position of the hand with respect to the joystick was checked before the beginning of each task.

A fixed, red circular cursor on the LCD screen indicated the position of the current target. The target's diameter was 0.5 cm in the joystick space, corresponding to 1 cm on the screen. A green circular cursor of the same size was printed on the screen, whose position along the y axis corresponded to the position of the joystick in the back and forth direction. The x position of the green cursor either denoted the lateral position of the joystick (actual visual feedback: VFA), or was set to zero (straight visual feedback: VFS). The latter mode corresponded to a cancellation of the left-right position error.

Subjects were asked to complete each reach (either forward or backward) in the time between two beeps of a metronome playing at 33 bpm (one beep every 1.8 s). The metronome was used to standardize the duration of the reaches among subjects. Subjects were allowed a 30 second warm-up to practice the rhythm dictated by the metronome. The devices, the metronome and the graphic rendering were controlled by a real-time software (Matlab/Simulink R2012b) running at 200 Hz.

During each task, a dynamic perturbation was introduced from the 11th to the 50th reach, after which it was removed. The perturbation consisted of a viscous curl field, rendered to the subject in five different ways:

- *Cutaneous + Kinesthetic Stimulation (CS+KS)*

The perturbation consisted of a viscous force f_x , generated by the joystick. The lateral force was computed as a function of the velocity along the motion axis (y):

$$\mathbf{f} = \begin{Bmatrix} f_x \\ f_y \end{Bmatrix} = \begin{bmatrix} b_{1,1} & b_{1,2} \\ b_{2,1} & b_{2,2} \end{bmatrix} \cdot \begin{Bmatrix} v_x \\ v_y \end{Bmatrix} \quad (1)$$

where all the elements of the viscosity matrix were set to zero except for $b_{1,2} = 20$ Ns/m. The variables are expressed in the International System of Units. It is worth noting that both the cutaneous and kinesthetic stimuli were provided by the haptic joystick, while the cutaneous devices were turned off.

- *Cutaneous Stimulation (CS)*

The perturbation, as of Eqn. 1, was provided by the cutaneous devices, while the haptic joystick was used to track the position of the hand only (it provided no force feedback). According to the sign of f_x , the cutaneous force was applied either to the index finger ($f_x > 0$) or to the thumb ($f_x < 0$). This stimulation resembled the force field presented in the previous mode, but without the kinesthetic part of the perturbation. This approach of subtracting kinesthesia from the complete haptic interaction by means of cutaneous devices was introduced in [11], and it is called *sensory subtraction*.

- *Kinesthetic Stimulation (KS)*

The joystick provided the same force feedback as in the first modality (CS+KS). Concurrently, the cutaneous devices were used to produce a 5 N force on the fingertip pushed by the joystick. In this way, the cutaneous stimulation originated by the joystick was

Perturbation	Visual feedback (VF)	
	Actual (A)	Straight (S)
<i>Haptic stimulation (CS+KS)</i>	A	F
<i>Cutaneous stimulation (CS)</i>	B	G
<i>Kineshetic stimulation (KS)</i>	C	H
<i>Visual distortion (VD)</i>	D	-
<i>Video-cutaneous stim. (VD+CS)</i>	E	-

Table 1. Experimental conditions. Each subject performed eight different tasks in a randomized sequence. Visual feedback was provided during all the experiment, while perturbations were provided from the 11th to the 50th reach. Note that in these reaches, for both the VD and VD+CS case, the visual feedback modality was switched from VFA to VD in order to generate the viscous visual distortion.

completely masked. In fact, above a threshold of ~ 2 N [25–27], the cutaneous receptors do not provide any perceivable sensation of increasing force. This condition is the closest to a pure kinesthetic stimulation.

- *Visual Distortion (VD)*

In this mode, both the joystick and the cutaneous devices were switched off, and the perturbation was generated by providing altered visual information on the lateral position of the hand (visuomotor transformation). The lateral (x) position of the green cursor on the screen was set equal to the position error e_x , computed as the difference between lateral joystick position (x_s) and a viscous distortion (x_r , reference position):

$$e_x = x_s - x_r = x_s - b \cdot v_y \quad (2)$$

where x_s and e_x are given in meters, v_y in meters per second, whilst b was set to -0.15 s. This distortion emulated the effects of a lateral viscous force field, without providing any kinesthetic or cutaneous stimuli.

- *Visual + Cutaneous Stimulation (VD+CS)*

The visual feedback provided to the subjects was the same as in the previous mode (VD). Concurrently, a cutaneous stimulation was generated as computed in the cutaneous mode (CS). This stimulation augmented the quality of the emulated force field, by combining the visuomotor transformation with the stimulation of fingertips.

The five perturbations were combined with the visual modes (VFA and VFS) into eight experimental conditions (see from A to H in Table 1).

The protocol consisted of eight tasks, each one corresponding to one of the experimental conditions. The conditions were alternated using randomized sequences. No information about the experimental conditions was provided to the subjects, neither on their nature nor on the particular order with which they were going to be presented.

2.4 Data analysis

We grouped the reaches of each task into 8 main *phases*, according to the motor adaptation literature [6, 7, 28]:

1. *Baseline*: the initial movements performed without perturbation (reaches 1–10).
2. *Direct effect*: the first reach with exposure to the perturbation (reach 11).
3. *Adaptation (Early)*: the following 12 reaches, during which the subjects started to adapt to the perturbation (reaches 12–24).
4. *Adaptation (Medium)*: the central phase of adaptation (reaches 25–37).
5. *Adaptation (Late)*: the last 12 reaches before removing the perturbation (reaches 38–50).
6. *After effect*: the first reach after removing the perturbation (reach 51).
7. *Re-adaptation (Early)*: the phase during which the subjects started to re-adapt to movements without perturbation (reaches 52–55).
8. *Re-adaptation (Late)*: the last phase of re-adaptation (reaches 56–60).

For each participant, the left–right *average weighted position error* [28, 29] was calculated as follows:

$$\frac{1}{M_k} \sum_{h=1}^{M_k} \left(\sum_{i=1}^{N_h} \frac{-\text{sign}(v_{yi}) \cdot (x_{si} - x_{ri})}{N_h} \right) \quad (3)$$

where k denotes the phase and h the reach number; M_k is the number of reaches in phase k ; x_{si} , x_{ri} and v_{yi} are, respectively, the current x position, the x reference position and the y velocity of the hand (i – th samples); N_h is the number of samples in reach h . The reference position was $x_{ri} = 0$ for all the experimental conditions except for conditions D and E, in which x_{ri} was the viscous distortion computed as in Eqn. 2.

Normality tests (Shapiro-Wilk normality test and D’Agostino-Pearson omnibus normality test) indicated a Gaussian distribution of position measures. We run a two-way within-subjects ANOVA, with the phases and the experimental conditions as within factors. In the presence of significant effects, pair wise post-hoc comparisons (Tukey’s test) were performed.

Two participants exhibited large variable errors and when questioned after the experiment it was apparent that they had misunderstood the task; thus their data were excluded.

3. RESULTS

Figure 2 shows the position metric and its inter-subject standard deviation in all phases. Statistical analysis indicated a significant interaction between experimental condition and phase (interaction: $F(49, 686) = 31.09$, $p < 0.0001$; condition: $F(7, 98) = 30.40$, $p < 0.0001$; phase: $F(7, 98) = 216.80$, $p < 0.0001$).

Pairwise post-hoc analyses indicated that all the conditions, except from B and G, exhibited significant direct effects when the force field was first applied ($p < 0.0001$, comparison with baseline). Indeed, conditions with CS alone, in presence of either VFA or VFS, showed no significant direct effects (B: $p = 0.9998$; G: $p = 0.8175$), regardless of whether the LCD screen provided information on the lateral position (comparison B–G: $p = 0.7931$).

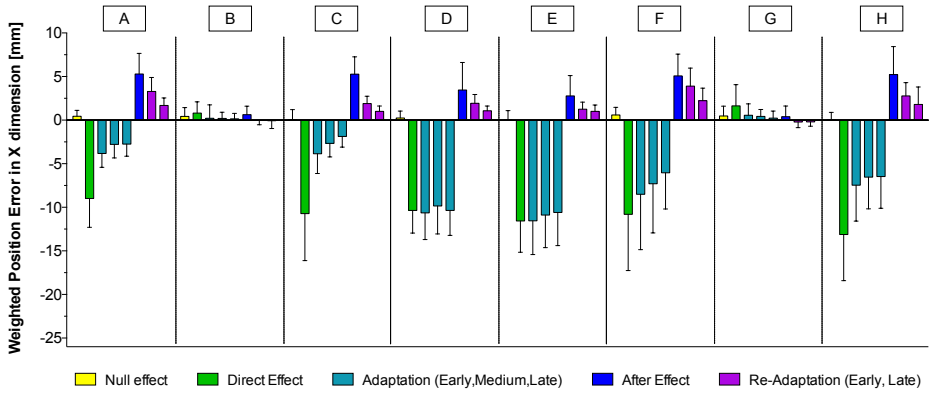


Figure 2. Average weighted position error in the x direction of all the experimental conditions (A: VFA+CS+KS; B: VFA+CS; C: VFA+KS; D: VD; E: VD+CS; F: VFS+CS+KS; G: VFS+CS; H: VFS+KS), for different phases of the experiment. The error bars represent the inter-subject standard deviation, i.e. the standard deviation computed in each phase by using the weighted position error of each subject as data set.

Regarding the magnitude of the direct effect, no difference was found between A and D ($p = 0.6530$), indicating that the visual perturbation, as provided in D, was effectively tuned to simulate the dynamic perturbation applied in A. Direct effects were comparable between conditions with the same visual feedback (A–C: $p = 0.3546$; D–E: $p = 0.7931$; F–H: $p = 0.0661$).

Thus, the first result is that the participants exhibited comparable direct effects when what was applied was a sudden perturbation in the presence of either a kinesthetic or an altered visual feedback, i.e., cutaneous feedback alone was not sufficient to generate direct effects. However, this last point needs deeper investigations.

The direct effect was also compared between similar perturbation modalities with different visual feedback (VFA and VFS respectively), without finding significant effects (A–F: $p = 0.2893$; C–H: $p = 0.0514$).

All the experimental conditions presenting direct effects showed also significant after effects when the perturbation was unexpectedly removed (A, C, F, H: $p < 0.0001$; D: $p = 0.0014$; E: $p = 0.0125$; comparison with baseline). Such effects were comparable in magnitude between conditions without visual distortion (A–C, F–H, A–F, C–H: $p > 0.9999$), while conditions D and E presented significantly smaller after effects with respect to the others ($p < 0.05$).

Following the direct effect, in the experimental conditions with VFA and VFS (A, C, F, H), the subjects adapted to the alteration provided, reducing their position error. Indeed, the error in the last adaptation phase differed significantly if compared with the direct effect ($p < 0.0001$). Instead, D and E didn't present significant adaptation (D: $p > 0.9999$; E: $p = 0.9227$), and the final errors were similar between the two conditions ($p > 0.9999$). These results suggest that kinesthetic stimulation plays a primary role in adaptation.

4. DISCUSSION AND CONCLUSION

4.1 Cutaneous and kinesthetic stimulation

In our experimental setting, cutaneous cues simulating the presence of a viscous force field did not bring any significant direct or after effects when used alone, regardless of the visual feedback provided to the subject (with or without cancellation of position error). On the other hand, all experimental conditions including kinesthetic stimulation (A, C, F, H) brought significant adaptation, aftereffects and re-adaptation, regardless of the cutaneous or visual feedback concurrently being provided. This result suggests that kinesthetic stimulation plays a primary role in robot-induced motor adaptation, while little contribution is provided by the cutaneous part of haptic interaction.

The lack of importance of cutaneous feedback in our experiments, partly conflicts with our initial hypothesis, and with the numerous works highlighting the prominent role of cutaneous forces in recognizing shapes [30], in curvature discrimination tasks [18, 31], and, more generally, in improving the illusion of presence in virtual and remote environments [11, 32, 33]. One explanation may be that the deformation of the finger pads, if not supported by a consistent measure of force by kinetic receptors, is not sufficient to produce the perception of viscosity [34]. It may also be that using wearable cutaneous devices, leaving the participant free to interact with the joystick in a more natural way [11, 12], would have helped in better outlining the role of cutaneous stimulation.

For example, in [11], Prattichizzo et al. analyzed the role of cutaneous feedback in teleoperation. They substituted haptic force feedback, provided by a common single-contact haptic interface, with cutaneous stimuli only, and registered the performance of 16 subjects during a 1-DoF telemanipulation task. Their results showed improved performance with respect to traditional sensory substitution techniques, but still not as good as employing a kinesthetic stimulation. A similar result was also presented in [23], where the role of cutaneous force in a more challenging telemanipulation task was analyzed. The participants were asked to perform a peg-in-hole experiment in a virtual scenario employing (1) cutaneous feedback only, (2) cutaneous and kinesthetic feedback, (3) kinesthetic feedback only, and (4) no force feedback at all. Similarly to [11], cutaneous force showed worse performances than for experimental conditions where kinesthesia was provided, but, unlike the results presented in this work, it showed better performances than for the case providing no force feedback at all.

The discrepancies between the results presented in this work and the ones in [11, 23] can be related to the fact that they dealt with very different environments as well as tasks. The cutaneous and kinesthetic feedbacks provided in the previous works were related to the properties of the virtual environment (i.e. the presence of an object) and were always coherent with the visual information being provided. Force feedback was always directed opposite to the motion of the user's hand and proportional to its displacement, as the haptic interaction was designed according to the god-object model [35]. Instead, in the work presented here, the force perturbation was always perpendicular to the motion of the user's hand and proportional to its velocity, measured along the direction of motion. Moreover, in [11, 23], visual feedback provided very limited information about the task being performed. This may have led users to concentrate more on the force cues than they did in the experiments presented here, where visual cues had a prominent role.

4.2 Viscous visual and video-cutaneous perturbations

The importance of kinesthetic stimulation is also clear if we compare tasks with visual distortion (D, E) to the ones in which kinesthetic stimuli were provided (A, C, F, H). All of

them showed significant direct effects, but the latter had greater aftereffects and adaptation.

It must be underlined that, in conditions D and E, the subjects were forced to learn a velocity-dependent trajectory model that consisted of moving along a non-straight curve. On the opposite, in all other tasks the target trajectory was straight. To this regard, tasks D and E appeared different if compared to the other experimental conditions. Nonetheless, conditions in which viscous visual (D) and video-cutaneous perturbations (E) were provided to the subjects showed some learning effects, indicated by significant aftereffect. This point, however, has to be cleared by a deeper analysis of the first and second half of each reach, separately, with the aim of catching differences in terms of feedforward control during adaptation.

For now, we may hypothesize that the contribution of kinesthesia to motor adaptation could only partially be replaced by visual information reproducing the alteration of motion which would result from the application of a lateral force field. This would suggest that the information provided through the visual sensory channel, if not corroborated by kinesthesia, is not sufficient to produce the same alterations in the subject's motor control. This conclusion is supported by Hwang et al. [36], who tested the hypothesis that proprioceptive states in which the limb is perturbed dominate the representation of limb state, by performing a task where position of the hand during a reach was correlated with patterns of force perturbation.

The additional cutaneous stimulation provided in our experiment during task E, which reproduced the same effect on the fingertips which would result from the application of a lateral force field, did not bring major improvements. In fact, tasks D and E were comparable in terms of direct and after effects, regardless of the presence of cutaneous stimuli.

4.3 Contribution of visual feedback

By comparing tasks A vs F and C vs H, we can notice that when visual feedback correctly resembles hand movements (A, C), motor adaptation becomes faster with respect to when visual cues are not informative on position error (F, H). This would suggest that visual feedback, if properly delivered, can influence adaptation to a dynamic environment. However, this difference in adaptation rate will have to be confirmed by a deeper analysis of the data. After that, we will be able to speculate on this possible result.

In our experiment, during tasks F and H, a straight visual feedback was provided to the users that is known in the literature as a visual channel [9]. This condition can be considered as a "false visual feedback" case, wherein the green cursor represented a projection of the hand's trajectory onto the straight line passing through the targets. Scheidt et al. [9] performed a series of experiments exploring the integration of visual and proprioceptive estimates of hand-path error during adaptation of reaching movements to a novel dynamic environment. Subjects grasped and moved the handle of an instrumented robot, which pushed the hand away from its intended target. They employed three visual feedback conditions: accurate visual feedback (concurrent visual and proprioceptive feedback), no visual feedback (proprioception feedback only), and visual channel feedback. The latter condition significantly impaired correction of initial direction errors during reaching. In fact, these errors increased with repeated exposure to the field. This result apparently contrasts with that found in our experiment. However, one must notice that the motion task in Scheidt's experiment differed from the one presented here, since it included the reach of eight target locations equally spaced around the periphery of a circle in the horizontal plane, and the viscous force field was a function of both directions (x and y). Secondly, no subject in that study reported being aware of the visual channel manipulation when asked to describe his/her experience after that session. On the contrary, in our experiment most subjects declared they had realized that the visual information had been altered. Implicit,

in this case, it is the possibility that the subjects used unaltered proprioceptive feedback of movement errors to drive adaptive improvements in motor performance, disregarding the visual information.

4.4 Concluding remarks

This study shows the first preliminary results on the contribution of the kinesthetic and the cutaneous parts of haptic feedback during the motor learning of a viscous field in reaching tasks. The analyses performed and the results found here can be considered as a first stage in the study of the haptic feedback as sensory summation of kinesthetic and cutaneous components in motor learning.

Obviously, this study presents some limitations that could be investigated in future experiments such as one-dimensional movements, the rate of introduction of the perturbation, the particular cutaneous devices employed, the use of other sensory modalities (e.g., auditory feedback [28, 29]), etc.

Also, there are some missed explorations in the analysis performed and described here. Indeed, it could be interesting to extract other importance information by these data.

First of all, it could be worth analyzing movement speeds, especially the velocity peak along the y axis and its temporal location to investigate possible differences in the movements trajectory within and between subjects for each task and in each phase.

Then, the extension of the analysis of the left-right average weighted position error in order to measure its values by considering separately both the first and second half of each reach. In this way, we could catch the differences in terms of feedforward (first half) and feedback control (second half) during adaptation. These metrics will be computed, and the complete report will be presented later.

REFERENCES

- [1] Hamed, A., Tang, S. C., Ren, H., Squires, A., Payne, C., Masamune, K., Tang, G., Mohammadpour, J., and Tse, Z. T. H., 2012. "Advances in haptics, tactile sensing, and manipulation for robot-assisted minimally invasive surgery, noninvasive surgery, and diagnosis". *J Robotics*, **2012**, pp. 1–14.
- [2] Reinkensmeyer, D. J., Emken, J. L., and Cramer, S. C., 2004. "Post-stroke upper extremity rehabilitation: a review of robotic systems and clinical results". *Annual Review of Biomedical Engineering*, **6**, pp. 497–525.
- [3] Krebs, H. I., Volpe, B., and Hogan, N., 2009. "A working model of stroke recovery from rehabilitation robotics practitioners". *J NeuroEng Rehabil*, **6**, p. 6.
- [4] Timmermans, A. A., Seelen, H. A., Willmann, R. D., and Kingma, H., 2009. "Technology-assisted training of arm-hand skills in stroke: concepts on reacquisition of motor control and therapist guidelines for rehabilitation technology design". *J NeuroEng Rehabil*, **6**.
- [5] Rosati, G., 2010. "The place of robotics in post-stroke rehabilitation". *Expert Review of Medical Devices*, **7**(6), pp. 753–758.
- [6] Shadmehr, R., and Mussa-Ivaldi, F. A., 1994. "Adaptive representation of dynamics during learning of a motor task.". *Journal of Neuroscience*, **14**(5 Pt 2), pp. 3208–3224.
- [7] Scheidt, R. A., Reinkensmeyer, D. J., Conditt, M. A., Rymer, W. Z., and Mussa-Ivaldi, F. A., 2000. "Persistence of motor adaptation during constrained, multi-joint, arm movements.". *Journal of Neurophysiology*, **84**(2), pp. 853–862.
- [8] Feygin, D., Keehner, M., and Tendick, R., 2002. "Haptic guidance: Experimental evaluation of a haptic training method for a perceptual motor skill". In *Haptic Interfaces for Virtual Environment and Teleoperator Systems*, 2002. HAPTICS 2002. Proceedings. 10th Symposium on, pp. 40–47.

- [9] Scheidt, R. A., Conditt, M. A., Secco, E. L., and Mussa-Ivaldi, F. A., 2005. “Interaction of visual and proprioceptive feedback during adaptation of human reaching movements”. *Journal of Neurophysiology*, **93**(6), pp. 3200–3213.
- [10] Morris, D., Tan, H., Barbagli, F., Chang, T., and Salisbury, K., 2007. “Haptic feedback enhances force skill learning”. In EuroHaptics Conference, 2007 and Symposium on Haptic Interfaces for Virtual Environment and Teleoperator Systems. World Haptics 2007. Second Joint, pp. 21–26.
- [11] Prattichizzo, D., Pacchierotti, C., and Rosati, G., 2012. “Cutaneous force feedback as a sensory subtraction technique in haptics”. *IEEE Transactions on Haptics*, **5**(4), pp. 289–300.
- [12] Pacchierotti, C., Tirmizi, A., and Prattichizzo, D., 2014. “Improving transparency in teleoperation by means of cutaneous tactile force feedback”. *ACM Transactions on Applied Perception*. In Press.
- [13] Birznieks, I., Jenmalm, P., Goodwin, A., and Johansson, R., 2001. “Encoding of direction of fingertip forces by human tactile afferents”. *The Journal of Neuroscience*, **21**(20), pp. 8222–8237.
- [14] Johnson, K. O., 2001. “The roles and functions of cutaneous mechanoreceptors”. *Current Opinion in Neurobiology*, **11**(4), pp. 455–461.
- [15] Hayward, V., Astley, O., Cruz-Hernandez, M., Grant, D., and Robles-De-La-Torre, G., 2004. “Haptic interfaces and devices”. *Sensor Review*, **24**(1), pp. 16–29.
- [16] Edin, B. B., and Johansson, N., 1995. “Skin strain patterns provide kinaesthetic information to the human central nervous system.”. *The Journal of Physiology*, **487**(Pt 1), pp. 243–251.
- [17] Gordon, J., and Ghez, C., 2000. “Muscle receptors and spinal reflexes: the stretch reflex”. In *Principles of Neural Science*, E. R. Kandel, J. H. Schwartz, and T. M. Jessell, eds. McGraw-Hill, pp. 564–580.
- [18] Prattichizzo, D., Chinello, F., Pacchierotti, C., and Malvezzi, M., 2013. “Towards wearability in fingertip haptics: a 3-DoF wearable device for cutaneous force feedback”. *IEEE Transactions on Haptics*, **6**(4), pp. 506–516.
- [19] Stanley, A. A., and Kuchenbecker, K. J., 2012. “Evaluation of tactile feedback methods for wrist rotation guidance”. *IEEE Transactions on Haptics*, **5**(3), pp. 240–251.
- [20] Lee, B. C., Chen, S., and Sienko, K. H., 2011. “A wearable device for real-time motion error detection and vibrotactile instructional cuing”. *IEEE Transactions on Neural Systems and Rehabilitation Engineering*, **19**(4), pp. 374–381.
- [21] Lieberman, J., and Breazeal, C., 2007. “TIKL: Development of a wearable vibrotactile feedback suit for improved human motor learning”. *IEEE Transactions on Robotics*, **23**(5), pp. 919–926.
- [22] Pacchierotti, C., Tirmizi, A., Bianchini, G., and Prattichizzo, D., 2014. “Improving transparency in passive teleoperation by combining cutaneous and kinesthetic force feedback”. In Proc. IEEE/RSJ Int. Symp. Intelligent Robots and Systems.
- [23] Pacchierotti, C., Chinello, F., Malvezzi, M., Meli, L., and Prattichizzo, D., 2012. “Two finger grasping simulation with cutaneous and kinesthetic force feedback”. In Haptics: Perception, Devices, Mobility, and Communication. Eurohaptics, Lecture Notes in Computer Science, pp. 373–382.
- [24] Cenci, S., Rosati, G., Zanotto, D., Oscari, F., and Rossi, A., 2010. “First test results of a haptic tele-operation system to enhance stability of telescopic handlers”. In Proceedings of the ASME 2010 10th Biennial Conference on Engineering Systems Design and Analysis ESDA2010.
- [25] Serina, E., Mote, C., et al., 1997. “Force response of the fingertip pulp to repeated compression—effects of loading rate, loading angle and anthropometry”. *Journal of Biomechanics*, **30**(10), pp. 1035–1040.
- [26] Vallbo, Å. B., Johansson, R., et al., 1984. “Properties of cutaneous mechanoreceptors in the human hand related to touch sensation”. *Human Neurobiology*, **3**(1), pp. 3–14.

- [27] Johansson, R. S., 1978. "Tactile sensibility in the human hand: receptive field characteristics of mechanoreceptive units in the glabrous skin area." *The Journal of Physiology*, **281**, p. 101.
- [28] Oscari, F., Secoli, R., Avanzini, F., Rosati, G., and Reinkensmeyer, D. J., 2012. "Substituting auditory for visual feedback to adapt to altered dynamic and kinematic environments during reaching". *Experimental Brain Research*, **221**(1), pp. 33–41.
- [29] Rosati, G., Oscari, F., Spagnol, S., Avanzini, F., and Masiero, S., 2012. "Effect of task-related continuous auditory feedback during learning of tracking motion exercises". *Journal of NeuroEngineering and Rehabilitation*, **9**(79).
- [30] Jansson, G., and Monaci, L., 2006. "Identification of real objects under conditions similar to those in haptic displays: providing spatially distributed information at the contact areas is more important than increasing the number of areas". *Virtual Reality*, **9**(4), pp. 243–249.
- [31] Frisoli, A., Solazzi, M., Salsedo, F., and Bergamasco, M., 2008. "A fingertip haptic display for improving curvature discrimination". *Presence: Teleoperators and Virtual Environments*, **17**(6), pp. 550–561.
- [32] Prattichizzo, D., Chinello, F., Pacchierotti, C., and Minamizawa, K., 2010. "Remotouch: A system for remote touch experience". In Proc. of IEEE International Workshop on Robot and Human Interactive Communication, pp. 676–679.
- [33] Okamura, A. M., 2004. "Methods for haptic feedback in teleoperated robot-assisted surgery". *Industrial Robot: An International Journal*, **31**(6), pp. 499–508.
- [34] Okamoto, S., Konyo, M., and Tadokoro, S., 2011. "Vibrotactile stimuli applied to finger pads as biases for perceived inertial and viscous loads". *EEE Transaction on Haptics*, **4**(4), Oct., pp. 307–315.
- [35] Zilles, C., and Salisbury, J., 1995. "A constraint-based god-object method for haptic display". In Proc. of IEEE/RSJ International Conference on Intelligent Robots and Systems, Vol. 3, pp. 146–151.
- [36] Hwang, E., Smith, M., and Shadmehr, R., 2006. "Dissociable effects of the implicit and explicit memory systems on learning control of reaching". *Experimental Brain Research*, **173**(3), pp. 425–437.

IMPROVED RIG FOR THE ANALYSIS OF KNEE BEHAVIOUR UNDER DYNAMIC MOTION TASKS

Nicola Sancisi
*Department of Industrial Engineering,
University of Bologna, Italy
E-mail: nicola.sancisi@unibo.it*

Michele Conconi
*Department of Industrial Engineering
Health Sciences and Technologies Interdepartmental Centre for Industrial Research
University of Bologna, Italy
e-mail: michele.conconi@unibo.it*

Margherita Forlani
*Department of Industrial Engineering
Health Sciences and Technologies Interdepartmental Centre for Industrial Research
University of Bologna, Italy
e-mail: margherita.forlani2@unibo.it*

Vincenzo Parenti Castelli
*Department of Industrial Engineering
Health Sciences and Technologies Interdepartmental Centre for Industrial Research
University of Bologna, Italy
E-mail: vincenzo.parenti@unibo.it*

Abstract. *The evaluation of the knee joint behaviour is of great interest for medicine. A new rig to test knees in vitro in loaded and unloaded conditions is presented in this paper. Its loading system based on a cable-driven parallel manipulator allows the application of general loads typical of common daily activities. Its force-control permits the evaluation of the joint natural response to the loads in terms of movement, measured thanks to a stereophotogrammetric system. In addition, the principal muscles that control the knee flexion and extension can be simulated and their contributions to the joint equilibrium can be evaluated thanks to a dedicated control system. The rig is an evolution of a previously presented version, of which it preserves the low cost and simplicity, together with the versatility and accuracy.*

Keywords: *knee behaviour, static analysis, dynamic analysis, test rig, in vitro test*

1. INTRODUCTION

The study of the behaviour of the knee joint and of the role of its articular structures is of great interest for the biomechanics community. A complete description of the knee joint behavior is fundamental to design and test new prostheses, to define and validate models of the joint, to develop rehabilitation strategies and to optimise surgical reconstruction techniques [1,2].

The evaluation of the knee joint behavior is performed by means of several tests: unloaded motion analysis, clinical tests and active motor tasks. They analyse the behaviour of the joint in different loading conditions and involving different structures: for instance, only articular surfaces and a limited number of ligaments are involved in passive motion, whilst all the joint active and passive structures are involved during active motor tasks.

Tests can be performed both *in vivo* and *in vitro*. *In vivo* tests allow the evaluation of the relative motion of the joint bones together with the muscle activation patterns; they require the use of complex and expensive motion evaluation techniques, like MRI or fluoroscopy, or invasive techniques, like intracortical pins, or conversely the acceptance of errors induced by soft tissue artifacts, if skin markers are used [3]. These limitations are not generally present when executing *in vitro* tests: the relative motion of the bodies can be analyzed in this case by directly measuring the motion of trackers fixed to the bones. However, active motion tasks that require muscle activation (such as standing from a chair) cannot be directly performed *in vitro*: loading conditions have to be previously measured *in vivo* and carefully reproduced on specimens during *in vitro* tests. Similarly, muscle activation patterns cannot be measured during tests on specimens.

Several test rigs have been developed in the last few years to execute *in vitro* tests in order to analyse the knee joint behaviour. Some of them are mainly devoted to the analysis of the kinematics of the joint in virtually unloaded conditions [4,5] or under the simulated body weight and quadriceps effects [6]. The principal limitation of these rigs is that they do not permit to test the knee during generic active motor tasks and under generic loading conditions. Other rigs are mainly devoted to the replication of *in vivo* tasks: the kinematics measured *in vivo* can be replicated on specimens and the necessary loads can be measured [7] or, conversely, the loads measured *in vivo* can be applied and the movements can be analysed [8]. Usually, these rigs are robot-based testing machines, thus they require complex control systems.

In this context, a new simple test rig is proposed in this study to evaluate the behaviour of the knee joint in both loaded and unloaded conditions. It allows the application of general loads to the knee joint in a wide range of flexion. Applied loads vary in real time according to flexion and to simulated task. All motion components of the joint (except for the flexion angle) are unconstrained, to not impose any reaction that could modify the joint response in terms of movements: forces are imposed, while joint rotations and displacements are measured. The rig is also equipped with a system that simulates and controls the leg main muscles, evaluating the muscle forces that guarantee the joint equilibrium at the considered loading conditions. The new rig represents an evolution of a previously proposed test rig, devoted to the execution of clinical tests [9]. It preserves the simplicity and low cost of the previous version, whilst showing flexibility and high accuracy and guaranteeing repeatability of measurements.

The rig specifications and the adopted solutions will be presented in the following sessions.

2. GENERAL REQUIREMENTS

Motion Tasks

The purpose of the new rig is the *in vitro* evaluation of the behavior of the knee joint in loaded and unloaded conditions.

To evaluate the knee behaviour in unloaded conditions, the relative motion between the tibia and the femur is measured during flexion when no external and no muscular loads are applied, and gravity is balanced. This kind of tests allows the analysis of the natural motion (passive motion) of the knee joint, that shows one degree of freedom in virtually unloaded conditions.

Besides, many different tests can be performed to evaluate the knee behavior in loading conditions: the relative poses between the tibia and the femur are measured while applying loads reproducing several given tasks, such as clinical tests and daily life activities. Clinical tests are usually performed by orthopaedists to assess any damage in the articular passive structures. They consist in applying static external loads to the knee joint at fixed flexion angles and evaluating the corresponding articular motion. Three types of test are usually performed on the knee joint: the drawer, the internal/external rotation and the ab/adduction tests. To describe the tests, a reference system St can be defined fixed to the tibia, where z is the medial/lateral axis, x is the anterior/posterior axis and y is perpendicular to the other two. The drawer test, which is showed in Fig. (1a), is performed by blocking the femur and, at a fixed flexion angle, by applying a force to the tibia directed in anterior/posterior direction (i.e. the x axis of St). The internal/external rotation test, which is showed in Fig. (1b), is performed by blocking the femur and, at a fixed flexion angle, by applying a couple to the tibia directed along the distal/proximal direction (i.e., the y axis of St). The abduction/adduction test, which is showed in Fig. (1c), is performed by blocking the femur and, at a fixed flexion angle, by applying a couple directed along the posterior/anterior direction (i.e., the x axis of St). These tests are repeated at different flexion angle values.

Beside the clinical ones, other tests replicating the loading conditions at which the knee is subjected during active motion tasks (like walking or standing from a chair) are necessary to evaluate the whole knee behaviour. During active motion tasks, the joint is subjected to a

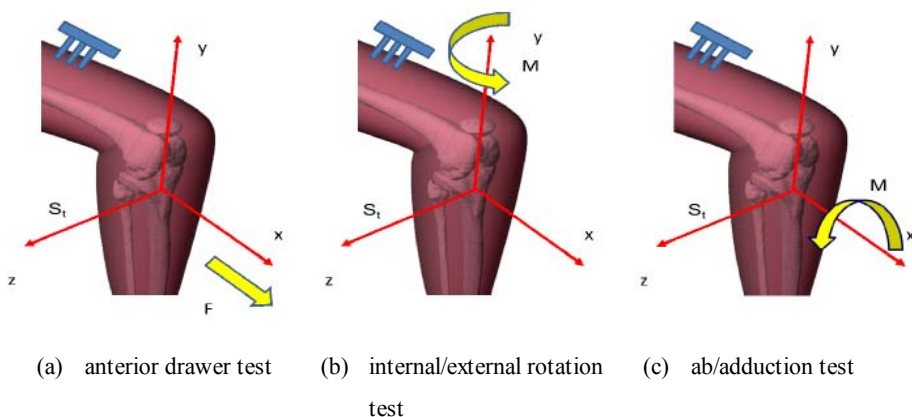


Figure 1. The clinical tests commonly executed on the knee joint.

complex system of forces and moments, due to forces exchanged between the foot and the ground and to forces exerted by the muscles. During daily activities, indeed, the muscles play an important role in guaranteeing the equilibrium and apply significant loads. The system of forces and moments, i.e. the wrench, exchanged between the foot and the ground varies with the tasks and the flexion of the knee. The muscle forces change accordingly, in order to guarantee the joint equilibrium.

Rig requisites

The rig is required to allow the test of the knee joint motion both when no loads and when certain loads are applied. A general wrench must be applied to the joint, variable with the task and the flexion angle. Several *in vivo* measurements of the forces exchanged between the foot and the ground during the most common daily activities have been performed in the literature [1,10,11]. They show how the walking is the most demanding activity in terms of generated forces: the ground reaction forces reach peaks of 125%BW in vertical direction and 30%BW in anterior direction. Furthermore, the most important muscle forces must be simulated, since muscles play an important role to provide the dynamic equilibrium during active motion tasks.

To guarantee the evaluation of the joint natural behaviour, the full range of motion of the joint must be guaranteed. In the design of the test rig, the range of motion of the knee joint has been considered with respect to diseased knees. In particular, if a coordinate system is defined according to [12], the following ranges of rotations and translations of the knee must be guaranteed: 130 degrees of flexion/extension, ± 30 degrees of ab/adduction and ± 40 degrees of internal/external rotation; ± 10 mm of medial/lateral, ± 40 mm of anterior/posterior and 40 mm of distraction displacements [2,13]. In all these rather wide ranges of motion, the test rig must be able to apply the loads typical of daily activities. No other loads must be applied to the joint, in order to not introduce further constraints that would alter the natural joint response.

Easiness of specimen unmounting and remounting, together with the possibility of a precise repositioning of the specimen itself within different tests must be guaranteed. Indeed, a number of experimental procedures and protocols require that some tests are repeated on the same specimen at a different time, (for example, before and after a prosthesis implantation), thus requiring to unmount the specimen from the test rig and to precisely remount it in the same position. Repeatability of the loading conditions is also required. In this context, a precise alignment of the specimen with the rig according to some anatomical landmarks guarantees that the applied loads have exactly the desired directions with respect to the joint. These characteristics are important to guarantee the consistency among the measurements from several tests on the same or different specimens.

In addition, since tests are performed on specimens with a wide range of sizes, the test rig is required to be versatile and easily adjustable for any leg size. The device has to be cheap and easy-to-clean, since it is used in contact with human tissues.

3. DESCRIPTION OF THE RIG

Overall Description of the Rig Architecture

The frame of the rig is formed by square section standard aluminum profiles, fixed together

by means of standard angle connections and bolts. In Fig. 2 a schematic of the rig is represented. The frame is composed by two parts: a base (5), fixed to the laboratory, and a portal (1). The portal is connected to the base via a rotational joint that allows its rotation with respect to the base about their common axis. The femur (3) is connected to the portal; while the tibia (10) is housed in the base and fixed to a ring (6) by means of proper clamping devices. At each fixed flexion angle, the relative position and orientation of the tibia with respect to the femur is determined solely by the constraints imposed by the joint structures and is measured by a stereophotogrammetric system. The knee flexion angle is set by rotating the portal and changing the position of the femur while keeping the axis of the tibia vertical, as described in the following. A flexion angle of 135 degrees can be reached. The specimen is mounted so that the transepicondylar femur axis (i.e., the physiological flexion axis) is coincident with the hinge joint axis. In this way, the relative motion between the tibia and the frame during flexion is minimized and the flexion angle of the joint and the applied loads can be controlled more easily and with a higher precision. The base is fixed with respect to the laboratory and contains the elements of the actuation system (8).

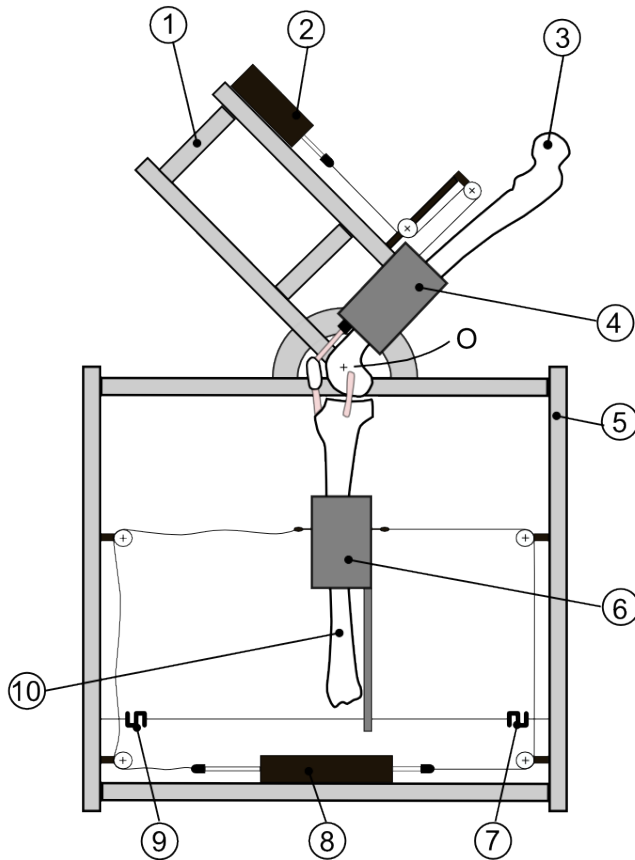


Figure 2. Schematic of the test rig: portal (1); single-acting pneumatic actuator (2); femur (3); femur fixation system (4); base (5); tibial ring (6); load cells (7) and (9); double-acting pneumatic actuator (8); tibia (10).

The femur is mounted on the rig by a fixation system that makes it possible to adjust the position of the specimen in the rig in all 6 DOFs in space, namely three translations and three rotations. The system consists of a femur fixation ring and a reference element; the former is provided with clamps that guarantee a rigid connection to the femur, while the latter is firmly connected to the portal. These two components can be univocally referred one another and can be unmounted and remounted in the same relative pose. The 6 DOFs can be regulated during specimen positioning and then they are locked, so that the femur is fixed to the portal and only the flexion angle can be regulated, by rotating the portal about the rotational joint axis. The pose of the femur with respect to the rig can thus be precisely controlled. The femur ring can be dismantled together with the femur. Thus the system permits also to accurately unmount and remount the femur in the same pose with respect to the rig, between two tests.

While the femur is fixed to the portal, the tibia is connected to the loading system. In particular, the tibial ring (6) is rigidly connected the tibia by means of high friction clamps; loads of the actuation system are applied to the ring, as it will be further described in the following section. Both the tibia and femur clamps are realized in stainless steel, since they enter into contact with the specimen, and are covered in sandpaper. They are designed to guarantee the anchoring of the bone by friction; thus, no bone preparation is needed and each single bone can be utilized for further tests.

Cable-driven Fully Parallel Loading System

A simple loading system has been studied to apply general wrenches to the tibia. Clinical tests require the application of constant loads directed along one of the axes of the defined reference system; conversely, motion daily activities require the application of complex wrenches, variable with the flexion angle.

As previously noted, the femur rotation is imposed by the frame portal while the tibia is free to change its pose. Five DOFs are left to the tibia with respect to the frame. Indeed, the tibia is free to move in order to reach the equilibrium pose, due to the effect of the loads and of the knee structures (articular surfaces, ligaments and muscles when activated). Only the tibia longitudinal axis is constrained to remain vertical, to control the flexion angle: this separate force control will be described in the following section.

A cable-driven fully parallel architecture has been adopted for the loading system. The tibial ring represents the movable platform of the system. The platform is actuated by 12 steel cables, two by two acting in the same direction and forming a closed loop with the actuator and the tibial ring. In each pair, one cable is always in tension and one always slack, so that only six actuators are necessary, namely one for each pair of cables; furthermore, this guarantees that while the tensioned side of the loop provides the load to the tibial ring, the natural motion of the tibia is not resisted by the untensioned side. Forces and moments are generated by pneumatic double-acting cylinders (8) with double-ended piston rod. One of the actuation closed loop is shown in Fig. 2.

The cables are connected to the tibial ring in a fashion that makes it possible to decouple the force and moment components along and about the three directions of the reference system defined in Sub-sect. 'Motion Task'. This particular configuration allows the application of general wrenches, within the desired range, guaranteeing simplified control, minimum forces at the actuators, and simple application of the loading conditions typical of the clinical tests. Considering the effect of friction in cylinders and pulleys, the

maximum applicable wrench components are: maximum force components of 2400 N for any of the three directions x , y and z previously defined; maximum moment components of 100 Nm about z axis and 300 Nm about x and y axes. These ranges of loads and moments guarantee the replication of all the loads of common daily activities.

This actuation system thus allows the simulation of several loading conditions, by applying to the tibia, through the tibial ring, a system of forces equivalent to those measured during both clinical tests and daily activities, like walking, squat and sit-to-stand tasks. For daily activities, the forces exchanged between the foot and the ground can be measured by means of a force platform during *in vivo* tests. The equivalent system of forces at the tibial ring can be calculated by considering the relative pose of the tibia with respect to the ground at each instant of the task and by an equivalence between force systems: ground forces are transformed in an equivalent system of 6 forces along the cables by the control code, that computes the pressure required by each cylinder.

The cylinder pressures are directly controlled, thus no feedback sensor is required and the control is simplified. The equivalent system of external loads is modified and applied to the tibia for each flexion angle, according to the specific task. When the flexion angle is changed by rotating the portal, a transducer communicates the flexion angle to the control system, that modifies the loads in the pneumatic actuators accordingly.

Simulation of muscle forces

While in unloaded motion and during clinical tests no muscle is involved, when executing daily activities muscles play an important role in guaranteeing the equilibrium of the knee joint. The system developed to reproduce muscle effects on specimens simulates and controls the effect of the most important muscles responsible of knee extension and flexion: in particular, the quadriceps on the anterior side, and the hamstrings and gastrocnemius on the posterior side.

With this system, the difference between muscle forces required by a given task can be experimentally obtained and not only imposed to the joint, by finding the equilibrium configuration that maintains the projections of the longitudinal tibial axis on the sagittal plane almost vertical. Two cables, one anterior and one posterior, connect the tibial ring to the frame distally, as shown in Fig. 2, and maintain the axis of the tibia vertical. Two load cells (7) and (9), positioned between each cable and the frame, measure the tension in the cables in the anterior/posterior direction. The difference between the two tensions controls the activation of the extensor or the flexor muscles in order to maintain the static equilibrium of the leg.

The quadriceps is simulated thanks to a single-acting pneumatic actuator (2) (Fig. 2), fixed to the portal and connected to the quadriceps tendon by means of a clamping device. Its position and orientation can be adjusted in order to align the quadriceps force to its anatomical direction. If, as a consequence of the external loads, the knee tends to flex, thus tensioning the anterior cable, the quadriceps actuator is activated to eliminate the tension.

Conversely, actuators strictly devoted to the simulation of the posterior muscles are not present on the rig. The muscles on the posterior side are simulated by applying an equivalent load to the tibial ring. In particular, if the knee tends to extend, thus tensioning the posterior cable, the effect of posterior muscles is simulated by applying a wrench to the tibial ring. In this case, thus, the total wrench applied to the tibial ring \overline{W}_{tot} is the sum of

two contributions: a wrench equivalent to the external loads measured during daily actions \overline{W}_{task} and a wrench equivalent to the resultant of the contribution \overline{W}_{res} of the two considered flexor muscles, i.e. gastrocnemius and hamstring which generate \overline{W}_{gas} and \overline{W}_{ham} respectively.

$$\overline{W}_{tot} = \overline{W}_{task} + \overline{W}_{res} = \overline{W}_{task} + \overline{W}_{ham} + \overline{W}_{gas} \quad (1)$$

For determining the resultant force of posterior muscles, information from the literature and subject-specific data are considered, together with a control system similar to that used for the quadriceps. In particular, the origin and insertion points of the hamstring (A_1 and B_1 , Fig. 3) and of the gastrocnemius (A_2 and B_2) are measured on the specimen to define the two lines of action of these muscles (represented by the unit vectors \overline{u}_{ham} for the hamstrings and \overline{u}_{gas} for the gastrocnemius) at each flexion angle. An estimation of the ratio k between the magnitude F_{ham} of the hamstring force \overline{F}_{ham} and the magnitude F_{gas} of the gastrocnemius force \overline{F}_{gas} is taken from the literature for each task. These information

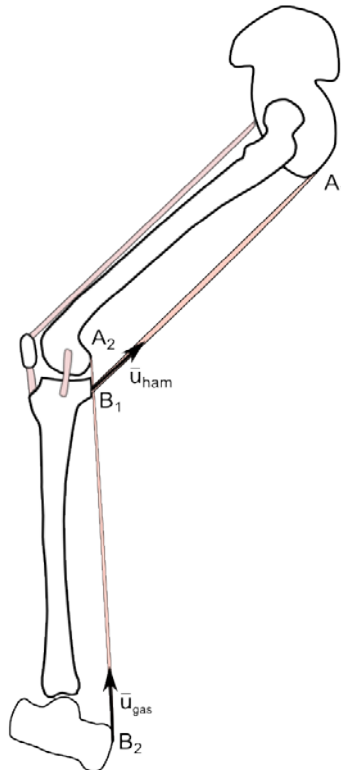


Figure 3. Schematic representation of the principal muscles responsible for knee flexion and extension.

are sufficient to obtain the line of action (unit vector \bar{u}_{res}) of the resultant of the posterior muscle forces \bar{F}_{res} :

$$\bar{F}_{res} = \bar{F}_{ham} + \bar{F}_{gas} = F_{ham} \bar{u}_{ham} + F_{gas} \bar{u}_{gas} = F_{gas} (k \bar{u}_{ham} + \bar{u}_{gas}) = F_{res} \bar{u}_{res} \quad (2)$$

The magnitude F_{res} of the resultant force is identified by the control system in order to guarantee the equilibrium.

This system makes it possible to simulate the effect of the muscles on the tested leg. Indeed, it applies a load that balances the knee flexion/extension moment. The load simulates the action of the quadriceps or the action of the posterior muscles, depending on the behavior of the knee joint. Therefore, this system allows the evaluation of the muscle contribution during daily activities. However, only the difference of the action of the antagonist muscles can be evaluated, since the present control system does not consider co-contraction of anterior and posterior muscles.

4. DISCUSSIONS AND CONCLUSIONS

In this work a new test rig has been presented as an evolution of a previously proposed one. Preserving the low cost and the simplicity of the previous version, the new test rig permits to evaluate the behavior of the human knee under loaded and virtually unloaded conditions in a wide range of motion.

The loading system based on a cable-driven fully parallel manipulator applies a general wrench to the knee. Furthermore, the action of the principal muscles of the leg is simulated: the dedicated system allows the evaluation of the force of the extensor and of the flexor muscles in guaranteeing the knee equilibrium at each flexion position, or at least the difference between contribution of antagonist muscles. The rig, thus, allows a precise replication of in vivo loading conditions on specimens. The force control adopted for the actuation allows the evaluation of the natural behavior of the tested joint, since the movement of the tibia and patella with respect to the femur due to the applied loads is not constrained. In addition, the possibility to evaluate the muscular loads is a key feature of the test rig, even if co-contraction of flexor and extensor muscles is not taken into account.

Moreover, the new test machine is versatile, with regards to both the kind of executable tests and the size of specimens, and easy to set up and clean. Actually, with some modifications also other joints, like the ankle, can be tested.

The developed rig was used to test a knee before and after the installation of a prosthetic device. The experimental set up is shown in Fig. 4. The rig showed good performances in terms of accuracy and repeatability. Finally, the design of the clamping and the adjustable device offers a good accuracy in positioning and in restoring the position if the specimen is unmounted between tests. Great accuracy was shown also in the loading and in the measuring systems. Since the experimental conditions were clearly defined and the machine proved to be accurate, experiments proved to be highly repeatable.



Figure 4. Experimental set up: a specimen is mounted on the rig, surrounded by the cameras of the stereophotogrammetric system.

Acknowledgements

The authors wish to acknowledge the Health Sciences and Technologies Interdepartmental Centre for Industrial Research (HST-ICIR) for supporting this research, and thank Dr. Benedetta Baldisserri and Dr. Diego Zannoli for their contribution to the construction of the rig.

REFERENCES

- [1] Anderson, F. C., and Pandy, M. G., 2001. "Dynamic optimization of human walking". *Journal of biomechanical engineering*, **123**(5), pp. 381-390.
- [2] Sancisi, N., Zannoli, D., Parenti-Castelli, V., Belvedere, C., and Leardini, A., 2011. "A one-degree-of-freedom spherical mechanism for human knee joint modelling". *Proceedings of the Institution of Mechanical Engineers, Part H: Journal of Engineering in Medicine*, **225**(8), pp. 725-735.

- [3] Leardini, A., Chiari, L., Croce, U. D., and Cappozzo, A., 2005. "Human movement analysis using stereophotogrammetry: Part 3. soft tissue artifact assessment and compensation". *Gait & posture*, **21**(2), pp. 212–225.
- [4] Ottoboni, A., Parenti Castelli, V., Sancisi, N., Belvedere, C., Leardini, A., 2010. "Articular surface approximation in equivalent spatial parallel mechanism models of the human knee joint: an experiment-based assessment". *Proceedings of the Institution of Mechanical Engineers, Part H: Journal of Engineering in Medicine*, **224**(9), pp. 1121 – 1132.
- [5] Ottoboni, A. and Parenti Castelli, V., 2006. "A simple system for the measurement of human joint passive motion", Proceedings of the 10th Mechatronics Forum Biennial International Conference, Penn State Great Valley, June 19-21, Malvern, PA, USA.
- [6] Zavatsky, A. B., 1997. "A kinematic-freedom analysis of a flexed-knee-stance testing rig". *Journal of biomechanics*, **30**(3), pp. 277–280.
- [7] Ding, B., Stanley, R. M., Cazzolato, B. S., and Costi, J. J., 2011. "Real-time fpga control of a hexapod robot for 6-dof biomechanical testing." In Proceedings of IECON 2011- 37th Annual Conference on IEEE Industrial Electronics Society, pp 252–257.
- [8] Varadarajan, K. M., Harry, R. E., Johnson, T., and Li, G., 2009. "Can in vitro systems capture the characteristic differences between the flexionextension kinematics of the healthy and tka knee?". *Medical engineering and physics*, **31**(11), pp. 899–906.
- [9] Zannoli, D., Sancisi, N., and Parenti Castelli, V., 2012. "A simple rig for precise measurements of the knee and ankle joint motion under static loading conditions". In Proceedings of Sesta Giornata di Studio Ettore Funaioli, pp. 160–16.
- [10] Guess, T.M., and Stylianou, A., 2012. "Simulation of anterior cruciate ligament deficiency in a musculoskeletal model with anatomical knees". *The open biomedical engineering journal*, **6**, pp.23–32.
- [11] Hirschfeld, H., Thorsteinsdottir, M., and Olsson, E., 1999. "Coordinated ground forces exerted by buttocks and feet are adequately programmed for weight transfer during sit-to-stand". *Journal of neurophysiology*, **82**(6), pp. 3021–3029.
- [12] Grood, E.S., and Suntay, W.J., 1983. "A joint coordinate system for the clinical description of three-dimensional motions: application to the knee". *Journal of Biomechanical Engineering*, **105**, pp. 136–144.
- [13] Grood, E.S., Stowers, S.F., and Noyes, F.R., 1988. "Limits of movement in the human knee". *The Journal of Bone and Joint Surgery*, **70-A**(1), pp.88–97.

LAVORAZIONI MECCANICHE ROBOTIZZATE DI PRECISIONE NELL'INDUSTRIA AUTOMOTIVE: UNA PROSPETTIVA EUROPEA

Angelo O. Andrisano

*Dipartimento di Ingegneria "Enzo Ferrari",
Università degli Studi di Modena e Reggio Emilia
E-mail: angelo.andrisano@unimore.it*

Francesco Leali

*Dipartimento di Ingegneria "Enzo Ferrari",
Università degli Studi di Modena e Reggio Emilia
E-mail: francesco.leali@unimore.it*

Fabio Pini

*Dipartimento di Ingegneria "Enzo Ferrari",
Università degli Studi di Modena e Reggio Emilia
E-mail: fabio.pini@unimore.it*

Matteo Ansaloni

*Dipartimento di Ingegneria "Enzo Ferrari",
Università degli Studi di Modena e Reggio Emilia
E-mail: matteo.ansaloni@unimore.it*

Abstract. *L'utilizzo di Robot Industriali per l'esecuzione di lavorazioni meccaniche è limitato da problemi legati alla loro precisione così che, attualmente, non risulta conveniente ridurre l'impiego delle tradizionali macchine a controllo numerico nemmeno laddove l'elevata flessibilità dei sistemi robotizzati potrebbe portare interessanti vantaggi competitivi. Il presente articolo, basato sull'esperienza accumulata durante il progetto europeo "COMET - Plug-and-produce COmponents and METHods for adaptive control of industrial robots enabling cost effective, high precision manufacturing in factories of the future", propone un approccio integrato per la progettazione di celle modulari robotizzate di lavorazione che integrano soluzioni tecnologiche innovative, con lo scopo di aumentare la precisione dimensionale e geometrica delle parti in lavorazione. In particolare si descrive un approccio progettuale che permette di realizzare celle caratterizzate da un significativo miglioramento delle prestazioni, sia attraverso la generazione preliminare di opportune traiettorie di lavoro (modalità offline) sia attraverso la correzione in tempo reale degli errori dinamici (modalità online). La descrizione dei risultati ottenuti attraverso una successiva campagna sperimentale permette di validare l'approccio sviluppato per un componente automotive e di valutare l'efficacia del metodo proposto attraverso la comparazione dei risultati ottenuti con quelli ottenibili con una macchina a controllo numerico a cinque assi.*

Keywords: *Engineering design, Robot machining, Robot accuracy*

1. INTRODUZIONE

La costante crescita delle applicazioni robotizzate degli ultimi 20 anni dimostra come i robot industriali rappresentino una soluzione ideale in termini di flessibilità operativa e convenienza economica, espressa in termini di ritorno sull'investimento iniziale [1, 2].

Tuttavia, è da osservare che la limitata precisione dei robot industriali ne limita l'impiego in processi di interesse industriale [3]. Il progetto europeo "COMET - Plug-and-produce Components and METHODS for adaptive control of industrial robots enabling cost effective, high precision manufacturing in factories of the future", attraverso un consorzio eterogeneo composto da università, partner tecnologici e integratori di sistemi, ha puntato ad investire sulla ricerca e sullo sviluppo di un'architettura per sistemi robotizzati in grado di migliorare la precisione necessaria ad eseguire lavorazioni meccaniche di finitura fino a raggiungere prestazioni paragonabili, in determinate condizioni, a quelle ottenibili con moderni centri di lavoro a controllo numerico [4].

L'architettura della soluzione COMET, come mostrato in Figura 1, si basa sull'integrazione di quattro tecnologie abilitanti, a partire da un robot industriale antropomorfo standard.

La prima di queste tecnologie abilitanti, PSIR, consiste nell'implementazione di un innovativo ambiente di programmazione e simulazione 3D per la creazione di percorsi di lavorazione robot. Basato su POWERMILL, software CAD/CAM sviluppato e commercializzato da DELCAM, il modulo PSIR dispone di funzioni per la previsione delle singolarità degli assi e delle collisioni, per la gestione delle strategie di lavorazione e dei parametri di processo, e per la generazione dei punti che compongono i profili di lavoro.

La seconda tecnologia, KDMIR, prevede l'identificazione delle caratteristiche cinematiche e meccaniche che descrivono univocamente ogni robot industriale, realizzata attraverso un modello matematico parametrico che permette una rappresentazione esatta del comportamento statico e dinamico in condizioni di lavoro.

La terza tecnologia implementata, ATIR, è legata alla prototipazione di un sistema di tracking ottico di ultima generazione, ottenuto dallo sviluppo degli attuali sistemi di misura NIKON METROLOGY, in grado di valutare le deviazioni degli assi robot dalle posizioni programmate, di calcolare le correzioni necessarie a minimizzarne gli errori di posizionamento sia in condizioni quasi statiche che dinamiche, e infine di comunicare in real-time i risultati al controllore del robot.

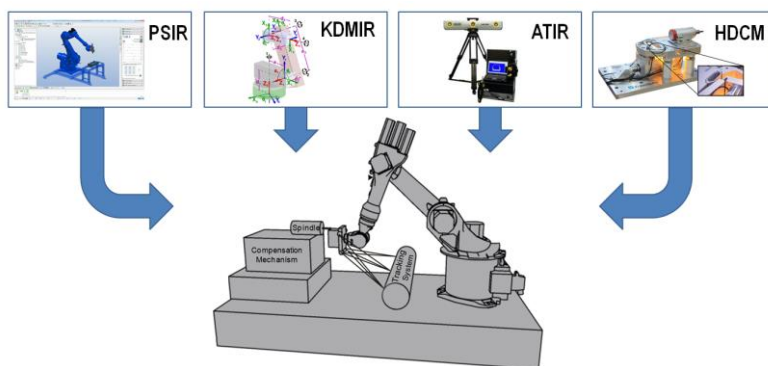


Figura 1. Integrazione delle quattro tecnologie abilitanti previste dal progetto COMET.

L'ultima tecnologia proposta riguarda un sistema di compensazione ad elevata dinamica, HDCM, che può compensare, all'interno di una larga ampiezza di banda, spostamenti di piccola entità legata ai fenomeni vibratorii indotti dalle lavorazioni, in modo da portare la precisione di esecuzione a valori superiori ai limiti meccanici dei robot stessi.

Il presente articolo descrive, in Sezione 2, la struttura ed il funzionamento di un prototipo di cella robotizzata modulare e riconfigurabile progettata e prodotta in collaborazione con l'azienda italiana SIR S.p.A., partner del progetto COMET, con l'obiettivo di integrare le tecnologie abilitanti all'interno di 4 diverse configurazioni denominate A, B, C e D. La Sezione 3 descrive il caso di studio realizzato al fine di dimostrare la validità industriale della cella robotizzata nella configurazione A. La sezione 4 illustra i risultati ottenuti. La sezione 5 raccoglie le conclusioni del lavoro a partire dall'analisi del confronto tra i risultati ottenuti dal sistema robotizzato e quelli riferiti all'esecuzione del medesimo ciclo di lavoro una tradizionale macchina CNC a cinque assi.

2. PROGETTAZIONE DI CELLE ROBOTIZZATE MODULARI E RICONFIGURABILI DI LAVORAZIONE MECCANICA

Le tecnologie COMET sono state integrate in diverse combinazioni ottenendo una cella robotizzata caratterizzata da 4 configurazioni, schematizzate in Figura 2:

- Configurazione A: PSIR
- Configurazione B: PSIR + KDMIR
- Configurazione C: PSIR + KDMIR + ATIR
- Configurazione D: PSIR + KDMIR + ATIR + HDCM

La configurazione A rappresenta la piattaforma di base ed include solo PSIR, il software di generazione e simulazione integrata del percorso del robot. La configurazione B aggiunge i modelli matematici descrittivi del robot (KDMIR) permettendo al software PSIR di calcolare un percorso compensato che consideri anche il comportamento cineto-dinamico del robot selezionato [5]. Il percorso compensato è inizialmente calcolato offline e quindi inviato al controller del robot per la successiva elaborazione.

Le configurazioni C e D aggiungono le tecnologie COMET in grado di correggere online la lavorazione del robot: ATIR e HDCM. La compensazione consiste nella correzione in tempo reale, calcolata dopo la misurazione della differenza tra le posizioni comandate e reali raggiunte dal robot, effettuata dal sistema ATIR. Nella configurazione C le correzioni misurate con ATIR vengono inviate al controllore robot per correggere il percorso di lavorazione. Nella configurazione D, oltre questa correzione, vi è anche la possibilità di correggere la posizione del mandrino che è fissato sulla piattaforma HDCM [6].

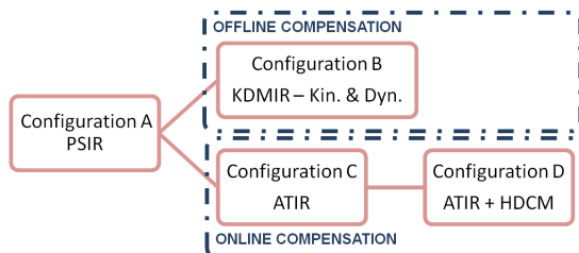


Figura 2. Configurazioni ottenibili con le tecnologie COMET.

A partire dallo studio delle tecnologie COMET si è proceduto, in collaborazione con gli ingegneri di SIR S.p.A. a progettare e costruire un prototipo riconfigurabile in grado svolgere automaticamente lavorazioni meccaniche ad alta precisione, il cui layout è mostrato in Figura 3.

L'equipaggiamento di base della cella prototipo è definito in base ai requisiti imposti dal progetto, che considera lavorazioni meccaniche eseguibili su un centro di lavoro CNC a 5 assi con un volume di lavoro da 1m^3 a 2.4m^3 .

Al fine di garantire caratteristiche operative analoghe a quelle del centro CNC, per la cella robotizzata è stato selezionato un robot ABB IRB 6640 con payload di 185kg, elongazione massima di 2800mm e controller IRC5, dotato di cambio rapido e pinza SCHUNK. Inoltre si è installato un elettromandrino HSD -939A con potenza nominale di 7.5kW e velocità di rotazione massima di 24000rpm, dotato di cambio utensile automatico, che funge da unità di lavoro fissa. La cella robot è inoltre dotata di sistemi ausiliari quali:

- Magazzino per il deposito degli organi terminali del robot (End-Effector) necessari all'esecuzione del ciclo di lavoro;
- Sistema di visione, utilizzabile in parte mobile a bordo robot per il riconoscimento e la localizzazione dei pezzi su pallet, e in parte fissa per la calibrazione e il controllo dimensionale online dei pezzi;
- Sistema di tasteggio, utilizzabile in parte mobile a bordo robot per la calibrazione degli elementi della cella e degli utensili di lavorazione, e in parte fissa per la calibrazione dei componenti;
- Sistema di cambio presa, impiegato per definire la posizione del pezzo rispetto alla pinza robot;
- Sistema di aspirazione e cabina insonorizzata per il contenimento delle emissioni acustiche, dei trucioli, degli olii di lubrificazione e raffreddamento, e per l'interdizione dell'area di lavoro agli operatori.

La soluzione sviluppata consente di svolgere automaticamente sia il ciclo di lavorazione previsto sia le fasi di presa dei pezzi grezzi, di controllo delle lavorazioni, di manutenzione programmata dei dispositivi e di rilascio dei pezzi finiti. In particolare, l'impiego combinato del sistema di tasteggio e del sistema di cambio presa permette di eseguire in autonomia la calibrazione della cella, impiegando il robot stesso come strumento di misura.

In Figura 4 è riportata la modalità di calibrazione proposte, già descritta in [7].



Figura 3. Layout della cella prototipale realizzata in collaborazione con SIR S.p.A.



Figura 4. A sinistra, calibrazione di un elemento fisso della cella, a destra, calibrazione della posizione del pezzo rispetto alla pinza robot.

Configurazione A

La configurazione A, come già introdotto, prevede l'implementazione del software PSIR per la programmazione offline dei percorsi di lavorazione. La novità di questo strumento è l'impiego di un approccio CAM per la programmazione robot, fondamentale per la definizione delle traiettorie di lavorazione necessarie a raggiungere elevati livelli di precisione. A partire dalle dimensioni nominali del componente, è possibile generare i percorsi in funzione dei parametri di processo, quali profondità di passata, direzione di avanzamento e impegno utensile. Molto importante è la possibilità di gestire le strategie di lavorazione, come traiettorie di ingresso e uscita dell'utensile.

In Figura 5 è presentata la cella virtuale che rispecchia le dimensioni e la configurazione della cella reale. La parte destra della figura, presenta il plug-in PSIR, così come integrato all'interno del prototipo.

Configurazione B

La configurazione B, il cui schema è mostrato in Figura 6, implementa il primo livello di correzione attraverso la definizione e l'impiego di un modello che tiene in considerazione le reali caratteristiche cinematiche e meccaniche del robot selezionato, in particolare dimensioni degli assi, giochi, attriti e cedevolezza dei giunti.

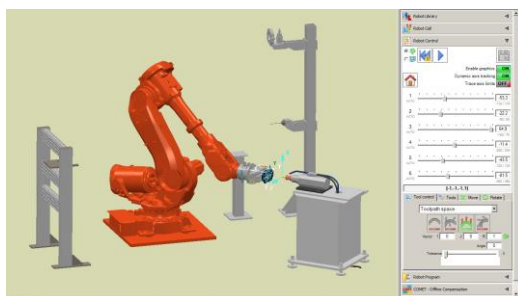


Figura 5. Interfaccia PSIR e configurazione A per la programmazione offline delle lavorazioni meccaniche.

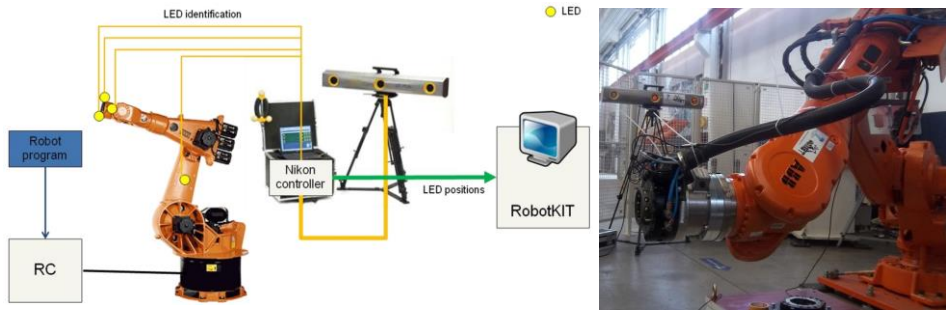


Figura 6. Calibrazione dei modelli cinematici e dinamici.

Le forze agenti sul robot durante la fase di lavorazione, inoltre, sono state calcolate impiegando modelli noti che legano tra loro i parametri di processo, ad esempio angoli di impegno, velocità di passata e profondità, e che sono successivamente organizzati attraverso librerie software.

La calibrazione dei modelli cinematici e dinamici ha richiesto l'esecuzione di numerose prove sperimentali basate sulla determinazione della differenza tra la posizione assoluta e la posizione relativa dei giunti del robot e sull'esecuzione di dati profili incrementali di moto ad asse 6 vincolato. Tale prova è stata realizzata seguendo la procedura descritta in [8] e utilizzando il dispositivo visibile in Figura 6 ai piedi del robot, il cui sviluppo è portato al deposito di un brevetto internazionale da parte di uno dei partner.

Configurazione C

Come accennato precedentemente, la compensazione online consiste nella correzione in tempo reale delle traiettorie del robot, calcolata dopo aver misurato il disallineamento tra la posizione del robot nominale e reale con il sistema di tracking ATIR.

La telecamera ATIR controlla la posizione reale e l'orientamento dell'End-Effector rispetto al mandrino. La misurazione è resa possibile da una serie di LED montati sui due elementi, come mostrato in Figura 7.

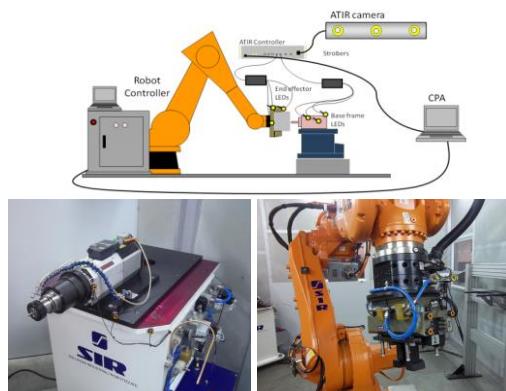


Figura 7. Schema funzionale della configurazione C (in alto) e dettaglio dei LED montati sul robot e sul mandrino (in basso).

I due aspetti fondamentali della configurazione sono legati al numero di LED che devono essere posizionati sul robot ed alla frequenza di acquisizione della camera che deve poter garantire il funzionamento real-time. Il numero di LED, in particolare, deve poter garantire la visibilità del robot per ogni configurazione degli assi e per ogni traiettoria seguita. All'aumentare del numero dei LED diminuisce proporzionalmente la massima frequenza di funzionamento per la camera, e quindi per il sistema.

Nella configurazione C, 3 LEDs sul mandrino e 3 LEDs sul robot sono sufficienti per il corretto funzionamento del sistema.

Configurazione D

La configurazione D ha il compito di compensare gli errori che non possono essere corretti agendo sulla posizione dei giunti del robot e sulla modifica delle traiettorie di lavoro. Questa configurazione richiede un sistema ad elevata dinamica che deve interagire in real-time con il controller del robot industriale. Il sistema è composto da attuatori piezo-elettrici agenti su elementi flessibili disposti lungo le tre direzioni cartesiane.

La complessità del sistema, gli alti costi di produzione e la complessità dell'interfacciamento con il controller robot, non accessibile alla comunicazione con sistemi non proprietari, non hanno permesso l'integrazione nella cella sperimentale. Il suo funzionamento è però stato testato presso i laboratori di Production Engineering and Automation (IPA) del Fraunhofer Institute di Stoccarda, dove sono state eseguite alcune prove sperimentali impiegando un controller aperto multifunzione a comando di un robot industriale tradizionale.

Figura 8 mostra il dispositivo HDCM nella sua configurazione finale.

3. VALIDAZIONE SPERIMENTALE

La validazione sperimentale della cella ha riguardato, in una prima fase di lavoro, la configurazione A del prototipo, ed è stata realizzata attraverso la lavorazione del componente descritto nel seguito. Infatti, al fine di validare l'approccio proposto, si è definito il processo di lavorazione di un componente rappresentativo dell'attuale contesto industriale, da confrontare rispetto all'approccio di lavorazione tradizionale impiegando una macchina CNC a 5 assi.

Il componente scelto, mostrato in Figura 9, è una pinza freno di dimensioni di 290mm x 155mm x 80mm e viene realizzato con una lega di alluminio AlSi7Mg0.5. La massa è di circa 2.7Kg.

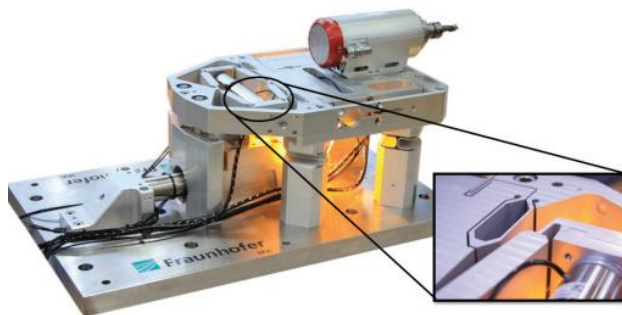


Figura 8. Meccanismo HDCM sviluppato dal Fraunhofer IPA di Stoccarda

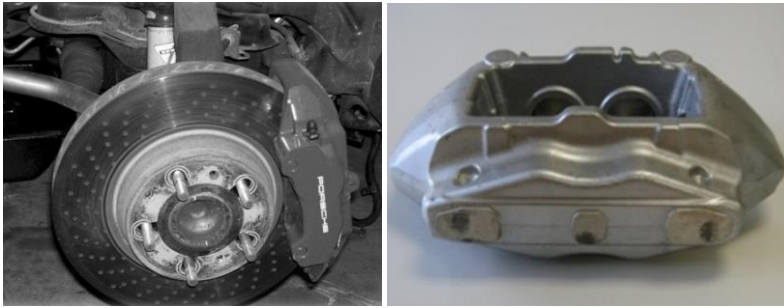


Figura 9. Pinza freno scelta per la definizione del ciclo di lavoro dimostrativo.

Dal punto di vista della precisione i requisiti dimensionali e geometrici sono i seguenti:

- ISO 2768 - f per le tolleranze dimensionali
- ISO 2768 - H per le tolleranze geometriche

La pinza freno è ottenuta da lavorazioni successive a partire da un semilavorato in alluminio pressofuso. Il ciclo di lavorazione di riferimento prevede 15 differenti lavorazioni fondamentali, quali foratura, fresatura, spianatura e smussatura, disposte sui diversi lati del componente.

In Figura 10 è riportato il dettaglio del cartellino di lavorazione con la tipologia e la sequenza delle lavorazioni proposte.

Al fine di avere un approccio rigoroso nella valutazione dei risultati ottenuti, le lavorazioni sono definite rispetto a elementi geometrici di riferimento univoci, Datum A, B e C, utilizzati anche per il successivo controllo dimensionale.

L'esecuzione del ciclo di lavorazione è preceduta da una campagna sperimentale volta alla identificazione dei parametri di taglio ottimali. In particolare, le operazioni di fresatura frontale sono state eseguite con una velocità di rotazione del mandrino di 7100rpm e un avanzamento di 5mm/s. La profondità di passata è variata da un massimo di 1 mm per finire a 0.25mm nelle ultime passate.

Nelle operazioni di finitura la velocità del mandrino è stata incrementata a 9000rpm. Le operazioni di foratura sono state eseguite con un avanzamento di 5mm/s e a 6000rpm. Infine, nelle operazioni di smussatura le velocità sono state incrementate: 16000rpm per il mandrino e 15mm/s per quanto riguarda l'avanzamento.

POSE 1 – Machining Operations			POSE 2 – Machining Operations		
10		Face 2 – Face Milling	70		Face 10 & Face 11 – Face Milling
20		Face 6 & Face 5 – Face Milling	80		Face 10 & Face 11 – Drilling
30		Face 1 (Datum A) – Face Milling	90		Face 3 & Face 4 – Drilling
40		Face 4 & Face 3 (Datum C) – Face Milling	100		Face 5 & Face 6 – Drilling
50		Face 8, Face 7 & Face 9 (Datum B) – Face Milling	110		Face 5 & Face 6 – Chamfering
60		Profile 1 – Contour Milling	120		Face 3 & Face 4 – Chamfering
			130		Face 10 & Face 11 – Chamfering

Figura 10. Lavorazioni previste sulla pinza freno.

4. RISULTATI

I percorsi robot per le operazioni di fresatura sono stati creati e simulati nel plug-in PSIR, Figura 11.

Al fine di migliorare la precisione di lavorazione sono state adottate le specifiche funzioni CAM offerte dalla soluzione PSIR, dipendenti dalla configurazione assunta dai giunti del robot, in particolare:

- Impostazione una bassa priorità per l'asse/i che presentano elevati valori di gioco
- Definizione di differenti strategie di avvicinamento per l'utensile / parte,
- Minimizzazione dell'inversione dei giunti del robot.

Figura 12 mostra due possibili approcci adottabili per minimizzare gli urti legati all'ingresso dell'utensile sul pezzo.

Figura 13 mostra la pinza freno al termine della lavorazione ottenuta con la cella in configurazione A.

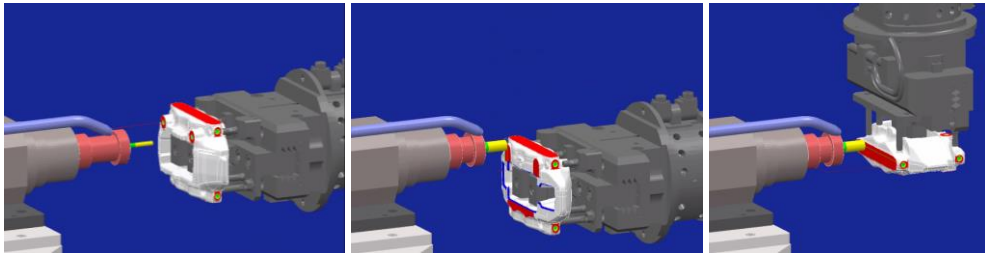


Figura 11. Simulazione dei percorsi robot con PSIR

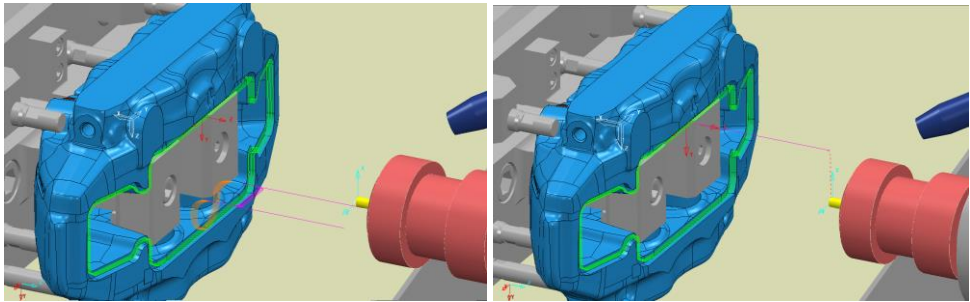


Figura12. Esempio di ottimizzazione delle strategie di avvicinamento al percorso.



Figura 13. Componente realizzato con la configurazione A

Rispettando i requisiti dimensionali definiti dalla norma ISO 2768 – f/H e considerando i Datum impiegati durante l’esecuzione delle operazioni di lavorazione, è stato individuato un campione rappresentativo di feature necessario a valutare distanze, planarità, perpendicolarità e parallelismo.

Figura 14 riassume le tolleranze misurate rispetto alle feature individuate. Nella tabella, a fianco di ogni caratteristica dimensionale e geometrica sono riportati i valori numerici nominali definiti dalla normativa e i valori misurati con una macchina a misura di coordinate, DEA Global Status equipaggiata con una testa Renishaw PH10M.

I risultati della tabella mostrano una buona capacità della configurazione A di produrre feature che siano geometricamente in tolleranza. Al contrario le dimensioni, legate alla precisione di posizionamento del robot, risultano fuori tolleranza.

5. CONCLUSIONI

Dalle sperimentazioni eseguite è possibile osservare come il solo impiego della configurazione A mostra un evidentemente miglioramento della precisione rispetto all’impiego di robot tradizionali. Infatti, l’approccio CAM proposto, integrato con alcuni strumenti specifici sviluppati nell’ambito del progetto COMET, consente un controllo completo delle strategie di lavorazione, dei percorsi e il controllo del comportamento del robot, elementi già sufficienti a mostrare un netto miglioramento delle prestazioni dei sistemi robotizzati impiegati per l’esecuzione di lavorazioni meccaniche.

In termini di processo, nell’ipotesi di lotti di ridotte dimensioni ad elevata variabilità, il costo della lavorazione robotizzata con la configurazione A è, inoltre, mediamente più basso di quello per la lavorazione con CNC, soprattutto a causa della riduzione del tempo di interazione operatore-pezzo durante le fasi di riposizionamento dei pezzi, necessari quando si lavori su più lati. In Configurazione A, l’operatore si limita alla disposizione dei pezzi grezzi su pallet mentre il robot procede a svolgere autonomamente tutte le operazioni successive, fino al controllo ed al rilascio dei pezzi finiti.

In termini di equipaggiamento, il costo di un robot dotato di un mandrino è inferiore rispetto a quello di una macchina utensile CNC a 5 assi. Considerando tutti i costi dovuti all’automazione di base del ciclo di lavoro, ad esempio il sistema di visione, riposizionamento delle parti, magazzino pinze, sistema di lubrificazione e sistema di calibrazione, il divario economico tra una soluzione robotizzata e una soluzione CNC è ridotta.

Feature	Tolerance	Required Value(s) [mm]	Measured Value(s) [mm]
Datum A	Flatness	0,2	0,075
Datum B	Flatness	0,2	0,057
	Perpendicularity	0,2	0,087
Datum C	Flatness	0,05	0,032
	Perpendicularity	0,2	0,0508
Plane A	Flatness	0,2	0,0657
Plane A2	Flatness	0,2	0,0411
Plane B	Flatness	0,2	0,177
Plane C	Flatness	0,05	0,0332
Datum D	Flatness	0,2	0,1255
Datum E	Flatness	0,2	0,2586
Plane_I_2	Flatness	0,2	0,1089
	Parallelism	0,2	0,172
Plane_II_2	Width	51(+/- 0,15)	51,3678
	Flatness	0,2	0,1305
Plane_II_2	Parallelism	0,2	0,2891
	Width	51(+/- 0,15)	51,3782
(inter-axis)	Width	120(+/- 0,15)	120,6461
Surface	Surface tolerance	0,1	0,504

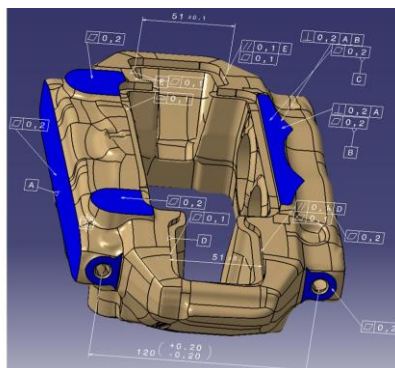


Figura 14. Tolleranze geometriche e dimensionali

Il principale vantaggio per la soluzione COMET consiste nel costo “processo per parte”, che considera non solo l'investimento ma anche la produttività del sistema. La configurazione A dimostra come il costo relativo all'introduzione delle tecnologie abilitanti PSIR e KDMIR sia facilmente giustificato da un punto di vista industriale. L'integrazione industriale di ATIR e HDCM, invece, richiede una successiva valutazione da svolgersi in base al rapporto tra la precisione desiderata e il costo della strumentazione.

In conclusione, sulla base dei risultati ottenuti è possibile affermare come l'integrazione delle tecnologie nella cella robotizzata permetta di impiegare i robot in lavorazioni robotizzate ad elevata precisione. Nelle prime due configurazioni di cella descritte, in particolare, l'incremento delle prestazioni avviene senza aumentare sostanzialmente l'investimento iniziale per l'installazione del robot e quindi diventa appetibile anche per PMI.

Le prove realizzate sul prototipo in configurazione A dimostrano effettivi vantaggi già ad un primo livello di integrazione delle tecnologie COMET. Ulteriori prove relative alle successive configurazioni sono in corso di realizzazione.

Ringraziamenti

Gli autori ringraziano gli ingg. Luciano e Davide Passoni e Lino Ferrari di SIR S.p.A. per il supporto alle attività e ricordano la ricerca è stata finanziata dalla Comunità Europea all'interno del European Economic Recovery Plan (EERP) e della misura Public-Private Partnerships (PPP) nel settore Factories of the Future (FoF).

RIFERIMENTI BIBLIOGRAFICI

- [1] In book, AA.VV., 2008, International Federation of Robotics: "World Robotics 2007, Statistical Yearbook".
- [2] Y. Chen, F. Dong, 2013, "Robot machining: recent development and future research issues", *International Journal of Advanced Manufacturing Technology*, vol. 66, Issue 9-12, pp.1489-1497.
- [3] U. Schneider, M. Ansaloni, M. Drust, F. Leali, A. Verl, 2013, "Experimental Investigation of Sources of Error in Robot Machining", *Robotics in Smart Manufacturing, Communications in Computer and Information Science*, Vol. 371, pp 14-26.
- [4] COMET, 2011, EU/FP7-project: Plug-and-produce COmponents and MEthods for adaptive control of industrial robots enabling cost effective, high precision manufacturing in factories of the future, [URL:http://www.cometproject.eu](http://www.cometproject.eu).
- [5] In Proceedings , C. Lehmann, M. Halbauer, J. van der Zwaag, U. Schneider, 2013, "Offline Path Compensation to Improve Accuracy of Industrial Robots for Machining Applications". In: Proc. of 14th Automation Congress, Baden-Baden, Germany.
- [6] U. Schneider, M. Drust, A. Puzik, A. Verl, 2013, "Compensation of Errors in Robot Machining with a Parallel 3D-Piezo Compensation Mechanism" , Forty Sixth CIRP Conference on Manufacturing Systems Vol. 7, pp. 305-310.
- [7] F. Leali, M. Pellicciari, F. Pini, A. Vergnano, G. Berselli," 2013, A Calibration Method for the Integrated Design of Finishing Robotic Workcells in the Aerospace Industry", *Robotics in Smart Manufacturing, Communications in Computer and Information Science* Vol. 371, pp 37-48.

- [8] In Proceedings C. Lehmann, B. Olofsson, K. Nilsson, M. Halbauer, M. Haage, A. Robertsson, O. Sörnmo, U. Berger, 2013, “Robot Joint Modeling and Parameter Identification Using the Clamping Method”, In Proceedings of IFAC Conference on Manufacturing Modelling, Management and Control (MIM 2013), Saint Petersburg, Russia.

CELLE ROBOTIZZATE FLESSIBILI A CONFIGURAZIONE VARIABILE

Aldo Rossi

Dipartimento di Tecnica e Gestione dei Sistemi Industriali

Università degli Studi di Padova, Italia

E-mail: aldo.rossi@unipd.it

Giulio Rosati

Dipartimento di Tecnica e Gestione dei Sistemi Industriali

Università degli Studi di Padova, Italia

E-mail: giulio.rosati@unipd.it

Simone Minto

Dipartimento di Tecnica e Gestione dei Sistemi Industriali

Università degli Studi di Padova, Italia

E-mail: simone.minto@mechatronics.it

Abstract. *L'assemblaggio flessibile è una necessità in forte crescita per molte realtà industriali, per motivi legati principalmente all'aumento della richiesta di piccoli lotti produttivi. Questa memoria vuole presentare il concetto di flessibilità di layout, esigenza molto sentita in ambito industriale, ovvero la possibilità di poter riconfigurare in tempi rapidi il layout di una cella robotizzata utilizzando strumenti software ed hardware a basso costo. L'articolo, dopo aver definito il workflow principale del processo di ricostruzione tridimensionale e d'importazione della geometria della cella in un ambiente CAD commerciale, presenta i primi risultati sperimentali che mettono in evidenza il comportamento reale del sistema.*

Parole chiave: *sistema di assemblaggio flessibile, cella robotizzata, flessibilità di layout, ricostruzione 3D, navigazione 3D.*

1. INTRODUZIONE

Al giorno d'oggi il mercato è caratterizzato da prodotti sempre più vari e con cicli di vita sempre più brevi. Per adattarsi a questo contesto e per restare competitive a livello internazionale, molte aziende stanno adottando dei sistemi di assemblaggio flessibili (FAS). Tali sistemi devono garantire anche un'elevata produttività ed un basso costo unitario diretto, il che richiede lo sviluppo di nuove tecnologie per i moderni sistemi di assemblaggio [1].

Oltre alla flessibilità di prodotto, ossia la possibilità di poter gestire diversi componenti con la stessa automazione, vi è una forte esigenza in ambito industriale di disporre di strumenti hardware e software al fine di poter aumentare la flessibilità di layout di una cella

robotizzata, ovvero la caratteristica di poter riconfigurare l'ambiente di lavoro in tempi rapidi.

Infatti, ad ogni modifica della planimetria di una cella di lavoro, ad esempio per la sostituzione di un componente con ingombri differenti, l'integrazione di ulteriori componenti o sottosistemi, è necessario compiere determinate operazioni come la ridefinizione dei punti di via del manipolare, la ridefinizione del ciclo di lavoro e la ricalibrazione della sensoristica utilizzata. Inoltre, è necessario porre molta attenzione al problema delle collisioni del robot, data la presenza di eventuali nuovi ostacoli. Tutte queste operazioni richiedono personale specializzato, tempo, con un conseguente fermo della produzione.

La soluzione presentata dagli autori permette di rendere più rapide ed intuitive, senza la necessità di ricorrere a personale altamente specializzato, le operazioni di aggiornamento della configurazione di una cella robotizzata. Essa prevede l'acquisizione tridimensionale dell'ambiente di lavoro e l'importazione dello stesso in un ambiente CAD commerciale. Un simulatore robotico permette la navigazione off-line di un manipolatore nella geometria acquisita, la memorizzazione off-line delle traiettorie robot e dei punti di via, oltre che alla gestione dei dati nel ciclo di lavoro in tempo reale.

2. CELLE ROBOTIZZATE FLESSIBILI A CONFIGURAZIONE VARIABILE: IL SISTEMA SVILUPPATO

Il sistema che proponiamo è schematicamente composto da due moduli:

- componente che permette l'acquisizione della geometria di una cella robotizzata mediante l'utilizzo del sensore Microsoft Kinect;
- simulatore robotico in grado di interfacciarsi con un ambiente CAD commerciale.

La scelta di utilizzo di questo specifico sensore è dettata dal suo sempre più diffuso uso in ambito di ricerca, in settori quali la robotica, sia per il controllo gestuale che per la realtà virtuale. Oltretutto, dispone di peculiari caratteristiche quali: velocità di acquisizione, adeguata precisione nella ricostruzione, facilità di utilizzo e costo ridotto.

Il Microsoft Kinect è un dispositivo dotato di una telecamera RGB con risoluzione di 640 x 480 pixel, un proiettore IR a luce strutturata da 1.2W, una telecamera IR composta da una matrice di 320 x 240 pixel, un array di microfoni ed una base motorizzata. Attraverso un hardware proprietario prodotto da PrimeSense, il Kinect è in grado di generare immagini depth di risoluzione pari a 640 x 480 pixel (11 bit, 2048 livelli di sensitività) ad una frequenza di 30 Hz, con un range di misura da 40 cm a 4 m. Lo strumento è in grado di generare un'immagine depth andando a rilevare le variazioni indotte dagli oggetti presenti nella scena nel pattern pseudo-causale proiettato.



Figura 1. Immagini depth RAW acquisite con il sensore Microsoft Kinect.

In Fig. 1 sono presenti alcune immagini depth acquisite con il sensore. È possibile osservare la presenza di numerosi “buchi” dove non è stato possibile rilevare correttamente il pattern IR emesso. Questa situazione può essere causata, come dettagliatamente spiegato in [5], da materiali a bassa o alta riflettività, particolare illuminazione di fondo, superfici eccessivamente inclinate, occlusioni e discontinuità degli oggetti.

Per il processo di ricostruzione tridimensionale è stato utilizzato, adattandolo al particolare ambiente di utilizzo, il framework Kinect Fusion studiato e sviluppato presso i laboratori Microsoft Research [2] [3]. La più importante classe degli algoritmi utilizzati sono basati sul concetto di *Iterative Closest Point* (ICP) introdotto in [4] che pone l'allineamento delle nuvole di punti come un problema di ottimizzazione non lineare in cui le corrispondenze tra le scansioni sono approssimate utilizzando le coppie più vicine dei punti trovati nella scansione avvenuta all'iterazione precedente, tenendo traccia costantemente della posa a 6 gdl della camera. In Fig. 2 viene schematicamente rappresentato il workflow del processo di acquisizione.

La procedura di acquisizione prevede che l'operatore impugni il Kinect, come raffigurato in Fig. 3, e si sposti lentamente all'interno dell'ambiente che vuole acquisire. Attraverso una porzione della GUI, visibile in Fig. 4, può verificare il risultato dell'acquisizione in tempo reale. Nel caso in cui si verificassero eventi o condizioni che impedissero il proseguimento della ricostruzione, l'operatore viene avvertito da un allarme sonoro e a video sarà raffigurato l'ultimo frame correttamente elaborato: in questo caso l'utente dovrà rimanere per qualche secondo fermo cercando di inquadrare l'ultima scena processata ed attendere che il processo di acquisizione continui.

La ricostruzione acquista dettagli con l'acquisizione di nuove misure di profondità. Nel caso in cui si desiderasse acquisire maggiori particolari di un determinato componente è necessario semplicemente riprenderlo con la telecamera per maggior tempo e con maggiori viste. I “buchi” vengono colmati ed il modello diventa sempre più completo e definito nel tempo. Le sottofigure (c) e (d) di Fig. 4 raffigurano quanto in precedenza esposto: è possibile notare come la spalla del robot acquisti definizione, particolari e volume.

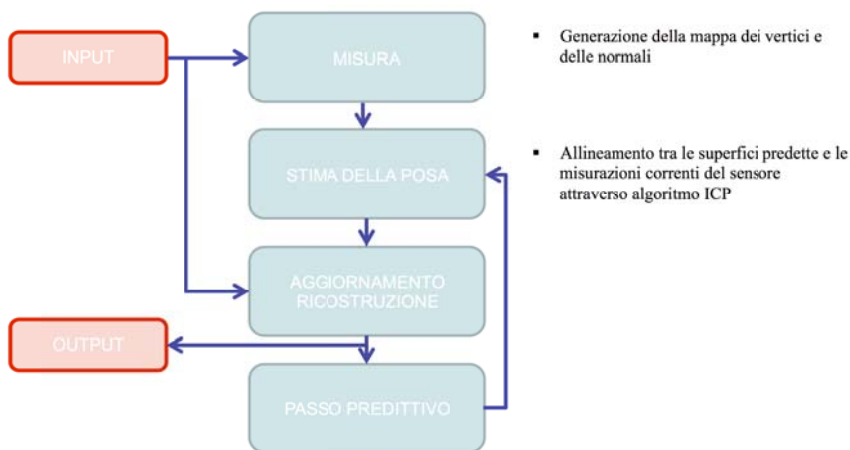
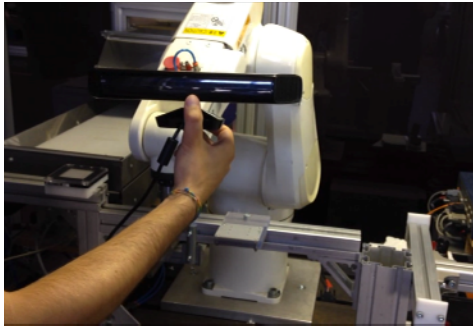
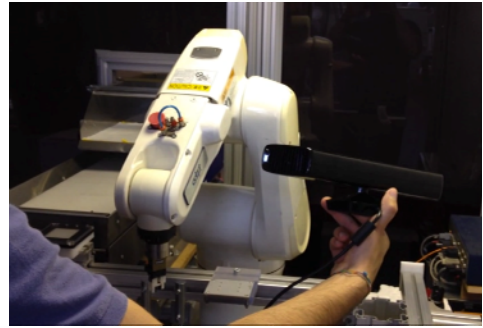


Figura 2. Workflow del processo di ricostruzione tridimensionale.

A procedura terminata è possibile esportare il risultato ottenuto in STL binario (STereo Lithography interface format). Con tale formato è possibile descrivere la superficie geometrica di un oggetto tridimensionale discretizzandola in triangoli, per tale motivo un'importante successiva operazione è quella di eseguire un apposito script per eliminare i vertici duplicati non necessari.

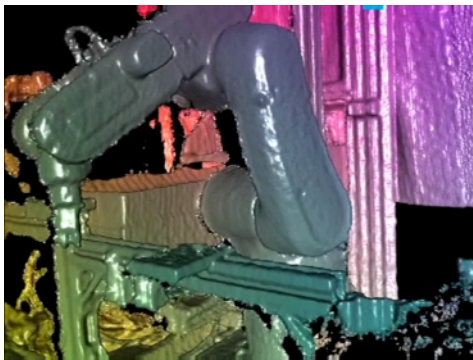


(a)

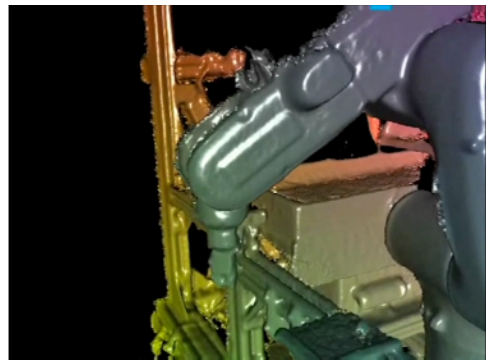


(b)

Figura 3. Processo di acquisizione della geometria della cella robotizzata.



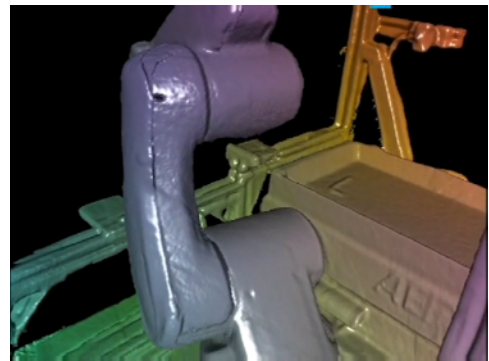
(a)



(b)



(c)



(d)

Figura 4. Frames in tempo reale durante il processo di acquisizione.

In Fig. 5 è possibile osservare il risultato della scansione ottenuto in due differenti viste. La risoluzione spaziale dell'acquisizione è pari a 5 mm, mentre il matching in tempo-reale avviene a 22 frame al secondo.

Il secondo modulo del sistema sviluppato prevede l'integrazione di un simulatore robotico sviluppato in linguaggio Matlab con il sistema CAD commerciale SolidWorks di Dassault Systems [6]. Il simulatore è in grado di comunicare in maniera bidirezionale con il processo attraverso un'interfaccia OLE-compliant COM server [7], utilizzando le interfacce messe a disposizione dalle API di SolidWorks. La movimentazione dei giunti del robot è effettuata invocando il metodo *DragAsUI* delle API fornite.

Poiché la scansione è stata eseguita in una precisa configurazione del manipolatore, le operazioni d'importazione della geometria della cella di lavoro nell'ambiente SolidWorks e di allineamento tra il modello CAD del robot e la nuvola di punti, corrispondente all'antropomorfo, può essere effettuata attraverso semplici e rapidi passaggi all'interno del software. In Fig. 6 è raffigurato il risultato dell'operazione di importazione.

Attraverso l'uso combinato della GUI in Matlab e dell'ambiente di disegno tecnico SolidWorks, è possibile compiere operazioni come:

- la navigazione off-line nella geometria acquisita simulando i movimenti del robot attraverso la GUI;
- la memorizzazione off-line delle traiettorie e dei via-point;
- la possibilità di progettazione di parti o specifici componenti che andranno ad integrare la cella di lavoro, potendo simulare le traiettorie direttamente nell'ambiente CAD commerciale e memorizzare successivamente i punti nella GUI.

Sfruttando la geometria acquisita, è possibile anche verificare il rischio di collisione del robot in tempo reale; problema importante in quelle fasi del ciclo di lavoro in cui il

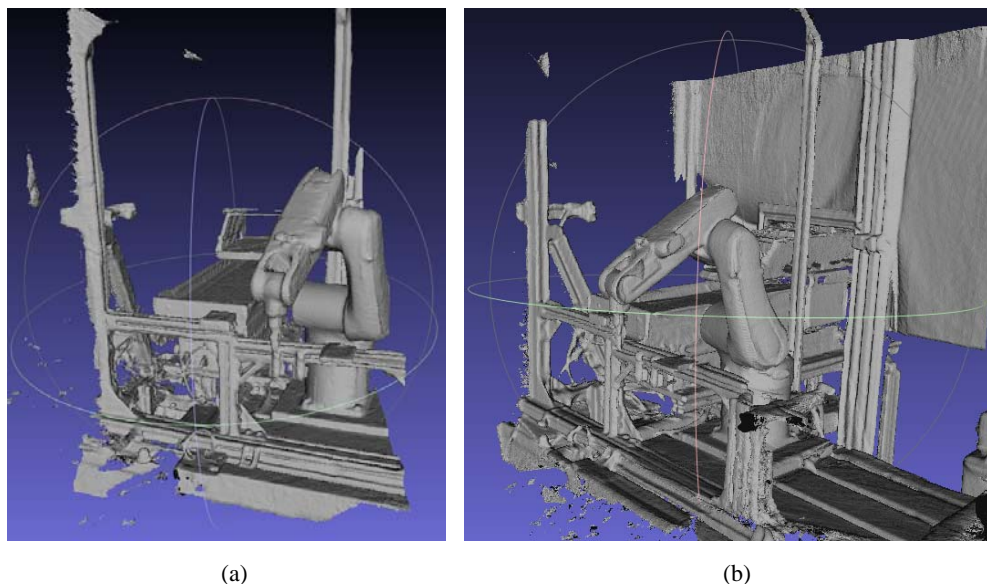


Figura 5. Risultato delle scansioni del volume di una cella robotizzata.

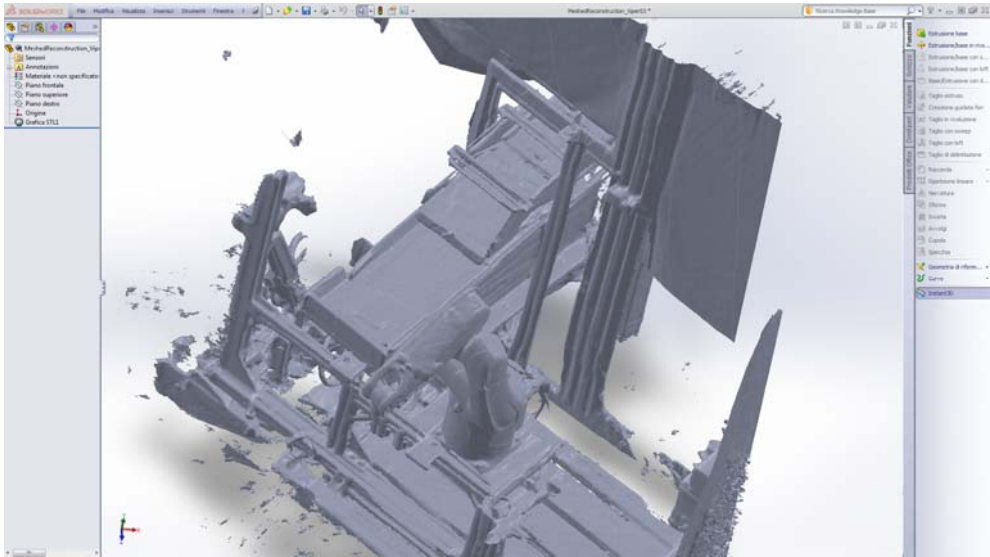
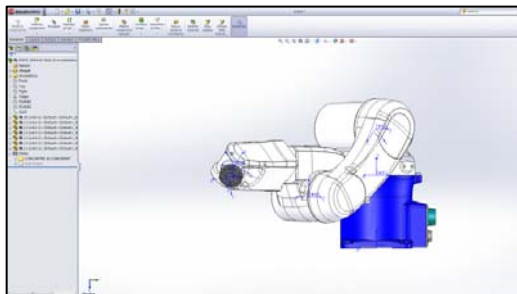
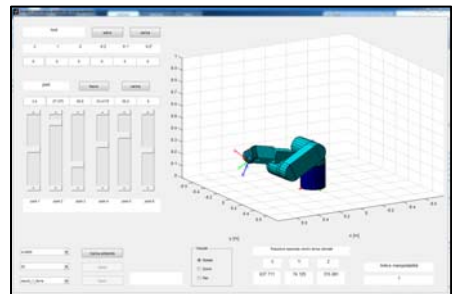


Figura 6. Importazione della geometria dell'ambiente scansionato nell'ambiente CAD commerciale.



(a)



(b)

Figura 7. Interfacciamento CAD-Simulatore: (a) importazione del robot antropomorfo – (b).

movimento del robot non sia pre-registrato ma venga comandato da coordinate calcolate, ad esempio, da sensori. Rappresentando gli ingombri del manipolatore attraverso semplici disequazioni (ad esempio: piano, cilindro, sfera) è possibile ottenere informazioni sull'eventuale compenetrazione di robot e ambiente. Il confronto della geometria di un antropomorfo con un oggetto di 1 dm^3 richiede circa 1 ms di tempo di calcolo.

3. CONCLUSIONI

Il presente contributo ha l'obiettivo di presentare una possibile strategia per la riconfigurazione rapida di una cella di lavoro robotizzata attraverso l'acquisizione della geometria tridimensionale della stessa, con l'integrazione di un simulatore robotico in un ambiente CAD 3D commerciale al fine di poter compiere off-line test di movimentazione per poter pianificare correttamente traiettorie ed acquisire via-point adeguati, disponendo di un motore di collision-detection in real-time.

RIFERIMENTI BIBLIOGRAFICI

- [1] Rosati G., Faccio M., Carli A., Rossi A., 2013. "Fully Flexible Assembly System (F-FAS): A New Concept in Flexible Automation". *Assembly Automation*. 33(1), pp. 8–21.
- [2] Besl, P. J., & McKay, N. D. 1992. "Method for registration of 3-D shapes". In *Robotics-DL tentative*, pp. 586-606. International Society for Optics and Photonics.
- [3] Izadi, S., Kim, D., Hilliges, O., Molyneaux, D., Newcombe, R., Kohli, P., ... & Fitzgibbon, A., 2011. "KinectFusion: real-time 3D reconstruction and interaction using a moving depth camera". In *Proceedings of the 24th annual ACM symposium on User interface software and technology*, pp. 559-568. ACM.
- [4] Newcombe, R. A., Davison, A. J., Izadi, S., Kohli, P., Hilliges, O., Shotton, J., ... & Fitzgibbon, A., 2011. "KinectFusion: Real-time dense surface mapping and tracking". In *Mixed and augmented reality (ISMAR), 2011 10th IEEE international symposium*, pp. 127-136. IEEE.
- [5] Dal Mutto, C., Zanuttigh, P., & Cortelazzo, G. M., 2012. *Time-of-Flight Cameras and Microsoft Kinect™*. Springer.
- [6] Dassault Systems, "Solidworks API Help" 1995-2014
<http://help.solidworks.com/2014/English/api/sldworksapiproguide/Welcome.htm>
- [7] Microsoft, "COM: Component Object Model Technologies" 2014
<https://www.microsoft.com/com/default.aspx>

PARAMETRIC MODELING OF EXPERIMENTAL DATA

Alessandro Freddi
Academy of Science of the Institute of Bologna
Department of Industrial Engineering,
University of Bologna, Italy
E-mail: alessandro.freddi@unibo.it

Abstract. *Experimental stress analysis was developed for solving structural mechanical problems, i.e. for determining states of stress, deformation and displacements in structural elements, starting from the knowledge of applied forces and system parameters, as alternative and complementary method of theoretical ones. This was the forward approach to problems for which theoretical solutions were limited to the cases treated by the classical theory of elasticity.*

The enormous development of numerical methods has largely overruled this task and the augmented accuracy of numerical applications has also confined the role of experimental verification to cases of complex and non conventional numerical modeling, as stress states resulting from bodies contacts, singularities, material anisotropy, etc.

Totally different is the case for which the knowledge of causes (as forces, impressed temperatures, imposed deformations) or of system parameters as geometry, materials and boundary conditions, is unknown. In these cases the experimental analysis is without alternatives. The present paper shows as it is possible to identify the Fracture Mechanics Parameters called Stress Intensity Factors for different kind of cracks in structural elements: e.g. identification is developed for parameters that are a mix of causes (applied stresses) and geometric parameters. 3D- Photoelasticity, Holographic interferometry and Strain gages are the methods utilized for solving linear and non-linear problems, applying them to paradigmatic cases, showing their capability and limitations.

Keywords: *Experimental Stress Analysis, Inverse Problems, Identification of Fracture Mechanics parameters, Photoelasticity, Holographic Interferometry, Strain Gages.*

1. INTRODUCTION

Experimental measurements are justified when prototypes or their representative physical models are available and when forces or stiffnesses or a function of them are unknown and must be identified.

Practical recent and promising applications of this method are in modern activities of reliability analysis [1], supervising and health-monitoring of existing systems, for controlling their deterioration and for estimating their residual life. For a complete presentation of inverse methods the author recommends the books of [2], [3] and [4] and relative bibliography. The approach to inverse solutions needs the following steps:

- Define the unknowns to be inversely identified.
- Arrange a forward theoretical or numerical model that must be representative of the physical problem, because inverse problems need models to fit to measured data.
- Estimate whether the system can be theoretically formulated or not in an explicit matrix form. The algebraic relationships in matrix form are suitable only for structural discretized systems.
- Develop a preliminary *Design of Experiment* on the forward problem for controlling sensitivity of the causes (factors) that must be independently influential to the system outputs (effects), searching to avoid the combined influence of more variable, i.e. interaction effects.
- Evaluate the level of experimental errors on the effects (e.g. signal to noise ratio) and select those effects less influenced by experimental errors. They can favor the *ill-posedness* of the problem (i.e. small variability of experimental data originate great variability on the estimation of unknown variables).
Note that direct problems can be also ill-posed when they are not well defined and inverse ones can be ill-posed when the experimental errors are relevant.
- Select the unknown parameters in such a way to result insensitive to other parameters of the physical model. An example on holographic interferometry will clarify this point.
- If the system can be formulated with matrix form and the number of known variables equals the number of unknown variables, the problem is determined or even-posed and inversion of the system - matrix (or transformation -, or operator - matrix) can be performed through classical algorithms to obtain the inverse solution.
When the number of known and unknown variables is not the same, different matrix inversion methods can be used, all of them bringing to approximate solutions. The pseudo-inverse matrix concept is introduced.
- Utilize regularization techniques for improving ill-posed problems. This technique will be not presented here.
- If the system cannot be formulated with matrix form, the problem must be dealt with formulation of a *functional of error* between forward and inverse solutions. It must be minimized through optimization/minimization techniques. This procedure provides the unknown parameters of forward model.
- Verify the solutions comparing the results obtained by the model with the experimental data.

2. SYSTEMS IN FUNCTIONAL FORM

Several minimization algorithms are offered by mathematical literature that greatly simplify the researcher task, as the *FindFit* of Mathematica $\text{\textcircled{R}}$, [5].¹ This algorithm is particularly

¹E.g., the algorithm `FindFit [data,expr,params,vars]` finds numerical values of the parameters *params* that make *expr* give a best fit to data as a function of *vars*. The expression *expr* can depend either linearly or nonlinearly on the par_i .

useful for minimizing functional of error because it allows the use of several alternatives that can be select, as *Conjugate Gradient*, *Gradient*, *Levenberg Marquardt*, *Newton*, and *Quasi Newton* methods, with the default use of the *Least-Squares* methods.

In the paper only the use of the *Least Square Method* is presented, to be considered the basic one in a first approach to minimization problems.

In next cases study, the forward problem is expressed in functional forms of this type:

$$\mathbf{y} = \mathbf{A}(\mathbf{p}_1, \mathbf{p}_2, \dots, \mathbf{p}_k, \mathbf{x}) \quad (1)$$

where \mathbf{y} is a vector of the effects, \mathbf{A} is the system transformation matrix, function of vectors parameters, and \mathbf{x} is the inputs vector, to be identified as solution of the inverse problem.

The error functional is the norm of a vector of the difference between the predicted output based on the forward model of Eq. 1 and the measured data that are presumed to be generated by the true value of input variables \mathbf{x}^{true} ; (n is the number of experimental data):

$$J(\mathbf{x}) = (\mathbf{y}^{pred} - \mathbf{y}^{meas})^T \cdot (\mathbf{y}^{pred} - \mathbf{y}^{meas}) = \sum_{i=1}^n [y_i^{pred}(\mathbf{x}) - y_i^{meas}(\mathbf{x}^{true})]^2 \quad (2)$$

If $\mathbf{x} \neq \mathbf{x}^{true}$:

$$J \geq 0$$

From this equation it is clear that if another type of functional is used, e.g. the L_1 norm that is the sum of absolute errors:

$$J = \sum_{i=1}^n |y_i^{pred}(\mathbf{x}) - y_i^{meas}(\mathbf{x}^{true})| \quad (3)$$

the values of the input variables that minimize this functional will be different from the values obtained, e.g., from L_2 norm.²

3. IDENTIFICATION OF FRACTURE MECHANICS PARAMETERS

Given a crack in a stress field, when it is not possible to determine analytically the stress intensity factors, the best way is identifying them by measurement of the stresses around the crack.

For this reason is advisable to express the generic field quantities σ_{ij} as a series expansion of this type [7],[8]:

$$\sigma_{ij} = \sum_{n=0}^N A_n r^{(n-1/2)} f_n(\theta) \sum_{m=0}^M B_m r^m g_m(\theta) + \dots \text{high order of } r \text{ terms} \quad (4)$$

where A_n and B_m terms are unknown coefficients and f_n and g_m are trigonometric functions.

The necessity to use more terms of the series expansion is related to the distance r from the crack tip where are selected (or it is possible) to select measurement points. In many cases three-dimensional stresses zone (close to the tip), sensors sizes and images resolutions, force the experimenter to locate the measurement points relatively far or almost not very close to

²For each kind of engineering problem it must be checked which inverse solution method meets best the requirements, because different solution algorithms applied to the same data can yield different answers.

the tip, where the condition $\eta \ll a$ is met. So it is advisable to have more terms of Eq. 4 to accurately describe the stress (strain) field.

Even remaining in the region close to the tip where K is dominant, it could be useful to have the solution for almost three ($n = 0, 1, 2$) up to six terms of the series. In this cases, *knott* equations must be modified, adding non singular terms to approximated classical Fracture Mechanics equations.

The field variables become in this hypothesis:

$$\begin{cases} \sigma_x = \operatorname{Re} Z - y \operatorname{Im} Z' - y \operatorname{Im} Y' + 2\operatorname{Re} Y \\ \sigma_y = \operatorname{Re} Z + y \operatorname{Im} Z' + y \operatorname{Im} Y' \\ \tau_{xy} = -y \operatorname{Re} Z' - y \operatorname{Re} Y' - \operatorname{Im} Y \end{cases} \quad (5)$$

where the stress functions are given as series in term of z as:

$$\begin{cases} Z(z) = \sum_{n=0}^N A_n z^{(n-1/2)} \\ Y(z) = \sum_{n=0}^M B_n z^n \end{cases} \quad (6)$$

The number of terms to select depends on r , on tip proximity to the boundaries and on the distance of the crack from applied loads. For distance close but not very close to the crack tip, the number of terms of series can be limited to three values (A_0, A_1, A_2) and only one value of B_m (B_0). Substituting Eq. 6 in Eq. 5 gives the following Equations:

$$\begin{aligned} \sigma_x &= A_0 r^{-1/2} \cos \frac{\theta}{2} \left(1 - \sin \frac{\theta}{2} \sin \frac{3\theta}{2} \right) + 2B_0 + \\ &+ A_1 r^{1/2} \cos \frac{\theta}{2} \left(1 + \sin^2 \frac{\theta}{2} \right) + \end{aligned} \quad (7)$$

$$+ A_2 r^{3/2} \left(\cos \frac{3\theta}{2} - \frac{3}{2} \sin \theta \sin \frac{\theta}{2} \right)$$

$$\begin{aligned} \sigma_y &= A_0 r^{-1/2} \cos \frac{\theta}{2} \left(1 + \sin \frac{\theta}{2} \sin \frac{3\theta}{2} \right) + \\ &+ A_1 r^{1/2} \cos \frac{\theta}{2} \left(1 - \sin^2 \frac{\theta}{2} \right) + \end{aligned} \quad (8)$$

$$+ A_2 r^{3/2} \left(\cos \frac{3\theta}{2} + \frac{3}{2} \sin \theta \sin \frac{\theta}{2} \right)$$

$$\begin{aligned} \tau_{xy} &= A_0 r^{-1/2} \cos \frac{\theta}{2} \sin \frac{\theta}{2} \cos \frac{3\theta}{2} + \\ &- A_1 r^{1/2} \sin \frac{\theta}{2} \cos^2 \frac{\theta}{2} - \end{aligned} \quad (9)$$

$$- 3A_2 r^{3/2} \sin \frac{\theta}{2} \cos^2 \frac{\theta}{2}$$

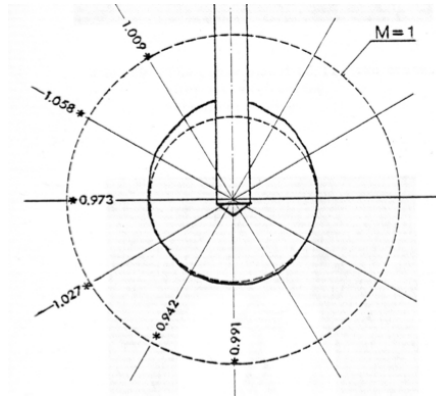


Figure 1. Circular crack obtained by an impact load on a sharp pin inserted into a small hole

4. IDENTIFICATION FOR CRACKS IN 3D BODIES BY PHOTOELASTICITY

The parameter $K (= M\sigma\sqrt{\pi a})$ is a combination of load and geometry data. Through a fatigue propagation of an initial defect and a photoelastic analysis by the frozen stress method at a certain propagation instant, the whole phenomenon of propagation and of stress distribution around the crack is clarified, [6]. Inadequacies of theoretical models and vice-versa the experimental capability in predicting crack directions are evident, especially when the analysis is not limited to a single image but is extended to a sequence taken during the propagation phase.

Single Crack in a Thick Body

For generating a circular crack in a block of epoxy resin (*Araldite*), a simple procedure is adequate:

- Very accurate cracks of circular form are obtained by impacts on a sharp pin inserted in small holes, Fig.1.
- The crack is propagate by cyclic pressurization up to a desired front diameter size.
- Up to a wanted size the crack is statically pressurized and stresses frozen . The stress state differs from one due to external uniform load by a constant value, Fig.2 so that the *Stress Intensity Factor* is not influenced by this modification of the load distribution.
- The *frozen* block is cut in slices in several radial directions, Fig.3, [9].

Extrapolation with a Regression Line For K_I Identification The Fracture Mechanics Equations for Mode I, give the following expression for the difference of the principal stresses in the plane, [6]:

$$\sigma_1 - \sigma_2 = 2A\sqrt{\sin^2 \frac{\theta}{2} \sin^2 \frac{3}{2}\theta + \sin^2 \frac{\theta}{2} \cos^2 \frac{3}{2}\theta} = 2A \sin \frac{\theta}{2}$$

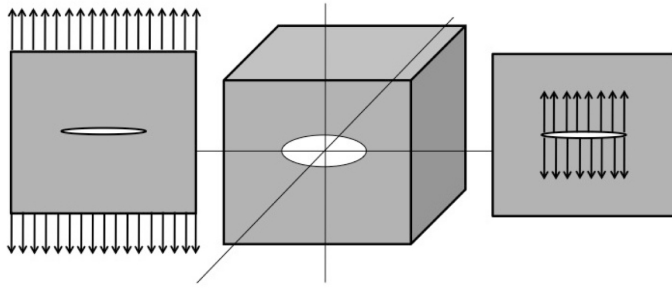


Figure 2. Equivalence of *SIF* (Stress Intensity Factor) for uniform internal and external load

Since

$$A = \frac{K_I}{\sqrt{2\pi r}} \cos \frac{\theta}{2}$$

the difference is:

$$\sigma_1 - \sigma_2 = 2 \frac{K_I}{\sqrt{2\pi r}} \sin \frac{\theta}{2} \cos \frac{\theta}{2} = \frac{K_I}{\sqrt{2\pi r}} \sin \theta$$

and for $\theta = \frac{\pi}{2}$

$$\sigma_1 - \sigma_2 = \frac{K_I}{\sqrt{2\pi r}} = f_\sigma \frac{N}{d}$$

then:

$$\frac{K_I}{\sqrt{2\pi}} \frac{d}{f_\sigma} = N \sqrt{r}$$

or, if $C = \frac{1}{\sqrt{2\pi}} \frac{d}{f_\sigma}$:

$$C \cdot K_I = N \cdot \sqrt{r} \tag{10}$$

Given a photoelastic fringe pattern, the elementary procedure for the determination of the Stress Intensity Factor of Mode I is reported in [10], where a linear extrapolation was utilized for the determination of K_I , Fig.4. The fringe pattern is shown in Fig.4.

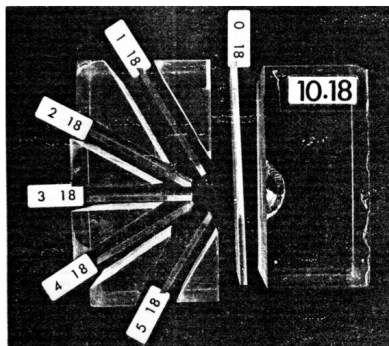


Figure 3. Block Slicing

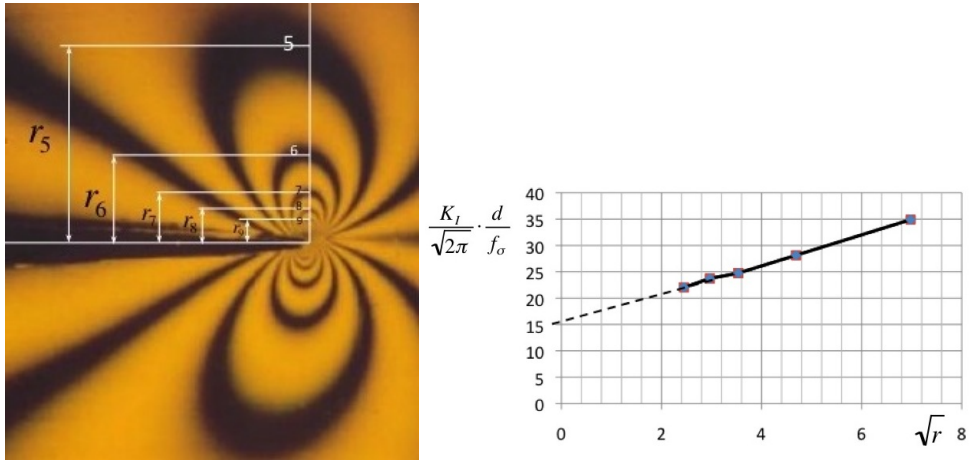


Figure 4. Photoelastic determination of K_I for a circular crack in a uniform stress field by a simplified linear extrapolation on a single direction. From [10]

However, it must be observed that linear extrapolation based on few points for estimating the straight line intercept on vertical axis is source of errors that could be unacceptable, leading to false results, Fig. 5. The error on intercept can be estimated, [3]. Given the straight line of equation:

$$y = a + bx \tag{11}$$

the standard deviation of the intercept a and of the slope b are:

$$\begin{cases} \sigma_a = \sigma \sqrt{\sum_i \frac{x_i^2}{\sigma_i^2} / \Delta} \\ \sigma_b = \sigma \sqrt{\sum_i \frac{1}{\sigma_i^2} / \Delta} \end{cases} \tag{12}$$

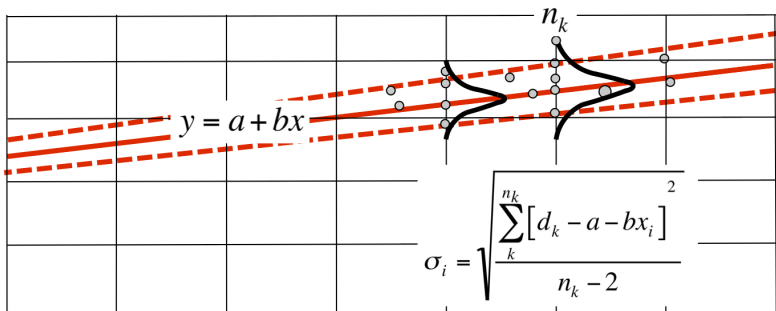


Figure 5. Error on the intercept on vertical axis of a regression straight line for extrapolating experimental data

where:

$$\sigma_i = \sqrt{\frac{\sum_{k=1}^{n_k} [d_k - a - bx_i]^2}{n_k - 2}} \quad (13)$$

and

$$\sigma = \sqrt{\frac{J^2}{n - 2}}$$

with

$$J^2 = \sum_i^2 [d_i - a - bx_i]^2 \quad (14)$$

and Δ is:

$$\Delta = \sum_i \frac{1}{\sigma_i^2} \sum_i \frac{x_i^2}{\sigma_i^2} - \sum_i \frac{x_i}{\sigma_i^2} \sum_i \frac{x_i}{\sigma_i^2} \quad (15)$$

Error (or Residuals) Functional Minimization Since the system cannot be formulated in an explicit matrix form, the error functional to minimize is given by Eq. 3. In this case the solution is obtained comparing a number of photoelastic orders N measured in several points of the interferometric pattern, with the theoretical predicted values in the same points, derived from the forward model and minimizing the difference as a function of theoretical unknown parameters K .

Eq. 3 gives:

$$J(K) = \sum_i^n [y_i^{pred}(K) - y_i^{meas}]^2 = \min \quad (16)$$

where: $y_i^{pred}(K)$ is theoretically predicted output and y_i^{meas} the experimental data. Then:

$$J = \| N^{pred} - N^{meas} \|^2$$

that can be written in this form:

$$J(K) = \sum_i^n \left[\frac{d}{f_\sigma \cdot \sqrt{2\pi}} \frac{K \cdot \sin \theta_i}{\sqrt{r_i}} - N(r_i, \theta_i) \right]^2 = \min \quad (17)$$

The value that minimizes J is the best estimation of K . Several optimization methods can be applied to solve the inverse problem as, e.g. the Least Square Method, through its normal equation:

$$\frac{dJ}{dK} = 0$$

$$\frac{dJ}{dK} = \frac{K}{f_\sigma \sqrt{2\pi}} \sum_i \frac{\sin^2 \phi_i}{r_i} - \sum_i \frac{N_i \cdot \sin \phi_i}{\sqrt{r_i}} = 0$$

from which:

$$\frac{K}{f_\sigma \sqrt{2\pi}} \frac{d}{dK} = \frac{\sum_i \frac{N_i \cdot \sin \phi_i}{\sqrt{r_i}}}{\sum_i \frac{\sin^2 \phi_i}{r_i}}$$

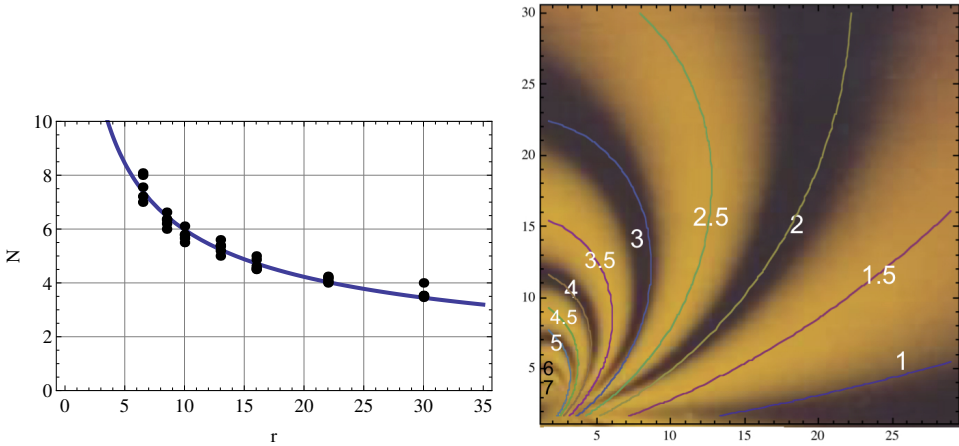


Figure 6. On left fitting the experimental data with a theoretical model along r for several values of θ on the whole field and on right comparison of experimental and theoretical distribution of fringes

In the following examples the application of *FindFit* algorithm of *Mathematica* [®], is utilized to estimate the Stress Intensity Factors for a single crack in a large body.

Example The constant C is:

$$C = \frac{d}{f_{\sigma} \sqrt{2\pi}} = \frac{16}{0.688} = 23.256$$

and model versus experimental data is:

$$C \cdot \frac{K \cdot \sin \phi_i}{\sqrt{r_i}} \rightarrow N(r_i, \phi_i)$$

It fits the experimental values according to Eq. 17. The advantage of an optimization technique is a comparison between theoretical and experimental K values on a large portion of the definition domain, unlike the extrapolation of data on a single direction. Versus a theoretical value of $0.825 \text{ MPa}\sqrt{\text{mm}}$ this procedure gives, Fig. 6: $0.812 \text{ MPa}\sqrt{\text{mm}}$ that is a good approximation of the theoretical value, against the extrapolation value of only $0.688 \text{ MPa}\sqrt{\text{mm}}$ by the simplified method.

Two Non-Coplanar Defects in a Thick Body

It has been planned an experiment with the aim of evaluating the stress intensity factor in the direction of maximum interaction between two circular cracks located in parallel planes of a large body, in a certain instant of time of their fatigue propagation due to a cyclic internal pressure, [11], Fig. 7. Material is assumed homogeneous and isotropic. Fig. 8 shows the vertical view of the variable front shapes of the same non-coplanar defects internally pressurized at increasing number of cycles and the perpendicular slice profile for photoelastic analysis in a selected propagation stage. It would be interesting to utilize this experiment for determining

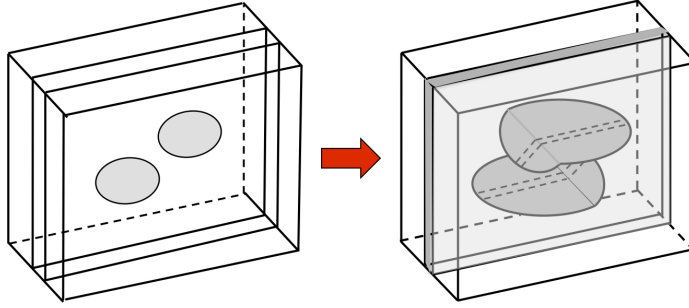


Figure 7. Two diverse configurations of non-coplanar defects, of initial circular shapes, internally cyclically pressurized with the view of the perpendicular slice profile for a photoelastic analysis

the state of stress for two interacting cracks externally loaded, instead of internally pressurized. The equivalence shown in Fig. 9 is valid for plane problems with plane cracks only. Fig. 10 shows the photoelastic fringe pattern around the tips of two interacting non-coplanar cracks internally pressurized, put in a large block of isotropic material.³ The model depends non-linearly on the unknown variables:

$$\left[\frac{f_\sigma}{d} N(r_i, \phi_i) \right]^2 = \frac{1}{2\pi r_i} \left[(K_I \sin \phi_i + 2K_{II} \cos \phi_i)^2 + (K_{II} \sin \phi_i)^2 \right] \quad (18)$$

The solution is possible through an *incremental/iterative* approach by the Least-Squares Method.

The error functional in two variables, starting from the previous equation, is:

$$J = \sum_i^n \left\{ \left(\frac{f_\sigma}{d} \right)^2 2\pi r_i N^2(r_i, \phi_i) - [(K_I \sin \phi_i + 2K_{II} \cos \phi_i)^2 + (K_{II} \sin \phi_i)^2] \right\}^2 = \min \quad (19)$$

³It can be considered valid with some approximations for 3-D cracks only with the restriction to the mean plane in which the state of stress is essentially two-dimensional.

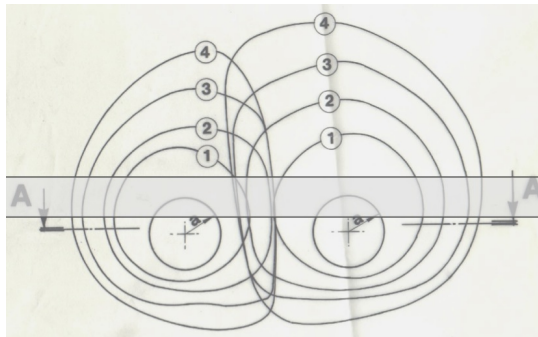


Figure 8. Front shapes of non-coplanar defects internally pressurized, at increasing numbers of fatigue cycles and profile of the analysis plane

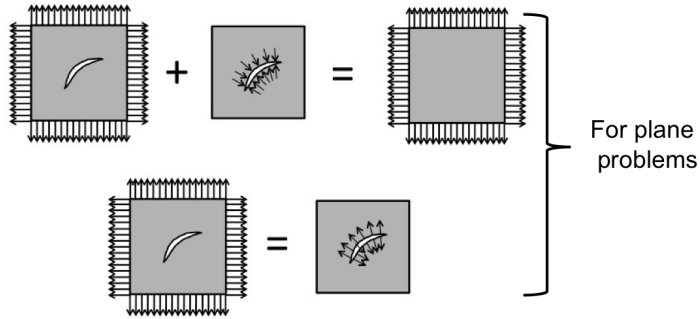


Figure 9. Approximate equivalence for SIF calculation in middle plane only between internal and external loading conditions

or:

$$J = \sum_i^n \left[M(N_i) - P(K_I, K_{II}, \phi_i) \right]^2 \quad (20)$$

where N are the measured orders and i is i -point label, variable from 1 to n , total number of measurements. The first term (M) of Eq. 20 is proportional to the fringe orders *measured* in points n and the second is the value (P) *predicted* by the theoretical relationship of Fracture Mechanics.

Approximation by Linearization The previous non linear expression is linearized by a Taylor series expansion, limited to the first term:

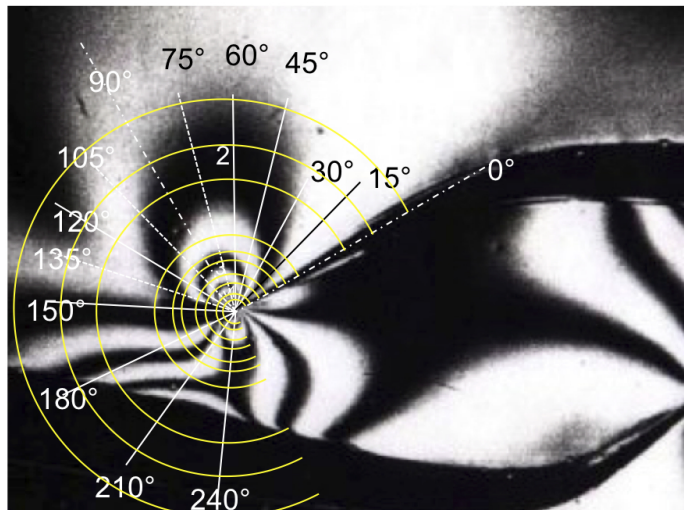


Figure 10. Frozen Fringes in the central plane of two non-coplanar interacting cracks in a large block, loaded by internal pressure

$$\begin{aligned}
P(K_I, K_{II}, \phi_i) &= [(K_I \sin \phi_i + 2K_{II} \cos \phi_i)^2 + (K_{II} \sin \phi_i)^2] \approx \\
&\approx P_0^2(r_i, \phi_i, K_{I0}, K_{II0}) + \left(\frac{\partial P^2}{\partial K_{I0}} \Big|_0 \Delta K_I + \frac{\partial P^2}{\partial K_{II0}} \Big|_0 \Delta K_{II} \right)
\end{aligned}$$

Substituting the first term of a Taylor series into the error function, the problem reduces to the minimization of a linear functional:

$$J = \sum_i^n \left\{ \left(\frac{f_\sigma}{d} \right)^2 2\pi r_i N^2(r_i, \phi_i) - P_0^2 - \left(\frac{\partial P^2}{\partial K_{I0}} \Big|_0 \Delta K_I + \frac{\partial P^2}{\partial K_{II0}} \Big|_0 \Delta K_{II} \right) \right\}^2 = \min \quad (21)$$

Linear Least-Squares Newton-Raphson Method In order to apply the *Linear Least-Squares Newton-Raphson Method* minimization proceeds to the generation of the corresponding normal equations in the variables

$$\Delta K_I, \Delta K_{II}$$

At the minimum, the derivative vector with respect to both parameters has its components equal to zero:

$$\begin{aligned}
\frac{\partial J}{\partial K_I} &= 2 \sum_i \left[\dots \right] \frac{\partial P^2}{\partial K_I} = 0 \\
\frac{\partial J}{\partial K_{II}} &= 2 \sum_i \left[\dots \right] \frac{\partial P^2}{\partial K_{II}} = 0
\end{aligned} \quad (22)$$

then:

$$\frac{\partial J}{\partial K_I} = \sum_i \left[\left(\frac{f_\sigma}{d} \cdot N(r_i, \phi_i)^2 - P_0^2 \right) \cdot \frac{\partial P^2}{\partial K_I} - \left(\frac{\partial P^2}{\partial K_I} \partial K_I + \frac{\partial P^2}{\partial K_{II}} \partial K_{II} \right) \cdot \frac{\partial P^2}{\partial K_I} \right] = 0$$

For the first vector component is:

$$\begin{aligned}
&\sum_i \left(\frac{\partial P^2}{\partial K_I} \cdot \frac{\partial P^2}{\partial K_I} \right) \partial K_I + \sum_i \left(\frac{\partial P^2}{\partial K_{II}} \cdot \frac{\partial P^2}{\partial K_I} \right) \partial K_{II} = \\
&= \sum_i \left((f_\sigma/d\sqrt{2\pi r})^2 \cdot N(r_i, \phi_i)^2 - P_0^2 \right) \cdot \frac{\partial P^2}{\partial K_I}
\end{aligned}$$

For the second vector component is:

$$\begin{aligned}
&\sum_i \left(\frac{\partial P^2}{\partial K_I} \cdot \frac{\partial P^2}{\partial K_{II}} \right) \partial K_I + \sum_i \left(\frac{\partial P^2}{\partial K_{II}} \cdot \frac{\partial P^2}{\partial K_{II}} \right) \partial K_{II} = \\
&= \sum_i \left((f_\sigma/d\sqrt{2\pi r})^2 \cdot N(r_i, \phi_i)^2 - P_0^2 \right) \cdot \frac{\partial P^2}{\partial K_{II}}
\end{aligned}$$

In matrix form, for finite differences ΔK_I and ΔK_{II} (remembering that all the partial derivatives as well as P_0^2 are functions of K_I , K_{II} and ϕ_i), the following relationships is valid:

$$\begin{aligned} & \begin{pmatrix} \sum_i \left(\frac{\partial P^2}{\partial K_I} \cdot \frac{\partial P^2}{\partial K_I} \right) & \sum_i \left(\frac{\partial P^2}{\partial K_{II}} \cdot \frac{\partial P^2}{\partial K_I} \right) \\ \sum_i \left(\frac{\partial P^2}{\partial K_I} \cdot \frac{\partial P^2}{\partial K_{II}} \right) & \sum_i \left(\frac{\partial P^2}{\partial K_{II}} \cdot \frac{\partial P^2}{\partial K_{II}} \right) \end{pmatrix} \cdot \begin{pmatrix} \Delta K_I \\ \Delta K_{II} \end{pmatrix} = \\ & = \begin{pmatrix} \sum_i \left((f_\sigma/d\sqrt{2\pi r_i})^2 \cdot N(r_i, \phi_i)^2 - P_0^2 \right) \cdot \frac{\partial P^2}{\partial K_I} \\ \sum_i \left((f_\sigma/d\sqrt{2\pi r_i})^2 \cdot N(r_i, \phi_i)^2 - P_0^2 \right) \cdot \frac{\partial P^2}{\partial K_{II}} \end{pmatrix} \end{aligned}$$

Briefly:

$$\mathbf{A} \cdot \Delta \mathbf{K} = \mathbf{B} \quad (23)$$

where \mathbf{A} and \mathbf{B} are two (2x2)- matrices and $\Delta \mathbf{K}$ is a (2x1)- vector.

Partial derivatives have the following expressions:

$$\begin{aligned} \frac{\partial P^2}{\partial K_I} &= 2K_I \sin^2 \phi_i + 4K_{II} \sin \phi_i \cos \phi_i \\ \frac{\partial P^2}{\partial K_{II}} &= 8K_{II} \cos^2 \phi_i + 4K_I \sin \phi_i \cos \phi_i + 2K_{II} \sin^2 \phi_i \end{aligned}$$

The minimization procedure starts with a guess for K_{I0} and K_{II0} and computes the values $P_0^2(r_i, \phi_i, K_{I0}, K_{II0})$. The Eq. 23 is solved for ΔK_I ΔK_{II} . The tentative values K_{I0}, K_{II0} must be incremented by this amount and the process repeated *incrementally and iteratively* until a minimum value for J is reached.

Example

- Internal pressure in both cracks: $p = 0.0866 \text{ MPa}$.
- External stress applied in longitudinal direction: $\sigma_{0x} = 0$.
- Number of fatigue cycles ($0 \div 0.0866$) of internal pressure $N_{cycl} = 32,400$.
- With reference to Fig. 10, starting state is given by two tentative values:
 $KI = 0.825 \text{ MPa} \sqrt{mm}$ $KII = 0.157 \text{ MPa} \sqrt{mm}$.
- A minimum of $J(= 10.76)$, is reached after about 27 iterations.
- The final reached values are: $K_I = 0.739 \text{ MPa} \sqrt{mm}$ and $K_{II} = 0.283 \text{ MPa} \sqrt{mm}$.

5. IDENTIFICATION OF STRESS INTENSITY FACTORS BY HOLOGRAPHIC INTERFEROMETRY

Holographic interferometry can be applied to the determination of fracture mechanics parameters, remembering the relationship that links the displacements field close to a crack with the Stress Intensity Factors, [6].

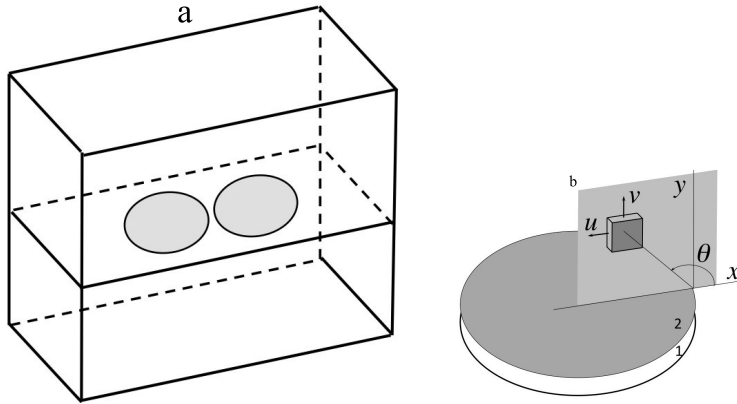


Figure 11. Two co-planar circular cracks in a large block and displacements field on a plane close to the cracks plane

Interference of Two Circular Co-planar Cracks

The application deals with the problem of two circular cracks lying in the same plane, uniformly loaded at a certain distance in a direction perpendicular to the plane. The experiment is set up through two cracks are artificially generated in the middle plane of a transparent plexiglass block of $300 \times 200 \times 110 \text{ mm}^3$. The experiment wishes investigate on the propagation effect for cycling load and verify if cracks tend to join forming a unique more dangerous crack. This intuitive conjecture needs a physical validation.

From the point of view of Fracture Mechanics the stress state in any points of cracks tips is equivalent to the state due to external uniform load for *plane strain condition*.

By holographic interferometry, [12] the displacements field Eq. 24 can be determined in

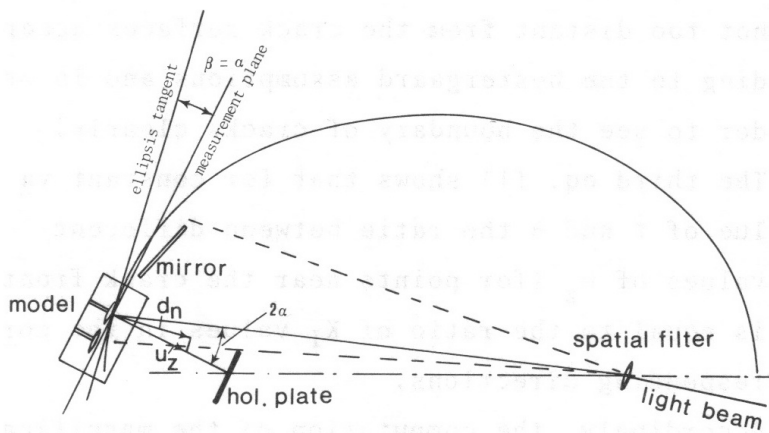


Figure 12. Positioning of the transparent model in the holographic bench

an opaque plane close and parallel to the cracks, Fig. 11. The transparent model is placed on the holographic bench as shown in Fig.12. The main model dimensions are the following:

- $2a = 60 \text{ mm}$ crack diameter.
- $h/a = 1.09$ distance between the centre of each crack and the symmetry plane over a .

Displacements contour lines for a given internal pressure are shown in Fig. 13.

It can be observed a small shift of the centre of the circular contour lines respect to the geometrical centre of the cracks, pointed out by the light eccentricity of the contour lines from the cracks tips (the distances in direction A are a little bigger than the distances in direction B). This small displacement is the symptom of a bigger value of the stress intensity factor in direction B respect to direction A , as it will be proofed in the following.

For the determination of the stress intensity factor in the two radial directions in points A and B the method of optimization based on the Least Square Solution has been utilized. Remembering the equations:

$$\begin{cases} u = \frac{K_I}{G} \sqrt{\frac{r}{2\pi}} \cos \frac{\theta}{2} (1 - 2\nu + \sin^2 \frac{\theta}{2}) \\ v = \frac{K_I}{G} \sqrt{\frac{r}{2\pi}} \sin \frac{\theta}{2} (2 - 2\nu - \cos^2 \frac{\theta}{2}) \end{cases} \quad (24)$$

solution can be found minimizing the object function:

$$J = \|v^{predict} - v^{meas}\|^2 = min \quad (25)$$

i.e. the norm of the vector of residuals. Substituting the second Eq. 24 in Eq. 25 gives:

$$J = \sum_i^n \left[\frac{K_I}{G\sqrt{2\pi}} \sqrt{r_i} \sin \frac{\theta_i}{2} (2 - 2\nu - \cos^2 \frac{\theta_i}{2}) - \frac{\lambda}{2 \cos \alpha \cos \beta} N(r_i) \right]^2 = min \quad (26)$$

where:

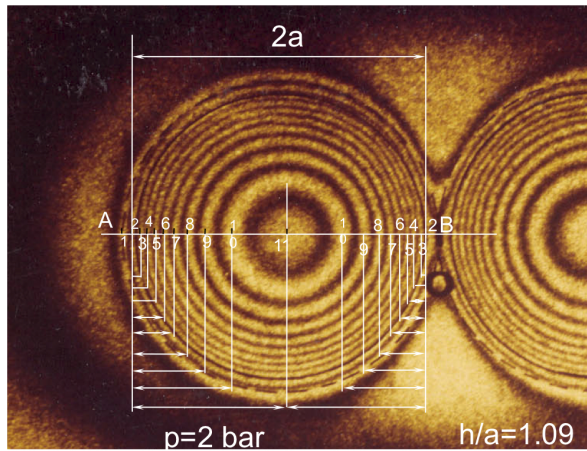


Figure 13. Contour lines of displacements field of the surfaces of two co-planar cracks in a transparent model in a uniform state of stress, internally pressurized at $p = 2 \text{ bar}$

- $G = \frac{E}{2(1+\nu)}$ = shear modulus of elasticity
- ν = Poisson's ratio
- r_i = distance from the crack tip
- θ_i = see Fig. 11 b)
- λ = wave length of laser light
- $\cos \alpha \cos \beta$ = geometrical position of the model on the holographic bench.

For $\theta = \pi$ the functional Eq. 26 becomes:

$$J = \sum_i^n \left[K_I \sqrt{r_i} - \frac{\lambda G}{2(1-\nu) \cos \alpha \cos \beta} \sqrt{\frac{\pi}{2}} N(r_i) \right]^2 = \min \quad (27)$$

where:

- $K_I \sqrt{r_i} = N^{predict}$
- $N(r_i) = N^{meas}$
- $\frac{\lambda G}{2(1-\nu) \cos \alpha \cos \beta} \sqrt{\frac{\pi}{2}} = C$

Normal equation The corresponding normal equation is:

$$\begin{aligned} \frac{\partial J}{\partial K_I} &= \frac{K_I}{G \sqrt{2\pi}} \sum_i^n \left[\sqrt{r_i} \sin \frac{\theta_i}{2} (2 - 2\nu - \cos^2 \frac{\theta_i}{2}) \right]^2 + \\ &- \sum_i^n \frac{N(r_i) \lambda}{2 \cos \alpha \cos \beta} \left[\sqrt{r_i} \sin \frac{\theta_i}{2} (2 - 2\nu - \cos^2 \frac{\theta_i}{2}) \right] = 0 \end{aligned}$$

The Least Square Solution gives:

$$K = \frac{\lambda G}{\cos \alpha \cos \beta} \sqrt{\frac{\pi}{2}} \cdot \frac{\sum_i^n N_i \left[\sqrt{r_i} \sin \frac{\theta_i}{2} (2 - 2\nu - \cos^2 \frac{\theta_i}{2}) \right]}{\sum_i^n \left[\sqrt{r_i} \sin \frac{\theta_i}{2} (2 - 2\nu - \cos^2 \frac{\theta_i}{2}) \right]^2} \quad (28)$$

K is obtained in directions A and B for a loading pressure ($p = 2$). The ratio of the two values is $KB/KA = 1.08$

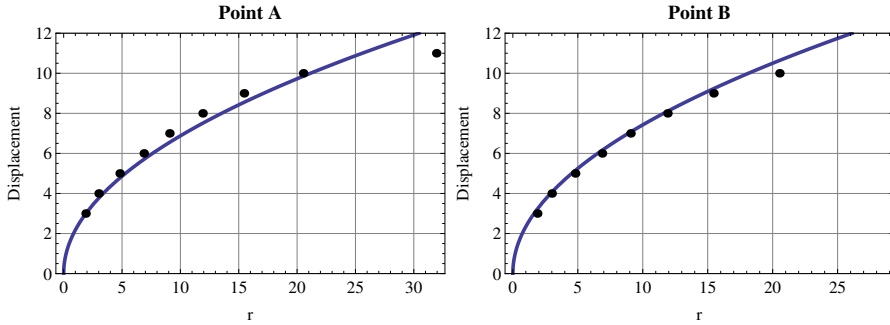


Figure 14. Theoretical curves in *A* and *B* directions from the *FindFit* algorithm for fitting experimental data in case of $p = 2 \text{ bar}$. The constant C is 0.580

Alternative Solution The application of LSM can be done by a direct algorithm. The application of *FindFit* algorithm of Mathematica® avoids calculation of normal equations because provides the expression of K_I in directions *A* and *B*. The algorithm works directly on the Eq.27 and Fig. 14 shows the two curves that fit the experimental data minimizing the residuals, giving directly both values of the stress intensity factors. For an internal pressure of $p = 2 \text{ bar}$ the values are the following:

K in Direction A $K = 1.261 \text{ MPa}\sqrt{\text{mm}}$

K in Direction B $K = 1.362 \text{ MPa}\sqrt{\text{mm}}$

The ratio is $K_B/K_A = 1.080$

The same procedure of LSM analysis for $p = 3 \text{ bar}$ gives a little different value of the ratio: $K_B/K_A = 1.102$ It can be concluded that the magnification effect in the direction of minimum distance between the cracks is about $10 \div 11\%$ and it is also worth observing the magnification factor $M = K_B/K_A$ is much more stable in the experiment than the single values K_A and K_B , highly dependent on the material parameters and loadings ($E, \nu, p, \text{etc.}$).

This example demonstrates that it is suitable to select the unknown output parameters in such a way to result insensitive to other parameters of the model, as it happens in this case where the material of the model (Plexiglass) is different from the prototype material in which the real cracks are located.

6. IDENTIFICATION OF STRESS INTENSITY FACTORS BY STRAIN GAGES MEASUREMENTS

Strain gages measurements offer several ways for identification of the plane-stress K value, with one or more higher order terms of series expansion of strain close to the crack. Let's assume that strain gages can be placed in a region near the crack tip along the crack line, with grids in a direction perpendicular to the crack plane, [8].

The case study deals with a corner crack in a component of rectangular section in a portal frame consisting of two columns subjected to tensile stress and two transversal elements.

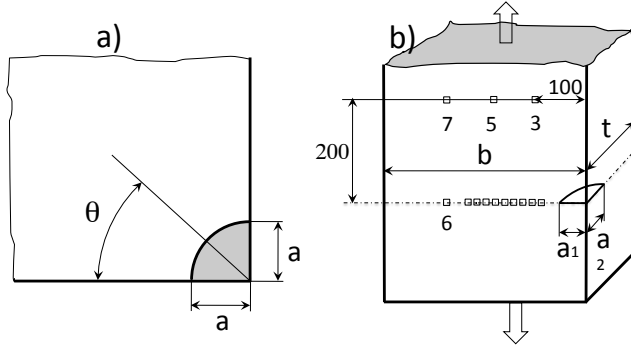


Figure 15. Sketch of angular crack in a tensile member. a) a theoretical form of a quarter of circular crack in infinite body; b) the real shape of angular crack after propagation

During the tests on a prototype, after a relevant number of working cycles, an angular crack enucleated in a corner that developed in the form of a quarter of circle and then in a more complex shape, Fig. 15 a).

Material and geometry data are:

- Mat.: Fe 510 with $E = 2.1 \cdot 10^5 \text{ MPa}$
- $\mu = 0.3$ Poisson's ratio
- $b > 400 \text{ mm}$ column width
- $t > 600 \text{ mm}$ column thickness
- $a_1 \geq 45 \text{ mm}$ crack length for $3.5 \cdot 10^6$ cycles
- $a_2 \geq 45 \text{ mm}$ that grows up to 200 mm for $3.5 \cdot 10^6$ cycles.

A chain of nine strain gages is located on the crack axis on the shorter side of the crack, at a distance $15 \div 30 \text{ mm}$ from the crack tip, Fig. 15 b). According to the model of linear elastic fracture mechanics (LEFM) three regions are defined surrounding the crack tip and it must be avoided to locate the strain gages either in the nonlinear zone very close to the tip where the material yields with large deformation or in a too far region where boundary effects dominates and the model is not more representative of the state of the local stress.

The measured values of nine strain gages along the crack plane are reported in Tab. 1.

Identification through the First Term of the Series

Measurements of strains along the crack plane can offer enough information for a proper K_I identification. In order to fit the theoretical model to the data, the least square method is applied as following:

$$J = \|\epsilon^{predict} - \epsilon^{meas}\|^2 = \min \quad (29)$$

$$J = \sum_i^n \left[\frac{(1-\nu)}{E\sqrt{2\pi}} \cdot \frac{K_I}{\sqrt{r_i}} - \epsilon^{meas}(r_i) \right]^2 = \min \quad (30)$$

Table 1. Strain measurements along along the crack plane

Distance r_i [mm]	Meas. Strain [$\mu\epsilon$]
15.30	762
16.90	699
19.15	656
20.80	623
22.80	591
24.70	566
26.90	557
29.10	537
30.70	527

being:

$$\epsilon^{predict} = \frac{(1 - \nu)}{E\sqrt{2\pi}} \cdot \frac{K_I}{\sqrt{r_i}} \quad (31)$$

Example Identification of K_I through the First term of Series Expansion with the previous data. The constant C is equal to:

$$C = \frac{(1 - \nu)}{E\sqrt{2\pi}} = \frac{0.7}{2.507 \cdot 2.1 \cdot 10^5} = 1.330 \cdot 10^{-6} \frac{1}{MPa}$$

By *FindFit* of *Mathematica*® [5], the identified value of the stress intensity factor with only *the first* term of series expansion is: $K_I = 2, 166.85 MPa\sqrt{mm}$, Fig. 16 at left.

Utilization of More Terms of Series Expansion for K_I Identification

In order to check the accuracy of K identification by strain gages, the use of more terms of the series expansion is suggested because the chain of strain gages, due to their natural transversal dimension, tends to overcome the limited area close to the crack tip supposed by the simplified theory and it is possible that they record strain contribution in points relatively far from the tip. For this reason it is recommended to use equations that take into account more terms (almost four) of the series expansion.

The relationships for the strains can be derived substituting Eq. 9 into the general stress-strain relations (Hooke law) [8, 108–109]. Strain component ϵ_y perpendicular to the crack line is obtained by the following Equation:

$$\begin{aligned} E\epsilon_y &= A_0 r^{-1/2} \cos \frac{\theta}{2} \left[(1 - \nu) + (1 + \nu) \sin \frac{\theta}{2} \sin \frac{3\theta}{2} \right] - 2\nu B_0 \\ &+ A_1 r^{1/2} \cos \frac{\theta}{2} \left[(1 - \nu) - (1 + \nu) \sin^2 \frac{\theta}{2} \right] + \\ &+ A_2 r^{3/2} \left[(1 - \nu) \cos \frac{3\theta}{2} + \frac{3}{2} (1 + \nu) \sin \theta \sin \frac{\theta}{2} \right] \end{aligned} \quad (32)$$

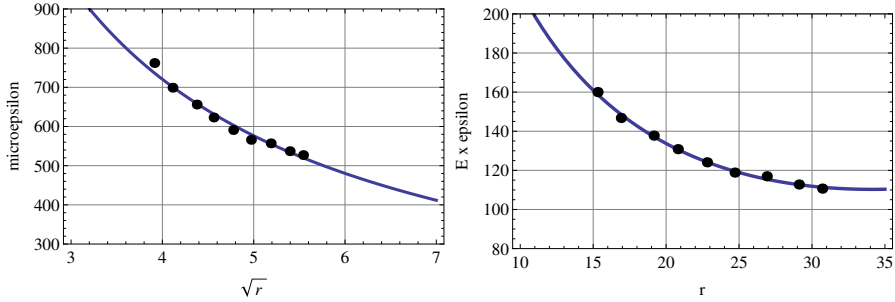


Figure 16. Theoretical model fitting experimental data according to Eq. 30 with one term, on left and with three terms of the series expansion on right

For $\theta = 0$ Eq. 32 holds:

$$E\epsilon_y = A_0 r^{-1/2}(1 - \nu) - 2\nu B_0 + A_1 r^{1/2}(1 - \nu) + A_2 r^{3/2}(1 - \nu) \quad (33)$$

Example Through the use of algorithm *FindFit* of *Mathematics*, the experimental values of Table 1 are fitted by Eq. 33 with three (A_0 , A_1 , A_2) terms of series expansion. The estimated value of the Stress Intensity Factor is $K_I = 2,973.38 \text{ MPa}\sqrt{\text{mm}}$, Fig. 16 on right side.

The improvement of this three terms model observing the differences between the diagrams of Fig. 16 seems minimum, but the estimation of the stress intensity factor changes considerably: 2,973.4 instead of 2,166.8 $\text{MPa}\sqrt{\text{mm}}$.

7. CONCLUSIONS

Given a structural problem, an inverse approach is able to *identify* causes as well as unknown system parameters or a combination of both, starting from stresses, displacements or strains measurements. For solving inverse problems it is necessary to set up a suitable theoretical model if a series of accurate experimental data is available. The accuracy of them and a proper selection of the quantities that must be measured have an important role for controlling the experimental errors that can be transmitted to the unknown variables, ill-conditioning the solutions.

Several methods have been utilized for the identification of Fracture Mechanics parameters, applying the methods to paradigmatic cases study, showing capability and limitations of them. They have different applications: these examples should show the most suitable for every case, [14].

3D-Photoelasticity is limited to the analogy and to the constraint of a different material, but its illustration capability of the total phenomenon is not overcome by any others. Holographic interferometry proves useful for special subtle cases and Strain Gauges allow the determination of Stress Intensity Factors when the Fracture Mechanics Theory can not be limited to the approximation of the first term, but strains are described by more terms of the series development.

From the point of view of technical sciences this is the best proof of the necessity to study structural problems joining theoretical/numerical models with experimental measurements. Only together they can satisfy modern quests for reliability, safety and life extension of technical systems.

References

- [1] Birolini, A., 2010. *Reliability Engineering*, 7 ed., Vol. 1. Springer Verlag, Berlin.
- [2] Laermann, K., 2008. *Inverse Problems in Experimental Structural Analysis*, 1 ed., Vol. 1. Shaker Verlag, Aachen.
- [3] Doyle, J.F., 2004. *Modern Experimental stress Analysis. Completing the solution of partially specified problems*, Vol. 1. J.Wiley N.Y.
- [4] Liu, G. R., and Han, X., 2003. *Computational Inverse Techniques In Nondestructive Evaluation*, Vol. 1. CRC Press LLC. Boca Raton, London, New York. ISBN 0-8493-1523-9.
- [5] Blinder, S. M., 2013. *Guide to Essential Math, A Review for Physics, Chemistry and Engineering Students, second edition*, Vol. I. Elsevier, Berlin. Mathematica 8.
- [6] Sharpe, W. J., 2008. *Handbook of Experimental Mechanics*, sem, ct, usa ed., Vol. 1. Springer Verlag. ISBN: 978-0-387-26883-5.
- [7] Knott, J., 1973. *Fundamentals of Fracture Mechanics*, Vol. 1. J. Wiley and Sons, London.
- [8] ESA991, ed., 1991. *Comment on Fracture Mechanics*, Vol. 1 of *Series Title*. Publisher Name, Publisher address, lesson at dep. aeron.& astron.,ncku. 4.3, pp. 94–122. See http://140.116.81.56/ESA991/Chap%4_2.pdf.
- [9] Kuske, A., and Robertson, G., 1974. *Photoelastic Stress Analysis*, 1 ed., Vol. 1. J. Wiley and Sons, London.
- [10] Freddi, A., 1991. *An Experimental Stress Analysis Syllabus and Course Design*, 1 ed., Vol. 1 of *Quaderni del DIN*. SocietaEditrice Esculapio, Via U. Terracini 30 40131 Bologna (Italy). <http://amsacta.unibo.it/3715/>.
- [11] Freddi, A., Olmi, G., and Cristofolini, L., 2008. *Experimental Stress Analysis in Materials and Structures*, (<http://www.springer.com/materials/mechanics/book/978-3-319-06085-9>) ed., Vol. 1. Springer Verlag. in press 2015.
- [12] Freddi, A., and Persiani, F., 1978. “Holographic measurement of magnification factors for embedded interacting defects in transparent models”. In 6th Int. Conf. on Exp. Stress Anal., A. Editor and B. Editor, eds., Vol. 1, VDI, VDI Berichte Nr.313.
- [13] Freddi, A., 2009. “Some reflections upon the design by experiment of mechanical structures”. In *Konstruktionsmethodik für Fahrzeugkonzepte : Kolloquium am 8. Mai 2009 anlässlich des Ausscheidens von Prof. Dr.-Ing. Hans-Joachim Franke aus dem aktiven Dienst und Übergabe des Instituts an Prof. Dr.-Ing. Thomas Vietor, G. für Konstruktionstechnik*, ed., Vol. 1, Institut für Konstruktionslehre, ITS Niedersachsen, Braunschweig 2010, pp. 159–176. Bericht 74.
- [14] Freddi, A., 2013. Some examples of system parameters identification by experimental stress analysis. unpublished, 24–28 April in Bari(Italy). Oral presentation at YSESM Symposium.

OPTIMAL DESIGN OF PAIRED TAPERED ROLLER BEARINGS UNDER CENTRED RADIAL AND AXIAL STATIC LOADS

Eugenio Dragoni

Department of Engineering Sciences and Methods

University of Modena e Reggio Emilia

E-mail: eugenio.dragoni@unimore.it

Abstract. *Based on the empirical relationships provided by the ISO 76 standard, this paper optimizes the internal dimensions of tapered roller bearings for maximum static load capacity. A bearing system formed by two identical bearings is assumed, subjected to whatever combination of radial force (applied at equal distance from the bearings) and axial force (applied to a centre shaft connecting the bearings). It is shown that the static load capacity increases linearly with the filling ratio (number of rollers divided by the maximum number which can fill the bearing) and the aspect ratio (ratio of length to mean diameter of rollers) and goes up with the square of the pitch diameter of the roller set. Further, given the ratio of axial to radial force, an optimal contact angle exists which maximizes the static load capacity of the bearing pair, regardless of actual size (pitch diameter) and proportions (ratio of roller diameter to pitch diameter).*

Keywords: *Radial rolling bearings, tapered rollers, static loading, optimization, design.*

1. INTRODUCTION

Ordinarily, rolling bearings are not designed and built in-house but are chosen by the designer from the catalogue of specialized manufactures. The high degree of specialization has fostered the development of standardized high-quality products, readily available off-the-shelf in a wide range of shape and dimensions at affordable prices. Under particular design circumstances, like very large bearings or tight mounting spaces, the need can arise for non-standard bearings which the regular market can satisfy only at a considerable cost of time and money. In such instances, rolling bearings of simple geometry (as with cylindrical or tapered rollers) can be manufactured by the end user itself to meet the specific requirements at a fraction of the costs and delivery time requested by the specialized suppliers.

When tackling the construction of custom bearings the designer has the control of all the variables and the design is conveniently conducted according to optimization methods. Unlike conventional machine elements, for which a wealth of optimization criteria have been developed since long [1, 2], the category of rolling bearings has received so far relatively little attention. May be due to the aforementioned passive design approach (selection from a catalogue) towards these components, until the turn of the century the technical literature has been limited to optimal bearing selectors [3] and simulators of bearing kinematics [4]. Papers dealing with the optimization of bearing features have appeared only lately, aimed at maximizing one or several performance properties of ball bearings [5–11], cylindrical roller bearings [12, 13] and tapered roller bearings [14–17].

As for ball bearings, Choi and Yoon [5] optimized an automotive wheel-bearing unit with double-row, angular-contact architecture using a genetic algorithm. They showed that

the system life can be improved over the standard design without any constraint violations. Kalita and coworkers [6] adopted a multi-objective optimisation approach for the design of ball bearings with enhanced dynamic capacity, static capacity and lubricant film thickness. The work uses both deterministic methods (penalty functions) and stochastic algorithms (simulated annealing and genetic search). The genetic approach was further explored by Chakraborty et al. [7] for ball bearings and its merits were compared to conventional techniques. Also based on genetic algorithms, a non-linear optimization procedure was developed by Rao and Tiwari [8] for the design of ball bearings with maximum fatigue life under kinematic constraints. The optimized bearing yielded better fatigue life as compared to standard catalogues. This study was further evolved [9] to achieve multi-objective optimization of the bearing in terms of static load capacity, fatigue life and elastohydrodynamic film thickness under inner and outer geometric constraints. Angular-contact ball bearings were optimized by Savsani et al. [10] for maximum static and dynamic loading ratings and minimum film thickness using a modified particle swarm optimisation technique. Both single and multi-objective optimisation tasks were considered, claiming advantages with respect to former, mainly genetic, numerical procedures. Wei and Chengzu [11] improved on the computational side of the problem introducing non-dominated sorting genetic algorithms to optimize high-speed, angular-contact ball bearings for fatigue life and frictional power losses.

The optimization of cylindrical roller bearings was first tackled by Kumar et al. [12] for maximum dynamic capacity using real-coded genetic algorithms and adopting, as design variables, the diameter of the rollers, the roller pitch diameter, the roller length and the number of rollers. This work was then expanded by adding the roller crowning (non linear profile) among the design parameters [13] and performing a Monte Carlo sensitivity analysis to investigate changes in the fatigue life of the bearing. The results showed that the multiplier of the logarithmic profile deviation parameter has more effect on the fatigue life as compared with other geometric parameters.

A pioneering instance of tapered roller bearing optimization can be traced back to the paper by Parker et al. [14], in which the performance of several large-bore (about 120 mm), tapered roller bearings were simulated and tested at shaft speeds up to 20 000 rpm under combined thrust and radial load. The computer-optimized bearing design proved superior to equal-sized standard bearings tested for comparison. Chaturbhuj et al. [15] optimized tapered roller bearings using genetic algorithms and demonstrated that the fatigue life of the bearing improved marginally compared with respect to standard bearings. However, some authors [12, 13] have pointed out that some optimization constraints introduced in this paper were unrealistic. A method for optimizing the geometry of tapered roller bearings at high speeds, was developed by Walker [16] with the main aim of determining the cup and cone angles which minimize the contact stresses. Walker found that at low speeds the optimum cup angle is 40 degrees, whereas the optimum value decreases to 10 degrees for the highest speeds. Wang et al. [17] presented a mathematical model for optimizing the design of four-column bearings with tapered rollers subject to several geometric constraints. By acting on a rearrangement of the classical variables (roller diameter and length, pitch diameter, number of rollers and cup angle), they improved the dynamic load rating by 22% and the life expectancy by 85% over a commercial competitor of like dimensions. Though interesting for the potential of improvements it shows, Wang et al.'s paper is rather obscure as concerns the optimization method behind the model and little can be taken away from the published results apart from the specific example presented.

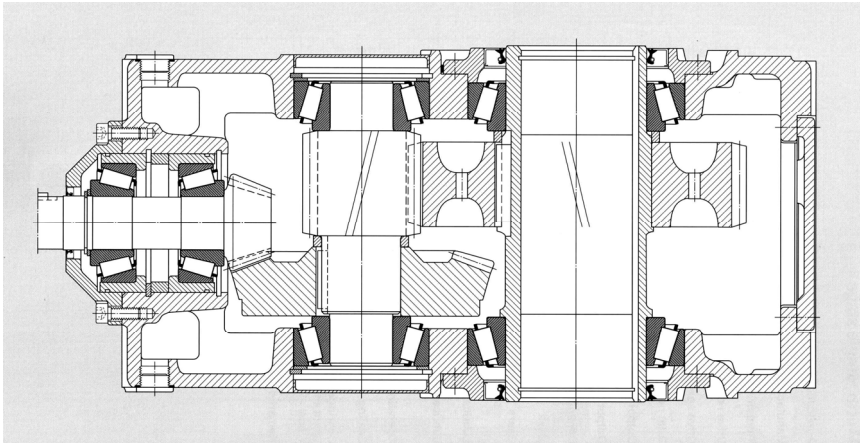


Figure 1. Longitudinal section of a two-stage bevel/spur gearbox with "O" and "X" arranged tapered roller bearings susceptible of customization and/or optimization.

In general, the above papers are focused on the methodological approach to the optimization problem and pay much less attention to the engineering value of the optimization results. If most of the numerical algorithms referenced above can be beneficial to the specialist's work, they are of little use for the general-purpose mechanical designer confronted with the task of designing simple custom bearings. As outcome of an applied research for a small Italian manufacturer of planetary gear drives, the present author has recently published an optimization procedure for radial cylindrical roller bearings [18], which overcomes these limitations. Relying on easy step-by-step calculations and with no need for specific optimization backgrounds, that procedure gives the macro-geometry of the bearing (roller diameter, roller length, pitch diameter of roller set, number of rollers) which maximizes the static and the dynamic load ratings under realistic size constraints.

In the wake of that fruitful effort, this paper tackles the engineering optimization of tapered roller bearings encountered in many industrial applications (see Fig. 1 for a typical instance). The optimization involves the static load capacity of bearing pairs, mounted according to either "O" or "X" arrangements, subjected to a combination of radial and axial forces. Each bearing is defined by the number, diameter and length of the rollers, by the contact angle (cup angle) and by the pitch diameter of the roller set. Following the equations provided by the standard ISO 76 [19], the safety factor of the bearing system is expressed in terms of three parameters: the ratio between roller diameter and pitch diameter, the cup angle and the ratio of axial to radial force. This simple expression gives engineering insight into the problem and shows that for each given load ratio an optimal contact angle exists which maximizes the static load capacity of the bearing, regardless of its actual size and proportions. Tables of optimal contact angles are provided for quick reference.

The optimization method presented here gives its best results for custom-made bearings, for which the design parameters can be varied with the greatest freedom. However, the results disclosed are useful also for identifying the best commercial bearings that can be selected from the manufacturers' catalogues to fit a particular application.

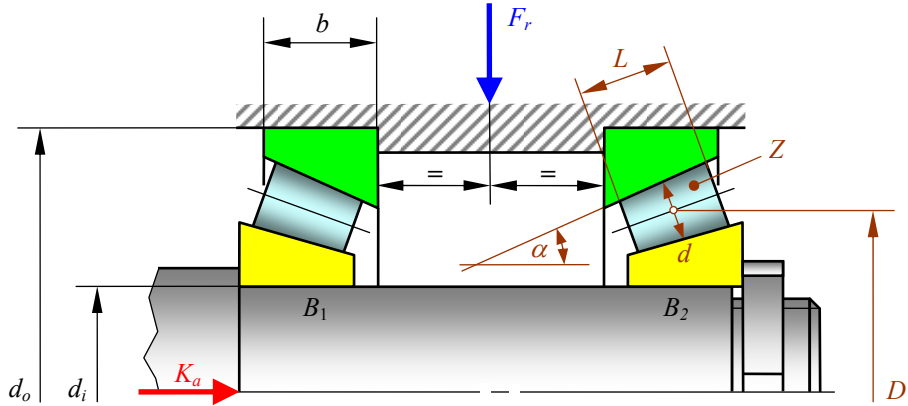


Figure 2. Reference configuration of the bearing system with applied loads and characteristic dimensions of the bearings.

2. PROBLEM STATEMENT

Fig. 2 shows the baseline configuration of the bearing system examined in this paper. The two bearings B_1 and B_2 are assumed to be equal and subjected to the radial force F_r , which is applied at the centre point of the pair. In addition to F_r , an axial thrust K_a also acts on the system through the centre shaft.

Geometrically, each bearing is defined by the following parameters: roller length, L ; mean roller diameter, d (measured at midlength of L); number of rollers, Z ; pitch diameter of the roller set, D ; contact angle, α . The ISO 76 standard [19] specifies that this angle should measure the slope of the raceway without retaining ribs, which is normally the outer one (cup) as shown in Fig. 2. Should the retaining rib be provided by the cup, the contact angle α should refer to the inner raceway (cone).

With reference to Fig. 2, the paper seeks the set of bearing parameters $\{d, D, L, Z, \alpha\}$ which maximizes the static load capacity of the system for given forces K_a and F_r . The search for the optimum will be based on the equations provided by the ISO 76 standard [19]. Although obtained explicitly for the particular bearing combination depicted in Fig. 2 (O arrangement with bearings removed from each other), the optimal solution presented will be applicable also to other combinations such as those shown in Fig. 3 (O and X arrangements with removed or paired bearings).

3. THEORY

Static Radial Load Rating

Subject to the conditions clarified below, the standard ISO 76 [19] gives the following field-tested expression for the static radial load rating, C_0 (N), of tapered roller bearings

$$C_0 = 44 \left(1 - \frac{d}{D} \cos \alpha \right) Z L d \cos \alpha \quad (1)$$

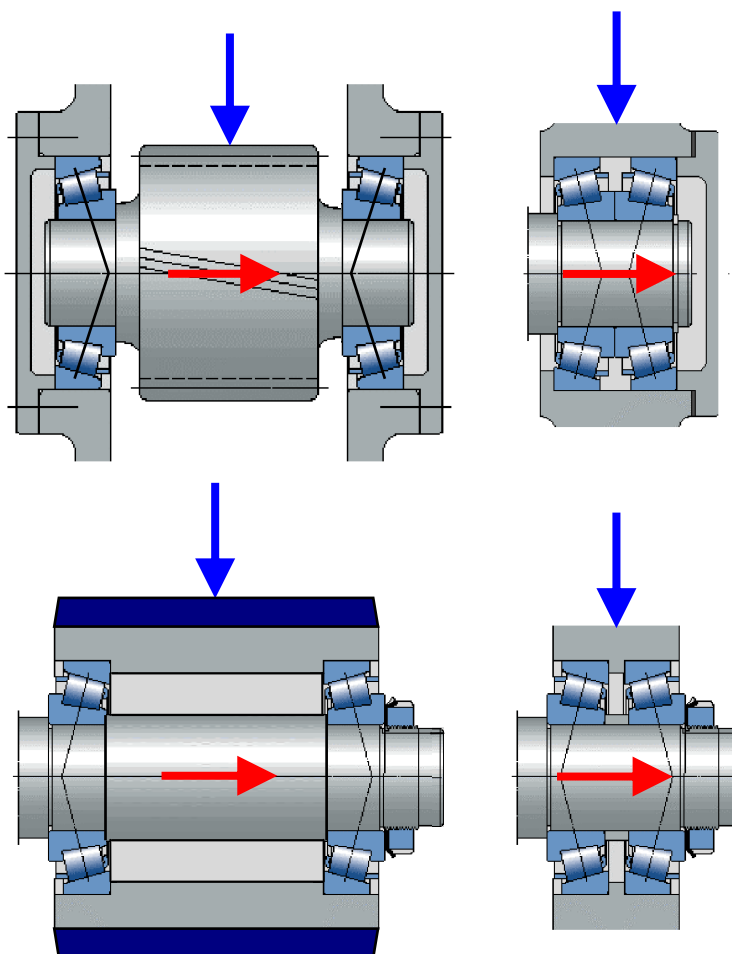


Figure 3. Examples of bearing systems to which the present theory is applicable: X-arrangement (top); O-arrangement (bottom); not paired (left); paired bearings (right).

Equation (1), in which the lengths are expressed in mm, holds true if the bearing is built and installed under the following assumptions: a) use of bearing steels with hardness $HRC \geq 58$; b) manufacture according to regular tolerances [20, 21]; accurate guide of rollers with rounded ends [22]; mounting onto stiff shafts and within rigid housings; working temperature not higher than 150°C . Significant deviations from these reference conditions can be accommodated by applying correction factors available in the literature [23]. Tab. 1 compares the static load ratings predicted by equation (1) with the actual load ratings of a selection of tapered roller bearings retrieved from the catalogue of a leading manufacturer (INA). The internal geometry of the bearings in Tab. 1 (properties from α to Z) were calculated starting from the catalogue properties (from d_i to Y_0) using the method described in Appendix 2.

Table 1. Comparison of predicted and catalogue static load ratings for a selection of commercial tapered roller bearings (INA).

Bearing	Properties from INA catalogue				Derived properties (see Appendix 2)					C_0 (kN)	
	d_i (mm)	d_o (mm)	b (mm)	Y_0 (-)	α (°)	d (mm)	D (mm)	L (mm)	Z (-)	INA	Eq.(1)
30210-A	50	90	17	0.79	15.6	10	70	14.1	20	96	103
30220-A	100	180	29	0.79	15.6	20	140	24.1	20	325	352
30230-A	150	270	38	0.76	16.1	30	210	31.6	20	630	692
30310-A	50	110	23	0.96	12.9	15	80	18.9	15	148	149
30320-A	100	215	39	0.96	12.9	28.75	157.5	32	16	500	519
30330-A	150	320	55	0.96	12.9	42.5	235	45.1	16	1 030	1 084
31310-A	50	110	19	0.4	28.8	15	80	17.3	15	125	126
31320-X	100	215	35	0.4	28.8	28.75	157.5	32	16	480	476
31330-X	150	320	50	0.4	28.8	42.5	235	45.7	16	1 040	1 007
T7FC050	50	105	22	0.38	30.1	13.75	77.5	20.3	16	135	144
T7FC070	70	140	27	0.38	30.1	17.5	105	25	17	237	242
T7FC095	95	180	33	0.38	30.1	21.25	137.5	30.5	19	400	406

By defining the filling ratio of the bearing, ζ , the aspect ratio of the rollers, λ , and the pitch ratio, δ , as follows

$$\zeta = \frac{Zd}{\pi D} \quad (2)$$

$$\lambda = \frac{L}{d} \quad (3)$$

$$\delta = \frac{d}{D} \quad (4)$$

equation (1) becomes

$$C_0 = 44 \pi \zeta \lambda D^2 (1 - \delta \cos \alpha) \delta \cos \alpha \quad (5)$$

Although the theoretical limits for the positive parameters ζ , λ and δ are $\zeta \leq 1$, $\lambda \geq 0$ and $\delta < 1$, in practice the following ranges are generally observed: $0.5 \leq \zeta \leq 1$, $0.5 \leq \lambda \leq 2$ and $\delta \leq 0.2$.

Static Equivalent Radial Load

Let $F_{r1} = 0.5F_r$ be the radial load on each bearing in Fig. 2 and F_a the actual axial load on the most loaded of the two bearings (bearing B_1 in Fig. 2). Following ISO 76 [19], the static equivalent radial load acting on the most loaded roller bearings of the pair is

$$P_0 = \text{MAX}\{F_{r1} ; X_0 F_{r1} + Y_0 F_a\} = \text{MAX}\{0.5F_r ; 0.5X_0 F_r + Y_0 F_a\} \quad (6)$$

where

$$X_0 = 0.5 \quad Y_0 = 0.22 \frac{\cos \alpha}{\sin \alpha} \quad (7)$$

For the loading configuration in Fig. 2 (centre radial load), the maximum axial force F_a is given by the following universally accepted equation [24]

$$F_a = K_a + 0.5 \left(\frac{F_{r1}}{Y} \right) = K_a + 0.25 \frac{F_r}{Y} \quad (8)$$

with [24]

$$Y = 0.4 \frac{\cos \alpha}{\sin \alpha} \quad (9)$$

Using (7)-(9) and introducing the load ratio, k , as

$$k = \frac{K_a}{F_r} \quad (10)$$

equation (6) becomes

$$P_0 = F_r \cdot \text{MAX} \left\{ 0.5 ; 0.25 + 0.22 \left(\frac{\cos \alpha}{\sin \alpha} k + 0.625 \right) \right\} \quad (11)$$

Static Safety Factor

ISO 76 [19] defines the static safety factor, S_0 , as

$$S_0 = \frac{C_0}{P_0} \quad (12)$$

By means of (5) and (11), equation (12) gives

$$S_0 = \frac{\zeta \lambda D^2}{F_r} \cdot \frac{44 \pi (1 - \delta \cos \alpha) \delta \cos \alpha}{\text{MAX} \left\{ 0.5 ; 0.25 + 0.22 \left(\frac{\cos \alpha}{\sin \alpha} k + 0.625 \right) \right\}} \quad (13)$$

which can be written as

$$S_0 = \varphi \cdot s_0 \quad (14)$$

with

$$\varphi = \frac{\zeta \lambda D^2}{F_r} \quad (15)$$

and

$$s_0 = \frac{44 \pi (1 - \delta \cos \alpha) \delta \cos \alpha}{\text{MAX} \left\{ 0.5 ; 0.25 + 0.22 \left(\frac{\cos \alpha}{\sin \alpha} k + 0.625 \right) \right\}} \quad (16)$$

4. OPTIMIZATION

Free Optimization

Equation (14) shows that the static safety factor, S_0 , is proportional to the functions φ and s_0 . From (15) we see that, for given radial load F_r , function φ increases linearly with the filling ratio, ζ , and the aspect ratio, λ , and goes up quadratically with the pitch diameter, D . Function φ can be regarded as a control factor through which the safety factor, S_0 , can easily be made large at will by increasing the pitch diameter.

Function s_0 can be interpreted as an intrinsic safety factor of the bearing system obtained when the filling ratio, the aspect ratio, the pitch diameter and the radial load assume unit value. From (16) we see that s_0 depends non-linearly on α , δ and k as shown by the three-dimensional charts in Fig. 4.

For any given load ratio k , the denominator of (16) achieves the absolute minimum value 0.5 when the following condition is met

$$0.25 + 0.22 \left(\frac{\cos \alpha}{\sin \alpha} k + 0.625 \right) = 0.5 \quad (17)$$

from which the optimum contact angle, α^* is obtained as

$$\tan \alpha^* = \frac{88}{45} k \approx 1.956 k \quad (18)$$

Letting $\xi = \delta \cos \alpha$, the numerator of (16) is maximum when

$$\frac{d}{d\xi} [(1 - \xi) \xi] = 0 \quad (19)$$

giving

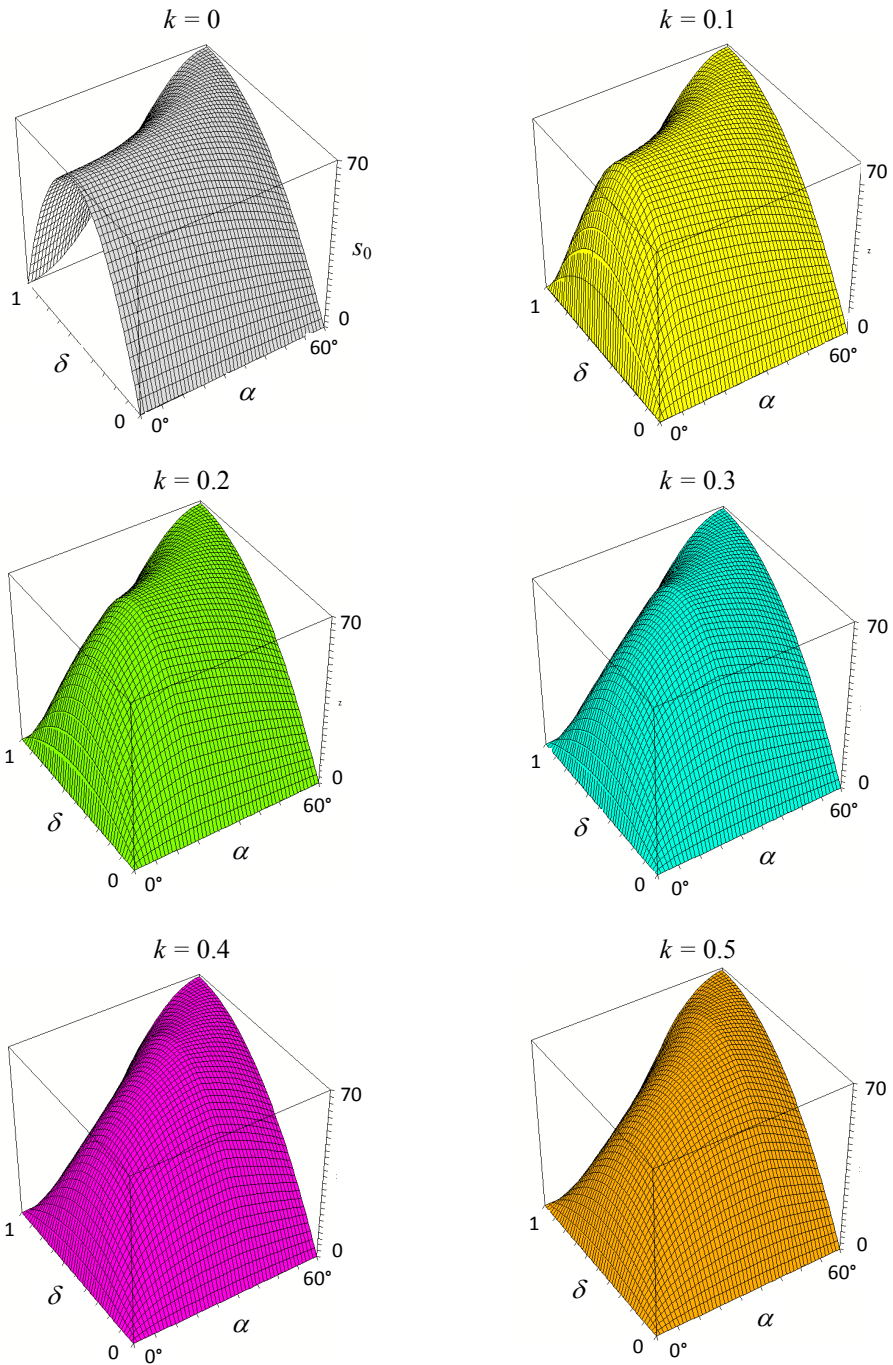


Figure 4. Charts of the intrinsic safety factor s_0 for a selection of load ratios k .

Table 2. Absolute optimum values of contact angle (α^*) and pitch ratio (δ^*) for a range of load ratios (k).

k	$\tan\alpha^*$	α^* (°)	δ^*
0	0	0	0.50
0.1	0.196	11.1	0.51
0.2	0.391	21.4	0.54
0.3	0.587	30.4	0.58
0.4	0.782	38.0	0.64
0.5	0.978	44.4	0.70
0.6	1.173	49.6	0.77
0.7	1.389	53.8	0.85
0.8	1.564	57.4	0.93
0.9	1.760	60.4	1.01
1.0	1.956	62.9	1.10

$$\xi = \delta \cos \alpha = 0.5 \quad (20)$$

Combination of (18) and (20) yields the optimal pitch ratio δ^* as

$$\delta^* = \frac{0.5}{\cos \left\{ \arctan \left(\frac{88}{45} k \right) \right\}} \quad (21)$$

Introducing (18) and (21) into (16) gives the following absolute maximum value, s_0^* , for the intrinsic safety factor

$$s_0^* = 22 \pi \approx 69.115 \quad (22)$$

The optimal contact angles and pitch ratios given by equations (18) and (21) are collected in Tab. 2 for the load ratio k ranging from 0 to 1. Fig. 5 depicts the shape assumed by the optimal bearing for $k=0$, $k=0.3$ and $k=0.6$.

Constrained Optimization

The proportions of the optimal bearings in Fig. 5 are too cumbersome, especially for $k > 0$, to be of practical use. A more fruitful approach is obtained by replotting the diagram of s_0 in Fig. 4 as shown in Fig. 6, in which the contour lines of s_0 are drawn as a function of the contact angle, α , and the pitch ratio, δ . The centre curve mn in Fig. 6 corresponds to the global optimum safety factor $s_0 = s_0^*$ given by equation (22). For any chosen load ratio k , the coordinates of point m in Fig. 6 provide the global optimal values α^* and δ^* listed in Tab. 2.

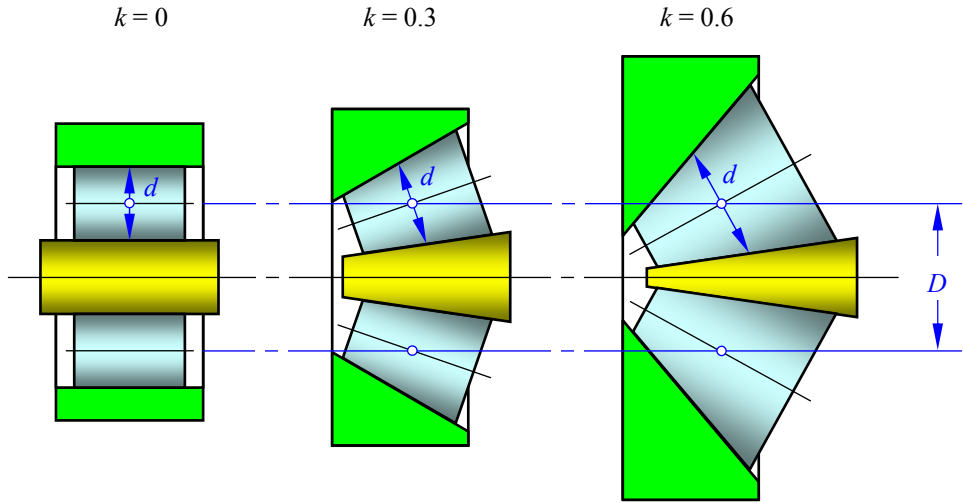


Figure 5. Optimal bearings for different load ratios k and constant pitch diameter D when no limits are put to the pitch ratio $\delta = d/D$.

Table 3. Optimum values of contact angle (α_δ^*) and corresponding intrinsic safety factors ($s_{0\delta}^*$) for given load ratios (k) and limit pitch ratios (δ_{lim}).

k	δ_{lim}									
	0.05		0.1		0.15		0.2		0.25	
	α_δ^* (°)	$s_{0\delta}^*$	α_δ^* (°)	$s_{0\delta}^*$	α_δ^* (°)	$s_{0\delta}^*$	α_δ^* (°)	$s_{0\delta}^*$	α_δ^* (°)	$s_{0\delta}^*$
0	0	13.13	0	24.88	0	35.25	0	44.23	0	51.84
0.1	11.0	12.89	11.0	24.44	11	34.67	11.0	43.56	11.0	51.14
0.2	21.5	12.26	21.5	23.33	21.5	33.20	21.5	41.87	21.5	49.35
0.3	29.5	11.41	30.0	21.79	30.0	31.14	30.0	39.45	30.0	46.73
0.4	32.0	10.62	32.5	20.31	33.0	29.07	34.0	36.91	35.0	43.87
0.5	34.0	9.98	34.5	19.09	35.0	27.36	36.0	34.79	37.0	41.41
0.6	35.5	9.43	36.0	18.06	37.0	25.90	38.0	32.98	39.0	39.31
0.7	37.0	8.95	37.5	17.17	38.5	24.65	39.5	31.41	40.5	37.48
0.8	38.5	8.54	39.0	16.38	39.5	23.54	40.5	30.03	41.5	35.87
0.9	39.5	8.17	40.0	15.68	41.0	22.55	41.5	28.80	42.5	34.43
1.0	40.5	7.84	41.0	15.06	42.0	21.67	42.5	27.69	43.5	33.14

Figure 6 can be used to find the optimal contact angle, α_δ^* , when the pitch ratio, δ , is limited upward. Take, for example the chart in Fig. 6 for $k = 0.4$ and assume $\delta \leq \delta_{lim} = 0.3$ meaning that only the region below line ab is feasible. The greatest value of s_0 that can be achieved in that region is obtained by moving on line ab and sweeping the contact angle from a to b until the optimum point M is reached. Point M is defined as the tangent point between ab itself and whichever contour line occurs to be touching the line ab . The abscissa of point M gives the optimal value α_δ^* for the contact angle ($\alpha_\delta^* \approx 36^\circ$ in this example). The contour line of s_0 passing from M gives the corresponding intrinsic safety factor ($s_{0\delta}^* \approx 50$ in the example).

This constrained optimization can be performed systematically once and for all using equation (16) for any combination of load ratios k and pitch ratios δ . For given k and δ , the intrinsic safety factor s_0 in equation (16) depends only on α and the optimum value α_δ^* is easily found numerically. Optimal values of α_δ^* and $s_{0\delta}^*$ obtained in this way are reported in Tab. 3 for load ratios in the range $0 \leq k \leq 1.0$ and pitch ratios $0.05 \leq \delta \leq 0.25$ (the most likely to occur in practice). Optimal bearings for $\delta_{lim} = 0.2$ are shown in Fig. 7 for $k = 0$ ($\alpha_\delta^* = 0^\circ$), $k = 0.3$ ($\alpha_\delta^* = 30^\circ$) and $k = 0.6$ ($\alpha_\delta^* = 38^\circ$).

The use of Tab. 3 for the optimal design of tapered roller bearings is easily performed as clarified by the following example. Assume that the bearing system in Fig. 2 has to be designed for the loads $F_r = 600\,000$ N and $K_a = 180\,000$ N with a safety factor $S_0 = 1.5$. Calculating from (10) $k = K_a/F_r = 600\,000/180\,000 = 0.3$ and assuming a limit pitch ratio $\delta_{lim} = 0.15$, Tab. 3 gives the optimal contact angle $\alpha_\delta^* = 30^\circ$ and the optimal intrinsic safety factor $s_{0\delta}^* = 31.14$. From equation (14) the value $\varphi_\delta^* = S_0/s_{0\delta}^* = 1.5/31.14 \approx 0.0482$ is calculated, which, adopting a filling ratio $\zeta = 0.8$ and an aspect ratio $\lambda = 1.5$ and using (15), gives $D_\delta^* = (\varphi_\delta^* F_r / \zeta \lambda)^{0.5} = (0.0482 \times 600\,000 / 0.8 \times 1.5)^{0.5} \approx 155$ mm. From (4), (3) and (2), the optimal mean roller diameter, optimal roller length and optimal number of rollers are finally obtained as $d_\delta^* = \delta_{lim} D_\delta^* = 0.15 \times 155 \approx 23.3$ mm, $L_\delta^* = \lambda d_\delta^* = 1.5 \times 23.3 \approx 35$ mm, $Z_\delta^* = \pi \zeta D_\delta^* / d_\delta^* = \pi \times 0.8 \times 155 / 23.3 \approx 17$.

5. DISCUSSION

Table 1 shows that, despite its simplicity, equation (1) predicts quite accurately the static load ratings of commercial tapered roller bearings. Within the wide range of dimensions and contact angles considered, the maximum error in Tab. 1 is less than 10 per cent (bearing 3023-A) while the average absolute error is just above 4 per cent. Errors of the same order of magnitude were calculated by Dragoni [18] for one standard cylindrical roller bearing for which the internal dimensions were known exactly and not simply guessed as in Tab. 1.

For the case of purely radial load ($k = 0$), Tab. 2 gives a global optimum solution with contact angle $\alpha^* = 0$ and pitch ratio $\delta^* = 0.5$, which means cylindrical rollers of diameter, d , equal to one half of the pitch diameter, D . This result coincides with the global optimal proportions reported by Dragoni [18] for the specific category of radial cylindrical roller bearings. For increasing axial loads ($k > 0$), the global optima for the pitch ratio collected in Tab. 2 become more and more unlikely for real-life applications (see Fig. 5).

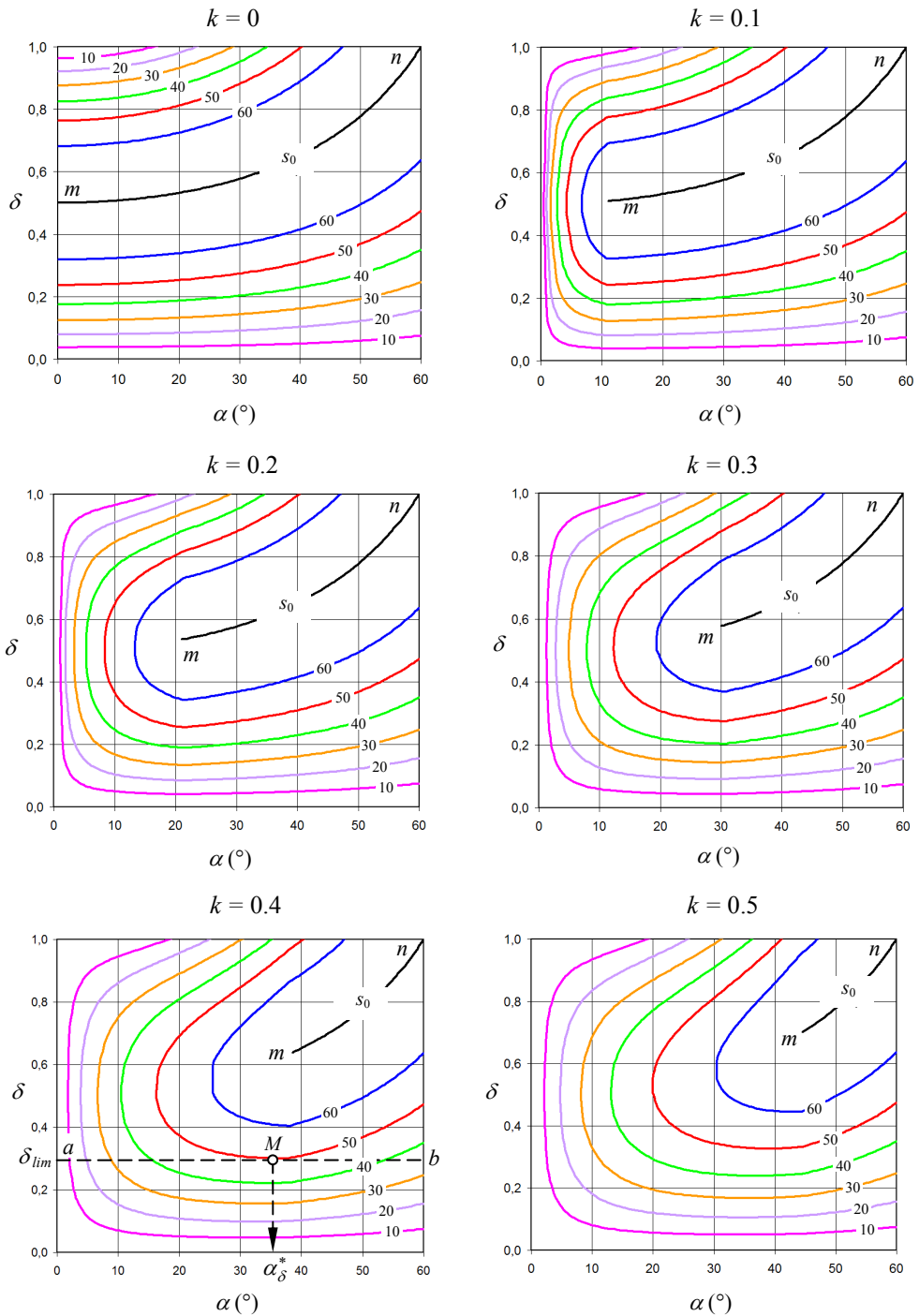


Figure 6. Contour lines of the intrinsic safety factor s_0 for a selection of load ratios k .

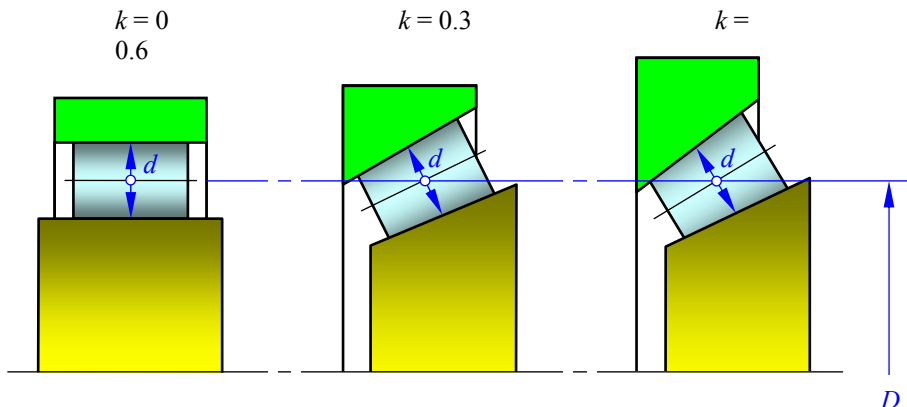


Figure 7. Optimal bearings for different load ratios k and limit pitch ratio $\delta_{lim} = 0.2$.

The reason why the theoretical optimization tends to these quite odd shapes is perhaps imputable to the fact that the empirical expression (1) was developed to fit the experimental behaviour of bearings with pitch ratios much lower than 0.5 as commonly encountered in practice (for example, the pitch ratios of the twelve commercial bearings in Tab. 1 range from 0.14 to 0.19).

Table 3, developed to take into account realistic geometric constraint on δ ($\delta \leq \delta_{lim} = 0.05 \dots 0.25$), shows that the optimum contact angle, α_{δ}^* , depends both on the load ratio, k , and the limit pitch ratio, δ_{lim} . However, while the effect of the load ratio is strong (with α_{δ}^* increasing monotonically with k), the dependence on the pitch ratio is weak (on passing from $\delta_{lim} = 0.05$ to $\delta_{lim} = 0.25$, the maximum relative increase of the optimum contact angle is about 10% and occurs for $k = 0.6$). For $k = 0.3$, the optimal contact angle in Tab. 3 is about 30° , which is the highest contact angle prescribed by the ISO 355 standard [25] and offered by most bearing manufacturers (see Tab. 1). For load ratios greater than 0.3, the optimal contact angle exceeds 30° and reaches the optimum value slightly above 40° for $k = 1$. In this range of operation, special supplies [26] or custom constructions are needed to achieve the maximum load capacity.

Table 3 also shows that the optimal intrinsic safety factor, $s_{0\delta}^*$, rapidly increases with the limit pitch ratio, δ_{lim} , and decreases with the load ratio, k . The increase of $s_{0\delta}^*$ with δ_{lim} is a consequence of the marked gradient of the surfaces of s_0 in Fig. 4 (confirmed by the density of the contour lines in Fig. 6) for pitch ratios in the range $0 \leq \delta \leq 0.5$. The decrease of $s_{0\delta}^*$ with k is due to the fact that, given the radial force F_r in Fig. 2, an increase of the load ratio k implies a greater total force on the bearing system with respect to the condition of pure radial loading.

With reference to the numerical example at the end of the Section *Constrained optimization*, it is easily verified that substituting the design data $F_r = 600$ kN and $k = 0.3$, together with the optimal results $\alpha_{\delta}^* = 30^\circ$, $d_{\delta}^* = 23$ mm, $L_{\delta}^* = 34.5$ mm, $Z_{\delta}^* = 17$ for F_r , k , α , d , L and Z , in equations (11) and (1), gives $P_0 = 300$ kN and $C_0 = 458.8$ kN,

respectively. These values imply a safety factor $S_0 = C_0/P_0 = 458.8/300 \approx 1.53$, slightly greater than the design value of 1.5. This small difference is due to roundoff of the variables involved in the calculations, especially as regards to the optimum number of rollers Z_δ^* (the exact value 16.72 was rounded to 17 in the example).

Spurred by the useful results obtained for the static loading covered in this paper, the next step of the research will focus on the optimization of the bearing system in Fig. 2 for maximum dynamic load-carrying capacity.

6. CONCLUSIONS

Using the empirical relationships provided by the ISO 76 standard, the internal dimensions of tapered roller bearings are optimized for maximum static load capacity. The bearing system investigated comprises two identical bearings undergoing whatever combination of radial and axial forces. Assuming that the radial force is applied at equal distance from the bearings of the pair, the closed-form optimization process leads to the following results:

- the static load capacity increases linearly with the filling ratio (number of rollers divided by the maximum number which can fill the bearing) and the aspect ratio (ratio of roller length to mean roller diameter of rollers) and goes up with the square of the pitch diameter of the roller set;
- given the ratio of axial to radial force, global optima exist for the contact angle and the pitch ratio (ratio of roller diameter to pitch diameter) which maximize the static load capacity;
- the bearing proportions at the global optima are too sturdy (contact angles greater than 60 degrees, pitch ratios equal to or greater than 0.5) to be used in practice;
- if the pitch ratio is constrained to stay below reasonable limits (≤ 0.25), an optimal contact angle exists which maximizes the static load capacity, regardless of the actual size and proportions of the bearing;
- the results of the optimization are conveniently summarized by a general table and a few simple equations that can be followed step-by-step to design the optimal bearing that suits any given application;
- the design procedure can either be used to design custom-made bearings (where the geometrical freedom can be exploited to the full) or to identify the best bearing from the manufactures' catalogues.

REFERENCES

- [1] Seireg, A., 1972. "A survey of optimisation of mechanical design". *J Eng Ind T ASME*, **94**(2), pp. 495–499.
- [2] Seireg, A.A., and Rodriguez J., 1997. *Optimizing the shape of mechanical elements and structures*. Cleveland, OH: CRC Press.
- [3] Ahluwalia, J., Gupta, S.K., and Agrawal, V.P., 1993. "Computer-aided optimum selection of roller bearings". *Computer-Aided Design*, **25**(8), pp. 493–499.
- [4] Aramaki, H., 1997. "Rolling Bearing Analysis Program Package 'BRAIN' ". *NSK Technical Journal Motion & Control*, no. 3, pp.15–24.

- [5] Choi, D-H., and Yoon K-C., 2001. "A Design Method of an Automotive Wheel-Bearing Unit With Discrete Design Variables Using Genetic Algorithms". *J Tribol T ASME*, **123**(1), pp. 181–187.
- [6] Kalita, K., Tiwari, R., and Kakoty, S.K., 2002. "Multi-objective optimisation in rolling element bearing system design". In *Proceedings of the Int. Conf. on Optimisation (SIGOPT 2002)*, Lambrecht, Germany, 17–22 February.
- [7] Chakraborty, I., Kumar, V., Nair, S.B., and Tiwari, R., 2003. "Rolling element bearing design through genetic algorithms". *Eng Optimiz.* **35**(6), pp. 649–659.
- [8] Rao, B.R., and Tiwari, R., 2007. "Optimum design of rolling element bearings using genetic algorithms". *Mech Mach Theory*, **42**(2), pp. 233–250.
- [9] Gupta, S., Tiwari, R., and Nair, S.B., 2007. "Multi-objective design optimisation of rolling bearings using genetic algorithms". *Mech Mach Theory*, **42**(10), pp. 1418–1443.
- [10] Savsani, V., Rao, R.V., and Vakharia, D.P., 2008. "Multi-objective design optimization of ball bearings using a modified particle swarm optimization technique". *Int J Des Eng*, **1**(4), pp. 412–433.
- [11] Wei, Y. and Chengzu, R., 2010. "Optimal design of high speed angular contact ball bearing using a multiobjective evolution algorithm". In *Proceedings of the IEEE Int. Conf. on Computing, Control and Industrial Engineering (CCIE 2010)*, Wuhan, China, 5–6 June.
- [12] Kumar, K.S., Tiwari, R., and Reddy, R.S., 2008. "Development of an optimum design methodology of cylindrical roller bearings using genetic algorithms". *Int J Comput Meth Eng Sci Mech*, **9**(6), pp. 321–341.
- [13] Kumar, K.S., Tiwari, R., and Prasad, V.V.N., 2009. "An Optimum Design of Crowned Cylindrical Roller Bearings Using Genetic Algorithms". *J Mech Des T ASME*, **131**(5), pp. 051011-1– 051011-14.
- [14] Parker, R.J., Pintel, S.I., and Signer, H.R., 1981. "Performance of Computer-Optimized Tapered-Roller Bearings to 2.4 Million DN". *J Tribol T ASME*, **103**(1), pp. 13– 20.
- [15] Chaturbhuj, N., Nair, S.B., and Tiwari, R., 2003. "Design optimization for tapered roller bearings using genetic algorithms". In *Proc. of the Int. Conf. on Artificial Intelligence (IC-AI 03 2003)*, Las Vegas, Nevada, 23–26 June, pp. 421–427. Volume 1, CSREA Press, ISBN 1-932415-12-2.
- [16] Walker, B., 2008. "High Speed Tapered Roller Bearing Optimization". *MS Thesis*, Rensselaer Polytechnic Institute, Hartford, Connecticut, April.
- [17] Wang, Z., Meng, L., Wensi, H., and Zhang, E., 2011. "Optimal Design of Parameters for Four Column Tapered Roller Bearing". *Appl Mech and Mater*, **63-64**(-), pp. 201– 204.
- [18] Dragoni, E., 2013 "Optimal design of radial cylindrical roller bearings for maximum load-carrying capacity". *Proc IMechE, Part C: J Mech Eng Sci*, **227**(11), pp. 2393–2401.
- [19] ISO 76, 2006. *Rolling bearings – Static load ratings*.
- [20] Wiesner, H., 2012. "Rolling bearings TC4 meets GPS TC213". *Evolution*, **19**(3), pp. 24–28.
- [21] ISO 492, 2002. *Rolling bearings – Radial bearings – Tolerances*.
- [22] Johnson, K.L., 1985. *Contact Mechanics*. Cambridge, UK: Cambridge University Press.
- [23] Harris, T.A., 2000. *Rolling Bearing Analysis*. 4th ed. New York: John Wiley & Sons.

- [24] Niemann, G., Winter, H., and Höhn B-R., 2005. *Maschinenelemente*. Vol. I Berlin, Germany: Springer.
- [25] ISO 355, 2007. *Rolling bearings – Tapered roller bearings – Boundary dimensions and series designations*.
- [26] TIMKEN, 2013. *Tapered Roller Bearing Catalogue*, <http://catalog.timken.com/WebProject.asp?CodeId=7.5.9.17&BookCode=trb12flx#> (access date 8/12/2013).
- [27] Niemann, G., 1981. *Maschinenelemente*. Vol. I Berlin, Germany: Springer.

APPENDIX I

Notation

b	Width of outer ring of bearing
C_0	Static radial load rating of the bearing
d	Roller diameter (measured at midlength of roller)
d_i	Inside diameter of bearing
d_o	Outside diameter of bearing
d_δ^*	Optimum value of d for $\delta \leq \delta_{lim}$
D	Pitch diameter of the roller set
D_δ^*	Optimum value of D for $\delta \leq \delta_{lim}$
F_a	Axial load acting on the most loaded bearing of the pair
F_r	External radial load applied to the bearing pair
F_{r1}	Radial load acting on each bearing of the pair ($= 0.5 F_r$)
k	Ratio of radial to axial external loads ($= K_a / F_r$)
K_a	External axial load applied to the bearing pair
L	Roller length
L_δ^*	Optimum value of L for $\delta \leq \delta_{lim}$
P_0	Static equivalent radial load acting on the most loaded bearing of the pair
S_0	Static safety factor of the bearing pair
s_0	Intrinsic static safety factor of the bearing pair
s_0^*	Global optimum of s_0
$s_{0\delta}^*$	Optimum value of s_0^* for $\delta \leq \delta_{lim}$

X_0, Y_0, Y	Load coefficients of the bearing
Z	Number of rollers
Z_δ^*	Optimum value of Z for $\delta \leq \delta_{lim}$
α	Contact angle of bearing
α^*	Global optimum of α
α_δ^*	Optimum value of α for $\delta \leq \delta_{lim}$
δ	Pitch ratio of bearing ($= d/D$)
δ^*	Global optimum of δ
ζ	Filling ratio of the roller set ($= Z d / \pi D$)
λ	Aspect ratio of the rollers ($= L/D$)
ξ	Auxiliary variable ($= \delta \cos \alpha$)
φ	Component of the static safety factor ($= \zeta \lambda D^2 / F_r$)
φ_δ^*	Optimum value of φ for $\delta \leq \delta_{lim}$

Table 4. Relationships between catalogue data (Y_0, d_i, d_o, b) and internal bearing properties (α, d, D, L, Z).

Internal property	Relationship	Numerical values	Source
α	$= \arctan\left(\frac{0.22}{Y_0}\right)$	–	Equation (7)
d	$= q_1(d_o - d_i)$	$q_1 = 0.25$	Textbook [27]
D	$= q_2(d_o + d_i)$	$q_2 = 0.5$	Assumption
L	$= q_3 \frac{b}{\cos \alpha}$	$q_3 = 0.8$	Assumption
Z	$= q_4 \frac{(d_o + d_i)}{d}$	$q_4 = 1.45$	Textbook [27]

APPENDIX 2

Internal Dimensions of Tapered Roller Bearings

The internal dimensions of the bearings, and the roller bearings are no exception, are proprietary data which the manufacturers do not provided in their catalogues. However, starting from the external dimensions of the bearings (d_i , d_o , b in Fig. 1) and the static coefficient, Y_0 , available from the catalogues, the internal properties (α , d , D , L , Z in Fig. 1) can be derived with acceptable precision. Tab. 4 shows how the internal properties displayed in Tab. 1 were obtained step-by-step from the catalogue data using elementary geometry, reasonable assumptions or capitalizing on characteristic proportions available from technical textbooks [27].

OPTIMIZATION METHODOLOGY FOR AN AUTOMOTIVE COMPOSITE HOOD

Antonio Strozzi

*Dipartimento di Ingegneria “Enzo Ferrari”
Università di Modena e Reggio Emilia, Italia
E-mail: antonio.strozzi@unimore.it*

Andrea Baldini

*Dipartimento di Ingegneria “Enzo Ferrari”
Università di Modena e Reggio Emilia, Italia
E-mail: andrea.baldini@unimore.it*

Matteo Giacomini

*Dipartimento di Ingegneria “Enzo Ferrari”
Università di Modena e Reggio Emilia, Italia
E-mail: matteo.giacomini@unimore.it*

Alberto Lazzarini

*Dipartimento di Ingegneria “Enzo Ferrari”
Università di Modena e Reggio Emilia, Italia
E-mail: alberto.lazzarini@unimore.it*

Alessandro Valgimigli

*Dipartimento di Ingegneria “Enzo Ferrari”
Università di Modena e Reggio Emilia, Italia
E-mail: alessandro.valgimigli@unimore.it*

Abstract. *The current emissions regulations lead car manufacturers to look carefully for weight reduction. In the automotive industry the classic trial-and-error approach to design is becoming inadequate and techniques based on optimization are necessary to improve the design process. In this study a methodology to design a sport-car front hood is proposed. The process carried out could also be extended to car components characterised by a similar configuration. Starting from the geometry of the actual part, a design volume has been defined. The first step consists of a topology optimization performed considering the material as isotropic (aluminium properties): the output is a rough structure which accomplishes all the imposed targets. The interpretation of the topology results brings to a re-design phase aimed at realising a feasible component.*

The subsequent optimization step is dedicated to composite material structures and acts on the component plybook, varying thickness and orientation of each ply to find the best solution complying with targets. Finally, the component has to be reviewed from a technological point of view in order to be virtually delivered and to proceed with the prototype phase.

Keywords: *optimization, composite, automotive, hood.*

1. INTRODUCTION

Nowadays, the need of respecting stringent regulations in terms of emissions for homologation is becoming more challenging for car manufacturers.

Fuel consumption reduction should be pursued: even though it appears an atypical goal for sport cars, it can lead to lower pollutant emissions and lower difficulties in reaching the homologation constraints. As shown in [1], a reduction in fuel consumption can be obtained both by acting on propulsion systems or fuel, and reducing global weight of the vehicle. Speaking about the propulsion system, new components and strategies are introduced to contain emissions. According to [2], slightly modified conventional gasoline vehicles by the introduction of start & stop system or regenerative breaking, may be an effective and inexpensive way to reduce fuel consumption and emissions. For what concerns fuel, automotive industry is looking for different and more ecological solutions like biodiesel or completely new approaches, such as hydrogenatural gas mixtures, as explained in [3].

Light-weight design could represent a different way of facing the problem: according to [4], vehicle mass is crucial for emissions. A lighter car, in fact, will have a lower fuel consumption and reduced emissions. Anyway, vehicle mass reduction, as objected by [5], could affect the safety performance in crash tests negatively. In fact, for this specific case study, crash behaviour has been taken into account during the design process of the component.

In view of weight reduction, design of composite materials structures has developed significantly because of the easily obtainable high stiffness-to-weight ratio. For automotive components in composite material, the classic trial-and-error design procedure is becoming inadequate. In this paper we describe a new methodology based on structural optimization processes applied to a specific case: a sport-car front hood. This approach could be dedicated to other car parts with a similar structure.

Mono-objective optimization processes were performed in order to achieve the main target of weight reduction, aiming also at respecting stiffness performance.

2. OPTIMIZATION PROCESSES

A typical optimization problem can be written in the form:

$$\min f(x), \quad x \in D \tag{1}$$

subject to optimization constraints $c(x) \geq 0$.

x is the vector of the optimization parameters, D the design space or domain, f the objective function, c the set of optimization constraints.

In order to set up an optimization process, the following needs to be defined:

1. the domain D of optimization (i.e. the Finite Element (FE) mesh of the object to be optimized, suitably subdivided into designable and non-designable areas);
2. the objective of optimization, to minimize the function $f(x)$;
3. the performance targets the component must satisfy (given in the form of optimization constraints $c(x)$), together with the loading conditions needed for computing the targets.

In this study, a design process based on different types of structural optimization is presented. The optimization techniques, which are provided by the Altair Engineering software Optistruct, could act sequentially or in loop.

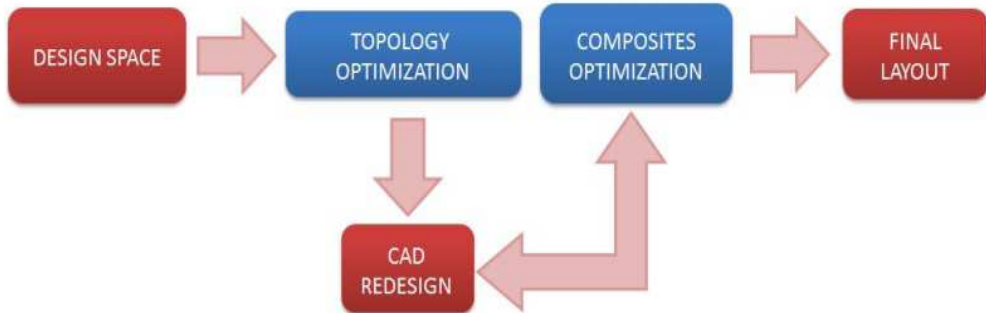


Figure 1. Design flow of the hood inner panel. It is possible to generate a loop with different type of optimization and CAD re-draw, the reviewed output of the last composite optimization is the final model. This model has to be verified for final validation.

Topology optimization purpose is to find the optimum structural mass distribution in a domain. The theory of topology optimization is laid down in the work of Bendsøe and Sigmund [6-8]. In topology optimization it is assumed that the material density of the structure can vary with continuity, and that mechanical properties of the material change accordingly with the density. The input variables of the optimization problem are given by the vector of density fractions of finite elements. A gradient descent optimization method is applied iteratively gradually defining the optimum material distribution.

Another optimization instrument applied to the component in this design process is related to composite material optimization. Two subsequent and strongly dependent steps were implemented in order to find a preliminary stacking sequence for the front hood.

The first phase of the composite optimization is called “Free-size”. Assuming a given basic stacking sequence, the purpose of composite free-sizing optimization is to change the total laminate thickness continuously throughout the structure, by varying the thickness of each ply with a particular fibre orientation for every finite element.

In OptiStruct, manufacturing constraints can be defined since free-sizing optimization and respected in later steps. Certain manufacturing requirements are necessary and influenced by material properties and chosen technology processes. For example, one typical constraint for carbon fibre reinforced composites is that plies of a given orientation cannot be stacked successively for more than 3 or 4 plies. In addition, balancing of a couple of ply orientations could be useful to eliminate twisting of a plate under bending load. Moreover, imposing constant thickness of a single ply (“manufacturing thickness”) has been necessary in order to achieve a higher level of feasibility. The standard result from a free-sizing optimization is thickness contribution of each orientation. Multiple ply shapes with the optimum thickness value per orientation can be generated from a free-sizing optimization.

In the second step, defined as “Size” optimization, thickness of each orientation is determined as a discrete multiple value of the “manufacturing thickness”.

The complete OptiStruct procedure includes also the third phase, called “Shuffle” optimization, which changes the order of plies in the laminate. In our methodology this step was not implemented, because the best sequence was decided in terms of technological constraints, addressed during the last design phase.

3. DESIGN METHODOLOGY

Topology optimization

At first, we set the FE model for the topology optimization step, carrying over some components from the aluminium former version of the hood. In particular, hinges and hood latch were not changed and joined to the hood with rigid elements (RBE2).

The outside panel (Fig. (2)) has been designed with a new configuration for what concerns air inlets and outlets and was meshed with 2D elements (mainly QUAD4). This component has a basic stacking sequence of carbon fibre cloths plies.

The outside panel was connected with a layer of structural adhesive (HEX8) to the under hood volume (TETRA4), as you can see in Fig. (3). This part, together with the adhesive layer, represents the domain of the optimization and is defined by a surface comprehensive of the engine cover and other under hood components. Aluminium, as an isotropic material, was chosen for the under hood volume domain. This is a reasonable approach for topology optimization because it has comparable stiffness properties to the other orthotropic materials and the main goal of this step is to find a rough frame structure. The glue was introduced to evaluate the importance of the link between domain and outer panel.

The definition of the objective of the optimization reflects the main goal of this methodology: minimizing the total mass of the hood.

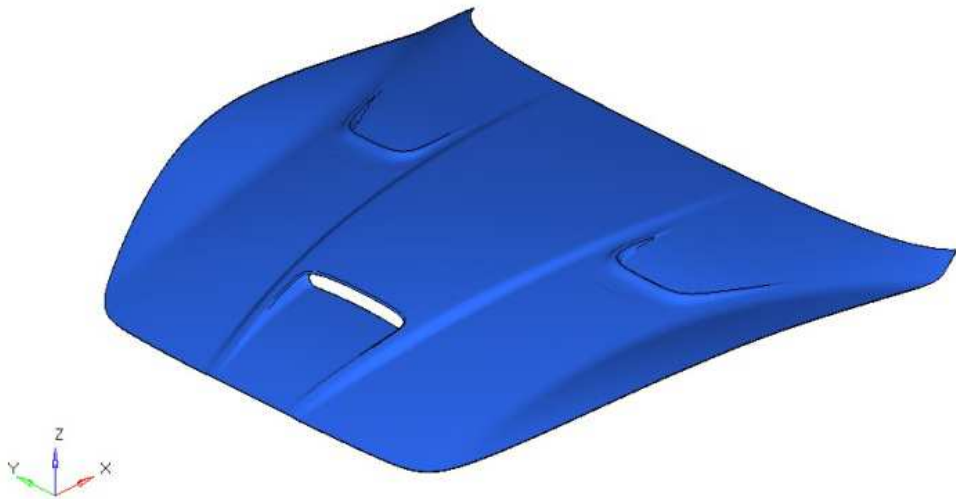


Figure 2. Hood outer panel.

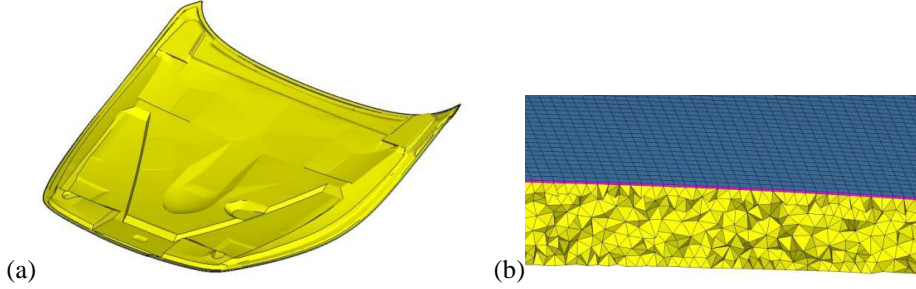


Figure 3. (a) Under hood design volume; (b) Detail of FE model: yellow elements - design volume (TETRA4), pink elements - adhesive layer (HEX8), blue elements - outer panel (QUAD4).

The optimization constraints, adopting a simple modus operandi, are represented by the performance targets required for this component:

1. Torsional stiffness:

$$K_t = \frac{M_t}{\theta} \quad (2)$$

where M_t is given by a force F applied at a certain lever arm b from the constrained front point and θ is the relative rotation angle between the front loaded cross section and the constrained one at the rear part of the hood.

2. Bending stiffness:

$$K_b = \frac{F}{\delta} \quad (3)$$

where F is the sum of the two forces applied at left and right side of the hood and δ is the average displacement of monitored loaded nodes.

3. Hood supports stiffness:

$$K_{hs} = \frac{P}{\delta_{Hs}} \quad (4)$$

where P is the force applied at the support of the hood and δ_{Hs} is the displacement of monitored loaded node.

4. Local deformation of the outer panel: δ_{def_i}

where δ_{def_i} refers to the magnitude of displacement vectors of different loaded nodes on the outer panel (6 areas from internal regulations).

5. Aerodynamic deflection: δ_{aero_i}

where δ_{aero_i} are the Z-displacement of 12 nodes of monitored areas on the outer panel (Fig. (4)).

In the optimization setup these constraints were assigned to the model as maximum displacements of monitored mesh nodes. From 1 to 4, targets are evaluated through load cases which are representative of experimental validations set in accordance with car manufacturer internal regulation. A slightly different approach was followed for aerodynamic performance, represented by the deformation of the hood evaluated at areas in Fig. (4). In the topology phase, 6 nodes per side in those areas were monitored.

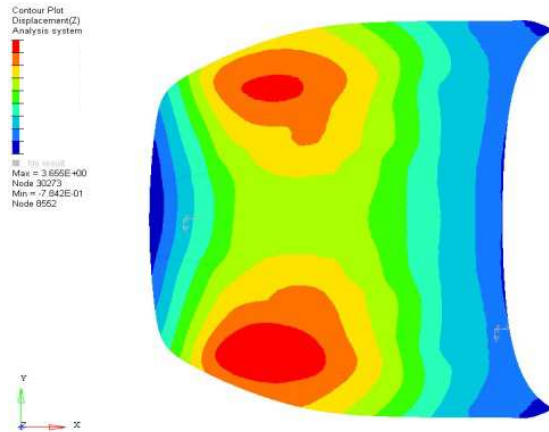


Figure 4. Z-displacement contour and monitored areas - aerodynamic load case (on aluminium hood).

The load case consists of a pressure distribution applied to the outer panel and the hood is constrained as in working conditions. The pressure distribution was already determined by a CFD analysis involving the whole car model at a certain critical speed performed by the car manufacturer. The comparison of FE structural analysis with the real case will be obtained performing track test measurements.

The topology process led to a distribution of density that clearly outlines a frame structure (Fig. (5)).

In Fig. (5a) the outer panel and elements of the domain with a value of normalized density greater than 0.1 are displayed. As you can see in Fig. (5b), areas of connection between the outer panel and the domain are spread in different position along the frame lines. With a distribution of higher density elements far from the outer panel, the solver tried to maximize the moment of inertia of the reinforcing structure.

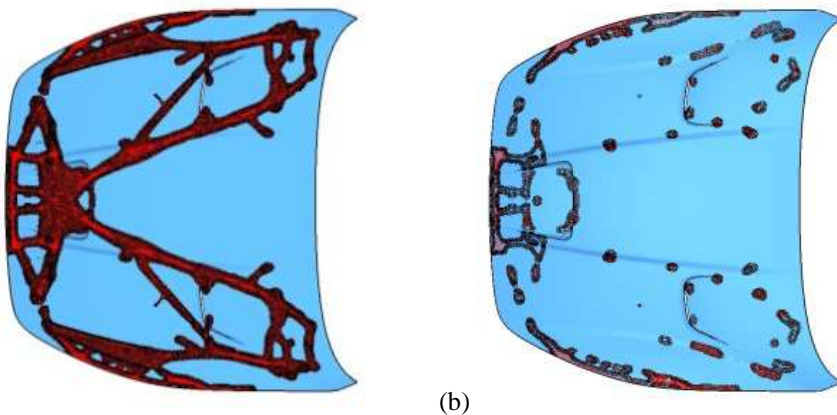


Figure 5. Topology results – elements with normalised density greater than 0.1. (a) inner panel structure; (b) connection areas between outer and inner panel.

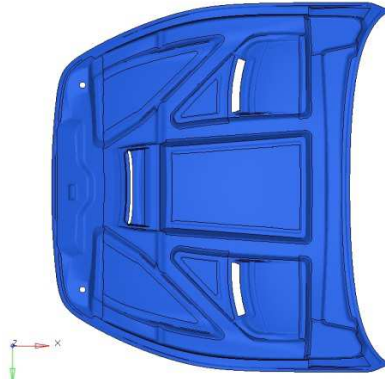


Figure 6. Redesigned hood inner panel.

CAD redesign phase

To begin the CAD reinterpretation phase, some considerations need to be done. For the optimized inner reinforcement frame, cross-sections of truss-like structures, typical of topology optimization results, were redesigned as thin-walled cross-sections. This choice was done in order to obtain more performing sections in terms of inertia-to-mass ratio. Moreover, this shape of the inner panel is in concordance with technologic guidelines.

As it is noticeable from Fig. (6), the geometry of the optimized component includes triggers in Y direction in view of front crash validation tests to be achieved for the whole car. Furthermore, Z-dimension of ribs was maximized in respect of under hood volume, while X and Y dimensions in some cases were limited by other car components. The inner panel displays plates with lower inertia-to-mass ratio to connect ribs. This decision was influenced more by compelling aesthetic requirements than by efficiency aspects.

The initial configuration shows a distribution of adhesive (Fig. (7)) which creates thin-walled closed-section beams between outer and inner panel ribs. In particular, the outer edges of the two panels are connected through a continuous line of structural epoxy adhesive. Central bonding is obtained with non-structural epoxy adhesive, positioned along separate lines, pursuing the main purpose of these connections, as explained before.

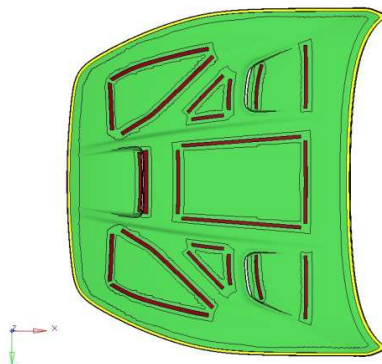


Figure 7. Adhesive bonding lines – view from the outer panel.

Composite material optimization

The next step of the design methodology was composite material optimization process, formed, as previously explained, by two subsequent and strongly related steps. This instrument could become part of a loop with geometric modifications to improve the design of the model: through the combination of these phases is possible, for example, to increase performance which have not been achieved yet or to reduce the mass if all the targets are fulfilled.

At first, the FE model for this optimization phase was implemented, starting from the former one set for the topology optimization. Outer panel, hinges and hood latch were not changed, while the redesigned inner panel was meshed with 2D elements (mainly QUAD4). Carbon fibre materials had an orthotropic material property card (MAT8) and composite stacking sequence were defined with a PCOMP property card, specifying material, thickness and orientation for each layer. These material properties were correlated with those from supplier datasheets in a previous activity. The adhesive was modelled with 3D elements (HEX8). Optimization constraints, at first, were represented by performance targets described before and the optimization goal was mass reduction. The domain incorporated both the outer panel and the inner one.

As discussed before, the composite material optimization process started with “free size” optimization. Two manufacturing requirements were imposed: thickness value of a single ply of each orientation package (manufacturing thickness) and constant thickness value (it cannot vary during optimization) of two and three plies respectively for inner and outer panel. These settings were introduced to reach a higher level of feasibility at this stage and to establish basic restraints received from the manufacturer. As in Fig. (8), various ply shapes with the optimum thickness value per orientation were created.

At the second step of the composite optimization process, “Size” optimization, each orientation package was converted into multiple plies characterised by the manufacturing thickness value. Final results of optimization constrained displacements (Tab. (1)) show that the optimized model achieves all the targets mentioned speaking about optimization constraints, with a mass reduction of 16.8%.

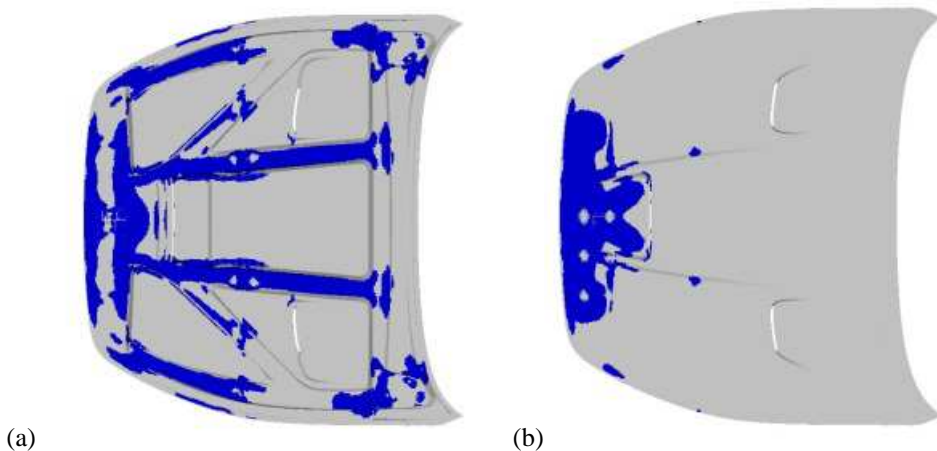


Figure 8. Composite optimization results – example of ply shapes. (a) a layer on the inner panel; (b) a layer on the outer panel.

Table 1. Results of composite material optimization process in terms of displacements referred to monitored nodes for load cases of torsion, bending, hood support stiffness, local deformation, aerodynamic deflection.

OPTIMIZATION CONSTRAINED VALUE	DELTA (from target)	OPTIMIZATION CONSTRAINED VALUE	DELTA (from target)
θ (torsion)	6%	δ_{aero_3}	1%
δ (bending)	1%	δ_{aero_4}	1%
δ_{Hs}	36%	δ_{aero_5}	28%
δ_{def_1}	2%	δ_{aero_6}	28%
δ_{def_2}	0%	δ_{aero_7}	2%
δ_{def_3}	7%	δ_{aero_8}	28%
δ_{def_4}	23%	δ_{aero_9}	2%
δ_{def_5}	3%	δ_{aero_10}	29%
δ_{def_6}	17%	δ_{aero_11}	1%
δ_{aero_1}	27%	δ_{aero_12}	27%
δ_{aero_2}	2%		

It can be noticed from Fig. (9) how the solver distributed total thickness on outer and inner panel.

For what concerns outer panel, the front area is much thicker than others. This is due to local deformation load case, which acts on 6 points positioned in this area, as prescribed by internal regulations. Experience with aluminium model demonstrates that FE representation of this test is quite more unfavourable than the real test. Consequently, this kind of result were not taken into account in the later phase of definition of final hood stacking sequence and layout. The whole outer panel was reinforced following manufacturer's know-how in order to achieve the local deformation experimental test.

Dealing with inner panel, results in terms of thickness and orientation clearly suggested which areas needed to be reinforced. These results were less influenced by a single load case and could be considered during stacking sequence definition.

Composite material optimization final results can be interpreted in two different ways. On one hand, it is possible to reinforce the component laminate in those areas characterised by increasing the number of plies with proper fibre orientation; on the other hand, geometric modifications with unchanged stacking sequence can be also effective. This choice had to be done evaluating each solution in terms of efficiency (stiffness-to-mass ratio) and feasibility. Referring to our methodology, choosing to redesign the geometry at this stage would mean to activate a loop between composite material optimization and CAD redesign. In this case, trying to modify inner panel shape was not possible, because the available volume was already employed during the previous design phase

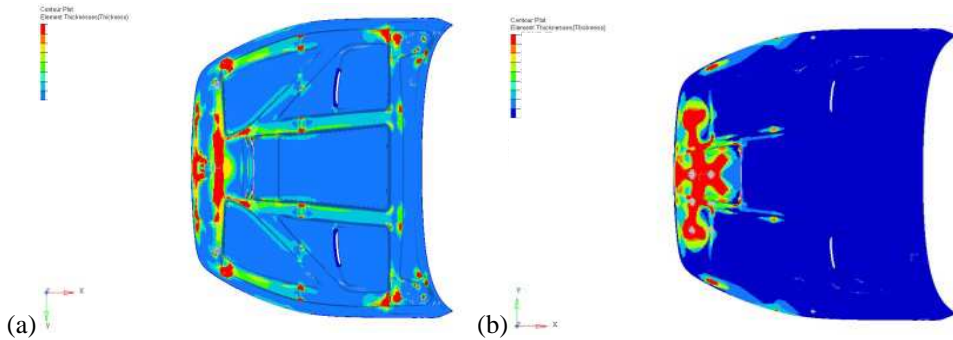


Figure 9. Composite optimization results – Total thickness. (a) inner panel; (b) outer panel.

Final layout

Once frozen the geometry of the inner panel, interaction with the hood manufacturer became much more intense to define technology requirements and try to match performance reached by the optimized model. A first configuration was designed, and in Fig. (10) it is possible to see a map of different stacking sequence areas.

In correspondence of adhesive bonding (both structural and non-structural) additional carbon fibre plies are required to stiffen those areas in order to avoid imprint on composite laminate during the autoclave curing process. Two carbon fibre clothes were introduced on the inner panel in correspondence of non-structural adhesive, one for structural adhesive. These patches were extended over ribs to follow the optimization thickness distribution, which shows higher values especially in these regions to create a link between hinges and hood latch.

In the front area, where hood latch and lateral supports are positioned, the stacking sequence displays four extra plies of carbon fibre cloth. The orientation of these plies was deduced from the results of composite material optimization.

Also steel plates for hood hinges need to be fixed at a stiffer carbon fibre structure, so two extra plies of carbon fibre cloth were introduced.

This first layout FE model is characterised by a weight reduction of 25%, showing higher torsional and bending stiffness (33% and 22% respectively) than aluminium hood. Optimization initial targets were acceptably decreased to aluminium hood reference values, in order to achieve a more consistent mass reduction with composite material configuration. Aerodynamic deflection is about 40% less than aluminium case. Hood supports stiffness is comparable to the reference model case.

At this stage a technological review started together with the prototype phase. Moreover, this was a crucial point because the methodology can be evaluated through the real case scenario.

From this step, only torsional and bending stiffness became performance parameters. In fact, aerodynamic load case seemed implicitly related to pure bending behaviour and areas involved in hinges stiffness could not be modified anymore; experimental tests will be carried on to validate the actual component for these targets.

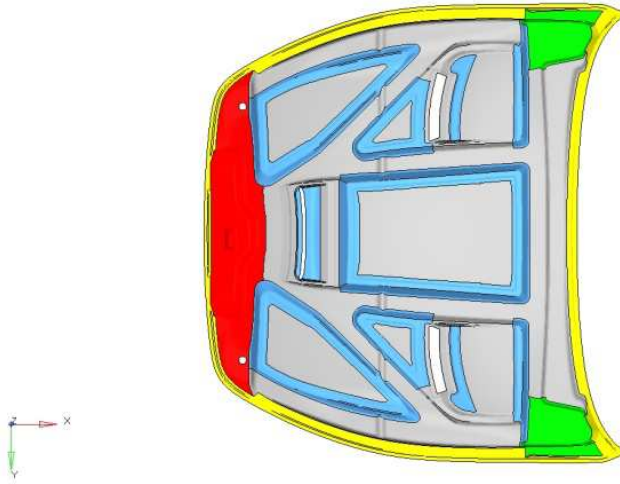


Figure 10. First layout of the inner panel.

The final configuration obtained from the design process was quite modified in view of additional hood manufacturer technology issues. In particular, adhesive bonding layout changed: autoclave cured components could be badly affected by too long and too close adhesive lines. As a result, some glue connections were suppressed and consequently reinforced stacking sequences were reduced both on inner and outer panel (Fig. (11)).

A FE analysis was carried on to obtain performance results of this new layout. This model shows a weight reduction of 27%, achieving higher torsional and bending stiffness (32% and 3% respectively) than aluminium hood. Furthermore, as noticeable from Fig. (11), triggers on the inner panel were positioned closer to the front central air inlet, because of preliminary front crash simulation results.

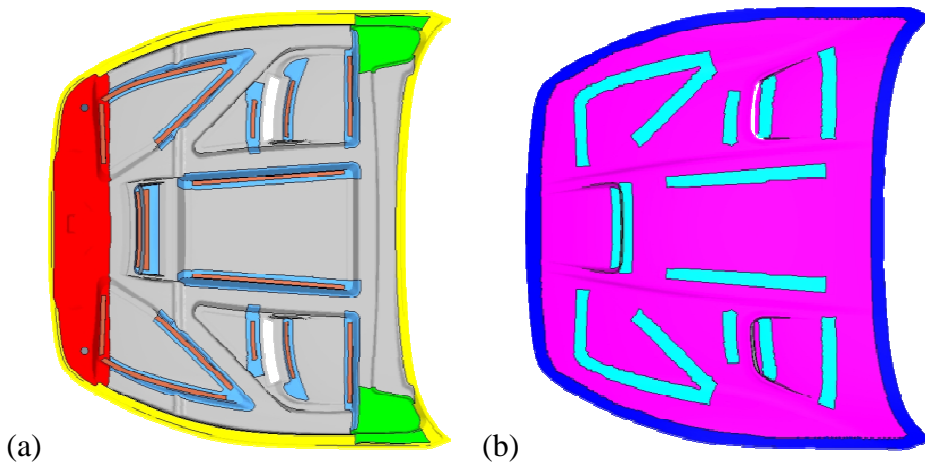


Figure 11. Prototype 1 layout - (a) inner panel; (b) outer panel.



Figure 12. Prototype 1 in painting room.

This solution represents a compromise between static and dynamic performance: it solves an unacceptable crash behaviour, although it significantly reduces bending stiffness. The first realised prototype is characterised by this configuration and was tested by the car manufacturer as imposed by internal regulations. Correlation gap between aluminium hood numerical model and experimental case is about 3%.

Mass comparison shows that prototype 1 FE model is about 20% lighter than the actual hood; this discrepancy is due to resin excess, to non-modelled composite material details and to a protective paint layer. The mass of tested real prototype 1 (Fig. (12)) is anyway 23% less than real aluminium hood.

The first prototype displayed some local aesthetic problems, due to non-structural adhesive lines. As a result, the manufacturer has decided to “break” adhesive bonding into several equidistant gluing points (Fig. (13)). Trying to balance a probable decrease of stiffness, gluing points were extended to other areas (around ribs, similarly to the initial layout) and reinforced stacking sequences dimensions on the outer panel were increased (Fig. (14)).



Figure 13. Dotted adhesive lines.

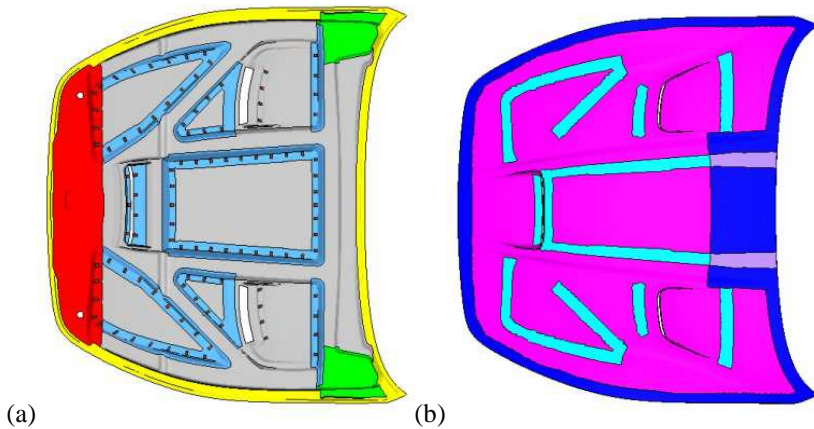


Figure 14. Prototype 2 layout - (a) inner panel; (b) outer panel.

A FE analysis has been executed and performance is about 2.7% of torsional and 3.5% of bending stiffness less than prototype 1.

Experimental results from torsional and bending tests on prototype 1 and 2 show a good matching between measured and expected outputs from FE analysis, particularly for prototype 1 (Tab. (2)).

Comparing real hood behaviour, prototype 2 has 13% higher torsional stiffness and 5% higher bending stiffness than aluminium hood.

Mass gap between numerical and actual hood is the same as prototype 1.

4. CONCLUSIONS

A methodology to design a sport-car composite material front hood was developed. The procedure can be easily applied to analogous car components.

Acting on the under hood volume, obtained from the geometry of the actual part, the first step consisted in a topology optimization, aimed at defining a rough frame structure connected to the outer panel. Imposed targets were reached. Interpretation of topology results led to a CAD re-design phase.

Later, a composite material optimization process was carried on to find the best solution in terms of stacking sequence complying with targets and manufacturer's technology requirements. The final layout was characterised by a weight reduction of 25% and a higher torsional and bending stiffness (33% and 22% respectively) than aluminium hood.

This configuration, which represents the final result of the new design process, was modified in view of hood manufacturer technology requirements for adhesive bonding.

Table 2. Gaps between numerical simulation and experimental tests.

	Numerical/Experimental gap	
	Proto1	Proto2
Kt	-3.5%	0.5%
Kb	2.9%	-11.2%

The first prototype version shows a decrease of adhesive bonding lines and repositioned triggers (closer to the central air inlet); in terms of performance, the FE model is characterized by a weight reduction of 27% and a higher torsional and bending stiffness (32% and 3% respectively) than aluminium hood. The correlation between numerical model and experimental tests is satisfactory (maximum gap of 3,5%).

The second prototype configuration presents dotted adhesive lines and slightly different stacking sequences. Mass comparison between prototype 1 and 2 and FE models shows that FE models are about 20% lighter than the actual hood. For what concerns real components, mass of prototype 2 is 23% less than aluminium hood; furthermore, prototype 2 has 13% higher torsional stiffness and 5% higher bending stiffness than aluminium hood.

Aerodynamic deflection, local deformation and hood supports stiffness will be assessed through experimental tests to validate the component.

REFERENCES

- [1] Bandivadekar, A., Bodek, K., Cheah, L., Evans, C., Groode, T., Heywood, J., Kasseris, E., Kromer, M., and Weiss, M., 2008. "Reducing the fuel use and greenhouse emissions of the US vehicle fleet". *Energy Policy*, **36**, pp. 2754-2760.
- [2] Silva, C., Ross, M., and Farias, T., 2009. "Analysis and simulation of "low-cost" strategies to reduce fuel consumption and emissions in conventional gasoline light-duty vehicles". *Energy Conversion and Management*, **50**, pp. 215-222.
- [3] Dimopoulos, P., Rechsteiner, C., Soltic, P., Laemmler, C., and Boulouchos, K., 2007. "Increase of passenger car engine efficiency with low engine-out emissions using hydrogen-natural gas mixtures: a thermodynamic analysis". *International Journal of Hydrogen Energy*, **32**, pp. 3073-3083.
- [4] Cuenot, F., 2009. "CO2 emissions from new cars and vehicle weight in Europe; how the EU regulation could have been avoided and how to reach it?". *Energy Policy*, **37**, pp. 3832-3842.
- [5] Tolouei, R., and Titheridge, H., 2009. "Vehicle mass as a determinant of fuel consumption and secondary safety performance," *Transportation Research Part D: Transport and Environment*, **14**, pp. 385-399.
- [6] Bendsøe, M.P., and Kikuchi, N., 1988. "Generating optimal topologies in structural design using homogenization method". *Computer Methods in Applied Mechanics and Engineering*, **71**, pp. 197-224.
- [7] Bendsøe, M.P., and Sigmund, O., 2004, *Topology optimization: theory, methods and applications*, Springer, Berlin.
- [8] Sigmund, O. 2001. "A 99 topology optimization code written in Matlab". *Structural and Multidisciplinary Optimization*, **21**, pp. 120-127.

TUNED MASS DAMPER DESIGN FOR VIBRATION SUPPRESSION OF STACKER CRANES

Enrico Carraro
SRcad technical study
E-mail: enrico.carraro@srcad.it

Emiliano Mucchi
Engineering Department in Ferrara(EnDIF),
University of Ferrara, Italy
E-mail: emiliano.mucchi@unife.it

Giorgio Dalpiaz
Engineering Department in Ferrara(EnDIF),
University of Ferrara, Italy
E-mail: giorgio.dalpiaz@unife.it

Abstract. *During a normal work cycle, stacker cranes can exhibit large vibration amplitude due to the impulsiveness of the loads to which they are subjected. In order to control and reduce these vibrations, a simple lumped parameter (LP) model of a stacker cranes has been developed. The parameters of the LP have been estimated by means of a more detailed finite element model. The LP model has been used in order to evaluate the effectiveness of a tuned mass damper (TMD) for vibration suppression. The TMD has been tuned by means of the model results. Eventually, a new prototype of a stacker crane has been designed including the TMA.*

Keywords: *Tuned mass damper, stacker crane, dynamic analysis.*

1. INTRODUCTION

A stacker crane (Fig. 1) is a special device designed to pallet handling in an automated warehouse. This system is composed of a portal consisting of two columns, a base, a beam on the top and a forklift truck. The stacker crane can move longitudinally through the wheels positioned on the base guided by fixed rails. The forklift truck can also move vertically, by means of wire ropes. Both movements cause vibrations of the structure: those caused by the longitudinal motion (X-direction) are attenuated by appropriate acceleration and deceleration run up, while those caused by the movement of the forklift truck (transverse movement in Z-direction) are the object of this research.



Figure 1. Example of a stacker crane (X is the longitudinal coordinate and Z is the transverse coordinate)

2. LUMPED PARAMETER MODELING OF THE STACKER CRANE

A one degree of freedom system model of the stacker crane has been developed. The equation that governs the system and the relative initial conditions in terms of displacement and velocity are:

$$\begin{cases} m\ddot{x}_1 + c\dot{x}_1 + kx_1 = 0 \\ x(t = 0) = 0 \\ \dot{x}(t = 0) = 0.005 \text{ m/s} \end{cases} \quad (1)$$

where x_1 is the degree of freedom that represents the transverse movement of the structure. The values of the initial conditions were achieved by experiments. The mass was concentrated in a single point and it was determined by the following relationship [1]:

$$m = m_{carr} + \frac{m_{col}}{3} \quad (2)$$

where m_{carr} is the mass of the forklift truck and m_{col} is the mass of the columns of the stacker crane. This equation is derived by analysing the total energy of the structure:

$$E_{tot} = E_{carr} + E_{col} \quad (3)$$

and then obtaining its natural frequency ω_n :

$$\omega_n = \sqrt{\frac{k}{m_{carr} + \frac{m_{col}}{3}}} \quad (4)$$

where k is global bending stiffness along the transverse direction. Damping coefficient c in Eqn. (1) has been estimated taking advantage of an experimental modal analysis carried out on the stacker crane. Thus, the damping factor $\xi = 0.02$ has been obtained and converted

into the damping coefficient c by the well-known equation $\xi = \frac{c}{2\sqrt{km}}$. Stiffness k in

Eqn. (1) represents the bending stiffness of the stacker crane. Firstly, it was estimated by using an analytical formulation:

$$k = \frac{48EI}{l^3} \quad (5)$$

where E is the Young's modulus, I is the moment of inertia and l is the length (in this case is the height) of the structure. Due to the presence of slots for lightening the columns, moment of inertia I was calculated in an approximate way, considering the slots as rectangles, as shown in Fig 2.

Thus, the bending stiffness (Eqn.(5)) leads to a value of 155973 N/m. This stiffness was then recalculated using a finite element model (FEM) of the stacker crane frame. The FEM was developed by using beam elements for the frame and shell elements for the forklift truck. A modal analysis was carried out by using the FEM. The first mode of vibration of the structure at a frequency of 0.84 Hz is depicted in Fig 3, which regards transverse motion. The FEM was validated using the same experimental modal analysis mentioned above, so the modal results can be considered reliable. By using Eqn. (4) in an inverse way, the stiffness can then be estimated leading to a value of 182020 N/m, slightly different from the value analytically calculated (155973 N/m). The differences between these two stiffness values can be attributed to the simplifications in the analytical calculation, in particular in the boundary conditions.

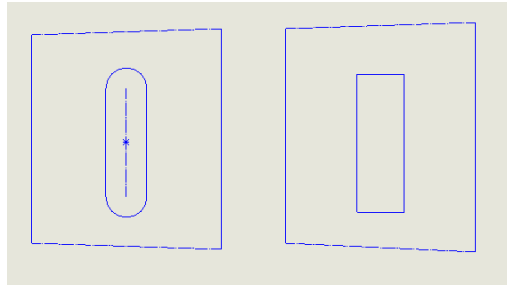


Figure 2. Simplification of the column geometry

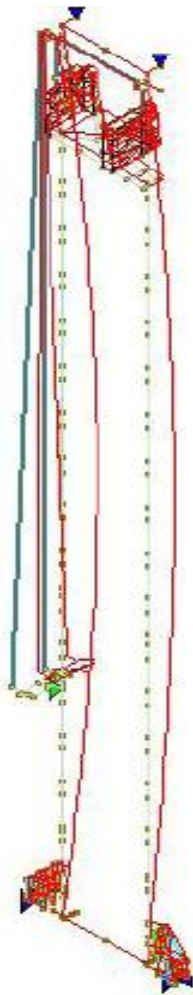


Figure 3. First mode shape at 0.84Hz: transverse motion.

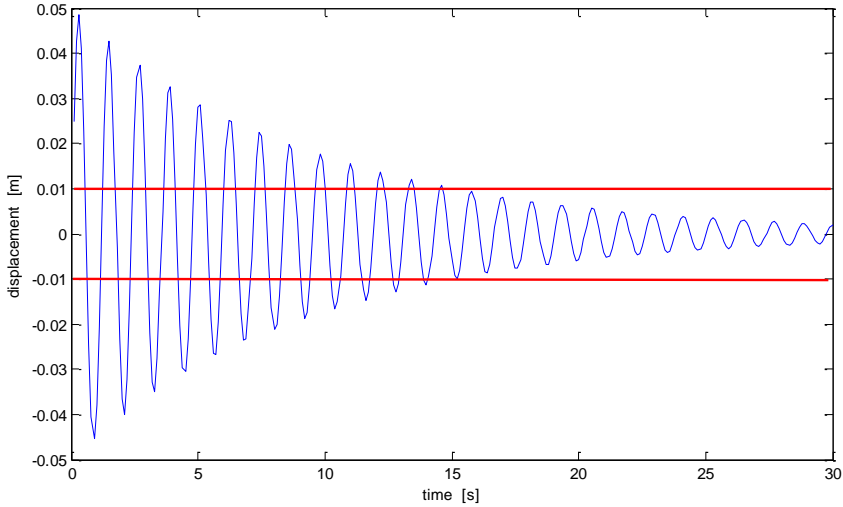


Figure 4. Vibration response of the system

Fig. 4 presents the vibration response of the LP model due to the initial condition of Eqn. (1). It is clear that the vibration amplitude involves a maximum amplitude of 5 cm. Due to functional constrains, the vibration amplitude can be considered acceptable for this application only when it is lower than 1 cm, thus after 15s, when the vibration amplitude become about 1 cm.

3. DESIGN OF PROPER VIBRATION SUPPRESSION SYSTEM

Once the actual behaviour of the system was determined, vibration suppression systems can be considered in order to reduce the vibration response till an acceptable threshold. These devices can be divided into active, semi-active and passive control systems. The first two systems have not been considered in this work due to the high cost. A number of passive control systems are available in the literature: i) systems which isolate the structure from the source exciter dissipating vibration energy before it is transmitted to the structure under consideration; ii) systems which dissipate vibration energy once it is already in the structure being studied. In our case, systems belonging to category i) cannot be used because the source of vibration belongs to the structure under consideration. On the contrary, systems belonging to category ii) seem adequate. In particular, the tuned mass damper (TMD) has been considered. The TMD is composed of a mass which is connected to the structure to be damped by means of spring and damper elements. In order to determine the stiffness and the damping coefficient of the spring and dampers of TMD, the value of mass ratio μ , defined as the ratio between the mass of the TMD and that of the structure to be damped should be defined. Then, parameter α can be calculated as:

$$\alpha = \frac{1}{1 + \mu} \quad (6)$$

In the literature, typical value of α are around 0.02. With this parameter the natural frequency of the TMD can be obtained as:

$$\omega_{TMD} = \omega_n \alpha \quad (7)$$

where ω_n is the natural frequency of the stacker crane. The mass of the TMD is determined by using mass ratio μ and the mass of the structure being studied:

$$m_{TMD} = \mu m_{strutt} \quad (8)$$

Damping factor ζ is calculated using the following relationship:

$$\zeta_{TMD} = \sqrt{\frac{3\mu}{8(1+\mu)}} \quad (9)$$

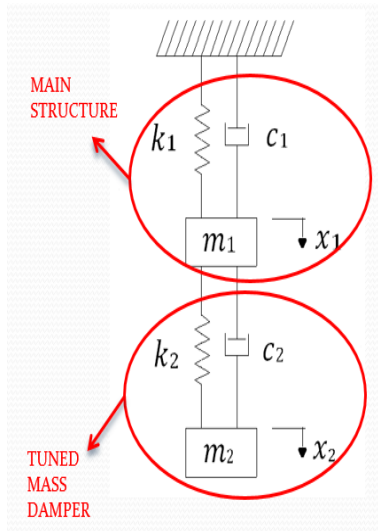
Eventually, the characteristic parameters of the TMD, i.e. stiffness and damping coefficients are obtained as:

$$k_{TMD} = \omega_{TMD}^2 m_{TMD} \quad (10)$$

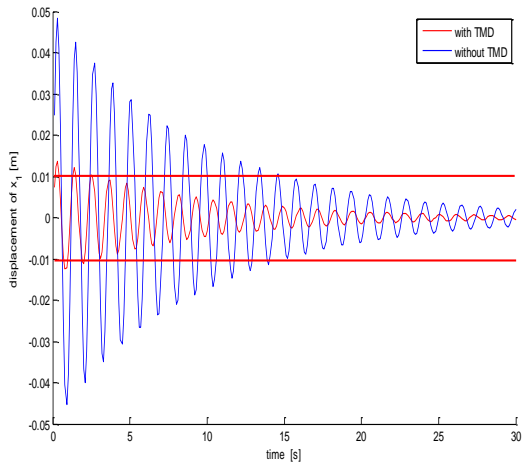
$$c_{TMD} = 2\zeta_{TMD} \omega_{TMD} m_{TMD} \quad (11)$$

Once the parameters of TMD have been design, the 1 degree of freedom model of the stacker crane has been modified in order to account the presence of the TMD, leading to a LP model with two degrees of freedom (DOFs) system, in which one degree of freedom accounts the bending deformation of the stacker crane and the other represents the Tuned Mass Damper (see Fig. 5a). The initial condition of the system remains the same as above. Fig.5b depicts the vibration response in time domain for the 2 DOFs systems and for the previous 1 DOF system. It can be seen that the vibration amplitude is strongly reduced and that the vibration amplitude does not excide the functional threshold of 1 cm .

Fig. 6 compares the frequency response function (FRF) of the two systems under study, the stacker crane model with and without TMD. The red curve (stacker crane model with TMD) show two peaks related to the two natural frequencies of the 2DOFs system. Moreover, the vibration amplitude is strongly reduced for the case with TMD. Fig 7 presents the comparison between the FRFs of the stacker crane model with and without TMD with different mass ratios, in order to find the optimal value. It can be noted that the mass ratio value that reduced at the maximum the vibration amplitude is 0.02, as found in the literature.



(a)



(b)

Figure 5. (a) 2 DOFs model. (b) Comparison between the vibration response in time domain of the stacker crane model with and without TMD.

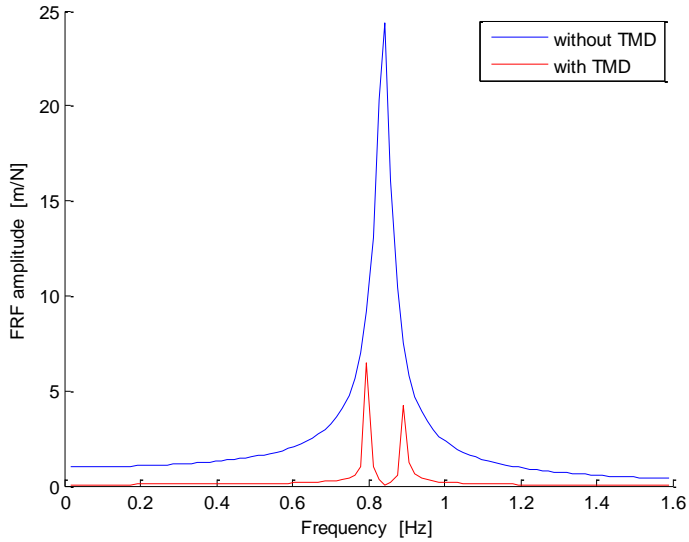


Figure 6. FRF amplitude of the stacker crane model with and without TMD ($\mu=0.02$).

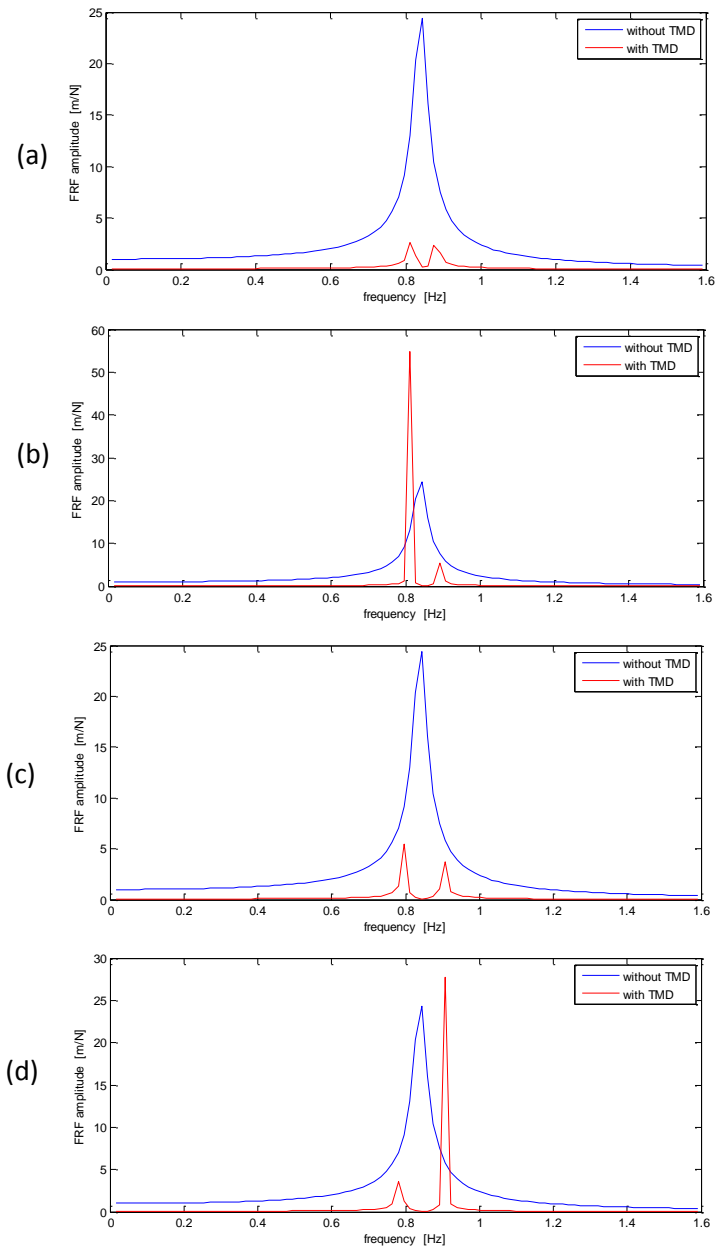


Figure 7. FRF amplitude of the stacker crane model with and without TMD, with different mass ratio: (a) $\mu=0.01$, (b) $\mu=0.015$, (c) $\mu=0.025$, (d) $\mu=0.03$.

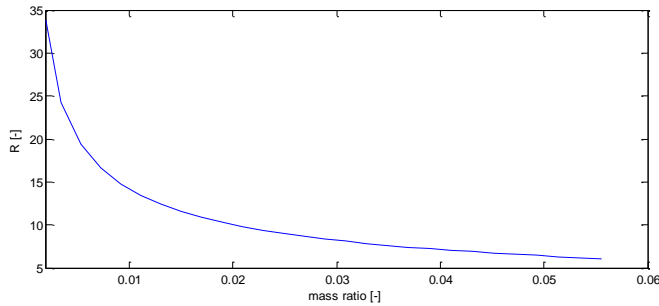


Figure 8. Influence on the mass ratio on the reduction of vibration of the structure

Table 1. Parameters of the designed TMD

Mass	131	kg
Stiffness	3499	N/m
Damping coefficient	116	Ns/m
Natural frequency	5.1745	rad/s

Fig 8. presents the influence on mass ratio μ on vibration reduction R of the structure; in particular, R is the ratio between the maximum dynamic displacement and static displacement. It is observed that the increase of this parameter determines a reduction of the vibration and at the same time an increase of the TMD size; thus, an increase of the mass to be added at the structure. Tab. 1 summarizes the parameters of the designed TMD.

4. DETAIL DESIGN OF THE TMD

In this section, the detail design of the TMD starting from the mail parameters collected in Table 1 is presented. Due to the overall dimensions and the available space, the TMD can only be placed within the columns of the structure. Two TMDs in parallel are used, each one inside a column and positioned at an half of the structure height. Each mass of the TMD is linked to the structure by means of four springs in parallel. The global stiffness, damping and mass properties of the two TMDs are similar to those in Table 1. Fig. 9 shows the 3D-Cad of the system. The spring-damper elements are connected to the main structure by means of revolute coupling and to the mass of the TMD by means of ball socket-ball stud elements. Fig. 10 shows the complete structure with the TMD. A supporting rope has been added in order to support the mass of the TMD together with a translational joint in order to avoid longitudinal oscillation of the mass. Two mechanical end stops have been designed to avoid breakage of the components of the TMD [2]; they serves to face large oscillations due to exceptional events to which the structure may be subjected, such as shock. The actual characteristics of the device are different from those calculated in the design phase (Table 1) of a very small amount. Table 2 collects the real parameters. Eventually, Fig 11 depicts the comparisons between the vibration reduction using the designed parameters of the TMD and the real ones: the behaviour is similar. In particular the vibration amplitude reduction changes from 72.5% to 72.44%.

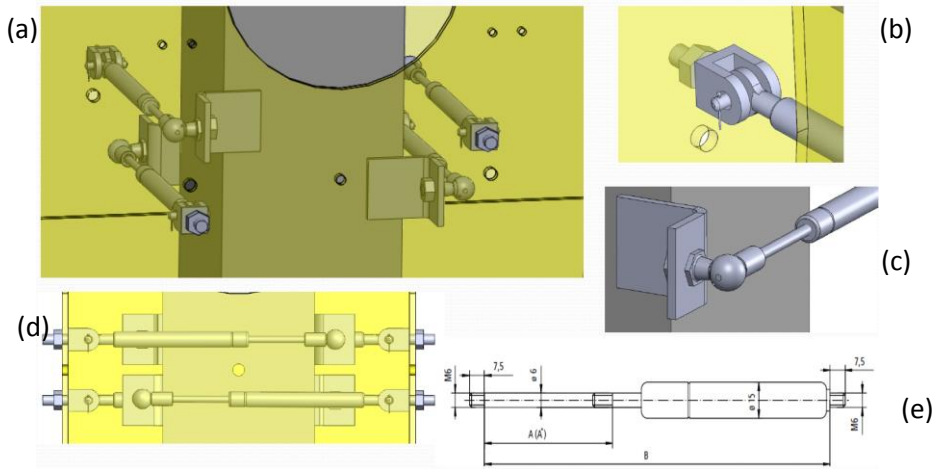


Figure 9. (a) mounting configuration of the TMD, (b) connection between spring-damper element and the column (c) connection between the spring-damper element and the mass of the TMD, (d) side view of the configuration of the TMD, and (e) drawing of the spring-damper element used.

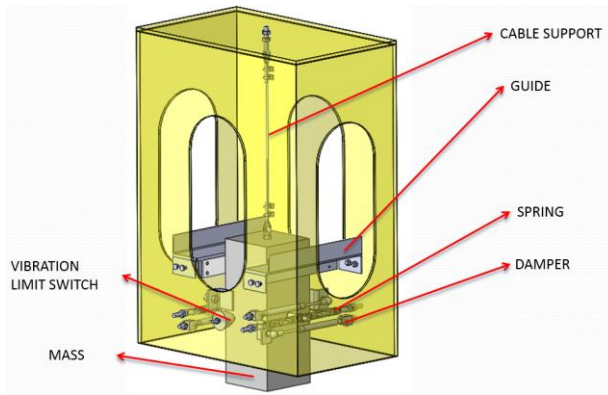


Figure 10. 3D- CAD of the TMD

Table 2. Parameters of the final TMD

Mass	131	kg
Stiffness	3502	N/m
Damping coefficient	116	Ns/m

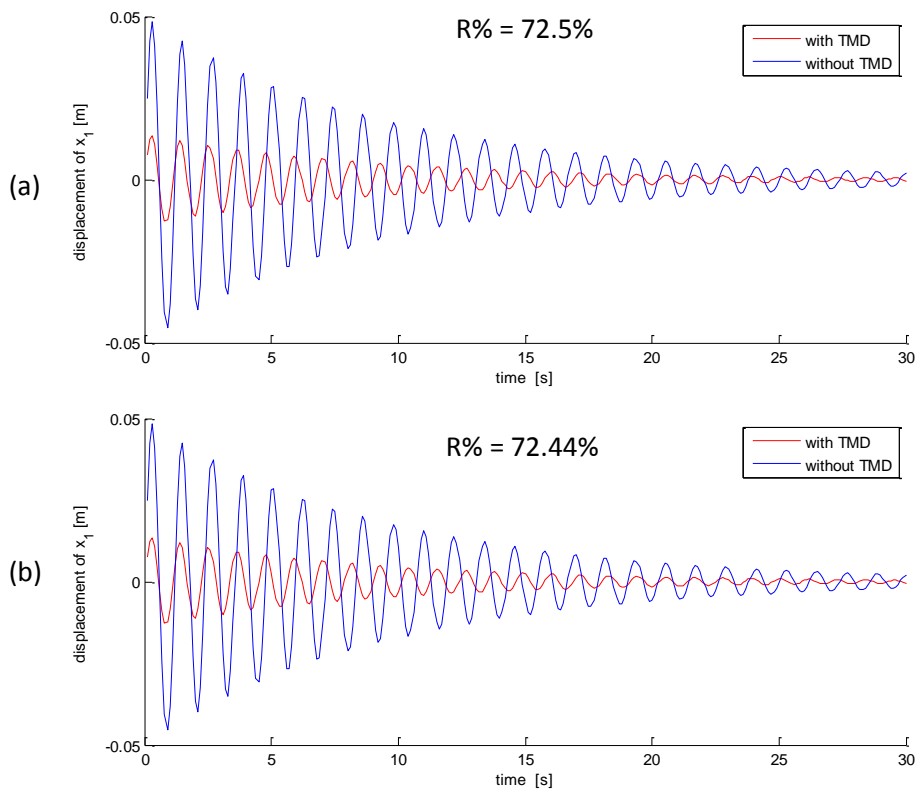


Figure 11. Vibration reduction of TMD with (a) designed and (b) real parameters.

5. CONCLUSIONS

This work has shown how simple lumped parameter (LP) modelling is effective for the dynamic analysis and optimization of the stacker crane. The finite element method makes possible an accurate estimation of the stiffness to be included in the LP model. This finite element model has been validated by experimental evidences. The use of the TMD leads to a vibration reduction of about 72% compared to the initial configuration without TMD. The 3D-Cad of TMD device was sent to the manufacturer and is currently under construction.

Acknowledgements

Part of this project has been carried out within the “Laboratorio di Acustica e Vibrazioni” which is supported by Regione Emilia Romagna - Assessorato Attività Produttive, Sviluppo Economico, Piano telematico - Fondi Obiettivo 2 (I). The authors wish to thank SRcad and Mazzali Renzo Studio Tecnico for active cooperation.

REFERENCES

- [1] In book, Meneghetti, U., Maggiore A., Funaioli, E., 2010. *Lezioni di Meccanica Applicata alle Macchine*, Vol. 3. Patron Editore, Chap. 3.
- [2] In book, Budynas, R., Nisbett, J., 2009. *Shigley - Progetto e costruzione di machine*, 2nd ed., McGraw-Hill Education.

STIFFNESS ANALYSIS OF SPATIAL STRIP-DRIVEN DEVICES

Fabrizio Nardini
*Department of Industrial Engineering,
University of Bologna, Italy
E-mail: fabrizio.nardini2@unibo.it*

Nicola Sancisi
*Department of Industrial Engineering,
University of Bologna, Italy
E-mail: nicola.sancisi@unibo.it*

Vincenzo Parenti Castelli
*Department of Industrial Engineering,
University of Bologna, Italy
E-mail: vincenzo.parenti@unibo.it*

Abstract. *Orthoses and exoskeletons require simple yet accurate devices to assist human joints in their motion. This paper presents the stiffness analysis of a spatial-strip driven device suitable for this application. The device features two cylinders guided by three flexible strips, so that a pure rolling relative motion between the two cylinders is generated. The analysis is conducted by defining analytical models to predict the equilibrium position of the device under different loading conditions. Only axial stiffness of the flexible strips is considered, while the effects of flexural and torsional stiffness are ignored as well as friction.*

Keywords: *orthoses, strip-driven device, stiffness analysis, analytical models*

1. INTRODUCTION

Orthoses are external devices placed besides injured human joints to provide a correct motion guidance as well as to decrease the loads on the anatomical structures. Therefore, the correct reproduction of the natural joint motion is a feature of great relevance in order to prevent the imposition of unnatural constraints to the anatomical structures. In the same way an appropriate load carrying capacity, together with lightness and simplicity, is highly important.

The aforementioned characteristics are often conflicting, since an accurate replica of the natural motion could be achieved by complex mechanisms, whereas simple devices would require a strong simplification of the motion. Thus, defining a device that combines both accuracy and simplicity is a big issue.

Recently, a new spatial device that combines these characteristics has been proposed [1]. The device is composed by two convex cones with the same vertex and with generic curvilinear

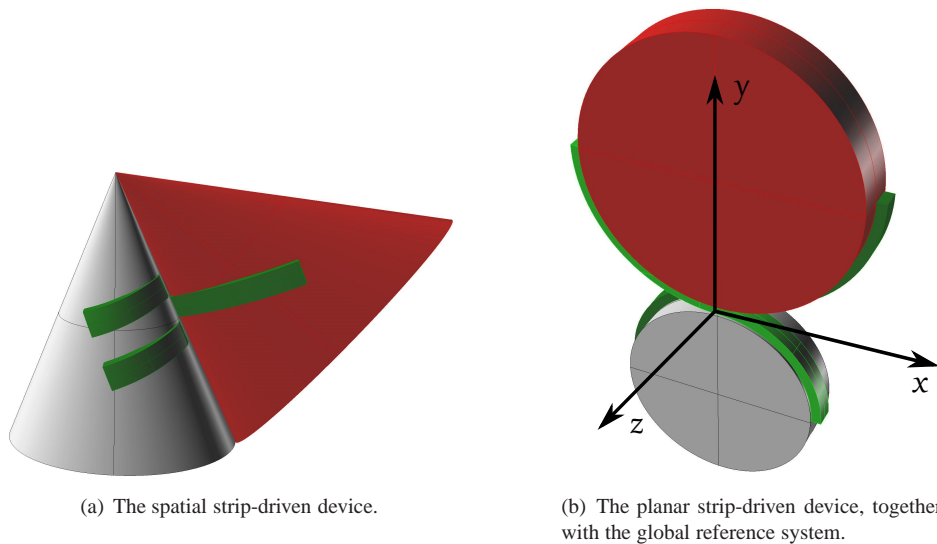


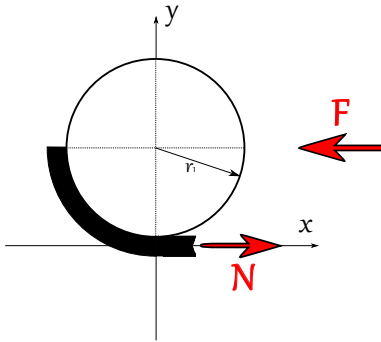
Figure 1. The strip-driven devices

ear directrix. The cones are interconnected by flexible strips that keep them in contact along a common line, as shown Fig. (1(a)). The device allows a one-degree-of-freedom (1-dof) spherical motion between the cones with no slipping (i.e. a pure rolling motion). Each strip wraps one cone from one end to the contact line and then wraps the other cone from the contact line to the other end. All the strips are connected in the same way to the cones but are crossed one after the other.

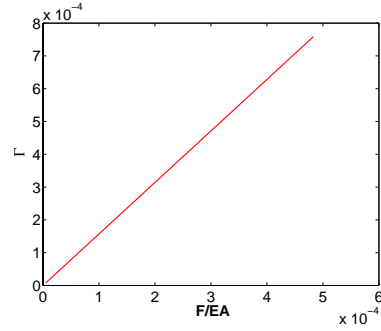
In this paper, a preliminary study of the stiffness of the planar device of which the aforementioned one is the spatial extension is presented. The device is similar to the one previously described: the shape of the strips and the way they are connected to the guided bodies are the same, but the cones are replaced by two cylinders. This type of device is well known in the literature [2, 3] and is used in a wide range of applications. Three analytical models based on geometrical considerations are proposed, each model dealing with a different loading condition in order to estimate the stiffness of the device.

2. GEOMETRIC MODEL

The analytical models obtained are based on a reference geometry for the device. Two cylinders with different radii r_1 and r_2 are considered. The strips are rectangular with the same unloaded length and the same rectangular cross section. In the following, the subscripts 1 and 2 are referred respectively to the upper and the lower cylinder. A device made with three strips is considered, therefore the rotations about the axis normal to the longitudinal axes of the cylinders are constrained; however, a higher number of strips could be used. Since the number of considered strips is odd, the device is not geometrically symmetrical and for some loading conditions some strips could be slack; in these cases only the loaded strips are considered in the model. However, in the reference starting configuration the strips are disposed symmetrically with respect to the line that connects the cylinder centers, and wrap



(a) Reference configuration used to derive the force-displacement relation for a load acting along the negative x direction.



(b) The linear relation between force and displacement. The plot shows on x axis the F/EA ratio and Γ on the y axis.

Figure 2. Reference configuration of the model and force-displacement relation

each cylinder for an angle equal to $\frac{\pi}{2}$.

All displacements are referred to the global reference system shown in Fig. (1(b)). The lower cylinder is considered fixed, while the upper one is moving.

A device composed by two cylinders with $r_1 = 20 \text{ mm}$ and $r_2 = 30 \text{ mm}$ and equipped with rectangular strips with a cross-sectional area $A = 1 \text{ mm}^2$ and a Young Modulus $E = 207 \times 10^3 \text{ MPa}$ is considered to give a numerical example of the displacements in a case of study.

3. STIFFNESS ANALYSIS

The three stiffness models are based on some simplifying assumptions:

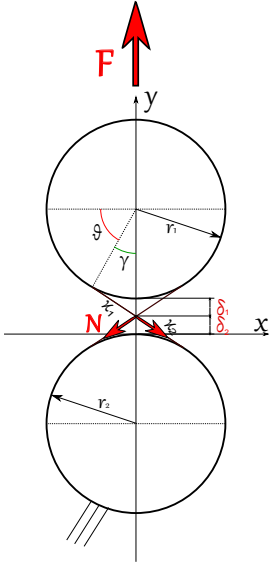
- Only the strip axial stiffness is considered;
- All degrees of freedom of the device are constrained except for the one along which the load acts. This degree of freedom corresponds to the motion component for which the largest displacement is expected for a given loading condition;
- The effects of friction are ignored.

Stiffness in x direction

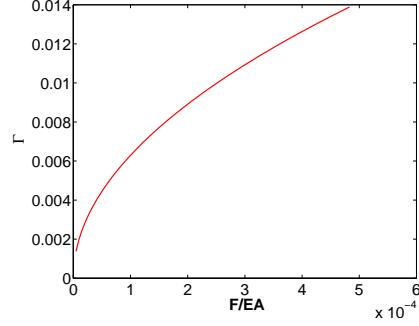
For this loading condition the stiffness of the device depends on the direction of the load. A load acting in the direction of negative x is considered: in this case, only one strip is loaded while the other two are slack, so they could be ignored in the model. The reference configuration is represented in Fig. (2(a)); for the sake of clarity only the upper part of the device and only the loaded strip are shown. Considering the well known relation:

$$\sigma = E\epsilon \quad (1)$$

where σ and ϵ are respectively the stress and the strain of the strip along the strip axis and E is the Young Modulus, under the aforementioned hypotheses the displacement δ of the moving



(a) Reference configuration used to derive the force-displacement relation for a load acting along the positive y direction. The device is represented in the final equilibrium configuration.



(b) The non-linear relation between force and displacement. The plot shows on x axis the F/EA ratio and Γ on the y axis.

Figure 3. Reference configuration of the model and force-displacement relation

cylinder could be written as:

$$\delta = \Delta l = \frac{Nl}{EA} \quad (2)$$

wherein N is the internal load, $l = \frac{\pi}{2} (r_1 + r_2)$ is the unloaded length of the strip and A is the cross-sectional area of the strip. For the equilibrium along x direction:

$$F = N \quad (3)$$

where F is the external load. Thus, from Eqn. (2) it is possible to write:

$$F = \frac{\delta EA}{l} = \frac{2\Gamma EA}{\pi} \quad (4)$$

where $\Gamma = \frac{\delta}{r_1 + r_2}$. The relation between the applied load and the obtained displacement is plotted in Fig. (2(b)) by using adimensional quantities to generalize the results. For a device with the characteristic dimensions reported in Section 2 and an acting load of 100 N , the obtained displacement is 0.0381 mm .

Stiffness in y direction

Figure (3(a)) shows the geometrical model, where a displacement $\delta = \delta_1 + \delta_2$ has been imposed by the external load F along the y direction. In this configuration, the free length

$\chi = \chi_1 + \chi_2$ of the strip can be written as:

$$\chi_{1,2} = \delta_{1,2} \sqrt{\frac{2r_{1,2}}{\delta_{1,2}} + 1} = \delta_{1,2} \sqrt{2d + 1} \quad (5)$$

where $d = \frac{r_1}{\delta_1} = \frac{r_2}{\delta_2}$. If θ is the angle for which the strip detaches itself from the cylinder, it is possible to express:

$$\begin{aligned} \cos \theta &= \frac{\sqrt{2d + 1}}{d + 1} \\ \sin \theta &= \frac{d}{d + 1} \end{aligned} \quad (6)$$

With geometrical considerations, the elongation of the strip is:

$$\Delta l = (\chi_1 + \chi_2) - (r_1 + r_2) \left(\frac{\pi}{2} - \theta \right) \quad (7)$$

From the stress-strain relation of Eqns. (1),(2), it is possible to express:

$$N = \frac{2EA\Delta l}{\pi(r_1 + r_2)} \quad (8)$$

For the equilibrium of the forces acting on the moving cylinder along the y direction, it is possible to write

$$F = 3N \cos \theta \quad (9)$$

since in this case all the three strips are tensioned. The final relation between the load force and the displacement of the moving cylinder can be obtained by substituting the results from Eqns. (5)–(8) in Eqn. (9):

$$\begin{aligned} F &= 6 \frac{EA \sqrt{2d + 1}}{\pi (d + 1)} \left[\frac{\sqrt{2d + 1}}{d} - \left(\frac{\pi}{2} - \arcsin \left(\frac{d}{d + 1} \right) \right) \right] \\ &= 6 \frac{EA}{\pi} \left[\Gamma \frac{2 + \Gamma}{1 + \Gamma} - \left(\frac{\pi}{2} - \arcsin \left(\frac{1}{(1 + \Gamma)} \right) \right) \frac{\sqrt{2/\Gamma + 1}}{1 + 1/\Gamma} \right] \end{aligned} \quad (10)$$

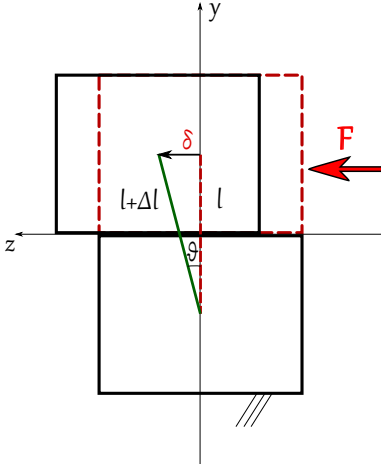
where $\Gamma = \frac{\delta_1 + \delta_2}{r_1 + r_2} = 1/d$.

Similarly to the previous case, the relation between force and displacement is shown in Fig. (3(b)), by using adimensional quantities. With the same reference device and load as the previous model, the obtained displacement is 0.6972 mm.

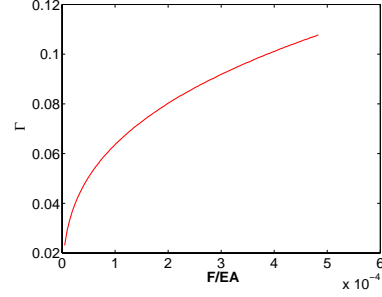
Stiffness in z direction

A scheme of the device in the zy plane is considered as shown in Fig. (4(a)). The two cylinders are represented developed in a plane as well as the strips (only one of which is shown in the figure for clearness). The dashed lines represent the initial position of the device while the final configuration is in solid line. The relation between the displacement and the angle θ between the initial and the deformed configuration of a single strip is given by:

$$\tan \theta = \frac{\delta}{l} \quad (11)$$



(a) Reference configuration of the developed cylinders used to derive the force-displacement relation for a load acting along the positive z direction. The device is represented in the final equilibrium configuration.



(b) The non-linear relation between force and displacement. The plot shows on x axis the F/EA ratio and Γ on the y axis.

Figure 4. Reference configuration of the model and force-displacement relation

where $l = \frac{\pi}{2} (r_1 + r_2)$. The elongation of the strip can be related to its initial length by means of the straightforward geometric relation:

$$\Delta l = \frac{l(1 - \cos \theta)}{\cos \theta} \quad (12)$$

For Eqns. (1),(2) it is possible to write:

$$N = \frac{EA(1 - \cos \theta)}{\cos \theta} \quad (13)$$

For the equilibrium of the forces acting on the moving cylinder along the z direction, it is possible to write

$$F = 3N \sin \theta \quad (14)$$

which makes it possible to relate θ to the external load:

$$F = 3EA \tan \theta (1 - \cos \theta) \quad (15)$$

The relation between the applied load and the displacement can be obtained from Eqns. (11)–(15):

$$F = \frac{3\delta EA(1 - \cos(\arctan(\frac{\delta}{l})))}{l} = \frac{6\Gamma EA(1 - \cos(\arctan(2\Gamma/\pi)))}{\pi} \quad (16)$$

where $\Gamma = \frac{\delta}{r_1 + r_2}$. In Fig. (4(b)) the relation between force and displacement is shown by means of adimensional quantities. With the same reference device and load as in the previous models, the obtained displacement is 5.41 mm .

4. CONCLUSIONS

A stiffness analysis of a strip-driven device under different loading conditions has been conducted and an analytical model for each case derived. Given the strong hypotheses made, the models supply a first evaluation of the stiffness of the device. The obtained models show a non-linear behavior of the device in two out of the three considered loading conditions. The device shows a high stiffness when loaded along the x or y axis, while the action of a load along the z axis is proved to be the most critical case.

REFERENCES

- [1] Sancisi, N., and Parenti-Castelli, V., 2011. "Strip-driven devices for the spatial motion guidance of human joints". In Proceedings of EMBC 2011, pp. 1–4.
- [2] Wilkes, D., 1969. Roller-band devices, June 24. US Patent 3,452,309.
- [3] Chironis, N., 1991. *Mechanisms & mechanical devices sourcebook*. McGraw-Hill.

FORZAMENTO ALBERO-MOZZO IN PRESENZA DI MOMENTO FLETTENTE: VALORE DEL MOMENTO FLETTENTE CHE PROVOCA IL DISTACCO TRA ALBERO E MOZZO

Antonio Strozzi

*Dipartimento di Ingegneria “Enzo Ferrari”
Università di Modena e Reggio Emilia, Italia
E-mail: antonio.strozzi@unimore.it*

Andrea Baldini

*Dipartimento di Ingegneria “Enzo Ferrari”
Università di Modena e Reggio Emilia, Italia
E-mail: andrea.baldini@unimore.it*

Matteo Giacomini

*Dipartimento di Ingegneria “Enzo Ferrari”
Università di Modena e Reggio Emilia, Italia
E-mail: matteo.giacomini@unimore.it*

Giuseppe Antonio Mulas

*Dipartimento di Ingegneria “Enzo Ferrari”
Università di Modena e Reggio Emilia, Italia
E-mail: giuseppeantonio.mulas@unimore.it*

Sara Mantovani

*Dipartimento di Ingegneria “Enzo Ferrari”
Università di Modena e Reggio Emilia, Italia
E-mail: sara.mantovani@unimore.it*

Abstract. *Si considera il problema di un forzamento albero-mozzo in presenza di coppia flettente applicata all'albero. Si sviluppa una simulazione analitica approssimata per determinare il valore della coppia che produce una situazione di incipiente distacco tra albero e mozzo. Tale situazione è ritenuta dannosa, perché favorisce problemi di fretting fatigue.*

Keywords: *albero, mozzo, forzamento, momento flettente, fretting fatigue.*

1. INTRODUZIONE

Si esamina in questo articolo il problema del forzamento albero-mozzo in presenza di una coppia flettente concentrata C applicata all'albero, Fig. (1). Si vuole definire il valore della coppia che provoca l'inizio del distacco tra albero e mozzo.

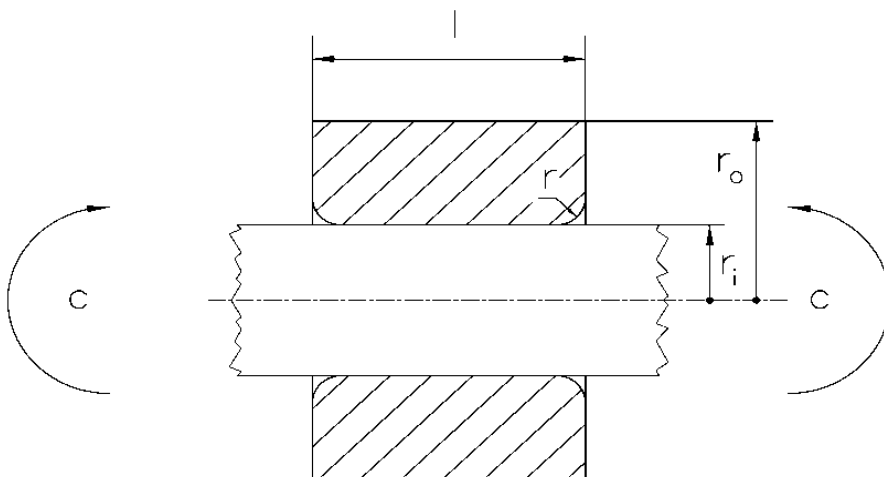


Figura 1. Schema del problema.

In altre parole, si vuole determinare il valore della coppia che vince il precarico del forzamento, causando l'inizio del distacco tra le superfici a contatto di albero e cavità del mozzo. La presenza di un distacco tra albero e mozzo costituisce un segno di cattiva progettazione, dato che esso favorisce fenomeni indesiderati di fretting fatigue.

In questo studio analitico preliminare, le tensioni dovute al solo forzamento ed alla sola coppia vengono analizzate separatamente; le tensioni dovute al solo forzamento vengono stimate col classico modello piano; le tensioni dovute alla sola coppia vengono analizzate con un modello a travi in contatto introducendo un suolo alla Winkler; imponendo che, nel punto di distacco, le pressioni di contatto dovute al solo forzamento siano uguali ed opposte a quelle dovute alla sola coppia, si stima la coppia di primo distacco.

Gli errori dovuti alle molte approssimazioni – trave tozza, deformabilità delle sezioni trasversali, picchi di contatto ignorati – potranno venire mitigati da una calibrazione del modello.

2. PRESSIONE DI SOLO FORZAMENTO

La pressione di solo forzamento p_{if} (l'indice sta per "interference fit"), nella zona centrale lontana dai picchi tensionali estremali, ref. [1], vale

$$p_{if} = \frac{EI}{2r_i} \frac{1}{1 + \frac{r_i^2 + r_o^2}{r_o^2 - r_i^2}} \quad (1)$$

dove r_i ed r_o denotano i raggi interno ed esterno del mozzo, e l'albero viene assunto pieno. Inoltre, E indica il modulo di Young dei materiali dell'albero e del mozzo, ed I denota l'inerzia diametrale.

Il fatto che ci si riferisca alla pressione centrale di forzamento, trascurando così i picchi di pressione estremali, può essere giustificato osservando che tali picchi sono molto

localizzati. Se si considera non la coppia di primo distacco, ma la coppia che produce un distacco tra albero e mozzo in direzione assiale per una lunghezza paragonabile a quella su cui insiste il picco di pressione (che in situazioni realistiche risulta dell'ordine del raggio di raccordo del foro del mozzo, ref. [1]), risulta corretto riferirsi alla pressione di contatto centrale trascurando i picchi estremali di pressione. Alla luce di queste osservazioni, il modello piano risulta accettabile.

3. PRESSIONE DI SOLA COPPIA FLETTENTE

Si esamina la pressione di contatto tra albero e mozzo in presenza di un contatto bilatero albero-mozzo di precisione, cioè senza gioco e senza interferenza iniziali, Fig. (2). Per semplicità, si ignora la possibile presenza di un arrotondamento agli spigoli del foro del mozzo. L'albero ed il mozzo vengono descritti in termini di travi; questa idealizzazione permette di determinare analiticamente la pressione di contatto, e.g. ref. [2]. Lo scopo principale è di determinare la pressione di contatto alle estremità del contatto albero-mozzo, dove l'albero inizia a staccarsi dal mozzo.

Più precisamente, si impiega per semplicità un modello puramente flessionale delle travi (e non flessotagliante). Il contatto tra le travi viene poi mediato da un suolo alla Winkler, che simula la deformazione delle sezioni trasversali delle travi. L'introduzione del suolo alla Winkler evita la presenza di forze o coppie concentrate alle estremità del contatto, che costituiscono una singolarità troppo forte rispetto alla soluzione nell'ambito della teoria dell'elasticità.

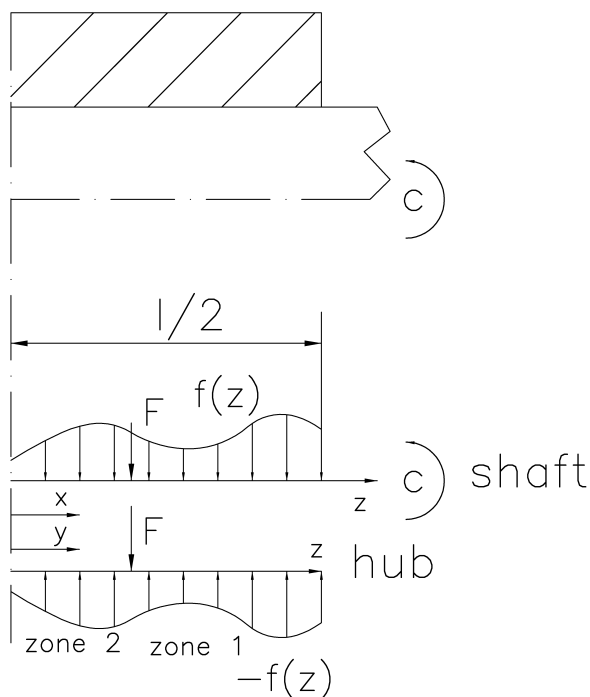


Figura 2. Pressione di sola coppia flettente.

Si presenta nel seguito una breve descrizione della determinazione della pressione di contatto ottenuta tramite il modello puramente flessionale a travi con l'introduzione di un suolo alla Winkler. Si impone una condizione di compatibilità tra le frecce dell'albero e del mozzo. Tali frecce vengono calcolate con l'ausilio del teorema di Castigliano; l'energia interna viene espressa in termini del momento flettente dovuto ad una forza lineare f e ad una forza concentrata ausiliaria F definita dalla coordinata assiale z , Fig. (2). Le frecce dell'albero e del mozzo vengono determinate derivando l'energia interna rispetto ad F , e successivamente ponendo $F=0$.

Si considerano nel seguito alcuni dettagli del calcolo. Il momento flettente nell'albero, M_s , e nel mozzo, M_h , la cui posizione è definita dalle coordinate assiale x , dovuto ad una forza lineare di contatto f e ad una forza concentrata ausiliaria F definita dalla coordinata z , vanno calcolati in riferimento alla Fig. (2). La lunghezza assiale del mozzo è l . L'espressione del momento flettente è diversa per i due intervalli 1 e 2 di Fig. (2), divisi dalla forza ausiliaria F la cui posizione è definita dalla coordinata z ; i due momenti flettenti sono indicati dagli indici 1 e 2:

$$\begin{aligned} M_{s,1}(x) &= C - \int_x^{l/2} f(y)(y-x)dy \\ M_{s,2}(x) &= C - \int_x^{l/2} f(y)(y-x)dy - F(z-x) \\ M_{h,1}(x) &= \int_x^{l/2} f(y)(y-x)dy \\ M_{h,2}(x) &= \int_x^{l/2} f(y)(y-x)dy - F(z-x) \end{aligned} \quad (2)$$

dove le origini delle coordinate x , y e z cadono al centro del mozzo. L'energia interna viene calcolata per l'albero e per il mozzo, e la sua derivazione rispetto ad F , seguita dall'imposizione $F=0$, produce le espressioni della freccia per l'albero e per il mozzo.

L'equazione di compatibilità è una generalizzazione del problema di una trave su supporto elastico alla Winkler (nel nostro caso, sono presenti due travi), ed esprime la condizione che la differenza tra le frecce dell'albero e del mozzo eguagli l'opposto della freccia, espresso come f/K , dove K è la costante di Winkler. Più esattamente, per tener conto di un possibile moto rigido verticale dei due corpi a contatto, l'estremità sinistra dell'albero viene assunta incastrata, mentre l'estremità sinistra del mozzo è libera di traslare verticalmente. Si osserva inoltre che questo problema di contatto è formulato in termini di una forza lineare f . Di conseguenza, invece di aggiungere alla freccia un termine costante che esprime lo spostamento rigido, risulta matematicamente più semplice aggiungere alla forza distribuita f un termine costante f_0 , che verrà determinato imponendo che la forza tagliante si annulli in mezzzeria del contatto.

Sfruttando la classica riduzione di integrali doppi, la condizione di compatibilità può essere espressa in termini di della seguente equazione integrale di Volterra

$$\begin{aligned} \frac{f(z) + f_0}{k} &= \left(\frac{1}{EJ_s} + \frac{1}{EJ_h} \right) \times \\ & \left[\frac{z^3}{6} \int_0^{l/2} [f(y) + f_0] dy - \frac{z^2}{2} \int_0^{l/2} y [f(y) + f_0] dy + \frac{1}{6} \int_0^z (y-z)^3 [f(y) + f_0] dy \right] + \frac{z^2}{2} \frac{C}{EJ_s} \end{aligned} \quad (3)$$

la quale, in seguito ad una differenziazione quarta rispetto a z , diventa la seguente equazione differenziale del quarto ordine in $f+f_0$

$$\frac{d^4[f(z)+f_0]}{dz^4} + K\left(\frac{1}{EJ_s} + \frac{1}{EJ_h}\right)[f(z)+f_0] = 0 \quad (4)$$

dove J_s e J_h sono i momenti di inerzia delle sezioni trasversali dell'albero e del mozzo, ed E è il modulo di Young,

Introducendo la costante β , ref. [2]

$$\beta = \frac{1}{\sqrt{2}} \sqrt[4]{\frac{K}{EJ_s + EJ_h}} \quad (5)$$

l'equazione differenziale assume la forma canonica, ref. [2]

$$\frac{d^4[f(z)+f_0]}{dz^4} + 4\beta^4[f(z)+f_0] = 0 \quad (6)$$

la cui soluzione è della forma, ref. [2]

$$f(z)+f_0 = e^{\beta z}(A \cos \beta z + B \sin \beta z) + e^{-\beta z}(C \cos \beta z + D \sin \beta z) \quad (7)$$

I quattro coefficienti A , B , C , D che appaiono in Eqn. (7) possono essere valutati inserendo la soluzione (7) nell'Eqn. (3). Infine, il valore della costante f_0 viene determinato imponendo che la tensione tagliente tra l'albero ed il mozzo si annulli per $z=0$. Le lunghe calcolazioni sono state relegate ad un manipolatore algebrico, e successivamente l'espressione di $f+f_0$ è stata compattata manualmente, ottenendo

$$f(z)+f_0 = \frac{2C \times J_h \beta^2}{(J_s + J_h) [\cos^2(\beta l / 2) + \cosh^2(\beta l / 2)]} \times \left\{ \begin{aligned} & \left[\cos(\beta l / 2) \sinh(\beta l / 2) - \sin(\beta l / 2) \cosh(\beta l / 2) + \frac{2}{l\beta} \right] \times \\ & \left[\cos(\beta z) \sinh(\beta z) - \sin(\beta z) \cosh(\beta z) \right] + \\ & 2 \cos(\beta l / 2) \cosh(\beta l / 2) \sin(\beta z) \sinh(\beta z) \end{aligned} \right\} \quad (8)$$

L'espressione (8) di $f+f_0$ è indipendente dal modulo di Young E , dato che la forza di contatto è attivata dall'imposizione della coppia C e non da uno spostamento tipo indentazione. Il valore di picco f_{\max} di $f+f_0$, che cade dove gli spigoli del foro del mozzo indentano l'albero inflesso, si ottiene imponendo $z=l/2$ nell'Eqn. (8), ottenendo

$$f_{\max} = \frac{2C \times J_h \beta^2}{(J_s + J_h)} \frac{\left\{ \begin{array}{l} \sin^2(\beta l / 2) + \sinh^2(\beta l / 2) + \\ \frac{2}{l\beta} [\cos(\beta l / 2) \sinh(\beta l / 2) - \sin(\beta l / 2) \cosh(\beta l / 2)] \end{array} \right\}}{[\cos^2(\beta l / 2) + \cosh^2(\beta l / 2)]} \quad (9)$$

Seguendo una approssimazione comunemente adottata in situazioni paragonabili, e.g. ref. [3], si assume che la pressione di contatto p sia distribuita cosinusoidalmente lungo la periferia della sezione:

$$p(r_i, \theta) = p \cos \theta \quad (10)$$

La pressione di contatto massima $p_{C,\max}$ causata dalla sola coppia C vale quindi

$$p_{C,\max} = \frac{f_{\max}}{\pi r_i} \quad (11)$$

4. DETERMINAZIONE DELLA COSTANTE DI WINKLER

In questo paragrafo si considera la valutazione della costante di Winkler K , che descrive la deformabilità delle sezioni trasversali dell'albero e del mozzo. La deformazione della sezione trasversale di una trave è causata dal campo di tensione distribuito lungo la sezione stessa. Se tale stato tensionale non è autoequilibrato, esso viene equilibrato dalla distribuzione delle tensioni taglianti lungo la sezione della trave, causate dallo scorrimento tra due sezioni contigue. Per determinare tale stato tensionale, occorre considerare simultaneamente la direzione assiale e quelle sul piano della sezione trasversale. Di conseguenza, la valutazione della deformabilità di una sezione trasversale costituisce generalmente un problema tridimensionale.

Tuttavia, questo problema può venire semplificato in termini di una idealizzazione piana adottando due semplificazioni.

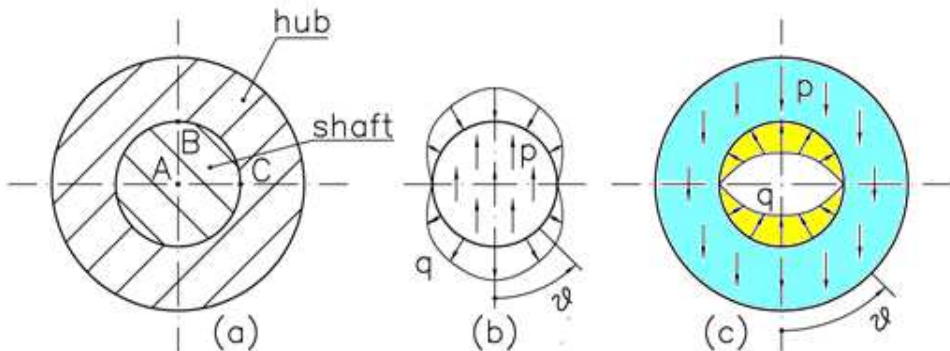


Figura 3. Equilibrio delle sezioni trasversali di albero e mozzo.

La prima semplificazione consiste nel rimuovere la tensione tagliante distribuita, sostituendola da tensioni taglianti applicate lungo la periferia della sezione, che equilibrano globalmente lo stato tensionale sul piano delle tensioni, vedi per esempio ref. [4]. Alternativamente, lo stato tensionale nel piano delle tensioni viene combinato con una distribuzione fittizia di forze di massa, di andamento possibilmente semplice, che ripristina l'equilibrio globale; un problema simile è trattato in ref. [5].

Si è deciso di adottare il secondo metodo, dato che l'assunzione di una forza di massa distribuita lungo la sezione meglio simula il meccanismo equilibrante effettivo, nel quale una tensione tagliante distribuita lungo la sezione equilibra le tensioni nel piano della sezione.

Si considera dapprima la deformazione dell'albero. Adottando la stessa approssimazione impiegata in Eqn. (10), la tensione radiale q viene assunta come distribuita cosinusoidalmente lungo la periferia dell'albero:

$$q(r_i, \theta) = q \cos \theta \quad (12)$$

dove la coordinate angolare θ ha origine dalla direzione verticale. La presenza di una tensione radiale trattiva, apparentemente fisicamente non corretta, viene giustificata ricordando che il vincolo al contatto tra albero e mozzo è inteso come bilatero. Quando le pressioni di contatto dovute alla sola coppia si sommano con quelle dovute al solo forzamento, le pressioni devono risultare tutte negative.

Per semplicità si assume che la forza gravitazionale p , distribuita uniformemente lungo la sezione circolare dell'albero, equilibri la tensione di bordo q . La risultante verticale Q della tensione radiale di bordo vale $q\pi r_i$. Il carico totale gravitazionale P agente verso l'alto vale $\rho g \pi r_i^2$. L'equilibrio tra Q e P impone $q = \rho g r_i$, e quindi il potenziale V della forza di massa diventa, ref. [6]:

$$V = \frac{q}{r_i} r \cos \theta \quad (13)$$

Le tensioni radiale, circonferenziale, e taglianti, espresse in coordinate polari, valgono

$$\sigma_r = \sigma_\theta = \frac{q}{r_i} r \cos \theta \quad ; \quad \tau_{r,\theta} = 0 \quad (14)$$

Seguendo ref. [6], gli spostamenti in tensione piana si ottengono tramite integrazione

$$u_r = \frac{(1-\nu)qr^2}{2Er_i} \cos \theta + S \cos \theta \quad ; \quad u_\theta = \frac{(1-\nu)qr^2}{2Er_i} \sin \theta - S \sin \theta \quad (15)$$

dove S è una costante di integrazione indefinita, che rappresenta una traslazione rigida verticale. La diminuzione della distanza tra i punti A e B del disco pieno è indipendente da S :

$$\Delta_{AB} = \frac{(1-\nu)qr_i}{2E} \quad (16)$$

Nel seguito si esamina la deformabilità del disco anulare che descrive la sezione del mozzo, Fig. (3). La tensione radiale q viene ancora assunta distribuita cosinusoidalmente lungo il bordo interno, mentre il bordo esterno viene ritenuto scarico. Si assume che una forza gravitazionale p , distribuita uniformemente lungo la sezione, equilibri la tensione radiale q applicata lungo il bordo interno dell'anello. Seguendo il precedente approccio, le tensioni radiale, circonferenziale e tangenziale nell'anello, espresse in coordinate polari, valgono:

$$\begin{aligned}\sigma_r &= \frac{(r_o^2 - r^2)}{r^3(r_o^2 - r_i^2)} \left[qr_i r^2 - 2C(r^2 - r_i^2)(r_o^2 - r_i^2) \right] \cos \theta \\ \sigma_\theta &= -\frac{1}{r^3(r_o^2 - r_i^2)} \left[2C(r_o^2 - r_i^2) r_i^2 r_o^2 + r^2(r_o^2 + r_i^2) - 3r^4 \right] + qr_i r^4 \cos \theta \\ \tau_{r\theta} &= -\frac{2C(r^2 - r_i^2)(r_o^2 - r^2)}{r^3} \sin \theta\end{aligned}\quad (17)$$

Gli spostamenti in tensione piana sono ottenuti tramite integrazione:

$$\begin{aligned}u_r &= \frac{qr_i}{8Er^2(r_o^4 - r_i^4)} \left[\begin{array}{l} -(1-\nu^2)r_o^2(r_i^2 r_o^2 + 3r^4) + \\ 2(3-\nu)(1+\nu)r^2 r_o^2(r_i^2 + r_o^2) \log r - \\ 4(1-\nu)r^4 r_i^2 \end{array} \right] \cos \theta + S \cos \theta \\ u_\theta &= -\frac{qr_i}{8Er^2(r_o^4 - r_i^4)} \left[\begin{array}{l} (1-\nu^2)r_o^2(r_i^2 r_o^2 - r^4) + \\ 2(3-\nu)(1+\nu)r^2 r_o^2(r_i^2 + r_o^2) \log r + \\ 2(1+\nu)^2 r^2 r_o^2(r_i^2 + r_o^2) + \\ 4(1-\nu)r^4 r_i^2 \end{array} \right] \sin \theta - S \sin \theta\end{aligned}\quad (18)$$

dove S è una costante di integrazione indefinita, che rappresenta una traslazione rigida verticale.

L'aumento delle distanza verticale tra i punti B e C dell'anello, Fig. (3), vale:

$$\Delta_{BC} = \frac{qr_i}{2E(r_o^4 - r_i^4)} \left[(1+\nu)r_o^2(r_i^2 + r_o^2) + 2(1-\nu)r_i^4 \right] \quad (19)$$

Alternativamente l'aumento in direzione verticale tra i punti B e D dell'anello vale:

$$\Delta_{BD} = \frac{qr_i}{4E(r_o^4 - r_i^4)} \left[\begin{array}{l} (1+\nu)(3-\nu)r_o^2(r_i^2 + r_o^2) \log \left(\frac{r_o}{r_i} \right) + \\ (1+\nu)^2 r_o^4 + (5-\nu^2)r_i^2 r_o^2 + 2(1-\nu)r_i^4 \end{array} \right] \quad (20)$$

In conclusione

$$\Delta = \Delta_{AB} + \Delta_{BC} \quad (21)$$

oppure

$$\Delta = \Delta_{AB} + \Delta_{BD} \quad (22)$$

Si impiegherà nei calcoli la definizione più aderente alle previsioni degli Elementi Finiti.

La costante di Winkler K è definita come il rapporto tra la forza f e la freccia Δ :

$$K = f / \Delta \quad (23)$$

dove

$$q = \frac{f}{\pi r_i} \quad (24)$$

5. CONDIZIONI DI INCIPIENTE DISTACCO

Si ricorda che il valore della coppia flettente C che produce una situazione di incipiente distacco è quello per cui la pressione di contatto dovuta al solo forzamento, Eqn. (1), eguaglia la pressione di contatto estrema imputabile alla sola coppia, Eqn. (11). Eguagliando quindi tali termini, si ottiene la seguente espressione della coppia flettente C di primo distacco:

$$\frac{Cl^2}{EI_s} = \frac{\pi l^2 \left(\frac{1}{J_s} + \frac{1}{J_h} \right) \left(1 - \frac{r_i^2}{r_o^2} \right) \left[\cos^2(\beta l / 2) + \cosh^2(\beta l / 2) \right]}{8\beta^2 \left\{ \begin{array}{l} \sin^2(\beta l / 2) + \sinh^2(\beta l / 2) + \\ \frac{2}{l\beta} \left[\cos(\beta l / 2) \sinh(\beta l / 2) - \sin(\beta l / 2) \cosh(\beta l / 2) \right] \end{array} \right\}} \quad (25)$$

6. CONCLUSIONI

Si è considerato il problema di un forzamento albero-mozzo in presenza di coppia flettente applicata all'albero. Si è sviluppata una simulazione analitica approssimata della deformazione dell'albero e del mozzo in termini di due travi puramente flessionali in mutuo contatto, con l'introduzione di un suolo alla Winkler. Si è stimato il valore della coppia che produce una situazione di incipiente distacco tra albero e mozzo. Tale situazione è ritenuta dannosa, perché favorisce problemi di fretting fatigue.

BIBLIOGRAFIA

[1] Strozzi, A., Baldini, A., Giacomini, M., Bertocchi, E., and Bertocchi, L., 2011. "Normalization of the stress concentrations at the rounded edges of a shaft-hub interference fit". *J. Strain Analysis*, **46**, pp. 478-491.

[2] Timoshenko, S., 1965. *Strength of Materials*, Vol 2, Van Nostrand, Canada.

- [3] Strozzi, A., and De Bona, F., 2005. "Hoop stresses in the con-rod small end". *Proc. IMechE, Part D: J. Automobile Engineering*, **219**, pp. 1331–1345.
- [4] Caputo, F., and Giudice, F., 1984. "Profili poligonali per trasmissioni di coppie: analisi delle tensioni e verifica sperimentale". In atti del XII National congress AIAS, pp. 697-710.
- [5] Castillo, J., and Barber, J.R., 1997. "Lateral contact of slender prismatic bodies". *Proc. R. Soc. Lond. A.*, pp. 2397-2412.
- [6] Barber, J.R., 2009, *Elasticity*, 3rd ed., Kluwer, Dordrecht.

STUDIO TEORICO DELLA LUBRIFICAZIONE IDRODINAMICA CON CARATTERIZZAZIONE VISCOELASTICA DI ANELLI DI TENUTA IN ELASTOMERO

Edzeario Prati
*Dipartimento di Ingegneria Industriale,
Università degli Studi di Parma
E-mail: prati@ied.unipr.it*

Alessandro Tasora
*Dipartimento di Ingegneria Industriale,
Università degli Studi di Parma
E-mail: tasora@ied.unipr.it*

Abstract. *Gli anelli di tenuta (o guarnizioni) a labbro per alberi rotanti operano normalmente in condizioni di interferenza iniziale di montaggio e di eccentricità statica e dinamica. In presenza di olio lubrificante, durante la rotazione dell'albero si forma un sottile film fluido fra il labbro e la superficie contrapposta, che impedisce il diretto contatto fra i due elementi cinematici della coppia, con conseguente riduzione dell'usura e del coefficiente di attrito. Fra labbro ed albero si instaura una lubrificazione idrodinamica caratterizzata da un meato molto sottile all'interno del quale la pressione del fluido dipende dalle caratteristiche del materiale elastomerico con cui è realizzata la guarnizione. Nel presente lavoro si riportano i risultati di uno studio teorico condotto per esaminare la risposta degli anelli di tenuta in presenza di eccentricità dinamica, situazione in cui è necessario considerare il comportamento viscoelastico del materiale elastomerico con cui gli anelli sono costruiti. Lo studio viene condotto determinando la pressione di contatto labbro-albero e l'altezza del meato, in presenza delle vibrazioni radiali dell'albero imposte dall'eccentricità dinamica, previa caratterizzazione viscoelastica dell'anello per via sperimentale. Si determina inoltre il valore del momento resistente per confrontarlo con i risultati sperimentali ottenuti in analoghe condizioni di esercizio.*

Parole chiave: *tenute radiali, contatto, lubrificazione idrodinamica*

1. ELENCO DEI SIMBOLI

- $OXYZ$: sistema di riferimento assunto
- U : velocità periferica dell'albero [m/s]
- P_i : forza radiale dovuta all'interferenza [N/m]

- E : Modulo elastico [N/m^2]
- δ : interferenza labbro-albero [m]
- R : Raggio dell'albero [m]
- $2b$: larghezza del labbro in direzione z [m]
- e_s : eccentricità statica [m]
- e_d : eccentricità dinamica [m]
- $\beta = x/R$: angolo che individua la posizione di un generico punto del labbro [rad]
- ω : velocità angolare dell'albero in rotazione [rad/s]
- E^* : modulo complesso [N/m^2]
- ψ : angolo di sfasamento fra forza e spostamento [rad]

2. INTRODUZIONE

Gli anelli di tenuta a labbro per alberi rotanti sono normalmente realizzati (vedi Figura 1) da un corpo in elastomero (con un anello metallico di irrigidimento), da un labbro (caricato da una molla elicoidale toroidale) e da una membrana che collega il labbro al corpo in elastomero.

Indagini sperimentali [1] mostrano che in condizioni operative si forma un sottile film fluido fra l'albero in rotazione e la superficie inferiore del labbro di tenuta.

Nel presente lavoro si studia la lubrificazione idrodinamica che porta alla formazione del suddetto film fluido in presenza del moto relativo fra i due membri che delimitano il meato e della pressione che provoca la deformazione del labbro dell'anello di tenuta.

La distribuzione della pressione di contatto labbro-albero, dipende dalle seguenti grandezze (vedi Figura 2):

- interferenza iniziale di montaggio: differenza fra il diametro dell'albero e il diametro della circonferenza che individua lo spigolo del labbro;
- eccentricità statica: distanza fra il centro della circonferenza che contiene lo spigolo del labbro e l'asse di rotazione dell'albero;
- eccentricità dinamica: distanza fra il centro geometrico dell'albero e il centro di rotazione dell'albero stesso.

Un generico punto del labbro, individuato dall'angolo β , subisce uno spostamento radiale di tipo statico dovuto all'interferenza δ e al valore di e_s . Con albero in rotazione il punto C percorre la circonferenza di centro B e raggio e_d , pertanto un punto del labbro è soggetto ad una vibrazione radiale il cui effetto è determinato dal comportamento viscoelastico dell'elastomero con cui è realizzata la guarnizione.

3. PRESSIONE DI CONTATTO LABBRO-ALBERO

L'interferenza di montaggio, genera una forza radiale per unità di lunghezza P_i , costante con x , agente lungo la circonferenza del labbro, esprimibile con la relazione:

$$P_i = E(\delta/2) \quad (1)$$

con E determinato operando come in [2].

Con riferimento alla Figura 2, considerando anche la presenza dell'eccentricità statica, la forza $P_{st}(x)$ dovuta alla deformazione statica del labbro, si potrà esprimere come:

$$P_{st}(x) = E[(\delta/2) - e_s \cos(x/R)] \quad (2)$$

Per effetto dell'eccentricità dinamica, lo spostamento del labbro in direzione radiale, dipende dalla posizione istantanea occupata dall'albero in rotazione con velocità angolare ω .

Con riferimento alle Figure 2 e 3, si assume:

- l'origine dei tempi $t_i = 0$ nell'istante in cui $C = C_0$
- l'angolo $\theta_i = \omega t_i$ l'angolo descritto dal segmento BC nel tempo t_i
- l'angolo $\beta = x/R$
- il tempo $t_{0\beta} = (2\pi - \beta)/\omega$ rappresenta il tempo necessario per passare dalla situazione in cui lo spostamento in β è massimo, alla successiva situazione in cui $C = C_0$
- il tempo $t = t_{0\beta} + t_i$

Lo spostamento radiale $\epsilon(\beta, t)$ dei punti del labbro dovuto all'interferenza δ , all'eccentricità statica e_s e all'eccentricità dinamica e_d , è esprimibile con la relazione:

$$\epsilon(\beta, t) = (\delta/2) - e_s \cos(x/R) + e_d \cos(\omega t) \quad (3)$$

Lo studio teorico della lubrificazione viene condotto considerando il comportamento viscoelastico dell'elastomero con cui è realizzata la guarnizione, sottoposta alla legge di spostamento corrispondente al movimento radiale dell'albero che, in presenza di e_d , comporta

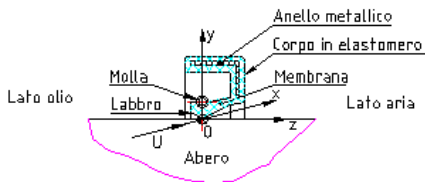


Figura 1. Anello di tenuta a labbro con il riferimento $OXYZ$ assunto e la velocità periferica U dell'albero (concorde con x).

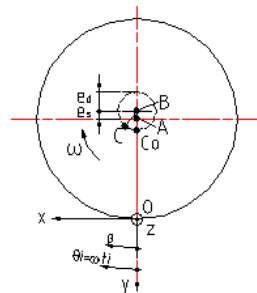


Figura 2. Guarnizione con eccentricità statica e_s e dinamica e_d . (A: centro del labbro, B: asse di rotazione albero, C: centro dell'albero).

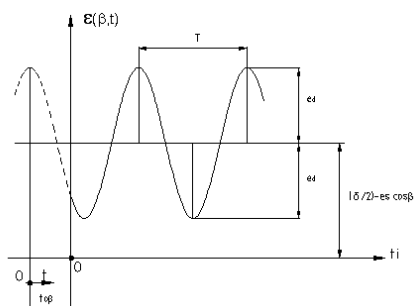


Figura 3. Spostamento radiale $\epsilon(\beta, t)$ dei punti del labbro in presenza di interferenza ed eccentricità statica e dinamica.

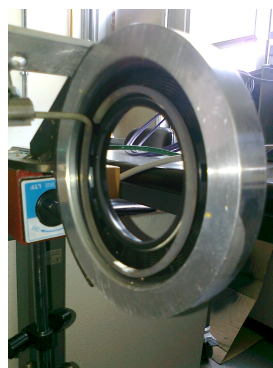


Figura 4. Controllo della temperatura con resistenza elettrica posizionata in prossimità del labbro dell'anello di tenuta.

un regime sinusoidale di forza e di spostamento. Per semplicità di trattazione, tale studio viene effettuato adottando il formalismo complesso, secondo il quale la forza viene espressa da un numero complesso σ^* e lo spostamento da un numero complesso ϵ^* . Si definisce poi *modulo complesso* E^* , la grandezza esprimibile col numero complesso:

$$\sigma^* / \epsilon^* = E^*(\omega) = E'(\omega) + iE''(\omega) \quad (4)$$

ove ω è la pulsazione, E' il *modulo di accumulazione* ed E'' il *modulo di perdita*.

L'angolo di sfasamento ψ tra forza e spostamento può essere determinato dalla relazione:

$$\tan(\psi) = E'' / E' \quad (5)$$

Considerando il comportamento viscoelastico del materiale della guarnizione, la forza $P_{din}(x, t)$ dovuta alla deformazione statica del labbro e alla presenza dell'eccentricità dinamica, è espressa con la relazione:

$$P_{din}(x, t) = E[(\delta/2) - e_s \cos(x/R)] + e_d |E^*| \cos(\omega t + \psi) \quad (6)$$

4. CARATTERIZZAZIONE VISCOELASTICA DELL'ANELLO DI TENUTA

Per la caratterizzazione in oggetto, si è condotta una indagine sperimentale su di una guarnizione in elastomero a base nitrilica (NBR), avente le seguenti dimensioni 70x110x12 mm (DIN 3760 type A).

Durante le prove, la temperatura dell'anello di tenuta è stata mantenuta a 50°C, corrispondente al valore mediamente raggiunto ad una velocità di rotazione dell'albero di 1000 giri/min ; per il riscaldamento si è utilizzata una resistenza elettrica con una forma ad anello (vedi Figura 4), appositamente realizzata, dotata di un adeguato sistema di controllo.

Nel punto inferiore del labbro si è appoggiato un sottile filo con applicato un peso di 3 N che consente di ottenere uno spostamento del punto di applicazione corrispondente all'interferenza radiale $\delta/2$.

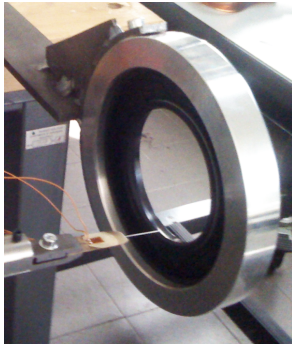


Figura 5. Trasduttore estensimetrico per rilevare lo spostamento del labbro.

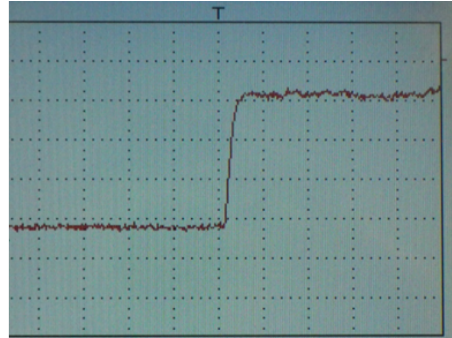


Figura 6. Traccia dello spostamento del labbro in funzione del tempo.

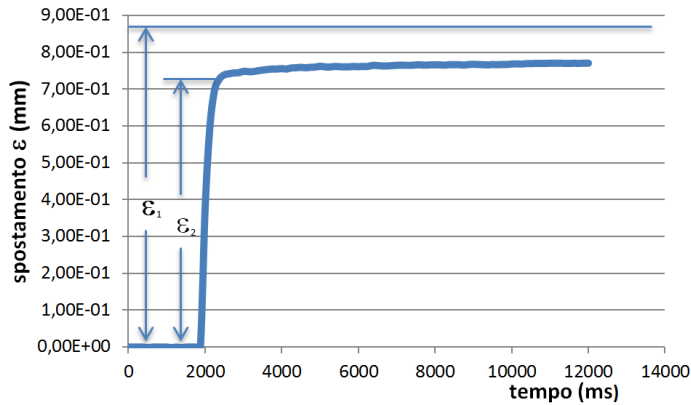


Figura 7. Spostamento del labbro alla temperatura di 50°C, successivo all'annullamento della forza di 3 N ad esso applicata.

Lo spostamento del labbro per effetto dell'annullamento istantaneo della forza peso, viene rilevato mediante un trasduttore estensimetrico costituito da uno spillo inserito nello spigolo del labbro dell'anello di tenuta (nella posizione di applicazione del carico) e fissato su una lamina metallica sulla quale si sono incollati, sulle due facce opposte, due estensimetri come riportato in Figura 5.

Nella Figura 6 è riportata la traccia del segnale, rilevato con l'impiego di una centralina estensimetrica, corrispondente allo spostamento del labbro in funzione del tempo.

Con una scheda di conversione analogico-digitale, si sono memorizzati i valori dello spostamento in funzione del tempo, coi quali si è ottenuto il grafico di Figura 7.

Con riferimento alla Figura 7, si è indicato con:

- ϵ_1 lo spostamento subito dal labbro per effetto dell'applicazione del carico $\sigma_0 = 3N$;
- ϵ_2 lo spostamento, praticamente istantaneo, di ritorno del labbro, conseguente all'annullamento istantaneo della forza σ_0 .

La Figura 7 mostra inoltre che a ϵ_2 segue uno spostamento fortemente influenzato dallo smorzamento viscoso con un tempo di rilassamento, necessario per recuperare lo spostamento ϵ_1 , notevolmente elevato.

Il particolare andamento della risposta dell'anello di tenuta alla prova sperimentale a cui è stato sottoposto e considerando i valori della pulsazione ω delle normali condizioni di esercizio, consente di potere ritenere che nella (4) sia $E'' = 0$, $E' = \sigma_0/\epsilon_2$, di conseguenza $E^* = E'$, e dalla (5) sia $\psi = 0$ rad.

5. STUDIO DELLA LUBRIFICAZIONE IDRODINAMICA

Con riferimento al sistema $OXYZ$ di Figura 1, considerando valide le ipotesi normalmente introdotte nella teoria classica della lubrificazione idrodinamica e in presenza di eccentricità dinamica (vedi Figura 2), poichè $p(x, z, t)$, $h(x, z, t)$ sono grandezze funzione anche del tempo, l'equazione di Reynolds assume la forma:

$$\frac{\partial}{\partial x} \left(h^3 \frac{\partial p}{\partial x} \right) + \frac{\partial}{\partial z} \left(h^3 \frac{\partial p}{\partial z} \right) = 6\mu U \frac{\partial h}{\partial x} + 12\mu \frac{\partial h}{\partial t} \quad (7)$$

Per una assegnata $p = p(x, z, t)$ la (7) rappresenta un'equazione differenziale a derivate parziali nella funzione incognita $h = h(x, z, t)$.

La particolarità dello studio in esame consente di introdurre ulteriori ipotesi semplificative:

- la larghezza $2b$ del labbro è dell'ordine del decimo di mm, mentre la lunghezza della sua circonferenza è dell'ordine del decimetro, di conseguenza a primo membro della (7) si trascura il termine relativo alla derivata parziale rispetto ad x nei confronti di quello relativo alla derivata parziale rispetto a z ;
- essendo inoltre $h \ll$ raggio della suddetta circonferenza, si trascura l'influenza della curvatura del meato;
- come conseguenza della prima ipotesi, si assume che l'altezza $h = h(x, z, t)$ non sia funzione di z , pertanto $h = h(x, t)$.

Con le ipotesi introdotte, la (7) diventa:

$$h^3 \left(\frac{\partial^2 p}{\partial z^2} \right) = 6\mu U \frac{\partial h}{\partial x} + 12\mu \frac{\partial h}{\partial t} \quad (8)$$

Indicando con (vedi Figura 8) :

$$P(x) = \int_{-b}^{+b} p(x, z) dz \quad (9)$$

la $p = p(x, z)$ si può scrivere come:

$$p(x, z) = f(z)P(x) \quad (10)$$

nella quale la funzione $f(z)$ che individua la legge di variazione della $p(x, z)$ lungo z , per la (10) deve rispettare la condizione di sottendere un'area unitaria.

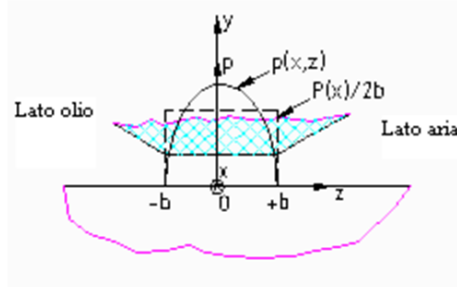


Figura 8. Andamento parabolico della $p(x, z)$ lungo z .

Il rapporto $P(x)/2b$ è indicativo della variazione della pressione media di $p(x, z)$ in direzione x .

Indicando con:

$$p_{zz} = \frac{\partial^2 p}{\partial z^2} \quad (11)$$

si può scrivere:

$$p_{zz} = \frac{\partial^2 f(z)}{\partial z^2} P(x) = f_{zz} P(x) \quad (12)$$

nella quale si è posto

$$f_{zz}(z) = \frac{\partial^2 f(z)}{\partial z^2}$$

Di conseguenza la (8) diventa:

$$p_{zz} h^3 = 6\mu U \frac{\partial h}{\partial x} + 12\mu \frac{\partial h}{\partial t} \quad (13)$$

Non essendo nota a priori la forma del meato, la trattazione analitica viene condotta applicando la teoria della lubrificazione idrodinamica *inversa*, che consiste nel determinare l'altezza del meato corrispondente ad una determinata distribuzione di pressione.

Fissato un punto z e valutato $f_{zz}(z)$, nota la funzione $P(x)$ è possibile esprimere $h(x, t)$ per il fissato valore di z .

Indagini sperimentali [3] suggeriscono per la $p(x, z)$ un andamento approssimativamente parabolico in direzione z (vedi Figura 8).

Assumendo per $p(x, z)$ una legge parabolica lungo z , la (10) diventa:

$$p(x, z) = \frac{3}{4b} (1 - (z^2/b^2)) P(x) \quad (14)$$

dalla quale si ottiene:

$$p_{zz} = -\frac{3}{2b^3} P(x) \quad (15)$$

$$f_{zz} = -\frac{3}{2b^3} \quad (16)$$

indipendente da z .

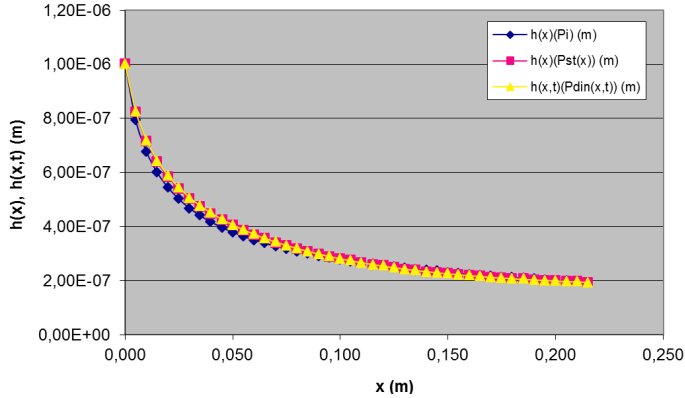


Figura 9. Andamento di $h(x)$ e di $h(x, t)$ assumendo come pressione idrodinamica del fluido P_i , $P_{st}(x)$, $P_{din}(x, t)$ (per $\theta_i = 0^\circ$).

Assumendo che la pressione $p(x, z, t)$ presenti un andamento parabolico lungo z , la (14) diventa:

$$p(x, z, t) = \frac{3}{4b} \left(1 - \frac{z^2}{b^2} \right) P_{din}(x, t) \quad (17)$$

Supponendo che in condizioni di lubrificazione idrodinamica la $P(x)$ coincida con la $P_{din}(x, t)$ espressa dalla (6), la $p_{zz}(x, t)$ assume l'espressione :

$$p_{zz}(x, t) = -\frac{3}{2b^3} P_i \left[1 - (2e_s/\delta) \cos\left(\frac{x}{R}\right) + (2e_d/\delta) \frac{|E^*|}{E} \cos(\omega t + \psi) \right] \quad (18)$$

Ponendo che nel punto $x = 0$ nell'istante $t = 0$ la $h(x) = h_0$, l'integrazione della (13) fornisce:

$$h(x, t) = \left\{ \frac{1}{h_0^2} + \frac{\mu U P_i}{2b^3} \left[x - \frac{2e_s}{\delta} R \sin\left(\frac{x}{R}\right) + \frac{e_d}{\delta} R \frac{|E^*|}{E} (\sin(\omega t + \psi) - \sin(\psi)) \right] \right\}^{-1/2} \quad (19)$$

La $h(x, t)$ è funzione periodica del tempo; nei vari punti β assume un valore che dipende dalla posizione dell'albero in rotazione con velocità angolare ω .

Nella Figura 9 si riportano gli andamenti di $h(x)$ ed $h(x, t)$ relativi ai seguenti tre casi:

- solo interferenza;
- interferenza ed eccentricità statica;
- interferenza, eccentricità statica ed eccentricità dinamica,

assumendo: $P_i = 120 \text{ N/m}$, $\mu = 0.0172 \text{ Pa s}$, $R = 0.035 \text{ m}$, $n = 1000 \text{ giri/min}$, $2b = 0.0004 \text{ m}$, $h_0 = 10^{-6} \text{ m}$, $e_s/\delta = 0.1$, $e_d/\delta = 0.015$, $|E^*|/E = 1.247$, $\psi = 0 \text{ rad}$.

Dalla Figura 9 si osserva che, lungo il tratto di labbro in esame, la $h(x)$ diminuisce continuamente all'aumentare di x ed il meato assume una forma convergente nel verso della velocità periferica U dell'albero, consentendo al fluido lubrificante di esercitare l'azione di

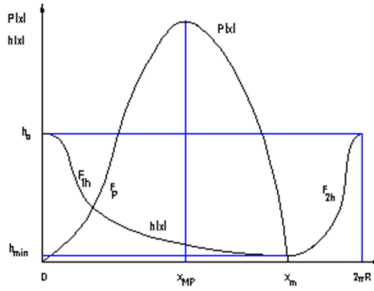


Figura 10. Andamento della $h(x)$ e della $P(x)$.

sostentazione idrodinamica. Poiché il meato deve rispondere ad esigenze di continuità, esso non può presentare brusche variazioni geometriche fra $x = 2\pi R$ ed $x = 0$. Pertanto si ritiene realistico ipotizzare che lungo tutto la circonferenza del labbro, la funzione $h(x)$ presenti un massimo h_0 per $x = 0$, assumendo quindi la forma di Figura 10.

Considerando l'andamento qualitativo della $P(x)$ sopra descritto, una possibile soluzione analitica nei tre casi sopra considerati può essere ottenuta nel modo seguente.

In presenza di sola interferenza, si assume per $P(x)$ un polinomio di terzo grado definito nell'intervallo $0 \leq x \leq x_m$:

$$P_{pl}(x) = \sum_{i=0}^{i=3} a_i x^i \quad (20)$$

i cui quattro coefficienti vengono determinati imponendo che: per $x = 0$ sia $P(x) = 0$, per $x = x_m$ sia $P(x) = 0$, per $x = x_{MP}$ sia $dP/dx = 0$ e infine sia $\int_0^{x_m} P(\xi) d\xi = P_i 2\pi R$.

La posizione di x_{MP} e di x_m si può definire introducendo i due coefficienti: $k_1 = x_m/2\pi R$, $k_2 = x_{MP}/2\pi R$.

Si può dimostrare analiticamente che per rispettare gli andamenti di $h(x)$ e $P(x)$ rappresentati in Figura 10, il coefficiente $k = k_2/k_1$ deve variare nell'intervallo $0.577 < k \leq 0.6$ indipendentemente dal valore di x_m (ovvero di k_1). Fissati k_1 e k si determinano i coefficienti del polinomio e si esprime $P_{vi}(x)$ mediante la (20).

Nel caso in cui oltre all'interferenza esista una eccentricità statica, si introduce il coefficiente $r_{vs}(x) = P_{st}(x)/P_i$ e si ipotizza che la pressione del fluido assuma l'espressione $P_{vs}(x) = r_{vs} P_{pl}(x)$. In [4] si sono determinati gli andamenti di $P_{vi}(x)$, $P_{vs}(x)$, e delle corrispondenti altezze del meato $h_{vi}(x)$, $h_{vs}(x)$, in funzione di k e k_1 .

In presenza di interferenza, eccentricità statica e dinamica, allo stesso modo si introduce il coefficiente $r_{vd}(x, t) = P(x, t)_{din}/P_i$ e si ipotizza per il fluido una pressione $P_{vd}(x, t) = r_{vd}(x, t) P_{pl}(x)$.

Integrando la (13) con la $P_{vd}(x, t)$, si determina la $h_{vd}(x, t)$.

Nella Figure 11 e 12 si riportano gli andamenti di $P_{vi}(x)$, $P_{vs}(x)$ e di $P_{vd}(x, t)$ nei tre casi sopra considerati, per $k_1 = 0.85$, $k = 0.6$, $\theta_i = 0^\circ$, e le corrispondenti altezze del meato $h_{vi}(x, t)$, $h_{vs}(x, t)$ ed $h_{vd}(x, t)$.

Dall'esame delle Figure 11 e 12, si osserva che l'altezza minima di meato è poco influenzata dall'andamento della pressione ed assume, per i normali valori di δ , e_s e di e_d , un valore che dipende principalmente dall'interferenza iniziale di montaggio.

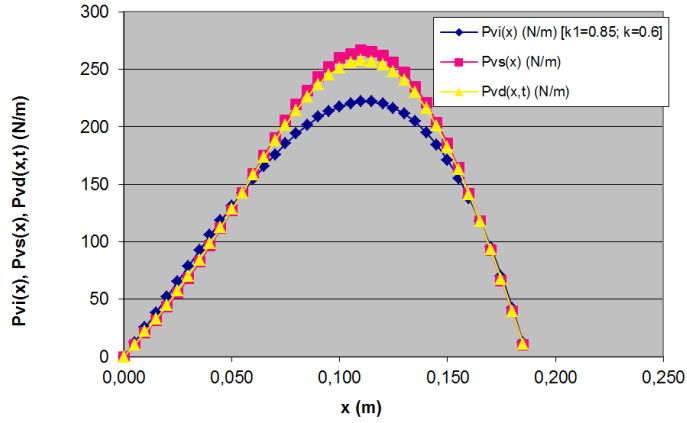


Figura 11. Andamento di $P_{vi}(x)$, $P_{vs}(x)$, $P_{vd}(x, t)$ (per $\theta_i = 0^\circ$).

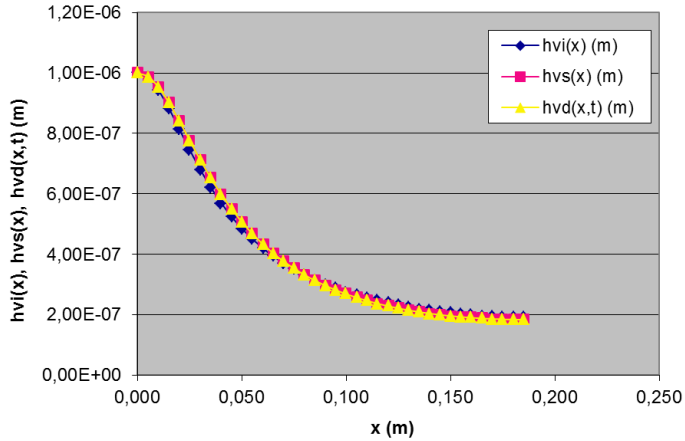


Figura 12. Andamento di $h_{vi}(x)$, $h_{vs}(x)$, $h_{vd}(x, t)$ (per $\theta_i = 0^\circ$).

La distribuzione complessiva della pressione influenza la forma e le dimensioni del meato e di conseguenza il valore delle tensioni tangenziali da cui dipende il momento resistente

6. MOMENTO RESISTENTE

Poichè $h(x)$ e $dP(x)/dx$ sono principalmente influenzati da δ e da e_s (vedi Figure 11 e 12), si può ritenere che nei vari punti β assumano valori indipendenti dal tempo.

Al fine di calcolare il Momento resistente M_r è necessario calcolare le tensioni tangenziali $\tau(x)$ applicate all'anello di tenuta. Con le ipotesi sopra introdotte e noti $P(x)$ ed $h(x)$, si ha

$$\tau(x) = -\frac{h(x)}{2} \frac{1}{2b} \frac{dP(x)}{dx} + \frac{\mu U}{h(x)} \quad (21)$$

nella quale si è assunta $\tau(x)$ positiva se orientata come l'asse x .

La forza tangenziale $T(x)$ per la larghezza $2b$ del labbro e per unità di lunghezza in direzione x , vale:

$$T(x) = 2b\tau(x) = -\frac{h(x)}{2} \frac{dP(x)}{dx} + \frac{2b\mu U}{h(x)} \quad (22)$$

dalla quale, considerando la lunghezza x_m di esistenza della $P(x)$, si ha:

$$M_r = R \int_0^{x_m} T(\xi) d\xi \quad (23)$$

Con le $P(x)$ ed $h(x)$ corrispondente ai grafici di Figura 11 e Figura 12, si ottiene $M_r = 0.51 \text{ Nm}$, valore mediamente misurato sperimentalmente [5] in condizioni operative confrontabili con quelle considerate nello studio analitico.

7. CONCLUSIONI

Nel presente lavoro si è condotto lo studio della lubrificazione idrodinamica che si instaura negli anelli di tenuta a labbro per alberi rotanti, in presenza di interferenza e di eccentricità statica e dinamica. Si è applicata la teoria della lubrificazione idrodinamica inversa che consente di determinare l'altezza del meato corrispondente ad una determinata distribuzione della pressione del fluido.

Dopo avere effettuato per via sperimentale una caratterizzazione viscoelastica della guarnizione realizzata in materiale elastomerico, si è individuata per via analitica la pressione di contatto labbro-albero nelle suddette condizioni di esercizio. Lo studio ha evidenziato come l'applicazione della citata teoria porti ad una forma e dimensione del meato che giustifica l'effetto di sostentazione idrodinamica del labbro anche in presenza delle vibrazioni radiali imposte dall'eccentricità dinamica dell'albero in rotazione. La validità dei risultati ottenuti viene confermata dal confronto fra il valore del momento resistente esercitato dall'anello di tenuta sull'albero determinato per via analitica, con quello determinato sperimentalmente in analoghe condizioni operative.

REFERENCES

- [1] Jagger, E. T., 1957. "Rotary shaft seals: the sealing mechanism of synthetic rubber seals running at atmospheric pressure". In Proc. Instn Mech Engrs, Vol. 171, pp. 597–616.
- [2] Tasora, A., Prati, E., and Marin, T., 2013. "A method for the characterization of static elastomeric lip seal deformation". *Tribology International*, **60**, pp. 119–126.
- [3] Hirano, F., 1961. "Friction and sealing characteristics of oil seals". In Int. Conf. On Fluid Sealing. BHRA, Harlow, Essex, England.
- [4] Silvestri, M., Prati, E., and Tasora, A., 2009. "A theoretical study of elasto-hydrodynamic lubrication in elastomeric lip seals". In ECOTRIB 2009, 2nd European Conference on Tribology, June 7-10, Pisa, Italy, pp. 585–590.
- [5] Silvestri, M., Prati, E., Tasora, A., and Marin, T., 2010. "Elastomeric seals behavior with oil pressure and lip support". In Proceedings of the 16th ISC International Sealing Conference - Stuttgart (Germany).

ON THE COMPLEMENTARITY FORMULATION OF LUBRICATED CAVITATED CONTACTS

Antonio Strozzi
*Engineering Department “Enzo Ferrari”
Università di Modena e Reggio Emilia, Italy
E-mail: antonio.strozzi@unimore.it*

Matteo Giacomini
*Engineering Department “Enzo Ferrari”
Università di Modena e Reggio Emilia, Italy
E-mail: matteo.giacomini@unimore.it*

Andrea Baldini
*Engineering Department “Enzo Ferrari”
Università di Modena e Reggio Emilia, Italy
E-mail: andrea.baldini@unimore.it*

Simone Sissa
*Engineering Department “Enzo Ferrari”
Università di Modena e Reggio Emilia, Italy
E-mail: simone.sissa@unimore.it*

Abstract. *The recently proposed complementarity formulation of lubricated cavitated contact is examined. For some particular situations it is demonstrated that the operator connecting the two complementary variables is coercive. This property entails the existence and uniqueness of the solution, and it provides a solid background to the employment of complementarity routines for locating the cavitated intervals.*

Keywords. *Lubrication, cavitation, complementarity, Reynolds equation.*

1. INTRODUCTION

The last decades have witnessed the transfer to lubrication problems of many theoretical-numerical procedures borrowed from the area of structural mechanics. Representative examples encompass the physical stability, a concept familiar to mechanics (e.g. the elastic stability of an Euler beam), extended in reference [1] to the analysis of the stability of steady-state solutions to lubricated contacts. Similarly, the “extended” variational formulation, which was initially conceived to improve the numerical convergence of the solution to nonlinear structural problems, has been extended to the elasto-hydrodynamic lubrication of soft contacts, references [2-4]. Finally, the concept of complementarity, initially applied to the area of structural mechanics with regard to unilateral contacts (see the ample literature review of reference [5]), has been transferred to lubrication problems, e.g. reference [6]. In reference [7], the lubrication problems of cavitation, tangential velocity slip, and mixed lubrication, have been given a unifying description in terms of complementarity.

This paper focuses upon a recently proposed modelling in terms of complementarity of lubricated contacts in the presence of cavitation, ref. [8]. This modelling corrects the limits of previous formulations, unable to guarantee the mass conservation. In addition, possible discontinuities of the fluid pressure and of the density when passing from a cavitated region to an active one or viceversa are correctly modelled.

To avoid confusion about the meaning of the connection between the fluid pressure and density in a lubricated contact subjected to cavitation, the following clarifications are introduced. In the cavitation problem, the fluid density depends on the pressure distribution (and viceversa), since the density attains its canonical value where the pressure is positive, whereas the density becomes lower than its canonical value where the pressure is null, i.e., where the fluid cavitates. This link between the pressure and the density is consistent with a description of the cavitation problem in terms of complementarity. The above link between the pressure and the density must not be confused with the link between the fluid pressure and the density in piezoviscous fluids.

The formulation of a problem in terms of complementarity requires the identification of two complementary variables, capable of detecting and describing the two distinct zones that constitute the problem. For instance, in a unilateral contact problem, the two complementary variables are the contact pressure and the gap in the deformed configuration between the mating surfaces. The extent of the contact between two bodies and the shape of the contact pressure are often unknown; with the aid of the complementarity approach, the extent of the contacting and separated zones may be defined together with the pressure distribution in the contacting intervals, as well as with the shape of the deformed gap in the separated regions.

Once the two complementary variables have been correctly identified, the task of solving the corresponding algebraic problem is left to robust routines, e.g. reference [5], rather than to heuristic procedures. A major practical advantage of the complementarity approach is that the mechanical behaviour of the two above distinct zones is described by the same equation, so that there is no need to employ switch functions to pass from one zone to the other, as thoroughly discussed in reference [8]. In other words, there is no need to guess the position of the transition zones; consequently, the numerical results are generally less sensitive to inaccuracies in describing the transition boundaries, and acceptable forecasts are achieved even with a coarse mesh.

Going back to the cavitation problem, and in particular to the identification of the correct complementary variables, the historically employed complementary variables are credited to Stampacchia, reference [9], p. 223, and they were the fluid pressure and the negative of the Reynolds residual, e.g. references [7,8], see also ref. [10]. It became however progressively clear that the adoption of such complementary variables produced physically incorrect predictions in some circumstances. In particular, the above adoption cannot correctly describe the reformation of an active zone that follows a cavitated interval, since the fluid mass conservation is violated, see reference [8] for details. To remove this deficiency, in reference [8] a new pair of complementary variables has recently been proposed, namely the fluid pressure and a variable connected to the fluid mass variation, often named void fraction. It is appreciated that such variables are commonly employed in tribological studies, e.g. reference [11]; nevertheless, they have not been previously employed within the framework of a complementarity approach.

In the cavitated zone, the relationship between the complementary variables degenerates into a mass conservation equation, thus overcoming the limits of the previous Stampacchia-type complementary variables. Selected examples have been presented in Fig.

(2) of reference [8] to evidence the differences in the results obtained with the traditional and with the new complementary variables. The recent paper [12], dealing with the lubrication of a piston ring, confirms the physical correctness of the two new complementary variables.

In all the cases examined, the complementarity numerical approach has efficiently defined the solution. It may therefore be expected that the numerical modelling of the cavitation problem in terms of complementarity possesses favourable mathematical properties. In particular, the matrix describing the complementarity problem is expected to be positive definite in most cases. It is known that coercive operators give rise to positive-definite matrices, ref. [13], and coercive operators are a means for demonstrating the uniqueness of the solution, [14]. Unfortunately, the cavitation problem is classified as non coercive in reference [15]. In addition, the cavitation problem is not covered in reference [16], specifically dealing with non coercive operators.

Results of general validity in terms of coercivity of the operator connecting the two complementary variables being impossible, the next best is to explore the coercivity property for particular situations. In the present paper, the Giacopini [8] pair of complementary variables is reconsidered, and it is shown that, under particular circumstances, the operator connecting the two complementary variables is coercive.

This paper is organized as follows. An initial section introduces the mathematical aspects of complementarity and coercivity. There follows a section devoted to the recently proposed complementarity variables describing the cavitation problem. The following sections show that in some particular circumstances the operator connecting the two complementary variables is coercive.

2. BASIC MATHEMATICAL ASPECTS OF THE COMPLEMENTARITY FORMULATION

The aim of this section is rather limited: to recall the basic knowledge regarding the complementarity approach. We introduce the Hilbert norm

$$\|f\| = \left(\int_0^a f^2 dx \right)^{\frac{1}{2}} \quad (1)$$

where f is a general function for which the above integral exists, and the integration interval is between 0 and a . We also introduce the inner product

$$(f, g) = \int_0^a fg dx \quad (2)$$

A description of a problem in terms of linear complementarity requires the knowledge of the linear relationship between the two complementary variables u and v

$$u = L(v) + T \quad (3)$$

where L is a linear operator, and T is a known term. In addition, the complementary variables u and v must be restricted in sign, and orthogonal

$$u \geq 0 \quad ; \quad v \geq 0 \quad ; \quad (u, v) = 0 \quad (4)$$

A sufficient condition for the complementarity problem to admit a unique solution is that the operator L is coercive, reference [14], that is

$$(L(v), v) \geq \alpha^2 \int_0^a v^2 dx \quad (5)$$

where α^2 is a positive constant.

3. THE TWO COMPLEMENTARY VARIABLES AND THEIR MATHEMATICAL LINK

The definition of the two complementary variables and their mathematical link according to ref. [8] is briefly recalled hereinafter. Variations of these definitions are proposed in the following sections

The unidimensional, hydrodynamic, steady state Reynolds equation for isoviscous fluids exhibiting a non constant density is

$$\frac{d}{dx} \left(\frac{\rho h^3}{6\mu} \frac{dp}{dx} \right) - U \frac{d(\rho h)}{dx} = 0 \quad (6)$$

where the fluid viscosity μ , the lubricated gap thickness h , and the velocity U , are known, whereas the fluid pressure p , and its density ρ are regarded as unknown variables. The coordinate x spans the lubricated interval between 0 and a .

Following reference [8], in Eqn. (6) the initial variables ρ and p are expressed in terms of the recently proposed complementary variables r and p

$$r = 1 - \frac{\rho}{\rho_0} \quad ; \quad p \quad (7)$$

where r is a variable connected to the variation of the fluid density ρ when passing from an active region to a cavitated one; the variable r is often named void fraction. Where the fluid is active, the density ρ equals its value ρ_0 , whereas ρ becomes lower than ρ_0 where the fluid cavitates. Consequently, $r \geq 0$. Similarly, the pressure p is positive in the active regions, and it becomes null where the fluid cavitates. Consequently, $p \geq 0$. Finally, where the fluid cavitates, $p=0$ and $r \neq 0$, whereas, where the fluid is active, $r=0$ and $p \neq 0$. Consequently, $pr=0$, that is, p and r are orthogonal variables. The sign restriction properties and the orthogonality property are summarised by classifying p and r as complementary variables.

By introducing in Eqn. (6) the above complementary variables (7), the following equation connecting the two complementary variables is obtained

$$\frac{d}{dx} \left(\frac{h^3}{6\mu} \frac{dp}{dx} \right) - \frac{d}{dx} \left(\frac{rh^3}{6\mu} \frac{dp}{dx} \right) - U \frac{d(h)}{dx} + U \frac{d(rh)}{dx} = 0 \quad (8)$$

In reference [8] it is noted that the following term (9) appearing in Eqn. (8)

$$\frac{d}{dx} \left(\frac{rh^3}{6\mu} \frac{dp}{dx} \right) \quad (9)$$

is null almost everywhere, since not only is p orthogonal to r , but also dp/dx is orthogonal to r . Consequently, the above term (9) may be omitted in Eqn. (8), which simplifies to

$$\frac{d}{dx} \left(\frac{h^3}{6\mu} \frac{dp}{dx} \right) - U \frac{d(h)}{dx} + U \frac{d(rh)}{dx} = 0 \quad (10)$$

Following again reference [8], Eqn. (10) is integrated once, thus obtaining

$$\frac{h^3}{6\mu} \frac{dp}{dx} - Uh + Urh = C_1 \quad (11)$$

from which

$$\frac{dp}{dx} = \frac{6\mu U}{h^2} - \frac{6\mu Ur}{h^2} + \frac{6\mu}{h^3} C_1 \quad (12)$$

A second integration leads to the following expression of p

By imposing $p=p_0$ for $x=0$, and $p=p_a$ for $x=a$, the following values of the constants C_1 and C_2 may be obtained, see reference [8]

$$p = 6\mu U \int_0^x \frac{1}{h^2} dx - 6\mu U \int_0^x \frac{r}{h^2} dx + 6\mu C_1 \int_0^x \frac{1}{h^3} dx + C_2 \quad (13)$$

$$C_1 = \frac{(p_a - p_o) + 6\mu U \int_0^a \frac{r}{h^2} dx - 6\mu U \int_0^a \frac{1}{h^2} dx}{6\mu \int_0^a \frac{1}{h^3} dx} \quad (14)$$

$$C_2 = p_o$$

The expression of the pressure p in terms of the complementary variable r thus becomes

$$p(x) = 6\mu U \left[\frac{\int_0^a \frac{r}{h^2} dy \int_0^x \frac{1}{h^3} dy}{\int_0^a \frac{1}{h^3} dy} - \int_0^x \frac{r}{h^2} dy \right] - 6\mu U \left[\frac{\int_0^a \frac{1}{h^2} dy \int_0^x \frac{1}{h^3} dy}{\int_0^a \frac{1}{h^3} dy} - \int_0^x \frac{1}{h^2} dy \right] + \frac{(p_a - p_o)}{\int_0^a \frac{1}{h^3} dy} \int_0^x \frac{1}{h^3} dy + p_o \quad (15)$$

where the coordinates x and y span the lubricated interval between 0 and a .

Eqn. (15) may be compactly formulated as

$$p(x) = L(r) + Q \quad (16)$$

where the linear operator L is

$$L(r) = \frac{6\mu U}{\int_0^a \frac{1}{h^3} dy} \left[\int_0^a \frac{r}{h^2} dy \int_0^x \frac{1}{h^3} dy - \int_0^a \frac{1}{h^3} dy \int_0^x \frac{r}{h^2} dy \right] \quad (17)$$

whereas the known term Q is

$$Q = -\frac{6\mu U}{\int_0^a \frac{1}{h^3} dy} \left[\int_0^a \frac{1}{h^2} dy \int_0^x \frac{1}{h^3} dy - \int_0^a \frac{1}{h^3} dy \int_0^x \frac{1}{h^2} dy \right] + \frac{(p_a - p_o)}{\int_0^a \frac{1}{h^3} dy} \int_0^x \frac{1}{h^3} dy + p_o \quad (18)$$

To demonstrate coercivity of the linear operator L , it should be necessary to show that, see Eqn. (5)

$$(L(r), r) \geq \alpha^2 \int_0^a r^2 dx \quad (19)$$

that is, assuming $U > 0$

$$\int_0^a \frac{r}{h^2} dy \int_0^a r dx \int_0^x \frac{1}{h^3} dy - \int_0^a \frac{1}{h^3} dy \int_0^a r dx \int_0^x \frac{r}{h^2} dy \geq \alpha^2 \int_0^a r^2 dx \quad (20)$$

Unfortunately, the authors have been unable to demonstrate the coercivity of the above operator even for simplified situations. However, it is possible to demonstrate coercivity for particular situations, examined in the following.

4. DEMONSTRATION OF COERCIVITY FOR A BOUNDARY CONDITION IMPOSING THE FLUID FLOW MASS

The pair of the classical boundary conditions consist in imposing $p=p_0$ for $x=0$, and $p=p_a$ for $x=a$, as it was done in formula (14). So doing, the expression of the constant C_1 includes an integral whose integrand is expressed in terms of the complementary variable r . Unfortunately, this feature impossibly complicates the analysis of the mathematical properties of the operator connecting the two complementary variables. A pair of mathematically favourable boundary conditions is discussed below.

A mathematically favourable boundary condition consists in imposing the value of the fluid flow mass in the lubricated region, see [15], after Eqn. 1.3. In fact, from Eqn. (11) the term $U\rho h$ is the fluid flow mass where the pressure derivative is null. Since the variables ρ and dp/dx change smoothly at the beginning of a cavitated region, see ref. [8], then $U\rho h = U\rho_0 h^*$, h^* being the lubricated gap height where the fluid begins to cavitate. If the fluid flow mass is known, h^* may be derived. In any case, $h_{\min} \leq h^* \leq h_{\max}$, so that h^* may be estimated.

From Eqn. (11), $C_1 = -Uh^*$. With this boundary condition, C_1 does no longer depend upon the complementary variable r , and the operator $L(r)$ assumes a more tractable form. This boundary condition describes a situation in which the fluid flow mass is experimentally measured, whereas the pressure of the sealed fluid is unknown.

To examine the mathematical properties of the operator connecting the two complementary variables, it is convenient to consider the variable r expressed in terms of the fluid pressure p (and/or of its derivatives) and not vice versa. By adopting the above discussed boundary condition, C_1 does no longer contain the complementary variable r . Consequently, from Eqn. (11) the expression of r in terms of dp/dx is

$$r = -\frac{h^2}{6\mu U} \frac{dp}{dx} + \frac{C_1}{Uh} + 1 \quad (21)$$

The operator $L(p)$ of Eqn. (3) assumes the form

$$L(p) = -\frac{h^2}{6\mu U} \frac{dp}{dx} \quad (22)$$

According to (5), the following integral should be examined to assess the coerciveness property of the operator L

$$-\frac{1}{6\mu U} \int_0^a \left(h^2 \frac{dp}{dx} \right) p dx = -\frac{1}{12\mu U} \left[h^2 p^2 \Big|_0^a - 2 \int_0^a p^2 h \frac{dh}{dx} dx \right] \quad (23)$$

which does not appear to be a useful result to demonstrate coerciveness. In fact, it would be particularly convenient if the integral in expression (23) were of the form of the right hand-term of the inequality (5).

It is noted that it is licit to modify a complementary variable by multiplying it by a positive weight function. The forms of integral (23) strongly suggests that, instead of assuming r as one of the complementary variables, the expression $s = r/h^2 = (\rho_0 - \rho)/(\rho_0 h^2)$. should be employed. This new expression of s is physically (as opposed to mathematically) equivalent to r , in the sense that both r and s should respect the properties that a) they remain positive together with the complementary variable p , and b) that r is orthogonal to p . Consequently,

$$s = -\frac{1}{6\mu U} \frac{dp}{dx} + \frac{C_1}{Uh^3} + \frac{1}{h^2} \quad (24)$$

and

$$L(s) = -\frac{1}{6\mu U} \frac{dp}{dx} \quad (25)$$

and the integral to be examined to assess the coerciveness property becomes

$$-\frac{1}{6\mu U} \int_0^a p \frac{dp}{dx} dx = -\frac{1}{12\mu U} [p^2(a) - p^2(0)] \quad (26)$$

which however is not yet a useful result to demonstrate coerciveness.

A further, physically based modification of the complementary variable describing the variation of the fluid density has been considered. The new, physically equivalent variable is $t = s \times x = (\rho_0 - \rho) \times x / (\rho_0 h^2)$. With this choice, the connection between the complementary variables becomes

$$t = -\frac{1}{6\mu U} x \frac{dp}{dx} + x \frac{C_1}{Uh^3} + x \frac{1}{h^2} \quad (27)$$

and the integral to be examined to assess the coerciveness property becomes

$$-\frac{1}{6\mu U} \int_0^a xp \frac{dp}{dx} dx \quad (28)$$

Integration by parts leads to

$$-\frac{1}{6\mu U} \int_0^a xp \frac{dp}{dx} dx = -\frac{1}{12\mu U} [ap^2(a) - \int_0^a p^2 dx] \quad (29)$$

By assuming that $p_a = 0$, the following result is obtained

$$-\frac{1}{6\mu U} \int_0^a xp \frac{dp}{dx} dx = \frac{1}{12\mu U} \int_0^a p^2 dx \quad (30)$$

It may be concluded that

$$(L(t), t) = \frac{1}{12\mu U} \int_0^a p^2 dx \geq \alpha^2 \int_0^a p^2 dx \quad (31)$$

Consequently, a value of $\alpha^2 < 1/(12\mu U)$ may be found for which inequality (5) is verified. It may be concluded that, within the limits of the boundary conditions imposed, the operator connecting the two complementary variables p and t is coercive, and, therefore, a solution exists and it is unique, e.g. ref. [14].

As a final observation, it was decided to detail in this section various modifications of one of the complementary variables, since a physical insight more than a mathematical ability is needed to understand up to what level of alteration the modified complementary variable still retains its physical meaning.

It has already been observed that the employment of the traditional boundary conditions (14) produces the negative fact that in formula (14) the constant C_1 depends on r , and, consequently, the above demonstration of coercive operator does no longer hold. It may however be observed that, since the constant C_1 depends on r in an integral manner, the above dependence is weak; this observation rationalizes the fact that the numerical routines have always found the solution without facing numerical troubles.

5. GENERALIZATION OF THE COERCIVITY RESULTS

It has already been noted that formula (15) expresses the variable p in terms of integrals involving the density ρ ; by introducing the variable r that is complementary to p , see reference [8] for details, it is possible to express p in terms of integrals involving r . With this formulation, the authors have been unable to demonstrate the coercivity of the corresponding operator even for simplified situations. As a result, a different approach is followed hereinafter, expressing ρ and, consequently, r , in terms of (the derivative of) p (and not p in terms of ρ). Moving back to the formulations expressed in (15), the connection between the variables (reciprocal of) ρ and (derivative of) p is

$$\frac{1}{\rho h^3} = \frac{dp}{dx} \frac{\int_0^a \frac{1}{\rho h^3} dx}{p_a - p_0 - 6\mu U \int_0^a \frac{1}{h^2} dx} - \frac{6\mu U \int_0^a \frac{1}{\rho h^3} dx}{h^2 \left(p_a - p_0 - 6\mu U \int_0^a \frac{1}{h^2} dx \right)} \quad (32)$$

The above expression (32) is reformulated in (33) to ease the introduction of the complementary variables, defined in the following section.

$$\left(\frac{\rho_0}{\rho} - 1 \right) \frac{1}{h^3} = \frac{dp}{dx} \frac{\int_0^a \frac{\rho_0}{\rho h^3} dx}{p_a - p_0 - 6\mu U \int_0^a \frac{1}{h^2} dx} - \frac{6\mu U \int_0^a \frac{\rho_0}{\rho h^3} dx}{h^2 \left(p_a - p_0 - 6\mu U \int_0^a \frac{1}{h^2} dx \right)} - \frac{1}{h^3} \quad (33)$$

The Introduction Of Three Weight Functions And The Examination Of The Corresponding Coercivity Properties

Three different situations have been detected for which the coercivity of the corresponding operator may be demonstrated. To this aim, both members of expression (33) have been multiplied by three linear weight functions remaining positive within the lubricated interval $(0, a)$. The following subsections separately consider these three situations.

The first weight function The first weight function is x . By multiplying both members of expression (33) by x , one obtains

$$\left(\frac{\rho_0}{\rho} - 1 \right) \frac{x}{h^3} = \frac{dp}{dx} \frac{\int_0^a \frac{\rho_0}{\rho h^3} dx}{p_a - p_0 - 6\mu U \int_0^a \frac{1}{h^2} dx} x - \frac{6\mu U \int_0^a \frac{\rho_0}{\rho h^3} dx}{h^2 \left(p_a - p_0 - 6\mu U \int_0^a \frac{1}{h^2} dx \right)} x - \frac{x}{h^3} \quad (34)$$

The two complementary variables connected to this weight function are

$$p \quad ; \quad r = \left(\frac{\rho_0}{\rho} - 1 \right) \frac{x}{h^3} \quad (35)$$

where r is a variable connected to the variation of the fluid density ρ when passing from an active region to a cavitated one and vice versa; the variable r incorporates the void fraction $(1-\rho/\rho_0)$. Where the fluid is active, the density ρ equals its value ρ_0 , whereas ρ becomes lower than ρ_0 where the fluid cavitates. Consequently, $r \geq 0$. Similarly, the pressure p is positive in the active regions, and it becomes null where the fluid cavitates. Consequently, $p \geq 0$. Finally, where the fluid cavitates, $p=0$ and $r \neq 0$, whereas, where the fluid is active, $r=0$ and $p \neq 0$. Consequently, $pr=0$, that is, p and r are orthogonal variables.

The sign restriction properties and the orthogonality property are summarised by classifying p and r as complementary variables. Mathematically, the complementarity conditions are

$$p \geq 0 \quad ; \quad r \geq 0 \quad ; \quad \int_0^a pr dx = 0 \quad (36)$$

It is recalled that, in the cavitated zones, Reynolds equation becomes the mass conservation equation.

Equation (34) is reformulated in terms of the complementary variables (35) as

$$r = \frac{dp}{dx} \frac{\int_0^a \frac{\rho_0}{\rho h^3} dx}{p_a - p_0 - 6\mu U \int_0^a \frac{1}{h^2} dx} x - \frac{6\mu U \int_0^a \frac{\rho_0}{\rho h^3} dx}{h^2 \left(p_a - p_0 - 6\mu U \int_0^a \frac{1}{h^2} dx \right)} x - \frac{x}{h^3} \quad (37)$$

It is appreciated that the integral

$$\int_0^a \frac{\rho_0}{\rho h^3} dx \quad (38)$$

appearing twice in expression (37) contains the unknown function ρ , and, therefore, it is an unknown, non null constant. However, for the time being, it will be treated as known, following an approach similar to a false position method. This aspect will be reconsidered later.

Formula (37) expressing r in terms of p may be given the following compact form

$$r = L(p) + Q \quad (39)$$

where L is the following linear operator

$$L(p) = \frac{\int_0^a \frac{\rho_0}{\rho h^3} dx}{p_a - p_0 - 6\mu U \int_0^a \frac{1}{h^2} dx} \frac{dp}{dx} x \quad (40)$$

and Q is treated as a known function for the time being

$$Q = -\frac{x}{h^3} - \frac{6\mu U \int_0^a \frac{\rho_0}{\rho h^3} dx}{h^2 \left(p_a - p_0 - 6\mu U \int_0^a \frac{1}{h^2} dx \right)} x \quad (41)$$

The coercivity properties must be examined for the following operator

$$L(p) = \frac{\int_0^a \frac{\rho_0}{\rho h^3} dx}{p_a - p_0 - 6\mu U \int_0^a \frac{1}{h^2} dx} \frac{dp}{dx} x \quad (42)$$

Coercivity requires that

$$\int_0^a L(p) p dx \geq \alpha^2 \int_0^a p^2 dx \quad (43)$$

In our case

$$\int_0^a L(p) p dx = \frac{\int_0^a \frac{\rho_0}{\rho h^3} dx}{p_a - p_0 - 6\mu U \int_0^a \frac{1}{h^2} dx} \int_0^a p x \frac{dp}{dx} dx \quad (44)$$

The following integral holds

$$\int_0^a p x \frac{dp}{dx} dx = p^2 x \Big|_0^a - \int_0^a p x \frac{dp}{dx} dx - \int_0^a p^2 dx \quad (45)$$

from which

$$\int_0^a p x \frac{dp}{dx} dx = \frac{1}{2} \left(p_a^2 a - \int_0^a p^2 dx \right) \quad (46)$$

If the following expression

$$\frac{\int_0^a \frac{\rho_0}{\rho h^3} dx}{p_a - p_0 - 6\mu U \int_0^a \frac{1}{h^2} dx} \quad (47)$$

appearing in Eqn. (44) is negative, and if $p_a=0$, whereas p_0 may assume any value, expression (47) holds true, where

$$\alpha^2 = \frac{\int_0^a \frac{\rho_0}{\rho h^3} dx}{2 \left(p_0 + 6\mu U \int_0^a \frac{1}{h^2} dx \right)} \quad (48)$$

Consequently, the operator L of expression (44) is coercive.

The treatment of integral (38) as a known constant requires specific comments. In reference [15], a boundary condition expressing the flow has been adopted. This condition contains integral (38), which may thus be regarded as known. In this paper a different, probably more general approach is followed.

Once the solution has been computed for a certain cavitation problem, integral (38) may be evaluated *a posteriori*. The previous passages show that, for any negative value considered for expression (37), which contains integral (38), operator (44) is coercive, and, therefore, a unique solution exists. Consequently, if expression (37) computed from the solution of a certain cavitation problem is negative and if $p_a=0$, the solution is unique for that problem. In other words, a unique pair of the variables p and r exists that solves the problem.

It is finally noted that the value of the pressure gradient computed, say, at the inlet, from (15) is

$$h^2 \left. \frac{dp}{dx} \right|_{x=0} = \frac{p_a - p_0 - 6\mu U \int_0^a \frac{1}{h^2} dx}{\rho h|_{x=0} \int_0^a \frac{1}{\rho h^3} dx} + 6\mu U \quad (49)$$

If the fluid does not cavitate at the inlet, $\rho=\rho_0$ at the inlet, and the above integral contains integral (37), which may thus be univocally correlated to the pressure gradient at the inlet.

The practical impact of the above result is as follows. For a solution obtained for a certain cavitation problem, it may be clarified *a posteriori* whether the conditions are fulfilled under which the solution obtained is unique.

The second weight function. The second weight function is $a-x$. The definition of r in (35) must be changed accordingly.

By employing in Eqn. (34) the term $(a-x)$ instead of x , the coercivity requirement (5) becomes

$$\int_0^a L(p)p dx = \frac{\int_0^a \frac{\rho_0}{\rho h^3} dx}{p_a - p_0 - 6\mu U \int_0^a \frac{1}{h^2} dx} \int_0^a p(a-x) \frac{dp}{dx} dx \quad (50)$$

The following integral holds

$$\int_0^a p(a-x) \frac{dp}{dx} dx = p^2(a-x) \Big|_0^a - \int_0^a p(a-x) \frac{dp}{dx} dx + \int_0^a p^2 dx \quad (51)$$

from which

$$\int_0^a p(a-x) \frac{dp}{dx} dx = \frac{1}{2} \left(p_0^2 a + \int_0^a p^2 dx \right) \quad (52)$$

If the following expression

$$\frac{\int_0^a \frac{\rho_0}{\rho h^3} dx}{p_a - p_0 - 6\mu U \int_0^a \frac{1}{h^2} dx} \quad (53)$$

appearing in (50) is positive, and if $p_0=0$, whereas p_a may assume any value, expression (5) holds true, where

$$\alpha^2 = \frac{\int_0^a \frac{\rho_0}{\rho h^3} dx}{2 \left(p_a - 6\mu U \int_0^a \frac{1}{h^2} dx \right)} \quad (54)$$

Consequently, the operator L of expression (34) (in which x must be substituted with $(a-x)$) is coercive.

The above result could have been derived directly from the conclusions regarding the first weight function, by changing p_0 with p_a , and by inverting the sign of U .

The third weight function. The third positive, linear weight function considered here is

$$p_a^2 + \frac{p_o^2 - p_a^2}{a} x \quad (55)$$

where p_0 and p_a are assumed to be different. The definition of r in (35) must be changed accordingly. In Eqn. (34), the term (55) must be employed instead of x .

The following integral holds

$$\int_0^a p \left(p_a^2 + \frac{p_o^2 - p_a^2}{a} x \right) \frac{dp}{dx} dx = p^2 \left(p_a^2 + \frac{p_o^2 - p_a^2}{a} x \right) \Big|_0^a - \quad (56)$$

$$\int_0^a p \left(p_a^2 + \frac{p_o^2 - p_a^2}{a} x \right) \frac{dp}{dx} dx - \frac{p_o^2 - p_a^2}{a} \int_0^a p^2 dx$$

Since

$$p^2 \left(p_a^2 + \frac{p_o^2 - p_a^2}{a} x \right) \Big|_0^a = p_a^2 p_o^2 - p_o^2 p_a^2 = 0 \quad (57)$$

integral (56) becomes

$$\int_0^a p \left(p_a^2 + \frac{p_o^2 - p_a^2}{a} x \right) \frac{dp}{dx} dx = -\frac{p_o^2 - p_a^2}{2a} \int_0^a p^2 dx \quad (58)$$

If the following expression

$$\frac{(p_a^2 - p_o^2) \int_0^a \frac{\rho_0}{\rho h^3} dx}{p_a - p_o - 6\mu U \int_0^a \frac{1}{h^2} dx} \quad (59)$$

appearing in the equivalent of (50) is positive, expression (5) holds true, where

$$\alpha^2 = \frac{(p_a^2 - p_o^2) \int_0^a \frac{\rho_0}{\rho h^3} dx}{2a \left(p_a - p_o - 6\mu U \int_0^a \frac{1}{h^2} dx \right)} \quad (60)$$

It is noted that this third approach does not include the first two approaches. For instance, the first approach holds for $p_o = p_a = 0$, a situation to which the third approach is not applicable.

The three above results on the coercivity of operator $L(p)$ hold when some restrictions are fulfilled. Unfortunately, it was not possible to derive, with the above approach, coercivity results of more general validity.

6. CONCLUSIONS

The recently proposed complementarity formulation of lubricated cavitated contact has been examined. For some particular situations it has been demonstrated that the operator connecting the two complementary variables is coercive. This property entails the existence and uniqueness of the solution, and it provides a solid background to the employment of complementarity routines for locating the cavitated intervals.

REFERENCES

- [1] Kostreva, M.M., 1984. "Pressure spikes and stability considerations in elastohydrodynamic lubrication models". *J. Tribol.*, **106**, pp. 386–393.
- [2] Strozzi, A., 1986. "The elastohydrodynamic problem expressed in terms of extended variational formulation". *J. Tribol.*, **108**, pp. 557–564.
- [3] Strozzi, A., 1992. "Contact stresses in hip replacements". PhD Thesis, University of Durham, U.K.
- [4] Strozzi, A., 1987. "An assessment of the numerical solution of the elastohydrodynamic problem for soft contacts". *Wear*, **115**, pp. 53–61.
- [5] Cannarozzi, A.A., 1980. "On the resolution of some unilaterally constrained problems in structural engineering". *Computer Methods in Applied Mechanics and Engineering*, **24**, pp. 339–357.

- [6] Oh, K.P., 1984. "The numerical solution of dynamically loaded elastohydrodynamic contact as a nonlinear complementary problem". *ASME J. of Lubrication Technology*, **106**, pp. 88–95.
- [7] Strozzi, A., 1985. "Formulation of three lubrication problems in terms of complementarity". *Wear*, **104**, pp. 103–119.
- [8] Giacomini, M., Fowell, M.T., Dini, D., and Strozzi, A., 2010. "A mass-conserving complementarity formulation to study lubricant films in the presence of cavitation". *ASME J. Tribol.*, **132**, pp. 1–12.
- [9] Kinderlehrer, D., and Stampacchia, G., 2000. *An introduction to variational inequalities and their applications*, Vol. 31., Siam.
- [10] Rohde, S. M., and McAllister, G. T., 1975, "A Variational Formulation for a Class of Free Boundary Problems Arising in Hydrodynamic Lubrication". *Int. J. Eng. Sci.*, **13**(9–10), pp. 841–850.
- [11] Grando, F.P., Prieta, M., and Prata, A.T. 2006. "A two-phase flow approach to cavitation modelling in journal bearings". *Tribology Letters*, **21**, pp. 233–244.
- [12] Avan, E.Y., Spencer, A., Dwyer-Joyce, R. S., Almqvist, A., and Larsson, R., 2013. "Experimental and numerical investigations of oil film formation and friction in a piston ring–liner contact". *Proceedings of the Institution of Mechanical Engineers, Part J: Journal of Engineering Tribology*, **227**, pp. 126–140.
- [13] Kirby, R.C., 2010. "From Functional Analysis to Iterative Methods". *SIAM Rev.*, **52**, pp. 269–293.
- [14] Nagurney, A., 2002. *Variational Inequalities*. Internal report, Isenberg School of Management, University of Massachusetts, Amherst, MA 01003.
- [15] Bayada, G., Mohamed El Alaoui T., and Khalid Ait H., 2007. "Existence and uniqueness for a non-coercive lubrication problem". *Journal of mathematical analysis and applications*, **327**(1), pp. 585–610.
- [16] Goeleven, D., 1996. *Noncoercive variational problems and related results*, Longman.

VISCOELASTIC AND MAGNETORHEOLOGICAL PROPERTIES OF MAGNETIC SILLY PUTTY

Nicola Golinelli

*Dipartimento di Scienze e Metodi dell'Ingegneria,
University of Modena and Reggio Emilia, Italy
E-mail: nicola.golinelli@unimore.it*

Andrea Spaggiari

*Dipartimento di Scienze e Metodi dell'Ingegneria,
University of Modena and Reggio Emilia, Italy
E-mail: andrea.spaggiari@unimore.it*

Eugenio Dragoni

*Dipartimento di Scienze e Metodi dell'Ingegneria,
University of Modena and Reggio Emilia, Italy
E-mail: eugenio.dragoni@unimore.it*

Abstract - In this work the elastic and viscous properties of the Silly Putty are considered. Silly Putty is a non-newtonian material whose properties depend on the rate at which it is deformed. For a rapid deformation it behaves as an elastic solid while over a relatively long time scale stress, the polymer molecules can be untangled and it flows as a fluid. The Silly Putty under study also presents a percentage of volume fraction of ferromagnetic particles. Thus, the purpose of this paper is to assess the behavior of this material under compression and shear tests combined with several value of magnetic field. The experimental test in compression mode show no dependence on the magnetic field, probably due to the perpendicularity among the magnetic flux and the force direction. Conversely, despite the poor mechanical properties of the Silly Putty, in shear mode an increment in the yield stress due to the magnetic field is found.

Keywords- silicone polymers, magnetorheological elastomers, design of experiment.

1 INTRODUCTION

Silly Putty is the commercial name of a material produced by Dow Corning Corporation (Dow Corning 3179 dilatant compound) based on silicone polymers which display unusual physical properties. Silly putty was discovered in 1943 by a Scottish engineer, James Wright, working for General Electric in Connecticut. During the second world war the supply of rubber in to the US was being cut off by the Japanese and so the government set industry the task

of developing a synthetic alternative. James Wright mixed boric acid with silicone oil and polyborosiloxane was created. Later, Wright found that the substance did not have all the properties needed to replace rubber, so it was not used for any purpose. This new polymer did not win widespread use until 1949, when Peter Hodgson bought the production rights from GE. Hodgson changed its name to *Silly Putty* and started to sell the bouncing putty as a toy. In 1961 *Silly Putty* went worldwide and other uses were found. The material's unique properties have found niche use in medical and scientific applications. Physical therapists use it for rehabilitative therapy of hand injuries. A number of other brands alter the material's properties, offering different levels of resistance. Because of its adhesive characteristics, it was even used by Apollo 8 astronauts to secure their tools in zero-gravity. *Silly Putty* is composed of 65% polydimethylsiloxane (PDMS), 17% silica (crystalline quartz), 9% Thixatrol ST (castor oil derivative), 4% dimethyl siloxane (hydroxy-terminated polymers with boric acid), 1% glycerine, and 1% titanium dioxide. *Silly Putty*'s unusual flow characteristics are due to the ingredient polydimethylsiloxane (PDMS), a viscoelastic liquid. Viscoelasticity is the property of materials that exhibits both viscous and elastic characteristics depending on the deformation rate. Viscous fluid materials, like honey, resist shear flow and strain linearly with time when a stress is applied. Elastic solid materials, strain when stretched and immediately return to their original state once the stress is removed. Viscoelastic materials behaves combining both the fluid and solid characteristic. Depending on the change of strain rate versus stress inside a material the viscosity can be categorized as having a linear, non linear, or plastic response.

Because the relation between shear stress and shear rate is not linear, *Silly Putty* may be characterized either as a dilatant fluid or a pseudoplastic fluid. A dilatant or shear-thickening materials (Figure 1) are mixtures that exhibit an increase in apparent viscosity as the rate of shear increases. When shear forces become larger in magnitude than repulsive interparticle forces, the molecules shift from a layered to a disordered structure, causing an increase in viscosity. In the opposite case, when the viscosity decreases with increases shear rate, the fluids are called pseudoplastic or shear-thinning fluids (Figure 1). There are two mechanisms (and hence two characteristic time scales) at work in this material. The high molecular weight PDMS has a characteristic relaxation time, defined by the time that a random walk allows the chain to relax from a stretched state through thermal vibrations. Moreover, due to the boric acid there are also transient Boron mediated "crosslinks" arising from associating Boron linkages. These act to give the *Silly Putty* a behavior more like an elastic solid than a liquid. However, since these "crosslinks" are dynamic the material is not permanently locked in place and can consequently flow under long time scale stress. In scientific literature a few studies were carried out to determine the viscoelastic properties of the *Silly Putty*. Cross et. al.[1] subjected the material to a rapid deformations by dropping different masses at different height onto one end of a *Silly Putty* cylinder, thus he was able to assess the deformations and the elastic forces at different speeds rate. Cross studied slow deformations by compressing the cylinder in a material testing machine at a fixed rate which was varied from 200 mm/min to 1000 mm/min. It was found an increase in the force by about a factor of 3, at any given displacement, when the compression rate increased by a factor of 5. Other tests have shown that the mechanical properties of *Silly Putty* are temperature dependent. Testing the material up to failure in temperature leads an elongation at break of 200% higher compared to an increase of 10°C. The volume percentage of the ferromagnetic particles of the commercial

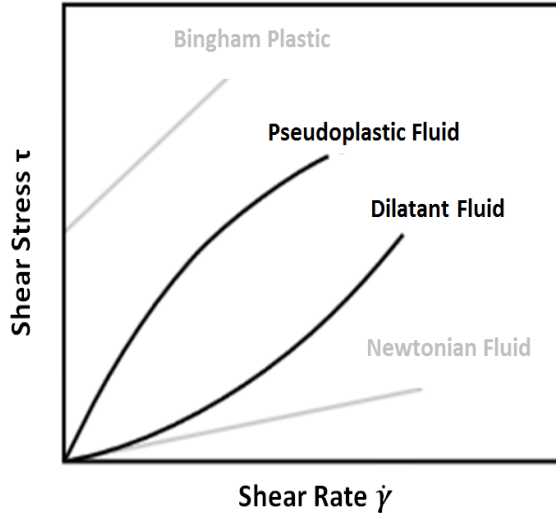


Figure 1. Different types of responses to a change in strain rate

magnetic *Silly Putty* is about 3.3%. In [2] four isotropic PDMS based magnetorheological elastomer samples with different percentages of iron particles were fabricated. Steady state and dynamic tests such as strain amplitude sweep and angular frequency sweep were used to test the magnetorheology of PDMS MREs and the results could be applied also to the magnetic *Silly Putty*. The steady state tests showed that the increase of iron particles in the sample would diminish the viscoelastic linear range of MREs. The dynamic and magnetic field intensity sweep test proved that the samples with higher iron weight fraction show higher initial storage and loss moduli and also higher MR effects.

The aim of this paper is to test the behavior of the magnetic *Silly Putty* and to evaluate whether or not there is a dependence on the magnetic field. Hence, a compression and shear tests were performed at different levels of deformation rate and intensity of magnetic field. A design of experiment technique was applied to the experimental tests, [3] to verify statistically the influence of each variable considered. Two kind of surfaces response were built, based on the experimental tests to link yield stress (σ for squeeze mode, τ for shear mode), magnetic field and time of application. An analysis of variance was used to verify whether or not the magnetic field is significant and it was found an influence of the applied magnetic field only in the shear tests.

2 MATERIALS AND METHODS

Experimental Apparatus

The experimental tests were carried out using the universal testing machine Galdabini Sun 500 (Figure 2) which is equipped with two different fixtures to perform both compression and shear tests. Since *Silly Putty* has an elastomeric nature due to PDMS, overconstraining would led to



Figure 2. Experimental apparatus

extremely high stresses, due to its Poisson's ratio close to 0.5. Hence, the material was placed confined only from the yoke of the magnetic system (Figure 3). The force was measured by a load cell located onto the head of the testing machine. These data sets were exported from the software of the testing machine to calculate by analytical formulae the yield stress values. The values of the velocities, of the magnetic field and the time of application of the latter are described in the Experimental Plan subsection. The current was supplied in DC mode to the coil by a stabilized TTI power supply system.

Magnetic System

One of the purposes of this paper is the study of the behavior of the magnetic *Silly Putty* under various magnetic fields, so the design of the magnetic system plays a key role. To increase the efficiency and the accuracy of the applied magnetic field during the experimental tests, particular attention was paid to the materials and the flux lines. On the one hand the compression tests (Figure 3(a)), both the support plate (A) and the punch (D) are made in aluminium, a paramagnetic material, in order to deflect as least as possible the magnetic flux through the *Silly Putty*. On the other hand in shear mode (Figure 3(b)) was used a steel punch, so in this way the magnetic flux lines may cross the two meatus of *Silly Putty* without deviations. The magnetic system was obtained by cutting a low carbon steel square bar, welded forming the traditional magnetic yoke shape and inserted in a copper coil. The copper coil was made using an AWG 22 wire (diameter 0.64 mm) with 1700 coils [4]. A finite element

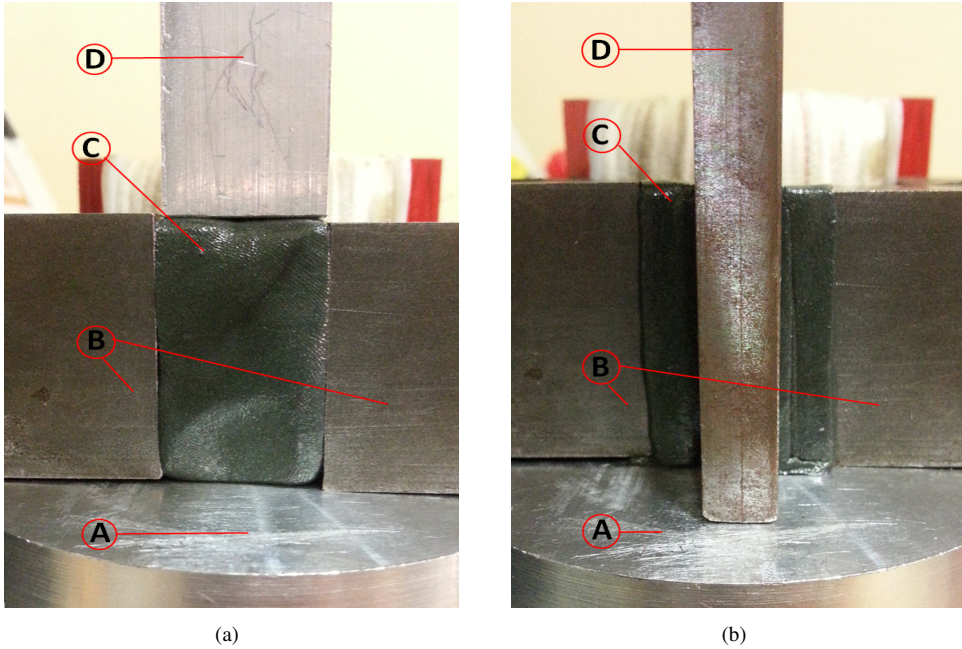


Figure 3. Compression (a) and Shear (b) mode settings

analysis of the magnetic system was performed by means of FEMM 4.2 software (Finite Element Method Magnetics, [5]), and in order to verify the values obtained it was used the hall effect probe of the Gaussmeter Hirst GM05. The model of the magnetic core can be considered as a 2D magnetostatic problem (Figure 4). Specifically, FEMM broken down the problem domain using 13043 discrete triangular elements and 6674 nodes. Over each element, the solution is approximated by a linear interpolation of the values of potential at the three vertices of the triangle.

Experimental Plan

Many experiments involve the study of two or more variables over the response. In general, factorial designs are very efficient for this type of experiments. Factorial design, means that in each complete trial or replication of the experiment all possible combinations of the levels of the factors are investigated. A variable is a characteristic under consideration while a level is a peculiar value of the variable. This method focuses on three variables which influence the behavior of the system, it is able to identify the interaction between these variables precisely, and to provide a reliable model to describe the system behaviour. In this experiment, both for compression and shear mode, the variables involved are the compression/shear rate (S), the applied magnetic field (B) and the time of application of the latter (seconds). The values adopted for the magnetic field are 0mT, 100mT and 200mT with a supply current of 0A, 1A and 2A respectively. Considering the compression rate and the shear rate, were adopted the

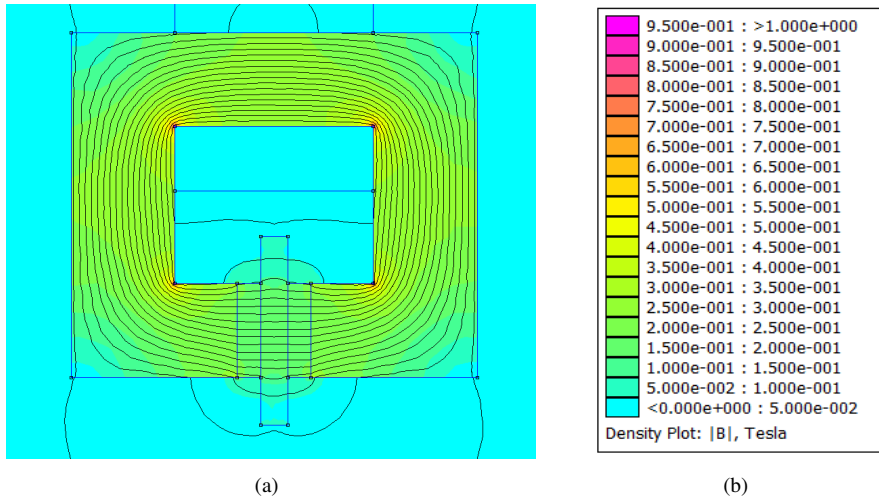


Figure 4. 2D FEMM simulation model (a) and magnetic field values (b)

Table 1. Experimental Plan for both compression and shear tests.

Levels	I	II	III
Magnetic Field, B, mT	0	100	200
Deformation Rate, S, mm/min	200	500	1000
Time, T, sec	0	150	300
Replicate	3 for each combination		
Experimental Points	27		
Grand total	81		

same values used by Cross [1] which are divided in three levels, 200mm/min, 500mm/min and 1000mm/min. The time of application of the magnetic field is also considered on three levels that is, 0 seconds, 150 seconds and 300 seconds. The completed experimental plan is reported in Table 1.

3 RESULTS AND DISCUSSION

Compression Mode

Experimental Results. Figure 5(a), 5(b), 5(c) show the experimental results in compression mode. The forces of the *Silly Putty* are a function of the applied 10mm displacement, at different compression rate (dashed lines are the tests at 1000 mm/min, dotted lines at 500 mm/min and solid lines at 200 mm/min). The figures depict the trends of the forces at different values of magnetic field applied and time of application. The data obtained are consistent to

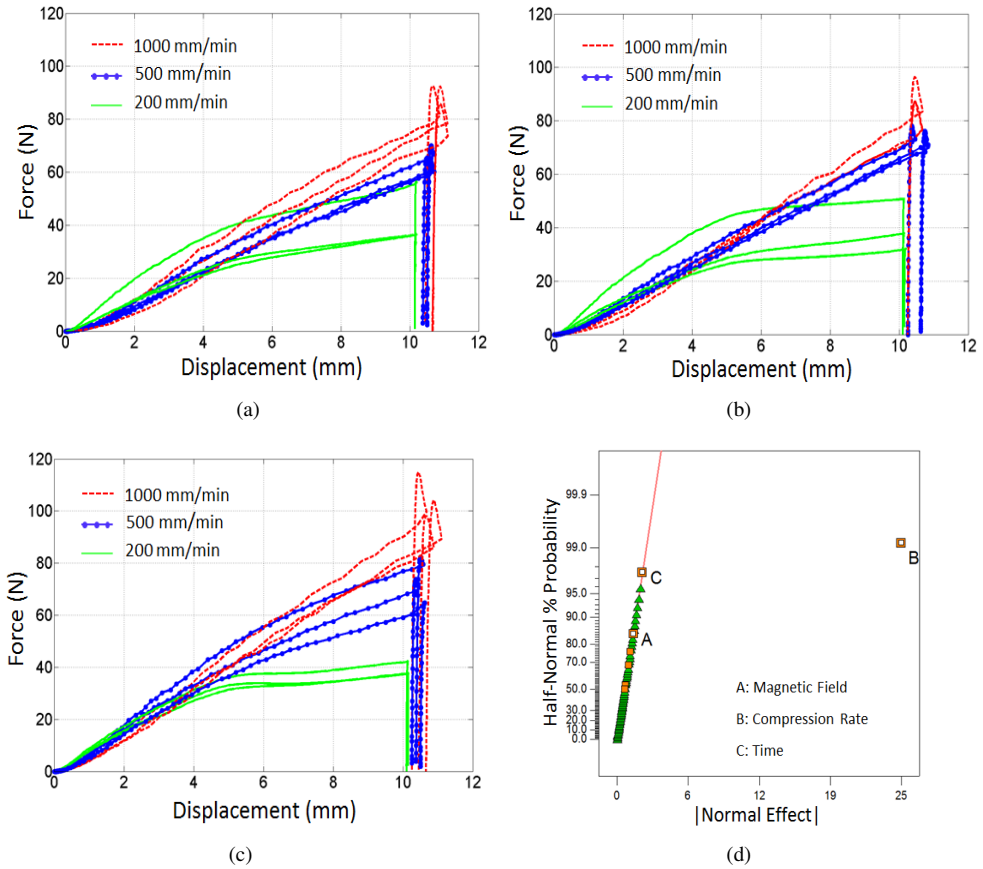


Figure 5. (a) Force-Displacement $B=0$ mT, $T=0$ sec, (b) $B=100$ mT, $T=150$ sec, (c) $B=200$ mT, $T=300$ sec., (d) Half-Normal plot of the yield strain stress: effect of the magnetic field A, compression rate B and time C.

those obtained from the experiment in [1]. It was found an increase in the force by about a factor of 3, at any given displacement, when the compression rate increased by a factor of 5. Furthermore, from the experimental curves, it is possible to qualitatively evaluate that both the applied magnetic field and the time does not significantly influence the yield stress. A possible reason is that the force direction and the magnetic flux lines are perpendicular to each other so they do not increase the mechanical properties of *Silly Putty*.

Analysis of Variance. Even though this is not a pure compression test the compressive stress σ is calculated as follows:

$$\sigma = \frac{F}{A} = \frac{F}{660} \text{ (MPa)} \quad (1)$$

Table 2. ANOVA of the considered variables. F values represent the influence of the variable on the response, p-value are the probability of error.

Variable	F-value	p-value
A-Magnetic Field	1.85	0.1651
B-Compression Rate	315.19	<0.0001
C-Time	3.58	0.0328

Table 3. Average values of compression stress σ . B is expressed in mT, S in mm/min.

	Magnetic Field (mT)			
	0	100	200	
Compression Rate (mm/min)	200	0.0524	0.0572	0.0580
	500	0.1044	0.1092	0.1100
	1000	0.1303	0.1351	0.1358

where A is the cross-section area of the punch. Having such estimates, one could then construct a list of the main effects and interactions ordered by the effect magnitude. Figure 5(d) called Half-Normal probability plot provided by Design Expert 8.0 [6], is a graphical tool that uses the estimated effects to assess which factors are significant. Since the half normal line starts at the origin, this produces a more sensitive scale for detection of significant outcomes [7] which are immediately detected at a glance. The X-axis represents the standardized effect associated with each factor considered (Table 1). The greater the standardized effect, the higher the influence of the variable on the response. The Y-axis represent the half-normal probability associated with each effect. The solid line interpolating the points represents the error of the test (given by the non influential interactions between the variables). The triangles are an expression of the sum of errors, which is calculated by the software. Since both magnetic field (A) and time of application (C) are superimposed on the error line of the normal distribution of the experimental error (stochastic distribution), ANOVA demonstrates that these variables does not influence the process. The compression rate point (B) fall off the error line so represent the only factor that mainly affect the tests.

In Table 2 are reported only the significant variables which are used to build the overall prediction models. The F value derives from the F-test [8], and gives a quantitative expression of the influence of each variable on the problem. The greater the F value, the greater the influence. Table 3 shows the averages of compression stress for each level of magnetic field and compression rate. It may be noted that the values increase from top to bottom (compression rate increase) but not from left to right (magnetic field increase), confirming that compression rate is the only significant variable.

Response Surface. This subsection deals with the construction of a response surface function of the factors involved in these tests. ANOVA analysis provides the final equation in

term of coded factor:

$$\sigma = 0.10 - 3.476e^{-3}A[1] + 1.357e^{-3}A[2] - 0.043B[1] + 8.7046e^{-3}B[2] \quad (2)$$

Coded factors transform the scale of measurement for a factor so that the high value becomes +1 and the low value becomes -1. Design descriptions and analysis for designed experiments are best done with coded factors. Coding reduces the range of each factor to a common scale, so the coefficients A[1], A[2], B[1] and B[2] are defined on a coded scale from -1 to +1 (Figure 6). For a two-level categoric factor the coefficient is half of the difference between the average at high and low levels. Conversely, for multilevel categoric factors the first coefficient is the difference of level 1 from the overall average, the second coefficient is the difference of level 2 from the overall average and so on. The negative sum of all the coefficients is the difference of the last level from the overall average.

Starting from these values and interpolating it has been possible to obtain the equation that characterize their behavior as a function of their associated variables. For values of magnetic field B between 0 and 100 mT:

$$A[1] = \frac{100 - B}{100}; \quad A[2] = \frac{B}{100} \quad (3)$$

while, for values greater than 100 mT up to 200 mT:

$$A[1] = \frac{100 - B}{100}; \quad A[2] = -2 \left(\frac{B - 100}{100} \right) + 1 \quad (4)$$

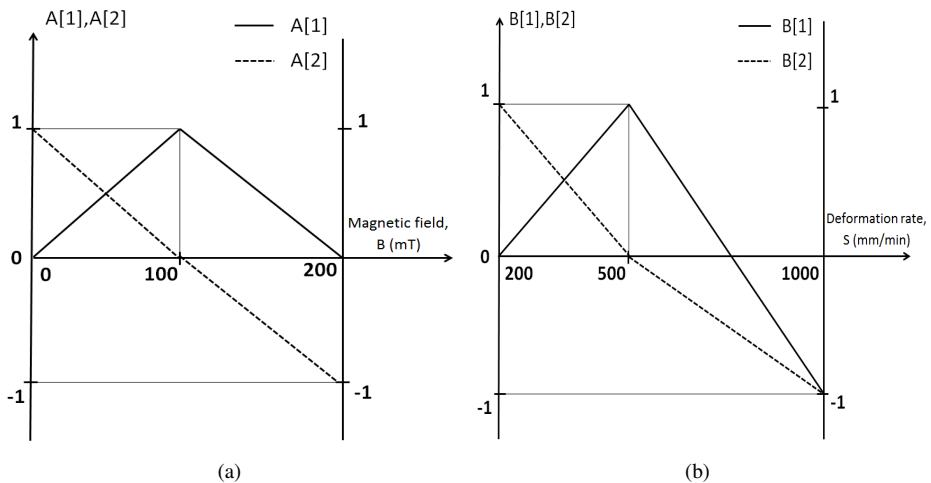


Figure 6. Coded factor diagram of Magnetic field (a) and Compression rate (b)

For values of compression rate S between 200 and 500 mm/min:

$$B[1] = \frac{500 - S}{300}; \quad B[2] = \frac{S - 200}{300} \quad (5)$$

and for values greater than 500 mm/min up to 1000 mm/min:

$$B[1] = \frac{500 - S}{500}; \quad B[2] = -2 \left(\frac{S - 500}{500} \right) + 1 \quad (6)$$

Figure 7 shows the response surface obtained using the Curve Fitting toolbox of Matlab ([9]). The accordance with the average values is good ($R^2=0.90$). A polynomial interpolation was adopted with the following equation (B is the magnetic field, S is the compression rate):

$$\sigma = \sum_{i=0}^2 \sum_{j=0}^2 a_{ij} B^i S^j \quad (7)$$

the coefficient a_{ij} reported in the matrix of coefficient of Table 4.

Table 4. Matrix of coefficient calculated to plot the surface response.

a_{ij}	j		
	0	1	2
0	8.358	0.272	-15e-5
i 1	0.073	3.763e-5	0
2	-31e-5	0	0

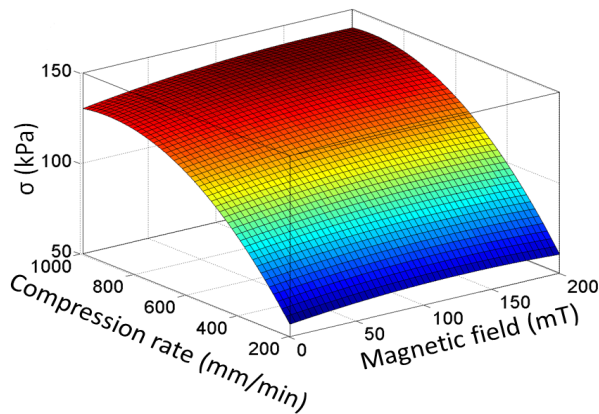


Figure 7. Response Surface (grid) for the yield strain stress

Shear Mode

Experimental Results. Figures 8(a), 8(b), 8(c) depict the trends of the forces as a function of the applied displacement which is 50mm. Each graph also shows the values of forces as a function of the shear rate. Dashed lines represent the tests carried out at 1000mm/min. Solid black lines show the tests at 500mm/min while solid gray lines are the tests at 200mm/min. In shear mode, it can be seen an increment in the shear strength of the material at constant strain rate. Due to magnetic field, at 200 mm/min strain rate, going to zero magnetic field to 200 mT with an application time of 300 sec., the maximum τ increases by 57.04 %. At 500 mm/min shear rate, the increase reported to τ max is 24,57 %, while at 1000 mm/min is 41,48 %. In shear mode, the force of attraction between the magnetic system and the punch is about 4 N, so can be neglected compared to the force exerted by the material. The percentage increase is greater when the speed value is at the lowest level because of the nature of the visco-elastic material. Increasing the shear rate leads to a predominant effect of the viscoelasticity over the magnetic effect.

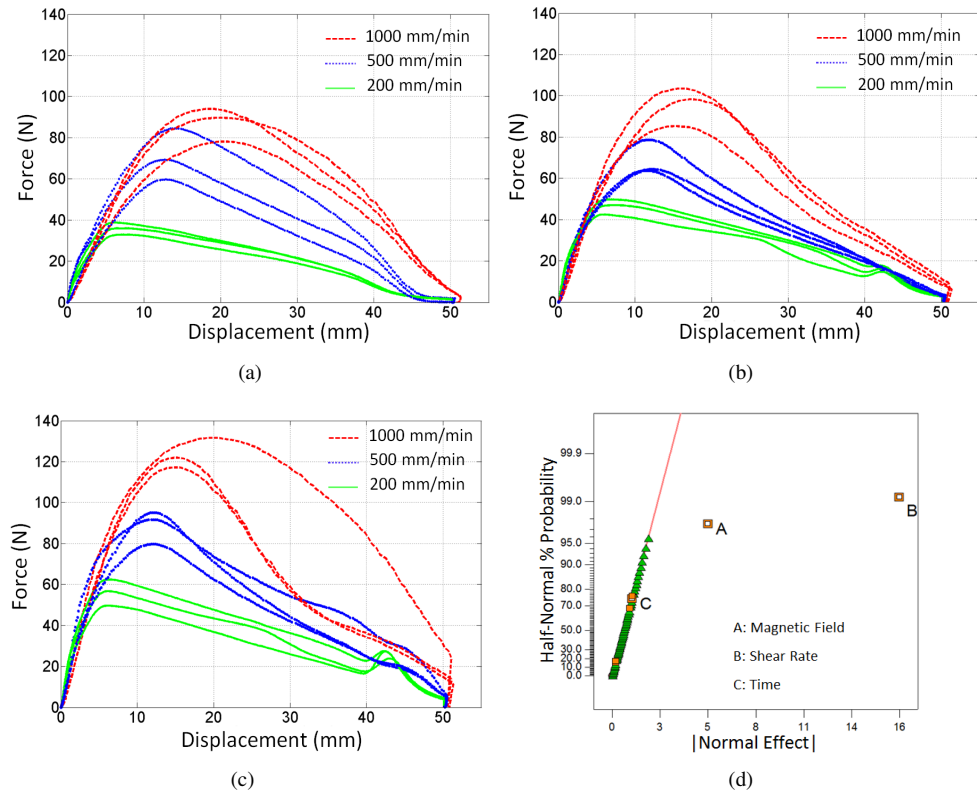


Figure 8. (a) Force-Displacement $B=0$ mT, $T=0$ sec, (b) Force-Displacement $B=100$ mT, $T=150$ sec, (c) Force-Displacement $B=200$ mT, $T=300$ sec, (d) Half-Normal plot of the yield shear stress: effect of the magnetic field A, share rate B and time C.

Analysis of Variance. The results of the experimental tests were analysed using shear stress rather than the forces. The stresses are a more significant parameter when studying the mechanical properties of a material and it can be compared with the compressive stresses. The shear stress is computed considering the forces provided by the universal testing machine and the contact surfaces and is:

$$\tau = \frac{F}{A} = \frac{F}{2 \cdot 30 \cdot 40} \text{ (MPa)} \quad (8)$$

The half-normal plot is able to show the influence of the factors on the variable response, that is in this case the shear stress τ . Figure 8(d), in contrast to compression tests, shows that the magnetic field becomes significant as well as the shear rate. For the sake of completeness, even in this case, the F values of the influence of each variable and the probability of error are reported in Table 5. Table 6 shows the average values of the shear stress τ for each level of magnetic field and shear rate. The influence of the applied magnetic field is confirmed by the fact that the values grow from top to bottom (shear rate increase) but also from the left to right (magnetic field increase).

Response Surface. In keeping with the former procedure, a coded equation was retrieved by Design Expert software. Since the factor and their levels are the same used in compression mode, the trends of the coefficients A and B are the same described in the subsection *Compression Mode - Response surface*.

$$\tau = 0.030 - 3.634e^{-3}A[1] - 5.151e^{-4}A[2] - 0.012B[1] + 2.116e^{-3}B[2] \quad (9)$$

Table 5. ANOVA of the considered variables. F values represent the influence of the variable on the response, p-value are the probability of error.

Variable	F-value	p-value
A-Magnetic Field	16.61	<0.0001
B-Compression Rate	135.58	<0.0001
C-Time	1.33	0.2695

Table 6. Average values of compression stress σ . B is expressed in mT, S in mm/min.

	Magnetic Field (mT)			
	0	100	200	
Shear Rate (mm/min)	200	0.0144	0.0175	0.0222
	500	0.0286	0.0318	0.0364
	1000	0.0365	0.0396	0.0443

Table 7. Matrix of coefficient calculated to plot the surface response.

b_{ij}	j		
	0	1	2
0	1.045	0.0785	-4.40e-5
i	1	0.018	-2.21e-6
	2	4.97e-5	0

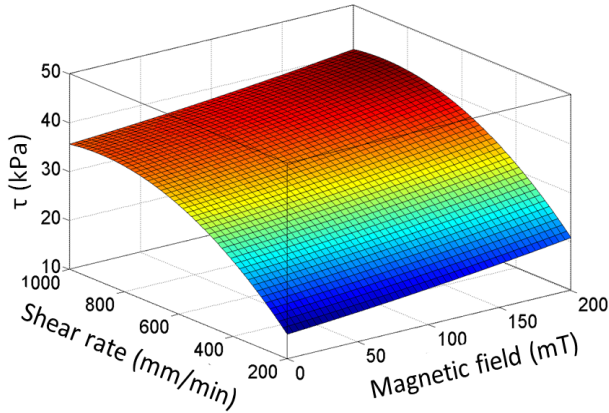


Figure 9. Response Surface (grid) for the yield shear stress

A response surface was built by the Curve Fitting toolbox of Matlab (Figure 9) using the equation 10. The coefficient used for the polynomial interpolation are showed in Table 7. Even in this case, the agreement with the experimental values is quite good ($R^2 = 0.93$).

$$\tau = \sum_{i=0}^2 \sum_{j=0}^2 b_{ij} B^i S^j \quad (10)$$

Compression vs Shear Mode

After analysing the influence of the magnetic field in compression mode and shear mode separately, in this subsection another analysis of variance was developed in order to assess the interaction between the field and test mode. In fact, performing an experimental plan including as a variable also the type of tests (compression mode or shear mode) was confirmed, in the half-normal plot of the ANOVA analysis, a significant influence of the interaction that exists among the tests mode and the strain rate (BD) (Figure 10). Even in this case, the F-values and the p-values for each variable are reported in Table 8.

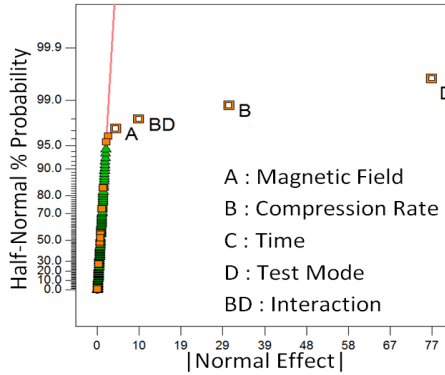


Figure 10. Half-Normal plot: effect of the magnetic field A, share rate B, time C, test mode D and BD interaction

Table 8. ANOVA of the considered variables. F values represent the influence of the variable on the response, p-value are the probability of error.

Variable	F-value	p-value
A-Magnetic Field	10.62	<0.0001
B-Deformation Rate	463.06	<0.0001
D-Test mode	2993.68	<0.0001
BD-Interaction	48.23	<0.0001

4 CONCLUSION

This work studies the behavior of magnetic *Silly Putty*. Several tests are carried out, by a universal testing machine, to evaluate the response of the material under compression and shear stress. Furthermore, a magnetic field is applied in order to assess the influence on the material properties. The tests are based on a design of experiment approach, thus all possible combinations of the levels of the factors are investigated. The presented results show that the forces retrieved in compression mode are not affected by the magnetic field, due to the perpendicularity between the force direction and the magnetic flux lines. Conversely, in shear mode, especially at slow shear rate (200 mm/min), applying magnetic field increases the maximum shear stress up to 50%.

REFERENCES

- [1] R. Cross, 2012. "Elastic and viscous properties of silly putty". *American Journal of Physics*, 8010:870.
- [2] T.F. Tian, X.Z. Zhang, W.H. Li, G. Alici, J. Ding, 2013. "Study of PDMS based magnetorheological elastomers". *Journal of Physics: Conference Series*, 412:012038.
- [3] D.C.Montgomery, 1997. *Design and Analysis of Experiment*. John Wiley and Sons, Inc., New York.

- [4] A. Spaggiari, E. Dragoni, 2012. "Effect of pressure on the flow properties of magnetorheological fluids". *Journal of Fluids Engineering*, 1349.
- [5] FEMM Finite Element Method Magnetics. <http://www.femm.info/wiki/homepage>.
- [6] Design expert 8.0, www.statease.com/dx8descr
- [7] M.J.Anderson,P.J.Whitcomb, 2007. *DOE Simplified: Practical tools for effective experimentation*. Productivity Press.
- [8] R.G. Lomax, 2012. *Statistical Concepts: a Second course for education and the behavioral sciences*, 4th ed. Routledge, London.
- [9] Matlab 7.14, <http://www.mathworks.com>.

A LOW FREQUENCY ENERGY CONVERTER FOR ELECTROMAGNETIC OR PIEZOELECTRIC ENERGY HARVESTING

Davide Castagnetti

Department of Engineering Sciences and Methods,

University of Modena and Reggio Emilia, Italy

E-mail: davide.castagnetti@unimore.it

Abstract. *Harvesting kinetic ambient energy usually involves the development of converters which operate in the low frequency range (from 0 to 100 Hz). A limit of the harvesters proposed in the literature is their relatively high operating frequency. This work deals with the development of a very low frequency energy harvester based on two counteracting Belleville springs. For a given height to thickness ratio, Belleville springs have nearly zero stiffness over a wide deflection range, thus giving the possibility to build a low frequency system. Either electromagnetic or piezoelectric transduction but also a hybrid of both can be applied to the proposed converter. A preliminary analytical and computational investigation of this solution is presented in the work showing promising results.*

Keywords: *energy harvesting, Belleville spring, low frequency, modeling*

1. INTRODUCTION

The work deals with the development of a very low frequency energy harvester exploiting Belleville springs. Kinetic ambient energy, which is the most common source for energy harvesting, usually occurs in the form of vibrations or random forces, being intrinsically frequency-variant in a low frequency range [1]-[3]. Therefore, it is challenging to develop energy harvesting systems able to efficiently harvest energy in the low frequency range. Among the available conversion techniques, electromagnetic and piezoelectric are surely the most promising in terms of simplicity, output current and voltage [2]-[3]. Many solutions have been presented in the literature either relying on electromagnetic [4]-[7] or on piezoelectric harvesting [8]-[15]. Recently, also non-linear harvesters have been proposed [12]-[13]. In addition, some hybrid harvesters combining piezoelectric and electromagnetic technology have been investigated [16]-[17].

A limit of the solutions proposed in the literature is their operating frequency. In case of electromagnetic harvesters, it falls in the range from 10 Hz to 100 Hz, while in case of piezoelectric harvesters, apart from few exceptions [11], [14]-[15], it is typically in the range from 50 Hz to 300 Hz.

The aim of this work is to overcome this limitation by proposing an innovative energy converter working at very low frequencies (below 10 Hz). This new solution is based on two counteracting Belleville springs and exploits their peculiarity, for a height to thickness ratio equal to 1.414, of nearly zero stiffness over a wide deflection range.

The paper is organized into three steps. In the first step we introduce the force-

deflection characteristic of Belleville springs and some engineering applications. In the second step, we propose and examine some conceptual solutions for an energy harvester relying on Belleville springs. The innovative nature of these solutions is their simple and compact structure, which can be organized either in series or parallel in order to improve the power output or achieve a multi-frequency behavior respectively. In the third step, the harvester is modeled both analytically and numerically.

Analytical and numerical results show a low operating frequency compared to solutions proposed in the literature, together with a high stroke providing an efficient energy conversion. Either electromagnetic or piezoelectric transduction but also a hybrid of both can be applied to this solution thus enhancing efficient energy conversion.

2. METHOD

Belleville springs: force-deflection behavior and applications

Patented by J. F. Belleville in 1867, the Belleville springs (Figure 1) are coned disk springs which have been extensively used in many engineering applications due to their peculiar characteristics. Belleville springs are compact along the loading axis, enable to obtain a wide variety of load-deflection characteristics by simply changing geometric proportions, and provide the possibility to vary the load-capacity and deflection range by using multiple springs in series and/or parallel.

Some examples of applications in industrial and machine constructions are spring suspensions, valves actuation, overload and slip clutches (to achieve the desired preload between friction discs), holding brake, backlash compensation, and in general applications involving energy storage or, more recently, impact energy dissipation [18]-[19].

An accurate analytical model for Belleville springs was proposed by Almen and Laszlo [20], which provided formulas for stresses and displacements calculation. According to this analytical model, the force-deflection relation of a Belleville spring (Figure 1) is given by the following formula:

$$P = 4K \frac{E s^4}{D^2} \eta \quad (1)$$

where E is the Young's modulus of the material, s represents the spring thickness, D the outer spring diameter, K is defined as:

$$K = \pi \left(\frac{c}{c-1} \right)^2 \left(\frac{c+1}{c-1} - \frac{2}{\ln c} \right) \quad (2)$$

being c the ratio between the outer and inner diameter of the spring ($= D / d$), and finally η is defined by the following formula:

$$\eta = \frac{1}{1-\nu^2} \frac{f}{s} \left[\left(\frac{h}{s} - \frac{f}{s} \right) \left(\frac{h}{s} - \frac{1}{2} \frac{f}{s} \right) + 1 \right] \quad (3)$$

where ν is the Poisson's ratio of the spring material, f is the axial deflection of the spring, and h is the free height of the conical spring measured as the elevation of the truncated

cone formed by either the upper or lower surface. By assuming P_0 as the load which flattens the conical spring producing a deflection $f = h$, the following dimensionless relationship between load and deflection is obtained:

$$\frac{P}{P_0} = \frac{f}{h} \left[\left(\frac{h}{s} \right)^2 \left(1 - \frac{f}{h} \right) \left(1 - \frac{1}{2} \frac{f}{s} \right) + 1 \right] \quad (4)$$

The above relationship highlights that the spring rate of a Belleville spring can be easily varied over a wide range by simply changing the height to thickness ratio (h/s) of the conical disc. The normalized force-deflection curves in Figure 2 show to which extent the characteristic of a Belleville spring can vary from linear to largely non-linear by increasing the height to thickness ratio from zero to two. The curves corresponding to a low height to thickness ratio are approximately linear. For a ratio $h/s = 1.414$ (dashed line) the curve shows a nearly constant load for a deflection range which extends symmetrically across the flat position, from about 0.6 up to 1.4 the f/h ratio. This almost zero stiffness across the flat position can be usefully exploited to develop structures for energy harvesters. Values of the height to thickness ratio higher than 1.414 provide highly non-linear curves, where the load reaches a local maximum and minimum respectively before and after the flat position.

Conceptual harvester solutions

Figure 3 shows the conceptual solution of an energy harvester exploiting Belleville springs. Two counteracting Belleville springs ($B1$ and $B2$) are fixed to an external tubular frame (F), separated by a spacer (S) at the inner diameter and preloaded to their flat position through fixtures (R) at the outer diameter. A circular rod (T), which is free to translate in the horizontal direction, is supported by the Belleville springs. According to Figure 2, for an h/s ratio equal to 1.414, the Belleville springs allow the system to oscillate across a central equilibrium position, with a stiffness which is nearly zero for a stroke on each side about 20% of the height h of the spring.

This solution can be exploited both for electromagnetic and piezoelectric energy harvesting. On the one hand, by applying a permanent magnet (M) to each end of the rod and enclosing each magnet in a coil (C), a simple electromagnetic energy harvester is obtained. On the other hand, piezoelectric patches bonded to the surface of the Belleville springs, which are deformed by external vibrations, provide a simple piezoelectric converter. By combining both solutions, a hybrid electromagnetic and piezoelectric harvester can be easily obtained.

This solution can be the base for a multi-frequency harvester which combines either in a series or in parallel many similar systems, simply differing for the Belleville spring dimensions.

Analytical model of the harvester

Figure 4 shows the model of the equivalent mass-springs system corresponding to the converter in Figure 3. The elastic force on the sliding rod (T) can be simply calculated summing the opposite forces exerted by each counteracting Belleville spring, which are provided by equation (1). By observing that the initial condition for the system is an axial deflection f of both springs equal to their free height h , and hence the displacement variable u ranges from $-h$ to h , it is possible to obtain the following expression of the elastic force:

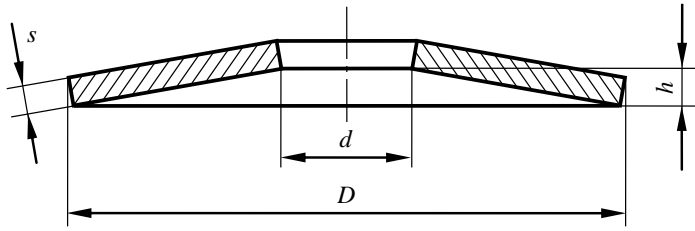


Figure 1. Section view of a Belleville spring.

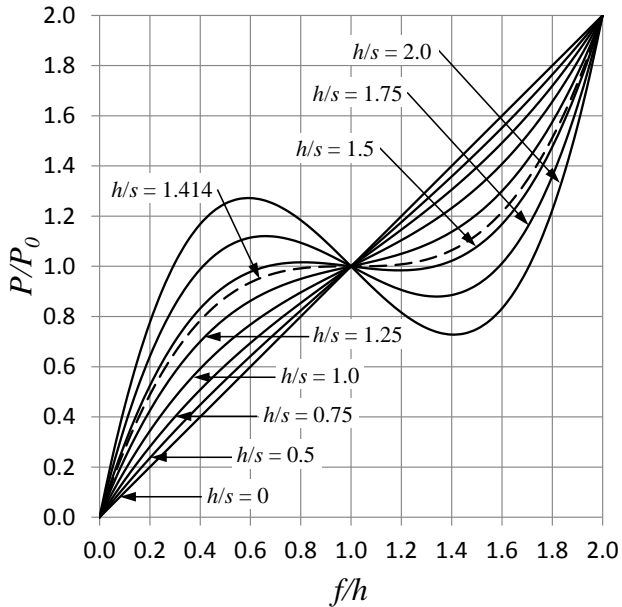


Figure 2. Dimensionless force-deflection curves for h/s ratios from 0 to 2.

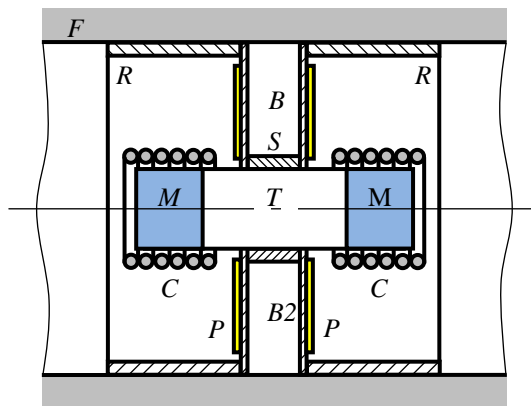


Figure 3. Conceptual solution for an energy harvester.

$$P = 4K \frac{E s^4}{D^2} (\eta_{B1} - \eta_{B2}) \quad (5)$$

where η_{B1} and η_{B2} refer to the Belleville springs *B1* and *B2* respectively, and according to equation (3) their expression is:

$$\eta_{B1} = \frac{1}{1-\nu^2} \frac{h-u}{s} \left[\left(\frac{h}{s} - \frac{h-u}{s} \right) \left(\frac{h}{s} - \frac{1}{2} \frac{h-u}{s} \right) + 1 \right] \quad (6)$$

$$\eta_{B2} = \frac{1}{1-\nu^2} \frac{h+u}{s} \left[\left(\frac{h}{s} - \frac{h+u}{s} \right) \left(\frac{h}{s} - \frac{1}{2} \frac{h+u}{s} \right) + 1 \right] \quad (7)$$

By replacing equation (6) and (7) into equation (5), the elastic force acting on the sliding rod (*T*) can be written as:

$$P = \frac{4K E s}{D^2 (1-\nu^2)} (u(h^2 - 2s^2) - u^3) \quad (8)$$

From equation (8) it appears that the elastic force on the rod (*T*) is non-linear with the displacement and equals zero when the rod is in central equilibrium position ($u = 0$).

The fundamental eigenfrequency of the system can be found from the differential equation of motion which governs the free motion of the undamped system:

$$m\ddot{u}(t) + \frac{4K E s (h^2 - 2s^2)}{D^2 (1-\nu^2)} u(t) - \frac{4K E s}{D^2 (1-\nu^2)} u^3(t) = 0 \quad (9)$$

where m is the mass of the rod (*T*). If small displacements across the equilibrium configuration in Figure 3 are considered, the linear part of the restoring elastic force (equation (8)) represents a good approximation. Therefore, equation (9) can be simplified to the following linear equation of motion:

$$m\ddot{u}(t) + \alpha u(t) = 0 \quad (10)$$

where:

$$\alpha = \frac{4K E s (h^2 - 2s^2)}{D^2 (1-\nu^2)}$$

By assuming a harmonic and symmetric motion for the system ($u(t) = u_0 \sin(\omega t)$), equation (10) provides the following fundamental circular frequency ω :

$$\omega = \frac{2}{D} \sqrt{\frac{K E s (h^2 - 2s^2)}{m(1-\nu^2)}} \quad (11)$$

Accordingly, the fundamental frequency f is equal to:

$$f = \frac{1}{\pi D} \sqrt{\frac{K E s (h^2 - 2s^2)}{m(1 - \nu^2)}} \quad (12)$$

Static and modal finite element analyses of the harvester

The finite element (FE) analyses which aimed at investigating the static and modal response of the harvester, involved two steps. First, a mass-spring FE model was implemented to assess the accuracy of the analytical model. Second, by exploiting the axisymmetry of the harvester, an axisymmetric FE model was implemented focused on its static response. Both FE models investigated a harvester including two Belleville springs with the geometry described in Table 1. The rod was assumed to be a solid cylinder 20 mm long and with a diameter equal to the inner diameter (d) of the Belleville springs.

The mass-spring model describes the rod (T) as a plane rigid body having the same mass of the rod itself. The two Belleville springs, which connect the mass to the outer frame, were described through non-linear spring connectors between the mass and the ground. The force-displacement characteristic of these connectors was defined according to equation (1), considering a height to thickness ratio (h/s) of the Belleville spring equal to 1.414. In order to simplify the FE model and directly coping with the harvester configuration, the force acted by the spring was set to zero in the initial configuration (zero displacement), thus corresponding to the central equilibrium position of the harvester. Built-in constraints were applied to the end of each spring, to reproduce its connection to the ground. Four static and one modal analysis steps are involved. The four static analysis steps displace the rod to f , 0, $-f$ and 0, respectively in order to reproduce a full load cycle. The final modal analysis step, which considers the rod free to oscillate across its center position, was performed with the Lanczos algorithm.

The axisymmetric model of the harvester describes both the rod (T) and the Belleville springs through semi-structural quadratic shell elements, having a thickness equal to the radius of the rod and to the thickness s of the Belleville spring, respectively. Both the rod and the Belleville springs have a Young's modulus equal to 210000 MPa and a Poisson's ratio equal to 0.3. An internal constraint (called kinematic coupling), which equals the translational degrees of freedom of the inner node of the Belleville springs to those of the corresponding nodes on the rod, ensures kinematic connection between the parts of the system. Five static analysis steps are involved. The first static analysis step deforms the Belleville springs to their flat position by applying counteracting displacements, equal to the height h of the spring, to the outer nodes. Keeping this condition, which corresponds to the central equilibrium position of the harvester, subsequent analysis steps perform a complete load cycle of the rod as in the mass-spring FE model.

3. RESULTS

Figure 5 shows the load-stroke curves of the rod (T) provided by the analytical model (solid black line), by the FE mass-spring model (solid red squares), and by the FE axisymmetric model (solid blue circles) for the same harvester geometry (Table 1).

The fundamental frequency retrieved from the analytical model (equation (12)) is equal to 6.03 Hz, while that from the mass-spring FE model is equal to 6.00 Hz.

The admissible stroke of the converter is equal to two times the height of the Belleville springs, since they can deform symmetrically from the initial flat condition.

Figure 6 shows the radial and hoop strains which originates on top and bottom surfaces of the Belleville springs. Hollow triangles and solid triangles represent the radial strain on the bottom and top surface respectively, while hollow circles and solid circles describes the hoop strains on the bottom and top surface respectively. The strain curves, which are plotted along the radial direction, are calculated as the difference between the strain at the end-stroke position and that at the central equilibrium position of the converter. The bottom surface of each Belleville spring is that on the inner side of the converter (Figure 3).

4. DISCUSSION

The load-stroke curves in Figure 5 highlights a quite close agreement between the analytical and FE predictions, in particular for the mass-spring FE model. The curves exhibit a nearly zero stiffness of the harvester across the central equilibrium position (Belleville springs deformed at flat position), since the Belleville springs reciprocally counteract each other. The prediction provided by the axisymmetric FE model, in the range from $-f/2$ to $f/2$, slightly differs from the analytical model and mass-spring FE model predictions. According to the axisymmetric FE model the stiffness of the harvester across the central equilibrium position is nearly four times higher than that obtained from the other models. This disagreement, which can be imputed to a slightly different constraining of the springs in the axisymmetric FE model compared to the analytical model, supports the need for an experimental validation of this harvester solution. On the whole, this load-stroke response of the harvester highlights a strongly non-linear behavior at high values of the rod stroke. Due to the stiffening of the system as the rod stroke increases, the stroke that can be conveniently exploited is nearly half of the total one.

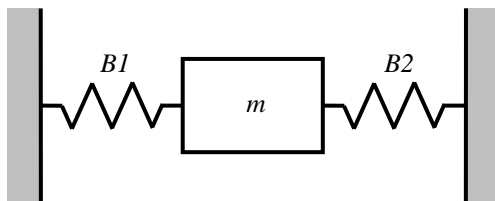


Figure 4. Equivalent mass-spring model of the elastic system.

Table 1 Dimensions of the Belleville springs.

Belleville spring dimensions	Value (mm)
Outer diameter, D	100
Inner diameter, d	20
Thickness, s	1
Height, h	1.414

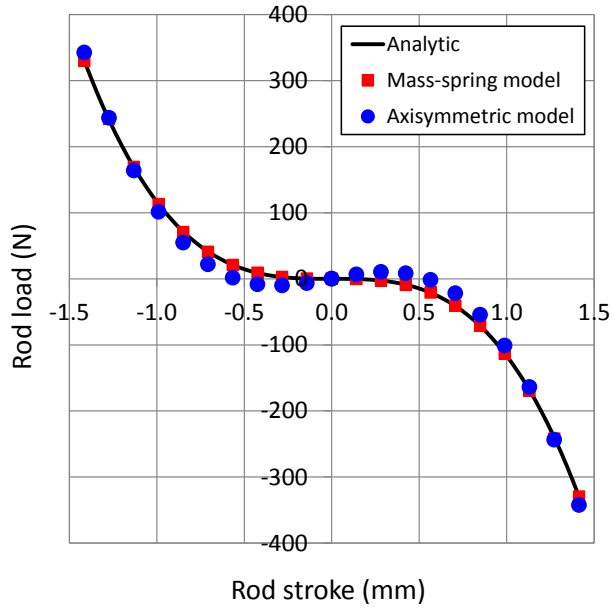


Figure 5. Load-stroke curves of the rod (T) as provided by the analytical and FE models.

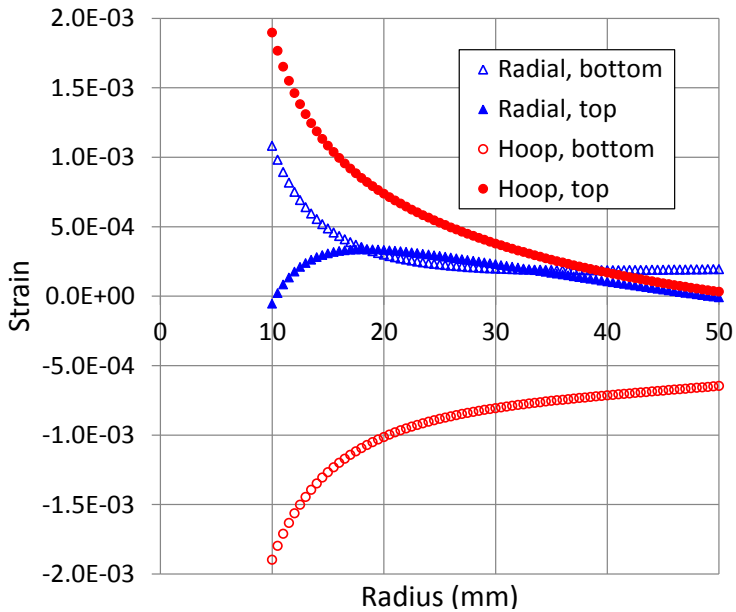


Figure 6. Radial and hoop strains which originate on top and bottom surfaces of Belleville springs during the loading cycle.

According to the analytical and mass-spring FE model, the fundamental frequency of the converter is quite low, with a very close agreement between the models. Since both these models provide a linear approximation of the modal behaviour of the harvester, experimental validation will be performed to assess the frequency response of the system as a function of the degree of non-linearity. The fundamental frequency of the system can be further decreased by using thinner Belleville springs, but with the drawback of reducing the admissible rod stroke.

The strain plots in Figure 6 show that from the equilibrium position up to the maximum rod stroke position large strains occur both in the radial and hoop directions. These strains, which extend over a wide annular region of the Belleville springs, can be exploited to harvest energy through piezoelectric patches applied on either sides of the springs.

On the whole, the proposed converter appears as a promising solution to harvest ambient energy at low frequency, through a hybrid electromagnetic and piezoelectric technology.

5. CONCLUSIONS

A very low frequency harvester based on two counteracting Belleville springs have been proposed and investigated. The harvester exploits the nearly zero stiffness of Belleville springs with a height to thickness ratio equal to 1.414 and can convert energy through a hybrid electromagnetic and piezoelectric transduction.

Both analytical and computational models provide a fundamental eigenfrequency of about 6 Hz. The large stroke of a sliding rod can be exploited for electromagnetic transduction. The relevant strains on the surfaces of the Belleville springs allow piezoelectric conversion. Since the proposed solutions appear promising, the next step will involve experimental tests on a prototype.

REFERENCES

- [1] Despesse, G., Jager, T., Chaillout, J.J., Le'ger J.M. Basrou, S., 2005, "Design and Fabrication of a New System for Vibration Energy Harvesting", *Proc. Ph.D. Res. Microelectron. Electron.*, **1**, pp. 225–228.
- [2] Beeby, S.P., Tudor, M.J., White, N.M., 2006, "Energy harvesting vibration sources for microsystems applications", *Meas. Sci. Technol.*, **17**, pp. R175–R195.
- [3] Dewei, J., Jing, L., 2009, "Human power-based energy harvesting strategies for mobile electronic devices", *Front. Energy Power Eng. China*, **3**, pp. 27–46.
- [4] von Büren, T., Tröster, G., 2007, "Design and optimization of a linear vibration-driven electromagnetic micro-power generator", *Sensors and Actuators*, **A 135**, pp. 765–775.
- [5] Sari, I., Balkan, T., Külah, H., 2010, "An electromagnetic micro power generator for low-frequency environmental vibrations based on the frequency up conversion technique", *J. of Microelectromechanical Systems*, **19**, pp. 14–27.
- [6] Ching, N.N.H., Wong, H.Y., Li, W.J., Leong, P.H. W., Wen, Z., 2002, "A laser-micromachined vibrational to electrical power transducer for wireless sensing systems". *Sensors Actuators*, **A97**, 98685–90.
- [7] Beeby, S.P., Torah, R. N., Tudor, M.J., Glynne-Jones, P, O'Donnell, T., Saha, C.R., Roy, S., 2007, "A micro electromagnetic generator for vibration energy harvesting. *J. Micromech. Microeng.*, **17**, pp. 1257–1265.

- [8] Glynne-Jones, F., Beeby, S.P., White, N. M., 2001, “Towards a piezoelectric vibration-powered micro-generator”, *IEE Proc. Sci. Mem. Technol.*, **148**, pp. 68-72.
- [9] Zurn, S., Hsieh, M., Smith, G., Markus, D., Zang, M., Hughes, G., Nam, Y., Arik, M., Polla, D., 2001, “Fabrication and structural characterization of a resonant frequency PZT microcantilever”, *Smart Mater. Struct.*, **10**, pp. 252-263.
- [10] Roundy, S., Wright, P.K., Rabaey, J., 2003, “A study of low level vibrations as a power source for wireless sensor nodes”, *Computer Communications*, **26**, pp. 1131–1144.
- [11] Benasciutti, D., Moro, L., Zelenika, S., Brusa, E., 2010, “Vibration energy scavenging via piezoelectric bimorphs of optimized shapes”, *Microsyst. Technol.*, **16**, pp. 657–668.
- [13] Singh, K., Michelin, S., de Langre, E., 2012, “Energy harvesting from axial fluid-elastic instabilities of a cylinder”, *J. of Fluids and Structures*, **30**, pp. 159-172.
- [14] Castagnetti, D., 2011, “Fractal-Inspired Multi-Frequency Structures for Piezoelectric Harvesting of Ambient Kinetic Energy” *J. of Mech. Design*, **133**, pp. 111005-1 - 111005-8.
- [15] Castagnetti, D., 2012, “Experimental modal analysis of fractal-inspired multi-frequency piezoelectric energy converters”, *Smart Mater. Struct.*, **21**, pp. 1-9.
- [16] Challa, V.R., Prasad, M.G., Fisher, F.T., 2009, “A coupled piezoelectric–electromagnetic energy harvesting technique for achieving increased power output through damping matching”, *Smart Mater. Struct.*, **18**, pp. 095029.
- [17] Khaligh, A., Zeng, P., Wu, X., Xu, Y., 2008, “A hybrid energy scavenging topology for human-powered mobile electronics”, *Proceedings of Industrial Electronics IECON 2008 34th Annual Conference of IEEE*, pp. 448-453.
- [18] Bagavathiperumal, P., Chandrasekaran, K., Manivasagam, S., 1991, “Elastic load-displacement predictions for coned disc springs subjected to axial loading using the finite element method”, *J. of Strain Analysis*, **26**, pp. 147-152.
- [19] Mubea disc spring handbook, 2012, (available at: http://www.mubea.com/uploads/media/Mubea_Disc_Springs_Manual_01.pdf).
- [20] Almen, J.O., Laszlo, A., 1936, “The uniform section disk spring”, *Trans. of the ASME*, **58**, pp. 305-314.

DIELECTRIC ELASTOMER MACHINES FOR THE CONVERSION OF OCEAN WAVE ENERGY

Rocco Vertechy
PERCRO Laboratory,
Scuola Superiore Sant'Anna, Italy
E-mail: r.vertechy@sssup.it

Marco Fontana
PERCRO Laboratory,
Scuola Superiore Sant'Anna, Italy
E-mail: m.fontana@sssup.it

Massimo Bergamasco
PERCRO Laboratory,
Scuola Superiore Sant'Anna, Italy
E-mail: m.bergamasco@sssup.it

Abstract. *Dielectric Elastomers (DEs) are a very promising technology for the development of energy harvesting devices that are based on the variable-capacitance electrostatic generator principle. This paper discusses the potentialities of DE technology for advancing the ocean wave energy sector. In particular, three innovative concepts of wave energy convert with DE-based power take-off system are introduced and described.*

Keywords: *dielectric elastomers, ocean wave energy.*

1. INTRODUCTION

Among the intermittent renewable resources, ocean-wave power is very persistent and highly spatially concentrated:

- The time-averaged wave-power intensity acting on an area placed just below the sea surface and lying perpendicular to the direction of wave propagation is typically between 2kW/m^2 and 3kW/m^2 ; that is nearly four times larger than the average wind-power intensity acting on an area perpendicular to the wind direction and nearly ten times larger than the average solar-power intensity acting on a horizontal surface of the earth [1].
- Depending on the specific location, wave-power time-availability ranges between 35% and 70%; that is larger than the typical 30% of wind and 15% of solar resources [1, 2].
- Wave-energy predictability is very reliable within 2 or 3 days; whereas wind-energy can be forecasted only within hours and solar-energy is almost unpredictable [2].

Similarly to off-shore wind, wave-energy provides optimal matching between resource availability and electricity consumption (a large part of the population indeed lives within

90km off a coastline), features a natural seasonal variability that follows electricity demand (especially in temperate climates alike in Europe), and brings limited environmental impacts with negligible necessity of land usage [2]. In addition, wave resources are usually complimentary to wind ones [2], and their absorption and conversion may help the prevention of coastal erosion.

Off the Europe coastline, the average theoretical wave-power potential has been recently estimated in 360GW (with roughly 75GW within the Mediterranean regions and 10GW in the Baltic sea) [3]. Despite this is only a small portion of solar and wind resources, for the reasons stated above, wave-power can be a good candidate to cover between 15% and 35% of the intermittent renewable energy mix in the future [2, 4].

Harvesting energy from waves is very challenging:

- ocean wave power is available at high forces and slow speeds (which limits the usability of direct drive generators and requires the adoption of speed reducers);
- machines need to operate well out of their nominal rating conditions;
- machine members must resist to extremely high occasional mechanical loads (especially during storms);
- machine components must resist to a very hostile (in particular, corrosive) environment;
- machines are difficult to install, maintain and test in real operational conditions;
- machine development, construction and testing is very expensive.

As compared to wind and solar, Wave Energy Converter (WEC) technology is still immature, high-risk and cost uncompetitive [2, 4, 5]. Since the forties in Japan and the seventies in Europe and US, nearly a thousand of WEC concepts have been proposed, and nearly a hundred of reduced-scale physical devices have been constructed and tested both at University laboratories and at Spin-Off companies. Today, nearly fifteen pre-commercial WECs have been deployed in the ocean for short-duration testing programs, with only few of them having undertaken the first step towards commercialization.

The proposed WEC architectures are rather diverse, and optimal designs have yet to be converged upon [2, 4, 5]. Different systems have been developed for being deployed either off-shore, near-shore or on the shore-line, and which exploit very dissimilar working principles alike (point, multi-body, or large) wave-absorbers, wave-terminators, wave-attenuators, overtopping reservoirs and submerged seabed devices [6].

Irrespective of the architecture, the considered WECs have relied on traditional mechanical components (such as turbines, oscillating plates or heaving buoys), mechanical/hydraulic transmissions and electromagnetic generators (electric machines). Made by stiff, bulky, heavy and costly metallic materials (and rare-earth materials), these components did not succeed in making the proposed WEC designs to overcome all the challenges mentioned above.

To make ocean wave energy exploitable in an affordable manner, a major technological breakthrough is required.

In this context, this paper describes Dielectric Elastomer Transducer (DET) technology and discusses its potentialities in the wave energy sector. In particular, three different concepts of DET-based WEC are introduced: the Poly-Surge [12], the Poly-Buoy [13] and the Poly-OWC [14-16].

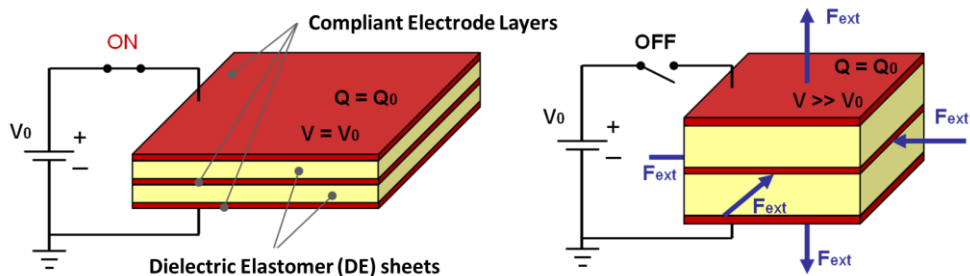


Figure 1: Schematic of a multi-layered DET: low electrical-energy and high elastic-energy state with no applied external force (left), high electrical-energy and low elastic-energy state with applied external force (right).

2. DIELECTRIC ELASTOMER GENERATORS

Dielectric Elastomers (DEs) are highly deformable rubber-like solids, which are mechanically incompressible and electrically non-conductive. The sequential stacking of multiple DE sheets separated by compliant electrode layers yields a deformable capacitive transducer (hereafter referred to as “Dielectric Elastomer Transducer”, or DET in short) that is capable of converting electricity into mechanical energy and vice-versa [9]. Typical materials used as DEs are natural rubbers, silicone elastomers, nitrile rubbers and polyacrylate elastomers (both in un-filled and filled form). Typical materials used for compliant electrodes are silicone compounds filled with conductive particles such as carbon black, carbon nanotubes, copper or silver.

DETs can be used as solid-state actuators, sensors and generators in any kind of machine featuring mechanical members with reciprocating motion [9]. In actuator mode, the deformations induced by the electrostatic attraction between oppositely charged electrodes are used to convert electricity into mechanical energy. In sensor mode, measurements of the deformable capacitance are used to infer DET strains or stresses (that is, displacements or forces). In generator mode, DETs operate via the variable capacitance electrostatic generation principle, thereby increasing the voltage of the charges that lie on the electrodes as the DET capacitance decreases.

A schematic of a simple DET generator made by three deformable electrode layers (in red) and two DE sheets (in yellow) is depicted in Fig. 1; the left figure shows the DET in its “low electrical-energy and high elastic-energy” state with no applied external force, whereas the right figure shows the DET in its “high electrical-energy and low elastic-energy” state with applied external force (figure on the right). In the schematic, V_0 indicates the battery voltage, V the DET voltage, Q the DET charge residing on each of its electrodes ($Q = Q_0$), and F_{ext} is an external force acting on the DET.

As shown, a possible operating sequence for a DET to convert mechanical energy into electricity is the following: 1) start from a configuration where DET capacitance is maximum and fully discharged (that is, with the DET having maximum area and minimum thickness as it is shown in Figure 1 on the left); 2) with the DET locked in the same configuration, connect the electrodes to a battery (with electric potential equalling V_0) so as to place there an amount of charge equalling Q_0 ; 3) as the charging process is completed, disconnect the DET from the power supply; 4) with the supply disconnected, apply the external force F_{ext} to reduce DET capacitance (which makes the electric potential

difference between electrode layers to increase to the value V , with $V \gg V_0$); 5) as the capacitance reaches its minimum value, connect the electrodes to an external electric circuit so as to withdraw the charge Q_0 that is at the electric potential V ; 6) as the discharging process is completed, bring the DET back to the starting configuration.

During this cyclical process, the amount of mechanical energy that can be converted into electricity equals

$$U = 0.5Q_0(V - V_0). \quad (1)$$

In practice, this energy results from the mechanical work that is performed by F_{ext} in a cycle to win the internal forces of electrostatic attraction that exist between oppositely charged electrodes of the DET as the electrodes are being separated. The related energy gain reads as

$$G = \frac{U}{0.5Q_0V_0} = \left(\frac{V}{V_0} - 1 \right). \quad (2)$$

The energy conversion process described above is only one of the possible alternatives. In practice, different energy conversion cycles can be performed by controlling in a different manner the flow of charge that enters/exits the electrodes as a function of DET deformation, with the best controller being the one that enables the regulation of the electric field acting within the DE sheets as the DET deforms [10, 11].

Irrespective of the considered control law, the maximal energy that can be converted by a specific DET in a cycle depends on: 1) type of deformation state (for instance, uniform and equi-biaxial or non-uniform and mono-axial); 2) dielectric strength and permittivity of the employed DE material; 3) elongation at break and stiffness of the employed DE material and compliant electrodes. For practical DETs, which feature:

- deformations up to 700% and Young's modulus in the range 0.01-20MPa;
- dielectric strength in the range 20-400MV/m and permittivity in the range 1.8-7;

typical values for the energy gain ranges between 3 and 15, which is significantly larger than those achievable with piezoelectric ceramics.

Due to the low mass density of DE materials (nearly 1000 kg/m³), values for the energy density of DETs (namely, the amount of energy converted in a cycle per kilogram of transducer) typically range between 0.1kJ/kg and 2kJ/kg, which, for generators operating at low frequencies (for instance, at less than 1Hz), compare very well (and sometimes are even better, especially as the operating frequency is smaller) with that of traditional electric machines.

Beside good energy density, other advantageous properties of DETs that could make them the optimal choice for the development of machines that generate electricity from low-frequency reciprocating motions are:

- rather good electromechanical conversion efficiency (usually in the range 60-90%);
- moderate or low cost (100€/kg for small batches and less than 10€/kg for large batches);
- solid-state monolithic embodiment with no sliding parts and very low internal friction;

- easy manufacturability, assembling and recyclability;
- good chemical resistance to corrosive environments;
- silent operation and no need of lubrication.

3. WAVE ENERGY CONVERTERS BASED ON DIELECTRIC ELASTOMERS TRANSDUCERS

In ocean waves, energy travels without any substantial overall motion of water. In fact, as a wave passes, water particles undergo orbital motions, with the energy of this movement being transmitted to succeeding water particles in a progressive manner. As such, ocean wave energy is available in both kinetic and potential forms; to be harvested, it requires machine elements undergoing slow reciprocating motions and capable to resist large forces/torques. In addition to motion and force requirements, machines (and components) for the conversion of ocean wave energy into electricity should also feature: good electro-mechanical conversion efficiency (in both directions); high impact and corrosion resistance; lightweightness and compactness; easy manufacturability and low cost; silent operation.

As described in the previous section, all these application requirements are perfectly matched by the properties of DETs, which are now opening a new frontier for the ocean wave energy sector.

Based on the different mode of interaction between the DET and the fluid, two families of dielectric elastomer machines for wave energy conversion can be identified:

- **First-Generation DET-based WECs:** they are characterized by the indirect interaction between DET and fluid. In this case, DE deformations are not directly generated by fluid pressures, but by a mechanical interface such as a flap or a buoy (see Figure 2 and Figure 3). Thus, in this case, two distinct bodies are identified: a primary interface, which is the body mechanically excited by the waves; a DET power take-off that converts kinetic and potential energy of the primary interface to electrical energy.
- **Second-Generation DET-based WECs:** they are characterized by direct interaction between DET and fluid, which occurs over wide contact surfaces. In this case, fluid-DET interaction is not mediated by any mechanical means, and DE membrane deformation is directly caused by wave-induced fluid pressures (see Figure 4).

As compared to first-generation systems, second-generation devices are highly-integrated machines that feature the minimal number of mechanical and electrical components beside the DET. Moreover, thanks to their intrinsic and tuneable compliance, such devices make it possible to optimize and control their radiation impedance in order to achieve maximal wave-energy extraction. Besides, first-generation systems are easier to model, design and control. Examples of first- and second-generation devices are provided below.

4. FIRST-GENERATION DET-BASED WECs

In this section, two concepts of first-generation devices are introduced and described.

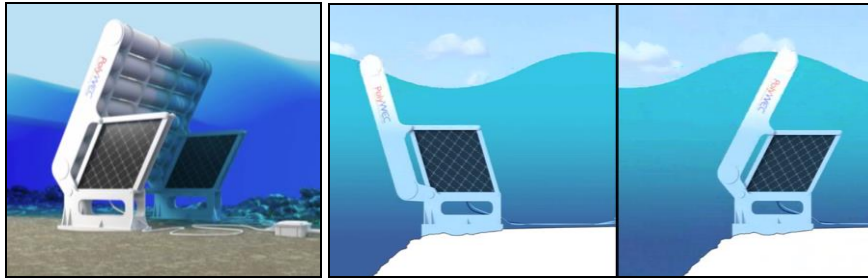


Figure 2: Poly-Surge - Oscillating Flap with a lozenge DET.

Poly-Surge

A first WEC architecture that could be suited for wave energy harvesting via DETs is the oscillating flap. This type of system consists of a buoyant flap hinged at the sea bottom and exploits the surging motion of waves. In traditional systems (such as the Oyster device by Aquamarine Power) the wave-induced oscillatory motion of the flap is used to pump water to the coast via hydraulic pistons and high-pressure flow lines. At the coast, the high-pressure water is then converted into electricity via a turbo-generator.

Replacement of the hydraulic power take-off system (and of the turbo-generator) with a lozenge DETs could enable local conversion of wave energy into electricity without requiring any mechanical or hydraulic transmission. Beside simplifying the system and reducing part count, this replacement could improve system efficiency, simplify installation and reduce the noise pollution emitted at the coast by the turbo-generator.

An artistic drawing of an oscillating flap equipped with a lozenge DEG (hereafter called Poly-Surge) is reported in Figure 2.

Since they need to be attached to the seabed, Poly-Surge systems are suited for near-shore installations at a nominal depth of nearly 10 m, possibly at locations where shoaling effects occur. At this depth, wave energy resource is still very significant, and usually characterized by limited maximum wave heights (due to wave breaking) and limited directional spread between longer and medium period waves.

As for the operating principle, Poly-Surge systems are excited by horizontal fluid accelerations mainly. Due to physical constraints in the oscillatory motion of the flap, Poly-Surge systems are likely to be not resonant in the working frequency range, and should be designed to maximize wave excitation force and to move at speeds that are adequate to limit vortex losses at the edges.

More details on Poly-Surge architecture, functioning principle, design issues and potential performances can be found in [12].

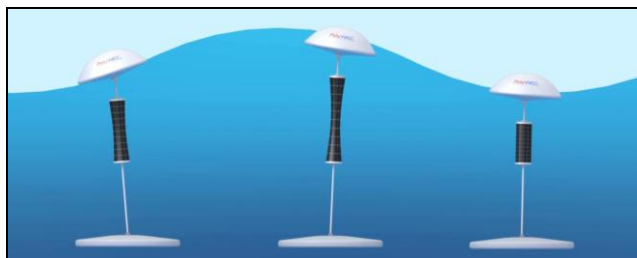


Figure 3: Poly-Buoy - Oscillating Buoy with a cylindrical DEG.

Poly-Buoy

A second WEC architecture that could be suited for wave energy harvesting via DETs is the oscillating buoy. An oscillating buoy WEC consists of a floating body, either submerged or semi-submerged, that moves under the action of sea waves with respect to an appropriate number of submerged and nearly fixed reaction points.

Depending on the water depth of installation, the reaction points can be located either on the seabed or on a floating body (namely a reaction body) that is submerged enough not to be excited by the wave field. Depending on the means of connection to the reaction points, the wave-induced oscillatory motion of the buoy can be in heave, surge or pitch (or a combination thereof).

During these oscillations, the distances between points of the buoy and those of reaction vary. These reciprocating changes in length can be used by power take off systems with linear motions to extract energy from waves. As alternative to the traditional hydraulic rams or linear electrical generators, cylindrical DETs can be used for this purpose. Depending on the size of the device, the considered DET can be placed either inside the buoy, close to the reaction points (in particular on the seabed or inside the reaction body) or along the line connecting the reaction points and the buoy.

An artistic drawing of an oscillating buoy connected to a reaction body via a cylindrical DET (hereafter called Poly-Buoy) is reported in Figure 3.

In terms of hydrodynamic properties, Poly-Buoys are point absorbers that can be installed both on-shore and off-shore. For standard buoy shapes and aspect ratios, Poly-Buoys are likely to be designed so as to be resonant in the working frequency range, which makes their performances very sensitive to the intrinsic passive stiffness of the DET.

More details on Poly-Buoy architecture, functioning principle, design issues and potential performances can be found in [13].

5. SECOND-GENERATION DET-BASED WECS

In this section, one concept of second-generation device is introduced and described.

Poly-OWC

Oscillating Water Column (OWC) wave energy converters are based on the movement of a water column enclosed in chamber (tube or duct) that has at least one submerged opening. The water inside the closed chamber is moved by wave-induced oscillating pressures on the opening.

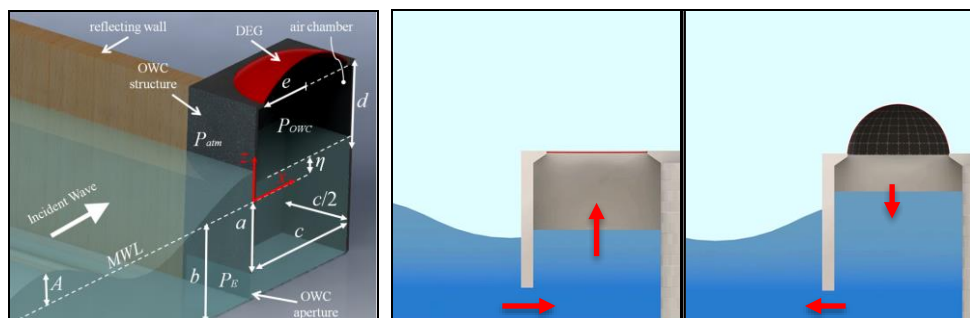


Figure 4: Poly-OWC – Oscillating Water Column with inflating circular diaphragm DET.

In traditional OWC concepts, the movement of the oscillating water column induces a pressure variation inside a closed air chamber; such a pressure variation is used to drive a turbo-generator, which converts the stored pneumatic power into usable electricity. Due to reciprocating air-flow, energy harvesting from traditional OWC devices requires either a self-rectifying turbine or a complex system of non-return valves that makes it possible to rectify the flow passing through a conventional turbine.

In OWCs, replacement of the turbo generator by an inflating diaphragm DET could significantly simplify overall system architecture and installation, improve overall energetic efficiency and climate adaptability, and reduce operating noise.

An artistic drawing of an OWC equipped with inflating circular diaphragm DET (hereafter called Poly-OWC) is reported in Figure 4.

In terms of hydrodynamic characteristics, Poly-OWCs can be installed both on the shore-line (with fixed structure) and off-shore (with floating structure); specifically, they are very suited for being integrated into breakwaters for harbour protection. For standard chamber shapes and aspect ratios, Poly-OWCs are likely to be designed so as to be resonant in the working frequency range, which makes their performances very sensitive to the intrinsic passive stiffness of the DET.

More details on Poly-OWC architecture, functioning principle, design issues and potential performances can be found in [14-16].

6. CONCLUSIONS

This paper presented three different concepts of Wave Energy Converters (WECs) that employ Dielectric Elastomer Transducers (DETs) to convert ocean wave power into direct-current high-voltage electricity. As compared to traditional WECs with hydraulic or electromagnetic power take-off system, the presented machines offer the following potential features: reduced capital costs; easy installation and maintenance; good shock and corrosion resistance; good energy conversion efficiency; good climate adaptability; reduced noise during operation.

As of today, DET technology is however not yet ready to deliver fully-functional WEC systems that are capable to operate in real seas for sufficient long periods of time. In this perspective, critical issues that need to be addressed are: assess the long-term fatigue, ageing, degradation and reliability of the employed materials; conceive better dielectric elastomers and conductive electrodes with improved electromechanical transduction properties and reduced dissipative effects; develop better design, optimization and control methodologies; conceive alternative system architectures with reduced part counts and integrating multiple functionalities in single components.

ACKNOWLEDGEMENTS

The work presented in this paper is developed in the context of the project PolyWEC (www.polywec.org), a FP7 FET–Energy project. The research leading to these results has received funding from the European Union Seventh Framework Programme [FP7/2007–2013] under grant agreement n° 309139.

REFERENCES

- [1] M. Leijon, A. Skoglund, R. Waters, A. Rehn, M. Lindahl, 2010. "On the physics of power, energy and economics of renewable electric energy sources". *Renewable Energy*, **35**, pp. 1729–1734.
- [2] "Oceans of Energy – European Ocean Energy Roadmap 2010-2050", 2009. *European Ocean Energy Association*.
- [3] G. Mork, S. Barstow, A. Kabuth, M.T. Pontes, 2010. "Assessing Global Wave Energy Potential". *OMAE2010, Proc. of 29th International Conference on Ocean, Offshore Mechanics and Arctic Engineering*, China.
- [4] "Future Marine Energy: Cost Competitiveness and Growth of Wave and Tidal Stream Energy", 2006. *Carbon Trust*.
- [5] "Implementing Agreement on Ocean Energy Systems - Annual Report 2010 and 2011", 2010 and 2011. *International Energy Agency*.
- [6] A.F.O. Falcao, 2010. "Wave energy utilization: A review of the technologies". *Renewable and Sustainable Energy Reviews*, **14**, pp. 899–918.
- [7] "Annual Energy Outlook 2010 With Projections to 2035", 2010. *Energy Information Administration*.
- [8] J. Huckerby, A. Brito Melo, 2011. "International Vision on Ocean Energy Systems". *Offshore Renewable Energy and its Potential for the Outermost Regions*, Portugal.
- [9] F. Carpi, D. De Rossi, R. Kornbluh, 2008. "Dielectric elastomers as electromechanical transducers: Fundamentals, materials, devices, models and applications of an emerging electroactive polymer technology". *Elsevier Science*.
- [10] R. Pelrine, R. Kornbluh, J. Eckerle, P. Jeuck, S. Oh, Q. Pei, S. Stanford, 2001. "Dielectric elastomers: Generator mode fundamentals and applications". *Proc. SPIE*, Vol. 4329, pp. 148–156 (2001).
- [11] A. Koh, C. Keplinger, T. Li, S. Bauer, Z. Suo, 2011. "Dielectric elastomer generators: How much energy can be converted?". *IEEE/ASME Transactions on Mechatronics*, **16**(1), 33–41 (2011).
- [12] G. Moretti, D. Forehand, R. Vertechy, M. Fontana, D. Ingram, 2014. "Modeling of an oscillating wave surge converter with dielectric elastomer power take-off". *Proc. of ASME 33rd International Conference on Ocean, Offshore and Arctic Engineering*, Paper No. OMAE2014-23559, San Francisco, CA, USA, 8-13 June.
- [13] G. Moretti, R. Vertechy, M. Fontana, 2014. "Modelling of a heaving buoy wave energy converter with stacked dielectric elastomer generator". *Proc. of ASME Conference on Smart Materials, Adaptive Structures and Intelligent Systems*, Paper No. SMASIS2014-7565, Newport, Rhode Island, Sept. 8-10.
- [14] R. Vertechy, M. Fontana, G.P. Rosati Papini, M. Bergamasco, 2013. "Oscillating-water-column wave-energy-converter based on dielectric elastomer generator". *Proc. of SPIE*, Vol. 8687, pp. 86870I-86870I.
- [15] G.P. Rosati Papini, R. Vertechy, M. Fontana, 2013. "Dynamic Model Of Dielectric Elastomer Diaphragm Generators For Oscillating Water Column Wave Energy Converters". *Proc. of ASME Conference on Smart Materials, Adaptive Structures and Intelligent Systems*, Paper No. SMASIS2013-3255, Snowbird, Sept. 16–18.
- [16] R. Vertechy, M. Fontana, G.P. Rosati Papini, D. Forehand, 2014. "In-tank tests of a dielectric elastomer generator for wave energy harvesting". *Proc. of SPIE*, Vol. 9056, pp. 90561G.

CLOSED-FORM MODAL ANALYSIS OF FLEXURAL BEAM RESONATORS BALLASTED BY A RIGID MASS

Giovanni Scirè Mammano
*Department of Engineering Sciences and Methods,
University of Modena and Reggio Emilia, Italy
E-mail: giovanni.sciremammano@unimore.it*

Davide Castagnetti
*Department of Engineering Sciences and Methods,
University of Modena and Reggio Emilia, Italy
E-mail: davide.castagnetti@unimore.it*

Eugenio Dragoni
*Department of Engineering Sciences and Methods,
University of Modena and Reggio Emilia, Italy
E-mail: eugenio.dragoni@unimore.it*

Abstract. *The work deals with the study of free flexural vibrations of constant cross-section elastic beams ballasted by a rigid mass with rotary inertia at any longitudinal position. We analyze five sets of boundary conditions of the beam (fixed-free, fixed-fixed, fixed-pinned, pinned-pinned, and free-free) and hypothesize that the structure is perfectly rigid, where the rigid mass is applied. By employing the Euler-Bernoulli beam theory, a single parametric matrix is obtained, which provides the characteristic equation of motion of the structure. When applied to specific configurations, the proposed analytical model predicts the eigenfrequencies and eigenmodes of the beam as accurately as ad-hoc analytical models available in the literature. The accuracy of the results is also confirmed by comparison with detailed two- and three-dimensional finite element analyses of a test case. By means of a 3D finite element model, the applicability of the rigid mass hypothesis to continuous beams with a composite thickened portion is finally assessed.*

Keywords: *transverse beam vibration, resonator, rigid mass, rotary inertia, modal analysis, MEMS, energy harvesting, tuning*

1. NOTATION

a	Length of the left beam portion (Figure 2)
A	Cross-section area of the beam
A_i	Cross-section area of the i -th layer of the inhomogeneous section
b	Half-length of the ballast mass (Figure 2)
c	Length of the right beam portion QR (Figure 2)

C_{in}	i -th parameter of the n -th eigenshape of the beam portion OP
D_{in}	i -th parameter of the n -th eigenshape of the beam portion QR
E	Young's modulus of the beam material
E_c	Elastic centre of the inhomogeneous section
E_i	Young's modulus of the material of the i -th layer of the inhomogeneous section
E_{mass}	Young's modulus of the ballast mass material
F_{im}	Inertia force in the transverse direction arising from the ballast mass
G	Centre of mass of the ballast mass
h_E	Distance between the centre of elasticity of the inhomogeneous section and the longitudinal axis of the beam
h_i	Thickness of the i -th layer of the inhomogeneous section
$\underline{\underline{H}}$	Characteristic matrix of the set of equations of motion
I_z	Inertia moment of the cross-section of the beam about the z -axis
$I_{iz'}$	Inertia moment of the cross-section of the i -th layer of the inhomogeneous section about the z' -axis
J_{Gz}	Inertia moment of the inertial element m , calculated in the centre of mass, about the z -axis
J_{Sz}	Inertia moment of the inertial element m , calculated in point S (Figure 1b), about the z -axis
L	Total length of the beam
m	Mass of the ballast mass
M_{Jm}	Moment originated by the inertial angular acceleration on the mass m
$M_n(\xi, t)$	Bending moment acting at ξ coordinate and time t of the beam portion OP for the n -th eigenmode
$M_n(\eta, t)$	Bending moment acting at η coordinate and time t of the beam portion QR for the n -th eigenmode
r	Width of the inhomogeneous section beam
$T_n(\xi, t)$	Shear force acting at ξ coordinate and time t of the beam portion OP for the n -th eigenmode
$T_n(\eta, t)$	Shear force acting at η coordinate and time t of the beam portion QR for the n -th eigenmode
t	Time coordinate
$v(\xi, t)$	Transverse displacement of the centre of mass of the beam portion OP at ξ coordinate and time t
$V_n(\xi)$	Amplitude of the transverse displacement of the centre of mass of the beam portion OP for the n -th eigenmode
$w(\xi, t)$	Transverse displacement of the centre of mass of the beam portion QR at ξ coordinate and time t
$W_n(\xi)$	Amplitude of the transverse displacement of the centre of mass of the beam portion QR for the n -th eigenmode
y_i	Ordinate of the geometric centre of the i -th layer of a inhomogeneous section
z	Axis normal to the page and directed outward in the xyz reference system

α	Ratio between the mass of the ballast mass and the mass of the beam
β_n	n -th root of the transcendental equation
γ	Ratio between the rotary inertia of the ballast mass and that of the beam
δ	Ratio between the length of the ballast mass and the free length of the beam
η	Curvilinear abscissa of the beam portion QR
ξ	Curvilinear abscissa of the beam portion OP
ρ	Mass density of the beam material
$\bar{\rho}$	Equivalent average mass density of the material constituting the inhomogeneous section
ρ_i	Average mass density of the material of the i -th layer of the inhomogeneous section
φ	Bending stiffness ratio between the cross section of the ballast mass and that of the beam
$\chi_{1,\dots,6}$	Parameters to define the specific set of boundary conditions
ω_n	Circular frequency of the n -th eigenmode
I, II, \dots, IV	Derivation order
$\langle EI \rangle_{beam}$	Bending stiffness of the cross-section of the beam section
$\langle EI \rangle_{mass}$	Bending stiffness of the cross-section of the ballast mass
$\langle EI_{iz} \rangle$	Equivalent bending stiffness of the inhomogeneous cross-section

2. INTRODUCTION

The study of transverse vibrations of beams has always been of great interest due to the extent of practical applications and pervasiveness of beam-like machine elements. Recently, the design of beam resonators with specific eigenfrequencies has gained particular attention in many technological devices, for example: sensors [1], energy harvesting devices [2]-[3], micro-electro mechanical systems (MEMS) [4], and vibration damping. The design of these structures requires to fulfil three main constraints: a given set of eigenfrequencies in a specific range, the global deformation of the beam under dynamic excitation, and the dimensions of the structure. The most simple and common solution to achieve these constraints is to introduce a distributed inertial element on the beam resonator in order to lower the eigenfrequencies and increase the bending strain, even by keeping the beam short. In particular, this strategy is fairly adopted in the design of energy harvesting devices [5]-[7].

Many works in the literature deal with the modal analysis of beam structures carrying a concentrated mass. Laura et al. [8] study cantilever beams with a tip mass. Yoo et al. [9] investigate a cantilever beam with a concentrated mass located at an arbitrary position, while Low et al. [10]-[15] examine a beam constrained at both ends, with the concentrated mass arbitrarily located. The same problem configuration but with compliant constraints is studied by De Rosa et al. [16]-[17].

The main limitation of these analytical models is that the mass carried by the beam is described as concentrated. The inaccuracy due to this hypothesis increases as the mass dimensions increase. A more accurate analytical model is developed in [18]-[21], where a rotary inertia is associated to the concentrated mass. In particular, in [18]-[19] a cantilever beam is examined while a simply supported beam is investigated in [20]-[21].

Frequently, the cross-section of the ballast mass is thicker than that of the beam. It comes that, as the length of the ballast mass increases a much stiffer structure is obtained. Two modelling techniques can be adopted to deal with this issue. The first technique describes the system as a beam composed by three portions, each with a specific cross-section. This model, which provides good results but is quite complex, is applied [22] where a Euler-Bernoulli beam theory is adopted, and also in [23] by using a Timoshenko beam model. The second modeling technique assumes the ballast mass as rigid, provided that its bending stiffness is higher than that of the beam. This second approach is chosen by Oguamanam [24] and Rama Bhat et al. [25], which investigate a cantilever beam with a distributed mass on the free end.

The aim of this work is to extend this approach to the modal analysis of elastic beams carrying a ballast mass arbitrarily located and undergoing different sets of boundary conditions. The ballast mass is described as a rigid body with mass and rotary inertia. The analysis of eigenmodes and eigenfrequencies refers to a two-dimensional space, describing the two beam portions through the Euler-Bernoulli formulation. Five sets of boundary conditions for the ends of beam are investigated: fixed-free, fixed-fixed, fixed-pinned, pinned-pinned, and free-free. These five sets of boundary conditions are analysed through a closed-form model involving six parameters, which allow to identify each set of boundary condition. Finally, the analytical model has been implemented in a software, which can be freely downloaded at http://www.machinedesign.re.unimore.it/publicazioni_eng.html.

The comparison, both with respect to the literature lumped-parameter models, and with respect to two- and three-dimensional finite element (FE) models, shows an excellent accuracy of the proposed method in the prediction of the eigenfrequencies and eigenmodes. Moreover, also the rigid mass hypothesis is assessed showing that it is applicable in all the configurations of practical interest.

3. MODEL DEVELOPMENT

Reference configuration

Figure 1a shows a cantilever beam having a length L , with a ballast mass. This configuration is assumed as reference for the analytical model development. Even if Figure 1a refers to a cantilever beam, the analytical model is developed according to a general formulation, in order to be applied to the following sets of boundary conditions: fixed-free, fixed-fixed, fixed-pinned, pinned-pinned, free-free. The beam structure in Figure 1a consists of three portions. The first, OP , is constituted by a beam with a length a and constant cross section. The second, PQ , represents a ballast mass m , with a length $2b$, and an arbitrary cross section. This ballast mass is characterized by a rotary inertia, J_{Gz} , calculated in its centre of mass G with respect to the z axis (Figure 1a). The distance between the centre of mass G and the centre of elasticity of the cross section of the beam is denoted by d (portions OP and QR). Obviously, in case the portion PQ would be a composite structure (an inner beam with a top and bottom distributed mass), the mass m and rotary inertia J_{Gz} would be those of the composite structure as a whole. Finally, the third portion, QR , is a beam with length c and the same cross-section as OP .

Since the bending stiffness $\langle EI \rangle$ of the ballast mass PQ is usually higher than that of the beam portions OP and QR , we assume the portion PQ as infinitely rigid (Figure 1b). Hence, PQ is described as a rigid bar, built-in to the portions OP and QR in P and Q respectively. Consequently, PQ is described by a concentrated mass m , and a rotary inertia

J_{S_z} , both applied at S , the mid-point of the PQ segment (Figure 1b). In particular, the rotary inertia J_{S_z} is obtained through the Huygens-Steiner theorem:

$$J_{S_z} = J_{G_z} + md^2 \quad (1)$$

In order to develop the analytical model, the following dimensionless ratios are introduced:

$$\alpha = \frac{m}{\rho A(a+c)} \quad (2)$$

$$\gamma = \frac{J_{S_z}}{\rho A(a+c)^3} \quad (3)$$

$$\delta = \frac{2b}{(a+c)} \quad (4)$$

The parameter α represents the ratio between the ballast mass and the mass of the beam itself, while γ is the ratio between the rotary inertia of the ballast mass and that of the beam. Finally, δ is the ratio between the length of the ballast mass and the length of the beam.

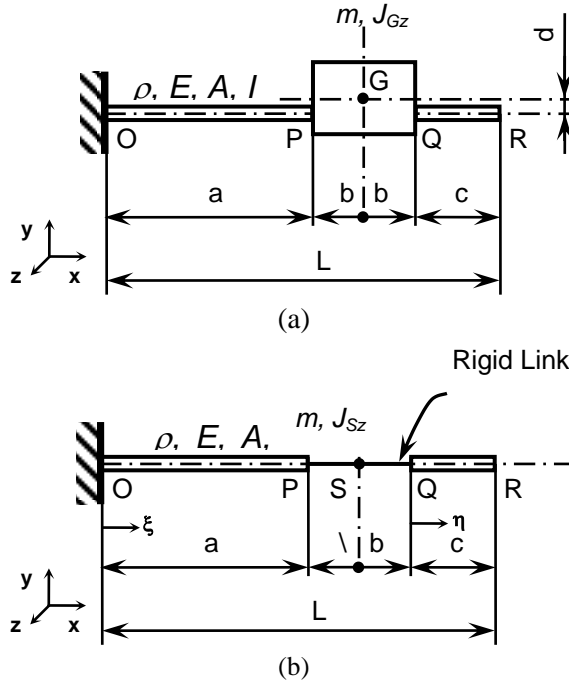


Figure 1. Sketch of the beam structure with ballast mass (a) and simplification of the structure into two beam portions connected by a rigid link (b).

Dynamic equilibrium

The motion of the beam portions OP and QR can be studied independently by applying appropriate compatibility conditions, which reproduce the rigid kinematic link between points P and Q . To this aim, a local abscissa is defined along the length of each beam portion (Figure 1b): ξ -axis on OP and η -axis on QR with domains $0 \leq \xi \leq a$ and $0 \leq \eta \leq c$ respectively. For the beam portion OP , we define $v(\xi, t)$ as the transverse displacement (y direction) at time t of the centre of elasticity at coordinate ξ . Thus, the equation of motion of OP can be written as [26]:

$$\rho A \frac{\partial^2 v(\xi, t)}{\partial t^2} + EI \frac{\partial^4 v(\xi, t)}{\partial \xi^4} = 0 \quad (5)$$

where ρ is the density of the beam material, A the cross section of the beam, E the Young's modulus of the beam material, and I the inertia moment about the z axis of the cross-section of the beam.

Similarly, for the beam portion QR we denote $w(\eta, t)$ as the transverse displacement at time t of the elastic centre of the cross section at coordinate η . Therefore, the equation of motion can be written in the following form:

$$\rho A \frac{\partial^2 w(\eta, t)}{\partial t^2} + EI \frac{\partial^4 w(\eta, t)}{\partial \eta^4} = 0 \quad (6)$$

A solution of equations (5) and (6) can be expressed as the product of two functions: one of them is a function of the position (ξ or η) and the other one is a harmonic function of time t . Since the two beam portions belong to the same vibrating system, the two harmonic functions must coincide. Thus, the solution of equations (5) and (6) can be conveniently expressed by the following functions for OP and QR respectively:

$$v(\xi, t) = V(\xi) \sin(\omega_n t) \quad (7)$$

$$w(\eta, t) = W(\eta) \sin(\omega_n t) \quad (8)$$

where V and W are the amplitudes of the transverse displacement in OP and QR respectively. Substitution of equations (7) and (8) into equations (5) and (6) respectively, yields the following ordinary differential equations:

$$V^{IV}(\xi) - \beta_n^4 V(\xi) = 0 \quad (9)$$

$$W^{IV}(\eta) - \beta_n^4 W(\eta) = 0 \quad (10)$$

where the Roman superscript indicate the differentiation order with respect to the curvilinear abscissa, while the term β_n^4 is defined as:

$$\beta_n^4 = \frac{\rho A}{EI} \omega_n^2 \quad (11)$$

A solution of the ordinary differential equations (9) and (10) may be expressed as:

$$V_n(\xi) = C_{1n} \cos(\beta_n \xi) + C_{2n} \sin(\beta_n \xi) + C_{3n} \cosh(\beta_n \xi) + C_{4n} \sinh(\beta_n \xi) \quad (12)$$

$$W_n(\eta) = D_{1n} \cos(\beta_n \eta) + D_{2n} \sin(\beta_n \eta) + D_{3n} \cosh(\beta_n \eta) + D_{4n} \sinh(\beta_n \eta) \quad (13)$$

Boundary conditions

The C_{in} and D_{in} coefficients (eight in total) in equations (12) and (13) respectively, together with the β_n coefficient have to be determined from the boundary conditions at the ends of each beam portion OP and QR respectively. In particular, four boundary conditions apply to the ends of each beam portion. These boundary conditions involve the displacement functions $V_n(\xi)$ (12) and $W_n(\eta)$ (13) and their derivatives up to the third order. Repeated differentiations of equations (12) and (13) give the following equations:

$$V_n^I(\xi) = -C_{1n} \beta_n \sin(\beta_n \xi) + C_{2n} \beta_n \cos(\beta_n \xi) + C_{3n} \beta_n \sinh(\beta_n \xi) + C_{4n} \beta_n \cosh(\beta_n \xi) \quad (14)$$

$$V_n^{II}(\xi) = -C_{1n} \beta_n^2 \cos(\beta_n \xi) - C_{2n} \beta_n^2 \sin(\beta_n \xi) + C_{3n} \beta_n^2 \cosh(\beta_n \xi) + C_{4n} \beta_n^2 \sinh(\beta_n \xi) \quad (15)$$

$$V_n^{III}(\xi) = C_{1n} \beta_n^3 \sin(\beta_n \xi) - C_{2n} \beta_n^3 \cos(\beta_n \xi) + C_{3n} \beta_n^3 \sinh(\beta_n \xi) + C_{4n} \beta_n^3 \cosh(\beta_n \xi) \quad (16)$$

$$W_n^I(\eta) = -D_{1n} \beta_n \sin(\beta_n \eta) + D_{2n} \beta_n \cos(\beta_n \eta) + D_{3n} \beta_n \sinh(\beta_n \eta) + D_{4n} \beta_n \cosh(\beta_n \eta) \quad (17)$$

$$W_n^{II}(\eta) = -D_{1n} \beta_n^2 \cos(\beta_n \eta) - D_{2n} \beta_n^2 \sin(\beta_n \eta) + D_{3n} \beta_n^2 \cosh(\beta_n \eta) + D_{4n} \beta_n^2 \sinh(\beta_n \eta) \quad (18)$$

$$W_n^{III}(\eta) = D_{1n} \beta_n^3 \sin(\beta_n \eta) - D_{2n} \beta_n^3 \cos(\beta_n \eta) + D_{3n} \beta_n^3 \sinh(\beta_n \eta) + D_{4n} \beta_n^3 \cosh(\beta_n \eta) \quad (19)$$

From Table 1, which collects the five sets of boundary conditions here examined, it appears that only four among the equations (12)-(19) are used to completely define each set of boundary conditions. Although different equations are used for each set of boundary conditions, it is possible to define the following system of four parametric expressions (involving C_{in} and D_{in} coefficients), which conveniently summarize all of them:

$$\begin{aligned} \chi_1 C_{1n} + C_{3n} &= 0 \\ -\chi_2 C_{1n} + (\chi_1 - \chi_2) C_{2n} + \chi_2 C_{3n} + (1 - \chi_2) C_{4n} &= 0 \end{aligned} \quad (20)$$

$$\chi_3 \cos(\beta_n c) D_{1n} + \chi_3 \sin(\beta_n c) D_{2n} + \cosh(\beta_n c) D_{3n} + \sinh(\beta_n c) D_{4n} = 0$$

$$-\frac{\chi_3 \sin(\beta_n c)}{\chi_5} D_{1n} + \chi_3 \chi_4 \chi_5 \cos(\beta_n c) D_{2n} + \frac{\sinh(\beta_n c)}{\chi_6} D_{3n} + \chi_6 \cosh(\beta_n c) D_{4n} = 0$$

By substituting the values collected in Table 2 to the six parameters $\chi_1, \chi_2, \chi_3, \chi_4, \chi_5, \chi_6$, the specific four equations are obtained for each of the five sets of boundary conditions here considered.

The remaining four parameters of equations (12) and (13) can be determined from the compatibility conditions between the beam portions OP and QR through the rigid link PQ . The rigid link PQ provides two compatibility conditions, the first dealing with the displacement, the second with the rotation of each beam portions at points P and Q .

The first condition correlates the transverse displacement of points P and Q , which can be conveniently written as:

$$W_n(Q) = V_n(P) + \delta(a+c)V_n'(P) \quad (21)$$

The second condition equals the rotation of the cross-sections of the beam portions at points P and Q , yielding the following equation:

$$V_n'(P) = W_n'(Q) \quad (22)$$

Table 1 Sets of boundary conditions of the beam.

End conditions of beam ($O-R$)	Boundary Conditions at O	Boundary Conditions at R
Fixed – Free	$V_n(\xi=0) = 0$	$W_n''(\eta=c) = 0$
	$V_n'(\xi=0) = 0$	$W_n'''(\eta=c) = 0$
Fixed – Fixed	$V_n(\xi=0) = 0$	$W_n(\eta=c) = 0$
	$V_n'(\xi=0) = 0$	$W_n'(\eta=c) = 0$
Fixed – Pinned	$V_n(\xi=0) = 0$	$W_n(\eta=c) = 0$
	$V_n'(\xi=0) = 0$	$W_n''(\eta=c) = 0$
Pinned – Pinned	$V_n(\xi=0) = 0$	$W_n(\eta=c) = 0$
	$V_n''(\xi=0) = 0$	$W_n''(\eta=c) = 0$
Free – Free	$V_n''(\xi=0) = 0$	$W_n''(\eta=c) = 0$
	$V_n'''(\xi=0) = 0$	$W_n'''(\eta=c) = 0$

Table 2 Values of the parameters $\chi_1, \chi_2, \chi_3, \chi_4, \chi_5, \chi_6$ as a function of the set of boundary conditions.

End conditions of beam ($O-R$)	χ_1	χ_2	χ_3	χ_4	χ_5	χ_6
Fixed – Free	1	0	-1	1	1	1
Fixed – Fixed	1	0	1	1	1	1
Fixed – Pinned	1	0	1	-1	$\tan(\beta_n c)$	$\tanh(\beta_n c)$
Pinned – Pinned	1	1	1	-1	$\tan(\beta_n c)$	$\tanh(\beta_n c)$
Free – Free	-1	0	-1	1	1	1

The remaining two equations are obtained by imposing the static equilibrium of the rigid link PQ (Figure 1b): first, the equilibrium of forces along the transverse y direction; second, the equilibrium of moments about the z -axis. The first condition deals with shear force T , which varies discontinuously between points P and Q due to the inertial force, F_{im} , of the concentrated mass m (at point S) and can be written as:

$$T_n(P) - T_n(Q) = -F_{im} \quad (23)$$

where the inertial force F_{im} is defined as:

$$F_{im} = m\omega_n^2 \sin(\omega_n t) [V_n(P) + V_n'(P)b] \quad (24)$$

Moreover, the bending moment M and shear force T for the beam portion OP satisfy the following expressions:

$$M_n(\xi, t) = EI V_n''(\xi) \sin(\omega_n t) \quad (25)$$

$$T_n(\xi, t) = EI V_n'''(\xi) \sin(\omega_n t) \quad (26)$$

By extracting the term ω_n^2 from equation (11) and taking advantage of equations (2) and (4), after little rearrangement we obtain:

$$[V_n'''(P) - W_n'''(Q)] + \alpha(a+c)\beta_n^4 [V_n(P) + (\delta/2)(a+c)V_n'(P)] = 0 \quad (27)$$

With regard to the second static condition, the discontinuity of moments is due to three different contributions: the bending moment originated by the shear force $T_n(Q)$, the bending moment generated by the inertia force F_{im} (equation (24)) of the concentrated mass, and the inertia moment M_{jm} due to the rotation of the rigid link PQ . Hence, the following expression is obtained:

$$M_n(P) - M_n(Q) = F_{im}(S)b - T_n(Q)2b - M_{jm} \quad (28)$$

In addition, the bending moment M and the shear force T for the beam portion QR can be written as:

$$M_n(\eta, t) = EI W_n''(\eta) \sin(\omega_n t) \quad (29)$$

$$T_n(\eta, t) = EI W_n'''(\eta) \sin(\omega_n t) \quad (30)$$

while the inertia moment M_{jm} is defined as:

$$M_{jm} = J_{sz} V_n'(P) \omega_n^2 \sin(\omega_n t) \quad (31)$$

Finally, by extracting the term ω_n^2 from equation (11) and taking advantage of equations (2)-(4), after some algebraic manipulations we obtain:

$$\begin{aligned} & \left[V_n^{II} (P) - W_n^{II} (Q) + W_n^{III} (Q) \delta (a+c) \right] + \\ & -\beta^4 \left\{ \alpha (a+c)^2 (\delta/2) \left[V_n (P) + V_n^I (P) (\delta/2) (a+c) \right] + \gamma (a+c)^3 V_n^I (P) \right\} = 0 \end{aligned} \quad (32)$$

General solution

The eight boundary and equilibrium conditions (20), (21), (22), (27) and (32) provide the following linear algebraic system in the eight unknowns $C_{in} \in D_{in}$:

$$\mathbf{H} \times [C_{1n}, \dots, D_{4n}]^T = \mathbf{0} \quad (33)$$

where the square matrix \mathbf{H} collects the coefficients of the set of equation:

Columns 1 through 2

$$\mathbf{H} = \begin{bmatrix} \chi_1 & 0 \\ -\chi_2 & \chi_1 - \chi_2 \\ -\cos(\beta_n a) + (a+c)\beta_n \delta \sin(\beta_n a) & -(a+c)\beta_n \delta \cos(\beta_n a) - \sin(\beta_n a) \\ \sin(\beta_n a) & -\cos(\beta_n a) \\ (a+c)\alpha\beta_n \cos(\beta_n a) + \sin(\beta_n a) & (a+c)\alpha\beta_n \sin(\beta_n a) - \cos(\beta_n a) \\ (a+c)^3 \alpha\beta_n^3 \delta^2 \sin(\beta_n a) - 2[2 + (a+c)^2 \alpha\beta_n^2 \delta] \cos(\beta_n a) & -4 \sin(\beta_n a) - (a+c)^2 \alpha\beta_n^2 \delta [(a+c)\beta_n \delta \cos(\beta_n a) + 2 \sin(\beta_n a)] \\ 0 & 0 \\ 0 & 0 \end{bmatrix}$$

Columns 3 through 4

$$\begin{bmatrix} 1 & 0 \\ \chi_2 & 1 - \chi_2 \\ -\cosh(\beta_n a) - (a+c)\beta_n \delta \sinh(\beta_n a) & -(a+c)\beta_n \delta \cosh(\beta_n a) - \sinh(\beta_n a) \\ -\sinh(\beta_n a) & -\cosh(\beta_n a) \\ (a+c)\alpha\beta_n \cosh(\beta_n a) + \sinh(\beta_n a) & \cosh(\beta_n a) + (a+c)\alpha\beta_n \sinh(\beta_n a) \\ [4 - 2(a+c)^2 \alpha\beta_n^2 \delta] \cosh(\beta_n a) - (a+c)^3 \alpha\beta_n^3 \delta^2 \sinh(\beta_n a) & 4 \sinh(\beta_n a) - (a+c)^2 \alpha\beta_n^2 \delta [(a+c)\beta_n \delta \cosh(\beta_n a) + 2 \sinh(\beta_n a)] \\ 0 & 0 \\ 0 & 0 \end{bmatrix}$$

Columns 5 through 8

$$\begin{bmatrix} 0 & 0 & 0 & 0 \\ 0 & 0 & 0 & 0 \\ 1 & 0 & 1 & 0 \\ 0 & 1 & 0 & 1 \\ 0 & 1 + (1/2)(a+c)^2 \alpha\beta_n^2 \delta & 0 & (1/2)(a+c)^2 \alpha\beta_n^2 \delta - 1 \\ 4 & -4[(a+c)^3 \beta_n^3 \gamma + (a+c)\beta_n \delta] & -4 & 4[-(a+c)^3 \beta_n^3 \gamma + (a+c)\beta_n \delta] \\ \frac{\chi_3 \cos(\beta_n c)}{\chi_5} & \chi_3 \sin(\beta_n c) & \frac{\cosh(\beta_n c)}{\chi_6} & \sinh(\beta_n c) \\ \frac{-\chi_3 \sin(\beta_n c)}{\chi_5} & \chi_3 \chi_4 \chi_5 \cos(\beta_n c) & \frac{\sinh(\beta_n c)}{\chi_6} & \chi_6 \cosh(\beta_n c) \end{bmatrix} \quad (34)$$

The linear system (33) has a non-trivial solution if and only if the determinant of the \mathbf{H} matrix equals zero:

$$\det(\mathbf{H}) = 0 \quad (35)$$

Equation (35) is the characteristic transcendental equation of the system that can be

solved for the variable β_n , obtaining infinite roots. According to equation (11), each root identifies a circular frequency ω_n of the n -th eigenmode of the beam. For each circular frequency ω_n it is possible to determine the C_{in} and D_{in} constants through the set of equation (33). Since the determinant of the characteristic matrix \mathbf{H} is zero, for each circular frequency ω_n the equations of the system are linearly dependent. Therefore, we need to set an arbitrary value for one of the unknown constants and then calculate the remaining ones. Upon substitution in equations (12) and (13) of the parameters C_{in} and D_{in} , the expressions of the eigenmodes associated to each circular frequency ω_n are obtained, up to a multiplicative coefficient.

In conclusion, this method, which will be called from now on Rigid Mass (RM) model, provides the eigenfrequencies and eigenmodes of an elastic beam under generic constraints, carrying a ballast rigid mass. It is observed that, by simply setting the semi-length b of the ballast mass equal to zero, the RM model simplifies to a model that describes the inertial element (m, J_{Sz}) as concentrated. This model, from now on called Concentrated Mass (CM) model, is analogous to the models retrieved in the literature [18]-[21]. If, in addition, also the rotary inertia J_{Sz} of the ballast mass is set to zero, the CM model describes a concentrated mass without inertial effects [8]-[17].

4. MODEL VALIDATION

In order to simplify the calculation procedure, the RM model has been implemented in a software (named Beam Frequency Calculator (BFC)), through the commercial tool Visual Basic 6.0. The software can be freely downloaded from the web at [27]. Appendix 1 describes, for a particular configuration, all the details of the software and its application.

In this section the assessment of the model is performed in three steps. The first assessment compares the CM model to analogous model taken from the literature. The second assessment, which is focused on a case study, compares the RM model with a two-dimensional FE model, a three-dimensional FE model, and finally with the literature models. The third assessment deals with the applicability of the rigid mass hypothesis.

Comparison between the CM model and literature models

In order to assess the correctness of the proposed model, in this section we compare the CM model to analogous models retrieved from the literature (either considering concentrated mass with rotary inertia or a concentrated mass without rotary inertia). The comparison is performed for all the five sets of boundary conditions considered in Section 2. The CM model is solved through the BFC software [27].

Four analytical models taken from the literature are used for comparison. First, the model presented in [15] for the case of a cantilever beam with a tip mass with rotary inertia. Second, the model proposed in [8], which is applied both to the case of a fixed-fixed beam and to the case of a fixed-pinned beam with intermediate concentrated mass without rotary inertia. Third, the model proposed in [17] for a pinned-pinned beam configuration having an intermediate concentrated mass with rotary inertia. Fourth, the model presented in [21] for the case of a free-free beam without any inertial element.

Table 3 compares, for each of the five sets of boundary conditions, the first four normalized eigenfrequencies provided by the literature models with those provided by the CM model. Specific values of the non-dimensional parameters m/m_{beam} , $J/(m_{beam} * L^2)$, a/L have been considered for each configuration.

Table 3 Comparison between the RM model reduced to concentrated mass with or without inertia and analogous models from the literature.

Structure under examination	m/m_{beam}	$J/(m_{beam} * L^2)$	a/L	Reference	Mode	f_{adim} reference model	f_{adim} RM model
Fixed – free tip mass and inertia	0.6	0.4	1	[15]	1	1.12305	1.12305
					2	2.08695	2.08695
					3	4.98723	4.98723
					4	8.02840	8.02840
Fixed-fixed intermediate mass	0.6	0	0.75	[8]	1	4.25570	4.25570
					2	6.68237	6.68237
					3	10.19053	10.19053
					4	13.96990	13.96990
Fixed-pinned intermediate mass	0.6	0	0.75	[8]	1	3.31928	3.31928
					2	6.29730	6.29730
					3	9.93266	9.93266
					4	13.29452	13.29452
Pinned-pinned intermediate mass and inertia	0.6	0.4	0.75	[17]	1	1.94099	1.94099
					2	3.79828	3.79828
					3	5.57670	5.57670
					4	9.59831	9.59831
Free-free no mass	0	0	0	[21]	1	4.73005	4.73005
					2	7.85321	7.85321
					3	10.99561	10.99561
					4	14.13717	14.13717

Comparison with respect to a cantilever having an intermediate ballast mass

Figure 2 shows the sketch of a cantilever with an intermediate ballast mass, eccentric with respect to the midplane of the beam. This configuration is taken as reference in this second step of assessment of the RM model. The structure consists of a beam with rectangular cross-section. Two ballast masses of different thickness are attached along the free length of the beam to the upper and bottom face respectively. On the whole, the region containing the ballast masses has a mass m (see Section 2).

The same steel material is assumed (Young’s modulus 210 GPa, Poisson’s ratio 0.3, and mass density 7850 kg/m³) both for the beam and for the inertial elements. We examined all the five sets of boundary conditions described in Table 1. In particular, in the case of asymmetric constraints (fixed-free and fixed-pinned) the fixed constraint is applied to the left end of the beam that is the farthest from the ballast mass.

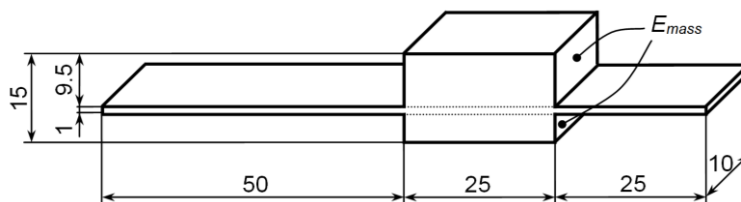


Figure 2. Sketch of the beam structure considered as case study in Section 3 (dimensions in mm).

RM model

The configuration in Figure 2 has been studied applying the RM model in its full formulation (ballast mass described as rigid and with finite length). Thus, in accordance with the sketch in Figure 1b, the beam in Figure 2 can be described by the geometric and inertial properties collected in Table 4 (RM model). The analysis has been performed through the BFC software.

Tables 5 and 6 report the first four eigenfrequencies provided by the RM model, and by the two- and three-dimensional FE models (see Section 3.2.2 and Section 3.2.3) respectively, for each set of boundary condition. Moreover, Tables 5 and 6 presents the percentage relative error, which was calculated with respect to the FE model.

Figure 3, 4, 5, 6 and 7 present, in normalized form, the first four eigenmodes provided by the RM model (hollow circles) for the fixed-free, fixed-fixed, fixed-pinned, pinned-pinned and free-free constraint respectively. The hollow circles are not plotted where the ballast mass occurs, in order to make it clearly visible.

Two-dimensional FE model

The two-dimensional FE model describes the configuration in Figure 2 and was implemented through the commercial FE software ABAQUS V6.9.1 [28]. The two beam portions have been described through linear Euler beam elements (B21H), with full integration. According to a convergence procedure, the element length was set to 0.05 mm, giving a total of 1500 elements.

The rigid mass linking the beam portions was described through a kinematic “wire connector”, available in ABAQUS. This is a rigid kinematic link between the ends (P and Q) of the beam portions, which equals their corresponding kinematic degrees of freedom (Figure 1). A mass m and a rotary inertia J_{Sz} (according to Table 4) are imputed to the midpoint of this kinematic link. The material of the beam is described as linear elastic with the mechanical properties of steel defined in Section 3.2.

Five different models have been implemented, one for each set of boundary conditions in Table 1, giving the results presented in Table 5, which is organized as described in Section 3.2.1.

Three-dimensional FE model

The three-dimensional FE model describes in details the configuration in Figure 2 and is assumed as the reference solution for the modal analysis of this case study. As the previous two-dimensional FE model, it was implemented through the ABAQUS software [28]. The whole structure has been described through eight-noded, linear, hexahedral

Table 4 Geometric and inertial parameters of the case study (Figure 2) for the implementation of the RM model and of the two-dimensional FE model.

Geometric and material properties	RM model	CM model		2D FE model
		With Inertia	Without Inertia	
a (mm)	50	62.5	62.5	62.5
b (mm)	12.5	0	0	12.5
c (mm)	25	37.5	37.5	25
m (kg)	2.9438E-2	2.9438E-2	2.9438E-2	2.9438E-2
J_{Sz} (kg m ²)	2.2691E-6	2.2691E-6	0	2.2691E-6

Table 5 Geometric and inertial parameters of the case study (Figure 2) for the implementation of the RM model and of the two-dimensional FE model.

Model Type		Eigenmode I		Eigenmode II		Eigenmode III		Eigenmode IV	
		Freq. (Hz)	Err %	Freq. (Hz)	Err %	Freq. (Hz)	Err %	Freq. (Hz)	Err %
Fixed - Free	RM model	39.05	0.1	420.30	0.0	1587.40	0.0	2325.27	0.0
	FE 2D	39.00		420.31		1587.50		2325.70	
Fixed - Fixed	RM model	255.45	0.0	1019.92	0.0	2316.82	0.0	5991.26	0.0
	FE 2D	255.35		1020.00		2317.00		5991.80	
Fixed - Pinned	RM model	188.00	0.0	775.98	0.0	2301.83	0.0	5925.05	0.0
	FE 2D	187.93		775.92		2301.80		5925.50	
Pinned - Pinned	RM model	128.54	0.0	688.18	0.0	1679.59	0.0	4876.72	0.0
	FE 2D	128.52		688.27		1679.70		4877.10	
Free - Free	RM model	519.26	0.0	1583.91	0.0	2303.23	0.0	5992.77	0.0
	FE 2D	519.24		1584.20		2303.60		5993.30	

Table 6 Comparison between the results provided by the three-dimensional FE model, by the RM model, by the concentrated mass model and by the concentrated mass and inertia model, for the first four eigenfrequencies of the case study (Figure 2).

Model Type		Eigenmode I		Eigenmode II		Eigenmode III		Eigenmode IV	
		Freq. (Hz)	Err %	Freq. (Hz)	Err %	Freq. (Hz)	Err %	Freq. (Hz)	Err %
Fixed - Free	FE 3D	38.76		415.03		1549		2294.6	
	RM model	39.05	0.7	420.3	1.3	1587.4	2.5	2325.27	1.3
	CM model without inertia	38.38	-1.0	373.7	-10.0	1193.95	-22.9	2828.96	23.3
	CM model	37.66	-2.8	280.17	-32.5	774.89	-50.0	1430.31	-37.7
Fixed - Fixed	FE 3D	253.5		1005.1		2288.9		5905.8	
	RM model	255.45	0.8	1019.92	1.5	2316.82	1.2	5991.26	1.4
	CM model without inertia	177.59	-29.9	1159.84	15.4	2839.86	24.1	3810.3	-35.5
	CM model	175.77	-30.7	557.94	-44.5	1429.2	-37.6	3787.47	-35.9
Fixed - Pinned	FE 3D	185.53		763.24		2274.1		5813.2	
	RM model	188	1.3	775.98	1.7	2301.83	1.2	5925.05	1.9
	CM model without inertia	118.36	-36.2	1093.43	43.3	2140.14	-5.9	3515.94	-39.5
	CM model	118.36	-36.2	500.76	-34.4	1428.46	-37.2	2678.07	-53.9
Pinned - Pinned	FE 3D	126.36		675.51		1648.3		4785.4	
	RM model	128.54	1.7	688.18	1.9	1679.59	1.9	4876.72	1.9
	CM model without inertia	84.78	-32.9	765.42	13.3	1988.24	20.6	2950	-38.4
	CM model	84.42	-33.2	455.79	-32.5	1032.1	-37.4	2678.07	-44.0
Free - Free	FE 3D	515.08		1554.5		2269.6		5875.1	
	RM model	519.26	0.8	1583.91	1.9	2303.23	1.5	5992.77	2.0
	CM model without inertia	410.96	-20.2	1181.19	-24.0	2828.44	24.6	3791.07	-35.5
	CM model	344.88	-33.0	777.07	-50.0	1411.93	-37.8	3783.27	-35.6

elements (C3D8R), with reduced integration and hourglass control [28]. According to a convergence analysis, not reported here for the sake of brevity, the element side length was set 0.25 mm, except in the thickness of the beam direction, where six layers of elements with the same transverse side length as above were applied (Figure 8). On the whole, the mesh consists of 320,000 elements, 346,983 nodes and 1,040,949 degrees of freedom. As in the previous two-dimensional FE model, the material was described as linearly elastic, according to the values of Section 3.2. Five different models have been implemented, one for each set of boundary condition described in Table 1.

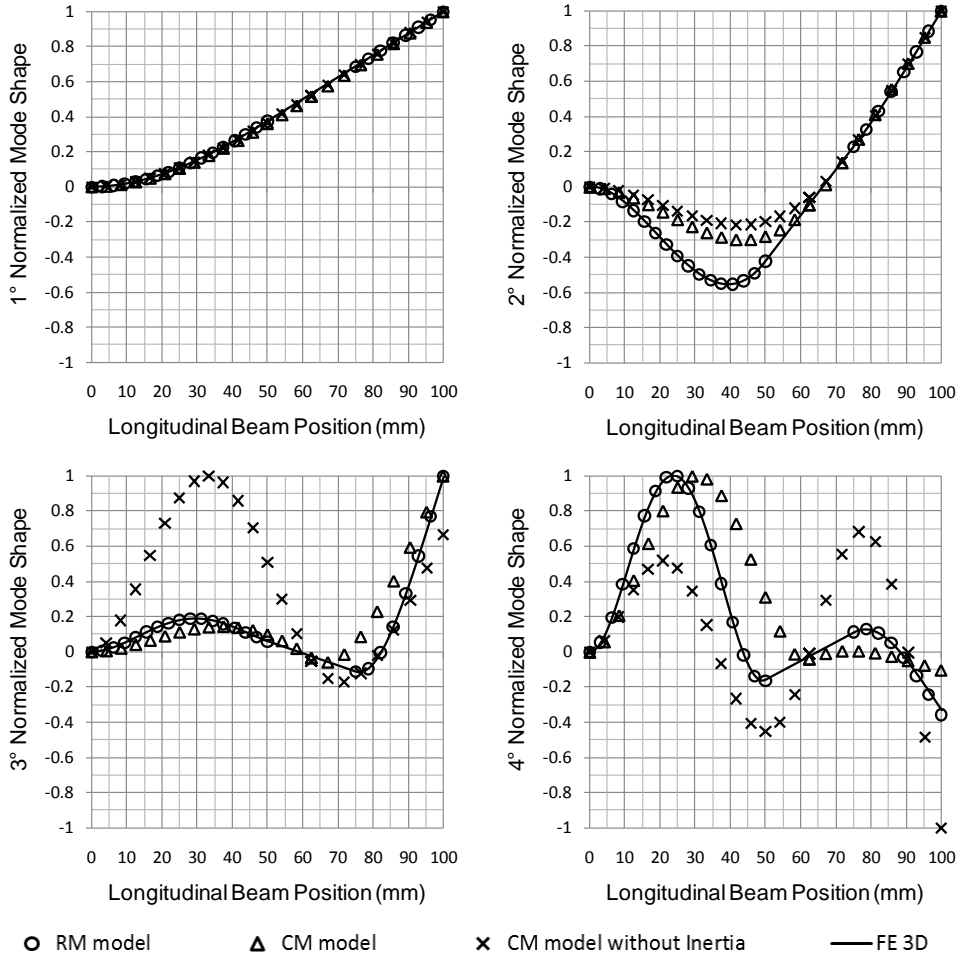


Figure 3. First four eigenmodes for the fixed-free beam.

Table 6 displays, for all the constraint conditions, the results provided by this computational model, organized as described in Section 3.2.1. Figures 3, 4, 5, 6 and 7 show, in normalized form, the first four eigenmodes provided by the computational model (solid line) for the fixed-free, fixed-fixed, fixed-pinned, pinned-pinned and free-free constraint respectively.

Three-dimensional FE model

The three-dimensional FE model describes in details the configuration in Figure 2 and is assumed as the reference solution for the modal analysis of this case study. As the previous two-dimensional FE model, it was implemented through the ABAQUS software [28]. The whole structure has been described through eight-noded, linear, hexahedral elements (C3D8R), with reduced integration and hourglass control [28]. According to a convergence

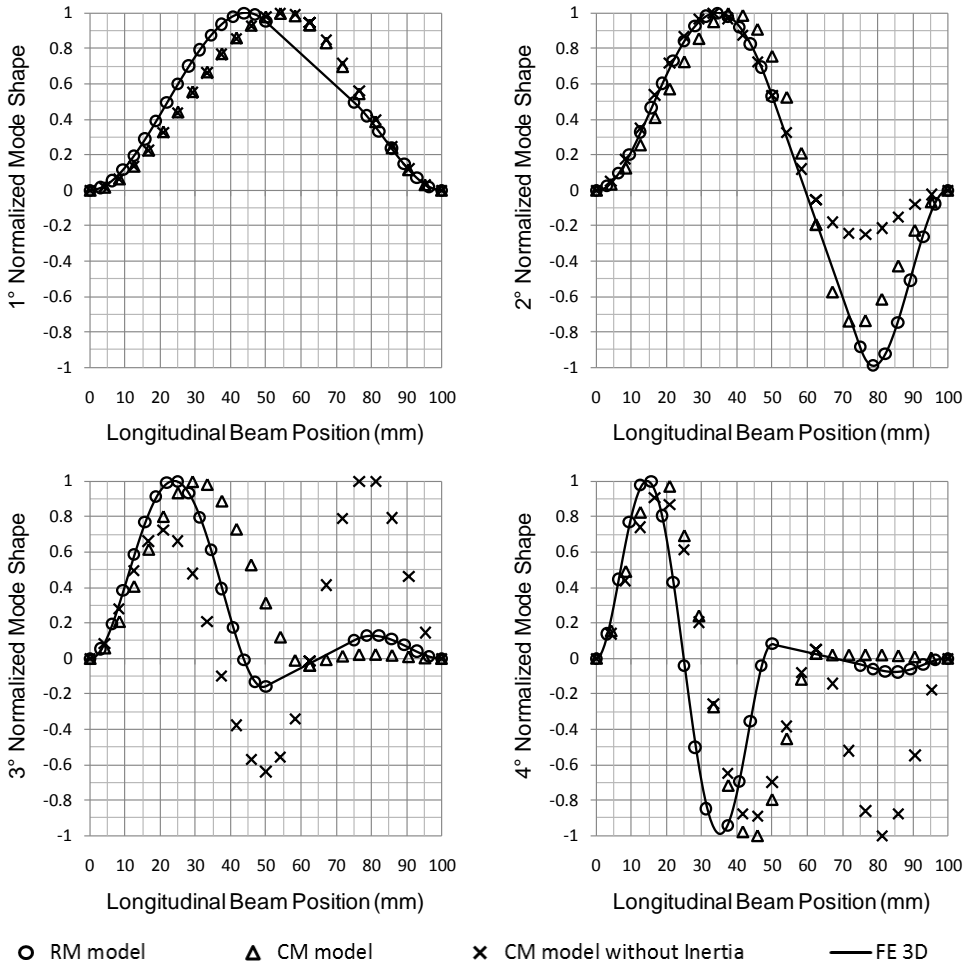


Figure 4. First four eigenmodes for the fixed-fixed beam.

analysis, not reported here for the sake of brevity, the element side length was set 0.25 mm, except in the thickness of the beam direction, where six layers of elements with the same transverse side length as above were applied (Figure 8). On the whole, the mesh consists of 320,000 elements, 346,983 nodes and 1,040,949 degrees of freedom. As in the previous two-dimensional FE model, the material was described as linearly elastic, according to the values of Section 3.2. Five different models have been implemented, one for each set of boundary condition described in Table 1.

Table 6 displays, for all the constraint conditions, the results provided by this computational model, organized as described in Section 3.2.1. Figures 3, 4, 5, 6 and 7 show, in normalized form, the first four eigenmodes provided by the computational model (solid line) for the fixed-free, fixed-fixed, fixed-pinned, pinned-pinned and free-free constraint respectively.

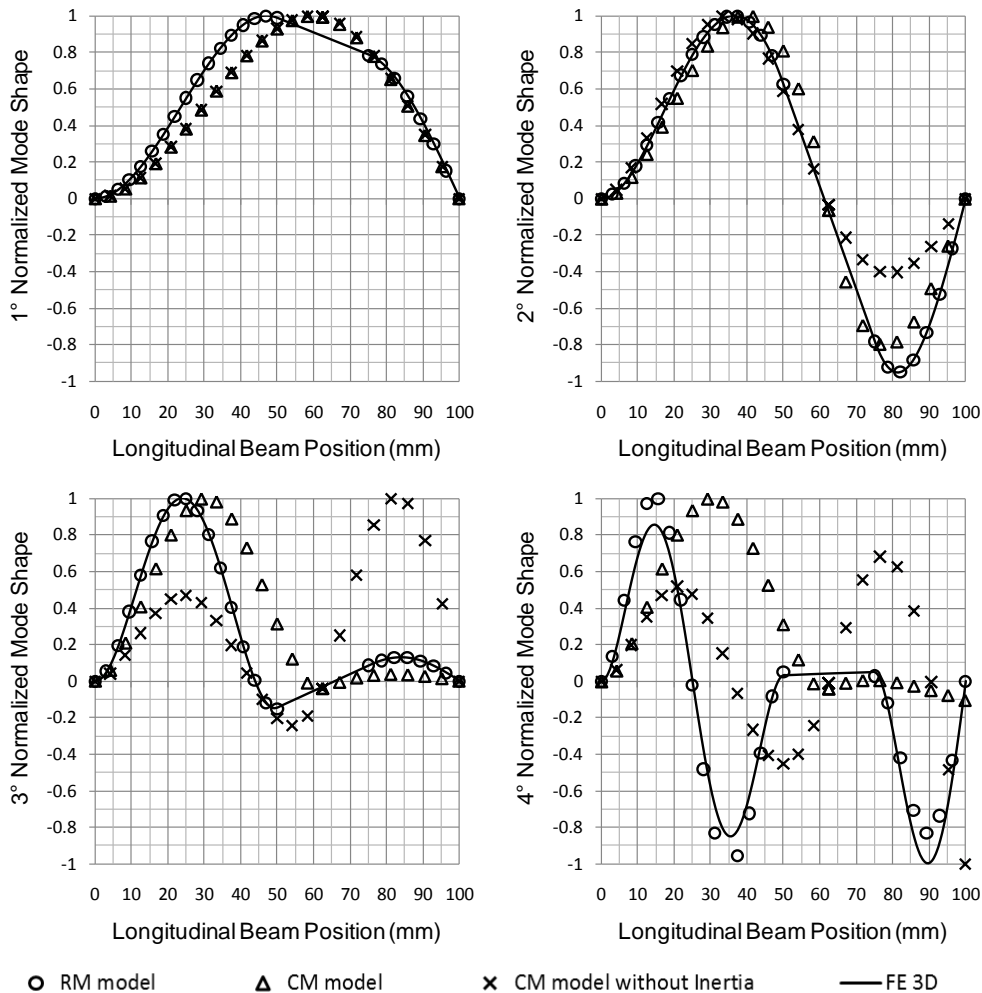


Figure 5. First four eigenmodes for the fixed-pinned beam.

Literature models

To the aim of evaluating the accuracy of the literature models in the prediction of the modal response of a beam carrying a ballast mass in arbitrary position, they are applied to the case study in Figure 2. The CM model was used as a substitute of the literature models due to its optimal agreement with the models taken from the literature (see Discussion section), to its easiest implementation, and to the need to investigate many sets of boundary conditions. The values of the geometric and inertial properties used in this comparison are collected in Table 4, for concentrated mass and rotary inertia and concentrated mass without rotary inertia respectively.

Table 6 shows, for all the constraint conditions in Table 1, the results provided by the CM model in both forms (with and without rotary inertia), organized as described in

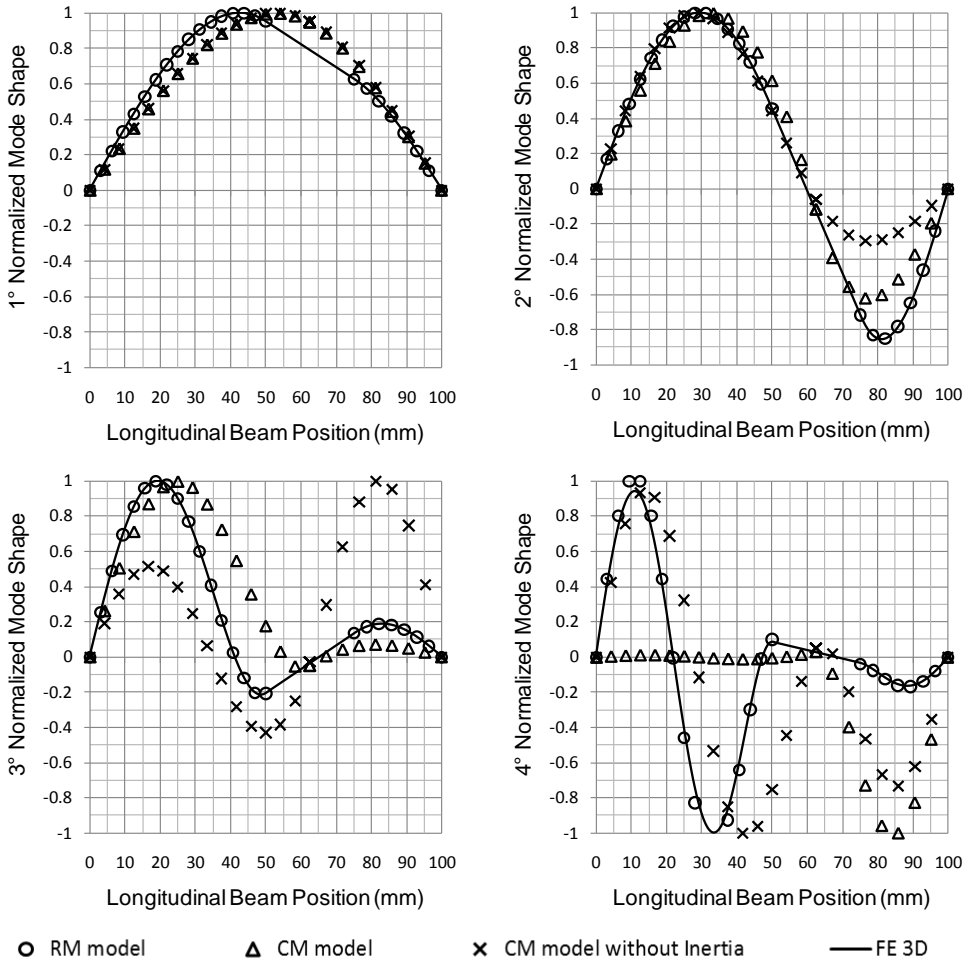


Figure 6. First four eigenmodes for the pinned-pinned beam.

Section 3.2.1. Figures 3, 4, 5, 6 and 7 display, in normalized form, the first four eigenmodes provided by the CM model, with rotary inertia (hollow triangles) and without rotary inertia (crosses), for the fixed-free, fixed-fixed, fixed-pinned, pinned-pinned and free-free constraint respectively.

Assessment of the rigid mass hypothesis

This last step aims at assessing the applicability of the rigid mass hypothesis (Section 2). Therefore, the analysis evaluates the sensitivity of the analytical model to the ratio between the bending stiffness of the ballast mass cross-section and that of the beam cross-section. Figure 2 highlights that both the beam and the ballast masses contribute to the bending stiffness of the ballast mass cross-section. Hence, it is possible to define the bending stiffness ratio φ as follows:

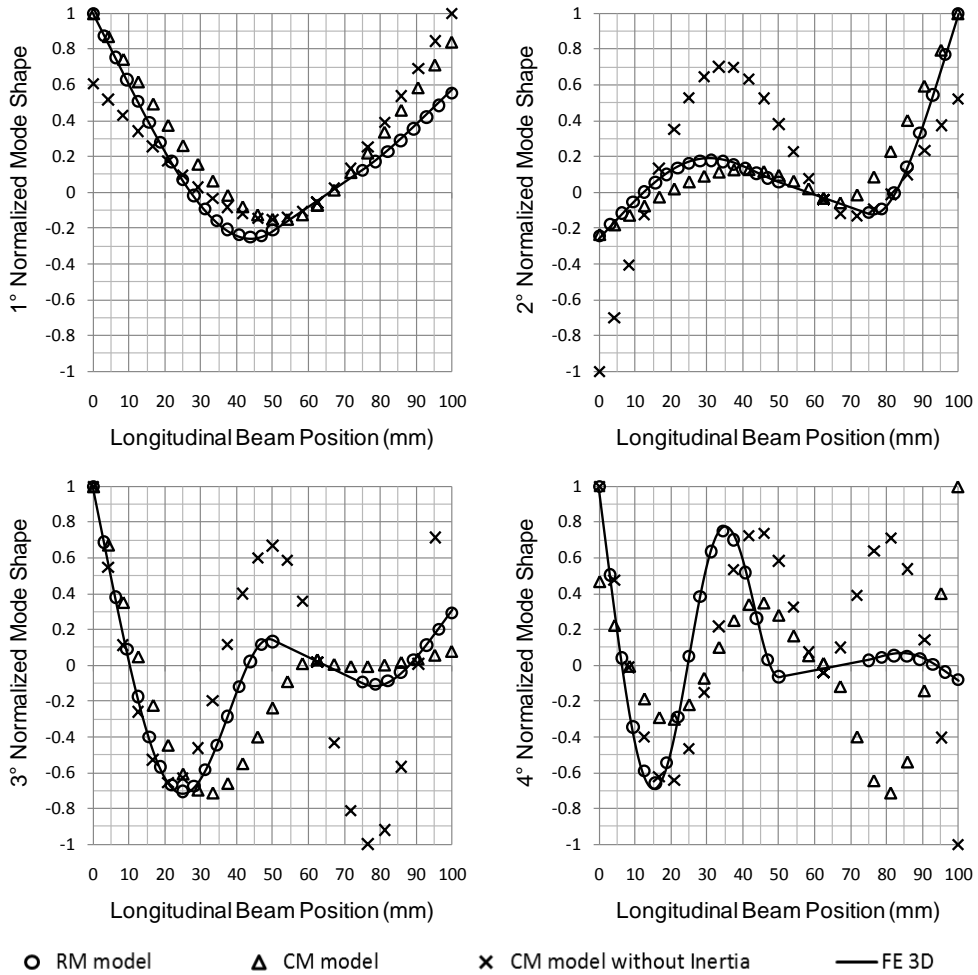


Figure 7. First four eigenmodes for the free-free beam.

$$\varphi = \frac{\langle EI \rangle_{mass}}{\langle EI \rangle_{beam}} \quad (36)$$

where $\langle EI \rangle_{mass}$ and $\langle EI \rangle_{beam}$ are calculated for a generic cross section, which can eventually be inhomogeneous (Appendix 2). The investigation was performed referring to the configuration of Figure 2, for two constraint conditions: fixed-free e fixed-fixed (Table 1).

In order to simplify the procedure, the bending stiffness ratio φ was varied by changing only the value of the Young's modulus of the inertial element E_{mass} , while keeping constant all the other parameters. Since the sensitivity analysis was performed through the three-dimensional FE model presented in Section 3.2.3, the same geometry and mass

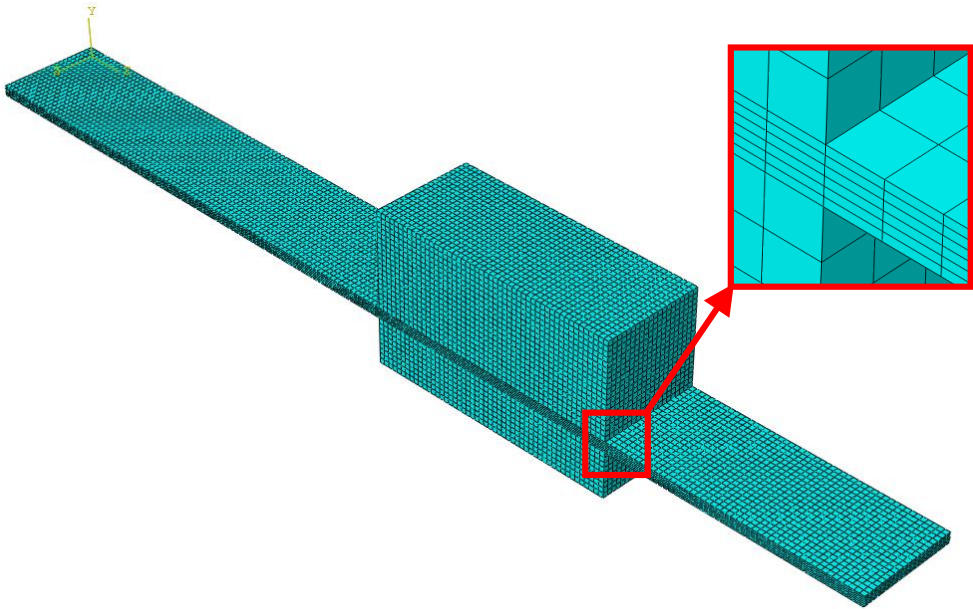


Figure 8. Image of the mesh performed on the three-dimensional FE model.

properties of the structure were used all along. Therefore, where the ballast masses are introduced, the cross-section of the structure comprises three layers with different Young's modulus.

Table 7 summarizes the values adopted for the elastic modulus of the ballast mass and the corresponding values of the bending stiffness ratio φ . Figures 9 and 10 show for the fixed-free and fixed-fixed beam respectively, the percentage relative error of the RM model on the first four eigenmodes, as a function of the bending stiffness ratio φ . The relative error was calculated with respect to the three-dimensional FE model.

5. DISCUSSION

The RM model consists of an algebraic system of eight linear equations in eight unknowns, represented, in matrix notation, by (33). These equations depend on the elastic and geometric properties of the beam and on the inertial properties of the rigid ballast mass.

Table 7 Young's modulus of the material of the ballast mass, corresponding bending stiffness both of the ballast mass and of the beam and bending stiffness ratio φ .

E_{mass} (GPa)	$\langle EI \rangle_{mass}$ (Nm ²)	$\langle EI \rangle_{beam}$ (Nm ²)	φ
632.2	1750	0.175	10000
210	591	0.175	3375
59.3	175	0.175	1000
28.25	87.6	0.175	500
4.95	17.5	0.175	100
2.375	8.76	0.175	50
0.4423	1.75	0.175	10

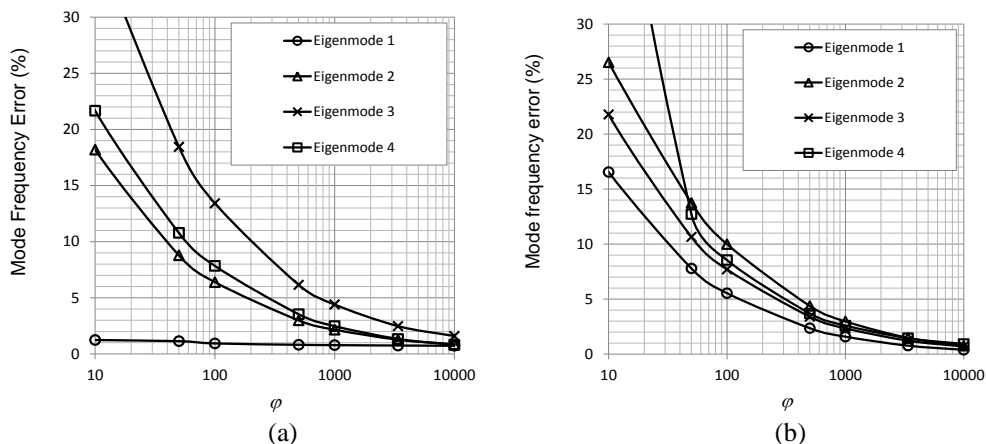


Figure 9. Plot of the percentage relative error in the prediction of the eigenfrequency as a function of the bending stiffness ratio: a) fixed-free beam, b) fixed-fixed

In addition, they include 6 parameters (χ_i , $i = 1..6$), which are a function of the set of boundary conditions of the structure being examined.

By examining the RM model, we observe that by setting to zero some of the model parameters, the model reduces to the classical analytical model presented in the literature [6]-[11], [14], [15] that describe the added ballast mass as concentrated. In particular:

- $b = 0$: concentrated ballast mass;
- $J_{sz} = 0$: ballast mass without rotary inertia;
- $m = 0$: ballast mass without mass.

Table 3 shows the excellent accuracy of the CM model when compared to the classical models from the literature, for all the eigenfrequencies and sets of boundary conditions examined. Therefore, the CM model unifies, in a general approach and for several sets of boundary conditions, the literature models.

Table 5 highlights that the results from the RM model and from the two-dimensional FE model closely match. The perfect agreement between the two methods, which testifies the accuracy of the RM model, is imputable to the same underlying hypotheses (Euler beam formulation and rigid mass).

Two observations can be made by examining Table 6. First, the RM model provides very accurate results also in comparison with the three-dimensional FE model, with an error ranging from 0.7% to 2%. In particular, the RM model always exceeds the FE model prediction since it assumes a rigid mass and does not account for the shear deformability of the beam. Second, literature models (represented by the CM model) provide an error ranging from 1.6% (at the first eigenfrequency for the fixed-free constraint), up to a maximum of 54% (at the fourth eigenfrequency for the fixed-pinned constraint). In particular, the forecasts of the literature models without rotary inertia either overestimate or underestimate the numerical forecasts. This alternate error is connected to a poor accuracy in the calculation of the eigenmode as can be seen from the diagrams in Figures 3-7. By

contrast, the literature models with rotary inertia always underestimate the numerical forecasts, with higher percentage relative errors. This is due to the fact that the underestimation of the stiffness in the region of the ballast mass (PQ). On the whole, in comparison to the literature models (represented by the CM model) the RM model predicts much more accurately the eigenfrequencies of the beam for whichever constraint is considered.

Figures 3-7 highlight the excellent agreement between the RM model (hollow circles) and the three-dimensional FE model (solid line). A little discrepancy between these models occurs only at the fourth eigenfrequency of the fixed-pinned beam (Figure 5). This is imputable to the complex curvature in the transition region between the beam and the ballast mass, which is described by the FE model. In addition, the straight deformed shape of the ballast mass (solid line in Figures 3-7) fully justifies the rigid mass hypothesis for the case study here examined.

Figures 3-7 highlight that the concentrated mass model without rotary inertia (crosses) and the concentrated mass model with rotary inertia (hollow triangles) provide with fair accuracy only the first or second eigenmodes depending on the set of boundary conditions.

By contrast, the predictions of the higher eigenmodes, which are fairly complex, are completely wrong. In conclusions, the models that describe the mass as concentrated, artificially alter the stiffness of the structure, thus providing an incorrect mode shape prediction.

From Figures 9 and 10 we can see that for both beam configurations examined, the error of the RM model decreases as the bending stiffness ratio φ increases. Obviously, this can be attributed to the hypothesis of rigid mass underling the RM model. In the case of the fixed-free beam (Figure 9), with exception of the third eigenmode, the error is lower than 11% up to φ equal to 50. The higher error for the third eigenmode (10% at a bending stiffness ratio equal to 200) is imputable to the significant bending strain occurring in this eigenmode near the rigid mass (solid line in Figure 3). Finally, Figure 9 highlight that the bending stiffness ratio does not affect the accuracy of the first eigenfrequency prediction for this constraint condition.

Figure 10 shows a higher error than in Figure 9 for all the eigenfrequencies at corresponding values of φ . On the whole, however, the error is more uniform between eigenmodes. This, once again, can be attributed to the higher deformation occurring for the eigenmodes in this constraint condition (fixed-fixed), which, consequently, can be less accurately described by the RM model.

On the whole, the hypothesis of a rigid ballast mass is fully justified when the bending stiffness ratio is high, as usually occurs in practice. For example, assuming the same material for the beam and ballast mass and a ratio between the cross-section in the region of the ballast mass and that of the beam equal to 2, 4 or 8, the bending stiffness ratio φ equals 8, 64, and 512 respectively. In the case study in Figure 2, the ratio φ is 3350. When the stiffness ratio is higher than 1000, the error is lower than 3% on the first four eigenfrequencies, thus comparable to a computational model.

In conclusion, the assessment of the RM model testifies its great accuracy for a wide range of beam configurations with ballast mass. The method can be applied to whichever beam section, including inhomogeneous section beam. Since the model relies on the Euler-Bernulli beam theory, its accuracy decreases when thick beams are examined, in particular in the prediction of the higher eigenmodes. Much more details about this can be found in the works from Grant [29] and Han et al. [30].

6. CONCLUSIONS

The paper develops the Rigid Mass (RM) model for the modal analysis of a constant cross-section beam, carrying a ballast mass for resonance tuning. As main hypotheses, the model describes the beam according to the Euler-Bernoulli formulation and the ballast mass as rigid, with mass and rotary inertia. Five sets of boundary conditions can be examined through the RM model, which reduces to a square matrix (dimension eight per eight) that provide the characteristic equation and thus the eigenfrequencies and eigenmodes of the structure. When reduced to describe the ballast mass as a concentrated mass either with or without inertia, the RM model provides results that match closely those of the analogous models from the literature. A very good agreement is obtained also in the comparison between the RM model and the two- and three-dimensional FE models. By contrast, the literature models describing the ballast mass as a concentrated mass either with or without rotary inertia, can lead to noticeable errors in the eigenfrequencies and eigenmodes prediction. With regard to the rigid mass hypothesis, the results show that it is a good approximation for the great majority of the resonator structures occurring in practice.

REFERENCES

- [1] Hassanpour, P.A., Cleghorn W.L., Mills J.K., Esmailzadeh E., 2007, "Exact solution of the oscillatory behaviour under axial force of a beam with a concentrated mass within its interval", *Journal of Vibration and Control*, **13**, pp. 1723–1739.
- [2] Roundy, S., and Wright, P.K., 2004, "A piezoelectric vibration based generator for wireless electronics", *Smart materials and structures*, **13**, pp. 1131–1142.
- [3] Jinkui, C., Haijun Z., Xiaozhen, D.U., Shuanghui, W., 2006, "The electrical characteristic simulation of Cantilever beam used in micro battery", *Proceedings of the International Technology and Innovation Conference*, Hangzhou, China, 6-7 November 2006, pp. 160-165.
- [4] Zurn, S., Hsieh, M., Smith, G., Markus, D., Zang, M., Hughes, G., Nam, Y., Arik, M., Polla, D., 2001, "Fabrication and structural characterization of a resonant frequency PZT micro-cantilever", *Smart Mater. Struct.*, **10**, pp. 252-263.
- [5] Brusa, E., De Bona, F., Gugliotta, A., Somà, A., 2003, "Dynamics modelling of microbeams under electrostatic load", *Proceedings of the DTIP*, Cannes-Mandelieu, 5-7 May 2003, pp. 181-186.
- [6] De Marquis, C., Erturk, A., Inman, D.J., 2009, "An electromechanical finite element model for piezoelectric energy harvester plates", *J. of Sound and Vibrat.*, **327**, pp. 9-25.
- [7] Ferrari, M., Ferrari, V., Guizzetti, M., Marioli, D., Taroni, A., 2008, "Piezoelectric multifrequency energy converter for power harvesting in autonomous Microsystems", *Sensors and Actuators*, **142**, pp. 329-335.
- [8] Laura, P.A.A., Pombo, J.L., Susemihl, E.A., 1974, "A note on the vibrations of a clamped-free beam with a mass at the free end", *Journal of Sound and Vibration*, **37**, pp. 161–168.
- [9] Yoo, H.H., Seo, S., Huh, K., 2002, "The effect of a concentrated mass on the modal characteristics of a rotating cantilever beam", *Proceedings of the Institution of Mechanical Engineers, Part C: Journal of Mechanical Engineering Science*, **216**, pp. 151–163.
- [10] Low, K.H. and Dubey, R.N., 1997, "A note on the fundamental shape function and frequency for beams under off-centre load", *Journal of Sound and Vibration*, **202**, pp. 134–138.
- [11] Low, K.H., 2001, "A comparative study of the eigenvalue solutions for mass-loaded beams under classical boundary conditions", *International Journal of Mechanical Sciences*, **43**, pp.

- [12] Low, K.H., 1998, “On the eigenfrequencies for mass loaded beams under classical boundary conditions”. *Journal of Sound and Vibration*, **215**, pp. 381–389.
- [13] Low, K.H., 1997, “Closed-form formulas for fundamental vibration frequency of beams under off-centre load”, *Journal of Sound and Vibration*, **201**, pp. 528–533.
- [14] Chai, G.B., and Low, K.H., 1993, “On the natural frequencies of beams carrying a concentrated mass” *Journal of Sound and Vibration*, **160**, pp. 161–166.
- [15] Naguleswaran, S., 1999, Lateral vibration of a uniform Euler-Bernoulli beam carrying a particle at an intermediate point. *Journal of Sound and Vibration*, **227**, pp. 205–214.
- [16] De Rosa, M.A., Ascoli, S., Nicastro, S., 1996, “Exact dynamic analysis of beam-mass systems” *Journal of Sound and Vibration*, **196**, pp. 529–533.
- [17] De Rosa, M.A., Franciosi, C., Maurizi, M.J., 1996, “On the dynamic behaviour of slender beams with elastic ends carrying a concentrated mass”, *Computers & Structures*, **58**, pp. 1145–1159.
- [18] Bruch, J.C. and Mitchell, T.P., 1997, “Vibrations of a mass-loaded clamped-free Timoshenko beam”, *Journal of Sound and Vibration*, **114**, pp. 341–345.
- [19] Swaminadham, M., and Michael, A., 1979, “A note on frequencies of a beam with a heavy tip mass..” *Journal of Sound and Vibration*, **66**, 144–147.
- [20] Hamdan, M.N., and Jubran, B.A., 1991, “Free and forced vibrations of a restrained uniform beam carrying an intermediate lumped mass and a rotary inertia”, *Journal of Sound and Vibration*, **150**, pp. 203–216.
- [21] Srinath, L. S., and Das, Y.C., 1967, Vibration of beams carrying mass, *Journal of Applied Mechanics: transaction of ASME*, **34**, pp. 784–785.
- [22] Naguleswaran, S., 2002, “Vibration of an Euler–Bernoulli beam on elastic end supports and with up to three step changes in cross-section”, *International Journal of Mechanical Sciences*, **44**, pp. 2541–2555.
- [23] Ju, F., Lee H.P., Lee, K.H., 1994, “On the free vibration of stepped beams”, *International Journal of Solids and Structures*, 1994, **31**, pp. 3125–3137.
- [24] Oguamanam, D.C.D. Free vibration of beams with finite mass rigid tip load and flexural-torsional coupling. *International Journal of Mechanical Sciences*, 2003, **45**, pp. 963–979.
- [25] Rama Bhat, B., and Wagner, H., 1976, “Natural frequencies of a uniform cantilever with a tip mass slender in the axial direction”, *Journal of Sound and Vibration*, **45**, pp. 304–307.
- [26] Kelly, S.G., 2000, *Fundamentals of mechanical vibrations*, 2nd ed., McGraw-Hill Science, p. 475.
- [27] Machine design group Reggio Emilia, http://www.machinedesign.re.unimore.it/pubblicazioni_eng.html, 2012.
- [28] 2008, Simulia ABAQUS *User’s Manual*. Dassault Systèmes Simulia Corp., (Providence, RI : HKS Inc.).
- [29] Grant, D. A., 1978, “The effect of rotary inertia and shear deformation on the frequency and normal mode equations of uniform beams carrying a concentrated mass”, *Journal of Sound and Vibration*, **57**, pp. 357–365.
- [30] Han, S.M., Benaroya H., Wei T., 1999, “Dynamics of transversely vibrating beams using four

engineering theories” *Journal of Sound and Vibration*, **225**, pp. 935–988.

[31] Gay, D., Hoa, S.V., Tsai, S.W., 2007, *Composite materials, design and applications*, 2nd ed., CRC PRESS.

Appendix A

The model developed in this work (RM model) has been implemented in software through the commercial tool Visual Basic 6.0, and can be freely downloaded from the web [27]. In the following we describe the simple procedure to perform an analysis.

From the main window of the software, click on the START button (or on File→New, or on the New button) to open the data logging interface (Figure 11). This window is organized in four input sections: the first collects the beam dimensions, the second the set of boundary conditions, the third the properties of the cross-section of the beam and the fourth the geometric and material properties of the ballast mass.

In order to describe how to use the software, in the following we will describe the calculation of the first four eigenfrequencies and eigenmodes of the case study (Section 3.2) in Figure 2, considering a simply supported configuration.

First, we define the length $a = 50$ mm of the beam portion OP , the length $2b = 25$ mm of the region PQ where the ballast mass is introduced, and the length $c = 25$ mm of the beam portion QR . Second, we select the proper boundary condition (pinned) at each ends of the beam (O, R) among that available (fixed, pinned, free). Third, we introduce the elastic properties of the material and the geometric properties of the cross-section of the two beam portions (OP, QR). For the most common cross-sections, these data can be defined through a simple automatic calculation tools by clicking on the “Calc beam section properties” button. As an alternative, we can type the values in the proper field. For this configuration we have: $E = 210000$ MPa, $\rho_{Beam} = 7850$ kg/m³, $A = 10$ mm², and $I = 0.833$ mm⁴. Finally, we have to introduce the inertial properties of the ballast mass. Again a simple automatic calculation tool is available by clicking on the “Calc mass property” button. For this configuration we have to define the following values: $m = 2.9438E-2$ kg, $J_{sz} = 2.2691E-6$ kg m².

In addition, by clicking on the “Option” button we can personalize the analysis through the following three options. First, the number of eigenfrequencies to be calculated. Second, the convergence criteria in the solution of the transcendental equation (35). Third, the resolution of the diagrams containing the plot of the eigenmodes.

Clicking on the “Frequency Analysis” button the calculation starts. Once the solution process is concluded, the window of the results appears (Figure 12). On the left, we can see the diagrams of the normalized eigenmodes, while on the right a table summarizes the eigenfrequencies and eigenmodes. A scroll bar is available, in case the window is larger than the screen. By selecting “Export Results” it is possible to save the results of the analysis in a text file containing both the eigenfrequencies and the eigenmodes.

Appendix B

In case of a inhomogeneous beam (Figure 13) having a constant width r , and constituted by n homogeneous layers with a thickness h_i , Young’s modulus E_i and mass density ρ_i , the equivalent bending stiffness is can be written as [31]:

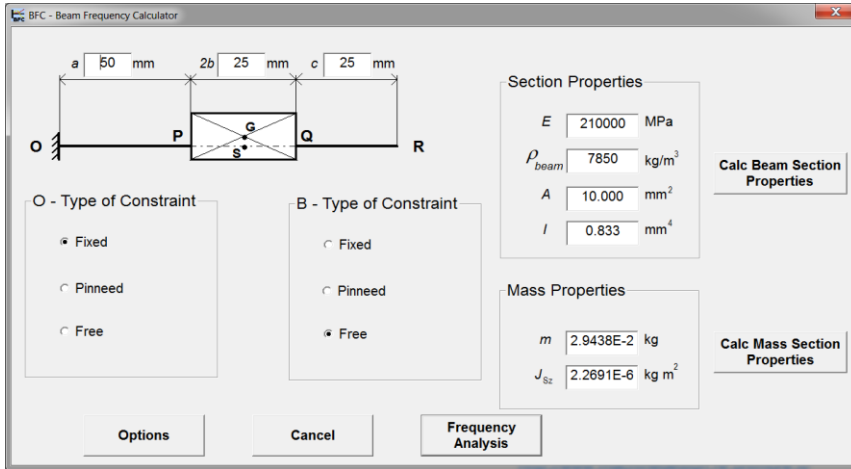


Figure 10. Data logging interface in the BFC software.

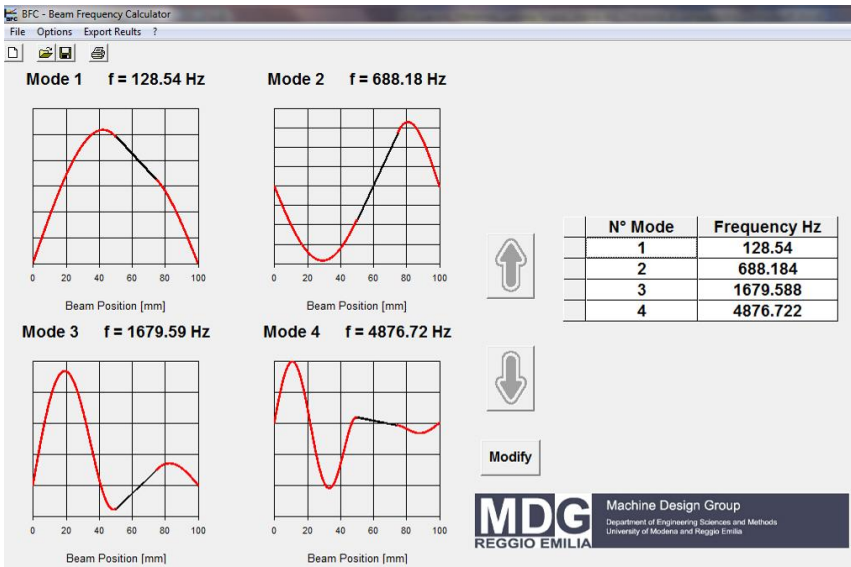


Figure 11. Results window of the BFC software.

$$\langle EI_z \rangle = \sum_{i=1}^n E_i f \left[\frac{h_i^3}{12} + A_i (y_i - h_E)^2 \right] \quad (B1)$$

where h_E is the distance between the centre of elasticity of the inhomogeneous section and the longitudinal axis of the beam. Similarly, the equivalent mass density $\bar{\rho}$ of the composite material results in the following expression:

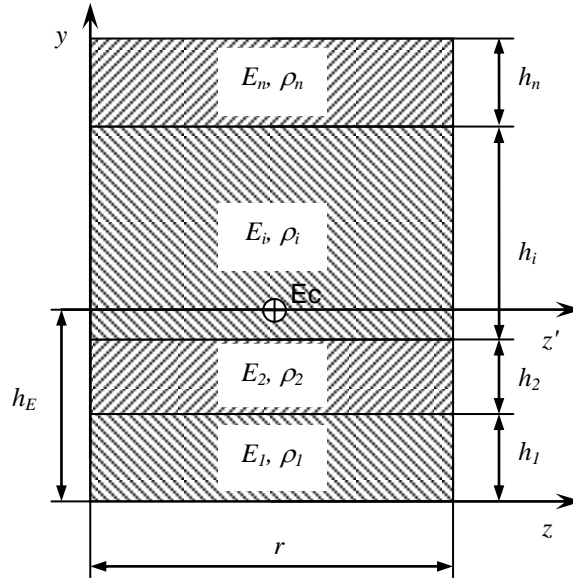


Figure 12. Sketch of the cross-section of a composite beam.

$$\bar{\rho} = \frac{\sum_{i=1}^n \rho_i A_i}{\sum_{i=1}^n A_i} \quad (\text{B2})$$

ON THE USE OF PIEZOELECTRIC STRAIN SENSORS FOR EXPERIMENTAL MODAL ANALYSIS

Emiliano Mucchi
Engineering Department
University of Ferrara, Italy
E-mail: emiliano.mucchi@unife.it

Giorgio Dalpiaz
Engineering Department
University of Ferrara, Italy
E-mail: giorgio.dalpiaz@unife.it

Abstract. Recently a novel miniaturized piezoelectric transducer has been manufactured. It is an Integrated Electronics Piezo Electric transducer which includes built-in microelectronics. This strain sensor can be suitable for EMA due to the low weight and little dimensions. Thus, the paper assesses the effectiveness of such a novel miniaturized sensor for application on experimental modal analysis. Comparisons between the results obtained by the accelerometers and the strain sensors are given, highlighting their pros and cons.

Keywords: modal analysis, strain sensor, strain frequency response function.

1. INTRODUCTION

Piezoelectricity arises from the cross-coupling of mechanical and electrical energy within certain materials; these materials can be used as both actuators and sensors. When a piezoelectric device is used as sensors, it actively generates charges in response to external loads, as compared to piezoresistive sensors where a voltage source is applied across the sensor to measure the strain. This cross-coupling from mechanical to electrical energy is called the direct piezoelectric effect [1].

Piezoelectric materials are commonly used to detect strain caused by structural vibrations in macro-scale structures or machinery. Strain sensors are applied to the mechanical structure to be monitored in industrial process controls and product quality. Assuming the presence of sensors has a negligible effect on the structure, the true strain can be measured by monitoring the electrical signals passing through the sensors and related to vibration of the structure. Moreover, the resultant strain measurand is an indirect measurement of stress forces acting along the structure to which the sensor is mounted. As such, these devices can provide insight into the behavior of mechanical systems or processes that generate machinery reactions. Monitoring such measurement signals can provide the necessary indication for process interrupt and pass/fail decisions or for determining wear and degradation of equipment and tooling. As an example, strain sensors are commonly used for monitoring the weld quality which is directly affected by electrode

clamping force. In this scenario, strain sensors may be used to verify that the clamping force has reached a desired minimum value before applying weld current. After reaching the minimum value, the strain sensor is used to immediately trigger weld current, which cuts cycle time and avoids electrode damage due to premature activation. Or the strain sensor may also be used to control the desired force value throughout the weld cycle leading to high quality parts with zero defects. Eventually, strain sensors are used for controlling processes in plastic injection molding, stamping, and pressing. It has to be underlined that the strain sensors suitable for condition monitoring or quality control have robust packaging for harsh industrial environments and large dimensions (generally 5X20X15mm) leading to relatively high weight. Thus, they are not suitable for applications in experimental modal analyses (EMA) of lightweight structures or mechanical systems, due to the mass loading effect. Mass loading is the effect caused by adding an additional mass to a dynamic structure. The aim of any measurement is to measure the response of a system as if the measurement equipment is not present. By adding a mass to a dynamic structure the dynamic behaviour of the structure will change. It is important to minimise this change to ensure the highest quality measurement. Usually, it is recommended to keep the ratio of mass of the item under test to the mass of the sensor below 10:1 [2,3].

Recently a novel miniaturized piezoelectric transducer (model PCB 740B02) that incorporates piezoelectric quartz sensing crystals that respond to a longitudinal change in distance has been manufactured. It is an Integrated Electronics Piezo Electric (IEPE) transducer which includes built-in microelectronics, i.e. it belongs to a class of sensors that has low impedance output electronics and works on a two wire constant current supply with voltage output. This strain sensor can be suitable for EMA due to the low weight (0.5 grams) and dimensions (5X1.8X15mm). Thus, the paper assesses the effectiveness of such a novel miniaturized sensor for application on experimental modal analysis.

An EMA campaign has been carried out on two types of brackets with different constraint conditions (freely-supported and clamped condition). These brackets are used in diesel engines to support different engine components such as gear pumps for steering systems, water pumps, fuel pumps, oil pumps, gas turbines, alternators. The EMA has been carried out by using both genuine piezoelectric accelerometers as well as the novel strain sensor. The results of the experimental measurements have been processed with different modal analysis algorithms in order to increase the robustness of the solution. Comparisons between the results obtained by the accelerometers and the strain sensors are given, highlighting their pros and cons. As this author is aware, this study is not present in the literature.

2. EXPERIMENTAL SETUP

For modal testing, it is necessary to measure the frequency response functions. For this reason an impact hammer (PCB 068C04) has been used to excite the different measurement points of the brackets and piezoelectric accelerometers (frequency range 1 to 10000 Hz) as well as strain sensors have been mounted on the brackets in order to measure the responses. The measurement locations were chosen in order to give an adequate spatial resolution to describe the global structural mode shapes. Measurements were acquired in three orthogonal directions in order to estimate the mode shapes in the 3D space. The procedure used to perform the EMA is the conventional procedure in which both excitation and response are measured simultaneously to obtain the Inertance, i.e. the FRF between

acceleration and force or the strain frequency response functions (SFRF), i.e. ratio the FRF between deformation and force [4].

During the EMA test, the response points were maintained fixed during the tests, while the excitation moved from one measurement point to another in order to obtain the FRFs among all the considered points. Figure 1 depicts the excitation points of the bracket being tested and the position where the responses in terms of acceleration and strain is measured (namely 1 and 2 for Bracket A, 3 and 4 for Bracket B). With the aim of assess the sensibility of the results to the sensor location, modal tests with strain sensors located in different positions have been carried out, maintaining always the same excitation points. In particular, concerning Bracket A, three different modal tests have been carried out: the first by located the accelerometer in point 1X (i.e. point 1 - direction X), the second by located the strain sensor in point 1X and the third by located the strain sensor in point 2Y. Concerning Bracket B, four different modal tests have been carried out: the first by located a triaxial accelerometer in point 4 (thus, measuring directions X,Y,Z), the second by located three strain sensors in point 4Y, 3Z and 3X, the third by located a strain sensor in point 3Z and the fourth by located the strain sensor in point 3X. The signals were acquired by using sampling frequency and frequency resolution according with the type of brackets and with the kind of constraint condition. An exponential window for the response signals and a force window for the force signals are used in order to reduce leakage. The input autopower-spectra, output autopower-spectra and cross-power-spectra are evaluated and stored for each measurement location. During the tests, the coherence function is monitored as an on-line check of data quality. The method used for mounting the strain sensor on the test surface is direct adhesive mounting with a quick-bonding gel, as for accelerometers. The surface should be flat with a minimum surface finish of $16\mu\text{m}$. The adhesive layer must be thin and uniform since excessive amounts of adhesive may affect the response of the transducer.

The brackets under test are identified with capital letters A and B. Bracket A is used in marine diesel engines to support the water pump for the cooling system; bracket B is used in automotive engines to support the pump for the steering system. The bracket material is aluminium. The brackets were tested in two different kinds of constraint conditions. The freely-supported condition was approximated by suspending the brackets using soft bungee cords (Table 1 and 2). The natural resonances of the bungee cords are much lower than the lowest natural frequencies of the brackets, so let assume that the modes of the bungee cords do not influence the analysis of the brackets. The brackets on the clamped conditions were analysed by screwing them to their engine block as in the actual condition (Table 1 and 2).

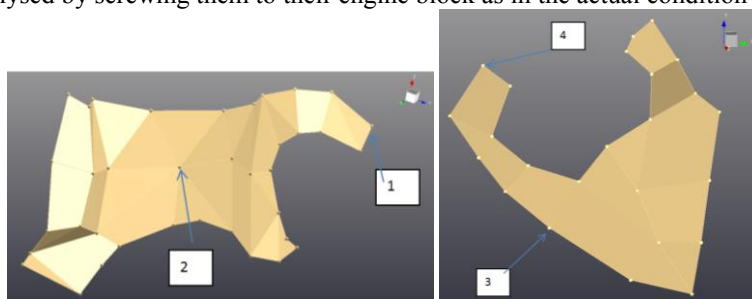


Figure 1. Wireframes of the excitation points and position of response points (namely 1,2,3,4) during the EMA of Brackets A and B.

Table 1. Results about bracket A.





	Freely-supported				Clamped			
<u>Bracket A</u>								
Modal frequencies and damping (mean value of LSCE and PolyMAX methods)	accelerometer		Strain sensor		accelerometer		Strain sensor	
	Fn [Hz]	ζ [%]	Fn [Hz]	ζ [%]	Fn [Hz]	ζ [%]	Fn [Hz]	ζ [%]
	1452	0.50	1510	0.32	510	1.45	535	1.6
	2551	0.09	2661	0.1	1258	0.67	1276	0.68
	2965	0.13	3129	0.12	1577	0.40	1586	0.5
	3921	0.08	3954	0.16	/	/	/	/
5003	0.18	5053	0.15	/	/	/	/	

Table 2. Results about bracket B.

	Freely-supported				Clamped			
<u>Bracket B</u>								
Modal frequencies and damping (mean value of LSCE and PolyMAX methods)	accelerometer		Strain sensor		accelerometer		Strain sensor	
	Fn [Hz]	ζ [%]	Fn [Hz]	ζ [%]	Fn [Hz]	ζ [%]	Fn [Hz]	ζ [%]
	1043	0.32	1068	0.29	511	0.10	525	0.22
	1218	0.51	1271	0.30	738	0.16	760	0.23
	2194	0.37	2229	0.30	886	0.12	887	0.1
	2994	0.17	3031	0.21	952	0.25	953	0.14
3088	0.39	3160	0.26	/	/	/	/	

3. RESULTS AND DISCUSSION

Once the experimental modal tests and analyses of the brackets have been performed, natural frequencies, modal damping and mode shapes are available for all modes in the frequency band of analysis, both using the acceleration as well as the strain as response.

The natural frequency (f_n) and modal damping (ζ) were obtained by averaging the values coming from the Least Square Complex Exponential (LSCE) [2][3] method and PolyMAX

method [2][5]. In fact, the results of the experimental measurements have been processed with two different modal analysis algorithms in order to increase the robustness of the solution: the LSCE method which works in the time domain and the frequency domain algorithm PolyMAX. In order to evaluate the effectiveness of the FRFs based on strain, the modal parameters (natural frequencies, modal damping and mode shapes) estimated by the accelerometers (that will be taken as reference) are compared with the modal parameters estimated by the strain sensor.

Figure 2 and Figure 3 reports the FRF-sum (i.e. the complex sum of FRFs of all the measured points) for the two brackets for the free-free and clamped EMA, both using the acceleration as well as the strain as response. The figures clearly present peaks which define the natural frequencies. It is interesting to note that the FRF-sum curves related to the strain sensor are clear, well-defined and easy to understand, in comparison to those related to the accelerometers. Table 1 and Table 2 collect the natural frequencies and the modal damping for the brackets being studied. Concerning Bracket A, the difference between the natural frequencies estimated by the accelerations and the strains is always less than 6%, while for Bracket B is less than 5%. Thus, the FRFs based on strain are very accurate in terms of precision in the natural frequency estimation. The comparison regarding damping is still rather good. The Modal Assurance Criterion (MAC) [2][3] has been used as a technique to determine the degree of correlation between mode shapes. This method has been applied in this paper in order to quantitatively compare the eigenvectors of the different analyses: MAC values close to one indicate a very good correlation (similar mode shapes), MAC values close to zero indicate that the two modes do not show any correlation (different shapes). Usually, MAC values higher than 0.7 indicate good correlation. Table 3, Table 4, Table 5 compare the mode shapes in terms of MAC. The MAC values presented in these tables clearly state that the three EMA lead to similar mode shapes, in fact the relative MAC values are always higher than 0.7. Thus, the mode shapes estimated by using strains in the FRFs are very accurate as those obtained by the accelerometers.

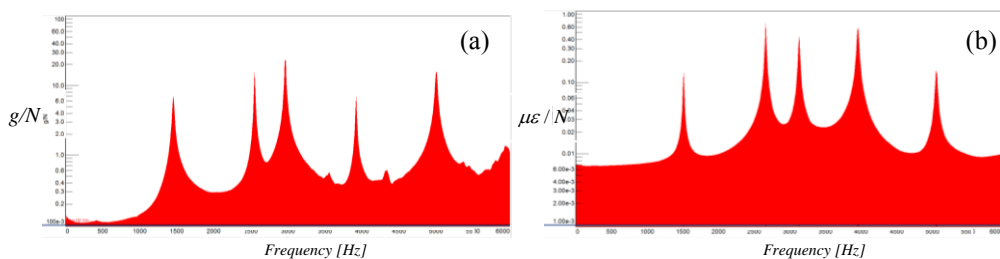


Figure 2. FRF-sum (amplitude) for the free-free EMA of Bracket A based on (a) acceleration and (b) strain.

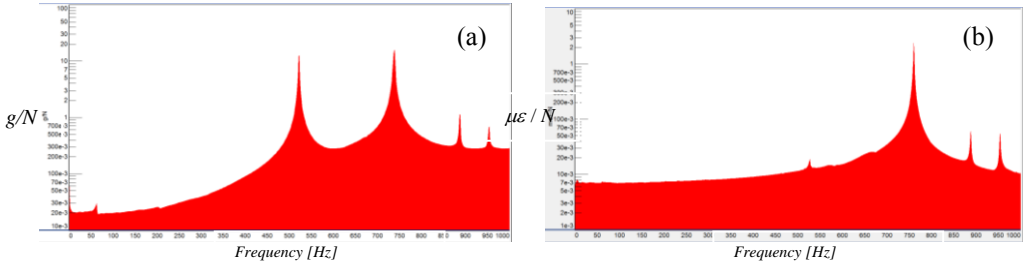


Figure 3. FRF-sum (amplitude) for the clamped EMA of Bracket B based on (a) acceleration and on (b) strain in point 3Z.

Table 3. MAC values between the Free-Free EMA of Bracket A with strain sensor in Point 1X and with accelerometer in Point 1X.

		Strain Sensor in 1X				
		F _n [Hz]	1510	2661	3129	3954
Accelerometer in 1X	1448	0.98				
	2538	0,01	0.83			
	2965	0.02	0.01	0.92		
	3921	0.06	0.04	0.01	0.86	
	5004	0.02	0.05	0.04	0.01	0.76

Table 4. MAC values between the Free-Free EMA of Bracket A with strain sensor in Point 2Y and with accelerometer in Point 1X.

		Strain Sensor in 2Y				
		F _n [Hz]	1510	2661	3129	3954
Accelerometer in 1X	1448	0.97				
	2538	0,01	0.88			
	2965	0.01	0.01	0.82		
	3921	0.06	0.07	0.01	0.83	
	5004	0.01	0.01	0.03	0.01	0.75

Table 5. MAC values between the Free-Free EMA of Bracket B with strain sensor in Points 4Y,3Z, 3X and with accelerometer in Points 4X,4Y,4Z.

	Fn[Hz]	Strain Sensor in 4Y,3Z, 3X				
		1070	1271	2230	3031	3170
Accelerometer in 4X,4Y,4Z	1041	0.80				
	1209	0,01	0.70			
	2194	0.05	0.01	0.80		
	2993	0.01	0.03	0.03	0.83	
	3092	0.01	0.01	0.01	0.02	0.88

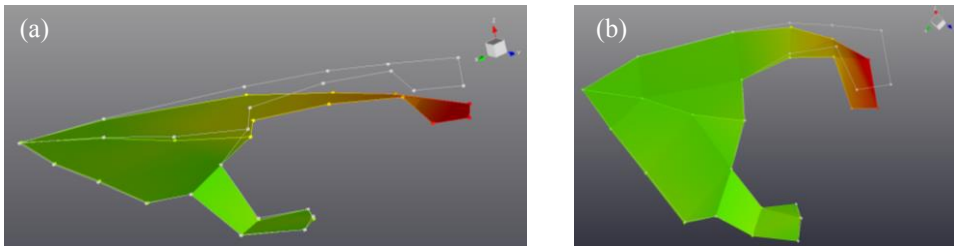


Figure 4. 1st and 2nd mode shape for the clamped EMA of Bracket B at 522 and 737 Hz, respectively. In the 1st mode (a) the main deformation regards Z direction, while for the 2nd mode (b) the main deformation is on the XY plane.

Table 6. MAC values between the clamped EMA of Bracket B with strain sensor in Points 3Z and with accelerometer in Points 4X,4Y,4Z.

	Fn[Hz]	Strain Sensor in 3Z			
		526	760	887	953
Accelerometer in 4X,4Y,4Z	522	0.02			
	737	0.01	0.06		
	886	0.01	0.03	0.71	
	952	0.01	0.06	0.37	0.47

Further modal tests have been carried out in order to assess the sensibility of the results to the sensor location. It is well known [2][3] that in genuine modal tests carried out with accelerometers, they should not be located in (or close to) nodal lines. Nodal lines [2][3][6] are lines or zones of zero displacement in a certain mode shape. Therefore, when the system being studied is hit on a point along these nodal lines, the system would not experience any vibration from that mode.

Obviously, it is expected that when the modal test is carried out with strain sensors, this rule should be respected. The modal tests hereafter presented and discussed aim at verifying this. Figure 4 depicts the first two mode shapes regarding Bracket B. It is clear that in the 1st mode the main displacement regards Z direction, while for the 2nd mode the main displacement occur on the XY plane. A modal test has been carried out by locating the strain sensor in point 3Z and the results has been compared with the accelerometer results (Table 5). It is interesting to note that the MAC values for the first two modes are very low (0.02 and 0.06). This behavior can be explained considering the particular shapes of the two modes (Figure 4), which they do not experience any deformation in point 3Z (i.e. point 3 – direction Z) , even if in point 3 a displacement along the Z direction occur. Thus, it is correct that the strain sensor located in point 3Z cannot capture the deformation regarding those two modes. On the contrary, modes 3 and 4 are correctly captured by the strain sensor since such shapes involve deformation of point 3Z. The reader might consider that the strain sensor can measure deformation and not displacement.

Thus, in case of acceleration-based modal analysis, it is necessary to locate the accelerometers in regions far from nodal lines where the level of displacement is high. On the other hand, in case of strain-based modal analysis, it is necessary to locate the strain sensors in regions where the level of deformation is high.

4. CONCLUSIONS

The paper presents a comparisons in terms of modal parameters between the genuine experimental modal analysis carried out by accelerometers and by strain sensors. The comparison has shown that the strain sensor are very useful and precise for the estimation of natural frequency, modal damping and mode shapes. Attention should be paid during the set up: in case of acceleration-based modal analysis, it is necessary to locate the accelerometers in regions far from nodal lines where the level of displacement is high; on the other hand, in case of strain-based modal analysis, it is necessary to locate the strain sensors in regions where the level of deformation is high.

Acknowledgements

This work has been developed within the Laboratory of Advanced Mechanics (MechLav) of Ferrara Technopole, realized through the contribution of Regione Emilia Romagna - Assessorato Attivita' Produttive, Sviluppo Economico, Piano telematico - POR-FESR 2007-2013, Attivita' I.1.1.

REFERENCES

- [1] Kona, S., Oldhamb, R., and Horowitz, R., 2007. "Piezoresistive and Piezoelectric MEMS Strain Sensors for Vibration Detection". *Sensors and Smart Structures Technologies for Civil, Mechanical, and Aerospace Systems*, **6529**, pp. 1-11.
- [2] In book, Heylen, W., Lammens, S., and Sas, P., 2003. *Modal analysis theory and testing*. Katholieke Univeriteit Leuven.
- [3] In book, Ewins D. J., 2000. *Modal Testing: Theory, Practice and Application*.
- [4] In Proceedings, Bernasconi, O., Ewins, D.J., 1989. "Application of strain modal testing to real structures". In Proceedings IMAC 1989, pp. 1453-1464.

- [5] In Proceedings, Guillaume, P., Verboven, S., Vanlanduit, Van der Auweraer H., Peeters, B., 2003. "A poly-reference implementation of the least-square complex frequency-domain estimator". In Proceedings IMAC 21, Kissimmee, USA, pp. 183-192.
- [6] Mucchi, E., 2013. "On the sweet spot estimation in beach tennis rackets". *Measurement*, **46**, pp. 1399–1410.

MULTIVARIATE ANALYSIS FOR BEARING CLASSIFICATION

Giuseppe Curcurù

*Department of Mechanical Technology, Production and Management Engineering,
University of Palermo, Italy*

E-mail: giuseppe.curcuru@unipa.it

Marco Cocconcelli

*Department of Engineering Sciences and Methods,
University of Modena and Reggio Emilia, Italy*

E-mail: marco.cocconcelli@unimore.it

Riccardo Rubini

*Department of Engineering Sciences and Methods,
University of Modena and Reggio Emilia, Italy*

E-mail: riccardo.rubini@unimore.it

Abstract. *Ball bearings are probably the most used components in mechanics. Since they usually connect mechanical parts with relative speed – like the rotor and stator in an electrical motor - they are at the core of the machine functionality. Damage in these components quickly lead to sudden and unexpected stop of machineries with a loss of production for industries. In a packaging machine, for example, an unexpected stop of a couple of hours may cause costs of loss-production which are several time the cost of the single broken component. The need to avoid unexpected stop becomes mandatory for Industry, which asked Academia ideas, algorithms and procedures to monitor the health of the bearings and predict any incipient fault. In the last decades a huge number of publications covered analysis of vibration data of monitored bearing. A massive number of signal processing techniques have been suggested both on a physical model of the component, or pure blind data analysis, such as the so-called artificial intelligent systems (Artificial Neural Networks, Support Vector Machines, etc...). Most of these intelligent systems require two steps: a training step that “teaches” the system about the correct classification of the incoming data (e.g. into “health bearing” class or “damaged bearing”), and a test step when the inner rules build in the training step are tested on unknown data. There’s a lot interest on intelligent system approaches, since they promise to automatically build the classification rules and they could be applied to different components, not only on the ball bearing. Unfortunately there is a hidden trouble: the intelligent systems work well if the incoming data vectors work well, i.e. they properly describe the signal changes related to an incipient damage. The aim of this paper is to prove that the RMS and Kurtosis values of the vibration data are good parameters that allow a proper classification of the bearing. Moreover the variability of these parameters is close related to the evolution of the damage, suggesting a simple procedure to make the bearings diagnostics.*

Keywords: *ball bearing, condition monitoring, cluster analysis, data variability, multivariate analysis.*

1. INTRODUCTION

The monitoring of rolling bearings in non-stationary motion conditions is a very topical issue [1], linked to the spread of the servomotors in the packaging industry. The classical methods of signal analysis for the support diagnostics [2,3], based on the mechanical model of the machine, require a pre-processing step of the vibration signal – enabled by the knowledge of the real motion law followed by the mechanical chain – for the application of the Computed Order Tracking [4,5]. Signal conditioning – which is focused on a re-sampling act to reconstruct the dynamics of the system as if it was detected at constant angles of rotation of the motor – necessarily introduces errors that may become relevant in case of complex motion laws with reversals of the direction of rotation.

The methodological approach provided by the application of expert systems is an effective alternative, conversely requiring a thorough harvesting of the characteristics of the signal in the different operation conditions of the machine, due to malfunction, wear or breakage. The Artificial Neural Networks, the most widely used algorithms for pattern recognition, must be trained with a considerable amount of information, even about the faulty machine, this constituting a strong limit for industrial applications.

The Hierarchical cluster analysis [6], introduced by Horowitz and Sahni [7], was developed and subsequently adopted for diagnostic purposes [8,9], for the identification of faults in bearings operating at constant speed [10,11]. The choice of appropriate features, sensitive to the amplitude and the statistical distribution of the signal, allows to make a diagnosis based on the only measurements in healthy conditions.

In this paper, the Hierarchical cluster analysis was applied to the monitoring of bearings following a complex motion law.

2. BACKGROUNDS

This paper started long ago in 2010 from the previous works of the authors [12, 13], where they successfully used Artificial Neural Networks and Support Vector Machines to make diagnostic of ball bearing in a variable speed application.

The ball bearing, a NSK 6309, was part of a brushless direct drive motor. Direct drive motors, also known as servomotors, are fully controlled by drive. The speed of the motor and the direction of the motion could be customized and continuously varied. Servomotors are increasing their presence in automatic machineries, since further components like gearboxes or mechanical cams were replaced. The speed variation can be completely defined by software.

In the experimental set-up a polynomial speed profile is considered. The corresponding angle position profile is shown in Figure 1. In particular the cyclic motion of the motor can be divided into two parts of different duration. At the end of the first part the motor slows down, stops and then starts the second part of the cycle in the opposite direction, until it reaches the initial condition. Should be noticed that such a complex motion makes classic diagnostic approaches (based on spectrum analysis) useless, since the high non-stationary components of the signal. This consideration justifies the use of artificial intelligent methods in order to overcome this limitation. Detailed explanation of the methods used and their results can be found in [12,13].

A piezoelectric monoaxial accelerometer (IEPE) was positioned near the bearing on the external case of the motor. The measuring direction was radial with respect to motor shaft and the bearing. An external load of 4kN was acting directly on the shaft by means of a belt. The duration of a complete cycle of the motor was 1.029 seconds sampled at 10kHz.

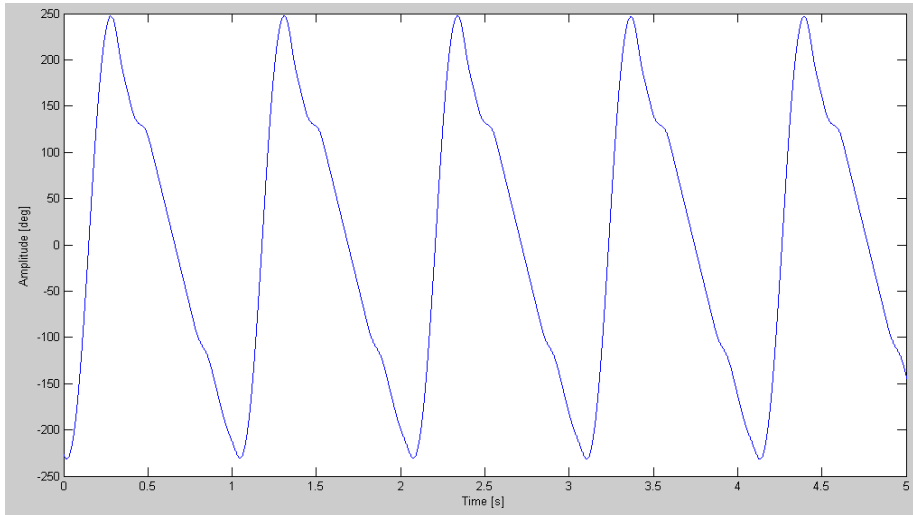


Figure 1. Polynomial position profile used in the experimental tests.

Table 1. Health status of the tested bearings

Bearing ref.	Health condition
1	Several working hours but still healthy
2	Several working hours but still healthy
3	Several working hours but still healthy
4	Distributed roughness
5	Distributed roughness, broken cage
6	Distributed roughness on the inner ring, localized damage on the outer ring
7	Distributed roughness on the inner ring, localized damage on the outer ring
8	Artificial damage on the outer ring
9	Artificial damage on the inner ring
10	New bearing
11	New bearing
12	Several working hours but still healthy
13	New bearing

The input vector for both Artificial Neural Networks and Support Vector Machines was made of the RMS value and Kurtosis value of the vibration data relative to a single cycle.

Thirteen bearings were available, seven of them were healthy bearing, and the others were claimed as faulty with different levels of wear. A complete list of the bearings with an explanation of health conditions is reported in Table 1.

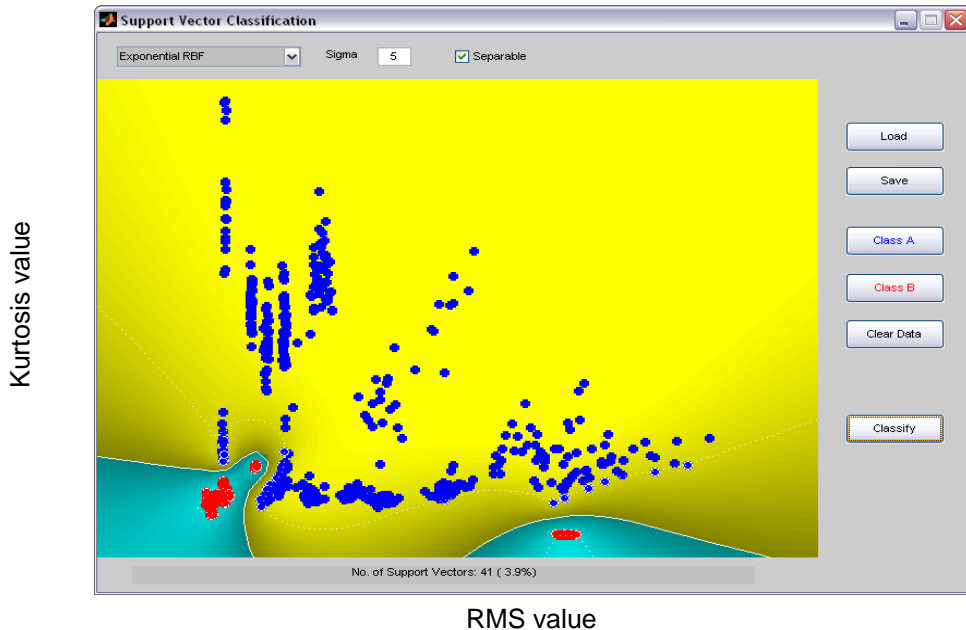


Figure 2. SVM classification of faulted (blue dots) and healthy bearings (red dots).

All the stated conditions of the bearings have been checked at the end of the test opening the bearings. The artificial damages refer to local fault made by an engraving cutter tool.

For each bearing 48 machine cycles data were available, and their distribution in a kurtosis-RMS map is shown in Figure 2, as a result of the Support Vector Machines classification [13]. Blue dots are faulted bearings while the red ones are the healthy.

The next section describes the use of cluster analysis to prove the usefulness of RMS and kurtosis as references of the bearing health status.

3. CLUSTER ANALYSIS

3.1 Methods

Cluster analysis aims to aggregate data on the basis of a greater or lesser similarity among the data elements. Should be noticed that the term cluster analysis doesn't refer to a specific algorithm, but a class of approaches that may be very different from one to another. Foundations on the cluster analysis could be found in [6].

In this paper the cluster analysis is made by means of Matlab Statistics Toolbox. This toolbox makes available a wide range of options regarding the type of clustering, metrics used, clustering methods, etc...

The chosen characteristics are:

- i. **Hierarchical clustering**, i.d. data are sorted and aggregated following a specific grouping method and a specific metric to quantify the similarity. At the base of the resulting dendrogram each data is separated from the others, while going on the top of the dendrogram the data start to be aggregated until all the data are considered as different realizations of a single class.

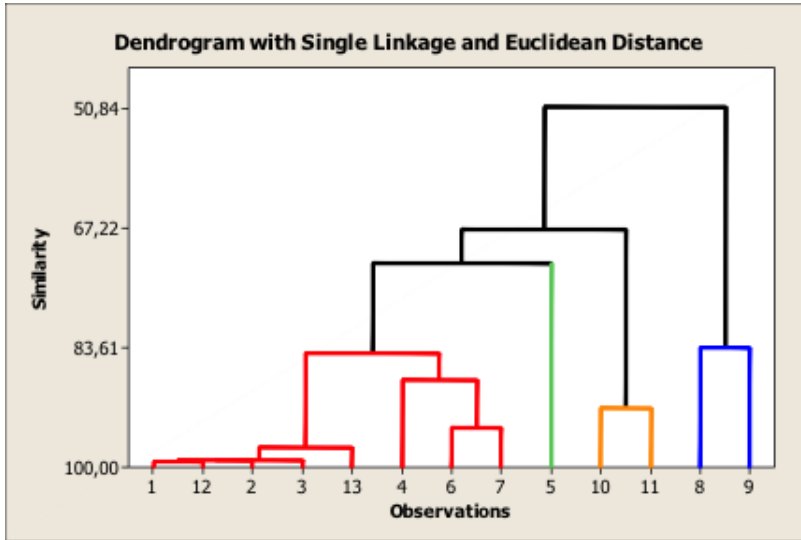


Figure 3. Dendrogram of the hierarchical clustering of bearings.

- i. **Single-linkage method** [14], i.d. data sets with the minimum distance to each other are aggregate at every iteration.
- ii. **aEuclidean metric**, i.d. the distance between two data set is computed by the Euclidean distance. Note: in this paper each data set is a two-element vector (RMS and kurtosis).

Since 48 complete cycles are available for each bearing, the clustering algorithm has been forced to works on the mean value of RMS and kurtosis computed for each cycle.

3.2 Results

The resulting dendrogram of the cluster analysis is shown in Figure 3. The labels on the x-axis (Observations) are the same bearing reference of Table 1.

The main classes are 5. The dendrogram starts to aggregate the healthy bearings (#1, #12, #2, #3), while the bearings subjected to distributed roughness (#4, #6, #7) constitute a different class. Surprisingly it seems that healthy bearings and distributed roughness bearings are more similar to each other with respect to remaining classes.

Two healthy bearings are classified together (#10, #11). Since these two bearings were out-of-box bearings, probably the resulting signal is due to the break-in period, with a more impulsive behaviour of the mechanical signal.

The artificially faulted bearings (#8, #9) constitute a specific class, while bearing #5 is a single class. Probably the late stage of damage in the bearing (broken cage) reflects a specific characteristic of RMS and kurtosis, which differ from the other cases.

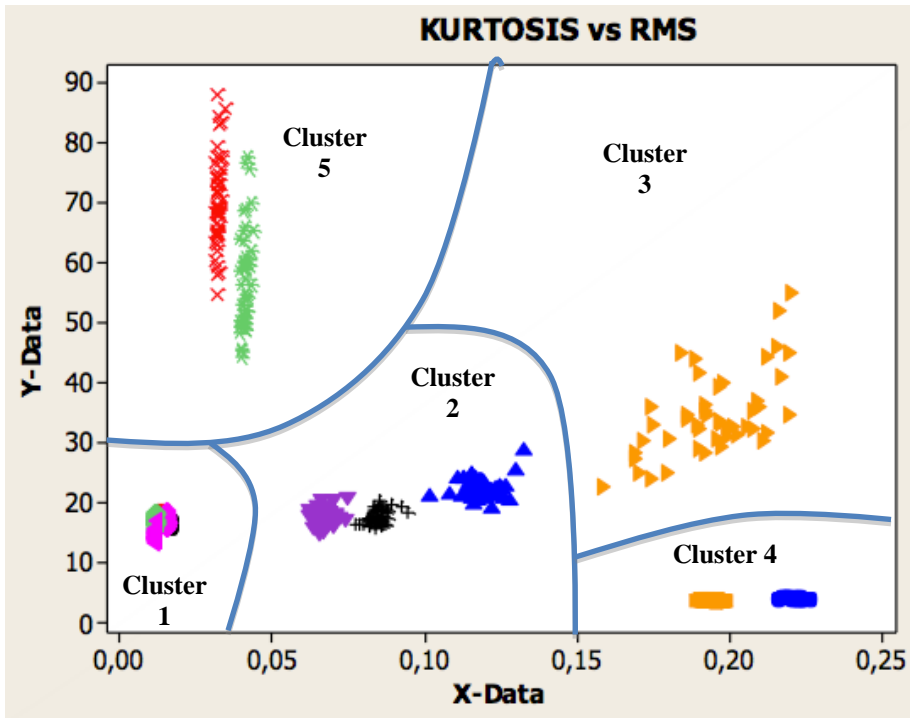


Figure 4. Separation of data into clusters.

With reference to the RMS-kurtosis map obtained from SVM approach (see Figure 2) the classification obtained by clustering data is reported in Figure 4, where X-Data is the RMS value and Y-Data is the kurtosis.

4. DISPERSION OF DATA

4.1 Discussion

In the previous section clustering analysis proved that the RMS and kurtosis values of vibration data are good parameters to clearly identify the health of the bearing, but also to characterize the fault evolution in time or the fault nature (artificial or natural fault).

Another interesting result come from the analysis of the Figure 4. There are a lot data points and each one has a specific colour and shape to clearly identify the bearing it belongs to. Same data points (same colour, same shape) are repetitions, i.e. different cycles, of the same bearing. The list of bearings in Table 1 shows that the number of healthy bearings (7) is higher than the faulted ones (6), but surprisingly the most area of the RMS-kurtosis is covered by the faulted bearings data. Healthy bearing data are very close one to the other, the same the dispersion of repetitions belonging to the same bearing. Faulted bearings data are characterized by a wide dispersion of the repetitions points. This could be justified by the second principle of thermodynamics: the entropy of the system increases with the fault evolution and consequently the statistic parameters (RMS and kurtosis) increase their variability.

The area of data dispersion in the RMS-kurtosis map characterizes the health status of

the bearings. In particular, the radius of the circumscribed circle, centred in the barycentre of the data points, defines the area and it is assumed as indicator to classify bearings. A suggested procedure to do diagnostics of ball bearings is described in the following section.

4.1 Big bang method

Let's introduce the "big bang method", because like in the origin of the Universe when all masses started to expand, it seems that the repetition points expand in the RMS-kurtosis map as damage increases.

The main idea of the procedure is shown in Figure 4. The radius of the circumscribed circumference increases as the damage level of the bearing increases. From an opposite point of view, the same radius circumscribes a different percentage of data available depending on the health status of the bearing.

All these information are used in the following anomaly-detection procedure:

- Fix a reference radius (i.e. an area) so that all the health bearing data points are supposed to belong to.
- Fix a percentage of repetition points that have to be included in the fixed area in order to classified as healthy (threshold).
- Acquire a sufficient number of working cycles of the bearing.
- Check if the bearing data satisfy the threshold and classify the bearing.

Just an example of application is shown in Figure 5:

- Suppose to fix an arbitrary reference radius (discontinuous dotted line) based on the experience of the user.
- Fix the threshold, i.e. the 80% of the dispersion of acquired data should be inside the reference radius to be classified as healthy bearing.

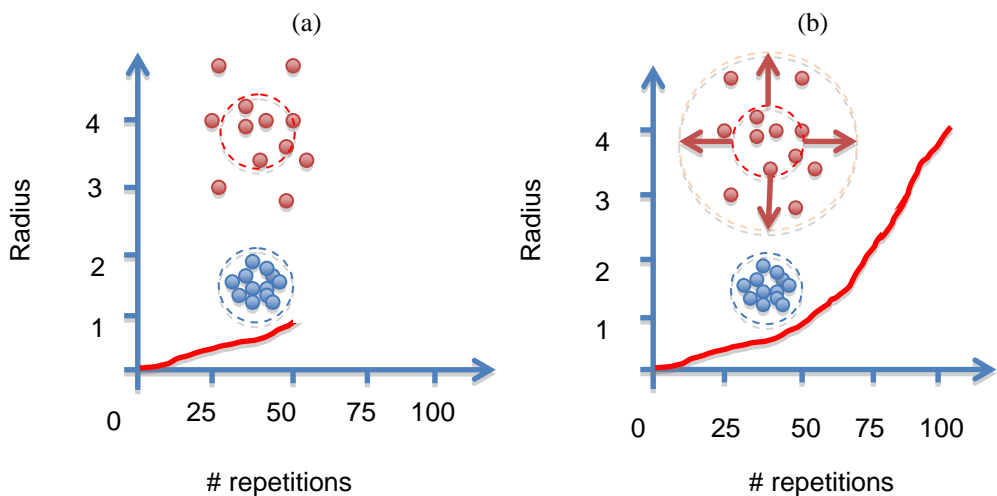


Figure 5. Circumscribed area radius for healthy (blue) (a) and faulty (red) (b) data.

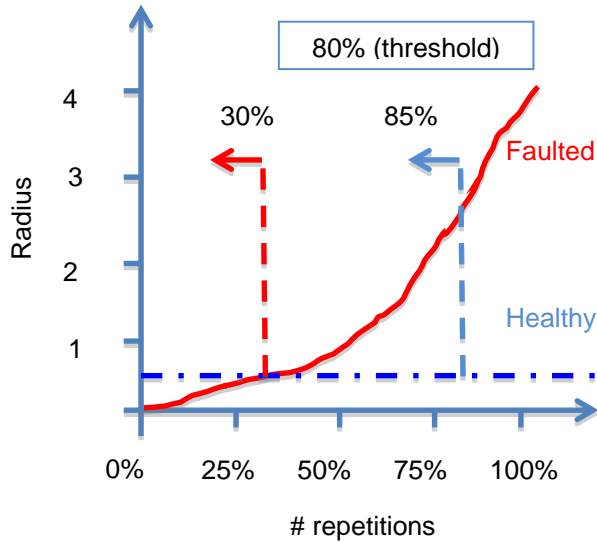


Figure 6. Example of the anomaly-detection procedure.

- Figure 5 shows also the radius of the circumscribed area as a function of the percentage of data included. In particular plots for two different bearings (red and blue line) are shown.
- At the reference radius, the 85% of blue line bearing data are included. Since this value overcome the fixed threshold (80%) the bearing is classified as healthy.
- At the reference radius, the 30% of red line bearing data are included. Since this value is lower than the fixed threshold (80%) the bearing is classified as faulted.

5. CONCLUSION

In this paper the use of RMS and kurtosis value as fault detector parameters has been examined. Based on past works of the authors, the choice of those two statistical parameters has been proved by means of a clustering analysis of the data available. In particular bearings in the same health conditions have been grouped together. Moreover the clustering process identifies also the type of damage, for example it divides the artificially damaged bearing from the natural one in a separate class.

Another advantage in the use of a RMS-kurtosis map is the high variance of data in faulted bearings. While an healthy bearing has a high repeatability of RMS and kurtosis value for each cycle of the working motion profile, a faulted bearing changes these value at each cycle, mainly because of the impulsive and non-stationary components of the signal.

All these comments lead to a procedure for the anomaly-detection in bearings. The procedure is very simple and requires only a small amount of historical data in order to set the thresholds. Comments and results on the usefulness of the proposed techniques are under developing and will be soon published.

6. ACKNOWLEDGEMENTS

The authors wish to thank the Inter Departmental Research Center INTERMECH MoRE of the University of Modena and Reggio Emilia for the financial support.

REFERENCES

- [1] Dalpiaz G., Rubini R., D'Elia G., Cocconcelli M., Chaari F., Zimroz R., Bartelmus W., Haddar M., 2014 "Advances in Condition Monitoring of Machinery in Non-Stationary Operations" Springer-Verlag, Berlin Heidelberg.
- [2] Randall R.B., Antoni J., 2011 "Rolling element bearing diagnostics: a tutorial" *Mechanical Systems and Signal Processing* Vol. 25(2), 485-520.
- [3] Rubini R., Meneghetti U., 2001 "Application of the Envelope and Wavelet Transform Analyses for the Diagnosis of Incipient Faults in Ball Bearings" *Mechanical Systems and Signal Processing* Vol. 15(2), 287-302.
- [4] Potter R., 1990 "A new order tracking method for rotating machinery" *Sound and Vibration* 24, 30-34.
- [5] Cocconcelli M., Bassi L., Secchi C., Fantuzzi C., Rubini R., 2012 "An Algorithm to Diagnose Ball Bearing Faults in Servomotors Running Arbitrary Motor Profiles" *Mechanical Systems and Signal Processing* Vol. 27, 667-682.
- [6] Hastie T., Tibshirani R., Friedman J. 2009 "The Elements of Statistical Learning", Springer New York.
- [7] Horowitz E., Sahni S. 1973 "Fundamentals of computer algorithms", Computer Science Press, Rockville, Maryland.
- [8] Skormin V.A., Popyack L.J., Gorodetski V.I., Araiza M.L., Michel J.D. 1999 "Applications of cluster analysis in diagnostics-related problems" *Proceedings of the 1999 IEEE Aerospace Conference* Vol 3, 161-168, Snowmass at Aspen, CO, USA.
- [9] Artes M., Del Castillo L., Perez J. 2003 "Failure prevention and diagnosis in machine elements using cluster" *Proceedings of the Tenth International Congress on Sound and Vibration* 1197-1203, Stockholm, Sweden.
- [10] Lei Y., He Z., Zi Y., Chen X. 2008 "New clustering algorithm-based fault diagnosis using compensation distance evaluation technique" *Mechanical Systems and Signal Processing* Vol. 22, 419-435.
- [11] Delgado Prieto M., Cirrincione G., Garcia Espinosa A., Ortega J.A., Heanao H. 2013 "Bearing fault detection by a novel condition-monitoring scheme based on statistical-time features and neural networks" *IEEE Transactions on Industrial Electronics* Vol 30(8) 3398-3407.
- [12] Cocconcelli M., Rubini R., Zimroz R., Bartelmus W. 2011 "Diagnostics of Ball Bearings in Varying-Speed Motors by Means of Artificial Neural Networks" *The Eight International Conference on Condition Monitoring and Machinery Failure Prevention Technologies*, Cardiff, UK.

- [13] Coconcelli M., Rubini R. 2011 "Support Vector Machines for Condition Monitoring of Bearings in a Varying-Speed Machinery" The Eight International Conference on Condition Monitoring and Machinery Failure Prevention Technologies, Cardiff, UK.
- [14] Sibson R. 1973 "SLINK: an optimally efficient algorithm for the single-link cluster method" The Computer Journal (British Computer Society) Vol 16 (1) 30–34.

FULL FIELD OPTICAL MEASUREMENTS FOR OPERATIONAL MODAL ANALYSIS AND MODEL UPDATING

Alessandro Zanmarini
Department of Industrial Engineering,
University of Bologna, Italy
e-mail: a.zanmarini@unibo.it

Abstract. Full field measurements, with their high accuracy in spatial definition of displacement patterns, are gaining increasing interest within the engineering community. Whereas in general the full field measurements can be more aimed at laboratory testing like traditional Experimental Modal Analysis (EMA), due to their complex equipment and the relation with the excitation sources, low cost image based & output only approaches like Hi-Speed Digital Image Correlation (DIC) can be challenged also in Operational Modal Analysis (OMA) framework. This work would then like to show Hi-Speed DIC usefulness also in the OMA procedures and consequent Model Updating (MU) technologies. In particular, the impact of many measurement points, or channels, is shown on the experimental identification of a vibrating plate and later on the numerical model refinement of the restraining conditions, with comments and details.

Keywords: operational modal analysis, model updating, full field measurements, optical techniques, non-contact measurements

1. INTRODUCTION

Optical full field measurements deliver displacement maps composed of many degrees of freedom (dofs), instead of one single channel as traditional transducers. Plus, the calculated fields are generally 3D, meaning that it is like having thousand of three-axial sensors precisely located on the surface under investigation, but without the mass loading they would bring. The advantage for light weight structure measurements in mechanical and aeronautical applications is straightforward. Optical measurements are a breakthrough for hi-resolution spatial description of a deforming surface, either statically or dynamically. They also open the path to a consistent experimental evaluation of dynamic strains and rotational dofs, both relevant for the updating process of complex models, together with fault detection [1], failure and fatigue evaluations [2–4] and substructuring frameworks. On the opposite side, nowadays the optical measurements have the drawback of having too many dofs to handle, compared to the quantity for which traditional approaches [5, 6] and, later, commercial software were devel-

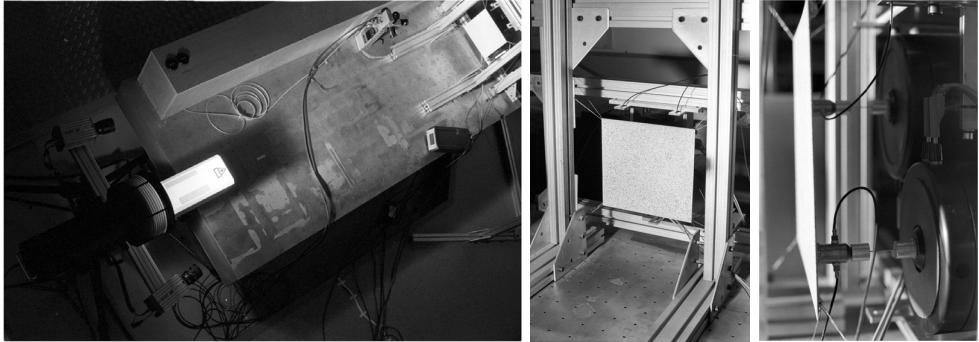


Figure 1. The experimental set-up for vibration measurements by means of optical equipment

oped: it is easy to deal with 30k dofs instead of few mono-axial channels, with clear impact on the whole identification & optimisation process. Image-based technologies are pushed by the recent advances in electronic components, from image capturing sensors, to computing engines, to hi-speed embedded RAM and solid state storage, together with a general rebate of the experimental equipment costs.

OMA has seen a recent accelerated development [7], especially dealing with civil engineering and big structures, for its ability to identify an experimental model (frequencies and shapes) from output only signals, but taken as a limited number of dataset. One of the recognised strength of OMA approach is the simplicity (and inherent low costs) of the experimental set-up, which can avoid the need of expensive controlled excitation sources and linked experimental procedures, while it can take advantage from natural excitation and generally white noise inputs, even if quantitatively unknown.

It came the idea to exploit in OMA the datasets obtained from Hi-Speed DIC in the framework of the full field experimental modal analysis project of the author¹, with their high spatial accuracy, simply disregarding the excitation data and restarting from the time domain full field displacement results, since these measurements were taken from broadband burst random noise excitations, with white noise spectra. The purpose is clearly to assess the impact of high spatial accuracy on the identification and model updating process. Besides, the original datasets could not be exploited at their maximal potential, but had to be spatially down-sampled to cope with an handable size by the identification and model updating software. The results obtained are reported below and commented in detail.

2. TEST CASE: FULL FIELD MEASUREMENTS ON A PLATE

In a growing field, such as that of full-field optical measurement technologies, comparative studies become of uttermost importance in assessing the achieved quality and the consistency with previous approaches. Full-field optical instruments still need to completely demonstrate their potentialities and benchmarks are missing in dynamic measurements.

A basic requirement for the set-up was that of showing a high modal density and closeness of the eigenmodes in a frequency range common to all three optical techniques, to stress

¹A. Zanarini, Project TEFMA - Towards Experimental Full Field Modal Analysis, Marie Curie FP7-PEOPLE-IEF-2011 PIEF-GA-2011-298543 grant, hosted at the Technische Universitaet Wien, Austria

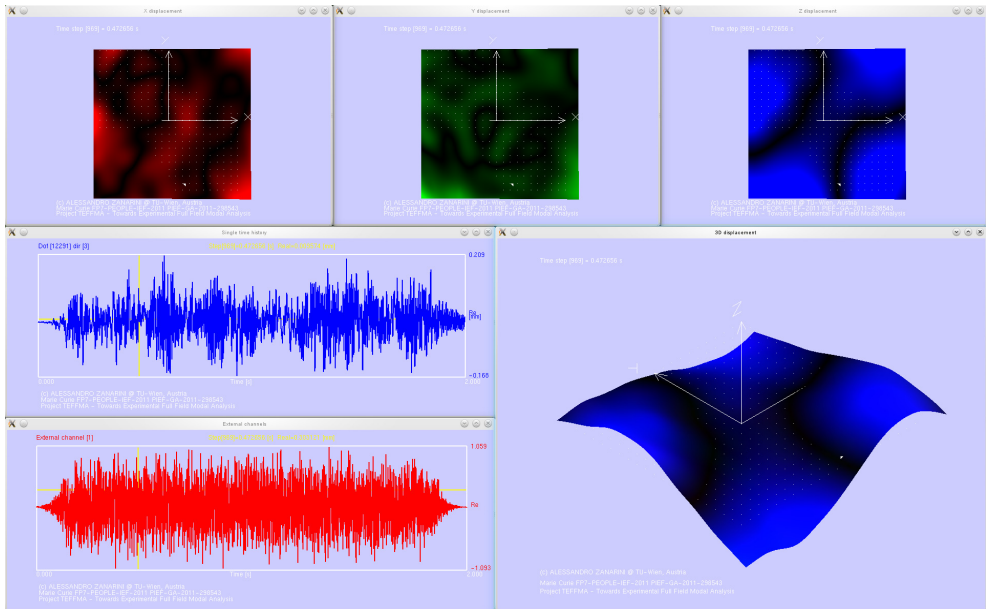


Figure 2. Screen shot from the custom software, coded to manage the full field datasets

the multi-input-*many*-output opportunity for extended analysis approaches [5, 6, 8] and to investigate the dependence of the vibration patterns from the specific excitation point.

For these reasons, a thin aluminium plate with the shape of a nearly perfect square was adopted. It was restrained by thin wires glued on the back at the four corners and fixed to pillars on the anti-vibration optical table, as shown in Fig.(1). The system of restrains had only to suppress the low-frequency rigid body motions and leave the plate in a quasi-free-free condition, to let appreciate the behaviour of the borders in dynamic motion. Two shakers were attached to the back of the plate and driven by the acquisition systems.

A linearity check was successfully performed on the test set-up that was prepared as common basis for a comparative study between different optical techniques (ESPI, DIC, SLDV). In fact, ESPI [9] is the most sensitive of the three technologies, but limited in displacement range, and required minimal power in the input, while DIC is less sensitive and generally requires bigger displacements and hi-power in the input source; SLDV works in an intermediate range of displacements and input power.

The tuning of the common experimental set-up was critical, especially in finding the right tension for the restraining wires, which were excited by so discrepant motions, from the sub-micron range while driving ESPI measurements to the sub-millimetre range in DIC. In spite of difficulties, the right adjustment was reached, to assure the wanted linear behaviour and avoid undesirable disturbing vibrations of the wires. The acquired data can be eventually compared also with those from ESPI measurements collected in 2005 [8].

In this work were used the Hi-Speed DIC measurements, which are already in the time domain, as OMA requires [7] to build the correlation matrices from them (see also Appendix A). The measurement system was placed in front of the plate, with acquisition direction

orthogonal to the flat surface and the centre of the plate as reference point for the alignment. It consisted in the 3D Hi-Speed DIC Dantec dynamics Q-450 and hi-speed cameras (Nanosense Mk III, 4 GB of memory - 1040 fps at 1280 x 1024 pixels maximal resolution) with hi-power & hi-frequency white light system. The field of view was maximized to retain the maximal spatial resolution available, according to the dynamic requirements. Due to these latter, the DIC pixel resolution was reduced to let the hi-speed cameras run at higher frame-per-second rates.

From a lab-based point of view, attention was put on the requirements of the DIC approach, in the terms of the random pattern to be applied by a spray paint coating (the thin paint coating gave a rough surface, avoiding any reflection) on the object under test and in the terms of the calibration of the stereo camera system, to calculate all the intrinsic and extrinsic parameters of the lenses, perspective and point of view. Relevant work was also done for the acquisition of random events through automatic triggering of the input.

Attention was paid to the possibility to read and elaborate the experimental results; software was thus developed for data reading & representation, as can be seen in Fig.(2), where a screen shot shows a hi-speed DIC full field displacement pattern at a time step, together with single channel time histories, which show the burst random noise used to drive the tests.

But in order to prepare the measurements for the next challenges, it was necessary to conceive and manage innovative & complex experiments, with a relevant work in the lab and on the computing facilities of TU-Wien, mixing the knowledge in experimental analysis [5,6] with the practice on the available optical techniques, pushed to their performance limits in terms of accuracy and repeatability of results. The conceived common set-up shown in Fig.(1) permitted the full-field vibration measurements, in a multi-input-*many*-output general scheme. The acquisitions were assured on the linearly behaving plate, in the broad frequency range up to 1 kHz, with a frequency resolution in the whole band of 1Hz: the hi-speed cameras used for DIC could not go over 2048 fps, which was the sampling frequency in this image-based case.

The acquisition of dynamic signals was very fast by DIC, like acquiring one measurement from a single lumped sensor such as a common accelerometer, but the off-line work was quite heavy: half an hour was required to download the DIC time series from the cameras, about 3 days to evaluate the corresponding displacement fields in the time domain. Strong power was needed by the shakers, due to the weaker sensibility to displacement of the DIC technology, compared to ESPI and SLDV. In fact, at TU-Wien DIC was intended for much larger displacements in the range of millimetres, but proved in this project to be able, once precisely calibrated, to sense quite small vibrations also in the sub-millimetre range. The quality obtained from the measurements is promising for the elaborations of this work. In Fig.(3,4) are shown in row order some full-field deflection shapes from DIC at different & increasing time steps, with the modal superposition result of the lower eigenmodes in evidence, highlighting the continuous mixing of the modal base vectors to generate complex displacement patterns with promising spatial consistency.

The structural dynamics retained in the measurements seems again to play a relevant role in determining the complex shaped distribution of flexural motion inside the surface area and reflect that high modal density searched for at the time of the design of the experiment.

The measurement system available worked in a single-input-*many*-output scheme, since it was not possible to drive the two shakers together and evaluate the transfer functions from a unique multi-input-*many*-output test, even if the LMS Test.Lab software suite & Scadas

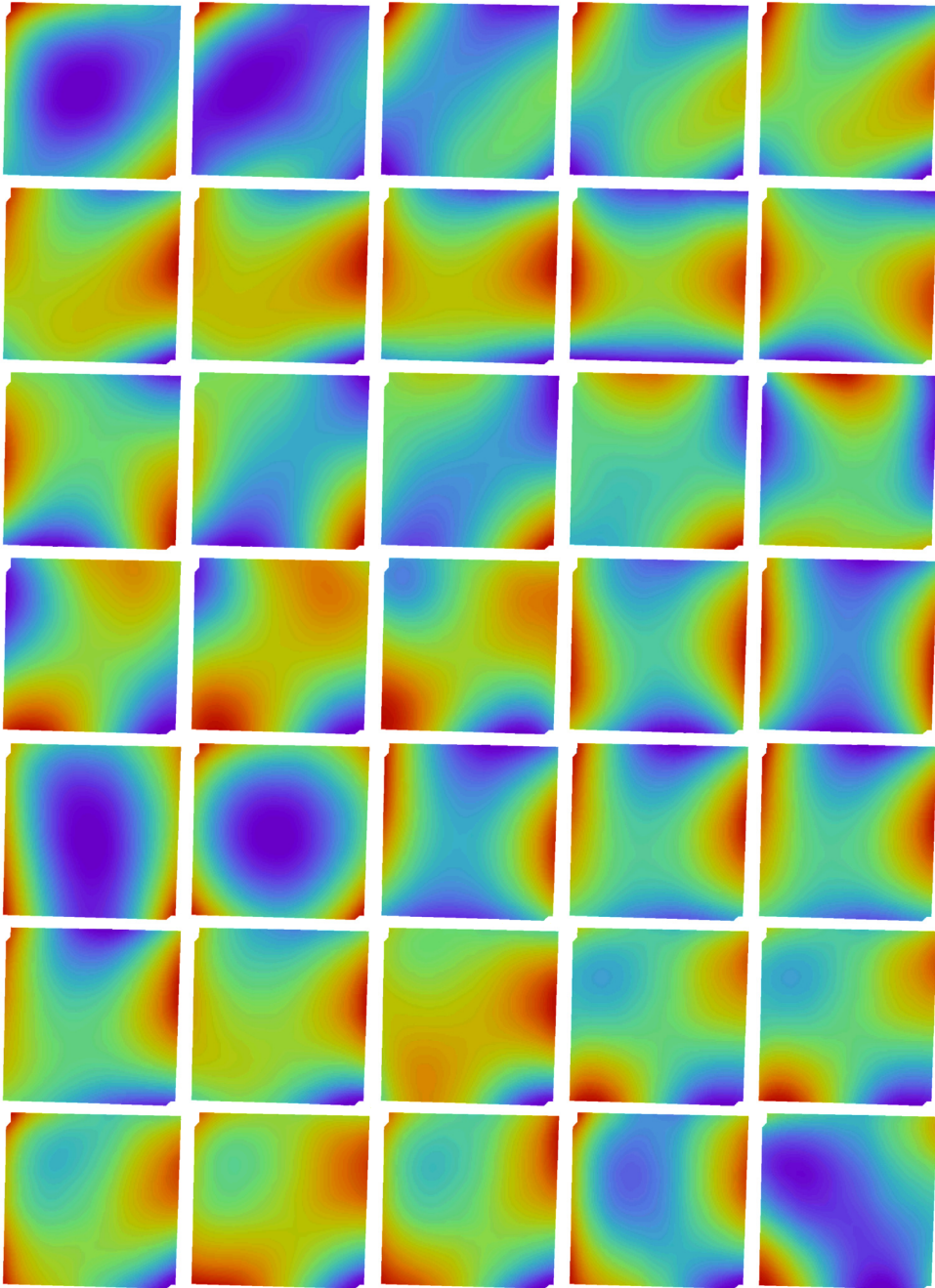


Figure 3. Displacement fields from input 1 at sequential frames in time domain, part I

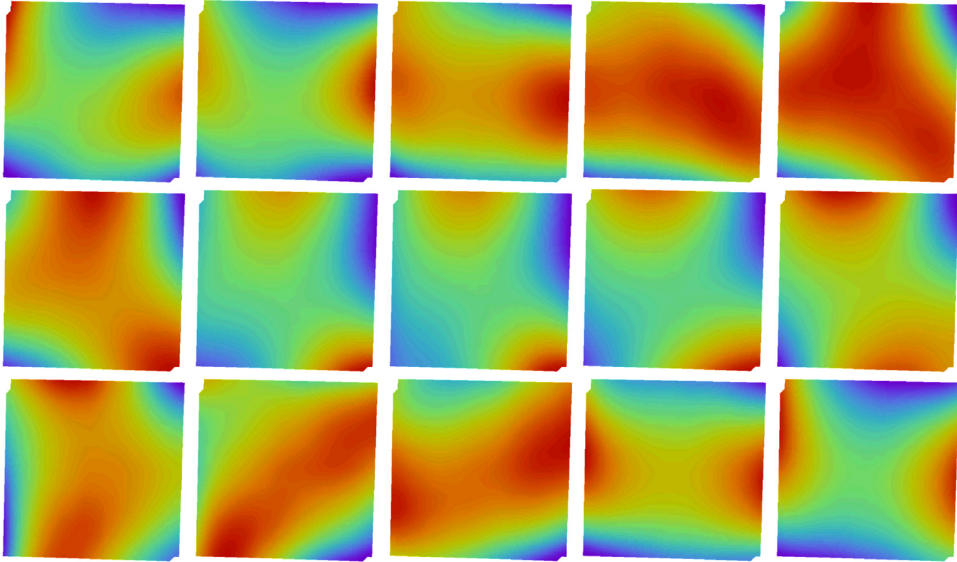


Figure 4. Displacement fields from input 1 at sequential frames in time domain, part II

front-end could have generated the right inputs to both shakers. Thus, to overcome this limitation and have a real multi-input-*many*-output dataset, separate tests were run for each shaker input.

The datasets were down sampled for the further processing in OMA and MU environments: from the original 120x120 grid, the files were generated from the custom software taking data every 5, 10, 13, and 20 points. Further, to reduce the size of the datasets, only out-of-plane data (Z-direction) were retained.

3. OMA IDENTIFICATIONS

From the Hi-Speed DIC measurements it was possible to extract the time series of the many dofs, with both set-ups from the two shakers, in order to better identify the presence of closely spaced or coupled modes [5–7]. Nevertheless, since output only measurements were taken into account, and not the impedances with their inherent knowledge of the excitation force, care should be taken, since the datasets might manifest the presence of the two attached shakers, in terms of added dynamic properties and local shape variations. As a minor refinement, attached cable influence and glue effect should be also considered. This should be reminded in a more advanced approach for model updating, as that of Fig.25. Attention must be paid on the selection of modes when the estimation releases complex-valued shapes, since they can be easily misunderstood as independent, especially with decreasing spatial resolution, while on a Modal Assurance Criterion (MAC) [5, 6] basis they result quite closely correlated, as in Fig.9, where the AutoMAC matrix is evaluated on two sets of identified modes, with 24 and 60 components each, showing correct and excessive (and not completely independent) mode identification.

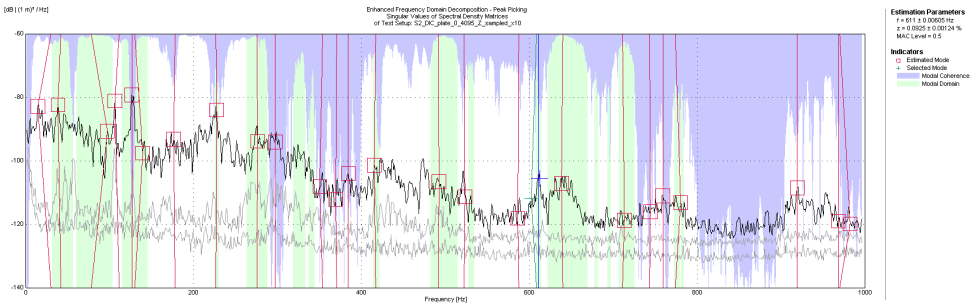


Figure 5. EFDD peak-picking from the first three SVD functions, merged datasets

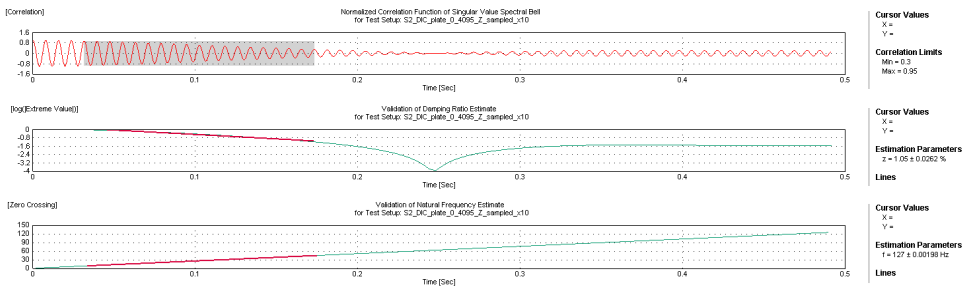


Figure 6. EFDD parameter estimation from the correlation functions

Different approaches

The OMA identification was run using the different approaches offered by the Structural Vibration Solutions ARTEMIS Extractor 5.3 software [10], delivering complex-valued spatially accurate shapes, with a clear advantage obtained from the higher spatial sampling that full field measurement can offer. The usage of multiple measurement sets helps in judging the pole scattering in frequency domain, in terms of standard deviation between the records. This is another parameter helpful also in the manual search of physical shapes. Furthermore, it is clear that some shapes are better identified from specific sets having different excitation conditions.

Enhanced Frequency Domain Decomposition. The singular value functions in Fig.5 clearly show [7], besides the sought high modal density and effectiveness of full field datasets, the presence of numerous peaks with double multiplicity, thus highlighting closely spaced eigenmodes. In fact, by means of the peaks on the second singular value function it was possible to identify, but with a worse quality, modes with a different shape than those on the first singular value function, not just coupled modes that might come from a structure with a high degree of symmetry. In Fig.6 is shown a typical case for a good estimation of the modal parameters, such as eigenfrequency and damping, with the assumption of a single acting mode [7]. Figure 7 displays the identified shapes by means of EFDD on both the

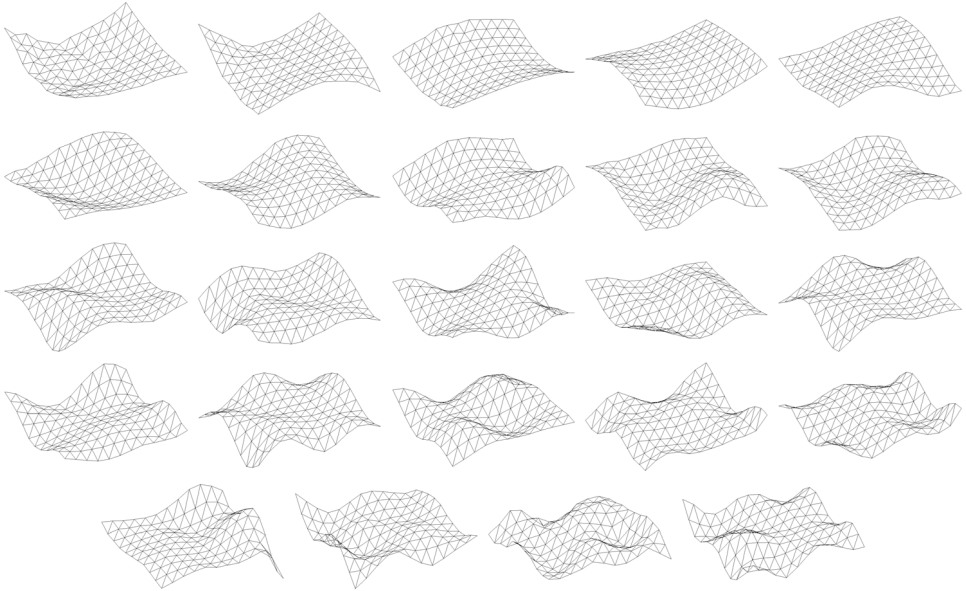


Figure 7. EFDD mode identification using both shaker responses, sampled x10

shaker datasets, which retain a very consistent spatial accuracy, even if down sampled every 10 points from the original unsmoothed measurements. In Fig.8 can be appreciated the high quality of the identification by means of very low correlation between the modes of the same set, with the frequency and damping details in Tab.1.

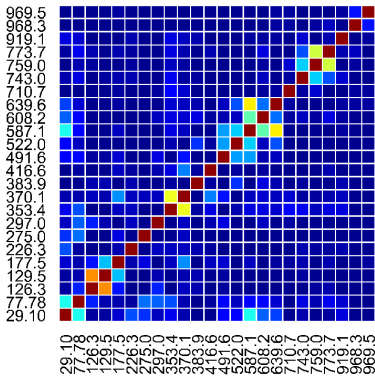


Figure 8. AutoMAC matrix from EFDD mode identification using both shaker responses, x10

Table 1. EFDD S1+S2, sampled x10

<i>freq.</i> [Hz]	<i>damp.</i> [%]	<i>freq.</i> [Hz]	<i>damp.</i> [%]
29.1	10.02	77.78	2.374
126.3	1.069	129.5	0.8001
177.5	2.938	226.3	0.4226
275.0	1.394	297.0	0.4928
353.4	0.4312	370.1	0.3191
383.9	0.285	416.6	0.1967
491.6	0.6268	522.0	0.3001
587.1	0.175	608.2	0.1091
639.6	0.1254	710.7	0.1535
743.0	0.1316	759.0	0.1314
773.7	0.1927	919.1	0.1059
968.3	0.0833	969.5	0.0769

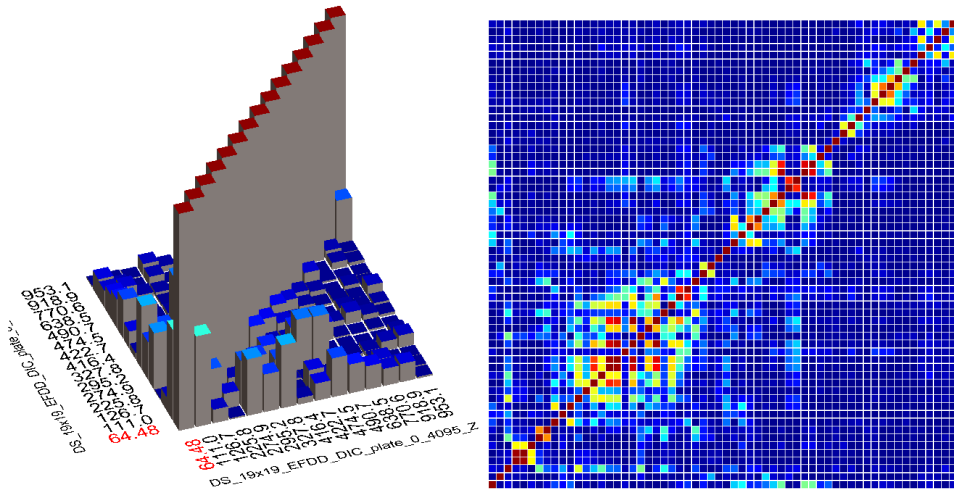


Figure 9. AutoMAC matrices showing low correlation (x10, 24 modes, left) and discrete correlation (x13, 60 modes, right) between OMA identified modes

On the other side, as in the MAC matrix on the right of Fig.9, when the selection of modes is excessive, mainly based on a visually driven peak-picking (when automated identification fails), the correlation between the identified modes can be quite relevant, delivering a modal base that has not completely orthogonal components, even if the measurement datasets were previously smoothed to avoid high frequency noise in the spatial domain. It must be pointed

Table 2. Excessive EFDD identification using S1+S2: 60 modes, x13

<i>freq.</i> [Hz]	<i>damp.</i> [%]	<i>freq.</i> [Hz]	<i>damp.</i> [%]	<i>freq.</i> [Hz]	<i>damp.</i> [%]	<i>freq.</i> [Hz]	<i>damp.</i> [%]
30.73	15.11	105.0	0.7569	126.3	0.5907	126.5	1.294
126.6	1.308	150.5	0.5905	155.6	0.593	177.6	3.287
225.8	0.5258	275.0	1.209	276.9	0.4045	296.0	?
297.2	0.4492	312.1	0.3595	313.9	0.2318	319.0	0.237
321.8	0.9947	322.5	0.2688	327.8	0.2597	331.0	0.2371
335.6	0.1639	335.8	0.393	347.2	0.1774	347.7	0.1526
352.5	0.1578	369.6	0.1741	381.1	0.2014	382.7	0.1413
383.7	0.2929	416.4	0.2109	438.0	0.8685	467.9	0.2062
474.2	0.3704	484.0	0.1269	490.8	0.1987	521.9	0.2539
525.5	0.1326	528.8	0.194	529.5	0.2574	536.2	0.1468
553.6	0.5782	587.3	0.08213	610.0	0.1359	638.2	0.7169
705.1	0.09335	758.9	0.1176	773.0	0.3718	798.5	0.08871
803.7	1.683	822.7	?	915.6	0.1236	929.5	0.1256
943.3	0.1385	953.3	0.2053	968.2	0.06881	980.3	0.06836
992.0	?	999.6	0.05118	1004.0	0.05228	1017.0	0.03872

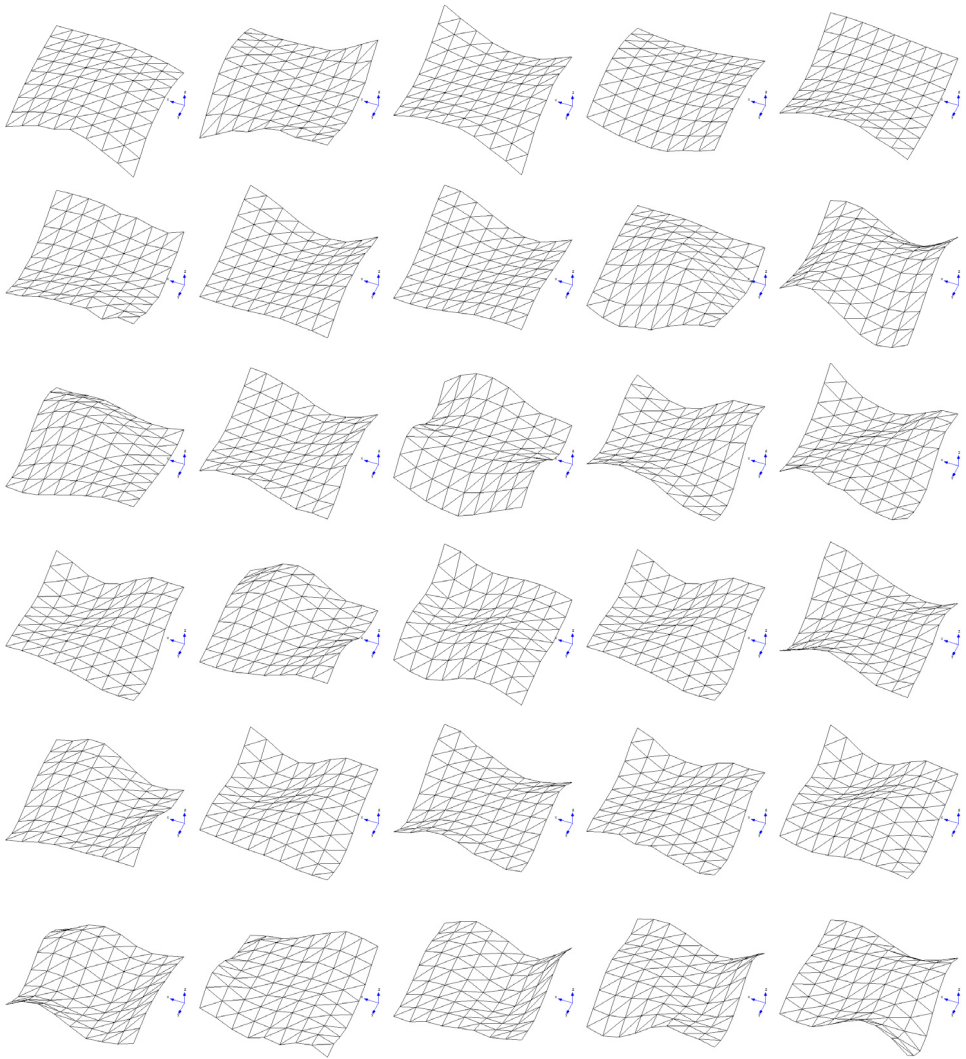


Figure 10. Excessive EFDD mode (1-30) identification using both shaker responses, x13

out that the complex-valued nature of the identified shapes can lead to misunderstandings on the visual discrimination between uncorrelated modes, due to local motion delays that can be interpreted as belonging to effectively separated shapes, especially if only a coarse spatial description is available. Also, it must be remarked that the modal damping factor can not be used as a key feature in rejecting non-physical modes, because, as in Tab.2, most of them have very low damping (3 null). In Figs.10-11 are shown 60 identified modes that are partially correlated. Although this is a sub-optimal identification, it showed to be a good driver for the following model updating stage, mainly for the redundancy of responses that gives.

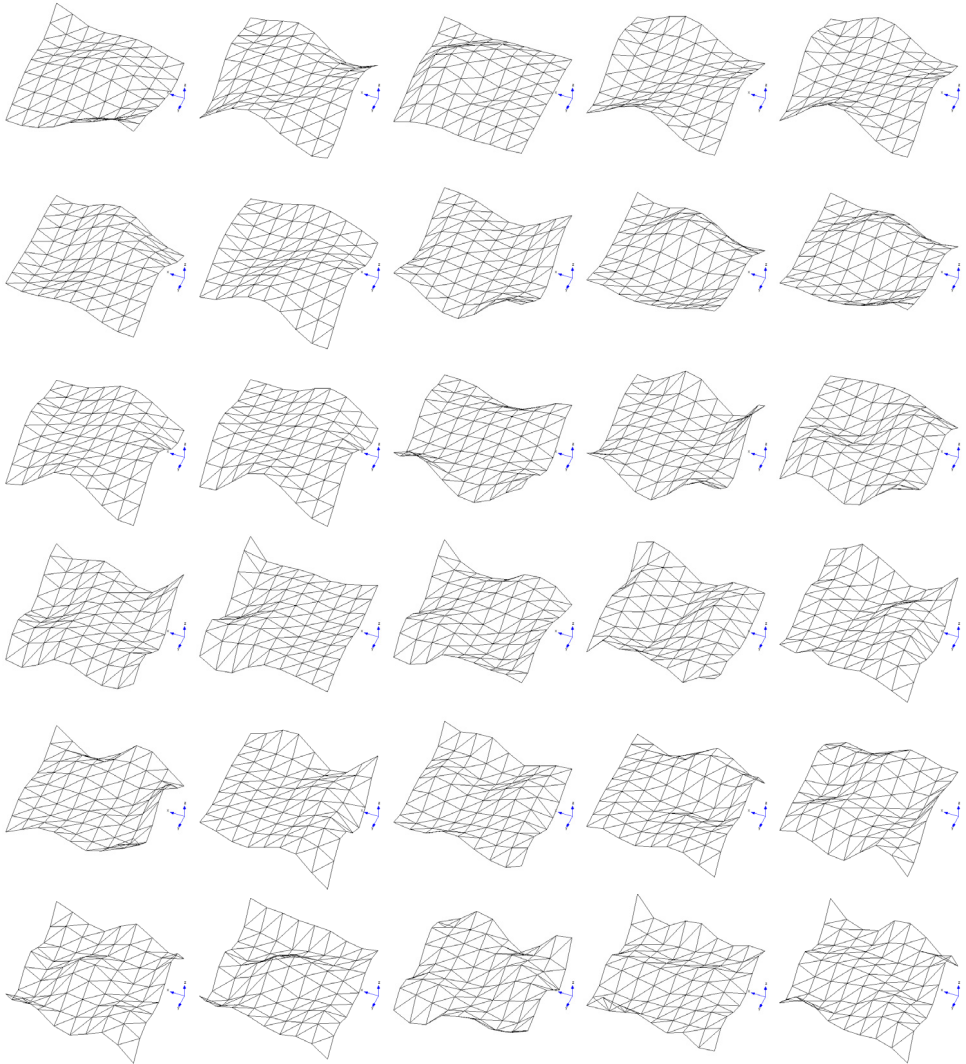


Figure 11. Excessive EFDD mode (31-60) identification using both shaker responses, x13

Curve fitting Frequency Domain Decomposition. CFDD and EFDD behaved in this test almost identically, as quantitatively assessed by MAC values of the identified modes that are very close to 1. Some minor differences might come from the standard deviation of frequencies and damping factors.

In Fig.12, with the finer spatial resolution available (down sampling every 5 points) in the datasets and also higher data redundancy for the identification, it can be outlined a different behaviour of the singular value functions, due to the location of the two shakers, even if in this test case it is not possible to speak about of many inputs, but just of multi (2) inputs.

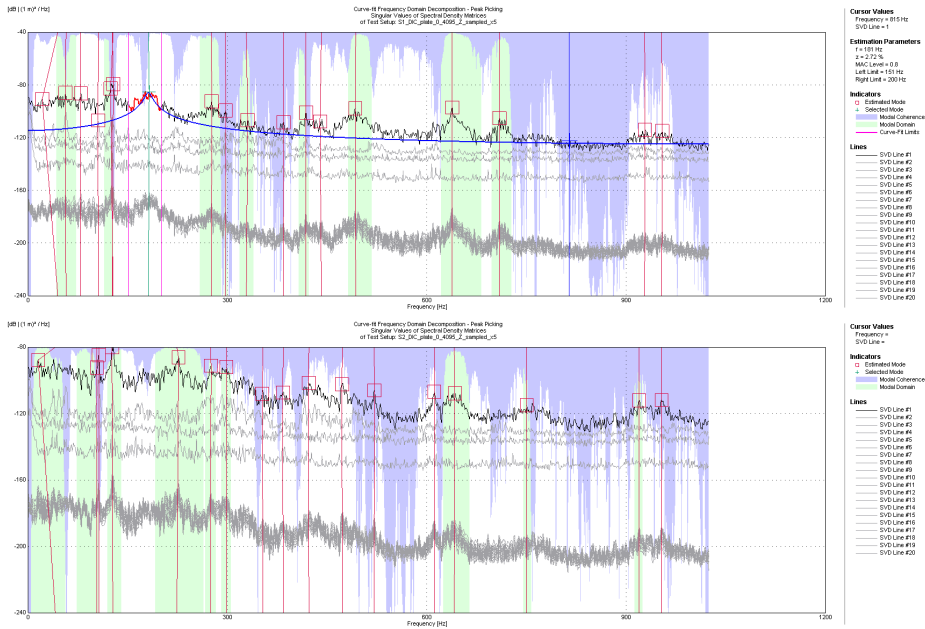


Figure 12. CFDD peak-picking from the SVD functions: shaker 1 and 2

There follows that the modes, which can be identified depending on the dataset that is on use, are slightly different, but with a remarkable spatial consistency retained also at the maximal resolution used in these EFDD-CFDD identifications: the frequencies, the modal damping factors and MAC values are reported in Tab.3, while the operational shapes are shown paired (black for shaker 1, red for shaker 2) in Figs.14-15; the MAC matrix is in Fig.13.

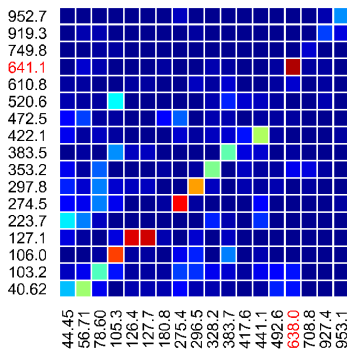


Figure 13. MAC matrix of the CFDD identified shapes with datasets from shaker 1 and 2, x5

Table 3. CFDD S1 vs S2, sampled x5

<i>freq.</i> [Hz]	<i>damp.</i> [%]	<i>freq.</i> [Hz]	<i>damp.</i> [%]	<i>MAC</i>
44.45	3.905	40.62	9.431	0.3144
78.60	5.147	103.2	1.249	0.4464
105.3	3.905	106.0	0.2514	0.8334
126.4	1.034	127.1	1.001	0.9317
127.7	1.404	127.1	1.001	0.9376
275.4	0.715	274.5	0.283	0.9003
296.5	0.2658	297.8	0.2067	0.7394
328.2	0.4598	353.2	0.3451	0.4944
383.7	0.0841	383.5	0.0834	0.4742
441.1	0.1715	422.1	0.5491	0.5491
638.0	0.2938	641.1	0.5639	0.9768
953.1	0.2197	952.7	0.0742	0.2663

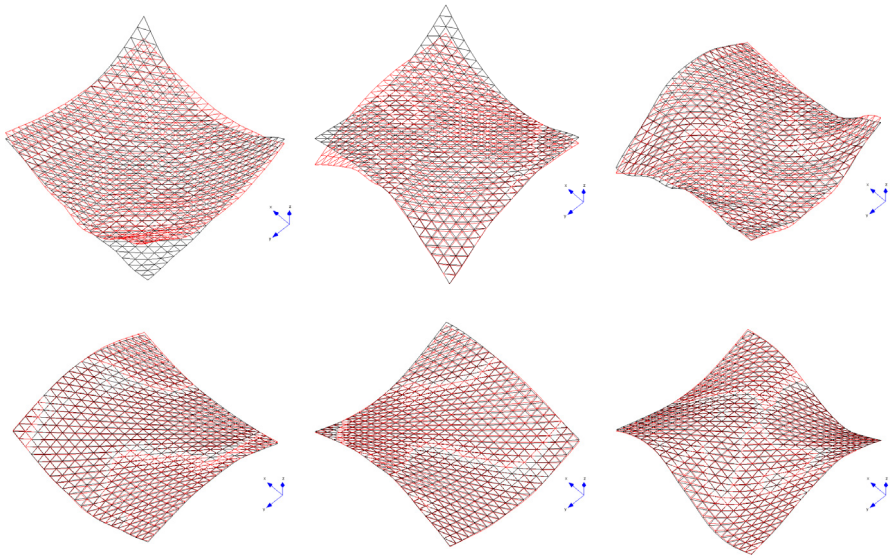


Figure 14. CFDD identified shapes (1-6) from the 2 datasets from shaker 1 & 2, x5

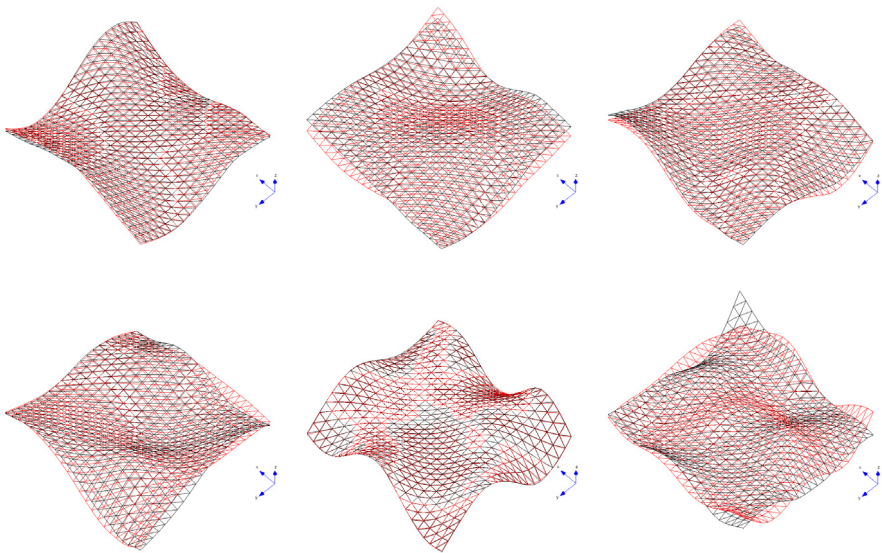


Figure 15. CFDD identified shapes (7-12) from the 2 datasets from shaker 1 & 2, x5

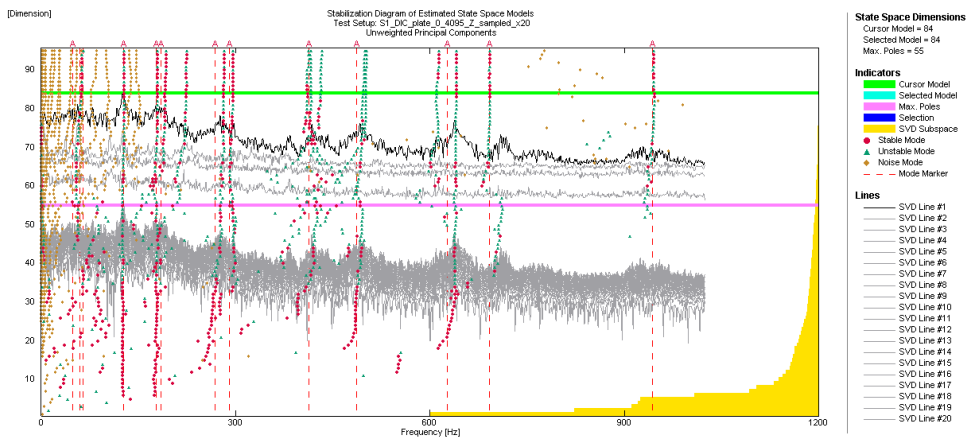


Figure 16. SSI - Unweighed Principal Components stabilization diagram, shaker 1

Stochastic Subspace Identification. Due to memory allocation limits of the commercial software, the order of the model was severely limited in using full field datasets. The SSI approach was thus not extensively tested to exploit the data redundancy of full field optical measurements. Only with the coarse grid of data points (down sampled every 20 points) it was possible to extract a decent, but limited in structural dynamics, model, otherwise the searchable poles were not sufficient to represent such a high modal density in the structural dynamics of the test case. Here are reported the obtained results, with merged datasets in the unweighed principal component identification: in Fig.16 is proposed a stabilisation diagram, obtained with extremely weak constraints of the pole stability criterion; in Fig.17 the shapes can show only coarse structural dynamics, while in Tab.4 the estimated modal damping factors are of one order greater than those obtained with the EFDD and CFDD approaches.

Dofs advantages & limits. It was suddenly clear that the number of available dofs influences the identification process. The smoothness of the correctly identified shapes, as a spatial consistency indicator, is preserved especially with a high spatial resolution, while it is severely damaged when a spurious or noise mode is selected. It must be remarked that operational modes identified by means of EFDD/CFDD peak-picking on the second singular value function showed lower smoothness along the geometry. There follows a clear indicator on the quality of the identification: the smoothness of the shape, or of the higher order derivatives, shall be preserved in order to represent a physical behaviour of the structure, being this valid until the spatial sampling respects the Shannon theorem for that shape.

While many more points/channels are available in the full field datasets, due to the cited memory allocation limits, the whole potential of the experimental source could not be used. This means that low frequency modes are always well depicted, while higher order shapes would surely have a clear benefit from a more accurate spatial description.

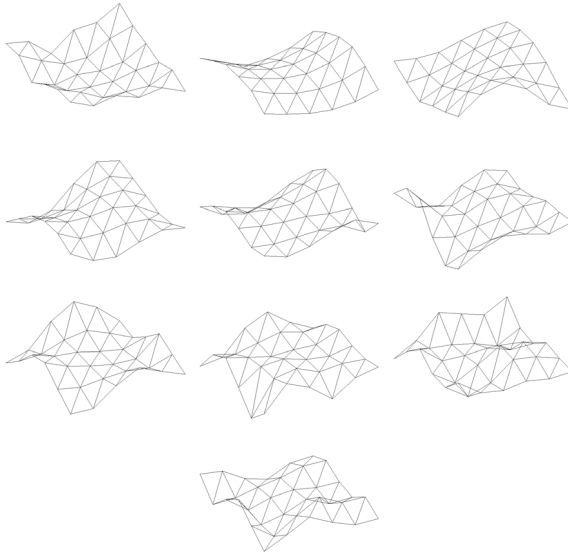


Figure 17. SSI-UPC modes identification using data from shaker 1, sampled x20

Table 4. SSI-UPC - S1 - x20

<i>freq.</i> [Hz]	<i>damp.</i> [%]
48.18	19.43
126.8	1.157
176.8	6.786
267.7	5.983
290.6	5.609
412.9	5.068
486.8	1.88
625.8	2.063
690.8	12.72
943.2	6.878

4. FE MODEL & UPDATING

The numerical model of the test case had to reproduce not only the thin aluminium plate, but also the restraining wires at the plate corners, as in Fig.18. It must be taken into account that the plate is not completely fixed, but is in a quasi-free-free conditions, since the wires were used as a high-pass filter with threshold at 20Hz (due to the limit of dynamic ESPI technology on very small displacements, which otherwise are masked by rigid body motion). The model was written by means of the script language of the FEMtools 3.6.1 software [11], which served also as solver and model updating driver.

Details of the numerical model

The aluminium plate itself, with dimensions as 250x236x1.5 mm, is modelled with thin shell isotropic elements and a grid of 60x58 nodes. The out-of-plane displacements are of interest in the comparison with tests in the updating procedure. Structural damping is added in the model.

Constraints. At each corner two different metallic rope assemblies were used to restrain the rigid body modes. There follows that 8 potentially different spring elements were added to the FE model, with higher stiffness for the 4 short wires. Also structural damping was modelled in these restraints. All the end points of the wires were then grounded by means of boundary conditions on their 3 dofs. The dynamic solution of the model searches for eigenmodes from 5 Hz up to 25% more than the upper frequency limit of the experimental data, thus 1250 Hz. In this way a mixture of rigid-body and elastic modes can be found at lower frequencies up to 90 Hz.

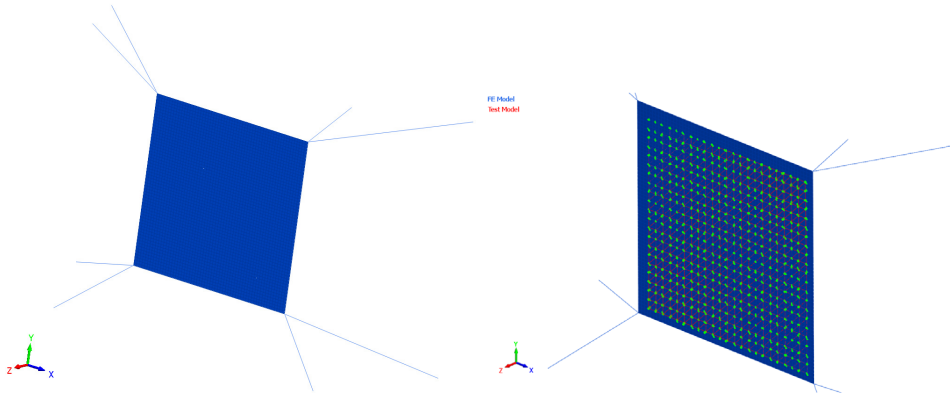


Figure 18. The FE model of the test set-up and the node-pair pairs with the measurements

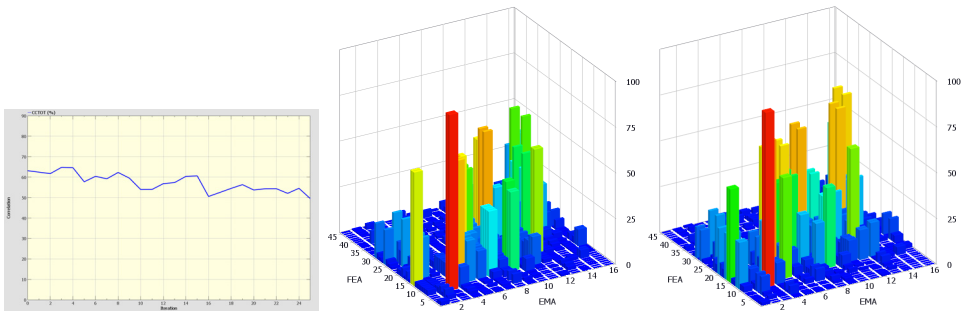


Figure 19. Error minimization function and MAC matrices (before & after) in FE model updating, using the dataset from shaker 2, high-spatial resolution sampling every 5 dofs, 16 modes from OMA

Complex-valued data. Since the OMA identified shapes were complex-valued, different combinations of eigensystem calculation were approached: real-valued Lanczos algorithm, but with rotational realization of the test datasets (to achieve the best shape assurance criterion), or complex-valued Lanczos algorithm with original test datasets; the latter gave the more consistent results in terms of final MAC value of the paired shapes. The eigenshapes were mass normalised.

Optimization strategy. The grid characteristics in the numerical model of the plate depended on the searched accuracy in the node-pair-table with the experimental dofs retained in the OMA identified shapes, having a minimal impact on the calculation time of this simple FE model. The attention was focused on the out-of-plane displacements only. The parameters of the updating were the Young modulus and structural damping coefficient of the plate, together with stiffness and structural damping properties of the 8 springs, for a total of 18 variables. Tests were also be run splitting the updating into two stages, with first stiffness parameters

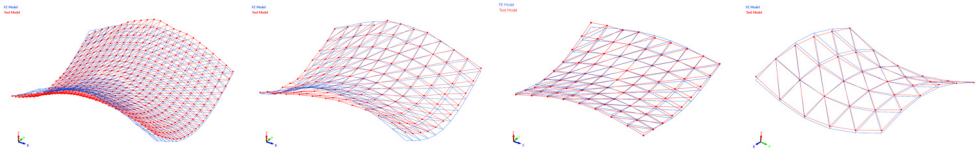


Figure 20. FE model updating as function of the resolution (x5, x10, x13, x20) of full field testing & OMA dataset at 127Hz: MAC value of 0.95, 0.87, 0.89, 0.95

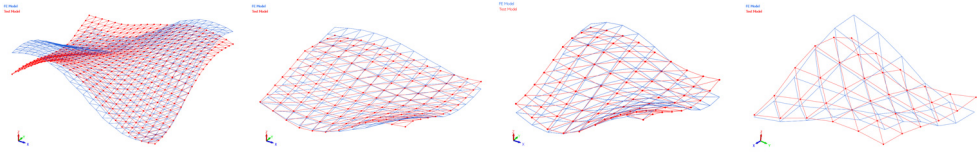


Figure 21. FE model updating as function of the resolution (x5, x10, x13, x20) of full field testing & OMA dataset at 175Hz: MAC value of 0.75, 0.79, 0.70, 0.46

then damping, but without appreciable advantage. Double modes could be considered (also due to the complex-valued solution) and only modes above 0.2 MAC value could be coupled. As optimisation function, eigenfrequency difference, eigenshape distance on most active dofs and MAC values were taken as responses: there resulted many responses, from 30 to hundreds, depending on the adopted thresholds. The sensitivity matrix calculation was thus computing intensive. The standard Bayesian sensitivity driven optimisation approach [11] was adopted, but also the pseudo-inverse solution was tested, due to the non-optimal convergence to the best compromise. Non linear optimisation was here not approached.

Updating results

It must be pointed out that for the model updating were used different OMA sets, in terms of spatial accuracy but also in terms of number of identified modes: for the high spatial accuracy case (x5) 16 EFDD operational modes were identified from the shaker 2 dataset, for the good accuracy case (x10) 24 modes from EFDD double shaker datasets, for discrete accuracy case (x13) 60 modes from EFDD double shaker datasets and for the low accuracy case (20x) 18 modes from SSI double shaker datasets. In Fig.19 a MAC matrix is displayed before and after updating, together with the error function after 25 iterations. In the captions of Figs.20-24 are shown the achieved MAC values of the coupled FEA-OMA modes after the last updating iteration, having different OMA identified shapes as targets. It is noticeable a 90 degrees rotation between different FEA/OMA datasets, may be due to complex-valued mode pairs coupling.

Furthermore, a more advanced FE model might also be introduced, with the shaker impedance head influences, as in Fig.25, but not tested in the updating routine. But it must be outlined that the advanced FE model highlights that asymmetry found in the displacement maps of the extensive full field measurement tests, showing nodal lines close to the location of the shaker inputs.

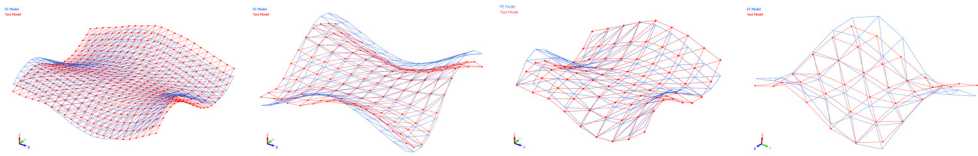


Figure 22. FE model updating as function of the resolution (x5, x10, x13, x20) of full field testing & OMA dataset at 297Hz: MAC value of 0.70, 0.70, 0.70, 0.57

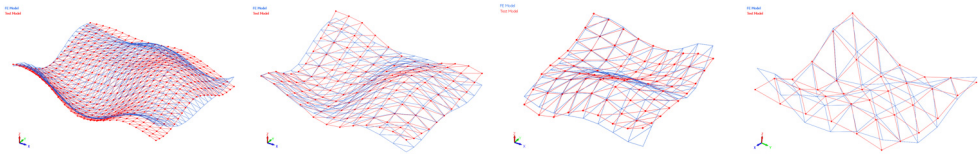


Figure 23. FE model updating as function of the resolution (x5, x10, x13, x20) of full field testing & OMA dataset at 511-529Hz: MAC value of 0.68, 0.62, 0.59, 0.52

Computational limits

The evaluations were run on a dual Intel Xeon Paxville DP (dual core 2.8GHz CPUs) 64bit workstation with 10GB of memory available: both software [10, 11], in the versions available for the OMA PhD Course², were not designed to take full advantage of the 64bit environment and of the multi-core computational platform, since most of the operations were sequential and not paralleled on all cores; the OMA identification [10] could not allocate more than 1GB of memory, limiting the size of the model in SSI technique when using many dofs; the updating procedure [11] could not run at the maximal speed using all cores, demanding high computational time on sensitivity evaluations, up to 2-3 hours for 25 iterations.

5. CONCLUSIONS

Full field datasets, even if here acquired for traditional EMA and only from 2 artificial inputs, proved to be with relevant content to run a successful operational modal identification, providing enhanced spatial description of the eigenshapes also at high frequency. The analyses carried out were consistent and promising, especially on the identification stage. For the updating task more attention should be paid on the management of the error minimization process, with eventually non-conventional approaches. Further coding work & testing is worth in searching to exploit all the potential inside the huge datasets coming from full field technologies, as will be part of the TEFFMA project of the author.

The combination of simpler testing equipment, fast & reliable estimation for OMA and the lowering of costs for high-speed cameras for DIC path the way for wider applications in industrial environment and in those case were the complexity of sources is not of easy replication on a test bench.

²PhD-course in operational modal analysis (OMA) and model updating, May 6-10, 2013 at the University of Minho, Guimares, Portugal, preceding the IOMAC2013 Conference, <http://www.iomac.dk/phd-summer-course/>

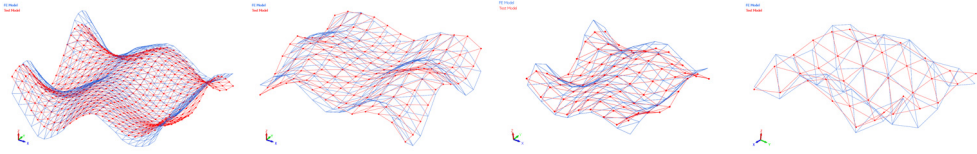


Figure 24. FE model updating as function of the resolution (x5, x10, x13, x20) of full field testing & OMA dataset at 758-775Hz: MAC value of 0.66, 0.48, 0.55, 0.39

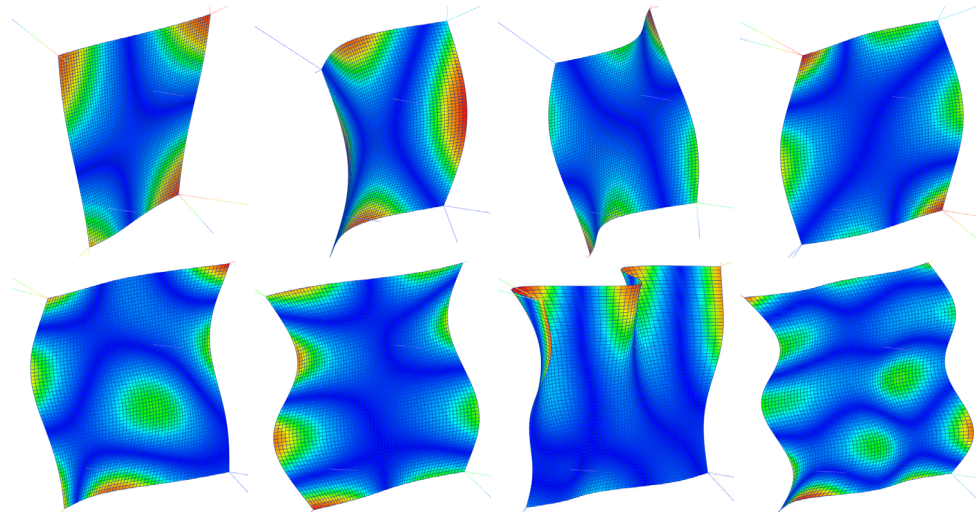


Figure 25. The advanced FE model of the test set-up with eigenshapes (at 104, 125, 219, 227, 403, 466, 747, 799 Hz) showing asymmetries and nodal lines close to shaker heads

Acknowledgements

The author wishes to thank Professors Rune Brincker, Carlos Ventura and Lingmi Zhang for the opportunity given to enter into contact with OMA&MU technologies during the course "PhD-course in Operational Modal Analysis (OMA) and Model Updating - Summer Course", held in Guimaraes, Portugal, in May 6-10, 2013.

Structural Vibration Solutions (ARTeMIS) [10] and FEMtools [11] software companies are acknowledged for having us given the trial version of their products to be tested in our real cases, also with the hope of future partnerships in structural dynamics projects.

This activity is part of the Project TEFFMA - Towards Experimental Full Field Modal Analysis, funded by the European Commission at the Technische Universitaet Wien, through the Marie Curie FP7-PEOPLE-IEF-2011 PIEF-GA-2011-298543 grant, for which the Research Executive Agency and TU-Wien are kindly acknowledged.

Appendix A SOME BASIC EQUATIONS ON OPERATIONAL MODAL ANALYSIS

Below are briefly recalled the main equations [7] that support the identification of operational modal analysis models, being in part close to, but also different from, traditional EMA & frequency response function based approaches.

A1 Time domain

Correlation Function matrix of the outputs vector $\mathbf{y}(t)$

$$\mathbf{R}_y(\tau) = E [\mathbf{y}(t)\mathbf{y}^T(t + \tau)] \quad (1)$$

Correlation Function of white noise input vector $\mathbf{x}(t)$

$$\mathbf{R}_x(\tau) = E [\mathbf{x}(t)\mathbf{x}^T(t + \tau)] = 2\pi \frac{\delta(\tau)}{2\Delta f} \mathbf{C} \quad (2)$$

with $\mathbf{C} = E [\mathbf{x}(t)\mathbf{x}^T(t)]$ as covariance matrix of the input.

Spectral Density of the white noise inside the Δf frequency band:

$$\mathbf{G}_x(\omega) = \frac{1}{2\Delta f} \mathbf{C} \quad (3)$$

Modal decomposition of the Correlation Function matrix, with N modeshapes

$$\mathbf{R}_{y+}(\tau) = 2\pi \sum_{n=1}^N \left(\mathbf{B}_n \mathbf{G}_x \mathbf{A}_n e^{\lambda_n \tau} + \mathbf{B}_n^* \mathbf{G}_x \mathbf{A}_n^* e^{\lambda_n^* \tau} \right) \quad (4)$$

$$\mathbf{R}_{y-}(\tau) = 2\pi \sum_{n=1}^N \left(\mathbf{A}_n \mathbf{G}_x \mathbf{B}_n e^{-\lambda_n \tau} + \mathbf{A}_n^* \mathbf{G}_x \mathbf{B}_n^* e^{-\lambda_n^* \tau} \right) \quad (5)$$

with:

$$\mathbf{A}_n = \frac{\Phi_n \Phi_n^T}{a_n} \quad \text{residual matrices}$$

Φ_n modeshape n

$$\mathbf{B}_n = \sum_{s=1}^M \left(\frac{\mathbf{A}_s}{-\lambda_n - \lambda_s} + \frac{\mathbf{A}_s^*}{-\lambda_n - \lambda_s^*} \right) \quad \text{weighted sum of residual matrices}$$

Modal decomposition of the Correlation Function matrix

$$\mathbf{B}_n \mathbf{G}_x \mathbf{A}_n = \mathbf{B}_n \mathbf{G}_x \frac{\Phi_n \Phi_n^T}{a_n} = \gamma_n \Phi_n^T, \quad \mathbf{A}_n \mathbf{G}_x \mathbf{B}_n = \Phi_n \gamma_n^T \quad (6)$$

with the Modal Participation vector $\gamma_n = \mathbf{B}_n \mathbf{G}_x \frac{\Phi_n}{a_n}$

$$\mathbf{R}_{y+}(\tau) = 2\pi \sum_{n=1}^N \left(\gamma_n \Phi_n^T e^{\lambda_n \tau} + \gamma_n^* \Phi_n^H e^{\lambda_n^* \tau} \right) \quad (7)$$

$$\mathbf{R}_{y-}(\tau) = 2\pi \sum_{n=1}^N \left(\Phi_n \gamma_n^T e^{-\lambda_n \tau} + \Phi_n^* \gamma_n^H e^{-\lambda_n^* \tau} \right) \quad (8)$$

A2 Frequency domain

Spectral Density matrix

$$\mathbf{G}_y(\omega) = \frac{1}{2\pi} \int_{-\infty}^{\infty} \mathbf{R}_y(\tau) e^{-i\omega\tau} d\tau \quad (9)$$

Modal decomposition of the Spectral Density matrix

$$\mathbf{G}_y(\omega) = \sum_{n=1}^N \left(\frac{\mathbf{B}_n \mathbf{G}_x \mathbf{A}_n}{-i\omega - \lambda_n} + \frac{\mathbf{B}_n^* \mathbf{G}_x \mathbf{A}_n^*}{-i\omega - \lambda_n^*} + \frac{\mathbf{A}_n \mathbf{G}_x \mathbf{B}_n}{i\omega - \lambda_n} + \frac{\mathbf{A}_n^* \mathbf{G}_x \mathbf{B}_n^*}{i\omega - \lambda_n^*} \right) \quad (10)$$

or

$$\mathbf{G}_y(\omega) = \sum_{n=1}^N \left(\frac{\Phi_n \gamma_n^T}{-i\omega - \lambda_n} + \frac{\Phi_n^* \gamma_n^H}{-i\omega - \lambda_n^*} + \frac{\gamma_n \Phi_n^T}{i\omega - \lambda_n} + \frac{\gamma_n^* \Phi_n^H}{i\omega - \lambda_n^*} \right) \quad (11)$$

REFERENCES

- [1] Zanarini, A., 2005. "Damage location assessment in a composite panel by means of electronic speckle pattern interferometry measurements". In Proceedings of the IDETC/CIE ASME International Design Engineering Technical Conferences & Computers and Information in Engineering Conference, Long Beach, California, USA, September 24-28, ASME, pp. 1–8. Paper DETC2005-84631.
- [2] Zanarini, A., 2008. "Fatigue life assessment by means of full field espi vibration measurements". In Proceedings of the ISMA2008 Conference, September 15-17, Leuven (Belgium), P. Sas, ed., KUL, pp. 1–15. Paper 326.
- [3] Zanarini, A., 2008. "Full field espi vibration measurements to predict fatigue behaviour". In Proceedings of the IMECE2008 ASME International Mechanical Engineering Congress and Exposition, October 31- November 6, Boston (MA) USA, ASME, pp. 1–10. Paper imece2008-68727.
- [4] Zanarini, A., 2008. "Esp measurements in structural dynamics: fatigue life assessment". In Proceedings of the Dantec Dynamics 15th International Conference and User Meeting, Dantec dynamics GmbH, pp. 1–20.
- [5] Heylen, W., Lammens, S., and Sas, P., 1998. *Modal Analysis Theory and Testing*. Katholieke Universiteit Leuven, Leuven (Belgium). ISBN 90-73802-61-X.
- [6] Ewins, D. J., 2000. *Modal Testing - theory, practice and application*, 2nd ed. Research Studies Press Ltd., Baldock, Hertfordshire, England. ISBN 978-0-86380-218-8.
- [7] R. Brincker, C. E. Ventura, L. Z., 2013. Notes of the phd-course in operational modal analysis (oma) and model updating. Guimaraes, Portugal, May 6-10.
- [8] Zanarini, A., 2007. "Full field espi measurements on a plate: challenging experimental modal analysis". In Proceedings of the XXV IMAC, Orlando (FL) USA, Feb 19-22., SEM. Paper s34p04.
- [9] Á. F. Doval, 2000. "A systematic approach to tv holography". *Measurement Science and Technology*, **11**(1), pp. R1–R36. IOP Pub Ltd.
- [10] Structural Vibration Solutions, 2013. Artemis extractor 5.3 software. <http://www.svibs.com>.
- [11] Dynamic Design Solutions, 2013. Femtools 3.6.1 software. <http://www.femtools.com>.

INDICE DEGLI AUTORI

Andrisano Angelo Oreste	47, 95
Ansaloni Matteo	95
Ascari Alessandro	1
Baldini Andrea	157, 191, 213
Bergamasco Massimo	255
Carminelli Antonio	29
Carraro Enrico	171
Carricato Marco	1, 57
Castagnetti Davide	245, 265
Catania Giuseppe	29
Cocconcelli Marco	303
Conconi Michele	83
Curcurù Giuseppe	303
Dalpiaz Giorgio	171, 293
Dragoni Eugenio	137, 229, 265
Fontana Marco	255
Forlani Margherita	83
Fortunato Alessandro	1, 57
Freddi Alessandro	115
Giacopini Matteo	157, 191, 213
Golinelli Nicola	229
Lazzarini Alberto	157
Leali Francesco	95
Liverani Erica	1
Manevitch Leonid I.	47
Mantovani Sara	191
Meoni Francesco	57
Minto Simone	107
Mucchi Emiliano	171, 293
Mulas Giuseppe Antonio	191
Nardini Fabrizio	183
Oscari Fabio	69
Pacchierotti Claudio	69
Parenti Castelli Vincenzo	83, 183
Pellicano Francesco	47
Pini Fabio	95
Prati Edzeario	201
Prattichizzo Domenico	69
Rosati Giulio	69, 107
Rossi Aldo	69, 107
Rubini Riccardo	303

Salsi Emilio	15
Sancisi Nicola	83, 183
Scirè Mammano Giovanni	265
Sissa Simone	213
Spaggiari Andrea	229
Squatrino Rosario	15
Strozzi Antonio	157, 191, 213
Strozzi Matteo	47
Tasora Alessandro	201
Todaro Ivan	15
Tomesani Luca	15
Valgimigli Alessandro	157
Vertechy Rocco	255
Zanarini Alessandro	313

In questo volume sono raccolte le memorie presentate in occasione della “Settima Giornata di Studio Ettore Funaioli”, che si è svolta il 19 luglio 2013 presso la Scuola di Ingegneria e Architettura dell’Alma Mater Studiorum – Università di Bologna. La Giornata è stata organizzata dagli ex allievi del Prof. Funaioli con la collaborazione del DIN – Dipartimento di Ingegneria Industriale e della Scuola di Ingegneria e Architettura dell’Alma Mater Studiorum – Università di Bologna, e con il patrocinio dell’Accademia delle Scienze dell’Istituto di Bologna e del GMA – Gruppo di Meccanica Applicata.

Questo volume è stato stampato con il contributo di G.D S.p.A.

AlmaDL è la Biblioteca Digitale dell’Alma Mater Studiorum Università di Bologna. AlmaDL ospita al suo interno gli archivi Open Access che rendono pubblicamente disponibili i contributi derivanti dalle attività di ricerca, didattiche e culturali dell’Ateneo bolognese. AlmaDL attua così i principi del movimento internazionale a sostegno dell’accesso aperto alla letteratura scientifica, sottoscritti dall’Università di Bologna assieme a molte altre istituzioni accademiche, di ricerca e di cultura, italiane e straniere.

<http://almadl.unibo.it>

